



HAL
open science

Self-assembly of platinum(II) complexes with tunable photophysical properties in confined spaces and in solution

Rémi Rouquette

► **To cite this version:**

Rémi Rouquette. Self-assembly of platinum(II) complexes with tunable photophysical properties in confined spaces and in solution. Other. Université de Strasbourg, 2017. English. NNT : 2017STRAF075 . tel-02003466

HAL Id: tel-02003466

<https://theses.hal.science/tel-02003466>

Submitted on 1 Feb 2019

HAL is a multi-disciplinary open access archive for the deposit and dissemination of scientific research documents, whether they are published or not. The documents may come from teaching and research institutions in France or abroad, or from public or private research centers.

L'archive ouverte pluridisciplinaire **HAL**, est destinée au dépôt et à la diffusion de documents scientifiques de niveau recherche, publiés ou non, émanant des établissements d'enseignement et de recherche français ou étrangers, des laboratoires publics ou privés.

ÉCOLE DOCTORALE DE SCIENCES CHIMIQUES
Institut de science et d'ingénierie supramoléculaires

THÈSE présentée par :

Rémi ROUQUETTE

soutenue le : **15 décembre 2017**

pour obtenir le grade de : **Docteur de l'université de Strasbourg**

Discipline/ Spécialité : Chimie

**Self-assembly of platinum(II) complexes with tunable
photophysical properties in confined spaces and in
solution**

THÈSE dirigée par :

Mme DE COLA Luisa

Professeur, université de Strasbourg

RAPPORTEURS :

Mme PIKRAMENOU Zoé

Professeur, university of Birmingham

M. GROS Philippe

Directeur de recherche, université de Lorraine

AUTRES MEMBRES DU JURY :

Mme POWELL Annie

Professeur, Karlsruhe Institute of Technology

M. KLYMCHENKO Andrey

Directeur de recherche, université de Strasbourg

To my Family, my friends and my soulmate

“There are no secrets to success. It is the result of preparation, hard work, and learning from failure”

-Colin Powell

Table of Contents

Summary.....	i
1. Introduction.....	1
1.1. Interaction between light and matter.....	2
1.2. Transition metal complexes.....	11
1.3. Classes of platinum(II) complexes.....	18
1.4. Supramolecular chemistry.....	20
1.5. Self-assembly of platinum(II) complexes.....	21
1.6. Introduction to copolymer and their self-assembly.....	29
1.7. Encapsulation of platinum complexes.....	34
1.8. Metallo-supramolecular block copolymer self-assembly.....	39
1.9. Surface functionalization.....	41
1.10. Platinum(II) complexes on silicon substrates.....	45
1.11. Scope of the thesis.....	46
1.12. References.....	47
2. Functionalization of silicon and gold substrates with platinum(II) complexes.....	55
2.1. Introduction.....	56
2.2. Result and discussions.....	58
2.2.1. Synthesis.....	58
2.2.2. Surface modification of silicon (100) via photochemical hydrosilylation.....	62
2.2.3. Surface modification of silicon (100) via click chemistry.....	70
2.2.4. Functionalisation of gold substrates.....	79
2.2.5. Growth of platinum (II) complexes nanowires by physical vapor deposition....	91
2.3. Conclusion.....	96
2.4. Experimental Part.....	97
2.5. References.....	112
3. Encapsulation of platinum(II) complexes by PMMA-PMAA diblock copolymer.....	117
3.1. Introduction.....	118
3.2. Results and discussions.....	121

3.2.1. Synthesis of the platinum(II) complex.....	121
3.2.2. Preparation of polymer particles.....	121
3.2.3. Encapsulation of platinum(II) complexes in PMMA-PMAA particles.....	126
3.2.4. Influence of the concentration of platinum(II) complex.....	138
3.2.5. Effect of the organic solvent: acetone vs THF.....	153
3.2.6. Order of PMMA-PMMA and platinum(II) mixing.....	158
3.2.7. Effect of the method of removal of the organic solvent.....	162
3.2.8. Effect of the method of addition of water on the encapsulation of the platinum(II) complex.....	166
3.2.9. Influence of the platinum(II) complex on the encapsulation.....	171
3.3. Conclusion.....	175
3.4. Experimental Section.....	175
3.5. References.....	181
4. Morphogenic effect of solvent mixture on aggregates of an amphiphilic platinum(II) complex.....	183
4.1. Introduction.....	184
4.2. Results and discussion.....	185
4.2.1. Synthesis of the complex.....	186
4.2.2. Preparation of the platinum aggregates in THF/water mixture.....	186
4.2.3. Effect of the concentration on the self-assembly properties of the platinum (II) complex.....	198
4.2.4. Effect of the rate of addition.....	200
4.2.5. Study of the morphology of the fibers at 80% water content via gradual- addition and flash-injection methods.....	206
4.2.6. Effect on the addition order of THF and water.....	208
4.2.7. Role of the solvent on the aggregation of the platinum (II) complex.....	213

4.2.8. Energy dispersive spectra (EDS) of platinum (II) complex aggregates.....	221
4.3. Conclusion.....	225
4.4. Experimental Section.....	226
4.5. References.....	228
5. Supramolecular co-assembly of two luminescent platinum (II) complexes.....	231
5.1. Introduction.....	232
5.2. Results and discussions.....	232
5.2.1. Platinum (II) complexes.....	234
5.2.2. Co-assembly at 70% water content in dioxane/water mixture.....	236
5.2.3. Co-assembly at 80% water content in dioxane/water mixture.....	248
5.2.4. Co-assembly at 60% water content in dioxane/water mixture.....	255
5.2.5. X-ray diffraction pattern.....	263
5.2.6. Selected Area Electron Diffraction (SAED).....	267
5.2.7. Reversibility.....	268
5.2.8. Aging	272
5.3. Conclusion.....	273
5.4. Experimental part.....	274
5.5. References	278
6. Instrumental part.....	281
Acknowledgements.....	295
Curriculum Vitae.....	299

Summary

The thesis titled “Self-assembly of platinum(II) complexes with tunable photophysical properties in confined spaces and in solution” tackles the preparation and the characterization of luminescent platinum(II) complexes and their photo-physical properties. Transition metal complexes have been used in many applications such as bio-imaging or optoelectronics devices due to the triplet and singlet excitons, which can lead to a 100% internal efficiency. In particular, platinum(II) complexes with their square planar geometry are able to self-assemble into various structures nanostructures with specific properties^{1,2}. Such rearrangement is possible due to the metallophilic interaction between the filled d_z^2 orbitals of neighboring platinum atoms supported by the π - π stacking of the coordinating ligands, or other supramolecular interactions, such as hydrogen bonding or electrostatic interactions.

This thesis manuscript opens with an introduction on the basic concepts of photophysics and more specifically, on the photophysical properties of d^8 platinum(II) complexes. An overview on the various types of platinum aggregates present in the literature is also reported³⁻⁶. A brief introduction to polymer particles⁷ and surface modification⁸ is also reported.

The first experimental chapter describes the different strategies explored for the covalent attachment of platinum(II) complexes on silicon. The first approach involved an UV- induced covalent grafting of 4-vinylpyridine molecules on hydrogen-terminated silicon wafers, as described in Figure 1⁹. The freshly formed pyridine-terminated substrates are coordinated to the platinum precursor $\text{PtCl}_2(\text{DMSO})_2$ and the tridentate ligand to form the platinum(II) complex¹⁰. The successive surface modifications were monitored by XPS analysis. The hydrogen-terminated substrates only showed the presence of adventitious carbon and oxygen. The grafting of 4-vinylpyridine molecules on Si-H substrates is demonstrated by the presence of the N 1s peak at 400 eV. Finally, the successful coordination of the platinum(II) complex to the substrate is evidenced by the presence of an additional Pt 4f and F 1s peaks, around 73 eV and 698 eV respectively. However, the density of the complexes on the silicon (100) substrate is relatively low and this limits further characterization. Direct coordination of the pre-synthesised platinum(II) complexes on the hydrogen-terminated substrate do not improve the surface coverage.

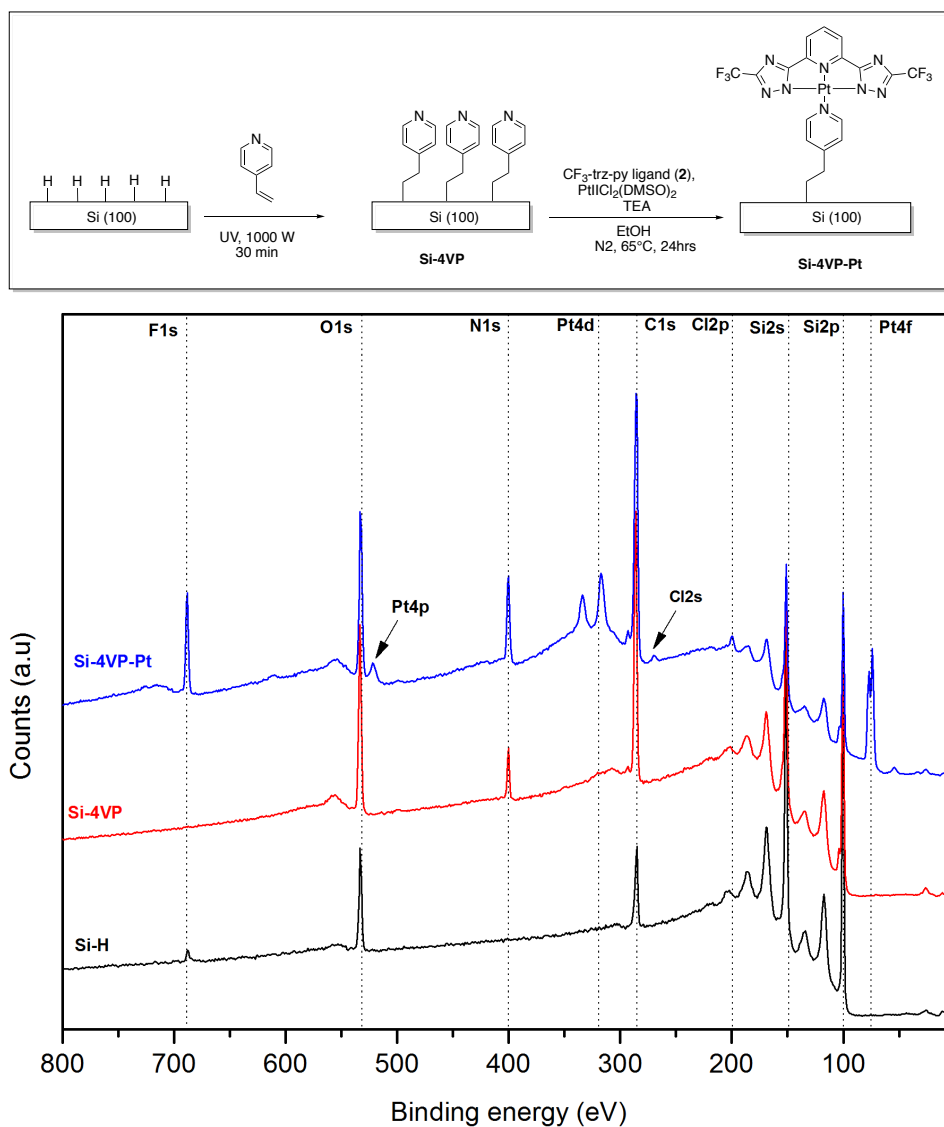


Figure 1. Schematic representation of the covalent linkage of luminescent platinum(II) complexes on silicon substrates via UV-induced photoreaction and corresponding XPS survey scans of the successive surface modifications.

The second approach began with the preparation of acetylenated substrates with alkyne molecules attached to the silicon substrates as depicted on Figure 2. A ligand with a polyethyleneglycol chain and an azide functional group at one end, and a pyridine moiety on the other side, was grafted to the acetylenated substrates by copper (I)-catalyzed alkyne-azide cycloaddition (CuAAC) click chemistry¹¹. The platinum(II) complex is formed the same method as previously reported. The successive surface modifications are monitored by XPS spectra. The covalent linkage of the ancillary ligand by “click-chemistry” is evidenced by the presence of the N 1s peak at 400 eV. Coordination of the platinum(II) complex on the surface is

demonstrated by the presence of additional Pt 4f and F 1s peaks at 73 eV and 698 eV respectively. However, even though the platinum(II) complex is strongly grafted to the silicon substrates, the surface coverage is also very low. The pre-synthesized platinum(II) complex is also directly attached to the alkyne-terminated substrate by click-chemistry and the surface coverage

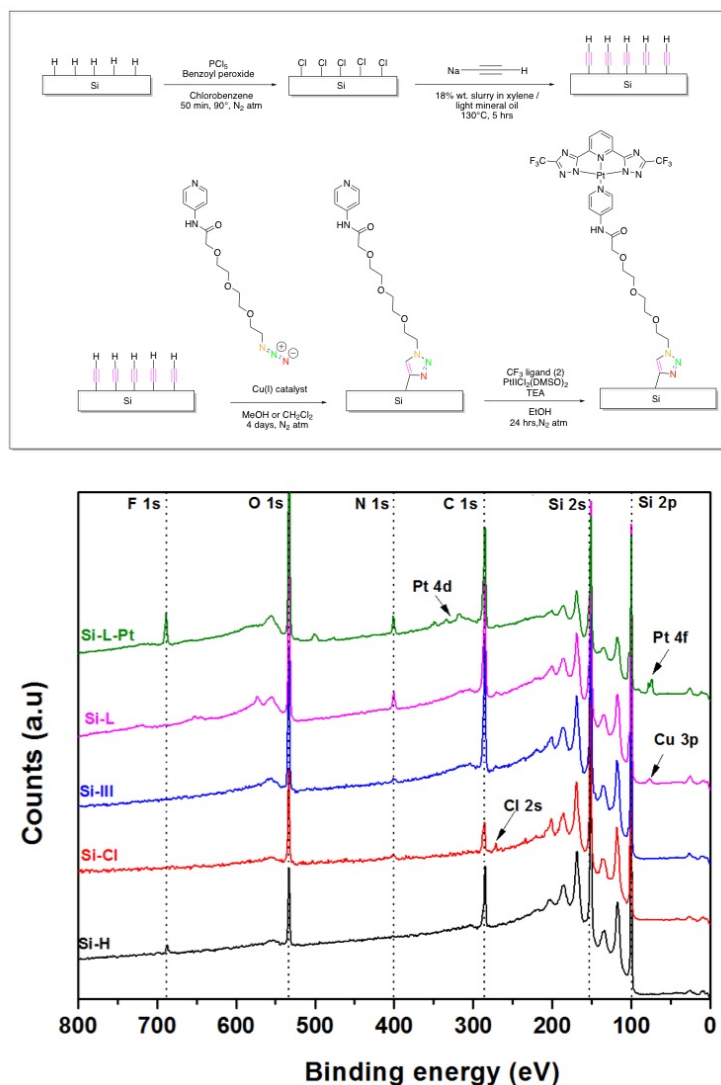


Figure 2. Schematic representation of the covalent linkage of luminescent platinum(II) complexes on silicon substrates via copper catalyzed alkyne-azide cycloaddition “click-chemistry” and corresponding XPS survey scans of the successive surface modifications.

slightly increases. However, the surface coverage is still very low and do not allowed further photophysical characterisation. In conclusion, obtaining functionalized silicon substrates with a high density of covalently linked platinum(II) complexes was unsuccessful. The attachment of platinum(II) complexes was achieved on gold substrates via the sulfur-gold bond^{12,13}. For

this purpose, complexes of different length with a disulfide-ending group were prepared. The freshly cleaned gold surfaces were immersed in a DMF solution containing the different platinum(II) complexes for 6 days before analysis. The successful attachment of the complexes on the gold substrates was demonstrated by the high resolution XPS analysis of the S 2p signal. This peak shifted from 163.0 eV (disulfide bond) to 161.5 eV (Au-S bond) when the complex was bonded to the gold substrate by sulfur-gold bond (Figure 3). The nature of the Au-S bond is still debated in the scientific community; however, the bond is known to be very strong¹³. The stability of the gold-sulfur bond was assessed by XPS after leaving the functionalized substrates at room temperature for a couple of months. The formation of sulfure oxide species (SO_x) was demonstrated by the presence of S 2p peaks at 169 eV. The density of complexes on the gold substrate was extremely low and limited further characterization, similar to the silicon substrate.

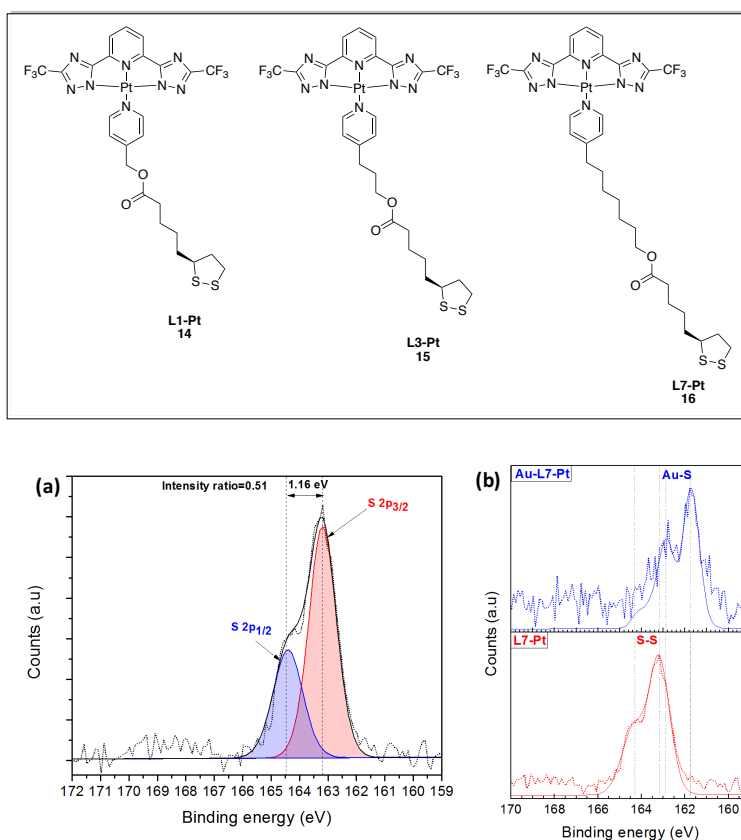


Figure 3. Chemical structures of the three platinum(II) complexes. High resolution spectra of the S 2p peak (a) and high resolution spectra of the S 2p signal of complex **L7-Pt** (red line, disulfide) and attached to the gold substrate **Au-L7-Pt** (blue line, gold-sulfur).

However, it is possible to use the functionalized gold substrates as sensing interfaces for the esterase agent¹⁴. Indeed, the platinum moiety is covalently linked to the disulfide-ending group by an ester group. It was then possible to remove the platinum moiety from the surface by cleavage of the ester bond with an esterase agent. As a reference, a platinum(II) complex with an amide bond instead of an ester bond was prepared as showed in Figure 2. The high-resolution spectra of the Pt 4f signal clearly showed the disappearance of the two peaks after incubation of the ester functionalized gold substrates in a solution containing the esterase. The signal of the complex with an amide bond did not disappear, meaning that the platinum moiety is still attached to the substrate. In conclusion, despite the coverage of platinum(II) complex on the gold substrate being relatively low, it could still be used as a sensing surface for an esterase agent.

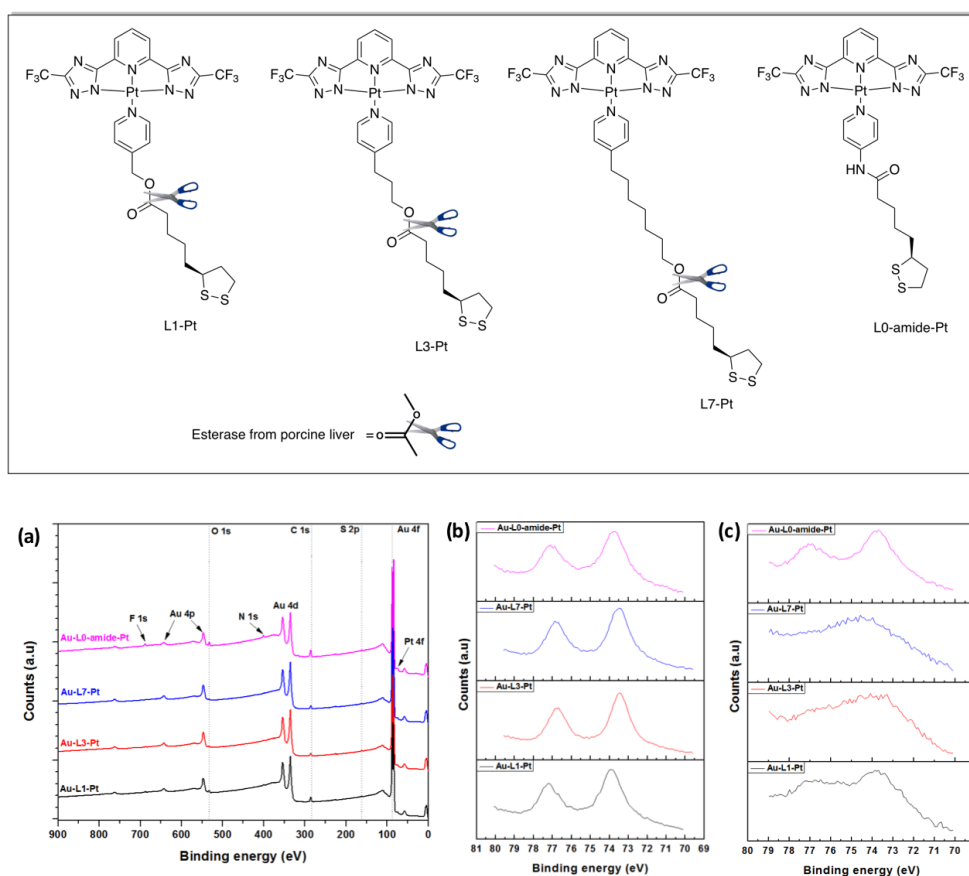
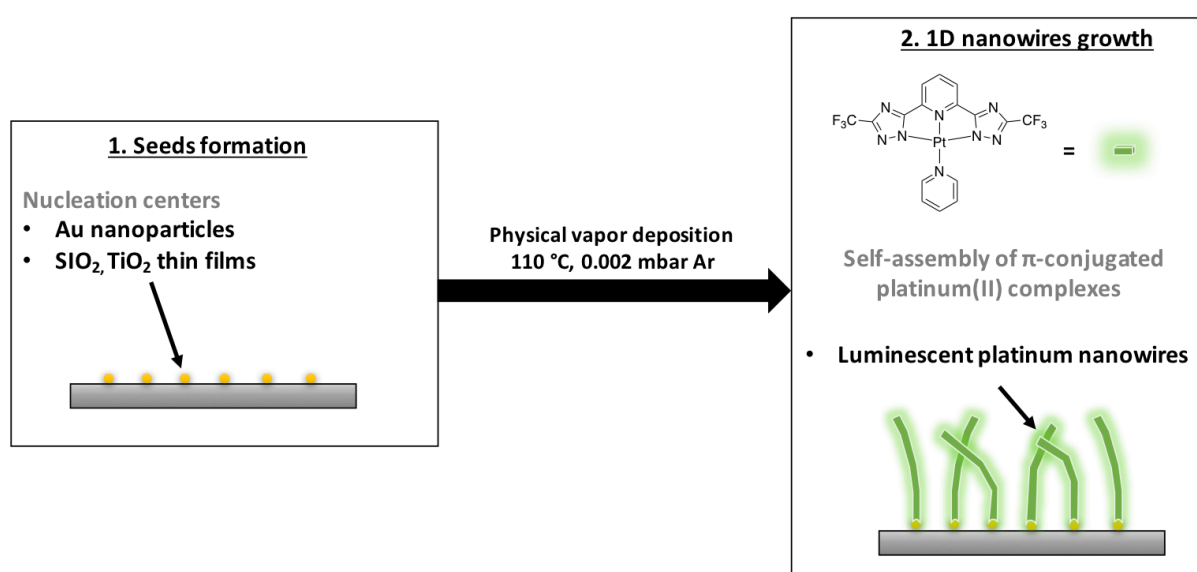


Figure 4. Chemical representation of the four platinum(II) complexes used for the sensing assay. Three complexes with an ester bond and one complex with an amide bond are linked to the gold substrates. In the presence of an esterase agent, the ester bond is cleaved and the platinum moiety removed from the surface. XPS survey scans of the functionalised gold substrates after cleavage of the ester bond (a) and high-resolution XPS spectra of the Pt 4f signal before (b) and after (c) cleavage of the ester group.

The aim of this study was to attach platinum(II) complexes onto surfaces and if possible, to trigger the self-assembly directly on the surface. However, it was not possible to reach this goal by wet chemical functionalization. For this reason, it was necessary to propose other strategies. We began collaboration with Dr. Ana Bórras of the University of Sevilla as they have previously reported the growth of nanowires of π -conjugated molecules on different substrates by physical vapor deposition (PVD)^{15,16}. The same method was used for a simple platinum(II) complex with a similar tridentate ligand and a pyridine moiety. After ensuring that the complex was stable by TGA, the nanowires were obtained on different substrates by sublimation at 110°C using the principle of PVD as displayed in Scheme 1.



Scheme 1. Illustration describing the PVD method used to grow nanowires of platinum(II) complex. 1) Nucleation centers are created on different substrates; 2) Self-assembly of π -conjugated platinum(II) complexes at 110°C.

Gold nanoparticles as nucleation centers provide bent platinum fibers perpendicular to the substrate (Figure 5). The mechanochromic property of the fibers was observed by a luminescence of the fibers that shifted from green to yellow after the application of pressure on the fibers¹⁷. Such a photophysical change was explained by the shortening of the platinum-platinum interactions within the fiber due to fiber contractions, which were caused by the application of a vertical pressure to the structure. In order to further characterize the mechanochromism properties from the bulk (powder) to the nanoscale (fibers), detailed AFM-fluorescence microscopy coupled studies are needed.

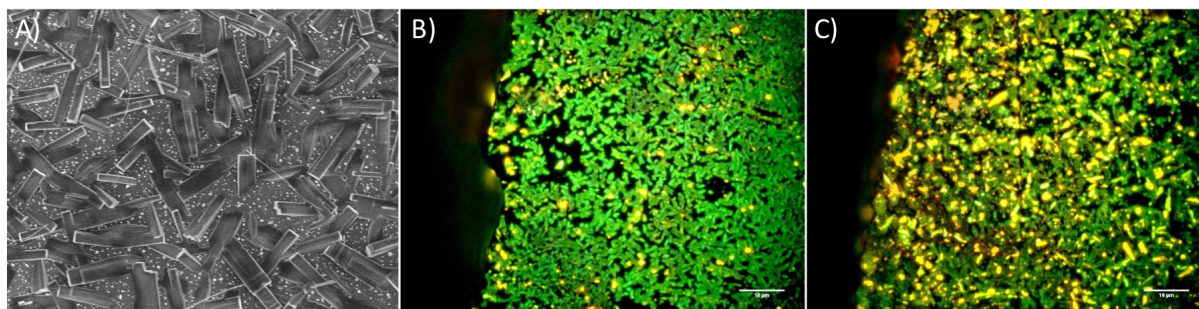


Figure 5. (A) SEM images of the fibers grown by PVD on gold nanoparticles on a silicon substrate. Fluorescence microscopy images of the platinum nanowires on Au (1nm) before (B) and after (C) mechanical activation of the nanowires by gentle pressing by hand through a PDMS foil.

In chapter 3, the encapsulation of luminescent platinum(II) complexes into polymer particles was investigated^{18,19}(Figure 6). Poly-(methyl methacrylate-co-methacrylic acid)(PMMA-PMAA) diblock copolymer with a long hydrophobic block and a short hydrophilic tail form particles in a THF/water mixture. Moreover, the hydrophobic core of the PMMA-PMAA particles is believed to be a suitable host for the hydrophobic platinum(II) complex. More interestingly, the platinum(II) complex aggregates into luminescent fibers in a THF/water mixture. The self-assembly properties of both the diblock copolymer and the platinum(II) complex were utilized in order to study the mechanism of encapsulation and the photophysical properties of the platinum-loaded particles. It appears that the luminescence coming from those particles is depending on the feed ratio between PMMA-PMAA and the complex and this is referred to as **R** in the manuscript. When the ratio **R** is below 30, the platinum(II) complex is mainly present in the THF/ water mixture as orange yellow emissive fibers. Upon increasing **R** to 50, the complex is encapsulated into the polymer particles and emits green. It is deduced that the complex is in the particles under an aggregative state. Interestingly the luminescence originating from the platinum loaded particles can be tuned depending on the ratio **R**. For example, when the ratio is high at 1000, blue emissive particles are observed. It is possible to obtain particles with an emission located between blue and green, *e.g* cyan or turquoise.

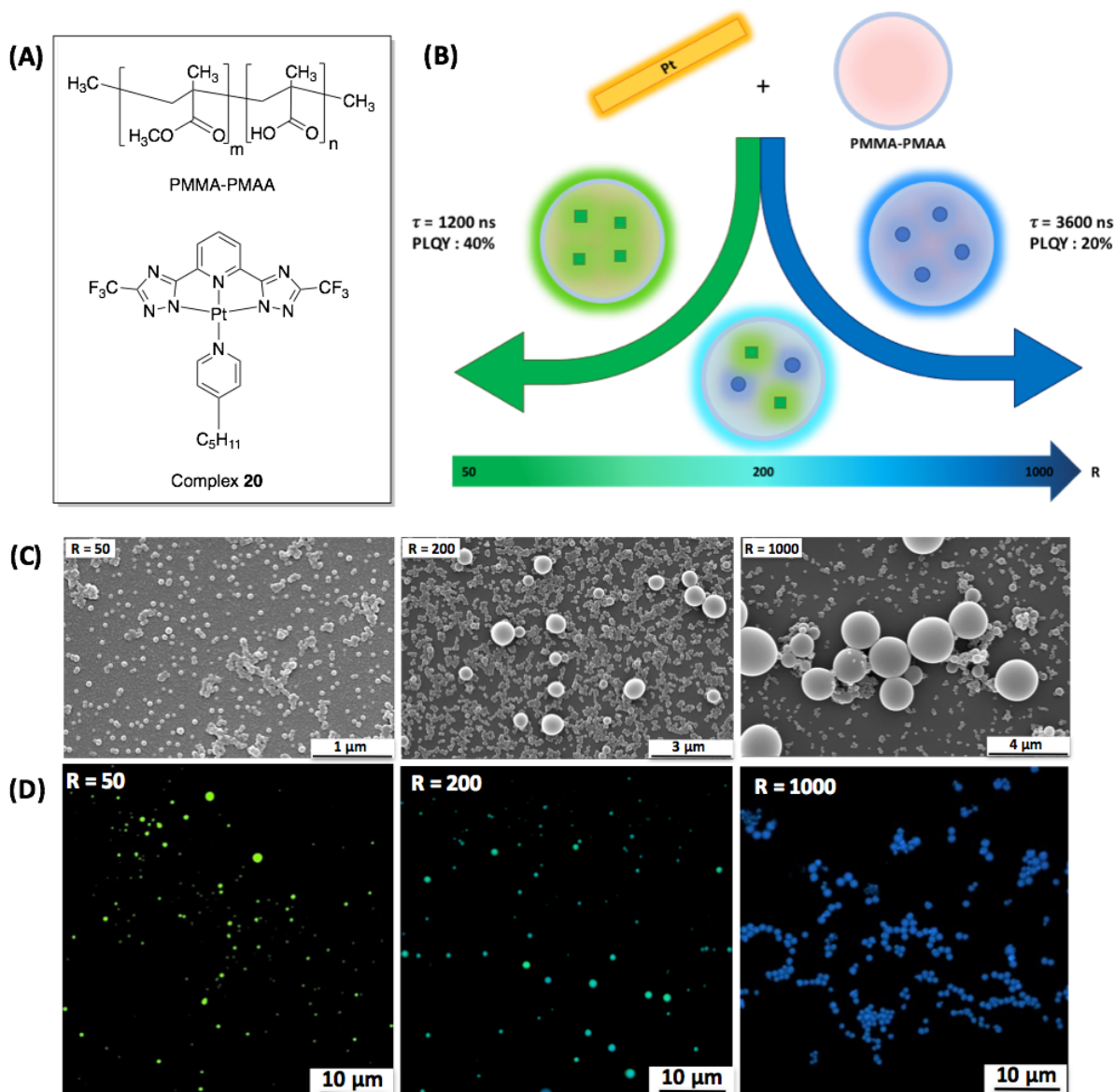


Figure 6. (A) Chemical structures of the PMMA-PMAA diblock copolymer and platinum(II) complex. (B) Schematic illustration of the encapsulation of the complex by polymer particles. The platinum fibers are disassembled in the presence of the polymer and two platinum species are formed, green emissive aggregates for R around 50 and blue emissive monomeric species at a higher R , above 500. A mixture of the two aggregates in a single particle can be observed for a ratio around 200. (C) SEM and (D) confocal fluorescence microscope images of the platinum-loaded particles at three distinct ratios. $\lambda_{\text{exc}} = 405\text{nm}$, the real emission color is displayed in lambda mode.

This is explained by the fact that the platinum(II) complex is diluted upon increasing the concentration in PMMA-PMMA. Thus, there are no more platinum aggregates in the particles

but only monomers. Consequently, the emission of the blue emissive particles is originating from the platinum monomeric species. When a turquoise emission is observed, a mixture of platinum aggregates and monomeric species is present in the same particle. It is also worth noting that the excited state lifetimes of the platinum-loaded particles increases from around 1 μ s to 3 μ s upon increasing **R**. Interestingly, the excited state of the monomeric species in the particles (3 μ s) is much longer than the monomeric species in THF (3 ns) and is comparable to the excited state lifetime of the platinum(II) complex at 77K, where most of the non-radiative relaxations are prevented by the rigidochromic effect²⁰. The complexes are confined in the rigid core of the polymer particles. The photoluminescence quantum yield of the platinum-loaded particles is also increased from less than 1% in THF to 20% when confined in the PMMA-PMAA particles. The method developed in this chapter is versatile as it is successful for different luminescent platinum(II) complexes. The same encapsulation behavior was observed for the other complexes with a tunable emission from green to blue. Moreover, it is also possible to obtain less polydisperse particles with similar encapsulation behavior with a modified method. The water was added dropwise to the PMMA/PMAA/complex **20**/THF mixture while stirring. The organic solvent was then removed from the solvent mixture by dialysis against water. Monodispersed smaller particles with indentations on their surfaces were obtained with tunable photophysical properties.

Chapter **4** is inspired by previous research on the different morphologies of diblock copolymer²¹. Multiple aggregates of such micelles, vesicles, rods, lamellae or large compounds micelles have been reported for diblock copolymers. The variety of morphologies observed is accounted for by the interactions of the hydrophobic and hydrophilic blocks with the solvent mixture. For example, In the presence of water, the hydrophobic blocks organize themselves in order to minimize interactions with the water molecules. Depending on the composition of the solvent, the copolymer adopts the most favorable morphology. An analogy is possible between the diblock copolymer and amphiphilic platinum(II) complex. To demonstrate this, a platinum(II) complex with a polyethylene glycol chain as a hydrophilic block and a chromophoric tridentate ligand as the hydrophobic block was selected. The presence of an amide functional group also favours the formation of directional hydrogen bonding N-H between adjacent complexes. The methodology used for the formation of platinum(II) complex aggregates is similar to the one reported for the formation of diblock copolymer

aggregates. The complex is dissolved in an organic solvent such as THF, DMF or dioxane, and water is gradually added while stirring. Solutions with the same concentration in complex by different THF/water ratio are obtained. The Critical Water Content (CWC) at which the platinum(II) complex starts to aggregate was measured by UV-VIS and emission spectroscopy is displayed in Figure 7.

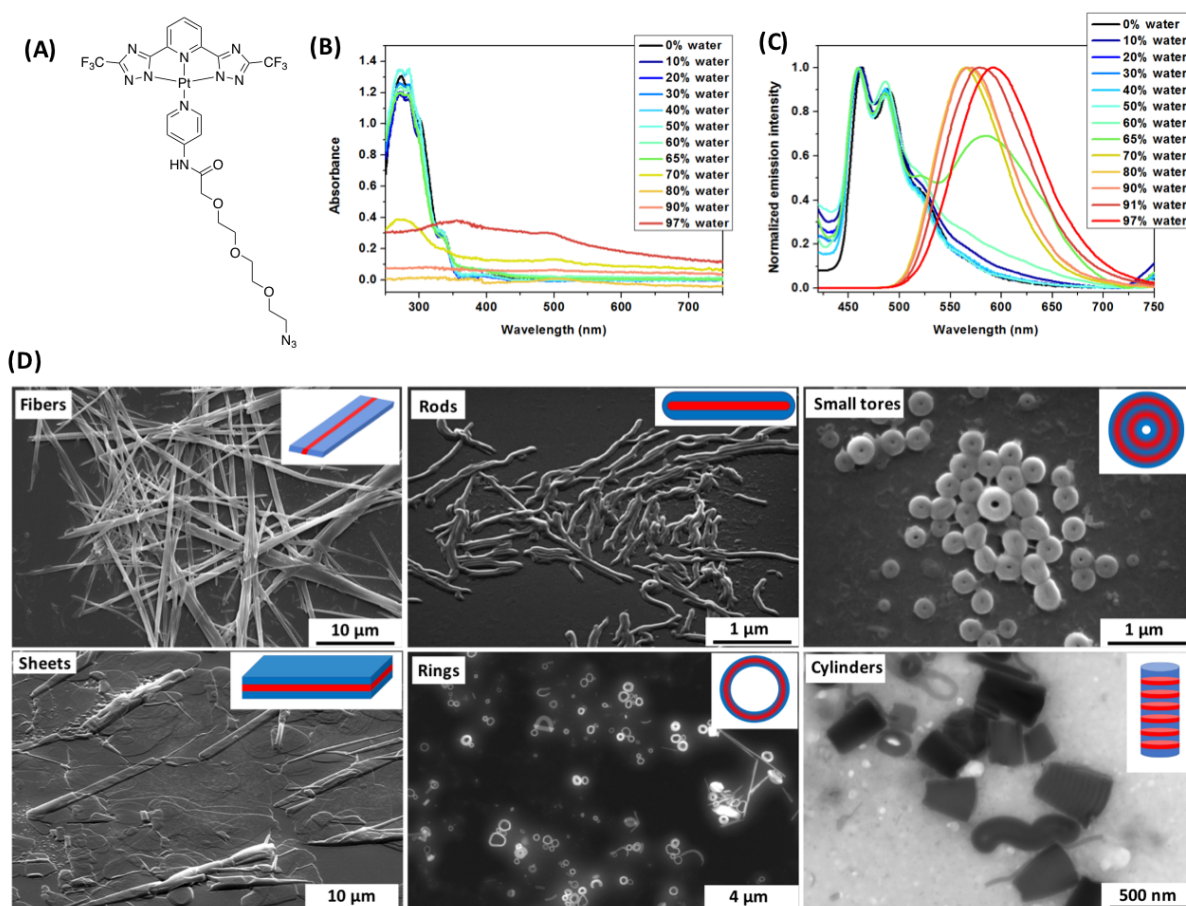


Figure 7. (A) Chemical structure of the amphiphilic platinum(II) complex. Absorption (B) and emission (C) spectra of complex 7 in different THF/water mixtures. (D) Scanning electron microscopy (SEM) and Scanning transmission electron microscopy (STEM) images and corresponding schematic representation of the various morphologies formed from the amphiphilic platinum(II) complex. In the schematic diagrams, red represents the hydrophobic platinum moiety and blue the hydrophilic polyethylene glycol chain.

The formation of platinum aggregates is observed with the rise of the ³MMLCT broad band centered approximately at 580 nm in the emission spectra. The CWC in a THF/water mixture is approximately 65%, dioxane/water mixture is 40% and DMF/water mixture is 30%. The water can also be flash-injected in the organic solvent or the order of addition can be inverted.

By varying different parameters, at least 6 different morphologies have been distinctively observed by electron microscopy as displayed in Figure 7D; fibers, rods, tores, sheet-like aggregates, rings and cylinders. All of those morphologies have already been reported for different platinum(II) complexes. However, this is the first time that such a diversity of morphologies is reported for a single complex. Fibers were the easily obtained when the water content is between 60% to 80% water content in a THF/H₂O solvent mixture. Tores of different sizes depending on the concentration were obtained when the water content was increased above 90%. Rods and cylinders were obtained when the water was flash-injected into the complex/THF mixture and the water content above 90%. Those two morphologies usually co-existed in solution. Additional fan-shaped aggregates can also be observed with the cylinders and rods. Sheet-like aggregates and rings were obtained when the complex/THF mixture was slowly added to the water at water content above 90%. Those two morphologies also co-existed in solution and were hard to separate. Each type of aggregates has specific photophysical properties, which make them unique. This study was essential to understand the behavior of platinum(II) complex in different solvent mixture. It also allowed the control of the morphology and its resulting photophysical properties.

The self-assembly properties of a single platinum(II) complex has been widely reported in literature²⁻⁶. In this regard, Chapter 5 focuses on the self-assembled properties of two complexes in a dioxane/water solvent mixture. Two parameters were explored for this purpose, the feed ratio between the two complexes and the composition of the solvent mixture²². Two platinum(II) complexes, which aggregate into fibers of different luminescence under similar conditions, were selected in order to easily compare the co-assembled aggregates as depicted in Figure 8.

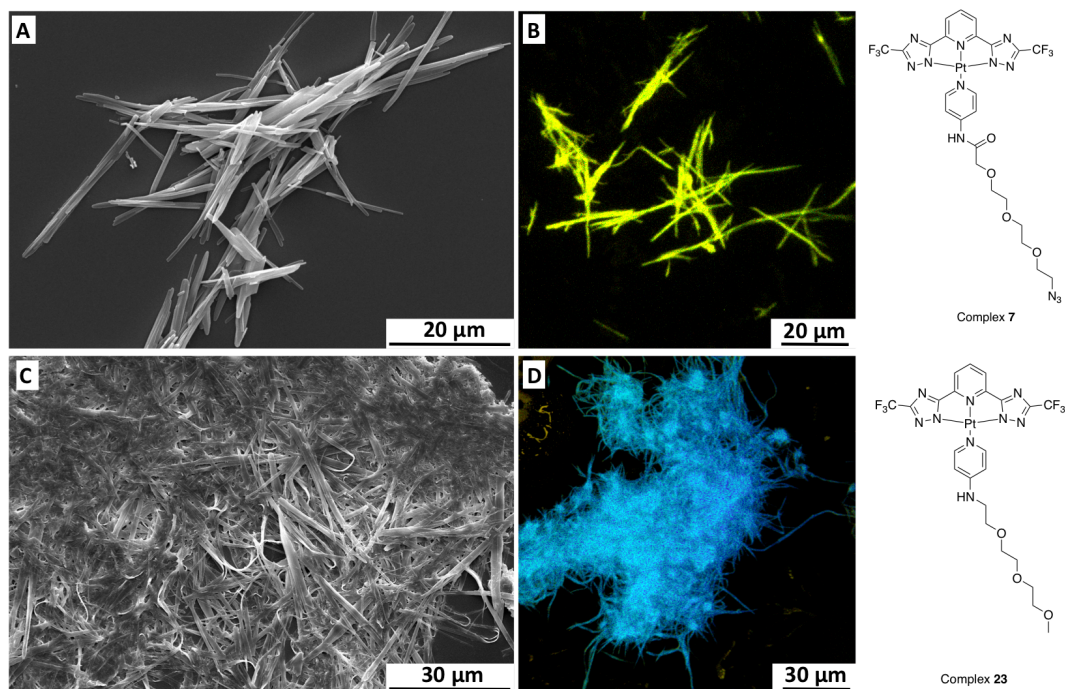


Figure 8. *a,c*) SEM and *b,d*) fluorescence confocal images of the fibers formed from complex **7** and **23** respectively in a 80% dioxane/water solvent mixture. The solution was drop-casted on a glass slide and dried under standard conditions. $\lambda_{exc} = 405 \text{ nm}$ in lambda mode.

The most interesting result was for the complex **23**/complex **7** mixture (1:0.2) at 70% water content in a dioxane/water solvent composition. The solution was blue emissive under the UV lamp but the fibers observed after drying were orange emissive. Real-time imaging of the evaporation the solution droplet as displayed in Figure 9 can be used to monitor the change in emission of the fibers. The emission of the fibers were originally blue emissive but gradually shifted to an orange emission. In the dioxane/water droplet, the dioxane evaporated slightly before the water. Consequently, the polarity of the solvent is increased because of the higher water content. The photoluminescent quantum yield was increased from 12% to 55% and the excited state lifetime from 450 ns to 550 ns upon luminescence transition. The change of photophysical properties upon varying the polarity of the solvent is referred to as solvatochromism. In this case, it can be referred to as positive solvatochromism because there was a bathochromic shift with increasing solvent polarity.

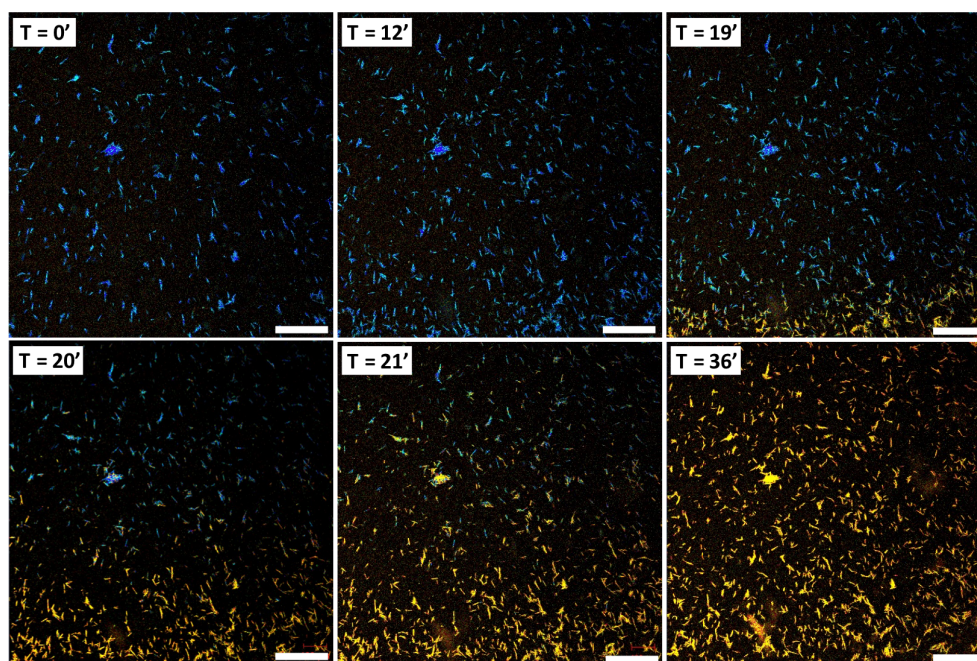


Figure 9. Real-time confocal imaging of the drop-casted solution of complex 27: complex 7 (1 :0.2) dioxane/water mixture (70% water content). $\lambda_{exc} = 405 \text{ nm}$ (real colors). Scale bar: 200 μm .

The X-ray diffraction (XRD) pattern analysis and Selected area diffraction pattern (SAED) clearly showed a d-spacing of 3.41 Å and 3.36 Å respectively, in accordance with the presence of platinum-platinum interactions within the orange emissive fibers. There were no patterns corresponding to platinum-platinum interactions for the blue emissive ribbons detected. It is concluded that the change in polarity induces a crystallographic transformation resulting in newly formed metallophilic interactions and a luminescence switch. This was the first time that such a change was observed without any morphological transformations. The luminescence transition of the fibers from blue to orange was also a reversible process when the water content was re-adjusted at 70%.

The supramolecular co-assembly at 60% water content provides millimetre-sized fibers with similar photophysical properties. For water content above 80%, blue emissive fibers coated with an orange emissive were observed. In this case, no luminescence transition was observed upon evaporation of the droplet.

Finally, chapter 6 describes of the techniques and instruments used in this work.

In conclusion, this PhD thesis focuses the study of different platinum(II) complex systems. The design, synthesis and characterization of several luminescent platinum(II) complexes with intriguing photophysical and self-assembly properties are reported. The behaviour of those complexes in confined spaces such as polymer particles, or spatially constrained on a surface, is explored with promising results. The meticulous study on the different morphologies of platinum(II) complexes aggregates and their implications on the photophysical properties have been carried out. Lastly, a supramolecular co-assembly of two complexes was demonstrated for the first time and opens the path to a new field of research in the self-assembly of more than one molecule.

References

1. V. H. Houlding; V. M. Miskowski, *Coord. Chem. Rev.*, **1991**, *111*, 145-152.
2. V. M. Miskowski; V. H. Houlding, *Inorg. Chem.*, **1991**, *30*, 4446-4452.
3. Yam, V. W. W., Wong, K. M. C., Zhu, N. Y. *J. Am. Chem. Soc.* **2002**, *124*, 6506–6507.
4. Po, Charlotte, Anthony Yiu-Yan Tam, Keith Man-Chung Wong, and Vivian Wing-Wah Yam, *J. Am. Chem. Soc.*, **2011**, *133*, 12136-12143.
5. Alessandro Aliprandi, Matteo Mauro, Luisa De Cola, *Nature Chem.* **2016**, *8*, 10-15.
6. Yong Chen, Kai Li, Wei Lu, Stephen Sin-Yin Chui, Chun-Wah Ma, Chi-Ming Che, *Angew. Chem. Int. Ed.*, **2009**, *48*, 9909-9913.
7. Sidharam P. Pujari, Luc Scheres, Antonius T. M. Marcelis, Han Zuilhof, *Angew. Chem. Int. Ed.*, **2014**, *53*, 6322-6356.
8. Yiong Mai, Adi Eisenberg, *Chem. Soc. Rev.*, **2012**, *41*, 5969-5985.
9. D. Xu, E. T. Kang, K. G. Neoh, Yan Zhang, A. A. O. Tay, S. S. Ang, M. C. Y. Lo and K. Vaidyanathan, *J. Phys. Chem. B*, **2002**, *106*, 12508-12516.
10. Deb Kumar Bhowmick, Linda Stegemann, Manfred Bartsch, Naveen Kumar Allampally, Cristian A. Strassert, Helmut Zacharias, *J. Phys. Chem. C*, **2015**, *119*, 5551–5561.
11. Kolb, H. C.; Finn, M. G., Sharpless, K. B., *Angew. Chem. Int. Ed.*, **2001**, *40*, 2004-2021.
12. Samuel J. Adams, David J. Lewis, Jon A. Preece, Zoe Pikramenou, *ACS Appl. Mater. Interfaces*, **2014**, *6*, 11598–11608.
13. Hannu Häkkinen, *Nature Chem.*, **2012**, *4*, 443-455.
14. Mei-Jin Li, Xing Liu, Mei-Juan Nie, Zhao-Zhen Wu, Chang-Qing Yi, Guo-Nan Chen, Vivian Wing-Wah Yam, *Organometallics*, **2012**, *31*, 4459–4466.

15. Manuel Macias-Montero, A. Nicolas Filippin, Zineb Saghi, Francisco J. Aparicio, Angel Barranco, Juan P. Espinos, Fabian Frutos, Agustin R. Gonzalez-Elipe, Ana Borrás, *Adv. Funct. Mater.*, **2013**, *23*, 5981–5989.
16. Ana Borrás, Myriam Aguirre, Oliver Groening, Carlos Lopez-Cartes, Pierangelo Groening, *Chem. Mater.*, **2008**, *20*, 7371–7373.
17. Damiano Genovese, Alessandro Aliprandi, Eko A. Prasetyanto, Matteo Mauro, Michael Hirtz, Harald Fuchs, Yasuhiko Fujita, Hiroshi Uji-I, Sergei Lebedkin, Manfred Kappes, and Luisa De Cola, *Adv. Funct. Mater.*, **2016**, *26*, 5271–5278.
18. 20. Nijuan Liu, Baoyan Wang, Weisheng Liu and Weifeng Bu, *Chem. Commun.*, **2011**, *47*, 9336–9338.
19. 21. N. Liu, Q. He, W. Bu, *Langmuir*, **2015**, *31*, 2262–2268.
20. Mark Wrighton, David L. Morse, Wrighton, M.; Morse, D. L., *J. Am. Chem. Soc.*, **1974**, *96*, 998–1003.
21. Zhang, L., Eisenberg, A., *Science* **1995**, *268*, 1728-1731
22. Kaka Zhang, Margaret Ching-Lam Yeung, Sammual Yu-Lut Leung, Vivian Wing-Wah Yam, *Chem* **2**, **2017**, 825–839.

Résumé

Cette thèse s'intitule "auto-assemblage de complexes de platine (II) aux propriétés photophysiques modulables dans des espaces confinés et en solution » traite de la préparation et de la caractérisation de complexes de platine(II) luminescents et leurs propriétés photophysiques. Les métaux de transition ont été utilisés pour de nombreuses applications tel que l'imagerie biologique et des appareils optoélectroniques à cause des excitons de nature triplet et singulet qui peuvent mener à des rendements proches de 100%. En particulier, les complexes de platine(II) avec leur géométrie carrée plan sont capables de s'auto-assembler en diverses nanostructures aux propriétés spécifiques^{1,2}. De tels arrangements sont possibles à cause des interactions métalophiliques entre deux orbitales pleines d_z^2 entre deux atomes de platines et favoriser par des empilements π - π des ligands de coordination ou d'autres interactions supramoléculaires tel que des liaisons hydrogène ou des interactions électrostatiques.

Ce manuscrit s'ouvre sur une introduction de concepts de bases de photophysiques et plus particulièrement sur les propriétés photophysiques de complexes de platine(II) d^8 . Un aperçu des différents types d'agrégats de platine présent dans la littérature est aussi reporté³⁻⁶. Une petite introduction sur les particules de polymère⁷ et la modification de surface⁸ est également reporté.

Le premier chapitre expérimental décrit les différentes stratégies explorées pour la liaison covalente de complexes de platine(II) sur des surfaces de silice. La première approche commence par l'attachement covalent de molécule de 4-vinylpyridine induit par irradiation UV sur des surfaces de silice avec des hydrogène terminaux comme décrit en figure 1⁹. Les surfaces fraîchement préparées avec des molécules de pyridine terminaux sont coordonnées au précurseur de platine $PtCl_2(DMSO)_2$ and le ligand tridenté pour former le complexe de platine¹⁰. Les modifications de surface successives sont contrôlées par spectrométrie photoélectronique X. Les surfaces hydrogénées ne montrent la présence de contamination de carbone et oxygène. L'attachement des molécules de 4-vinylpyridine sur les substrats Si-H est démontré par la présence du pic N 1s à 400 eV. Finalement, la coordination du complexe de platine(II) au substrat est mise en évidence par la présence de pics Pt 4f et F 1s autour de 73 eV et 698 eV respectivement. Cependant, la densité de complexe sur la surface de silice (100)

est relativement faible et limitent des plus amples analyses. La coordination directe de complexes de platine(II) déjà synthétisés sur les surfaces hydrogénées n'ont pas amélioré la densité sur de complexes sur la surface.

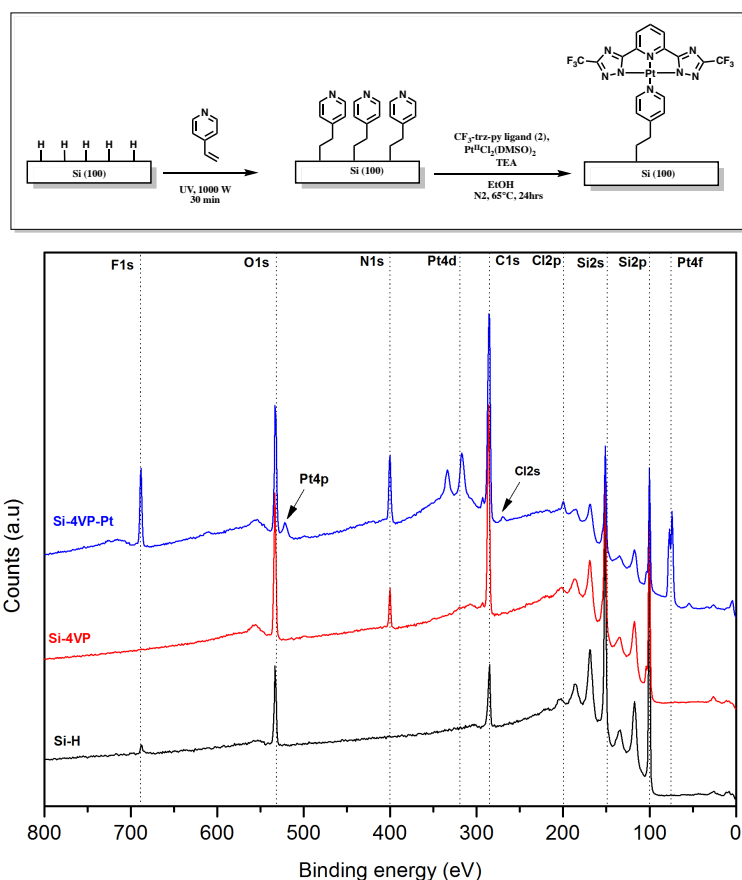


Figure 1. Représentation schématique de l'attachement covalent de complexes de platine(II) luminescents induit par irradiation UV et spectroscopie photoélectronique X des différentes modifications de surface.

La seconde approche commence par la préparation de surface acétylène avec des molécules alcyne attachées à la surface de silice comme montré en figure 2. Un ligand contenant une chaîne polyéthylenglycolée, un groupement azoture à une extrémité et une pyridine de l'autre sont attachés aux surfaces acétylènes par cyclo addition alcyne-azoture catalysé par cuivre (I) (chimie-click). Le complexe de platine(II) est attaché de la même manière que précédemment. Les modifications successives des surfaces sont contrôlées par spectroscopie photoélectronique X. L'attachement covalent du ligand auxiliaire par « chimie-click » est mis en évidence par la présence par le pic d'azote N 1s à 400 eV. La coordination du complexe est montrée par la présence des pics de Pt 4f et F 1s à 73 eV et 698 eV respectivement. Cependant,

même si le complexe est fortement attaché à la surface de silice, la densité en complexe est très faible à la surface. Le complexe de platine(II) a également été attaché directement au substrat acétylène par « chimie-click » augmentant légèrement la densité à la surface. Malheureusement, la densité à la surface est trop faible pour faire des analyses plus poussées.

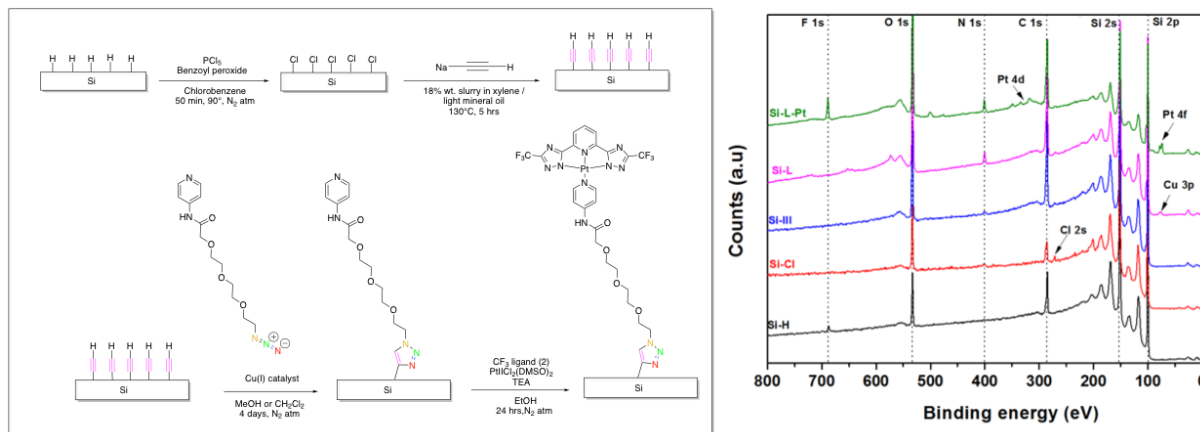


Figure 2. Représentation schématique des attachements covalents de complexes de platine(II) luminescents sur des surfaces de silice par chimie-click et spectroscopie photoélectronique X des différentes surfaces.

En conclusion, même si le complexe de platine(II) a été attaché avec succès de manière covalente à la surface, la densité à la surface était trop faible pour l'utilisation que nous voulions en faire.

L'attachement de complexes de platine(II) a été réalisé sur des surfaces d'or par des liaisons sulfure-or^{12,13}. Pour cette raison, des complexes avec des chaînes de longueurs différentes avec des groupement disulfures ont été préparé. Des surfaces fraîchement nettoyées sont immergées dans une solution de DMF contenant les différents complexes pendant 6 jours avant d'être analysés. L'accrochage des complexes de platine(II) sur les surfaces d'or ont été démontré par spectroscopie photoélectronique X haute résolution du signal S 2p des atomes de sulfures. Le pic est déplacé de 163 eV (liaison disulfure) à 161.5 eV (liaison sulfure-or) lorsque que le complexe est attaché à la surface d'or (figure 3). La nature des liaison or-sulfure est toujours sujette à discussions et ne sera pas débattue dans cette thèse. Il est néanmoins convenu que cette liaison est très forte¹³. La stabilité des liaisons sulfure-or est également évaluée par SPX après avoir laissé les surfaces fonctionnalisées à l'air libre pendant 2 mois. La formation d'oxydes de sulfure (SO_x) est établie par la présence de pics à 169 eV caractéristiques de ces oxydes. La densité de complexes sur les surfaces d'or est néanmoins

très faible, comme c'était le cas sur les surfaces de silice et ne permet pas de faire de plus amples analyses.

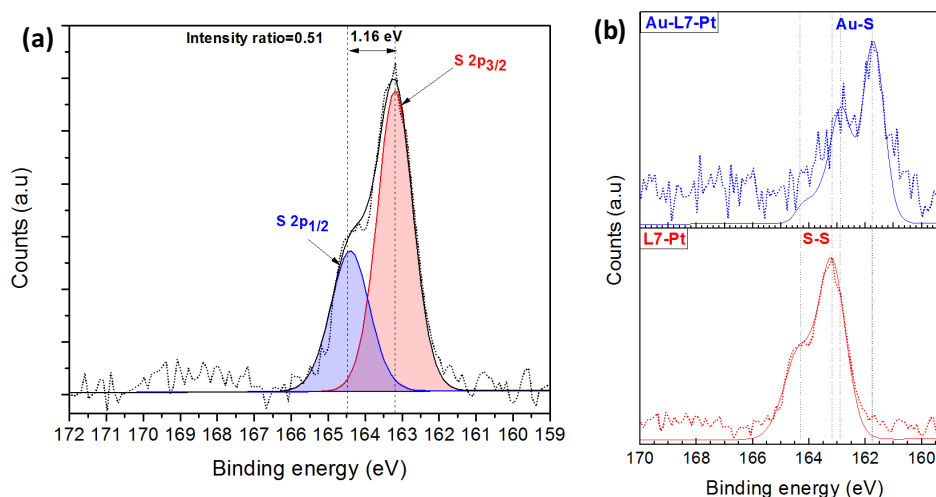
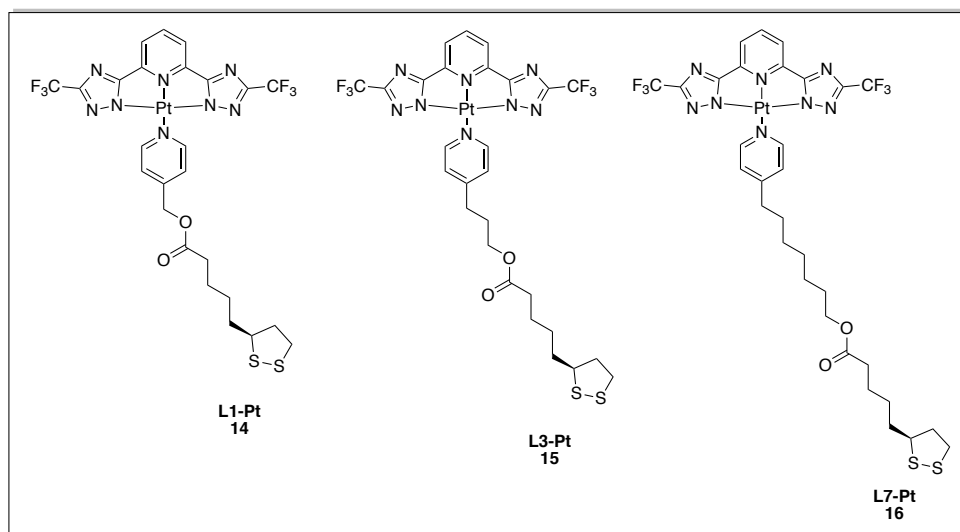


Figure 3. Structure chimique des trois complexes de platine(II). Spectres haute résolution du pic S 2p (a) du complexes L7-Pt seul (rouge, disulfure) et attaché à la surface d'or (bleu, sulfure-or).

Cependant, il est possible d'utiliser ces surfaces d'or fonctionnalisés comme des interfaces sensibles aux agents esterase¹⁴. En effet, l'atome de platine est lié à la surface d'or par une fonction ester. Il est alors possible de retirer la partie comprenant le platine par rupture de la liaison ester avec le bon agent. Pour prouver cette théorie, un complexe de platine avec groupement amide au lieu d'ester a été préparé comme référence comme montré en figure 2. Les SPXs haute résolution du pic du platine Pt 4f montrent clairement la disparition des deux pics après incubation des surfaces fonctionnalisés dans des solutions contenant l'agent

estérase. Par contre le signal du platine pour le complexe avec la fonction amide ne disparaît pas, prouvant que la partie contenant l'atome de platine est toujours attaché à la surface. En conclusion, malgré la faible densité de platine, la surface fonctionnalisée peut quand même servir de senseurs pour la détection d'agent estérase.

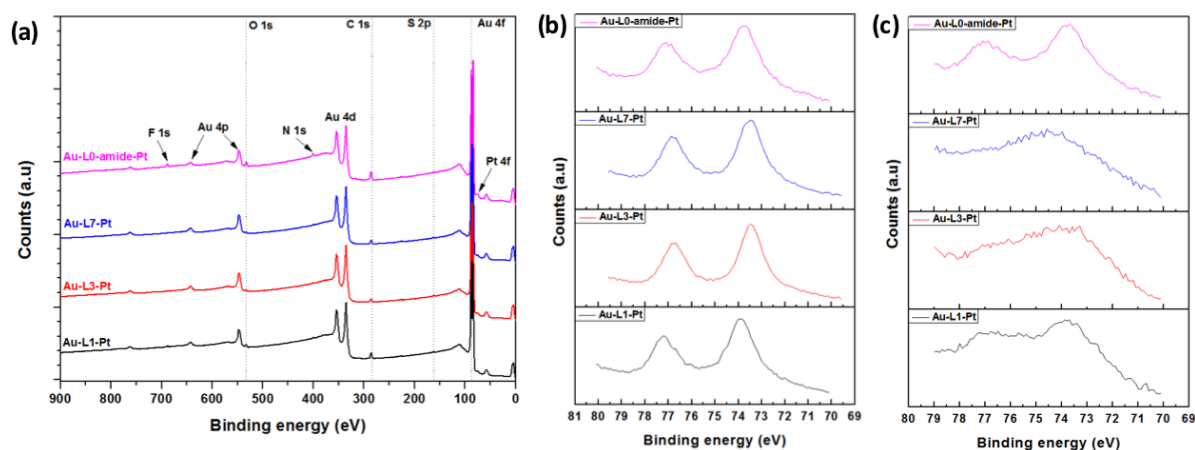
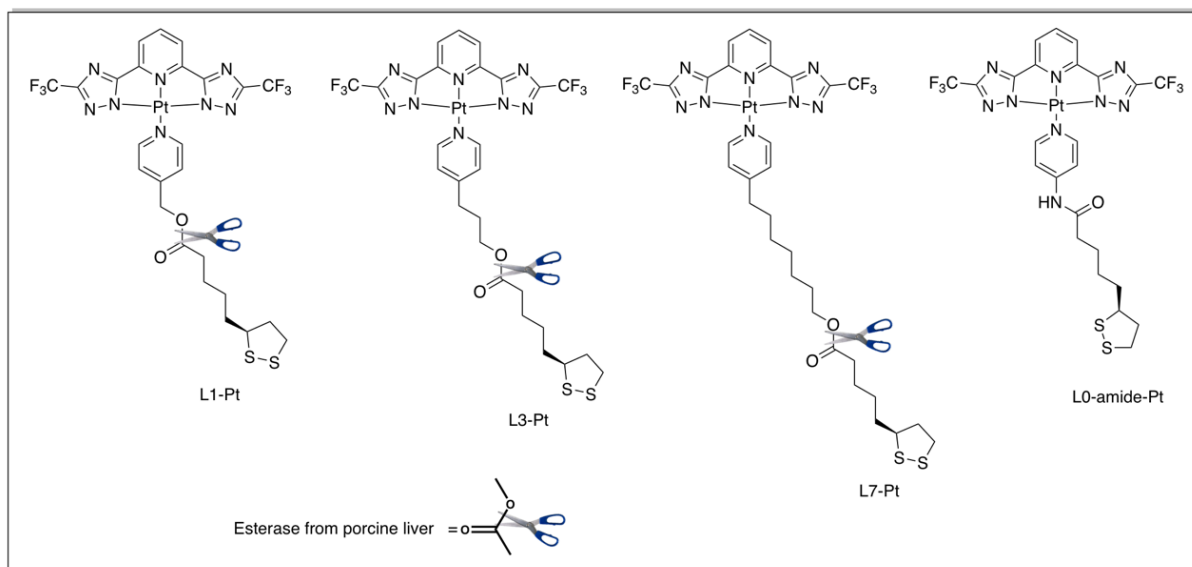


Figure 4. Représentation chimique de quatre complexes de platine(II) utilisé par l'essai sensorial. Trois complexes avec de fonctions ester et un complexe avec une fonction amide sont attaché à des surfaces d'or. En présence d'un agent estérase, les fonctions esters sont rompues et la partie comportant l'atome de platine est détaché de la surface. Les scans par spectroscopie photoélectronique X de ces surfaces (a) et spectroscopie haute résolution du signal Pt 4f avant (b) et après (c) rupture de la fonction ester.

Le but de cette étude était d'attacher des complexes de platine à des surfaces et si possible de déclencher l'auto-assemblage de ces complexes directement sur la surfaces. Cependant,

cela n'a pas été possible d'atteindre cet objectif par des fonctionnalisation en solution. Il était alors nécessaire de réfléchir à de nouvelles stratégies. Pour ces raisons, il était nécessaire de penser à une nouvelle approche. Nous avons démarré une collaboration avec Dr. Ana Bõrras de l'université de Séville qui est spécialisée dans la croissance de fil de systèmes conjugués π sur différentes surfaces par déposition physique en phase gazeuse^{15,16}. La même méthode a été utilisé sur un simple complexe de platine(II) avec un ligand tridenté and une pyridine en ligand auxiliaire. Après s'être assuré que le complexe de platine(II) est stable par analyse thermogravimétrique, les fils moléculaires sont obtenus sur différent substrat par sublimation à 110°C en utilisant les principes de déposition physique en phase gazeuse comme montré en schéma 1.

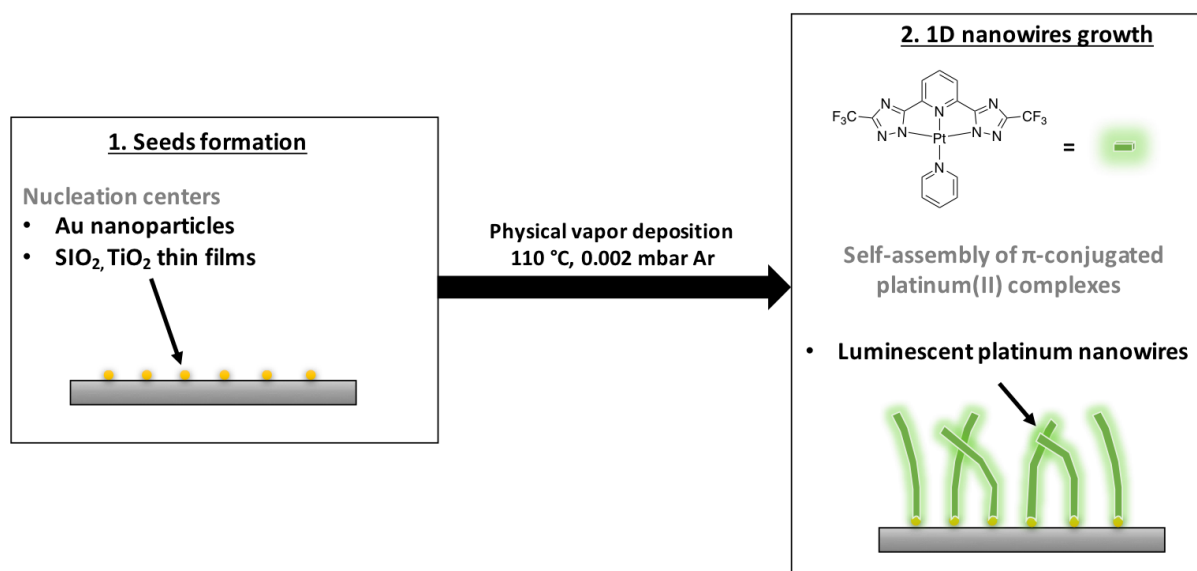


Schéma 1. Illustration décrivant la déposition physique en phase gazeuse utilisé pour la formation de fibres de complexe de platine(II). 1) Les centres de nucléation sont créés sur différent substrats ; 2) auto-assemblage de de complexes de platine(II) π -conjugué à 110 °C.

Les nanoparticules d'or comme centre nucléophiles procurent des fibres de platine courbées orthogonal à la surface (Figure 5). Les propriétés mécanochromiques des fibres sont observés par la luminescence des fibres qui est décalé de vert à jaune après application d'une pression sur ces fibres¹⁷. De tels changements photophysiques sont expliqués par un raccourcissement des distances entre deux atomes de platine dans les fibres de platine après application d'une pression le long de l'axe directionnel des structures. Pour étudier en profondeur et comparer

les propriétés méchanochromiques des poudres par rapport aux fibres, microscopie à force atomique couplé à un microscope à fluorescence est nécessaire.

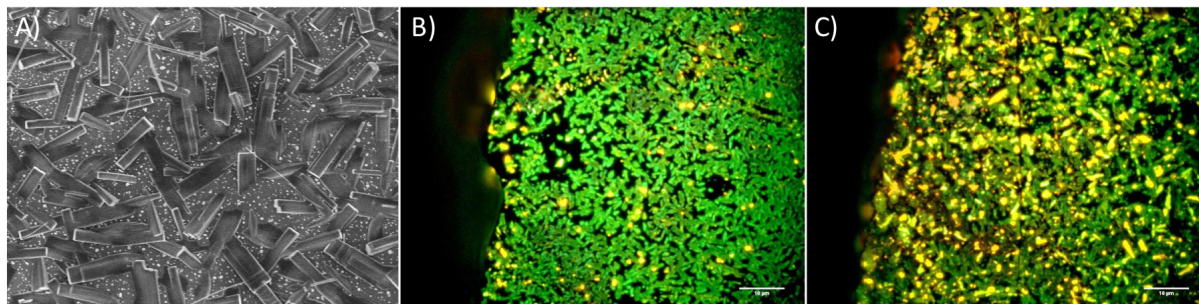


Figure 5. (A) Image MEB des fibres obtenues par déposition physique en phase gazeuse sur des nanoparticules d'or (1 nm d'épaisseur équivalente) sur une surface de silice. Images de microscopie à fluorescence des fibres de platine avant (B) et après (C) application d'une pression verticale sur les fibres.

Dans le chapitre 3, encapsulation de complexes de platine(II) dans des particules de polymère est étudié^{18,19} (Figure 6). Poly-(methyl methacrylate-co-methacrylic acid)(PMMA-PMAA) polymère di-bloc avec une longue chaîne hydrophobe et une courte chaîne hydrophile forment des particules dans un mélange H₂O/THF. Le noyau hydrophobe de ces particules est un environnement adapté pour des complexes de platine(II) hydrophobes. En plus, ces complexes s'auto-assemblent également en fibres luminescentes dans un mélange H₂O/THF. Les propriétés d'auto-assemblage à la fois des polymères et des complexes de platine(II) sont utilisés pour étudier les mécanismes d'encapsulation et des propriétés photophysiques des particules chargées en platine. On s'est rendu compte que la luminescence venant de ces particules dépend du ratio entre PMMA-PMAA et le complexe et est référé à **R** dans ce manuscrit. Quand le ratio est en-dessous de 30, le complexe de platine(II) est majoritairement présent dans le mélange H₂O/THF en tant que fibres émettant une coloration orange. Lorsque le ratio est augmenté à 50, le complexe est encapsulé dans les particules de polymère et émettent alors verte. Il a été déduit que le complexe est maintenant dans les particules à l'état agrégé. La luminescence venant des particules peut être modulé en fonction du ratio **R**. Par exemple, quand le ratio est haut à 1000, des particules émettant une coloration bleue sont observés. Il est également possible d'obtenir des particules avec des émissions comprises entre bleues et vertes comme par exemple turquoise ou cyan.

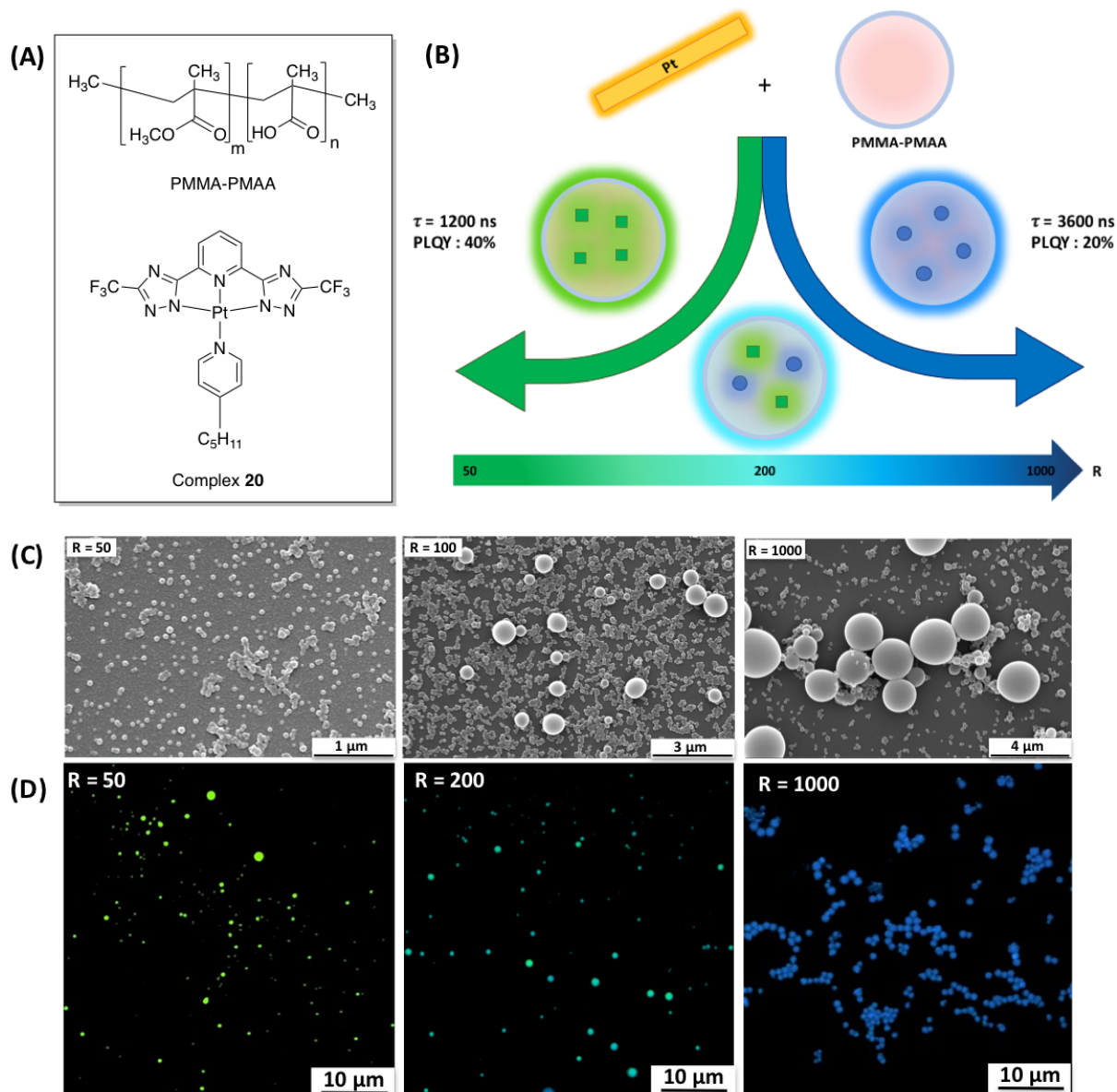


Figure 6. (A) Structures chimiques du copolymère di-bloc PMMA-PMAA et du complexe de platine(II). (B) Représentation schématique de l'encapsulation des complexes par les particules de polymère. Les fibres de platine sont désassemblées en présence de polymères et deux espèces sont formées dans les particules : des agrégats émettant vert quand R est autour de 50, des monomères émettant bleus quand R est supérieur à 500. Un mélange de ces deux espèces dans une particule simple peut être observé quand R est autour de 200. Images de (C) Microscopie électronique à balayage (MEB) et (D) microscopie confocale à fluorescence des particules chargées en platine à trois différents ratios. $\lambda_{exc} = 405\text{nm}$, les couleurs réelles sont montrées en lambda mode.

Ceci est expliqué par le fait que les complexes de platine(II) est dilué dans les particules en augmentant la concentration en polymère. Ainsi, il n'y a plus d'agrégats de platine dans les

particules mais seulement des molécules seules. Par conséquent, l'émission bleue venant des particules est dû au monomère de platine(II). Quand une coloration turquoise est observée, un mélange d'agrégat et de monomère est présent dans la même particule. Il est également important de mentionner que les temps de vie à l'état excité de ces particules chargé en platine augmentent d'environ 1 à 3 μs en augmentant le ratio **R**. Le temps de vie des monomères dans les particules (3 μs) est beaucoup plus long que les monomères en solution dans le THF (3 ns) et est comparable au temps de vie des complexes de platine(II) à 77K lorsque la plupart des relaxations non radiatives sont empêchées par effet rigidochromique²⁰. Les complexes sont alors confinés dans le noyau rigide des particules de polymère. Le rendement quantique de photoluminescence de ces complexes de platine(II) est augmenté de moins de 1% dans le THF à 20% lorsque encapsulé dans les particules. La méthode développée dans ce chapitre est très polyvalent car il fonctionne avec la plupart des complexes de platine(II) utilisé dans cette thèse. Le même comportement a été observé pour les autres complexes de platine(II) avec des émissions comprises entre le vert et le bleu. En plus, il est possible d'obtenir des particules de tailles similaires avec des propriétés d'encapsulation similaire en changeant légèrement la méthode de préparation. L'eau est ajoutée goutte-à-goutte au mélange PMMA-PMAA/complexe **20** dans le THF. Le solvant organique est alors enlevé du mélange réactionnel par dialyse contre de l'eau. Des particules de tailles plus similaires avec des petits défauts à leurs surfaces sont obtenus avec des propriétés photophysiques modulables.

Le chapitre **4** s'inspire des travaux de recherches sur les différentes morphologies des copolymère dibloc²¹. De nombreux agrégats tels que des micelles, des vésicules, des tiges, des lamelles ont été reporté pour différent polymères. La variété des morphologies observés est en parti dû par les interactions entre les block hydrophobes et hydrophiles dans un mélange de solvants. Par exemple, en présence d'eau, les blocs hydrophobes s'organisent de manière à minimiser les interactions entre les molécules d'eau. En fonction de la composition du solvant, les copolymères adoptent la morphologie la plus adapté à l'environnement. Une analogie est possible entre les copolymères di-bloc and un complexe de platine(II) amphiphile. Pour démontrer cela, un complexe de platine avec une chaîne polyéthylèneglycolée comme bloc hydrophile et un ligand tridenté chromophore comme bloc hydrophobe a été préparé. La présence d'une fonction amide favorise également l'établissement de liaison hydrogène entre molécules adjacentes. La méthode utilisée pour la formation d'agrégats de complexes de

platine(II) est similaire à celle décrit pour la formation d'agrégats de copolymère di-bloc. Le complexe est dissout dans un solvant organique tel que le THF, DMF ou dioxane et de l'eau est ajouté graduellement. Des solutions à la même concentration en complexe mais avec compositions THF/H₂O différentes sont obtenues. La teneur critique en eau à laquelle les complexes de platine(II) commencent à s'auto-assembler est mesuré par UV-Vis et émission spectroscopie comme montré en Figure 7.

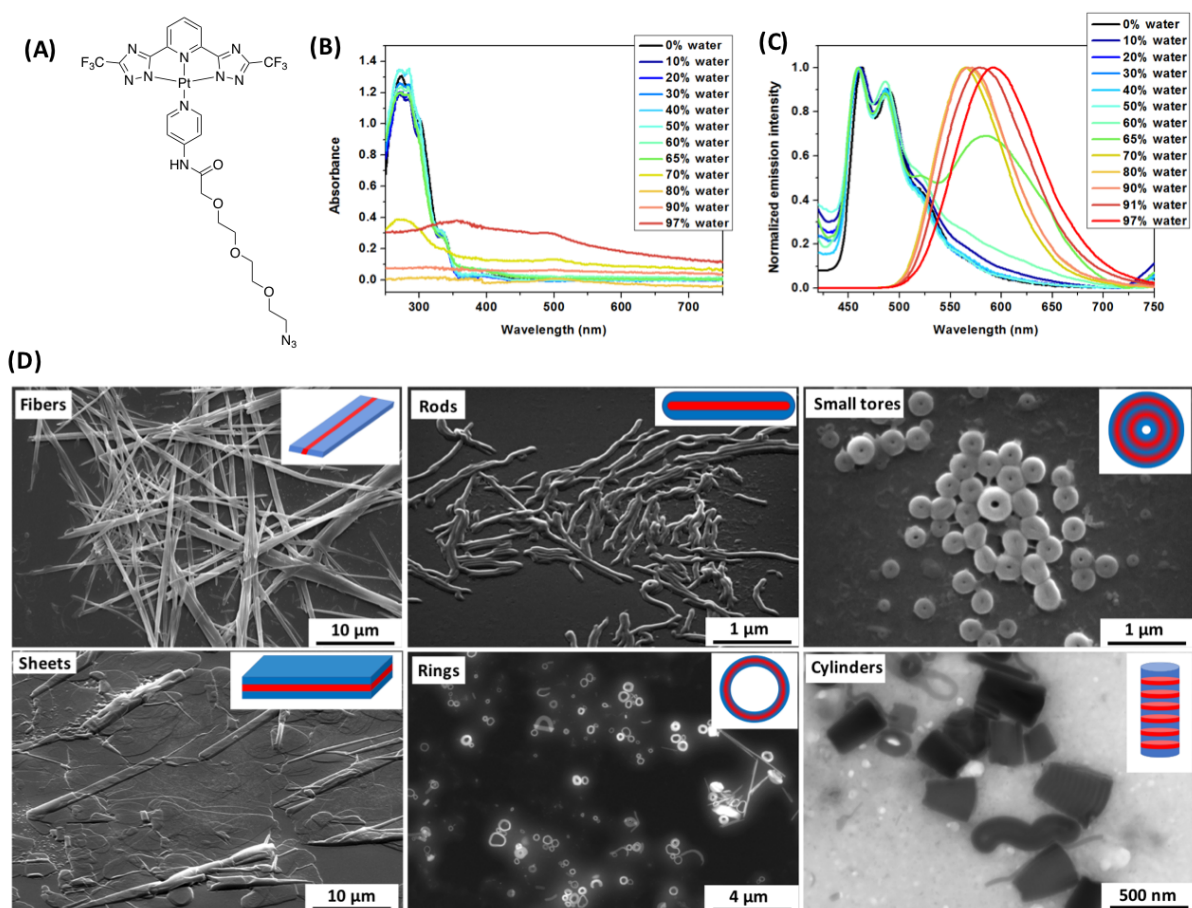


Figure 7. (A) Structure chimique du complexe de platine (II) amphiphile. Spectres d'absorption (B) et d'émission (C) du complexe 7 dans différents mélanges THF/H₂O. Images de (D) microscopie électronique à balayage (MEB) et microscopie électronique à balayage par transmission (MEBT) et représentation schématique des différentes. Dans les représentations schématiques, la partie rouge représente le partie hydrophobe (ligand tridenté) et la partie bleu la partie hydrophile (chaîne polyéthylèneglycolée).

La formation d'agrégats de platine est observée avec la présence de large ³MMLCT band centré approximativement autour de 580 nm dans les spectres d'émission. La teneur critique en eau dans un mélange H₂O/THF est d'environ 65%, 40% pour un mélange dioxane/H₂O et

30% pour un mélange DMF/H₂O. L'eau peut aussi être ajoutée en une fois et l'ordre d'addition dans le solvant organique inversé. En variant les différents paramètres, au moins 6 différentes structures ont été clairement observées par microscopie électronique comme montré en figure **7D** ; fibres, tiges, tores, feuillets, cercles et cylindres. La plupart de ces morphologies ont déjà été rapportées pour différents complexes de platine(II). Cependant, c'est la première fois qu'une telle diversité de morphologies est reportée pour un unique complexe. Les fibres sont facilement obtenues quand la teneur en eau est située entre 60% et 80% dans un mélange H₂O/THF. Tores de différentes tailles sont obtenus quand la teneur en eau est au-dessus de 90. Tiges et cylindres sont obtenues quand l'eau est rapidement ajoutée et que la teneur en eau est au-dessus de 90%. Ces deux morphologies coexistent en solution et sont difficilement séparables. Des agrégats en forme d'éventail peuvent également être observés à côté de cylindres et tiges. Des feuillets et des cercles sont obtenus quand le complexe de platine(II) dans le THF est ajouté lentement à l'eau et la teneur en eau supérieure à 90%. Ces deux morphologies coexistent également en solution. Chaque agrégat possède des propriétés photophysiques spécifiques ce qui les rend uniques. Cette étude est essentielle pour comprendre le comportement de complexe de platine(II) dans un mélange de solvant et permet le contrôle des morphologies et leurs propriétés.

L'auto-assemblage de complexe de platine(II) seul a été reporté de maintes fois dans la littérature²⁻⁶. Chapitre 5 se focalise sur les propriétés d'auto-assemblage de deux complexes dans un mélange H₂O/dioxane. Deux paramètres sont modifiés pour cette étude, le ratio entre les deux complexes et la composition du solvant²². Deux complexes de platine(II) qui s'auto-assemblent en fibres aux propriétés photophysiques différentes sous les mêmes conditions ont été sélectionnés afin de comparer leur co-auto assemblages comme montré en Figure **8**.

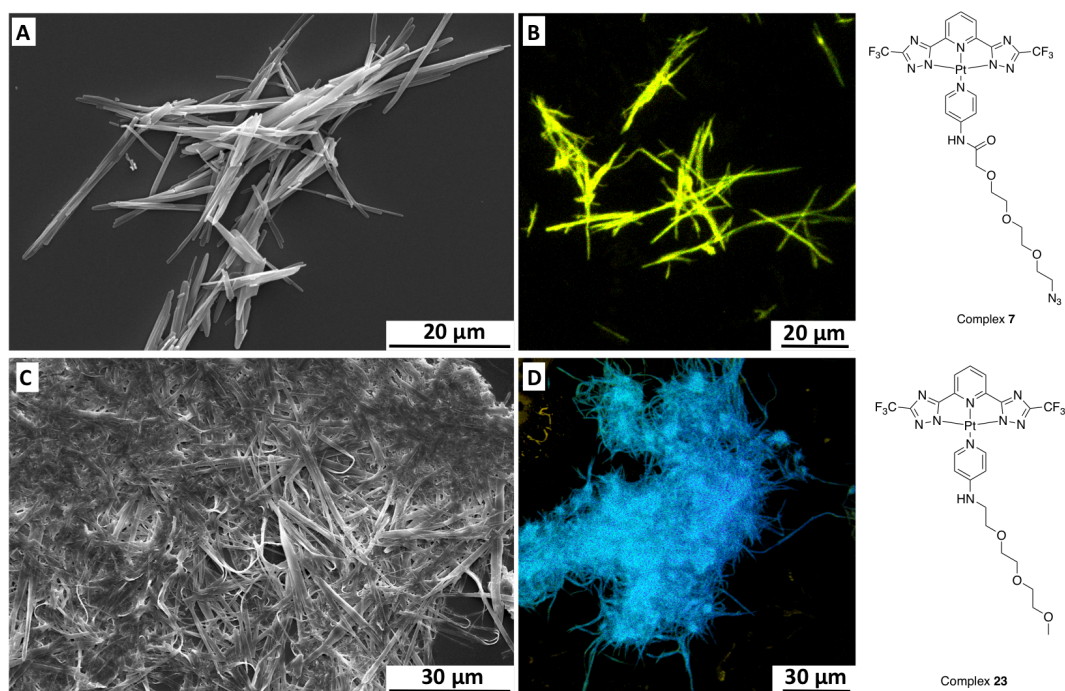


Figure 8. Images de a,c) MEB et b,d) microscopie confocale à fluorescence des fibres formées à partir du complexe 7 et 23 respectivement à une teneur en eau de 80% dans un mélange dioxane/H₂O. $\lambda_{exc} = 405 \text{ nm}$ en lambda mode.

Le résultat le plus important est pour le mélange complexe 23/complexe 7 (1 :0.2) à une teneur en eau de 70% dans un mélange dioxane/H₂O. La solution émet une coloration bleue sous la lampe UV alors que les fibres observées au microscope confocale à fluorescence émettent orange. Le visionnage en temps réel de l'évaporation d'une goutte de solution est montré en Figure 9 et peut être utilisé pour observer le changement de luminescence des fibres. L'émission des fibres est initialement bleu mais change graduellement à l'orange lors de l'évaporation de la goutte. Dans une goutte dioxane/eau, le dioxane s'évapore légèrement plus rapidement que l'eau. Par conséquent, la polarité du solvant augmente parce que la teneur en eau dans la goutte augmente lors de l'évaporation. Le rendement quantique de photoluminescence est augmenté de 23% à 55% and le temps de vie de 450 ns à 550 ns lors de la transition du bleu à l'orange. Le changement de propriétés photophysiques par variation de polarité du solvant est appelé solvatochromisme. Dans ce cas, il s'agit de solvatochromisme positif à cause de l'effet bathochromique dû à l'augmentation de la polarité du solvant.

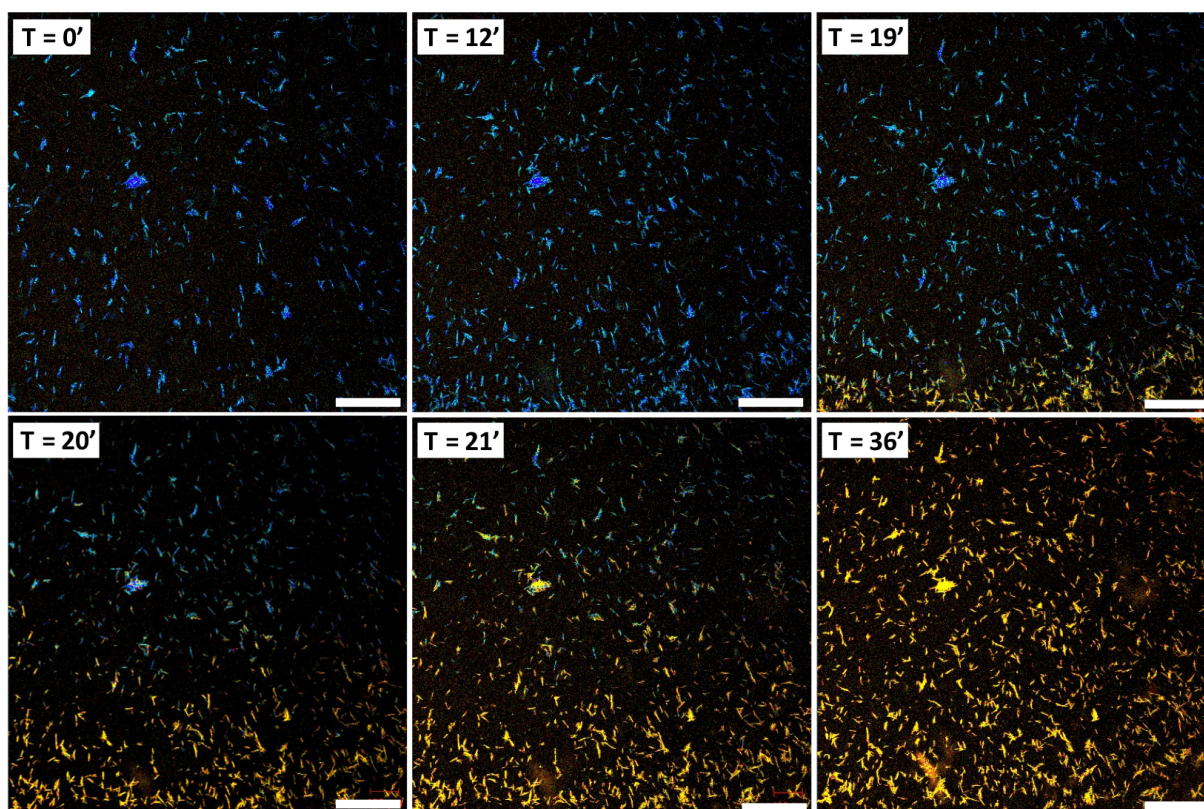


Figure 9. Visionnage en temps réel d'une goutte de solution contenant complexe **27**: complexe **7** (1 :0.2) dans un mélange dioxane/water (teneur en eau 70%). $\lambda_{exc} = 405 \text{ nm}$ (couleurs réelles). échelle : $200 \mu\text{m}$.

La diffraction des rayons X et la diffraction des électrons dans une zone sélectionné montrent clairement un espacement-d de 3.41 \AA et 3.36 \AA respectivement, en accord avec la présence d'interactions platine-platine dans les fibres émettant orange. Il n'y a d'interactions Pt-Pt dans les fibres bleues. Il a été conclu que le changement de polarité du solvant induit un changement cristallographique dans les fibres résultant en nouvelles interactions métalophiliques et changement de luminescence. Il s'agit du premier exemple de changement d'émission sans changement de morphologie. Le changement de luminescence de bleu à l'orange est un phénomène réversible lorsque la teneur en eau est réajustée à 70%. L'auto-assemblage supramoléculaire à une teneur en eau de 60% mène à la formation de fibres de l'ordre du millimètre aux propriétés photophysiques similaires. Pour une teneur en eau de 80%, des fibres bleues recouvertes d'une couche émettant orange sont observées. Dans ce cas, la transition de luminescence n'est pas observée lors de l'évaporation de la goutte.

En conclusion, cette thèse se focalise sur l'étude de différents systèmes de complexes de platine(II). Le design, la synthèse et la caractérisation de plusieurs complexes luminescents aux propriétés photophysiques et d'auto-assemblage intrigantes ont été démontré. Le comportement de ces complexes dans des espaces confinés tels que des particules de polymère ou attachés à des surfaces a été étudiés avec des résultats prometteurs. L'étude méticuleuse des différentes morphologies pour des agrégats de complexe de platine(II) et leurs propriétés photophysiques ont également été étudié. Finalement, le co-auto-assemblage supramoléculaire de deux complexes de platine a été démontré pour la première fois et ouvre la voie à un nouvelle angle de recherche sur l'auto-assemblage d'un système avec plus d'une molécule.

References

1. V. H. Houlding; V. M. Miskowski, *Coord. Chem. Rev.*, **1991**, *111*, 145-152.
2. V. M. Miskowski; V. H. Houlding, *Inorg. Chem.*, **1991**, *30*, 4446-4452.
3. Yam, V. W. W., Wong, K. M. C., Zhu, N. Y. *J. Am. Chem. Soc.* **2002**, *124*, 6506–6507.
4. Po, Charlotte, Anthony Yiu-Yan Tam, Keith Man-Chung Wong, and Vivian Wing-Wah Yam, *J. Am. Chem. Soc.*, **2011**, *133*, 12136-12143.
5. Alessandro Aliprandi, Matteo Mauro, Luisa De Cola, *Nature Chem.* **2016**, *8*, 10-15.
6. Yong Chen, Kai Li, Wei Lu, Stephen Sin-Yin Chui, Chun-Wah Ma, Chi-Ming Che, *Angew. Chem. Int. Ed.*, **2009**, *48*, 9909-9913.
7. Sidharam P. Pujari, Luc Scheres, Antonius T. M. Marcelis, Han Zuilhof, *Angew. Chem. Int. Ed.*, **2014**, *53*, 6322-6356.
8. Yiong Mai, Adi Eisenberg, *Chem. Soc. Rev.*, **2012**, *41*, 5969-5985.
9. D. Xu, E. T. Kang, K. G. Neoh, Yan Zhang, A. A. O. Tay, S. S. Ang, M. C. Y. Lo and K. Vaidyanathan, *J. Phys. Chem. B*, **2002**, *106*, 12508-12516.
10. Deb Kumar Bhowmick, Linda Stegemann, Manfred Bartsch, Naveen Kumar Allampally, Cristian A. Strassert, Helmut Zacharias, *J. Phys. Chem. C*, **2015**, *119*, 5551–5561.
11. Kolb, H. C.; Finn, M. G., Sharpless, K. B., *Angew. Chem. Int. Ed.*, **2001**, *40*, 2004-2021.
12. Samuel J. Adams, David J. Lewis, Jon A. Preece, Zoe Pikramenou, *ACS Appl. Mater. Interfaces*, **2014**, *6*, 11598–11608.
13. Hannu Häkkinen, *Nature Chem.*, **2012**, *4*, 443-455.
14. Mei-Jin Li, Xing Liu, Mei-Juan Nie, Zhao-Zhen Wu, Chang-Qing Yi, Guo-Nan Chen, Vivian Wing-Wah Yam, *Organometallics*, **2012**, *31*, 4459–4466.

15. Manuel Macias-Montero, A. Nicolas Filippin, Zineb Saghi, Francisco J. Aparicio, Angel Barranco, Juan P. Espinos, Fabian Frutos, Agustin R. Gonzalez-Elipe, Ana Borrás, *Adv. Funct. Mater.*, **2013**, *23*, 5981–5989.
16. Ana Borrás, Myriam Aguirre, Oliver Groening, Carlos Lopez-Cartes, Pierangelo Groening, *Chem. Mater.*, **2008**, *20*, 7371–7373.
17. Damiano Genovese, Alessandro Aliprandi, Eko A. Prasetyanto, Matteo Mauro, Michael Hirtz, Harald Fuchs, Yasuhiko Fujita, Hiroshi Uji-I, Sergei Lebedkin, Manfred Kappes, Luisa De Cola, *Adv. Funct. Mater.*, **2016**, *26*, 5271–5278.
18. 20. Nijuan Liu, Baoyan Wang, Weisheng Liu and Weifeng Bu, *Chem. Commun.*, **2011**, *47*, 9336–9338.
19. 21. N. Liu, Q. He, W. Bu, *Langmuir*, **2015**, *31*, 2262–2268.
20. Mark Wrighton, David L. Morse, Wrighton, M.; Morse, D. L., *J. Am. Chem. Soc.*, **1974**, *96*, 998–1003.
21. Zhang, L., Eisenberg, A., *Science* **1995**, *268*, 1728-1731
22. Kaka Zhang, Margaret Ching-Lam Yeung, Sammual Yu-Lut Leung, Vivian Wing-Wah Yam, *Chem* **2**, **2017**, 825–839.

Chapter 1

Introduction

Abstract: This chapter introduces the basic concepts of photophysics and the interaction between light and matter. The primary focus will be on the photophysical properties of d^6 and d^8 transition metal, and particularly platinum(II) complexes, which will be discussed in this chapter. The self-assembly of platinum(II) complexes into supramolecular architectures and their properties will also be highlighted. Finally, a brief discussion of polymer and surface functionalization will also be introduced in this chapter.

1.1. Interaction between light and matter¹⁻⁵

Light is the main source of energy for living organisms on earth. It provides the driving force for photosynthesis, which is the first step in the storage of energy that can be available for physiological processes. Understanding how light can be absorbed, produced, or transformed in chemical species in assembled components is a major objective of numerous scientists from different disciplines.

Light consists of electromagnetic waves, which are synchronized oscillations of electric and magnetic fields. The oscillation of the two fields are perpendicular to each other, and perpendicular to the direction of the wave. The resulting electromagnetic spectrum and the corresponding interactions with matter are depicted in Figure 1.1.

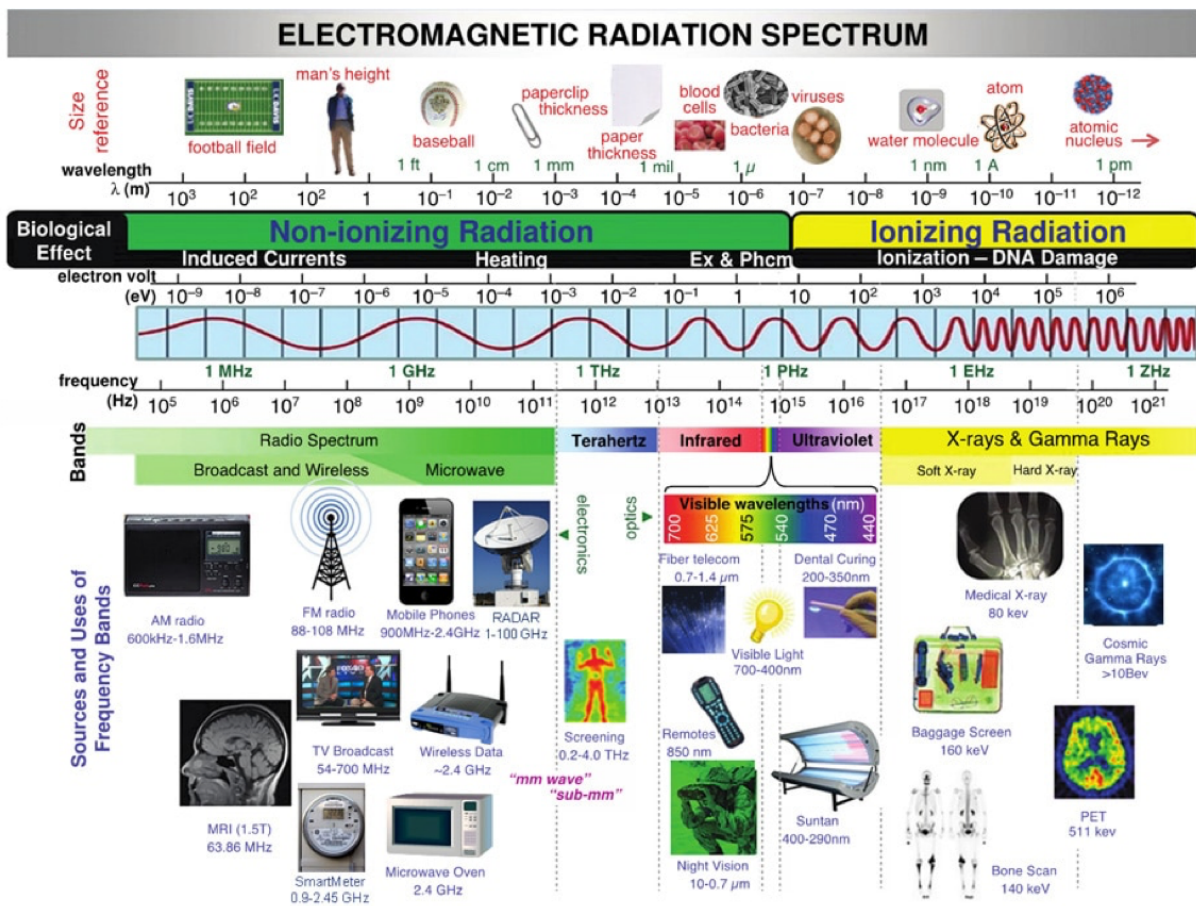


Figure 1.1. Electromagnetic magnetic spectrum showing the different types of electromagnetic radiation in terms of wavelength and frequency. The UV-visible region is where photochemistry takes place.

The interaction of light with matter as a natural phenomenon and/or as an artificial process permeates most branches of science, from biology to materials science. For example, photosynthesis is a process used by plants and other organisms to convert light energy into chemical energy that can later be released to fuel organisms' activities. Solar energy consists of radiant light and heat from the sun. Moreover, it is an important source of renewable energy that is being harnessed using photovoltaic systems. Its' energy is artificially converted into a useful energy form via photophysical and photochemical processes.

Most molecules have higher energy excited electronic states in addition to the ground electronic state. These states are the result of the promotion of one of the electrons from the occupied orbital in the ground state to a vacant higher energy orbital.

The excitation of an electron from the occupied orbital to a higher energy orbital occurs when a photon with energy that matches the difference between the two states interacts with the molecule (Figure 1.2).

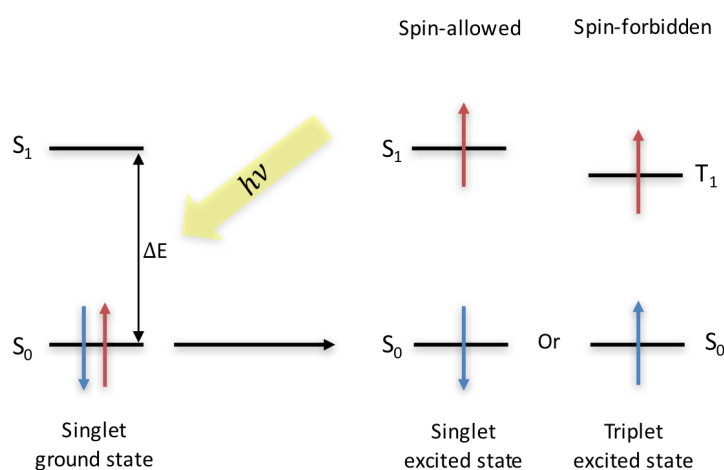


Figure 1.2 Schematic representation of state diagram. Each state is indicated by the energy of the lowest vibrational level.

$$\Delta E = h\nu \quad \text{(eq. 1.1)}$$

where,

ΔE = Energy difference between the two levels (J)

h = Planck constant ($6.62607004 \times 10^{-34}$ J.s)

ν = frequency of the radiation (s^{-1} or Hertz)

The frequency can be converted into wavelength, since:

$$\nu = \frac{c}{\lambda} \quad (\text{eq. 1.2})$$

Where,

c is the velocity of the light (299,792,458 m.s⁻¹ exactly)

λ is the wavelength of the radiation (m)

Eq.s (1.1) and (1.2) correlate the energy difference and the wavelength of the radiation required for the promotion of an electron:

$$\Delta E = \frac{hc}{\lambda} \quad (\text{J}) \quad (\text{eq. 1.3})$$

$$\Delta E = N_A \frac{hc}{\lambda} \quad (\text{J.mol}^{-1}) \quad (\text{eq. 1.4})$$

Where,

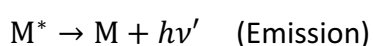
N_A is the Avogadro constant (6.022,136,7(36) x 10²³ mol⁻¹)

Each electron in a molecule carries a spin angular momentum with a spin quantum number $s = \frac{1}{2}$. In the presence of a magnetic field, and electrons of the molecule have a magnetic moment. The magnetic moment can be aligned in the direction of the lines of force of the applied magnetic field or opposed to it, giving rise to two different energy states of the electron. The electron possesses a “spin-up” or “spin-down” property, which is indicated by the use of arrows, \uparrow or \downarrow . The arrows represent the alignment of the electron magnetic moment with respect to the applied magnetic field. The total spin angular momentum possessed by all the electrons of an atom or a molecule is represented by the total spin quantum number S . Two electrons each possessing $s = \frac{1}{2}$ may be present with their spins parallel or opposed. If the spins are opposed ($\uparrow\downarrow$), the total spin quantum number S is equal to zero ($S = \frac{1}{2} + (-\frac{1}{2}) = 0$). If the spins are parallel ($\uparrow\uparrow$ or $\downarrow\downarrow$), the total spin quantum number is equal to 1 ($S = \frac{1}{2} + \frac{1}{2} = 1$). The spin multiplicity generates the number of states expected in the presence of magnetic field, which is given by $2S+1$. Thus, if a molecule with all electrons are spin-paired, $S=0$ and the spin multiplicity will be equal to 1. This electronic state will be

referred to as a singlet state S_0 . The promotion of one electron from the ground state to the excited state (without any changes in the electron spin), results in the total spin quantum number being equal to 0 and the excited state will be a singlet state S_1 . If the promotion of one electron from the ground state to the excited state is coupled with a change in the spin of the electron, it then becomes aligned with the electron of the ground state, $S = 1$ and therefore it will have a spin multiplicity of 3. The excited state is now referred to as a triplet state abbreviated T_1 .

The excited triplet state usually has a lower energy than the excited singlet state. In essence, when two unpaired electrons occupy different orbitals there is a minimum energy of electron-electron repulsion when their spin is parallel. This repulsion energy determines the energy difference between the excited singlet state and triplet state.

What is the fate of an electronically excited molecule? A molecule at its excited state possesses an extra energy $h\nu$ and can not persist in an excited state indefinitely, since it represents an unstable situation with respect to the ground state. Note that an excited molecule can be considered as a new chemical species. Thus, generally the chemical and physical properties differ between the molecule at its excited state and the molecule at its ground state. Electron de-excitation must somehow occur, with the excess energy being released as thermal or radiation energy.



Where,

M is the molecule at its ground state (S_0)

$h\nu$ is the energy of the exciting photon

$h\nu'$ is the energy of the emitted photon

M^* is the molecule in an electronically excited state

The Franck-Condon principle states that because the rearrangement of electrons is considerably faster than the motion of nuclei, the nuclear configuration does not change significantly during the energy absorption process (Born-Oppenheimer approximation). Thus,

the absorption or emission of molecules is characterized by the vertical excitation energies (Franck-Condon principle, Figure 1.3).

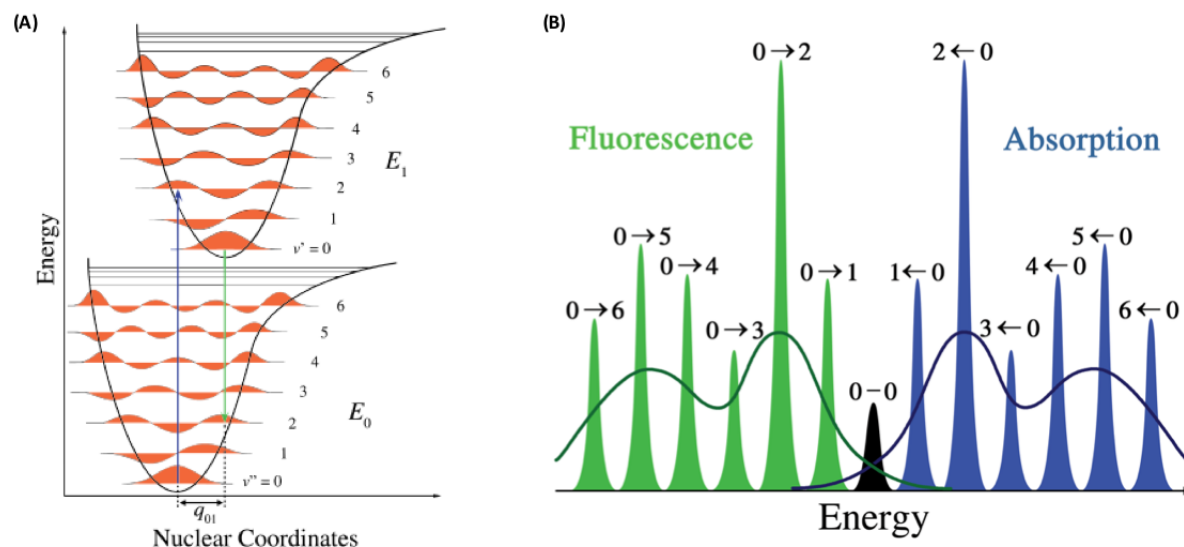


Figure 1.3. (A) Franck-Condon principle energy diagram. Vibrational levels are favored when they correspond to a minimal change in the nuclear coordinates. The potential wells are shown favoring transitions between $v = 0$ and $v = 2$. (B) The narrow line scan is usually only observed in the spectra of dilute gases. The darker curves represent the inhomogeneous of the same transitions that occur in liquids or solids.

The ground state (E_0) supports numerous vibrational energy levels. At room temperature, only the lowest vibrational level is populated, and electronic transitions originate from the $v''=0$ vibrational level. The bound excited state (E_1) also supports several vibrational levels. However, because the excited state potential energy curve is typically shifted, the vertical excitations from the lowest vibrational level of the ground electronic state take the system into one of several vibrational levels of the excited electronic state.

Vibronic transitions are the simultaneous changes in electronic and vibrational energy levels of a molecule due to the absorption or the emission of a photon at the appropriate energy.

The principle also states that during an electronic transition, a change from one vibrational energy level to another is more probable to occur if the two vibrational wave functions overlap more significantly. The spectra of molecules in solvents that interact strongly with the chromophore are broad and often featureless.

Relaxation to the ground state can occur via both radiative and non-radiative processes. The various transitions involving electronic states of similar or different spin multiplicities are represented in the Jablonski diagram⁶ (Figure 1.4).

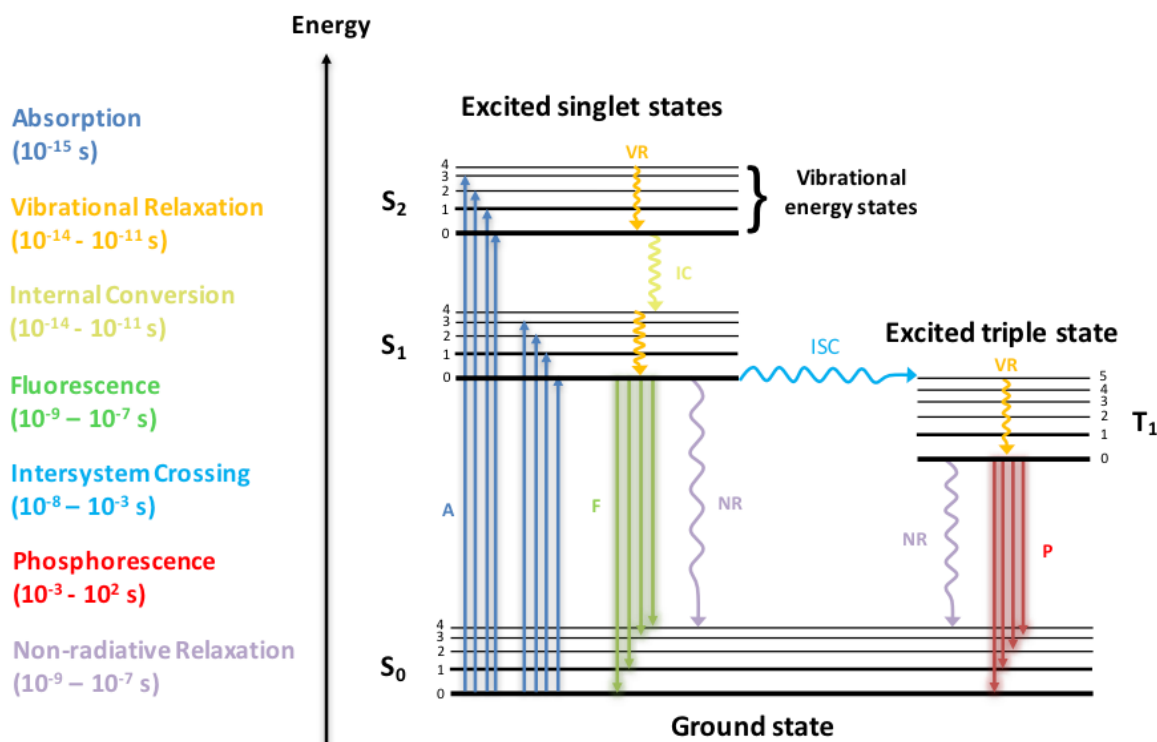


Figure 1.4. Jablonski diagram showing the excitation of a molecule from the ground state and all the radiative and non-radiative processes that can occur during its relaxation. Straight lines indicate radiative processes, whereas wavy lines denote non-radiative transitions.

Upon interaction with the light, a molecule can be promoted from the lowest electronic state S₀ (Kasha's rule) to an excited electronic state. Due to spin selection rules, the excited state that is reached generally has the same spin multiplicity as the ground state, typically a singlet-singlet transition.

This event can occur in the femtosecond time scale (10⁻¹⁵s). Absorption of a photon leads to the population of the matching vibronic state. Then, the vibrational relaxation (VR) to the lowest vibrational state is followed by internal conversion (IC) to the lowest singlet state (S₁). The radiative relaxation between the lowest excited state and one vibronic state of ground state is called fluorescence, which occurs with conservation of electronic spin (10⁻⁷ - 10⁻⁹ s). As the equilibrium geometry of the molecule in the lowest excited state and the surrounding environment may differ from the Franck Condon state reached upon absorption of light, a

shift in the emission is observed as compared to the absorbed light (Stokes shift). When an electron in a molecule with a singlet ground state is excited to a higher energy level, an excited singlet state or an excited triplet state will form. A singlet state is a molecular electronic state where all electron spins are paired. In essence, the spin of the excited electron is still paired with the ground state electron (Pauli exclusion principle). In a triplet state, the excited electron is no longer paired with the ground state electron; they are parallel and have the same spin. Since excitation to a triplet state involves an additional forbidden spin transition, it is less probable that a triplet state will form when the molecule absorbs radiation.

Nonetheless, spin-orbit coupling (SOC) can overcome the selection rule as the flip of the electronic spin is coupled to a change of the orbital angular moment (El-Sayed's rules). The size of the interaction between the electron spin and orbital motions depends on the fourth power of the atomic number. In particular, heavy molecules, such as transition metals, can induce SOC very efficiently. The time scale of ISC is on the order of 10^{-8} to 10^{-3} s, one of the slowest forms of relaxation.

The radiative relaxation from an excited triplet state back to a singlet state is known as phosphorescence. However, if the SOC is strong enough, singlet and triplet states can be mixed leading to excited states with partial singlet and triplet characters. In this case, the emission is referred to as "luminescence". Finally, the molecule in an excited state (S_1 or T_1) can undergo non-radiative relaxation in which the excitation energy is dissipated as heat to the solvent. Non-radiative relaxation can also occur through interaction with a second molecule via fluorescence quenching. For example, the molecular oxygen (O_2) is an extremely efficient quencher of fluorescence because of its unusual triplet ground state.

If we consider the fluorescence of the S_1 state of a molecule to be in direct competition with internal conversion and intersystem crossing, then the rate of decay is given by

$$-\frac{d}{dt}[M^*] = k_f^0[M^*] + k_{ISC}[M^*] + k_{IC}[M^*] \quad (\text{eq. 1.5})$$

Where,

k_f^0 is the natural fluorescence rate coefficient (s^{-1})

k_{ISC} is the rate coefficient for intersystem crossing (s^{-1})

k_{IC} is the rate coefficient for internal conversion (s^{-1})

$[M^*]$ is the concentration of electronically excited molecule

The deactivation of the excited states follows a first order kinetics and the lifetime of the excited states (S_1 or T_1) are defined as the reciprocal of the radiative and non-radiative rate coefficients.

$$[M^*] = [M^*]_0 e^{-k_f t}, \quad k_f = k_f^0 + k_{ISC} + k_{IC} \quad (\text{eq. 1.6})$$

Where,

k_f is the sum of all the possible pathways by which M^* may be deactivated

The measured fluorescence lifetime is thus given by

$$\tau_f(S_1) = \frac{1}{k_f} = \frac{1}{\sum k_i} = \frac{1}{k_f^0 + k_{ISC} + k_{IC}} \quad (\text{eq. 1.7})$$

In a similar way, the measured phosphorescence lifetime is given by

$$\tau_p(T_1) = \frac{1}{k_p + k'_{ISC}} \quad (\text{eq. 1.8})$$

The photoluminescence quantum yield (PLQY) is known to be another crucial parameter, used to measure the efficiency of various photo-induced pathways. The PLQY (Φ) can be defined as the ratio between the emission and the absorption by a molecule. In fact, it is directly related to the ratio between the rate coefficient of the radiative photophysical pathway and the sum of all the radiative and non-radiative photo-induced pathways:

$$\Phi_f = \frac{k_f}{k_f + k_{ISC} + k_{IC}} \quad (\text{eq. 1.9})$$

Where,

Φ_f is the fluorescence quantum yield

Substitution of eq. (1.7) into (1.9) gives

$$\Phi_f = k_f \tau_f \quad (\text{eq. 1.10})$$

The phosphorescence quantum yield depends on the product of the rate coefficients for intersystem crossing and for phosphorescence from the triplet state, divided by the product of the sums of the rate coefficients for all the photo-induced deactivation pathways of both the singlet and triplet states. The quantum efficiency (η_{ISC}) is thus introduced as

$$\eta_{ISC} = \frac{k_{ISC}}{k_f + k_{ISC} + k'_{IC}} = k_{ISC} \tau_f \quad (\text{eq. 1.11})$$

$$\Phi_p = \frac{k_p}{k_p + k'_{ISC}} k_{ISC} \quad (\text{eq. 1.12})$$

Where,

Φ_p is the phosphorescence quantum yield

The value of Φ and η_{ISC} can vary from 0 to 1. By knowing the excited state lifetime and the quantum yields, it is possible to calculate the radiative and non-radiative decay constants.

$$k_r = \frac{\Phi}{\tau} \quad (\text{for fluorescence } k_r = k_f \text{ and for phosphorescence } k_r = k_p) \quad (\text{eq. 1.13})$$

$$k_{nr} = \frac{1-\Phi}{\tau} \quad (\text{for fluorescence } k_{nr} = (k_{IC} + k_{ISC}) \text{ and for phosphorescence } k_{nr} = (k_{IC} + k'_{ISC})) \quad (\text{eq. 1.14})$$

1.2. Transition metal complexes

Transition metal complexes (TMCs) have attracted a great deal of attention because of their peculiar photophysical properties and redox properties⁷⁻²⁰. They have been studied and applied in many fields from bio-sensing²¹, bio-imaging²², photo-catalysis²³⁻²⁵,

electrochemiluminescence^{26,27} and energy conversion²⁸. They have also been used as active materials in organic light emitting diodes (OLEDs), light emitting electrochemical cells (LEECs)²⁹⁻³⁵, spin-cross over (SCO)³⁶, and dye sensitized solar cells (DSSCs)³⁷. Transition metal complexes are more appealing compared to general fluorescent organic molecules due to generally having longer excited state lifetimes, a high photoluminescence quantum yield and a large Stokes shift. Nevertheless, the first row transition metal complexes cannot be used for this purpose as their low lying d-d states are thermally accessible leading to fast non-radiative deactivation. Our interest is focused on the second and third row transition metals with d^6 , d^8 and d^{10} electronic configuration such as Ru(II), Os(II), Ir(II), Re(I), Pt(II), Pd(II), Ag(I) and Au(I). As mentioned previously, the presence of heavy metal atoms coupled with a judicious choice of metal ions and ligands, leads to strong spin-orbit coupling (SOC). As a result, the luminescent compounds show promising and tunable photophysical properties from UV to near infra-red (NIR) from both singlet and triplet states. The mixed nature of the luminescent state emission can in some cases approach 100%.

1.2.1. Crystal field theory and ligand field theory^{38,39}

In order to describe the various spectroscopies of transition metal coordination complexes, physicists Hans Bethe and John Hasbrouck Van Vleck developed the Crystal Field Theory (CFT). The theory describes the disintegration of degeneracies of electron orbital states, usually d or f orbitals, due to the static electric field produced by the neighboring charge distribution. According to CFT, an octahedral metal complex forms because of the electrostatic interactions of a positively charged metal ion with a six negatively charged ligand. The lowest energy-arrangement of six identical negative charges is an octahedron, which minimizes repulsive interactions between the ligands (Figure 1.5). The five d-orbitals of free metal ions are initially degenerate, so they have the same energy. In a ligand field, if six negative charges are uniform over the surface of a sphere, the energy of all five d orbitals rises due to repulsive electrostatic interactions between the negative charges and electrons in the d orbitals. The five d orbitals split into two sets of orbital energy levels. The d_z^2 and $d_{x^2-y^2}$ orbitals (called e_g orbitals) point directly at the six negative charges located on the x, y and z axes.

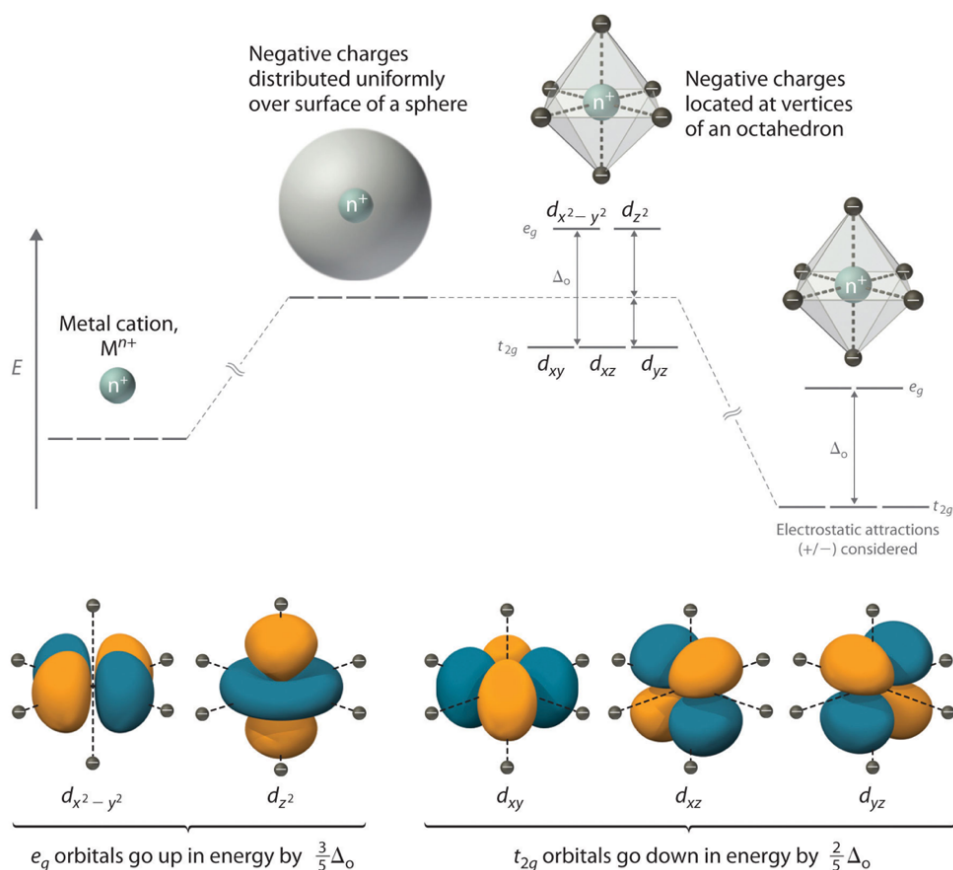


Figure 1.5. Splitting of the five degenerate d-orbitals of a transition metal ion in the presence of a crystal field for octahedral complexes

Consequently, the energy of an electron in these two orbitals will be greater than the initial energy. In contrast, the three other orbitals (d_{xy} , d_{xz} , d_{yz} , collectively called t_{2g} orbitals) are oriented 45° angle to the axes so they point between the six negative charges. The energy of an electron in these three orbitals is lower than the initial energy. The energy difference between the two sets of orbitals is called the crystal field splitting energy (Δ_o). It is important to note that the splitting of the d orbitals does not change the total energy.

Tetragonal and square planar geometry can be correlated to distorted octahedral complexes. Moving the two axial ligands away from the metal ion along the z axis initially generates an elongated octahedral complex (center) and eventually produces a square planar complex (right) (Figure 1.6). As shown in the below the structures, an axial elongation causes the z-component orbitals (d_{z^2} , d_{xz} and d_{yz}) to decrease in energy and the $d_{x^2-y^2}$ and d_{xy} orbitals to increase in energy. Nevertheless, the change in energy is not the same for all five d orbitals.

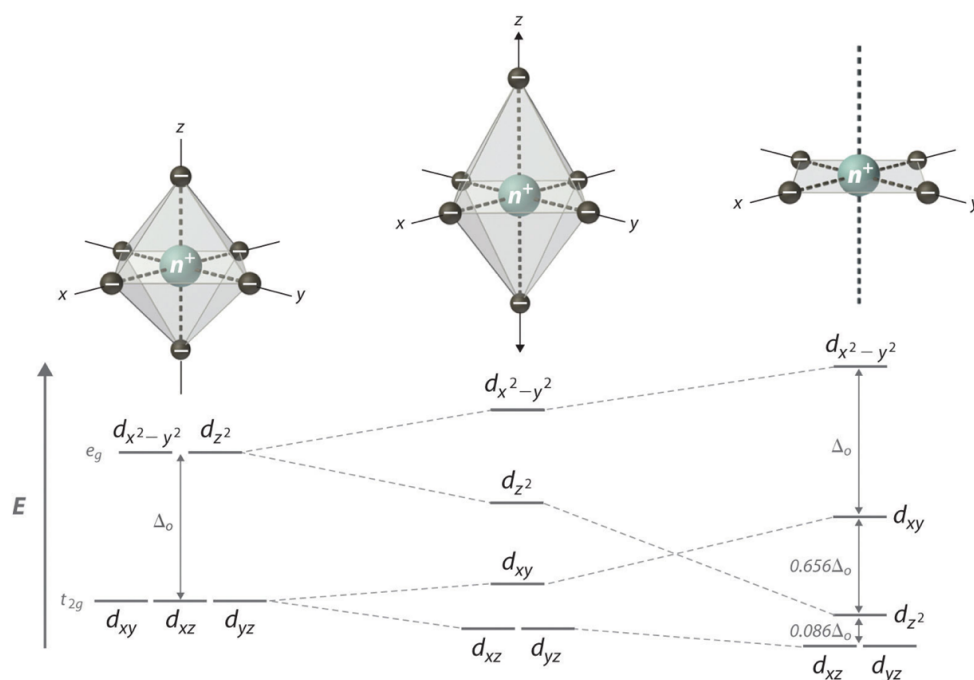


Figure 1.6. Energy level splitting diagram of the five degenerate d-orbitals of a transition metal ion in the presence of a crystal field for tetrahedral and square planar complexes.

Removing the two axial ligands results in the energy of the d_{z^2} orbital to decrease significantly, so that the order of the d_{z^2} and d_{xy} orbitals is reversed. However, the CFT provides only a simple conceptual model; it treats ligands as point charges or dipoles and does not take into account the overlap of ligand and metal atom orbitals. A more thorough approach is given by the Ligand-Field Theory (LFT),³⁸ which is an application of Molecular Orbital Theory (MOT). In fact, the LFT describes the molecular orbitals of a d-metal complex as being similar to polyatomic molecules. The metal and ligand valence orbitals generally form symmetry-adapted linear combinations and the relative energies of the molecular orbitals are then estimated by using empirical energy and overlap considerations.

In order to comprehend the photochemical processes that involve both d^6 and d^8 , it is important to briefly describe what happens upon excitation of the system.

d^6 Metal Complexes

Figure 1.7 depicts the interactions between orbitals of the metal ion and coordinated ligands for an octahedral geometry. If a metal is coordinated by conjugated ligands, the set of s, p and d orbitals of the metal are mixed with symmetry-adapted orbitals from the ligands. Upon

optical excitation, electronic transitions between the different orbitals can occur and such processes can be described as electron density redistributions between part of the molecules, where filled and virtual orbitals with a certain nature are located. These orbitals can be classified according to the contributions.

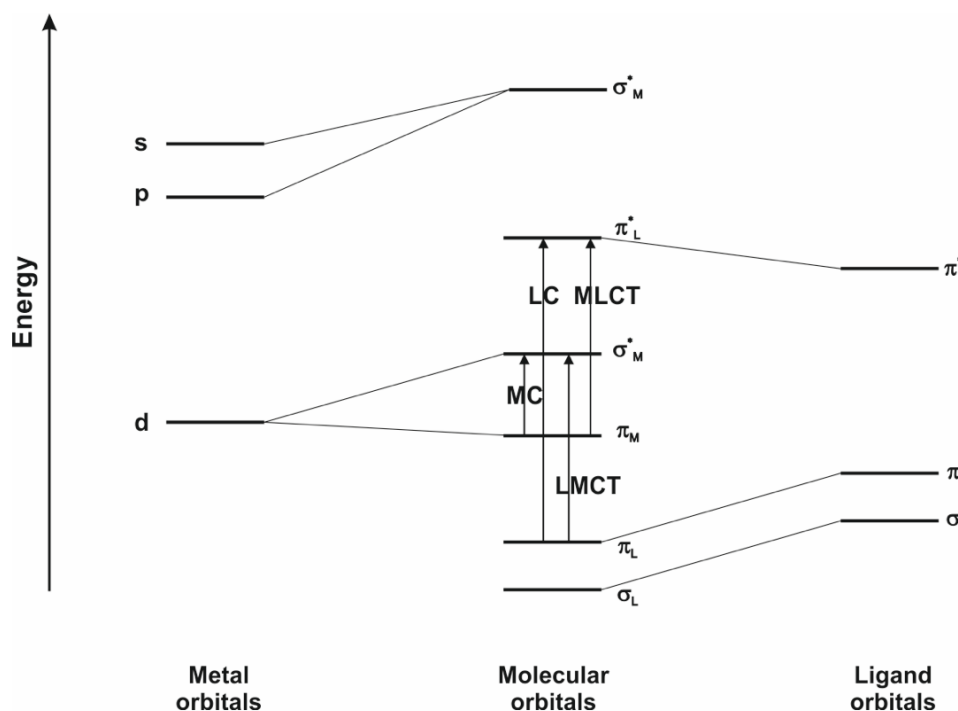


Figure 1.7. Simplified MO diagram for an octahedral transition metal complex and relative spectroscopic excitation transitions. M stands for metal and L for ligands.

σ_L : strongly bonding, predominantly ligand-centered (σ -MOs);

π_L : bonding, predominantly ligand-centered (π -MOs);

π_M : non-bonding, predominantly metal-centered (π -MOs of t_{2g} symmetry);

σ_M^* : antibonding, predominantly metal-centered (σ -MOs of e_g symmetry)

π_L^* : bonding, predominantly ligand-centered (π -MOs);

σ_M^* : strongly antibonding, predominantly metal-centered (σ -MOs of e_g symmetry)

There are essentially four possible types of excited states, named after the comparison of their electronic configuration with the one of the ground state:

MC: Metal Centered states, mainly involving d-orbitals, occupied non-bonding orbital $\pi_M(t_{2g})$ and anti-bonding unoccupied $\sigma_M^*(e_g)$ orbitals. Deactivation to the ground state occurs through

a non-radiative pathway, as the equilibrium geometry of the excited state strongly differs from the ground state due to the placement of electron density in the anti-bonding orbitals.

LC: Ligand Centered mainly involving occupied bonding orbital (π_L) and unoccupied anti-bonding orbital (π_L^*) located on the ligands. These states are also known as intra-ligand states, and can have also charge transfer character such as inter-ligand or ligand-to-ligand charge transfer (ILCT or LLCT).

MLCT: Metal to Ligand Charge Transfer state, mainly involving occupied metal centered bonding orbitals (π_M) and unoccupied ligand centered anti-bonding orbitals (π_L^*).

LMCT: Ligand to Metal Charge Transfer, mainly involving occupied ligand centered bonding orbitals (π_L) and unoccupied metal centered anti-bonding orbitals (σ_M^*).

The relative energies of these states depend on many factors. For example, if the size of the metal increases, the interaction of d-orbitals with the ligand orbitals is more effective, so the MC states are pushed to higher energy levels. In a similar way, oxidation state of the metal center, type, strength and substitution of ligands (electron donating or withdrawing groups) alter the character and energy of the state. According to the perturbation theory, the character of two states can be mixed in nature, leading to new states (mixing of states by configuration interaction or spin orbit coupling).

d⁸ Metal Complexes

Metal ions with d⁸ electronic configuration, such as Pd(II), Pt(II), Au(II), Ir(I) and Rh(I) usually form square planar complexes irrespective of the strength of the ligands.

Most of the work reported in this thesis is based on Pt(II) complexes. Hence, from here onwards, only the d⁸ configuration is considered for Pt(II) complexes. Figure 1.6 shows the simplified splitting of the degenerate d orbitals in the presence of a square planar ligand field. Considering that the d_{z^2} orbital is more destabilised than d_{xy} , a plausible MO diagram is shown in Figure 1.8.

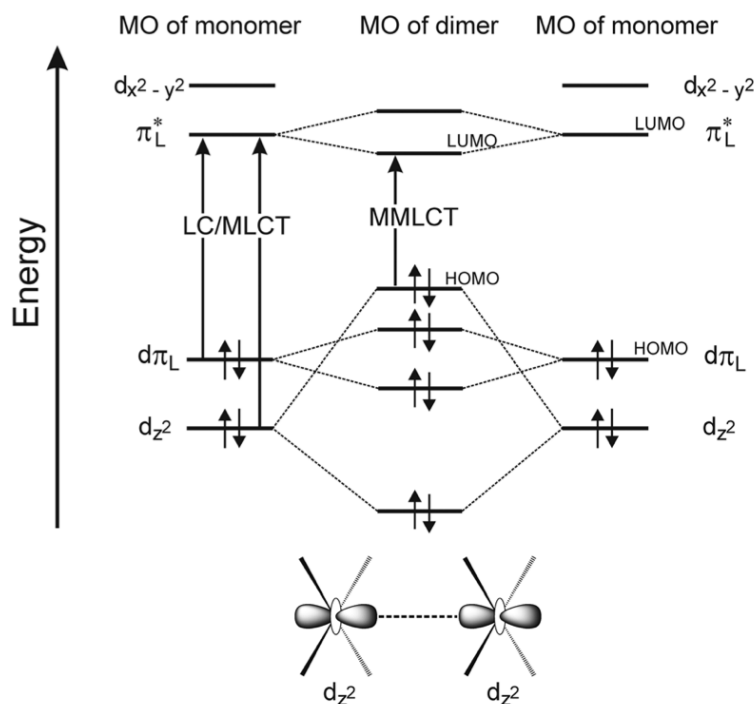


Figure 1.8. Simplified MO diagram for a Pt(II) square planar complex showing intermolecular d_{z^2} orbital overlap in the ground state and its influence on energy of the MOs d_{z^2} .

Platinum (II) square planar complexes are generally 16 valence electron systems (8 electrons from the metal center and 8 electrons from the ligands). Generally, for the monomeric form of the complex, the d_{z^2} orbitals lie below the HOMO, which is mainly constituted by bonding orbitals of the ligand (π_L). The LUMO is also mainly ligand centered with main contributions from the anti-bonding orbitals of the ligands (π_L^*). The relative energy levels of MLCT and LC states depend on the energy gap between the HOMO (d_{z^2}, π_L) and LUMO (π_L^*) of the orbitals involved in the electronic configuration of the excited state. For instance, in Figure 1.8, the lowest electronic transition is LC, as mainly HOMO (π_L) and the LUMO (π_L^*) are involved in the change of electronic configuration with respect to the ground state. If the energy gap between the MC (d orbitals of the metal) and the lowest excited state is comparable to kT (k is the Boltzmann constant and T is the temperature in kelvin), it can be deactivated non-radiatively as shown in Figure 1.9.

On the basis of the LFT, for a metal center set in a square planar geometry of the coordinating ligands, relaxation of the degeneracy of the d orbitals leads to a filled d_{z^2} orbital normal to

the plane of the molecule. This filled orbital may weakly interact with the ligands coordination sphere, and energetically lies below the HOMO level.

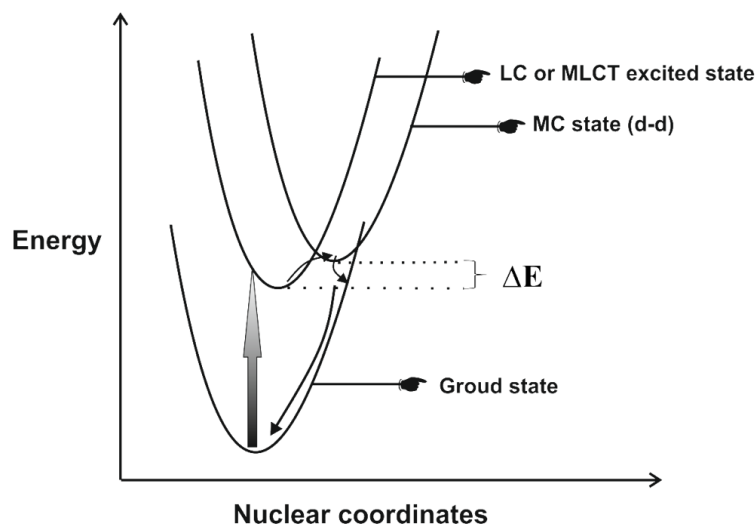


Figure 1.9. Potential energy surface of the d-d excited state in Pt(II) complexes is displaced relative to the ground state, owing to the strong antibonding character of the $d_{x^2-y^2}$ orbital that is populated. The d-d transition (MC state) can provide a thermally activated pathway of non-radiative decay. The thick arrow represents the absorption of light and the thin ones represent IC, ISC and VR processes.

The exposure of the metal center and its d_{z^2} orbital to the surrounding environment, (for example, solvent molecules or neighboring platinum(II) complexes) when aggregation occurs, enables electronic coupling⁴⁰⁻⁴⁹. Aggregation can be enhanced or supported by extended π -conjugation of the coordinating ligands and the absence of bulky ligands. In the latter case, the formation of such ground-state metallophilic interactions through the free axial position destabilizes the filled d_{z^2} orbitals, leading to the splitting of d-orbitals upon Pt \cdots Pt interaction, typically for intermetallic distances between $<3.5 \text{ \AA}$. As a result, the nature of the HOMO is changed from $d\pi_L$ to d_{z^2} orbital. Conversely, the splitting of the $d\pi_L^*$ renders a stabilized LUMO in the aggregated species. Due to the new Pt \cdots Pt interaction, new excited-states are formed such as Metal-Metal-to- Ligand Charge transfer (MMLCT) and Ligand-to-Metal-Metal Charge transfer (LMMCT) which appears stabilized compared to the MLCT of the monomeric species (Figure 1.8). The non-radiative deactivation via MC states is therefore avoided, as the lowest lying excited state is stabilized when compared to ground state.

Two closed-shell metal cations, *e.g.* Pt(II), would generally be expected to repel each other. However, the attractive interactions between closed shell metal ions have been increasingly studied and are often referred as to metallophilic interactions⁴⁹.

The best evidence for these metallophilic interactions has been found in the solid state where structural data obtained by X-ray diffraction provides precise information about the distance between the metals involved. Metallophilic interactions involving d^{10} ions,⁵⁰⁻⁵³ d^8 ions,⁵⁴⁻⁵⁷ or the combination of both in heterometallic systems⁵⁸⁻⁶¹ have been reported in the last decade. Numerous theoretical studies on metallophilic interactions continue to be carried out at various levels, which take into account relativistic and correlation effects to describe these van der Waals-type interactions^{62,63}. The strength of such metallophilic interactions has been compared to that of hydrogen bonding ($7-11 \text{ kcal.mol}^{-1}$)⁵¹ which is strong enough to be used for the preparation of supramolecular structures.

1.3. Classes of platinum(II) complexes

Several classes of Pt(II) complexes have been explored, namely bidentate ($N^{\wedge}N$), tridentate ($N^{\wedge}N^{\wedge}N$) and cyclometalated (bi and tridentate) compounds (Figure 1.10).

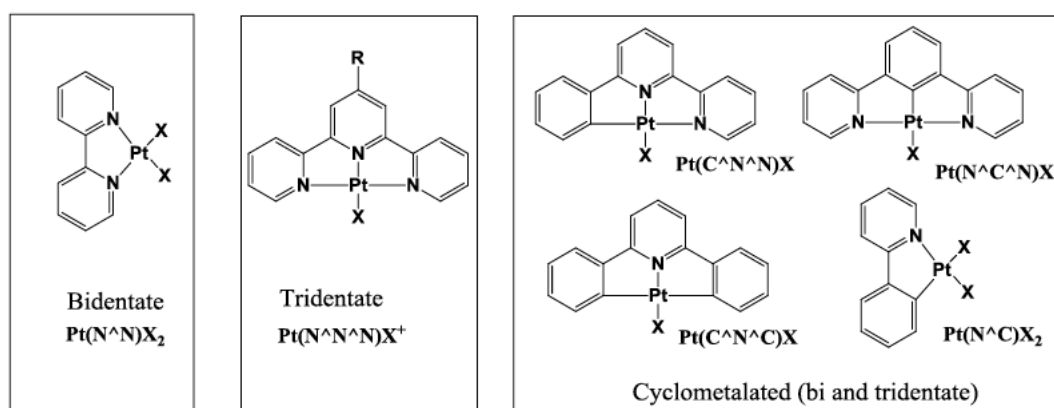


Figure 1.10. Chemical structures of the different classes of platinum(II) complexes.

Bidentate $Pt(N^{\wedge}N)X_2$ complexes have been studied to tune the photophysical properties by changing two different types of ancillary ligands, namely monodentate ligands⁶⁴⁻⁶⁶ ($X = Cl^-$, CN^- , SCN^- , NCO^- and acetylide) or bidentate ligands^{64,67} (acetylacetonato (acac), ethylenediamine(en) and tolan-2,2-diacetyl (tdaH₂). The advantage of bidentate ancillary ligands over monodentate ligands is that the non radiative deactivation can be reduced by the

enhancement of rigidity which results in longer lifetimes and higher photoluminescence⁶⁷. Conversely, one of the potential advantages of tridentate ligand over bidentate ligands is the inhibition of the D_{2d} distortion that bis-bidentate complexes can undergo, for example, the twisting of the two coordination planes relative to one another. The first terpyridine based Pt(II) complex ($Pt(N^3)$) was described in 1934⁶⁸ and it was discovered that it has numerous applications⁶⁹⁻⁷². It is non-luminescent in solution at room temperature (rt) due to the efficient non-radiative deactivation via the MC state^{73,74}. To avoid this non-radiative pathway, one solution is to increase the energy gap between MLCT and MC states. This can be achieved by either lowering the energy of the LUMO or increasing the energy of the HOMO. There have been numerous modifications to the terpyridine ligand including varying the substitution with an electron withdrawing groups or extending π -conjugation^{73,75}. For example, the insertion of an electron-donating group in the terpyridine ligand stabilizes the lowest excited state. Substitution with an electron withdrawing group stabilizes the MLCT state as compared to unsubstituted complex. Thus, the MC states can not be thermally populated and luminescence can be observed in solution at ambient temperature^{73,76}. On the second part of the molecule, the ancillary ligand also plays a major role on the energy of the excited states. Stronger field ancillary ligands π -accepting or σ -donating such as CN ⁷⁷, OH ⁷⁸, SCN ⁷⁸ and arylalkynyl⁷⁹ can push the MC states effectively to higher energy, giving luminescence in solution. Later, the replacement of one or two of the N atoms by C atoms to form cyclometalated ($Pt(C^2N^2)X$), ($Pt(N^2C^2N)X$) or ($Pt(C^2N^2C)X_2$) leading to mono- or doubly charged species with bright luminescence in solution were reported⁸⁰. Modifications of the tridentate/cyclometalated ligand can lead to enhanced luminescent characteristics. It is possible for instance to take advantage of the strong effect of cyclometalated ($Pt(C^2N^2)$) with σ -alkynyl ligand on the electronic properties to tune the structural, photophysical characteristics of a set of platinum(II) complexes⁸¹.

1.4. Supramolecular chemistry

Type of interactions	Strength (kJ.mol ⁻¹)	Description	Example
Covalent bond	100-400	Chemical bond that involves the sharing of electron pairs between atoms.	
Ionic	250	Chemical bond that involves the electrostatic interaction between oppositely charged ions.	
Hydrogen	10-65	Electrostatic attraction between hydrogen atom covalently bound to a highly electronegative atom.	
Ion-dipole	50-200	Electrostatic interaction between an ion and a neutral molecule that has a dipole.	
Dipole-dipole	5-50	Electrostatic interactions between permanent dipoles in molecules.	
$\pi - \pi$ interaction	0-50	Interactions between the π – orbitals of a molecular system.	
Van der Waals	< 5	Attraction or repulsion between atoms or molecules caused by correlations in the fluctuating polarizations of nearby particles.	
Hydrophobic	N/A	Desire of non-polar molecules to aggregate in aqueous solution in order to separate from water.	
Metal-ligand	0-400	Interaction of certain ligands with a metal with a bond order greater than one.	

Figure 1.11. Examples of the different types of interactions in chemistry.

Supramolecular chemistry is a term introduced by the 1987 Chemistry Nobel Prize winners Profs. Jean-Marie Lehn, Charles John Pedersen and Donald James Cram. This branch of chemistry concerns the development of organized assemblies formed by the association of single molecules through the interplay of non-covalent interactions⁸². Supramolecular

chemistry has been defined as “Chemistry beyond the molecules”, based on covalent and non-covalent interactions leading to the association between two or several chemical species, and of intermolecular bonds. It involves the selective recognition of molecules through non-covalent interactions such as hydrogen bonding, Van der Waals interactions, hydrophobic interactions, metallophilic interactions, π - π stacking, electrostatic interactions, halogen bonding and coordination bonding. While a covalent bond normally has a homolytic bond dissociation energy that ranges between 100 and 400 $\text{kJ}\cdot\text{mol}^{-1}$, non-covalent interactions are generally weak. These interactions can vary from less than 5 $\text{kJ}\cdot\text{mol}^{-1}$ for Van der Waals forces through hydrogen bonding (50 $\text{kJ}\cdot\text{mol}^{-1}$) or coulombic interaction (250 $\text{kJ}\cdot\text{mol}^{-1}$) aggregates (see Figure 1.11)⁸³. Understanding the effect of all the interactions is crucial as they affect the properties of the final. The chemical assembly of relative small and simple molecules into macroscopic, hierarchically organized, and complex structures allows to bridge the gap between the nano- and the macro- world. Furthermore, the functions of a supramolecular structure are much more complex than the single acts of a small components and new emerging properties rise from the assemblies.

1.5. Self-assembly of platinum(II) complexes

The self-assembly of luminescent platinum(II) complexes containing π -conjugated ligands through π - π and Pt \cdots Pt interactions has been intensively studied over the years as an efficient bottom-up approach towards the preparation of supramolecular materials up to the micrometer scale⁸⁴⁻⁸⁹. Because of the non-covalent nature of those interactions, the self-assembled architectures can be monitored and tuned by varying parameters such as temperature, mechanical forces, counter ion, etc.... Moreover, when stimuli-responsive groups are incorporated into these building blocks, the self-assembled properties can be controlled by the application of external stimuli such as pH, temperature, and UV exposure.^{90,91} As discussed previously, remarkable spectroscopic properties, such as lower-energy and/or emission bands, have often been observed and considered as a fingerprint of the establishment of Pt \cdots Pt interactions and used to probe dynamic transformations of the supramolecular assemblies. Several varieties of supramolecular functional architectures

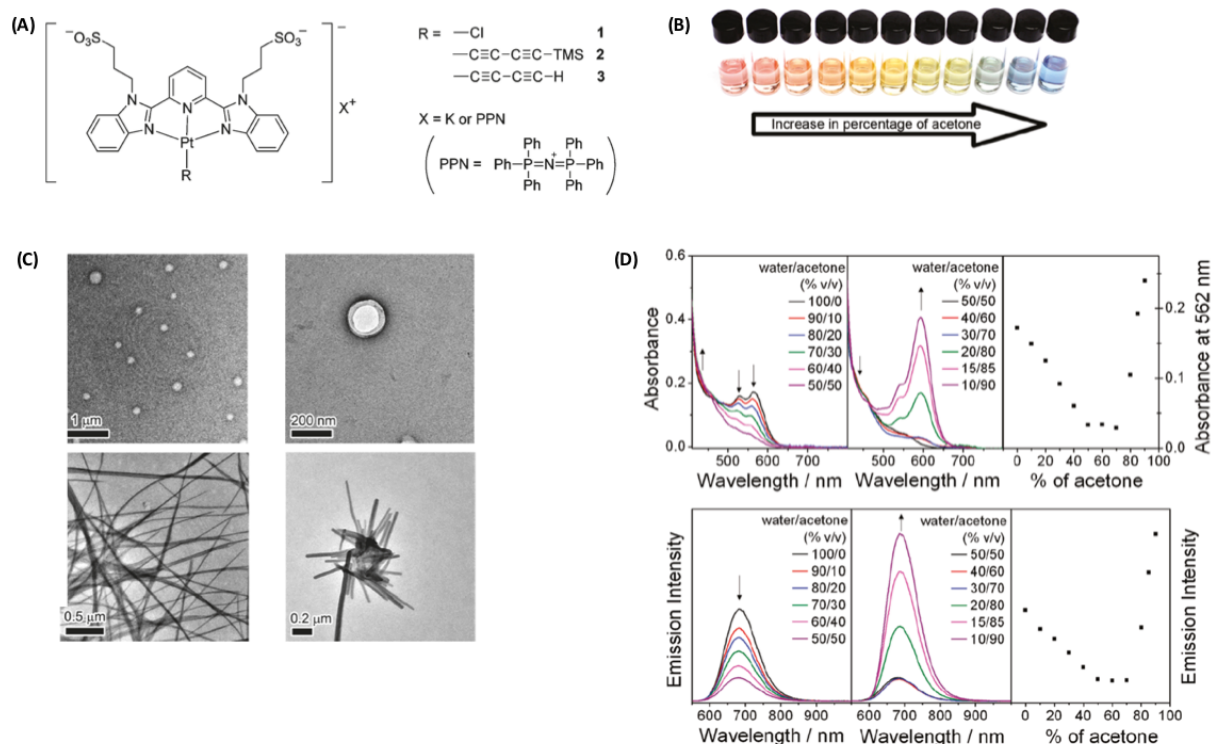


Figure 1.12. (A) Structures of the amphiphilic anionic platinum(II) bzimpy complexes. (B) Solutions of complex 1.K in water- acetone mixture. (C) TEM images prepared from aqueous solutions (top) and 90% acetone-water mixture (bottom) of complexes 1.K and 3K. (D) UV-vis absorption and emission spectra of complex 1.K increasing the acetone content in water and plot of the absorbance at 562 nm versus percentage of acetone⁹⁵.

have been reported which range from 0D structures (for example, micelles), to 1 dimensional arrays, 2D layers and up to 3D networks. Due to their square-planar molecular arrangement, Pt(II) complexes tend to often self-assemble into 1D fibers. Those fibers tend to bungle into entangled 3D networks leading to, in some cases, the formation of supramolecular gels⁹²⁻⁹⁴.

As mentioned previously, platinum (II) complexes with tridentate ligands have attracted considerable attention in recent years due to their photoluminescent properties.

Among them, alkynylplatinum(II) complexes bearing an amphiphilic anionic bzimpy moiety on the tridentate ligand and a chlorine atom as ancillary ligand have shown remarkable self-assembled properties associated with spectroscopical changes in the photophysical properties (refer to Figure 1.12)⁹⁵. When the molecule is solubilized in water, pseudo-0D micellar structures have been observed due to its amphiphilic character. These types of assembly are characterized by a broad featureless emission band ($\lambda_{em} = 675-585$ nm) attributed to a ³MMLCT band due to the Pt...Pt interactions. Upon gradient addition of an

organic solvent (acetone in this example) to the aqueous solution, the color of the solution containing the Pt(II) complex is shifted from red to yellow to blue as the solvent mixture is varied from 100% water to 90% acetone. Such spectroscopic changes were attributed to the variation of the low-lying ¹MMLCT absorption bands. The decrease of the absorption bands at 530 nm and 560 nm upon adjusting the water content from 100% to 50% in a acetone/water mixture was attributed to the partial disaggregation process with disruption of Pt···Pt and π - π interactions. Above 50% in acetone, the formation of intense ¹MMLCT absorption bands at lower energy (600nm) was observed and attributed to the formation of a second kind of aggregates with stronger Pt···Pt and π - π interactions. These changes in spectroscopic properties were monitored by electron microscopy. In aqueous solution platinum(II) complex form vesicles. Upon increasing the acetone content, long fibers were formed.

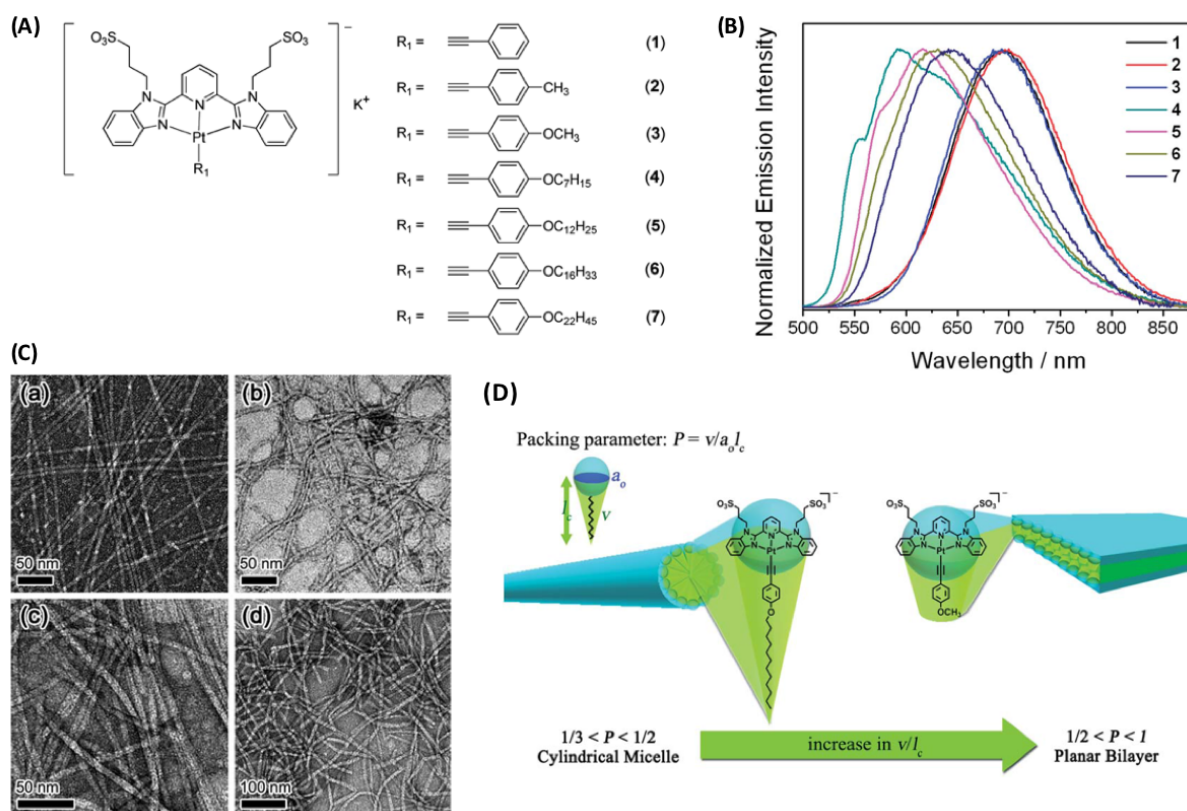


Figure 1.13. (A) Structure of the amphiphilic alkyneplatinum(II) bzimpy complexes. (B) Normalized emission spectra of complexes 1-7 in aqueous media. (C) TEM images (negatively stained) prepared from an aqueous solution of (a) 4, (b) 5, (c) 6, (d) 7. (D) Relationship between packing parameter and morphologies⁹⁶.

In a more recent study, the same group have reported the molecular structural changes on self-assembly of amphiphilic sulfonate-pendant platinum(II) bzimpy complexes in aqueous

medium (see Figure 1.13)⁹⁶. The introduction of alkyl chain of different lengths has been found to have an important effect on controlling the molecular packing and thus on the spectroscopic changes. Complexes with short alkyl chain aggregates produce sheet-like structures. Upon increasing the length of the alkyl chain, the platinum(II) bzimpy complexes tend to form cylindrical micelles. The change in morphology was attributed to the variation of the packing parameters of amphiphilic molecules. Indeed, longer alkyl chain lead to an increase in the hydrophobicity of the complexes. Packing parameters and its consequence on the morphology of amphiphilic molecules will be discussed in the next part.

In our group, neutral platinum(II) complexes self-assembling into highly emitting microcrystalline fibers have been reported. The solvent-assisted, self-assembled fibers show high PLQY, longer lifetimes and red-shifted polarized light emission compared to the molecularly dissolved blue-emitting platinum(II) complex. SAXS/WAXS measurements of these fibers showed an intermolecular distance of 3.28 Å, attributable to of Pt...Pt interactions along the growth axis of the fibers (refer to Figure 1.14)⁹⁷.

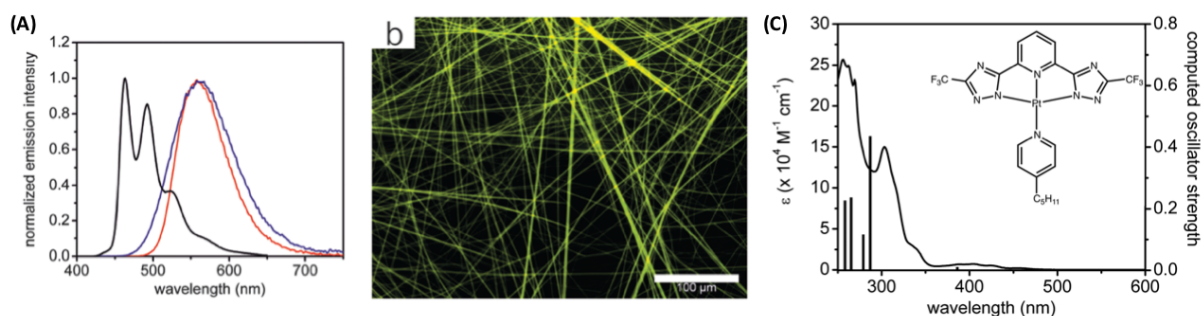


Figure 1.14. (A) Emission spectra of Pt(II) complex in CHCl₃ (black line, 5x10⁻⁵M), fibers obtained from acetone (red line, 4 mg.mL⁻¹) and fibers obtained from CH₂Cl₂ (blue line, 4 mg.mL⁻¹). (B) Fluorescence microscopy image of the fibers from acetone. (C) Absorption spectrum obtained for Pt(II) complex in CHCl₃ and TD-DFT vertical transitions with the corresponding computed oscillator strength⁹⁷.

Platinum(II) complexes, depending on their design, can self-assemble into various morphologies, mainly through platinum-platinum and π - π stacking interactions. Nevertheless, a comprehensive control of the final structures of these aggregates is yet to be achieved. In our group, the supramolecular landscape of an amphiphilic platinum(II) complex has been fully characterized and controlled through a combination of supramolecular and photochemical approaches⁹⁸. The different supramolecular assemblies for the same molecule

has been monitored by following the different photophysical properties of the aggregates as a fingerprint for each species (see Figure 1.15).

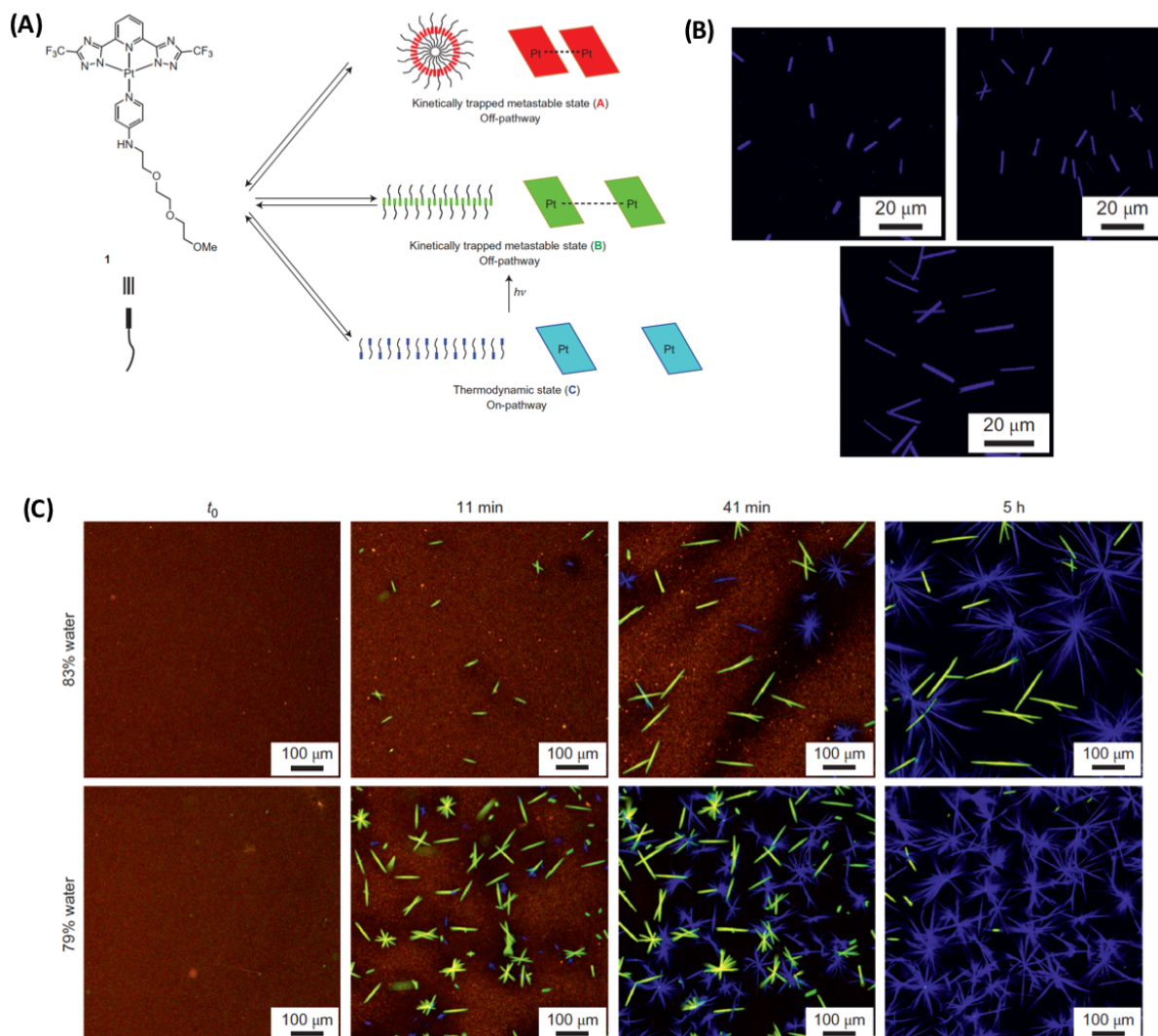


Figure 1.15. (A) Chemical structure of platinum(II) complex 1 and schematic representation of the three assemblies in dynamic equilibrium with the monomeric species. (B) Confocal images of the fibers obtained from the seeded polymerization at different $[A]/[C]$ ratio. (C) Snapshots from the supramolecular polymerization at 83% water-dioxane (top) and 79% water-dioxane (bottom) at different time. These show the time-dependant evolution of assembly A (red) into B (green) and C (blue)⁹⁸.

The platinum(II) complex can self-assemble whether into two kinetic assemblies or one thermodynamic counterpart. It was possible to control the dynamic pathways of the three species by adjusting the parameters, such as solvent composition and light. The novelty of the

approach was to follow in real time the evolution of the self-assembly until reaching the thermodynamic species (C) passing by two kinetically trapped species (A and B). Due to the change in the color of the emission of the different assemblies, the process was recorded by confocal microscopy. Moreover, it has also been demonstrated that the size of the assemblies can be controlled by seeded growth under living supramolecular polymerization conditions.

Other ligand systems were also explored for metallo gels of platinum(II) complexes. By definition, if a gelator contains a metal center, the gel is known as a metallo gel. The presence of metal center in the gelator can offer particular functionalities to the macrophase (gel state) such as stimuli responsiveness, bio-imaging and luminescent properties. To increase the solubility and gelating capacity of metal complexes, the ligands are functionalized with long alkyl chains, cholesterol moieties and polyethylene glycol chains.

De Cola *et al.* reported a metallo gel of Pt(II) complex showing a high PLQY (90%)⁹⁹. Interestingly, the complex is not emissive in solution, whereas Pt...Pt interactions are switched on upon gelation, to give aggregate emission from ³MMLCT state (Figure 1.16).

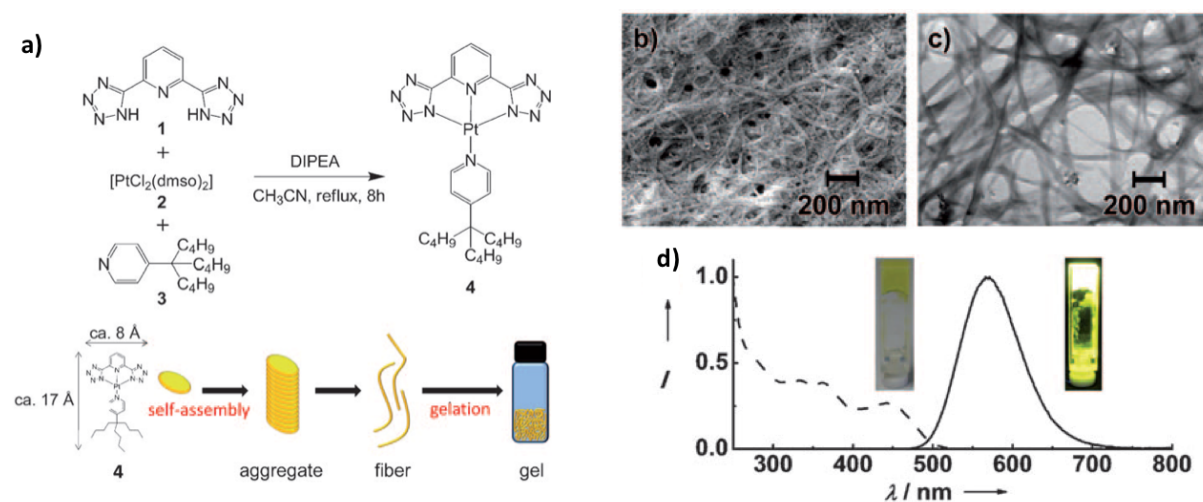


Figure 1.16. a) One pot synthesis of platinum(II) complex 4 and representation of the self-assembly process, going from luminescent aggregates to fibers and gel. b) SEM and c) TEM of the gel. d) Emission and excitation spectra of the gel and photographs of the luminescent gel⁹⁹.

Another interesting approach to build up soft nanomaterials with phosphorescent organoplatinum(II) complexes consists of combining metallophilic interaction with ionic self-assembly. Chen *et al.* reported that cationic platinum(II) complexes were non-soluble in apolar solvents until addition of a counter-ion with a highly lipophilic anion¹⁰⁰. The photophysical properties observed in apolar solvent show a bathochromic shift in absorption and emission

spectra. When complex 3 in dichloromethane (0.5 wt%) is drop-casted on a silica wafer under a moist airflow, honeycomb mesostructures can be observed by SEM (see **Figure 1.17**). The resultant film shows this pattern covering an area of tens of square millimeters. The regular hexagonal arrangement could also be confirmed by the fast Fourier transform image. Non-covalent metallophilicity and ionic self-assembly has a key role in holding the building blocks together in the supramolecular nanostructures and ordered honeycomb structures.

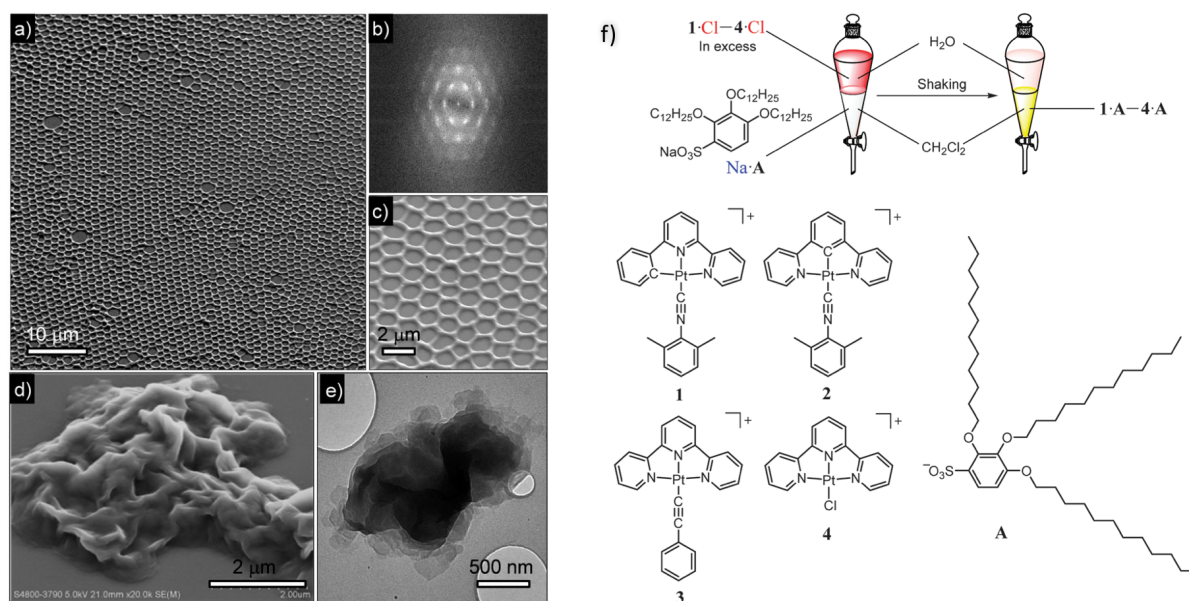


Figure 1.17. SEM micrograph (a) and its corresponding fast Fourier transform image (b) of the honeycomb mesostructure formed by complex 1.A. on the surface of a silicon wafer. (c) Amplified SEM image of the mesostructure. (d) SEM and (e) TEM images of complex 1.A obtained from a dodecane solution¹⁰⁰.

Introduction of chiral moieties into the molecular structures can lead to the formation of chiral supramolecular structures such as helicoidal fibers. Respectively, a recent example of the formation of chiral supramolecular structures has been reported by Yi and coworkers,¹⁰¹ who synthesized a series of amphiphilic bipyridyl alkynylplatinum(II) complexes bearing cholesteric groups and ethylene glycol chains (see **Figure 1.18**).

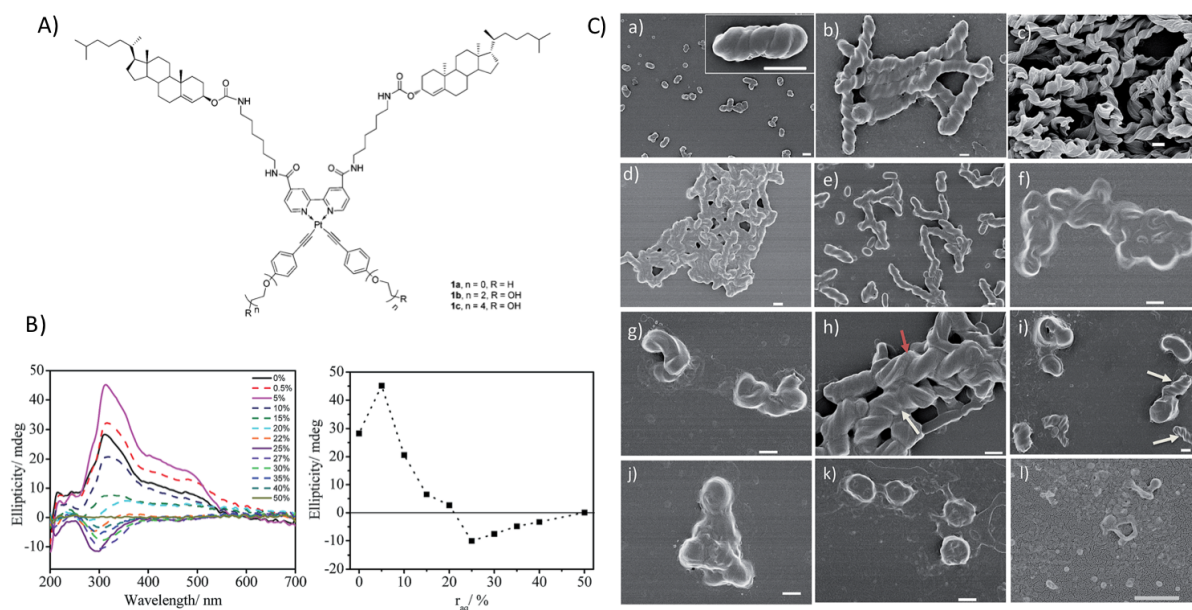


Figure 1.18. A) Chemical structure of complex 1a, 1b, and 1c. B) CD spectra of complex 1c in water-ethanol mixture with increase water-ethanol volumic ratio (r_{aq}). C) SEM images of 1c in water-ethanol with increasing r_{aq} from (a) 0% to (l) 50%. The scale bar is 500 nm^{101} .

Interestingly, a solvent-dependent chiral switching of self-assembled structures has been observed, where the longer ethylene glycol chains form regular left-handed helical structures in aqueous ethanolic solution at H_2O content $< \text{vol } 5\%$. As the H_2O ratio was increased, the chirality changed from left- to right-handed helix as shown by circular dichroic (CD) spectroscopy, with concomitant alteration of the packing mode from monolayer to hexagonal motifs. At water content greater than 50 vol% the structure finally transforms into bilayer vesicles with the loss of CD signal. The observed morphological changes were ascribed as due to a delicate balance between hydrophobic and hydrophilic interactions. Another example of supramolecular self-assembly of chiral structures has been reported by Yam and coworkers¹⁰² who have shown how achiral alkynylplatinum(II) complexes can interact with carboxylic β -1,3-glucan motifs leading to chiral helicoidal structures. Interestingly, the distribution of this two-component helical assembly is affected by different parameters such as temperature, aging, components ratios and mode of preparation and was tentatively rationalized in terms of kinetic vs. thermodynamic control.

In summary, square planar Pt(II) complexes that yield highly luminescent supramolecular self-assembled structures have been introduced. The design of both chelating ligand and ancillary

ligands in terms of both bulkiness and electronic properties allows the formation of architectures with different morphologies and tunable and enhanced photophysical properties compared to the monomeric platinum(II) complex.

1.6. Introduction to copolymer and their self-assembly

1.6.1. Generality

A polymer (from greek *poly-*, “many” + *-mer* “parts”) consists of repeated subunits (monomers) chemically bonded into long chains. A polymer is a large molecule, or a macromolecule with a high relative molecular mass and various properties. Polymers that contain only a single type of repeat unit are known as homopolymers, while polymers containing a mixture of repeat units are known as copolymers. The microstructure of a polymer relates to the physical arrangement of the monomer unit along the backbone of the chain. The polydispersity is a measure of the heterogeneity of sizes of of polymer. The dispersive index as a measure of the distribution of molecular mass of a polymer is defined as :

$$PDI = \frac{M_w}{M_n} \quad (\text{eq. 1.15})$$

Where,

M_w is the weight average molecular weight (sensitive to molecules of high molecular mass)

M_n is the number average molecular weight (sensitive to molecules of low molecular mass)

The glass-transition temperature T_g of a polymer characterize the range of temperatures over which the glass transition occurs. Below T_g , the polymer is hard, brittle, rigid and glassy. Above T_g , the polymer is rubbery and leathery.

A polymer architecture is a critically important chain parameter that affects many of its physical properties including viscosity, solubility, glass transition temperature, size and morphology in solution. A great variety of complex but well-defined chain architectures, such as dendritic¹⁰³, hyperbranched¹⁰⁴, block¹⁰⁵, star¹⁰⁶ or comb¹⁰⁷ and many others have been synthesized (see Figure 1.19).

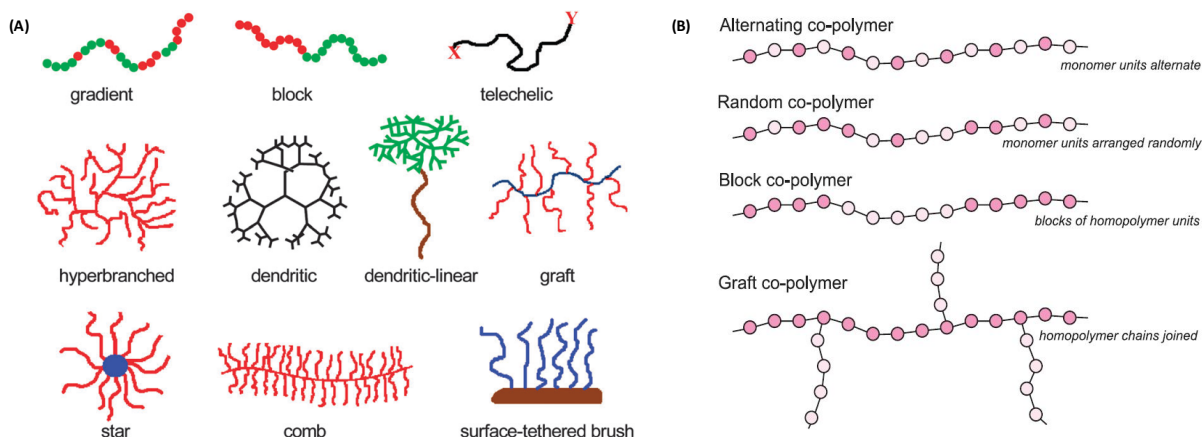


Figure 1.19. (A) various polymer architectures and (B) different types of copolymer.

1.6.2. Diblock copolymers

Most of the work reported in this thesis is based on the study of block copolymers and their self-assembly properties in solution. The most commonly and extensively studied systems are those of linear amphiphilic block copolymers, which are typically defined as macromolecules consisting of two or more chemically distinct and frequently immiscible blocks linked together by covalent bonds. When an amphiphilic block copolymer is dissolved in a thermodynamically ideal solvent for one of the blocks, the copolymer self-assembled into various morphologies including spherical micelles, cylindrical micelles, lamellae, vesicles, discontinuous structures or large micelles compound¹⁰⁸⁻¹¹⁰. The self-assembly arises from the need of the copolymer chains to minimize the interface energy. The solvent compatible block has a tendency to form the hydrophilic coronas whereas the solvent incompatible block tends to form the hydrophobic core of the aggregates. This is called the hydrophobic effect¹¹¹⁻¹¹². The morphology of the resulting aggregates is a result of the molecular curvature arising from the relative sizes of the soluble and insoluble blocks. The dimensionless packing parameter¹¹³, p , can be used to define the relative size of the insoluble region of the copolymer and is defined as:

$$p = \frac{v}{a_0 l_c} \quad (\text{eq. 1.16})$$

Where,

a_0 is an effective cross-sectional area per the amphiphilic block copolymer at the interface.

l_c is the statistical critical length normal to the interface, which correlate with the contour length of the polymer chain

v is the volume occupied by the densely packed copolymer block (hydrophobic for aqueous media). The packing parameter defines the ratio of the insoluble chain molecular volume to the volume occupied by the copolymer in the assembly (see Figure 1.20)¹¹⁴.

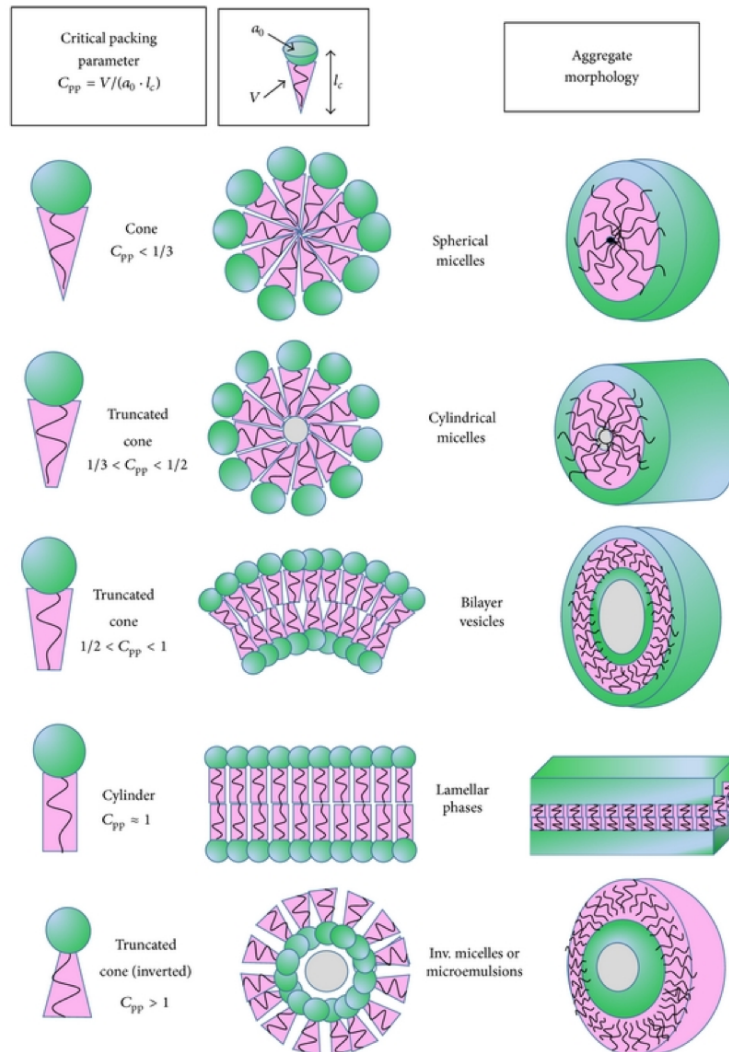


Figure 1.20. Amphiphile shape factors and overview of the possible aggregates predicted from the critical packing parameter.

Amphiphiles with $p < 1/3$ generally form spherical micelles. When $1/3 < p < 1/2$, amphiphiles form micelles with the spherical cylindrical (worm-like) morphology. If $1/2 < p < 1$. A gradual variation from a cylindrical micelle through to vesicles and then to a planar bilayer at $p=1$ is expected. When the packing parameter $p > 1$, more complex systems of the inverted aggregates may form. It is worth mentioning that it is a balance between all the free energy contributions to the self-assembly and also kinetic factors that determine the morphology of the final structure. The packing parameters are considered to be more theoretical than an empirical estimation. For instance, the same block copolymer can self-assemble into micelles,

vesicles, lamellae and large vesicles compounds under different conditions. The different morphologies reported for a poly(styrene)-block-poly(acrylic acid) (PS-*b*-PAA) amphiphilic diblock copolymer are depicted in Figure 1.21.

*Spherical micelles*¹¹⁵. The most common morphology is spherical micelles. The self-assembly of a classical, amphiphilic diblock copolymer leads to two different types of micelles, depending on their relative block lengths: star-like and crew-cut. Systems in which the hydrophobic blocks are much longer than the hydrophilic segments are named “crew-cut” aggregates (or reverse micelles). They have a bulky core and a relatively short corona. By contrast, systems in which the hydrophilic blocks are much longer than the hydrophobic segments are named ‘star-like’ aggregates (regular micelles)¹¹². The spherical micelles are usually the first aggregates to form, thus they can be considered as the starting morphology for aggregates. The size of polymeric micelles is usually between 10 and 100 nm.

*Cylindrical or wormlike micelles*¹¹⁶ (*rods*). They are composed of cylindrical core and a corona surrounding the core. Generally, they have diameters of the same order of magnitude of the spherical micelles but can extend to tens of micrometers in length.

Lamellae and vesicles^{117,118} (*bilayers*). Lamellae are flat or slightly curved bilayers. Vesicles are closed bilayers, typically hollow spheres with a hydrophobic wall and internal and external hydrophilic coronas.

*Large compound micelles*¹⁰⁹ (*LCMs*). They consist of an aggregation of inverse micelles and their outer surface is stabilized in solution by a thin layer of hydrophilic chains. LCMs are frequently seen in many polymer systems. They have a much larger diameter than spherical micelles and are highly polydisperse.

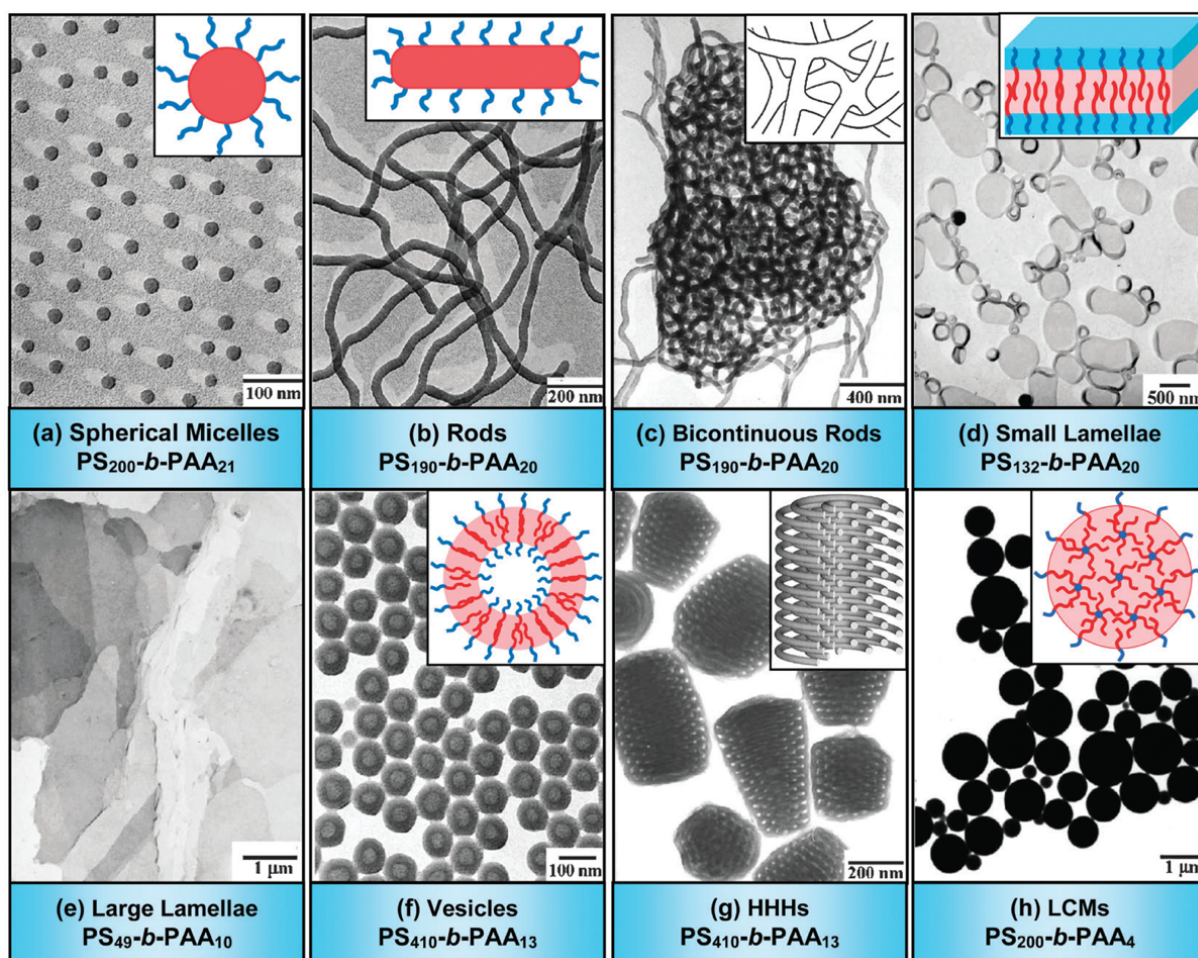


Figure 1.21. TEM images and corresponding schematic representation of various morphologies formed from amphiphilic $PS_m-b-PAA_n$ copolymers. Red represents hydrophobic PS block and blue represents hydrophilic PAA segments¹¹⁶.

There are several methods for the preparation of block copolymer in solution¹⁰⁹⁻¹¹³. Generally, for a block copolymer with a high T_g , a co-solvent method is used. Basically, the amphiphilic block copolymer is dissolved in a common solvent (generally dioxane, THF or DMF which are ideal solvents for both of the blocks). Then a selective solvent, *e.g* water which is a nonsolvent for the hydrophobic block), is slowly added to the solution. The water addition is continuous until the water content is much higher that at which the aggregation process starts. Then the aggregates are usually quenched in an excess of water to freeze the kinetic processes and morphologies. Finally, the common solvent is removed by dialysis of the resulting solution against water or evaporated.

1.7. Encapsulation of platinum complexes

Metal-based anticancer drugs, in particular platinum-drugs, have been investigated for the treatment of cancer. One of the most widely used platinum-based anticancer drugs is the cisplatin, discovered in 1965 and then FDA-approved in 1978¹¹⁹. However, this drug was associated with major side effects and drug resistance. To overcome these issues, drug delivery systems have been developed to load, transport and delivery the drugs in a controlled manner. Two strategies have been developed throughout the years; the platinum-based drug can be either physically encapsulated into a polymer matrix¹²⁰ or they can be covalently bonded to the polymer¹²¹. For many years, numerous studies have been carried out and techniques have been developed with a range of drug carriers including dendrimers, micelles and solid polymer particles¹²².

The metallodrugs may have higher or lower oxidation states that are either inactive or too toxic. The active oxidation state for platinum or ruthenium is +2. This metal ion is surrounded by ligands, which can be sorted into two groups. The permanent ligands, amines or phosphines, are permanently bound, while labile ligands, carboxylates or halogenates, tend to leave the complex (see Figure 1.22)¹²³. These labile ligands are often the key to the efficiency of the drug since the replacement of this ligand by water activates the drug.

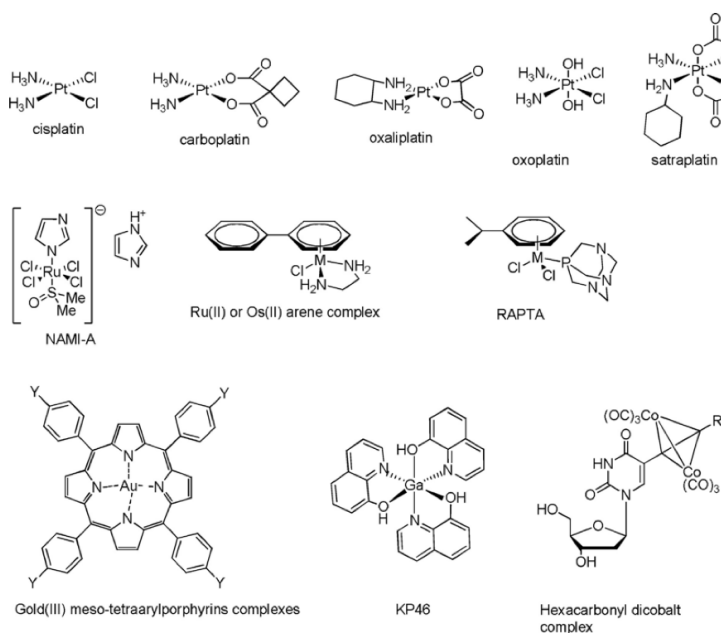


Figure 1.22. Chemical structures of common metal-complex drugs¹²³.

Polymeric micelles have also been successfully used for the encapsulation of platinum(IV) drugs. For instance, Dhar *et al.* used nanoparticles of PLGA-PEG nanoparticles to deliver Pt(IV) drugs to prostate cancer^{124,125}. The anticancer activity of the Pt(IV)-encapsulated nanoparticles was found to be superior to that of free cisplatin. Pt(IV) drugs provides better stability and expanded coordination spheres compared to Pt(II) drugs. The major drawback of the physical encapsulation is the limited drug retention in the polymer matrix. The release of the drug is generally rather fast, usually with an initial burst release (see Figure 1.23).

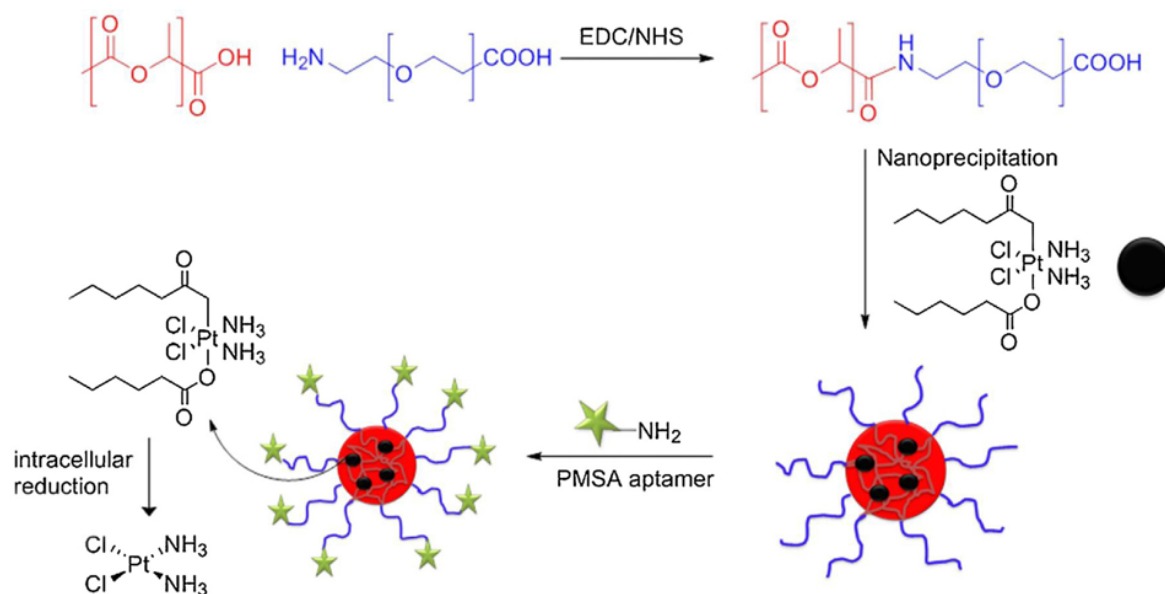


Figure 1.23. Encapsulation of Pt(IV) drugs into polymeric micelles with prostate-specific membrane antigen on the micelle surface¹²⁶.

The other proposed method for the encapsulation of platinum-based drugs is the formation of macromolecular platinum complexes via covalent attachment to the polymer backbone. The advantages of this method include enhanced cellular uptake, prolonged circulation time in blood vessels, drug retention time in tumors and high loading capacity and water solubility. During the micelles formation, the platinum drugs are incorporated into the inner core by chemical conjugation. One example of this system is NC-6004, which is a block copolymer of PEG poly (ethyleneglycol) and poly(glutamic acid) (PGlu) coordinated with *cis*-diammineplatinum moieties (Figure 1.24)¹²⁷. The hydrophilic PEG chain constitutes the outer shell of the micelles, and the PGlu-Pt complex chain constitutes the inner core of the micelles. The *cis*-platin micelles have an average size of 28 nm and are stable in distilled water for a long time.

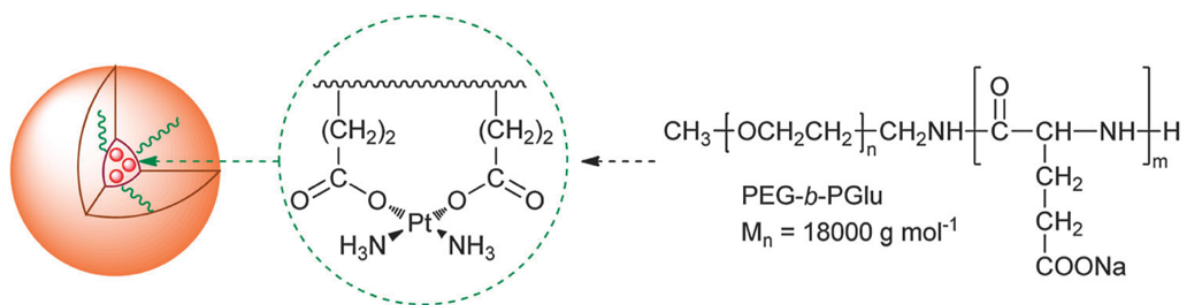


Figure 1.24. NC-6004 : Polymeric micelle carrier systems for Platinum drugs.

Nevertheless, intensive photophysical studies of platinum(II) complexes inside confined architectures are of interest for this work.

De Cola *et al.* recently reported a highly reactive platinum precursor that enables facile labelling of aza-heterocyclic compounds in aqueous media through the formation of highly emissive Platinum (II) complex aggregates inside Pluronic P123 micelles (see Figure 1.25)¹²⁸.

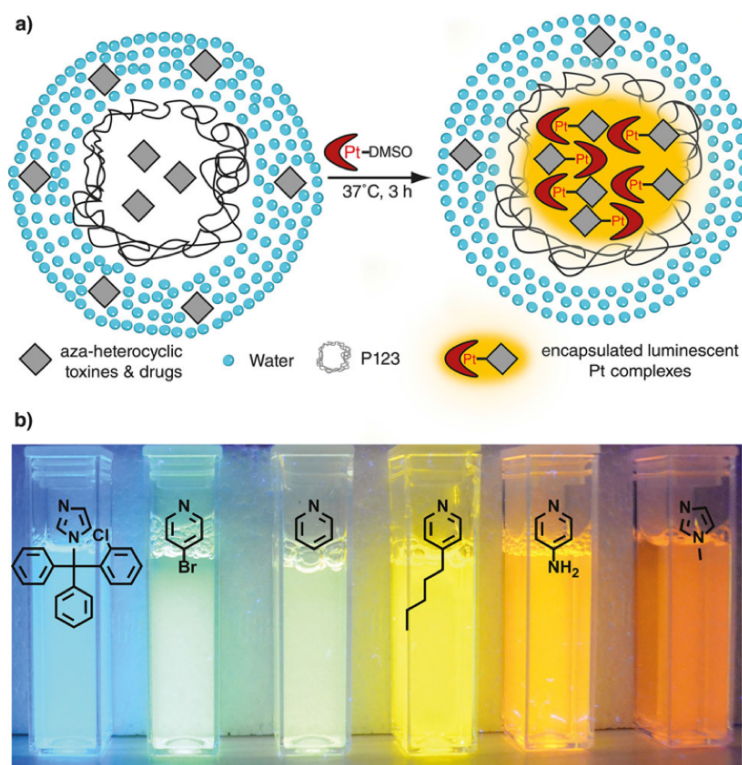


Figure 1.25. a) Schematic representation of the reaction of aza-heterocyclic analytes with Pt(II) precursor in water containing P123 surfactant. b) Photographs of the different luminescent of the Pt(II) complexes under UV lamp¹²⁸.

A luminescent assay for the *in situ* labelling, detection and differentiation of pyridines, imidazols, and related species in aqueous solution and biological environment were

developed and based on the remarkable spectroscopic properties of Pt(II) aggregates. The use of Pluronic P123 as a surfactant prevents the precipitation of the hydrophobic complexes in solution. The micelles formed in water were measured to be 30 nm diameter and were suitable for biological environment. Discrimination of the analytes from one another was possible by the collection and differentiation of all emission and excitation spectra as well as the excited state lifetime of the Pt(II) aggregates formed in the micelles.

Bu *et al.* reported the preparation of luminescent polymeric hybrids formed by platinum(II) complexes and block copolymers (see Figure 1.26)¹²⁹.

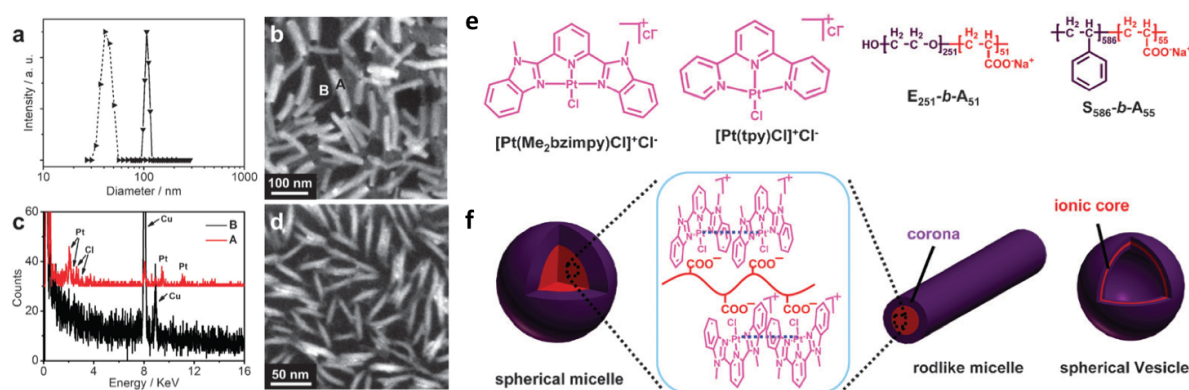


Figure 1.26. a) DLS plot of the diameter of the morphologies formed. b) HAADF-STEM image of the rod-like micelles formed with $[Pt(Me_2bzimpy)Cl]^+ Cl^-$ and (c) EDX spectra showing the presence of Platinum. d) HAADF-STEM image of the rod-like micelles formed with $[Pt(tpy)Cl]^+ Cl^-$. e) Chemical structures of platinum(II) complexes¹²⁹ and block copolymers. f) Schematic representation of their self-assembling morphologies in solvents¹²⁹.

The incorporation of cationic platinum(II) complexes into anionic block copolymers leads to the formation of luminescent architectures from spherical or rod-like micelles as well as vesicles. The two platinum(II) used in this study are nonemissive or weakly emissive in aqueous solutions due to the quenching effect by efficient radiationless decay. Upon increasing the concentration of the cationic amphiphilic copolymer ($E_{250}-b-A_{51}$), the MMLCT bands in absorption and emission was increased gradually. Such results were the consequence of a successful electrostatic binding of the platinum(II) cations to the carboxylate groups of the polymer. As a result, the platinum(II) cations were brought into close proximity with each other leading to platinum-platinum and π - π stacking interactions. STEM images revealed the presence of rod-like aggregates. A similar study was performed with another cationic polymer,

S₅₈₆-b-A₅₅. They observed a dominant morphology of rod-like micelles along with a few spherical micelles and vesicles. A similar approach was used by the same group to study the self-assembly of star-like micelles with a polystyrene corona and a small ionic core bearing platinum(II) complexes. The micelles were able to self-assemble to form vesicles in which the micelles shrank significantly and were distributed on the vesicles surface (see Figure 1.27)¹³⁰.

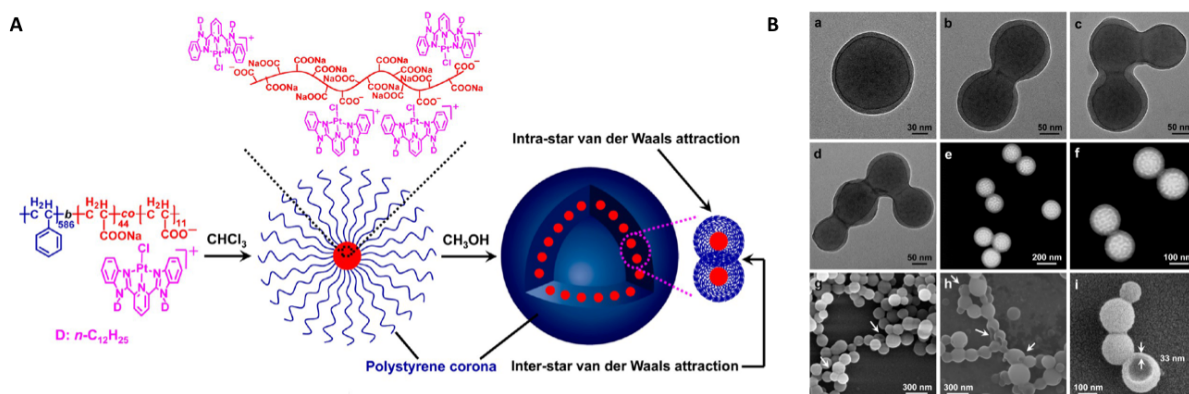


Figure 1.27. A) Structural formula of SAPt-1 and schematic drawing of its self-assembling morphologies from micellar to vesicles. B) BF-TEM (a-d), HAADF-STEM (e,f) and SEM (g-f) images obtained from chloroform/methanol dispersion¹³⁰.

In the last few months, the first supramolecular co-assembly between a platinum (II) complex and poly(ethylene glycol)-*b*-poly(acrylic acid) (PEG-*b*-PAA) diblock copolymer in aqueous solution was reported¹³¹. The resulting co-assembly combined the tendency of the platinum (II) complex to aggregate toward anisotropic supramolecular structures and the solubility of the diblock copolymer. Moreover, platinum-platinum interactions were detected within the fibers resulting in enhanced photophysical properties (Figure 1.28).

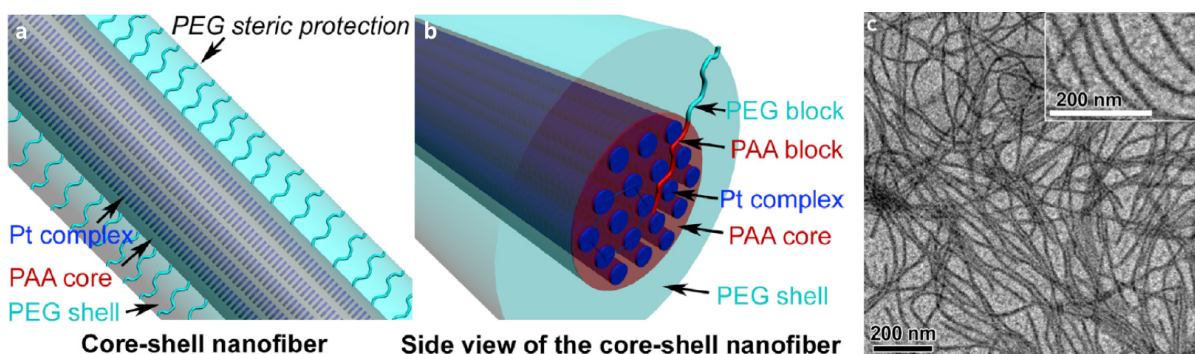


Figure 1.28. (A) and (B) Schematic representation and (C) TEM images of the fibers formed by co-assembly of platinum(II) complex and PEG₄₅-*b*-PAA₆₉ in acetonitrile-methanol-water (1:1:8, v/v/v) solvent mixture.

1.8. Metallo-supramolecular block copolymer self-assembly

Metallo-supramolecular chemistry is by definition a combination of supramolecular chemistry and polymer chemistry. Contrarily, in this case the platinum moiety is covalently linked to the hydrophilic and hydrophobic blocks. Moreover, the presence of a metal complex in the copolymer structure introduces additional electrochemical, photophysical and redox properties.

Yam and coworkers reported the synthesis of thermo-responsive luminescent metallo-supramolecular triblock copolymers based on platinum (II) complexes (Figure 1.29)¹³².

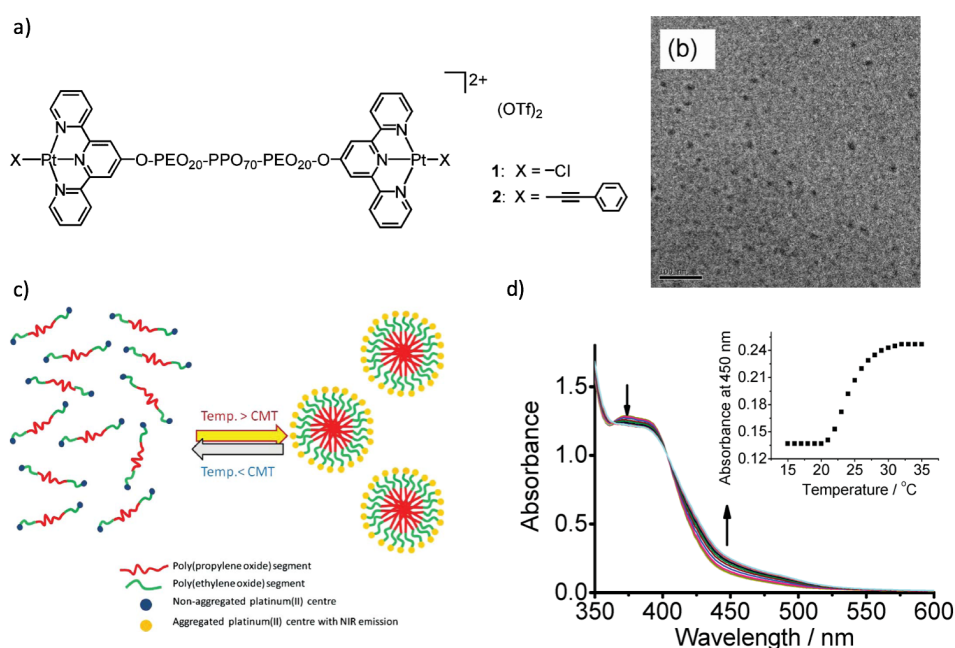


Figure 1.29. a) Chemical structures of Pt(II) complexes 1 and 2. b) TEM images of an aqueous solution of complex 1 at 30 °C. c) Schematic representation of the aggregation of platinum(II) complex due to the micellization of PEO-PPO-PEO copolymers. d) Absorption spectra of complex 1 in water upon increasing the temperature. Inset: plot of the absorbance at 450 nm versus temperature¹³².

PEO-PPO-PEO triblock copolymer consisting of hydrophilic PEO segments and hydrophobic PPO segments undergoes the micellization process in water when the critical micelle temperature (CMT) is reached. An increase of the temperature leads to the formation of polymeric micelles and the platinum(II) moieties become closer in proximity. An increase of the MMLCT bands were observed resulting from the aggregation of platinum(II) complexes through to Pt...Pt and π - π stacking interactions. Moreover, the micelle formation is a

reversible, self-assembly, temperature-dependant process. They reported a 19-fold emission intensity switch when the temperature was increased from 15°C to 31°C. The same group also have reported an amphiphilic platinum(II)-containing diblock copolymer, with pH and solvent-responsive micellization properties that may induce drastic UV-vis and emission spectral changes *via* modulation of Pt...Pt and π - π stacking interactions, both in aqueous and organic media (Figure 1.30)¹³³. The aggregation sizes of the micelles in water and acetone-water-mixture were found to be a gaussian distribution with a peak distribution at around 38 nm. The reversible micellization properties were correlated with the emergence of ³MMLCT bands around 750 nm and were attributed to Pt...Pt interactions in the so-formed micelles.

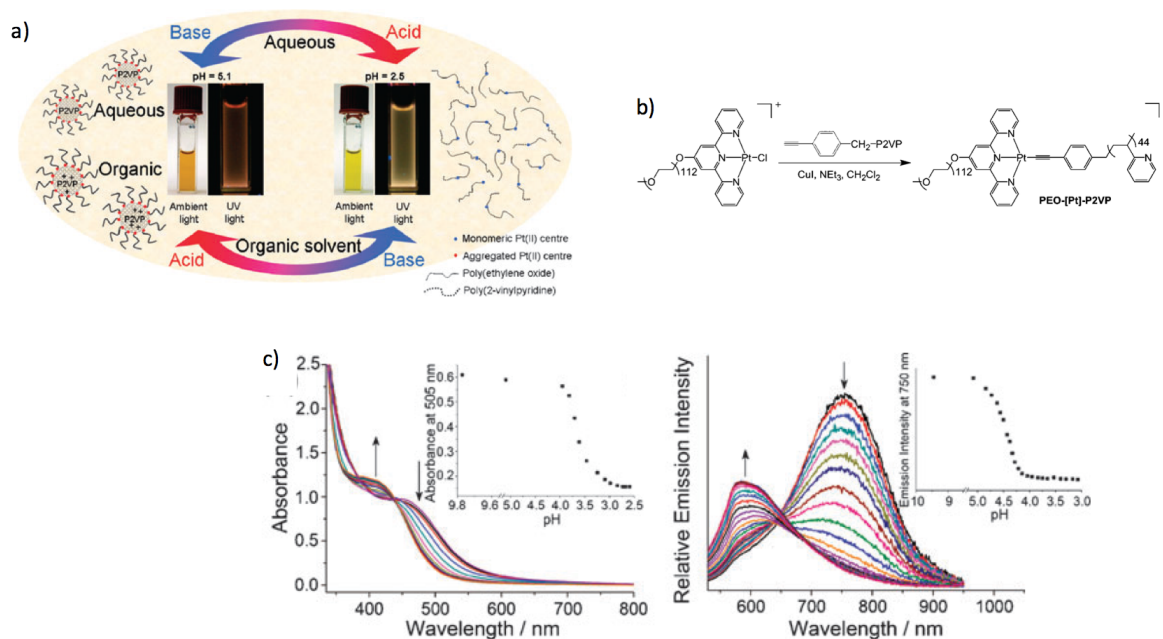


Figure 1.30. a) Reversible pH and solvent-responsive micelle-mediated self-assembly of PEO-[Pt]-P2V. b) Molecular structure of the amphiphilic platinum(II)-containing diblock copolymer. c) UV-vis absorption and emission spectra of PEO-[Pt]-P2V in water upon decreasing pH. Plot of the absorbance at 505 nm and emission at 750 nm versus pH¹³³.

Metallo-supramolecular block copolymer is an elegant method to encapsulate the platinum moiety within polymer micelles. However, the synthetic effort and the difficulty of handling such molecules are limitations of the method. The encapsulation of platinum(II) complexes by block copolymers is a versatile method which enables the complex and polymer to be handled separately. For example, the feed ratio between the polymer and the complex can be varied or the mixing of the two molecules can be controlled.

1.9. Surface functionalization

1.9.1. Silicon¹³⁴

Silicon, before the emergence of graphene, was the most promising and important material utilised in microelectronic computing. A wide range of functionalities can be synthesized and incorporated on the surface which allows a finer tailoring of the surface characteristics and properties for a broad range of applications¹³⁵⁻¹³⁸.

Single crystal silicon wafers of high purity are currently relatively cheap due to their use in a lot of different fields. The most common surface orientations are Si (111) and Si(100)¹³⁹. Silicon crystals have a diamond structure, *i.e* the atoms are sp^3 hybridized and bonded to the four nearest neighbors in a tetrahedral coordination. The covalent bonds are 2.35Å long and each has a bond strength of 226 KJ.mol⁻¹¹⁴⁰. Silicon wafers are grown from crystal and have a regular crystal structure. When cut into wafers, the surface can be aligned in one of several relative directions known as crystal orientations. The (100) planes have a square unit cell, and each silicon atom below the surface is bonded to two atoms in the plane below and two atoms in the plane above. In the (111) direction, the silicon crystal has a double-layer structure, with each Si atom having three bonds to atoms in the other layer of the double layer and one bond to an atom in a different double layer. Upon exposure to air, single crystal silicon structures become rapidly coated with a thin, native oxide layer that can be removed chemically with a fluoride ion. Silicon wafers can also be doped in a controlled fashion with electron donating (P, As, Sb: n-type) or withdrawing (B: p-type) impurities to make it more conductive. The modification of silicon wafer is possible from two starting materials: oxide silicon layer or non-oxide layer.

1.9.2. Surface modification of oxide surfaces¹⁴¹

Surface modification with alkoxy silanes is one of the most commonly used methods to prepare monolayers on oxides¹⁴². The main advantage is the quick and efficient formation of covalent linkage between the substrate and the anchoring group¹⁴³. This covalent bond stabilizes the monolayer, and also allows for further chemical modification. The modification of silicon oxide substrates has been initially reported by Sagiv¹⁴⁴ and since then different

methods have been reported. The most reproducible technique for the preparation of silane SAMs is the immersion of a clean, freshly prepared Si-OH substrate in millimolar solution of alkoxysilane precursor^{145,146}.

Phosphonic acids [R-PO₃H₂] and their phosphonate ester derivatives [R-PO₃R₂] are attractive alternatives, for use as anchoring groups for hydroxylated surfaces^{147,148}. Both functional groups have the ability to react with oxide substrates. In comparison with silane analogues, phosphonate derivatives are considerably less susceptible towards self-condensation reactions, which makes them easy to handle and store in ambient conditions.

Carboxylic acid-based SAMs can also form densely packed and highly organized monolayer films^{149,150}. The advantages of these layers are the wide range of carboxylates available and the environmentally friendly nature of the carboxylates, which make them attractive for “green” chemistry.

More recently, catechol and dopamine have been used for oxide surface-modification¹⁵¹. Their mode of attachment is a biomimetic one, as it hinges on chemistry that is also found in the adhesive-pad proteins secreted by marine mussels to produce extremely strong binding. The binding of catechol-derivate is advantageous for three main reasons: the reaction works on a wide variety of surfaces; the so-formed bond is extremely strong; and any annealing or heating is required during the formation of the monolayer.

Alkene and alkyne-based monolayers have also been formed by photochemical and thermal attachments^{152,153}. One of the advantages of alkene/alkyne onto -OH terminated surfaces is the stability of the resulting layers. In most cases, those monolayers display a significantly higher stability than silane-based monolayers. Such stable monolayers can also be used to construct photopatterned monolayers on oxide surfaces.

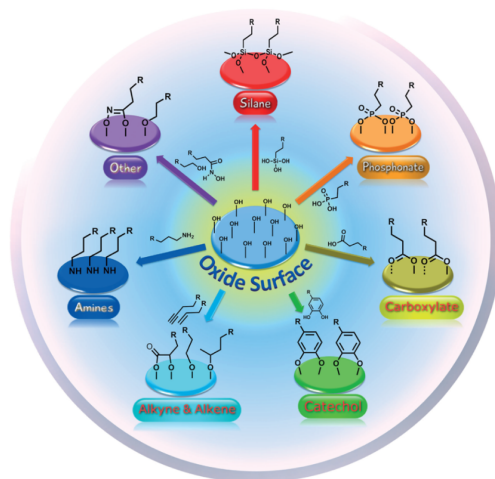


Figure 1.31. Different ways to covalently attach monolayer on silicon oxide surfaces¹⁴¹.

1.9.3. Surface modification of silicon surfaces through Silicon-Carbon bond¹⁵⁴

Preparation of monolayers through silicon-carbon bond on flat substrate has been studied for more than 20 years in order to precisely tailor the interface properties and increase the stability of the formed monolayer^{155,156}. For the functionalization of non-oxidized silicon substrates, silicon-hydride terminated surfaces are generally used as starting point. Silicon (100) wafer treated with fluoride sources provide dihydride Si-H₂ surface when silicon (111) provides monohydride Si-H terminated surface¹⁵⁷. Si-H surfaces are prone to oxidation under ambient conditions but can however be handled in air for several minutes with little degradation. The preparation of these surfaces is thus accessible for the chemist using Schlenk line and glovebox techniques¹⁵⁸ (Figure 1.32). Due of the anisotropic nature of the ammonium fluoride etching, this procedure has been limited to the (111) orientation since it has been reported to roughen the (100) surface. The superior chemical homogeneity of the fluoride etched Si (111) surface relative to the Si (100) has been reported in scientific literature.

Hydrogenated silicon surfaces are attractive because of their ease of preparation and lack of reactivity toward a range of common solvents. Several reactions on the hydride-terminated silicon surfaces have been developed since the early nineties. Hydrosilylation involves the insertion of an unsaturated bond on a silicon-hydride substrate. Chidsey et al. reported the first work on hydrosilylation of non-oxidized Si-H substrate in 1993¹⁵⁵. Covalent attachment of alkenes onto the surface in the presence of a radical initiator provided high quality alkyl monolayers. Those monolayers showed good stability towards ambient conditions and boiling

in basic and acidic conditions. Another approach is the functionalization of the surface through chlorination is possible¹⁵⁹ and results in surfaces that are suitable candidates for numerous applications¹⁶⁰⁻¹⁶². Silicon-carbon linked monolayer provides a relatively simple approach to obtain chemically passive silicon substrates, with minimal traces of silicon oxides.

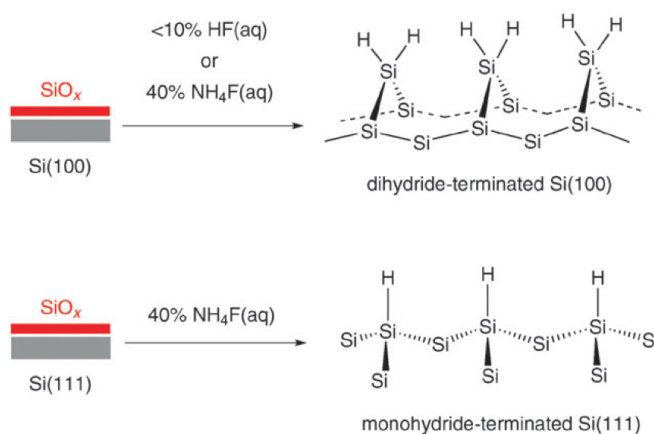


Figure 1.32. Preparation of hydride terminated Si(100) and Si(111) surfaces by chemical etching.

1.9.4. Gold¹⁶³

Gold is historically the most studied substrate for the formation of self-assembled monolayer because it is simple to obtain, relatively inert and easy to modify. The spontaneous adsorption of organic molecules on a variety of surfaces can generate self-assembled monolayers of one molecule thickness. The seminal work of Nuzzo and Allara involved the use of a series of disulfides to form monolayers from solution¹⁶⁴. An extended study showed that well-organized organic monolayers could be formed from spontaneous adsorption onto gold substrates¹⁶⁵. The most common protocol for preparing SAMs on gold and other materials is the immersion of a freshly prepared clean gold substrate into a solution containing the organosulfur compounds^{166,167,168} (thiols, disulfides, sulfides). Dense coverage is rapidly obtained, however the reorganization process requires a longer time in order to minimize the defects in the SAM. They are moderately stable at room temperature but can degrade over time and desorb upon moderate heating. SAMs formed from sulfides suffer from severe

stability issues and conformational defects, and SAMs formed from disulfides are subject to multilayer contamination due to the low solubility of the adsorbate precursor. However, these SAMs still remain appealing for the functionalization of gold substrates and gold nanoparticles. These SAMs have been utilized in a myriad of applications including biosensing¹⁶⁹, and electrode modifications¹⁷⁰. Although the formation of self-assembled monolayer on gold has been studied for three decades, the nature of the sulfur-gold bond is still discussed among scientists¹⁷¹.

1.10. Platinum(II) complexes on silicon substrates.

The coordination chemistry of metals can be utilized to form molecular films of organometallic complexes on solid substrates and leads to organized and directed intermolecular aggregation. Strassert *et al.* reported a new strategy for the functionalization of quartz and silicon carbide with platinum complexes¹⁷². A pyridine-terminated silane linker was grafted on the substrates followed by the coordination of the phosphorescent platinum(II) complexes (Figure 1.33). The formed complexes are forced to aggregate due to surface constraints regardless of the bulkiness of the tridentate ligand. The degree of functionalization of the surface was monitored by surface characterization techniques, *e.g.* XPS and ATR FT-IR. The photoluminescent properties of the functionalized substrates indicate the presence of MMLCT bands in emission and excitation due to the Pt...Pt interactions at the surface. These substrates could be used for electroluminescent devices consisting of emissive layers of oriented aggregates. To date, this appears to be the only report of self-assembled platinum complexes on silicon-based substrates.

The self-assembly at the solid/liquid interface of platinum(II) complexes on gold¹⁷³ and highly oriented pyrolic graphite¹⁷⁴ (HOPG) have also been reported. Formation of sophisticated ordered monolayers on the substrates was driven by non-covalent hydrogen bonding and van der Waals forces. However, the photophysical properties of the monolayers formed from platinum (II) complexes were not investigated and the presence of the Pt...Pt interactions not demonstrated.

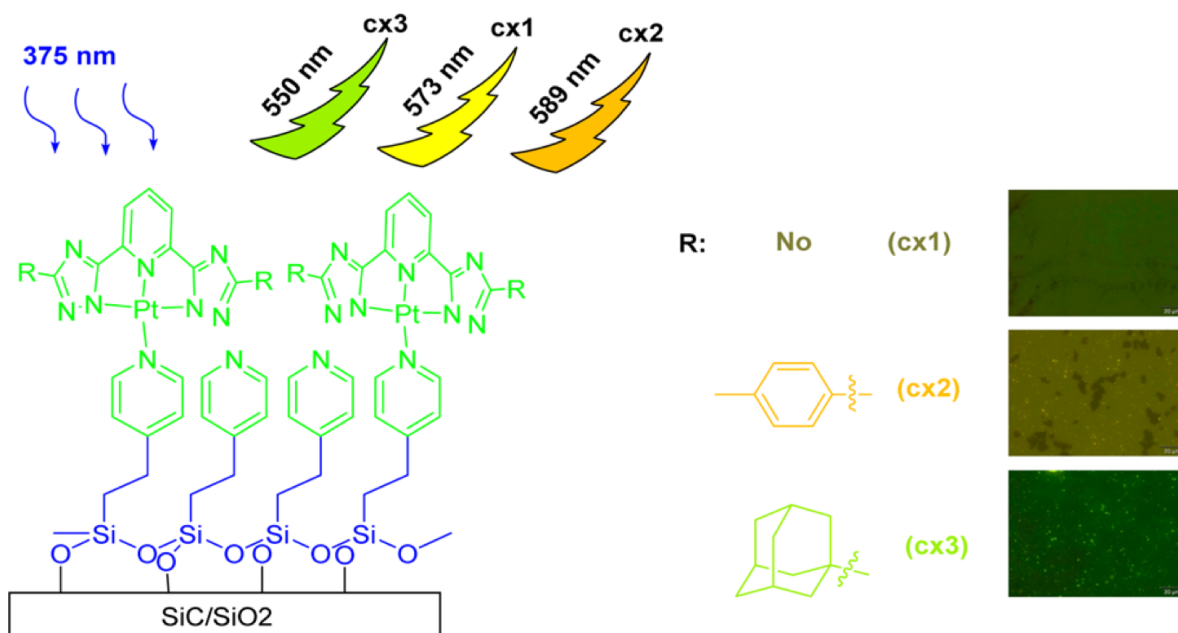


Figure 1.33. Luminescent platinum(II) complexes on quartz and Silicon carbide substrates via pyridine-terminated alkoxy silane linker.

1.11. Scope of the thesis

This thesis focuses on the synthesis, photophysical and self-assembly properties of luminescent platinum(II) complexes and their behaviour in solution, inside polymer particles and on different substrates.

Chapter 2 explores different strategies for the covalent linkage of platinum(II) complexes on gold and silicon substrates. Growth of platinum nanowires by physical vapor deposition is also investigated.

Chapter 3 is dedicated to the encapsulation of platinum(II) complexes by polymer particles. The mechanism is studied in detail by electron and fluorescence microscopy and correlated to the intriguing photophysical properties.

Chapter 4 demonstrates an analogy between the behavior of diblock copolymer and amphiphilic platinum(II) complex in different organic solvent/water mixtures. Different morphologies such as fibers, rods or cylinder were observed by microscopy and their photophysical properties were studied.

Chapter 5 explores the supramolecular co-assembly of two different platinum(II) complexes for the first time, and the resulting morphological and photophysical properties of the so-formed aggregates.

1.12. References

1. J. R. Lakowicz, in *Principles of Fluorescence Spectroscopy*, 3rd edn., **2006**, pp. 1-26.
2. N. J. Turro, V. Ramamurthy and J. C. Scaiano, *Principles of molecular photochemistry: an introduction*, **2009**.
3. B. Valeur, *Molecular fluorescence: principles and applications*, **2001**.
4. K. Rohatgi-Mukherjee, *Fundamentals of photochemistry*, **1978**.
5. A. Credi, L. Prodi, M. Gandolfi and M. Montalti, *Handbook of Photochemistry*, **2006**.
6. A. Jabłoński, *Zeitschrift für Physik*, **1935**, 94, 38-46.
7. C. S. Peyratout, T. K. Aldridge, D. K. Crites and D. R. McMillin, *Inorg. Chem.*, **1995**, 34, 4484-4489.
8. G. Arena, L. M. Scolaro, R. F. Pasternack and R. Romeo, *Inorg. Chem.*, **1995**, 34, 2994-3002.
9. N. Farrell, *Comments on Inorganic Chemistry*, **1995**, 16, 373-389.
10. M. Howe-Grant, K. C. Wu, W. R. Bauer and S. J. Lippard, *Biochemistry-U.S.*, **1976**, 15, 4339-4346.
11. B. M. Zeglis, V. C. Pierre and J. K. Barton, *Chem. Commun.*, **2007**, 4565-4579.
12. F. Puntoriero, S. Campagna, M. L. Di Pietro, A. Giannetto and M. Cusumano, *Photochem. Photobiol. Sci.*, **2007**, 6, 357-360.
13. I. Eryazici, C. N. Moorefield and G. R. Newkome, *Chem. Rev.*, **2008**, 108, 1834-1895.
14. S. D. Cummings, *Coord. Chem. Rev.*, **2009**, 253, 1495-1516.
15. A. M. Krause-Heuer, R. Grunert, S. Kuhne, M. Buczkowska, N. J. Wheate, D. D. Le Pevelen, L. R. Boag, D. M. Fisher, J. Kasparkova, J. Malina, P. J. Bednarski, V. Brabec and J. R. Aldrich-Wright, *J. Med. Chem.*, **2009**, 52, 5474-5484.
16. G. H. Clever and M. Shionoya, *Coord. Chem. Rev.*, **2010**, 254, 2391-2402.
17. J. K. Barton, E. D. Olmon and P. A. Sontz, *Coord. Chem. Rev.*, **2011**, 255, 619-634.
18. Q. Zhao, C. Huang and F. Li, *Chem. Soc. Rev.*, **2011**, 40, 2508-2524.
19. K. K.-W. Lo, M.-W. Louie and K. Y. Zhang, *Coord. Chem. Rev.*, **2010**, 254, 2603-2622.
20. H. Yang, K. L. Metera and H. F. Sleiman, *Coord. Chem. Rev.*, **2010**, 254, 2403-2415.

21. A. Ruggi; F. W. B. van Leeuwen; A. H. Velders, *Coord. Chem. Rev.*, **2011**, *255*, 2542-2554.
22. V. Fernandez-Moreira; F. L. Thorp-Greenwood; M. P. Coogan, *Chem. Commun.*, **2010**, *46*, 186-202.
23. M. S. Lowry; J. I. Goldsmith; J. D. Slinker; R. Rohl; R. A. Pascal; G. G. Malliaras; S. Bernhard, *Chem. Mater.*, **2005**, *17*, 5712-5719.
24. S. Rau; D. Walther; J. G. Vos, *Dalton Trans.*, **2007**, 915-919.
25. R. Reithmeier; C. Bruckmeier; B. Rieger, *Catalysts*, **2012**, *2*, 544.
26. M. Staffilani; E. Höss; U. Giesen; E. Schneider; F. Hartl; H.-P. Josel; L. De Cola, *Inorg. Chem.*, **2003**, *42*, 7789-7798.
27. M. M. Richter, *Chem. Rev.*, **2004**, *104*, 3003-3036.
28. The Exploration of Supramolecular Systems and Nanostructures by Photochemical Techniques, ed. Springer Netherlands, **2011**
29. Highly Efficient OLEDs with Phosphorescent Materials, ed. Wiley, **2008**
30. Comprehensive organometallic chemistry III: Applications I: main group compounds in organic synthesis, ed. Elsevier, **2007**
31. C. Cebrian; M. Mauro; D. Kourkoulos; P. Mercandelli; D. Hertel; K. Meerholz; C. A. Strassert; L. De Cola, *Adv. Mater.*, **2013**, *25*, 437-442.
32. M. Mauro; C. H. Yang; C. Y. Shin; M. Panigati; C. H. Chang; G. D'Alfonso; L. De Cola, *Adv. Mater.*, **2012**, *24*, 2054-2058.
33. M. Mydlak; M. Mauro; F. Polo; M. Felicetti; J. Leonhardt; G. Diener; L. De Cola; C. A. Strassert, *Chem. Mater.*, **2011**, *23*, 3659-3667.
34. R. D. Costa; E. Ortí; H. J. Bolink; F. Monti; G. Accorsi; N. Armaroli, *Angew. Chem. Int. Ed. Engl.*, **2012**, *51*, 8178-8211.
35. T. Hu; L. He; L. Duan; Y. Qiu, *J. Mater. Chem.*, **2012**, *22*, 4206-4215.
36. Spin-Crossover Materials: Properties and Applications, ed. Wiley, **2013**
37. B. E. Hardin; H. J. Snaith; M. D. McGehee, *Nat. Photon.*, **2012**, *6*, 162-169.
38. Shriver and Atkins' Inorganic Chemistry, ed. OUP Oxford, **2010**
39. V. Balzani, **2006**
40. J. Muniz; C. Wang; P. Pyykkö, *Chem. Eur. J.*, **2011**, *17*, 368-377.
41. V. H. Houlding; V. M. Miskowski, *Coord. Chem. Rev.*, **1991**, *111*, 145-152.
42. V. M. Miskowski; V. H. Houlding, *Inorg. Chem.*, **1991**, *30*, 4446-4452.

43. *Adv. Inorg. Chem.*, ed. Rudi van, E., Grażyna, S., Academic Press, **2011**
44. I. M. Sluch; A. J. Miranda; O. Elbjeirami; M. A. Omary; L. M. Slaughter, *Inorg. Chem.*, **2012**, *51*, 10728-10746.
45. B. Ma; P. I. Djurovich; M. E. Thompson, *Coord. Chem. Rev.*, **2005**, *249*, 1501-1510.
46. D. Kim; J.-L. Brédas, *J. Am. Chem. Soc.*, **2009**, *131*, 11371-11380.
47. M. Kato; C. Kosuge; K. Morii; J. S. Ahn; H. Kitagawa; T. Mitani; M. Matsushita; T. Kato; S. Yano; M. Kimura, *Inorg. Chem.*, **1999**, *38*, 1638-1641.
48. H. B. Gray; A. W. Maverick, *Science*, **1981**, *214*, 1201-1205
49. P. Pyykkö, *Chem. Rev.*, **1997**, *97*, 597-636
50. H. Schmidbaur; A. Schier, *Chem. Soc. Rev.*, **2012**, *41*, 370-412.
51. S. Sculfort; P. Braunstein, *Chem. Soc. Rev.*, **2011**, *40*, 2741-2760.
52. H. Schmidbaur, *Gold Bull*, **2000**, *33*, 3-10.
53. H. Schmidbaur, *Chem. Soc. Rev.*, **1995**, *24*, 391-400.
54. M. J. Katz; K. Sakai; D. B. Leznoff, *Chem. Soc. Rev.*, **2008**, *37*, 1884-1895.
55. Y. Kajitani; K. Tsuge; Y. Sasaki; M. Kato, *Chem. Eur. J*, **2012**, *18*, 11196-11200.
56. D. L. M. Suess; J. C. Peters, *Chem. Commun.*, **2010**, *46*, 6554-6556.
57. T. Murahashi; H. Kurosawa, *Coord. Chem. Rev.*, **2002**, *231*, 207-228.
58. M. Kim; T. J. Taylor; F. P. Gabbaï, *J. Am. Chem. Soc.*, **2008**, *130*, 6332-6333.
59. E. J. Fernandez; A. Laguna; J. M. Lopez-de-Luzuriaga, *Dalton Trans.*, **2007**, 1969-1981.
60. R. Józszai; I. Beszedá; A. C. Bényei; A. Fischer; M. Kovács; M. Maliarik; P. Nagy; A. Shchukarev; I. Tóth, *Inorg. Chem.*, **2005**, *44*, 9643-9651.
61. B.-H. Xia; H.-X. Zhang; C.-M. Che; K.-H. Leung; D. L. Phillips; N. Zhu; Z.-Y. Zhou, *J. Am. Chem. Soc.*, **2003**, *125*, 10362-10374.
62. F. Scherbaum; A. Grohmann; B. Huber; C. Krüger; H. Schmidbaur, *Angew. Chem. Int. Ed. Engl.*, **1988**, *27*, 1544-1546.
63. P. Pyykko; M. Straka, *Phys. Chem. Chem. Phys.*, **2000**, *2*, 2489-2493
64. V. M. Miskowski, V. H. Houlding, C. M. Che and Y. Wang, *Inorg. Chem.*, **1993**, *32*, 2518-2524.
65. W. B. Connick, R. E. Marsh, W. P. Schaefer and H. B. Gray, *Inorg. Chem.*, **1997**, *36*, 913-922.
66. M. Hissler, W. B. Connick, D. K. Geiger, J. E. McGarrah, D. Lipa, R. J. Lachicotte and R. Eisenberg, *Inorg. Chem.*, **2000**, *39*, 447-457.

67. F. Hua, S. Kinayyigit, J. R. Cable and F. N. Castellano, *Inorg. Chem.*, **2006**, 45, 4304-4306.
68. G. T. Morgan and F. H. Burstall, *J. Chem. Soc.*, **1934**, 1498-1500
69. H. Hofmeier and U. S. Schubert, *Chem. Soc. Rev.*, **2004**, 33, 373-399.
70. K. M. Wong and V. W. Yam, *Acc. Chem. Res.*, **2011**, 44, 424-434.
71. C. Yu, K. H. Chan, K. M. Wong and V. W. Yam, *Chem. Commun.*, **2009**, 3756-3758.
72. K. Suntharalingam, A. J. White and R. Vilar, *Inorg. Chem.*, **2010**, 49, 8371-8380
73. D. R. McMillin and J. J. Moore, *Coord. Chem. Rev.*, **2002**, 229, 113-121.
74. S. D. Cummings, *Coord. Chem. Rev.*, **2009**, 253, 449-478.
75. R. McGuire, M. C. McGuire and D. R. McMillin, *Coord. Chem. Rev.*, **2010**, 254, 2574-2583.
76. D. K. Crites, C. T. Cunningham and D. R. McMillin, *Inorg. Chim. Acta*, **1998**, 273, 346-353.
77. M. H. Wilson, L. P. Ledwaba, J. S. Field and D. R. McMillin, *Dalton Trans.*, **2005**, 2754-2759.
78. T. Aldridge, E. Stacy and D. McMillin, *Inorg. Chem.*, **1994**.
79. A. Y. Tam, K. M. Wong and V. W. Yam, *J. Am. Chem. Soc.*, **2009**, 131, 6253-6260
80. C. Cornioley-Deuschel, T. Ward and A. Von Zelewsky, *Helv. Chim. Acta*, **1988**, 71, 130-133; Develay, S.; Blackburn, O.; Thompson, A. L.; Williams, J. A. G. *Inorg. Chem.* **2008**, 47, 11129-11142; Williams, J. A. G. *Chem. Soc. Rev.*, **2009**, 38, 1783-1801; Schneider, J.; Du, P.; Jarosz, P.; Lazarides, T.; Wang, X.; Brennessel, W. W.; Eisenberg, R., *Inorg. Chem*, **2009**, 48, 4306.
81. W. Lu, B. X. Mi, M. C. Chan, Z. Hui, C. M. Che, N. Zhu and S. T. Lee, *J. Am. Chem. Soc.*, **2004**, 126, 4958-4971.
82. J.-M. Lehn, *Science*, **2002**, 295, 2400-2403
83. F. J. M. Hoeben; P. Jonkheijm; E. W. Meijer; A. P. H. J. Schenning, *Chem. Rev.*, **2005**, 105, 1491-1546
84. C. Yu; K. H. Chan; K. M. Wong; V. W.-W. Yam, *Proc. Natl. Acad. Sci. U.S.A*, **2006**, 103, 19652-19657.
85. J. Moussa; K. M.-C. Wong; L. M. Chamoreau; H. Amouri; V. W.-W. Yam, *Dalton Trans.*, **2007**, 3526-3530.
86. T. Cardolaccia; Y. Li; K. S. Schanze, *J. Am. Chem. Soc.*, **2008**, 130, 2535-2545.

87. M. Y. Yuen; V. A. Roy; W. Lu; S. C. Kui; G. S. Tong; M. H. So; S. S. Chui; M. Muccini; J. Q. Ning; S. J. Xu; C. M. Che, *Angew. Chem. Int. Ed. Engl.*, **2008**, *47*, 9895-9899.
88. W. Lu; Y. Chen; V. A. Roy; S. S. Chui; C. M. Che, *Angew. Chem. Int. Ed. Engl.*, **2009**, *48*, 7621-7625.
89. W. Lu; S. S. Chui; K. M. Ng; C. M. Che, *Angew. Chem. Int. Ed. Engl.*, **2008**, *47*, 4568-4572.
90. A. Y.-Y. Tam; K. M.-C. Wong; V. W.-W. Yam, *J. Am. Chem. Soc.*, **2009**, *131*, 6253-6260.
91. V. W. Yam; Y. Hu; K. H. Chan; C. Y. Chung, *Chem. Commun.*, **2009**, 6216-6218
92. T. Cardolaccia; Y. Li; K. S. Schanze, *J. Am. Chem. Soc.*, **2008**, *130*, 2535-2545
93. F. Camerel; R. Ziessel; B. Donnio; C. Bourgogne; D. Guillon; M. Schmutz; C. Iacovita; J.-P. Bucher, *Angew. Chem. Int. Ed. Engl.*, **2006**, *119*, 2713-2716.
94. M. Chen; C. Wei; X. Wu; M. Khan; N. Huang; G. Zhang; L. Li, *Chem. Eur. J.*, **2015**, *21*, 4213-4217
95. C. Po; A. Y. Tam; K. M. Wong; V. W. Yam, *J. Am. Chem. Soc.*, **2011**, *133*, 12136-12143
96. C. Po, A. Y. Tam, V.W. Yam, *Chem. Sci.*, **2014**, *5*, 2688-2695
97. M. Mauro, A. Aliprandi, C. Cebrian, D. Wang, C. Kübel, L. De Cola, *Chem. Commun.*, **2014**, *50*, 7269-7272
98. A. Aliprandi, M. Mauro, L. De Cola, *Nature Chem.*, **2016**, *8*, 10-15
99. C. A. Strassert, C. H. Chien, M. D. G. Lopez, D. Kourkoulos, D. Hertel, K. Meerholz, L. De Cola, *Angew. Chem. Int. Ed.*, **2011**, *50*, 946-950
100. Y. Chen, C. M. Che, W. Lu, *Chem. Commun.*, **2015**, *51*, 5371-5374
101. Y. Mao; K. Liu; L. Meng; L. Chen; L. Chen; T. Yi, *Soft Matter*, **2014**, *10*, 7615-7622
102. C. Y. Chung; S. Tamaru; S. Shinkai; V. W. Yam, *Chem. Eur. J.*, **2015**, *21*, 5447-5458
103. S. M. Grayson and J. M. J. Fréchet, *Chem. Rev.*, **2001**, *101*, 3819-3868
104. B. I. Voit and A. Lederer, *Chem. Rev.*, **2009**, *109*, 5924-5973.
105. N. Hadjichristidis, S. Pispas and G. Floudas, *Block Copolymers: Synthetic Strategies, Physical Properties, and Applications*, *John Wiley & Sons*, Hoboken, New Jersey, **2003**.
106. A. Blencowe, J. F. Tan, T. K. Goh and G. G. Qiao, *Polymer*, **2009**, *50*, 5-32.
107. S. S. Sheiko, B. S. Sumerlin and K. Matyjaszewski, *Prog. Polym. Sci.*, **2008**, *33*, 759-785
108. J. C. M. van Hest, D. A. P. Delnoye, M. W. P. L. Baars, M. H. P. van Genderen and E. W. Meijer, *Science*, **1995**, *268*, 1592-1595.
109. L. Zhang and A. Eisenberg, *Science*, **1995**, *268*, 1728-1731.
110. L. Zhang, K. Yu and A. Eisenberg, *Science*, **1996**, *272*, 1777-1779.

111. L. Zhang and A. Eisenberg, *J. Am. Chem. Soc.*, **1996**, *118*, 3168–3181.
112. L. Zhang and A. Eisenberg, *Polym. Adv. Technol.*, **1998**, *9*, 677–699.
113. D. E. Discher and F. Ahmed, *Annu. Rev. Biomed. Eng.*, **2006**, *8*, 323–341
114. J. N. Israelachvili, *Intermolecular and Surface Forces*, Elsevier, Amsterdam, **2011**.
115. R. K. O'Reilly, C. J. Hawker, and K. L. Wooley, *Chem. Soc. Rev.*, **2006**, *35*, 1068–1083
116. N. S. Cameron, M. K. Corbierre and A. Eisenberg, *Can. J. Chem.*, **1999**, *77*, 1311–1326.
117. L. Zhang and A. Eisenberg, *Macromolecules*, **1996**, *29*, 8805–8815
118. D. E. Discher and A. Eisenberg, *Science*, **2002**, *297*, 967–973
119. B. Rosenberg, L. VanCanp, J.E. Trosko, V. H. Mansour, *Nature*, **1969**, *222*, 385
120. S. H. Bai, C. Thomas, A. Rawat and F. Ahsan, *Crit. Rev. Ther. Drug Carrier Syst.*, **2006**, *23*, 437–495
121. R. Duncan, *Nat. Rev. Cancer*, **2006**, *6*, 688–701
122. M. E. Gindy, R. K. Prud'homme, *Expert Opin. Drug Delivery*, **2009**, *6*, 865–878.
123. L. Kelland, *Nat Rev Cancer*, **2007**, *7*, 573–84
124. S. Dhar, F. X. Gu, R. Langer, O.C. Farokhzad, S. J. Lippard, *Proc Natl Acad Sci*, **2008**, *105*, 17356–17361
125. N. Kolishetti, S. Dhar, P. M. Valencia, L. Q. Lin, R. Q. Karnik, S. J. Lippard, R. Langer, O. C. Farokhzad, *Proc Natl Acad Sci*, **2010**, *107*, 17939–17944
126. Shive M, *Adv. Drug Delivery Rev.*, **1997**, *28*, 5–24
127. Y. Matsumura, *Adv. Drug Delivery Rev.*, **2008**, *60*, 899–914
128. S. Sinn, F. Biedermann, L. De Cola, *Chem. Eur. J.* **2017**, *23*, 1 – 8
129. N. Liu, B. Wang, W. Liu, W. Bu, *Chem. Commun.*, **2011**, *47*, 9336–9338
130. N. Liu, Q. He, W. Bu, *Langmuir*, **2015**, *31*, 2262–2268
131. Kaka Zhang, Margaret Ching-Lam Yeung, Sammual Yu-Lut Leung, Vivian Wing-Wah Yam, *Chem 2*, **2017**, 825–839
132. Y. Hu, K. H. Y. Chan, C. Y. S. Chung, V.W. W. Yam, *Dalton Trans.*, **2011**, *40*, 12228–12234
133. Y. Hu, K. H. Y. Chan, C. Y. S. Chung, V.W. W. Yam, *Chem. Commun.*, **2009**, 6216–6218
134. H. N. Waltenburg, J. T. Yates Jr., *Chem. Rev.*, **1995**, *95*, 1589–1673
135. Paula M Mendes, *Chem. Soc. Rev.*, **2008**, *37*, 2512–2529
136. Q. Li, G. Mathur, S. Gowda, S. Surthi, Q. Zhao, L. Yu, J. S. Lindsey, D. F. Bocian, V. Misra, *Adv. Mater.*, **2004**, *16*, 133–137

137. S. Kobayashi, T. Nishikawa, T. Takenobu, S. Mori, T. Shimoda, T. Mitani, H. Shimotani, N. Yoshimoto, S. Ogawa, Y. Iwasa, *Nat. mat.*, **2004**, *3*, 317-322
138. H. Maeda, R. Sakamoto, Y. Nishimori, J. Sendo, F. Toshimitsu, Y. Yamanoi, H. Nishihara, *Chem. Commun.*, **2011**, *47*, 8644–8646
139. H. N. Waltenburg, J. T. Yates, *Chem. Rev.*, **1995**, *95*, 1589
140. R. Walsh, *Acc. Chem. Res.*, **1981**, *14*, 246.
141. Sidharam P. Pujari, Luc Scheres, Antonius T. M. Marcelis, Han Zuilhof, *Angew. Chem. Int. Ed.*, **2014**, *53*, 6322 – 6356.
142. N. Herzer, S. Hoepfener, U. S. Schubert, *Chem. Commun.*, **2010**, *46*, 5634 – 5652
143. M. Grandbois, M. Beyer, M. Rief, H. Clausen-Schaumann, H. E. Gaub, *Science*, **1999**, *283*, 1727 – 1730.
144. J. Sagiv, *J. Am. Chem. Soc.*, **1980**, *102*, 92–98
145. M. Grandbois, M. Beyer, M. Rief, H. Clausen-Schaumann, H. E. Gaub, *Science*, **1999**, *283*, 1727 – 1730.
146. N. Herzer, S. Hoepfener, U. S. Schubert, *Chem. Commun.*, **2010**, *46*, 5634 – 5652.
147. H. E. Ries, Jr., H. D. Cook, *J. Colloid Sci.*, **1954**, *9*, 535 – 546.
148. P. Thissen, M. Valtiner, G. Grundmeier, *Langmuir*, **2010**, *26*, 156 – 164.
149. D. L. Allara, R. G. Nuzzo, *Langmuir*, **1985**, *1*, 45 – 52.
150. 20. A. Raman, R. QuiÇones, L. Barriger, R. Eastman, A. Parsi, E. S. Gawalt, *Langmuir*, **2010**, *26*, 1747-1754.
151. Q. Ye, F. Zhou, W. Liu, *Chem. Soc. Rev.*, **2011**, *40*, 4244 – 4258.
152. M. Rosso, M. Giesbers, A. Arafat, K. Schron, H. Zuilhof, *Langmuir*, **2009**, *25*, 2172 – 2180.
153. T. K. Mischki, R. L. Donkers, B. J. Eves, G. P. Lopinski, D. D. M. Wayner, *Langmuir*, **2006**, *22*, 8359 – 8365.
154. Simone Ciampi, Jason B. Harper, J. Justin Gooding, *Chem. Soc. Rev.*, **2010**, *39*, 2158–2183.
155. Matthew R. Lindford, Christopher E. D. Chidsey, *J. Am. Chem. Soc.*, **1993**, *115*, 12631–12632.
156. M. R. Linford, P. Fenter, P. M. Eisenberger, C. E. D. Chidsey, *J. Am. Chem. Soc.*, **1995**, *117*, 3145–3155.
157. H. Ubara, T. Imura, A. Hiraki, *Solid State Commun.*, **1984**, *50*, 673–675.

158. G. S. Higashi, Y. J. Chabal, G. W. Trucks, K. Raghavachari, *Appl. Phys. Lett.*, **1990**, *56*, 656–658.
159. A. Bansal, X. Li, I. Lauermann, N. S. Lewis, S. I. Yi, W. H. Weinberg, *J. Am. Chem. Soc.*, **1996**, *118*, 7225–7226.
160. A. Bansal and N. S. Lewis, *J. Phys. Chem. B*, **1998**, *102*, 1067–1070.
161. R. D. Rohde, H. D. Agnew, W.-S. Yeo, R. C. Bailey, J. R. Heath, *J. Am. Chem. Soc.*, **2006**, *128*, 9518–9525.
162. E. J. Nemanick, P. T. Hurley, B. S. Brunshwig and N. S. Lewis, *J. Phys. Chem. B*, **2006**, *110*, 14800–14808.
163. J. Christopher Love, Lara A. Estroff, Jennah K. Kriebel, Ralph G. Nuzzo, George M. Whitesides, *Chem. Rev.*, **2005**, *105*, 1103-1169.
164. R. G. Nuzzo, D. L. Allara, *J. Am. Chem. Soc.*, **1983**, *105*, 4481–4483.
165. R. G. Nuzzo, F. A. Fusco, D. L. Allara, *J. Am. Chem. Soc.*, **1987**, *109*, 2358-2368.
166. Bain, C. D.; Troughton, E. B.; Tao, Y. T.; Evall, J.; Whitesides, G. M.; Nuzzo, R. G., *J. Am. Chem. Soc.*, **1989**, *111*, 321-335.
167. Dannenberger, O.; Wolff, J. J.; Buck, M., *Langmuir*, **1998**, *14*, 4679-4682.
168. Strong, L.; Whitesides, G. M., *Langmuir*, **1988**, *4*, 546.
169. Paula M Mendes, *Chem. Soc. Rev.*, **2008**, *37*, 2512–2529
170. Amanda L. Eckermann, Daniel J. Feld, Justine A. Shaw, Thomas J. Meade, *Coord. Chem. Rev.*, **2010**, *254*, 1769–1802.
171. Hannu Häkkinen, *Nature Chem.*, **2012**, *4*, 443-455.
172. Deb Kumar Bhowmick, Linda Stegemann, Manfred Bartsch, Naveen Kumar Allampally, Cristian A. Strassert, Helmut Zacharias, *J. Phys. Chem. C*, **2015**, *119*, 5551–5561.
173. Pascal R. Ewen, Jan Sanning, Tobias Koch, Nikos L. Doltsinis, Cristian A. Strassert, Daniel Wegner, *Beilstein J. Nanotechnol.*, **2014**, *5*, 2248–2258.
174. Mohamed El Garah, Stephan Sinn, Arezoo Dianat, Alejandro Santana-Bonilla, Rafael Gutierrez, Luisa De Cola, Gianauelio Cuniberti, Artur Ciesielski, Paolo Samori, *Chem. Commun.*, **2016**, *52*, 11163-11166.

Chapter 2

Functionalization of silicon and gold substrates with platinum(II) complexes

Abstract: This chapter describes the different strategies developed for the functionalisation of gold and silicon substrates through silicon-carbon and sulfur-gold bonds. Several platinum (II) complexes with different anchoring groups were prepared and characterized. Surface modifications were carried out followed by measurements and the analysis of the XPS spectra. The photophysical properties of the functionalised substrates were also studied by luminescence spectroscopy and fluorescence microscopy. A new method based on physical vapor deposition (PVD) by sublimation of the platinum (II) complexes enabled the growth of nanowires perpendicular to the surface. The morphological and photophysical properties of those ordered structures were studied by scanning electron microscopy (SEM) and fluorescence microscopy.

2.1. Introduction

The formation of organized monolayers consisting of oriented molecules on gold and silicon substrates have attracted a vast amount of attention for the last forty years¹⁻⁴. It began with the seminal work of Jacob Sagiv, who first reported the formation of homogeneous mixed monolayers on polar solid surfaces by adsorption from organic solutions⁵. It was demonstrated that a monolayer containing both chemisorbed and physisorbed components could be produced in a one step procedure via covalent silane bonds on substrates with –OH groups. A few years later, Nuzzo and Allara reported the adsorption of bifunctional organic disulfides on gold surfaces leading to the formation of self-organized monolayers⁶. From those two pioneering works, many applications have been discovered, including electrochemistry⁷, sensing⁸⁻¹¹, field effect transistor¹², photovoltaic¹³. Different approaches have been developed to form well-defined monolayers on silicon wafers. Among them, modification of the native oxide surface, typically silicon, was extensively studied¹⁴. One of the most widely used strategies for the modification of an oxide surface was the use of alkoxy silanes. The silanization reaction occurred between the hydroxyl groups on the surface, which attack and displace the alkoxy groups on the silane, thus forming a covalent Si-O bond. The polycondensation reaction between the oxide surfaces and the alkoxy silane molecules across the surface leads to the formation of stable monolayers^{15,16}. Phosphonate^{17,18}, carboxylate^{19,20}, catechol²¹ or alkene/alkyne^{22,23} were also used for the formation of stable monolayers on silicon oxide and other oxide surfaces. Many techniques were developed to covalently attach the aforementioned anchoring groups on the oxide surfaces: photochemical attachment^{24,25}, thermal grafting^{26,27} and wet chemical functionalization²⁸⁻³⁰. There have also been various developments involving the formation of self-assembled monolayers on gold substrates³¹. Metal-organic self-assembled monolayers have been widely studied and there are numerous field applications³²⁻³⁴. Deposition of organometallic complexes on different substrates can lead to the formation of ordered structures with interesting photophysical properties³⁵⁻³⁸. In particular, because of the d_z^2 orbitals and the d^8 electronic configuration of platinum (II) complexes, the molecules show a high tendency to stack favoured by weak non-covalent metal...metal and/or π - π ligand-ligand interactions^{39,40}. The self-organization of luminescent platinum (II) complexes has been employed as an efficient *bottom-up* approach towards the preparation and development of novel molecular materials from the molecular-

to micrometer-scale⁴¹⁻⁴⁵. Luminescent platinum (II) complexes are also known for their high photoluminescent quantum yield, long excited state lifetimes (compared to organic fluorescent labels), tuneable emission and significant Stokes shift. Most studies on the self-assembly of platinum (II) complexes were carried out in solution, and there are very few studies on the aggregation on solid substrates. Strassert and a co-worker recently developed a new strategy for the anchoring of platinum (II) complexes on quartz and silicon surfaces⁴⁶. Pyridine-terminated silane linkers were covalently bonded to amorphous quartz and silicon carbide by polycondensation reactions on the substrates, followed by coordination of the luminescent platinum (II) complexes. Islands of luminescent platinum (II) aggregates were observed on the surface, meaning that platinum-platinum interactions occurred on the surface. However, the density of the platinum complex was relatively low (less than 10% coverage in the best case) and there are limited applications in optoelectronics or electroluminescent devices. Another possible approach is to grow platinum fibers perpendicular to the substrate. The preparation of organic nanowires from π -conjugated molecules has been accomplished by several methods including vapor deposition^{47,48}. This method allowed direct control over the morphology and the composition of the nanowires. Similar methods at low pressure or physical vapor deposition also represent alternative methods for the formation of aggregation of π -conjugated molecules⁴⁹.

In this chapter, we report the functionalisation of gold and silicon substrates with different platinum (II) complexes. Silicon substrates were firstly treated in order to obtain reactive hydrogen terminated surfaces (Si-H). The first strategy chosen was to covalently attach 4-vinylpyridine molecules on the Si-H substrates by UV induced photoreaction. The second strategy developed was to transform the Si-H surface into acetylenated substrates with an alkyne bond perpendicular to the substrate. A molecule with an azide functional group on one side and a pyridine moiety on the other side was linked to the surface by CuAAC click chemistry. For the two strategies, platinum (II) complexes consisting of a tridentate chelating ligand were coordinated to the functionalised substrates under surface constraints. The resulting surfaces were characterised by X-ray photoelectron spectroscopy (XPS) in order to determine the density of platinum (II) complexes on the surface. Gold substrates were also functionalised via sulfur-gold bonds with platinum (II) complexes of different lengths bearing a disulfide-ending group. The modified gold substrates were analysed by XPS to determine the density of platinum complexes on the surface and confocal fluorescence microscopy to study the

photophysical properties. A sensing essay based on the removal of the platinum moiety from the substrate via cleavage of the ester functional group was also demonstrated. Finally, nanowires of platinum (II) complexes were also grown by PVD perpendicularly to different substrates. The shape and density of the platinum (II) nanowires were assessed by (SEM) and fluorescence microscopy. The mechanochromic effect upon application of a pressure force directed along the axis of the platinum-platinum interactions on luminescent platinum nanowires were also studied by SEM and fluorescence microscopy.

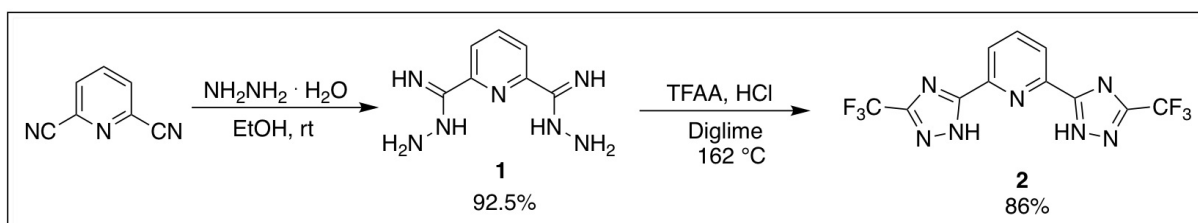
2.2. Results and discussions

2.2.1. Synthesis

All the compounds were characterised by ^1H NMR, ^{13}C NMR and ^{19}F NMR when possible. Additional elemental analysis and mass spectrometry analysis were performed for all the platinum (II) complexes.

Synthesis of tridentate ligand **2**

The synthetic route for the preparation of the chromophoric tridentate ligand **2** used for the preparation of all the platinum (II) complexes is depicted in Scheme 2.1⁴⁵. This particular ligand has been synthesised to address different features. The tridentate ligand provides a rigid chelating unit for the platinum (II) complex. The CF_3 electron withdrawing group stabilizes the HOMO and increases the energy gap between the HOMO and the LUMO. Moreover, the presence of the "small" CF_3 group provides a hydrophobic character and favours aggregation of the platinum (II) complex without steric hindrances.



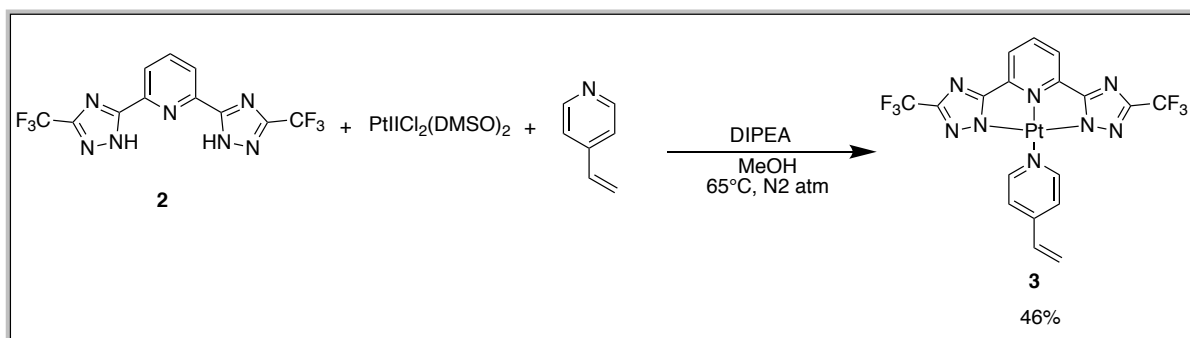
Scheme 2.1. Synthetic route for the preparation of the tridentate ligand **2**.

In the first step, commercially available 2,6-pyridinebiscarbonitrile was reacted with hydrazine monohydrate in ethanol and the nucleophilic addition hydrazine of the two nitrile functional

groups resulted in pyridin-2,6-bis(carboximidhydrazone) (**1**). Then, condensation between **1** and **2** equivalents of trifluoroacetic anhydride was carried out in diethylene glycol dimethyl ether (“diglime”) at reflux, leading to acylation and ring closure. Diglime was chosen as solvent for its high boiling point required for the formation of the triazole. The addition of water to the reaction mixture precipitated compound **2**, which was easily collected as a whitish powder with an overall high yield.

Preparation of the platinum (II) complexes

Two strategies were employed to functionalise the silicon wafer 1) UV induced coupling of 4-vinylpyridine with hydrogen-terminated substrate, 2) Cu(I)-catalyzed Huisgen 1,3-dipolar cycloaddition click-chemistry between acetylenylated substrate and azide terminated platinum (II) complex. For this reason, two different platinum (II) complexes were prepared. The synthetic route for the preparation of vinyl-terminated platinum (II) complex (**3**) is depicted in Scheme 2.2. Complex **3** was then covalently linked to the silicon substrate by polycondensation reactions induced by UV irradiation.

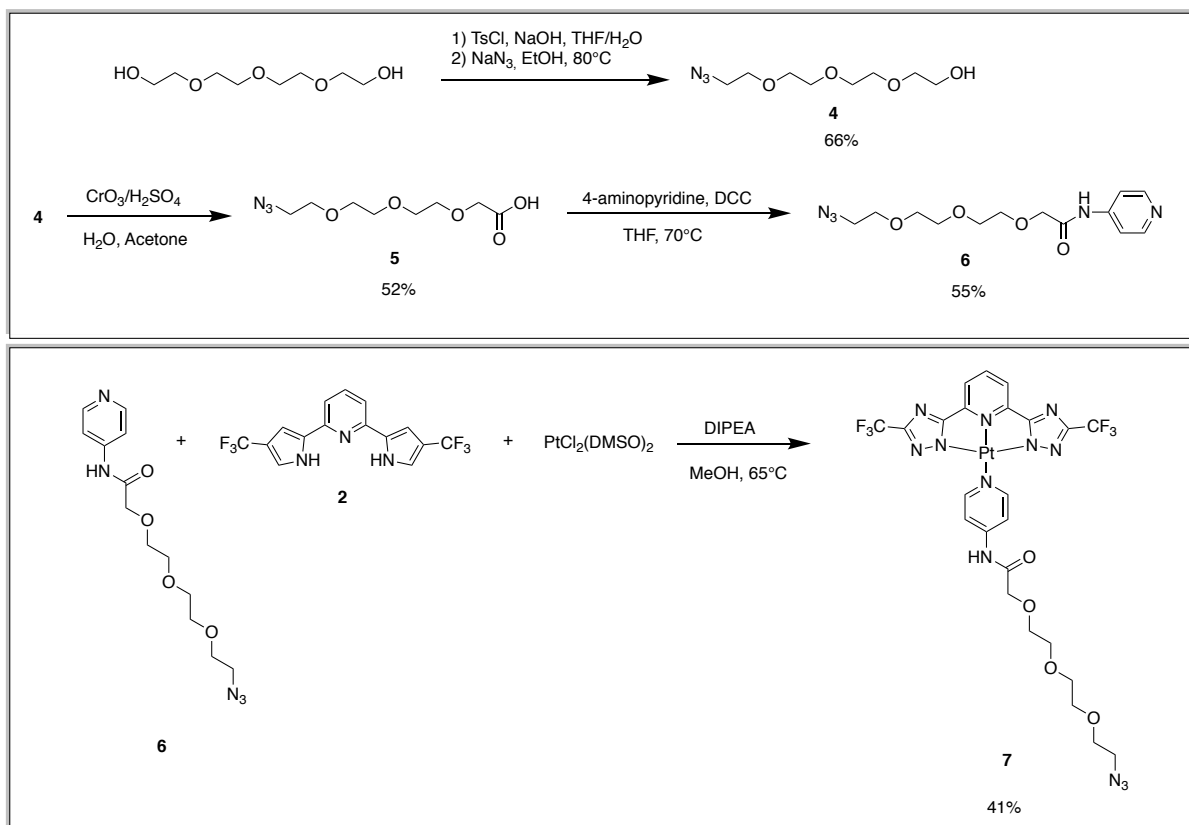


Scheme 2.2. Synthetic procedure for the preparation of vinyl-terminated platinum (II) complex **3**.

The tridentate ligand was coordinated to the platinum precursor PtCl₂(DMSO)₂ by deprotonation of its triazole rings in the presence of a non-nucleophilic base, diisopropylethylamine (DIPEA), and heating under inert atmosphere. The coordination sphere was then completed by addition of the 4-vinylpyridine as an ancillary ligand. Compound **3** was obtained after column chromatography purification as an orange powder.

The synthetic routes for the syntheses of the azide-terminated ligand **6** and the corresponding platinum (II) complex (**7**) is depicted in Scheme 2.3. Commercially available tetra(ethyleneglycol) was successively converted into a monotosylate and azide derivate (**4**)⁵⁰.

The hydroxyl group of compound **4** was then oxidized with freshly-prepared Jones reagent to give compound **5**⁵¹. Condensation of compound **5** with 4-amino pyridine in the presence of a coupling agent (dicyclohexylcarbodiimide, DCC) led to the desired ancillary ligand **6**. The corresponding platinum (II) complex was prepared as reported above.



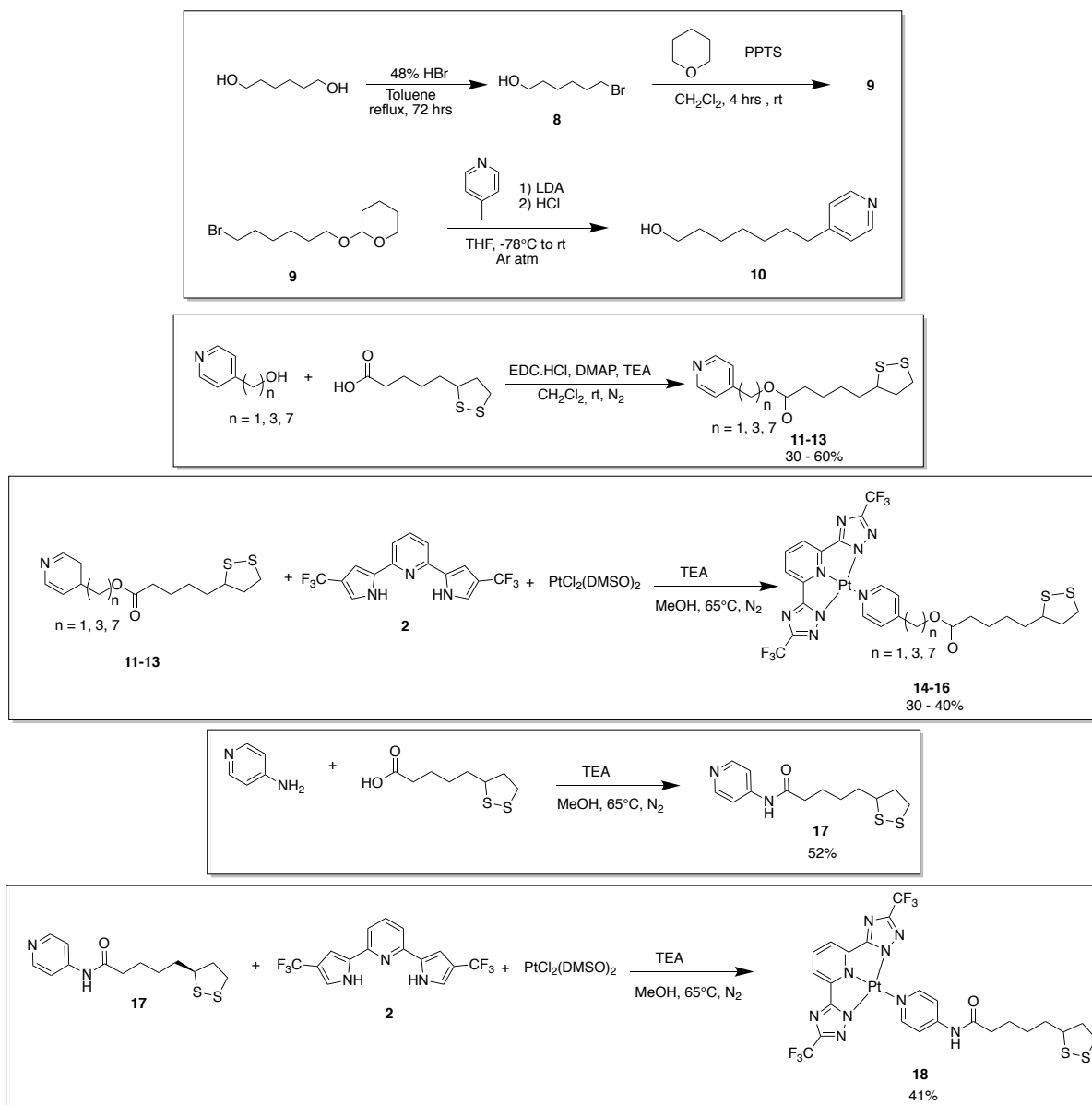
*Scheme 2.3. Synthetic route for the synthesis of the azide-terminated ligand and the corresponding platinum(II) complex **7**.*

The tridentate ligand was coordinated to the platinum precursor PtCl₂(DMSO)₂ and heated in methanol in the presence of a base diisopropylethylamine (DIPEA) under nitrogen atmosphere. The coordination sphere was completed by ancillary ligand **7**. The compound was obtained after column chromatography purification as an orange powder.

Gold

In order to attach platinum (II) complexes on the gold substrates, disulfide terminated ligands were firstly synthesized as depicted in Scheme **2.4**⁵². Pyridine with a short alkyl chain (1 or 3 - CH₂) as spacer and a hydroxyl functional group at the end in para position was commercially available. A longer spacer with a 7-members carbon chain was synthesised by bromination of

one hydroxyl group of 1,6 hexane-diol (**8**). Due to the presence of monobromo, dibromo, and non-brominated products, the reactional mixture was purified by column chromatography. The different spots of the TLC were revealed by a potassium permanganate solution. The single hydroxyl group of compound **8** was protected with 3,4-



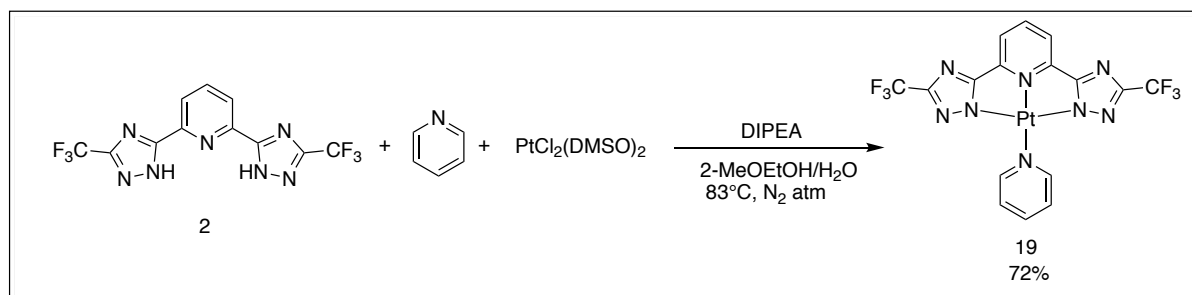
*Scheme 2.4. Synthetic route for the synthesis of disulfide terminated ligands and their corresponding platinum (II) complexes **14-16** and **18**.*

dihydro-2H-pyran to provide compound **9**. Bromide was substituted by deprotonated 4-picolone molecules in presence of a strong base lithium diisopropyl amide (LDA) and intermediate **10** was obtained after deprotection of the hydroxyl group in acidic conditions.

The ancillary ligands **11-13** were obtained after esterification of 4-(hydroxyalkyl) pyridines of differing chain lengths and α -lipoic acid, each as pale yellow oils. The oils were dissolved in methanol solutions and stored in the fridge. The corresponding platinum (II) complexes were prepared via the mixing of tridentate ligand **2**, the platinum precursor $\text{PtCl}_2(\text{DMSO})_2$ and ligands **11-13**. The complexes **14-16** were obtained after column chromatography purification as a yellow/orange coloured powders. An additional platinum (II) complex with an amide functional group instead of the ester was also prepared. 4-aminopyridine was coupled with α -lipoic acid via an amide bond and the resulting ligand (**17**) was coordinated to the platinum (II) complexes as mentioned above. The reactional mixture was purified by column chromatography and the resulting platinum (II) complex was obtained as an orange powder.

Physical vapor deposition (PVD)

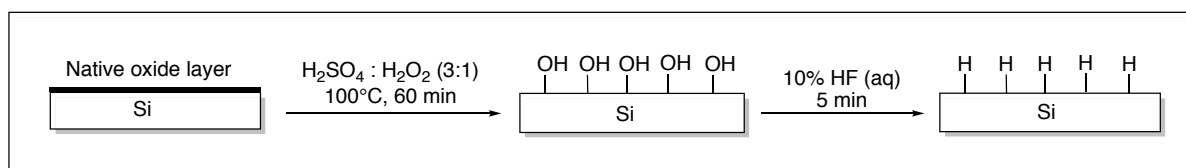
For the PVD by sublimation of the platinum (II) complex, a platinum (II) complex stable under reduced conditions and prone to self assemble into fibers was prepared as depicted on Scheme 2.5.



Scheme 2.5. Synthetic route for the preparation of two simple platinum(II) complexes.

2.2.2. Surface modification of silicon (100) via photochemical hydrosilylation

Silicon substrates (2 cm^2) were cleaned in a piranha solution for 60 min at 100°C and etched in 5% HF solution for 5 min. The substrate was smoothly agitated if bubbles appeared on the surface. A hydrogen-terminated surface was obtained and was stable for a couple of hours (Scheme 2.6).



Scheme 2.6. Preparation of H-terminated silicon substrates.

The cleaning and etching of the native silicon (100) wafer was followed by XPS analysis (survey and spectra are shown in Figure 2.1). The main difference between the XPS surveys spectra of the Si-H and Si-OH samples is the presence of an intense O 1s peak at 532 eV for Si-OH (Figure 2.1A). This was accounted for by the presence of numerous hydroxyl groups on the surface of the substrate.

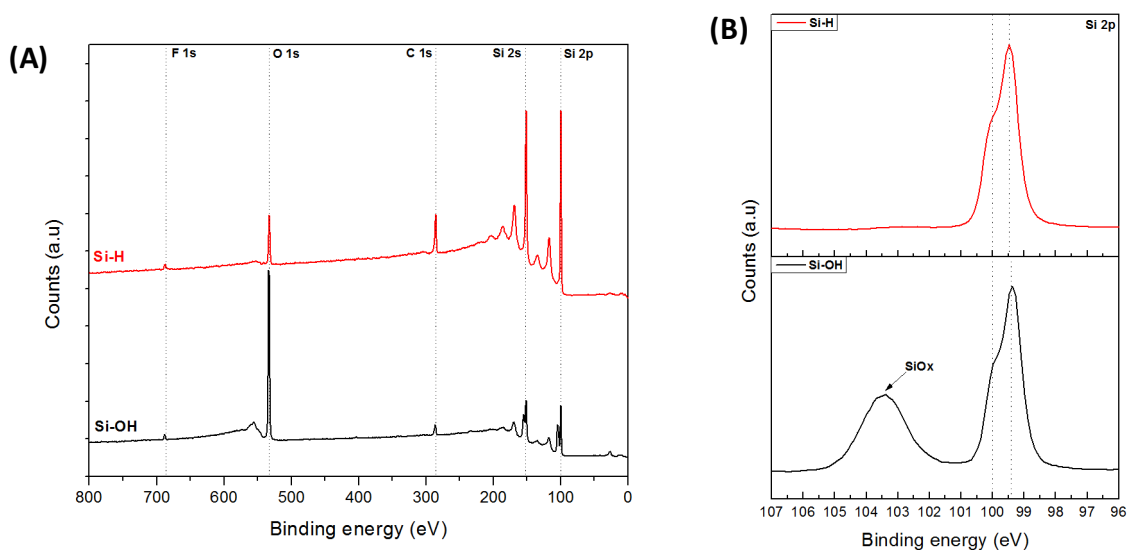
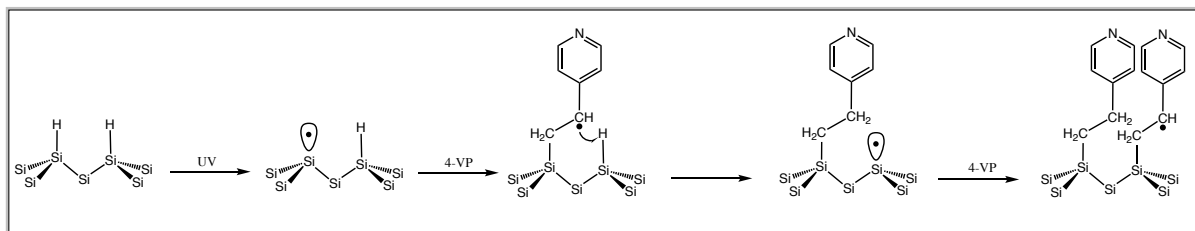


Figure 2.1. XPS survey (A) and high resolution spectra of the Si2p line (B) of Si-OH and Si-H substrates.

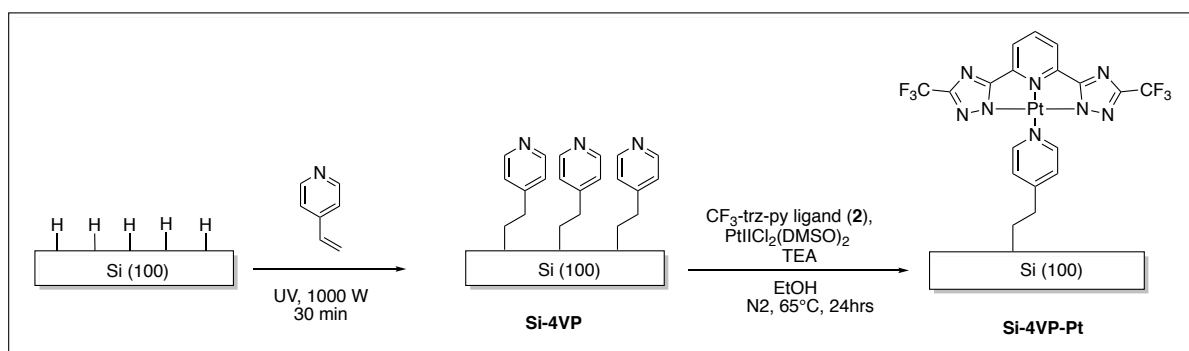
Consequently, the high-resolution XPS spectra of the Si 2p line for Si-OH, reported in Figure 2.1B, shows a broad peak around 103.5 eV for silicon oxides (SiO_x). The peaks at 99.4 eV and 100 eV are attributed to the two spin-orbit components $\text{Si } 2p_{1/2}$ and $\text{Si } 2p_{3/2}$ of the elemental Si^0 silicon. Upon etching, the hydroxyl groups were removed from the surface and the newly exposed material formed a hydride layer, which was only stable for a short time. As a result, the component of the Si 2p line for silicon oxides at 103.5 eV disappeared in the hydrogen-terminated sample (Si-H) as displayed in the high resolution spectra of the Si 2p signal (Figure 2.1B). The radical mechanism of the reaction between 4-vinylpyridine and Si-H surface is illustrated in Scheme 2.7 and is typical of radical polymerizations. In the initiation stage, UV irradiation (1000 W) causes the homolythical breakage of silicon-hydride bonds, to yield an immobilized silicon radical (or “dangling bond”) on the substrate. This reactive species readily reacts with olefins, such as 4-vinylpyridine, to form a secondary carbon radical. The reaction

propagates with the radical abstracting a nearby hydrogen atom to produce another dangling bond. The reaction keeps repeating as the chain reaction propagates along the surface⁵³.



Scheme 2.7. Schematic representation of the UV-induced free radical reaction between the 4-vinylpyridine and the H-terminated silicon substrate.

The coordination reaction of the platinum (II) complex to the pyridine-terminated surfaces is illustrated in Scheme 2.8. The Si-4VP substrate was immersed into a methanol solution containing the platinum precursor $\text{PtCl}_2(\text{DMSO})_2$, the tridentate ligand **2** and triethylamine. The substrate was rinsed thoroughly with ethanol to remove all of the uncoordinated 4-VP molecules.



Scheme 2.8. Schematic representation of the functionalisation of silicon wafer by UV-induced coupling.

Characterization of the surfaces by XPS

The functionalisation process was investigated by XPS. The high resolution XPS spectra are generally calibrated with the C-C peak at 284.8 eV as a reference. However, it was difficult to locate the C-C component in the C 1s peak because of the few C-C bonds on the Si-4VP and Si-4VP-Pt substrates. For this reason, the high resolution XPS spectra were calibrated on the Si $2p_{3/2}$ peak at 99.4 eV which did not move upon the different functionalisation. The survey scans of the successive surface modifications are displayed in Figure 2.2. Hydrogen-terminated substrate (Si-H) survey scans reveals C 1s, O 1s, Si 2s and Si 2p peaks along with a

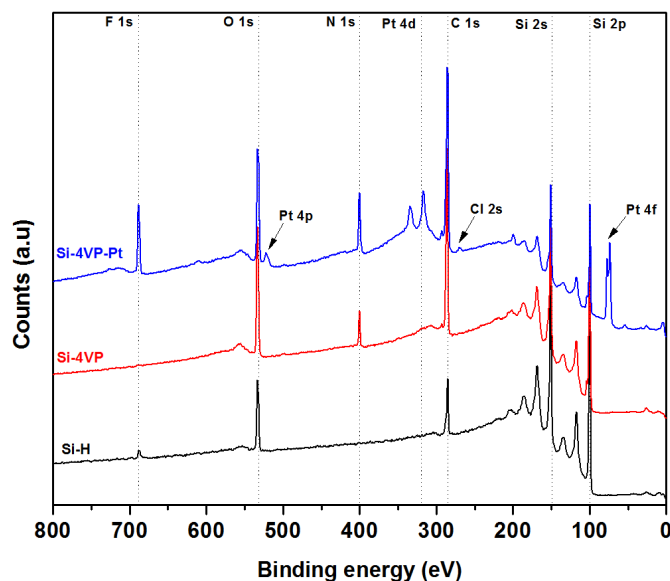


Figure 2.2. XPS survey scans of the freshly prepared hydrogen terminated surface (Si-H, black graph), after the grafting of 4-vinylpyridine (Si-4VP, red graph) and the formation of the platinum (II) complex (Si-4VP-Pt, blue graph).

small peak at 700 eV attributed to F1s. The chemical composition on the Si-H substrate is reported in Table 2.1. The Si2p line appears at 99.48 eV, close to the energy of the elemental silicon (99.4 eV). C1s and O1s peaks were attributed to adventitious carbon and oxygen contamination from the atmosphere. The F1s peak was a result of the remaining fluorine left on the surface after etching by 5% HF solution. The coupling between the 4-vinylpyridine and the Si-H substrate was confirmed by the presence of the N1s band around 398.9 eV, and attributed to the imine (-N=) of the pyridine. The chemical composition of the substrate is reported in Table 2.2. The Si2p band appears at a lower binding energy (98.7 eV) compared to the elemental silicon (99.4 eV). This indicates the formation of silicon-carbon bonds and a greater electropositive environment around the silicon atoms. Consequently, the binding energy was shifted to lower energies. The coverage of the 4-vinylpyridine (4-VP) on the silicon surface can be easily expressed as the $[N\ 1s]/[Si\ 2p]$ ratio because each molecule of 4VP contains one nitrogen atom. The ratio calculated from Table 2.2 was equal to 0.23, which is almost 4 times higher than reported in the literature for similar substrates²⁵. The formation of a monolayer of 4VP may be limited by the steric hindrance of the pyridine moiety and by the repulsion between pyridine units. After complexation of the platinum (II) complex, additional bands from Pt4f_{7/2}, Pt4f_{5/2}, Pt4d_{5/2}, Pt4p_{3/2}, and Pt4p at 73.13 eV, 76.24 eV, 315.45 eV, 332.41 eV and 520.63 eV were observed, along with an intense F1s band at 682.22 eV. The binding

energy of the Pt bands was higher in energy compared to the elemental platinum (71.2 eV) because of its oxidative state of +2 due to the platinum atom in the complex. The platinum atom in the platinum (II) complex is surrounded by four nitrogen atoms which stabilizes the binding energy of the electron of the platinum ion. The chemical composition of the Si-4VP-Pt substrate is reported in Table 2.3. The atomic percentage of platinum on the substrate was measured to be 1.61%. It is possible to determine the density of platinum (II) complexes on the surface by comparing the signals of the Si 2s, Pt 4d_{5/2}, and the Pt 4d_{3/2} peaks reported in Table 2.4⁴⁶. The chemical compositions of the silicon substrates are reported in Tables 2.1, 2.2 and 2.3. The XPS spectra were calibrated using the C 1s binding energy (284.80 eV) as standard.

Table 2.1. Chemical composition of the Si-H substrate.

Name	Peak BE	FWHM eV	Area (P) CPS.eV	Atomic %
Si 2p	100.09	2.27	776906.19	64.13
C 1s	285.41	1.81	281115.83	23.34
O 1s	533.06	2.87	315404.83	10.84
F 1s	687.83	3.19	61714.06	1.69

Table 2.2. Chemical composition of the Si-4VP modified substrate.

Name	Peak BE	FWHM eV	Area (P) CPS.eV	Atomic %
C 1s	286.29	2.69	671781.07	43.82
Si 2p	100.18	2.38	559370.87	36.26
O 1s	533.36	2.76	537281.95	14.50
N 1s	400.38	1.66	128996.21	5.42

Table 2.3. Chemical composition of the Si-4VP-Pt modified substrate.

Name	Peak BE	FWHM eV	Area (P) CPS.eV	Atomic %
C 1s	285.99	3.16	859805.21	50.49
Si 2p	100.05	2.43	345366.23	20.16
O 1s	532.95	2.95	422894.63	10.27
N 1s	400.68	2.06	263540.61	9.97
F 1s	688.41	2.87	334815.93	6.50
Pt 4f	74.32	2.82	519164.63	1.61
Cl 2p	199.34	3.61	48942.19	0.99

Table 2.4. Area ratios of the Pt 4d and Si 2s XPS signals in the survey spectra

	Si 2s	Pt 4d _{5/2}	Pt 4d _{3/2}	Si 2s/ Pt 4d _{5/2}	Si 2s/ Pt 4d _{3/2}
Si-4VP-Pt	352097	266282	178428	0.76	0.51

The (Si 2s/ Pt 4d_{5/2}) and (Si 2s/ Pt 4d_{3/2}) ratio were calculated to be below 1 meaning that the density of platinum (II) complexes was very low. Upon coordination of the platinum (II) complex on the substrates, traces of chlorine were observed with two peaks at 198.15 eV and 268.35 eV, attributed to Cl2p and Cl2s, respectively. One hypothesis was that the chlorine signal was due to the platinum (II) precursor PtCl₂(DMSO)₂. However, no traces of sulfur from DMSO were observed. High resolution XPS spectra of the C1s, N1s, Si2p and Pt4f (displayed in Figure 2.3) provided additional information on the surrounding environments of those atoms and the stability of the substrates. The native silicon (100) was efficiently etched by the 5% HF solution, evidenced by the fact that no oxidized silicon was observed between 101-104 eV (Figure 2.3A). Upon functionalization of Si-H substrate with 4-vinylpyridine and coordination of the platinum (II) complex, a broad low-lying band centered at approximately 103 eV was formed and confirmed the formation of silicon oxides. The intensity of the band of the silicon oxide was less than 10% of the intensity of the Si 2p bands. As previously mentioned, the shift in the lower energies of the Si 2p peak was the result of the formation of Si-C bonds, rather than the Si-H bonds. The high resolution XPS of the C 1s signal showed a low-lying band centered at approximately 292.5 eV for the Si-4VP-Pt substrate and was attributed to the –CF₃ moiety of the triazole ligand of the platinum (II) complex (Figure 2.3B). The high-resolution XPS spectra of N 1s displayed a sharp peak at 398.9 eV, originating from the single nitrogen of the pyridine. When the platinum (II) complex was coordinated to the substrate, a broader band centered at approximately 399.5 eV was observed. The signal was originating from the nitrogen atoms of the pyridine and from the different nitrogen atoms of the triazole ligand (Figure 2.3C). A comprehensive, detailed analysis of the high-resolution spectra of C 1s and N 1s will be provided in the section related to the functionalisation of gold substrates. These results confirmed the successful coordination of platinum (II) complexes on Si (100) substrates at a relatively low density. The direct addition of the platinum (II) complex (3) with the 4-vinylpyridine as ancillary ligand was also carried out. The hydrogen-terminated substrates were immersed in chloroform solution containing complex 3 and irradiated with UV lamp for 30 min. The procedure was exactly the same than for the coupling of 4VP on Si-H substrates. However, the XPS analysis did not show the presence of any platinum 4f peaks, meaning that the complex was not covalently bond to the silicon substrate. That was the reason why a detailed stepwise method, displayed in Scheme 2.8, was used in this study.

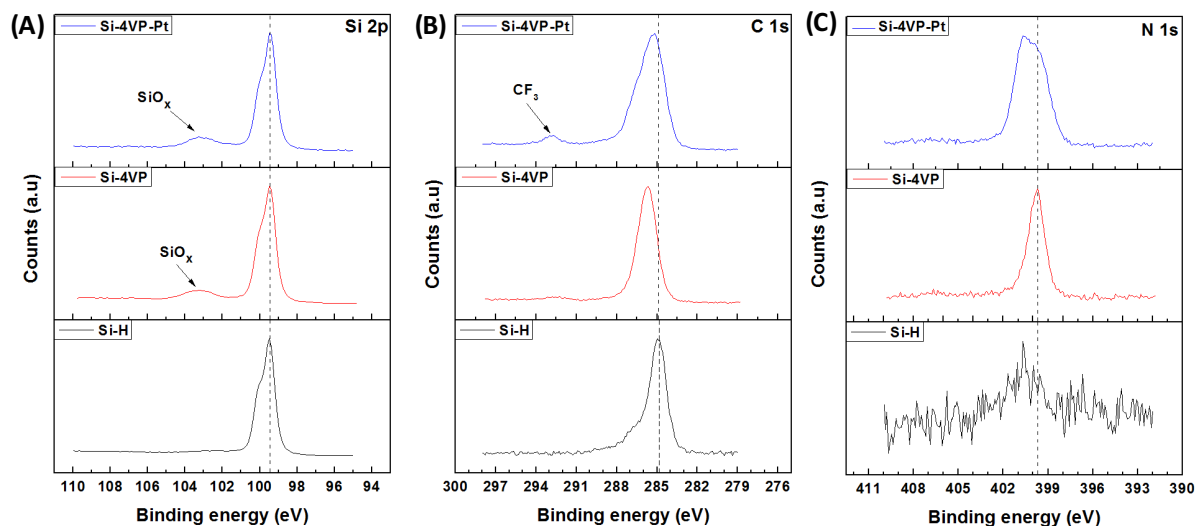


Figure 2.3. High resolution XPS spectra of C 1s(a), N 1s(b) and Si 2p(c) signals of Si-H, Si-4VP and Si-4VP-Pt substrates.

Water contact angle

Another method to determine if the surface was modified involved measuring its water contact angle. The water contact angles of the different substrates are reported in Table 2.5. The native silicon (100) wafer had a water contact angle of approximately 40°. This value decreased to 25° when the substrate was treated with a piranha solution, which removed traces of organics absorbed on the surface, while further oxidizing it to increase the number of –OH groups. Upon HF etching, the surface was mostly covered with hydrides, increasing the contact angle from 25° to 83°. The pyridine terminated substrate also provided a hydrophobic surface with a water contact angle of around 57°, but was not as hydrophobic as the Si-H surface. Finally, when the platinum (II) complex was coordinated to the substrate, there was a small change in the water contact angle compared to that of Si-4VP. The Si-4VP-Pt substrate was hydrophobic due to the presence of the triazole chelating ligand of the complex on the top of the surface.

Table 2.5. Water contact angle of the different substrates.

Native Si	Si-OH	Si-H	Si-4VP	Si-4VP-Pt
40.3 ± 0.25 °	27.3 ± 1.60 °	82.9 ± 0.77°	58.6 ± 0.36°	62.4 ± 0.55°
41.8 ± 1.60°	25.5 ± 1.65°	83.0 ± 0.73°	56.3 ± 0.32°	60.6 ± 0.52°

Atomic force microscopy (AFM)

The topographies of the functionalised silicon substrates were studied by AFM. Figure 2.4 shows the AFM images of the native silicon (100) wafer and Si-4VP and Si-4VP-Pt modified substrates. Additional information regarding the roughness (R_A , calculated as the root-mean-square difference from the average of the surface height) of the different surfaces were also reported.

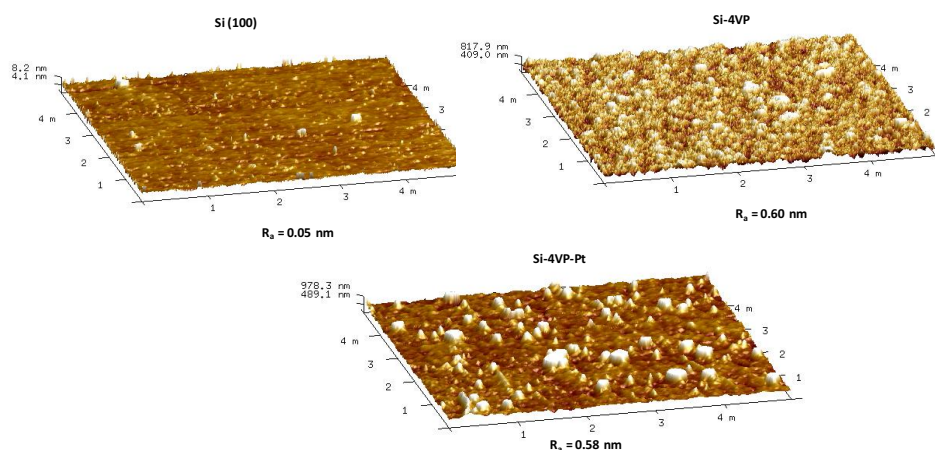


Figure 2.4. Topography of the native Si(100) wafer and modified Si-4VP and Si-4VP-Pt substrates. R_A is the root-mean-square surface roughness value.

The surface of the native silicon (100) wafer was quite smooth and uniform with a R_A value of approximately 0.05 nm. After hydrosilylation, R_A increased to 0.60 nm, indicating a modification of the surface topology. The increased roughness could also be associated to the formation of silicon oxide. Finally, when the platinum (II) complex was coordinated to silicon substrate, the roughness of the surface slightly decreased in value to 0.58 nm. The height of the monolayer could not be determined due to the lack of a reference on the substrate.

Photophysical properties.

The emission spectra of the native silicon substrate, Si-4VP and Si-4VP-Pt are displayed in Figure 2.5 and are all similar. It was hypothesized that the concentration of platinum (II) complex on the substrate was below detectable levels and the broad band around 680 nm was attributed to the silicon wafer. Indeed, the XPS analysis showed a low density of platinum (II) complexes on the surface. Another hypothesis was that the silicon substrate interacted

with the platinum (II) complex and quenched the luminescence. The final hypothesis was that the complexation reaction failed and only the non-emissive physisorbed platinum precursor was detected by the XPS. However, the substrate was rinsed several times with various solvents and thus the presence of physisorbed molecules was highly unlikely.

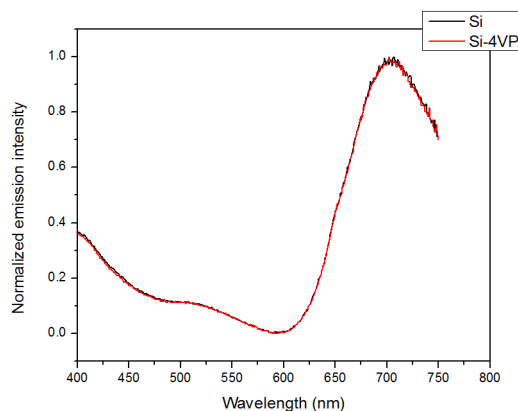
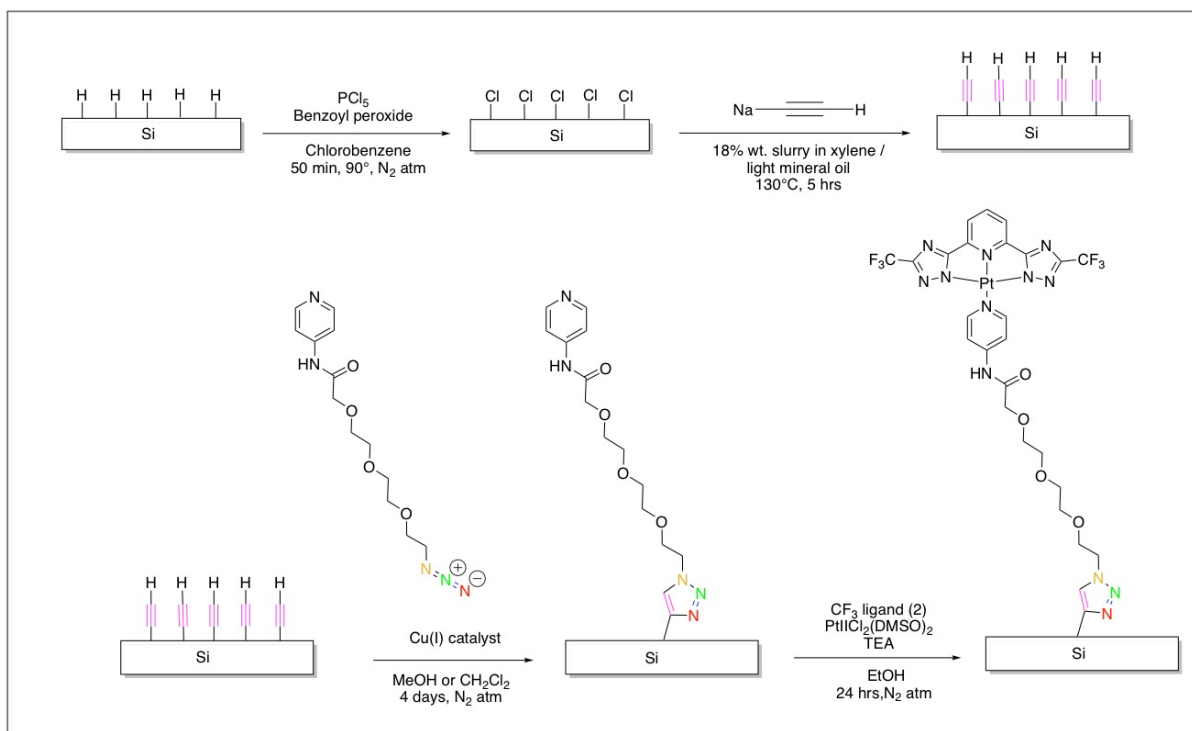


Figure 2.5. Emission spectra of native silicon (100) wafer (black line) and functionalised Si-4VP substrate (red line). $\lambda_{em} = 300$ nm.

2.2.3. Surface modification of silicon (100) via click chemistry

The second strategy explored the attachment of platinum (II) complexes on silicon substrates and involved the use of copper (I)-catalyzed alkyne-azide cycloaddition, a well-known example of click-chemistry. The preparation route is illustrated in Scheme 2.9. Native silicon (100) substrates were again cleaned with a piranha solution and etched with 5% aqueous HF. Surface hydrides were then substituted by chlorine in the presence of the benzoyl peroxide. Acetylene molecules were then attached to the substrate by acetylenylation reaction, immersing the chlorinated substrates in a sodium acetylide solution. The coverage of the acetylene molecules on the substrates was estimated to be around 90% and this was consistent with other studies⁵⁵. The C 1s signal of acetylenated substrates was compared to the C 1s signal of freshly prepared Si-CH₃, which were used as a reference, and 100% coverage of CH₃ on the surface. The intensity of the peaks around 284 eV attributed to the silicon-carbon bond were then compared. Three Si-methyl and Si-acetylene substrates were prepared and their C 1s signals compared to determine an average 90% coverage of the acetylene molecules on the silicon substrates.



Scheme 2.9. Schematic representation of the functionalisation of silicon (100) wafer by click-chemistry between an azide terminated platinum (II) complex and acetylenated substrate.

In principle, according to Scheme 2.9, it would make no difference having the azide immobilized on the surface and the alkyne moieties on the ancillary ligand. However, azides tend to be unstable compared to alkynes, easily losing the nitrogen to yield other species such as amines. This, together with the ease of surface modification with alkynes, made the alkylation of the silicon surface a preferable method to immobilize the ancillary ligand. Moreover, azides and alkynes are tolerant to other functionalities and are highly specific, as the coupling can only occur between these two groups⁵⁶. Copper(I) iodide was chosen as a catalyst for the reaction between the acetylenated substrates and the azide terminated ligand. Cu(I) acetate and Cu(II)SO₄ (in presence of sodium ascorbate as reducing agent) were also successfully used with similar results to Cu(I) iodide. The final step was the complexation reaction between the anchored ligand, the platinum precursor and the triazole ligand in solution.

Characterization of the surfaces by XPS

The high resolution XPS spectra were calibrated on the Si 2p_{3/2} peak at 99.4 eV. Survey and high resolution XPS scans of the different substrates are displayed in Figure 2.6. XPS survey scan of the hydrogen terminated silicon substrates (Si-H) displayed the presence of the C 1s

and O 1s peaks at 284.8 eV and 532 eV, which originated from the atmosphere contamination on the substrates.

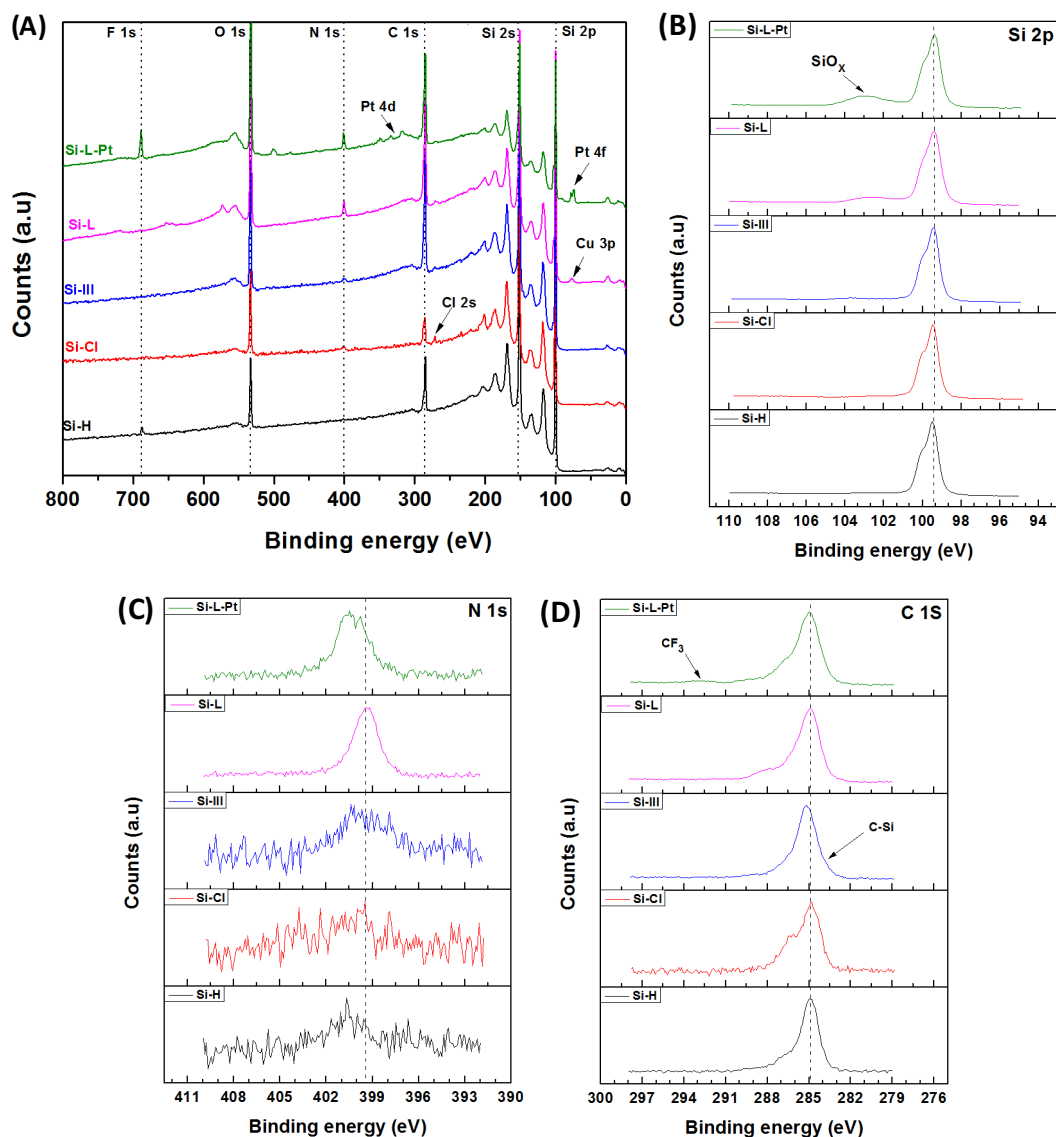


Figure 2.6. XPS survey scans (A) and high-resolution C 1s (B) and N 1s (C) scans of the successive surface modifications from Si-H (black curve) to Si-L-Pt (green curve).

The chlorination of the substrate (Si-Cl) was confirmed by the presence of the Cl 2s peak at 270 eV. The attachment of acetylene molecules on the surface was confirmed by the presence of a shoulder at 283.2 eV in the high-resolution spectra of C 1s peak (Figure 2.6B). The success of the “click” reaction between the acetylenated substrate and the azide-terminated ligand was confirmed by the presence of the N 1s peak in the survey spectra. Traces of the copper catalyst were also left on the sample. Finally, the coordination of the platinum (II) complex was confirmed by the presence of the Pt 4f peak at 73.8 eV in the survey spectra and a low-

lying band at 293 eV in the high-resolution XPS spectra of C 1s signal. It is worth noting that the peak of the platinum at 73.8 was very weak compared to Si 2p. The evolution of the recorded elemental composition on the modified silicon substrates is reported in Tables 2.5-2.9.

Table 2.5. Chemical composition on the Si-H substrate

Name	Peak BE	FWHM eV	Area (P) CPS.eV	Atomic %
Si 2p	100.09	2.27	776906.19	64.13
C 1s	285.41	1.81	281115.83	23.34
O 1s	533.06	2.87	315404.83	10.84
F 1s	687.83	3.19	61714.06	1.69

Table 2.6. Chemical composition of the Si-Cl substrate

Name	Peak BE	FWHM eV	Area (P) CPS.eV	Atomic %
Si 2p	100.85	1.48	173540.57	63.06
C 1s	286.28	3.25	49490.53	18.09
O 1s	533.19	2.77	91659.84	13.86
Cl 2p	201.40	3.36	22489.71	2.84
N 1s	402.13	3.50	9108.39	2.15

Table 2.7. Chemical composition of the Si-III substrate.

Name	Peak BE	FWHM eV	Area (P) CPS.eV	Atomic %
Si 2p	100.20	2.32	498951.90	47.88
C 1s	286.01	2.93	345807.74	33.38
O 1s	533.35	2.93	380409.88	15.20
Cl 2p	201.34	3.88	67144.09	2.24
N 1s	399.97	4.60	20940.80	1.30

Table 2.8. Chemical composition of the Si-Ligand substrate

Name	Peak BE	FWHM eV	Area (P) CPS.eV	Atomic %
C 1s	285.43	2.96	623693.50	39.74
Si 2p	100.05	2.42	538534.93	34.12
O 1s	532.38	2.83	757725.77	19.97
N 1s	400.04	2.89	93780.09	3.85
Cu 2p _{3/2}	934.10	4.16	341031.47	2.13
I 3d	619.95	2.99	97946.49	0.19

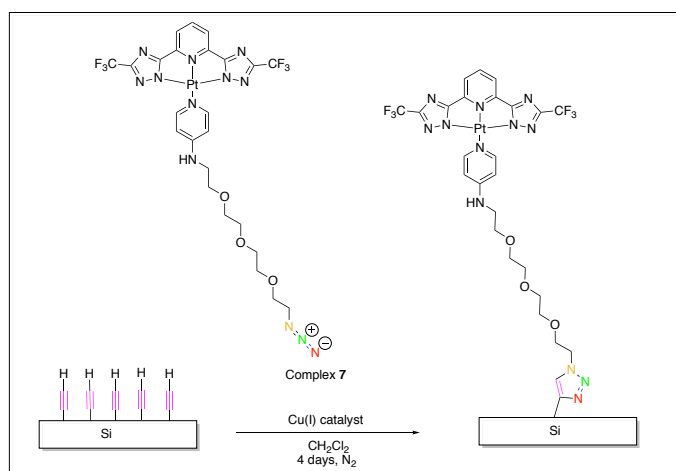
Table 2.9. Chemical composition of the Si-L-Pt substrate

Name	Peak BE	FWHM eV	Area (P) CPS.eV	Atomic %
Si 2p	100.13	2.50	598898.41	36.37
C 1s	285.86	3.18	523752.19	32.00
O 1s	533.02	2.88	1036457.41	26.20
N 1s	400.96	3.27	71109.92	2.80
F 1s	689.18	3.18	119950.73	2.43
Pt 4f	75.18	3.63	64595.67	0.21

Table 2.10. Area ratios of the Pt 4d and Si 2s XPS signals in the survey spectra.

	Si 2s	Pt 4d _{5/2}	Pt 4d _{3/2}	Si Pt 4d _{5/2} / Si 2s	Si Pt 4d _{3/2} / Si 2s
Si-L-Pt	556951	27434	16145	0.049	0.029

Platinum only represented 0.35% atomic of the overall substrate. The (Si 2s/ Pt 4d_{5/2}) and (Si 2s/ Pt 4d_{3/2}) ratio reported in Table 2.10 were extremely low compared to the method studied previously via UV induced polycondensation and the literature⁴⁶. The density of platinum (II) complex on the final substrate was very low. This could be accounted for by the successive surface modification, which degraded the quality of the substrate. It could also be attributed to the size of the platinum(II) complex, which prevents a high coverage due to steric hindrance. Another theory is the efficiency of the click-chemistry. In order to optimise the CuAAC, more optimal reaction conditions may be investigated. In order to improve the platinum (II) complex coverage, a direct click-chemistry between the complex 7 and the acetylenated substrate was performed as depicted in Scheme 2.10.



Scheme 2.10. Schematic representation of the acetylenated surface with complex 7 by CuAAC click-chemistry.

To study the role of the concentration of complex **7** in solution, the substrates were immersed in solutions with 0.1 mM, 1.0 mM, and 10 mM concentrations in anhydrous dichloromethane and copper(I) iodide. The XPS survey scan and high-resolution spectra of the N 1s, C 1s and Pt 4f of complex **6** powder are displayed in Figure 2.7. The high resolution of the Pt 4f signal displayed the spin-orbit splitting of the platinum and the Pt 4f_{7/2} and Pt 4f_{5/2} with an area ratio of 3 :4 under the peaks. The most interesting feature was the presence of a small peak around 404.5 eV peak in the high-resolution spectra of the N 1s signal (Figure 2.7c). It was attributed to the positively charged central nitrogen atom of the azide functional group⁶⁴. It could be used as a reference for the success of the click chemistry as the azide functional group was transformed in a triazole group.

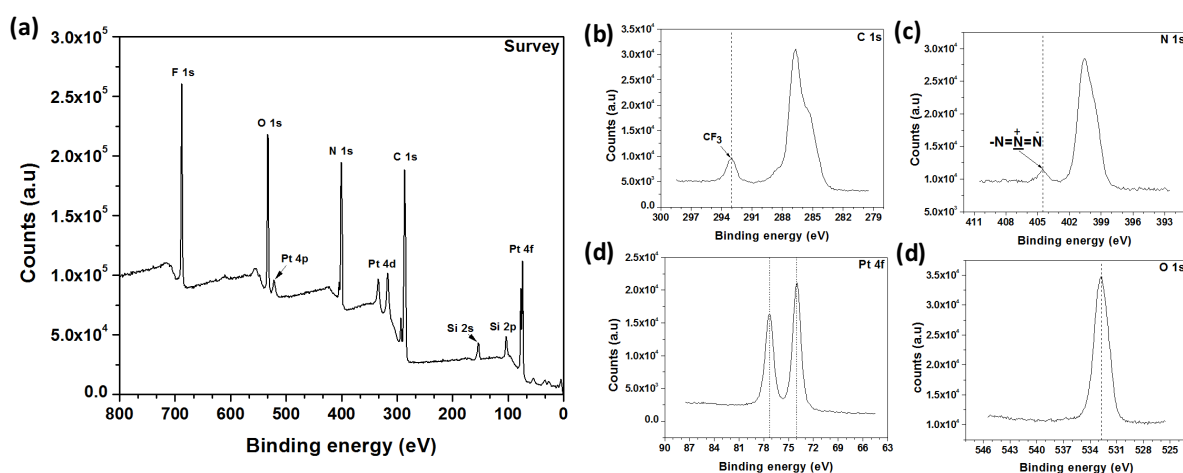


Figure 2.7. XPS survey scan (a) and high resolution XPS spectra of C 1s (b), N 1s (c), pt 4f (d) and O 1s (e) of the platinum(II) complex **7** powder.

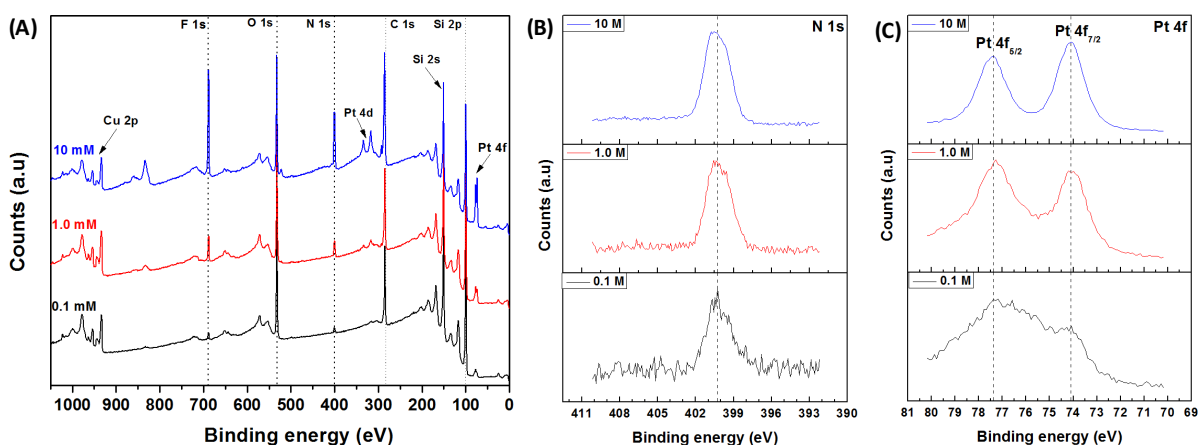


Figure 2.8. XPS survey scans (a) and high resolution XPS spectra of N 1s (b) and Pt 4f (c) signal of the functionalised substrates immersed in complex **6** dichloromethane solution of different concentration.

The XPS spectra of the functionalised silicon substrates are displayed in Figure 2.8. Upon increasing the concentration of complex 6 in solution, the intensity of the Pt 4f peak at 74.0 eV and 77.4 eV was clearly increased in the survey spectra and better resolved in the high resolution XPS spectra of Pt 4f signal (Figure 2.8c). Moreover, there was no peak at 404 eV (previously attributed to the central nitrogen of the azide functional group) on the high-resolution XPS spectra of the N 1s signal on the substrates (Figure 2.8b). Consequently, most of the azide groups reacted with the surface and transformed into triazole groups. Additional peaks at 932 eV and 952 eV were attributed to the Cu 2p₃ signal, which confirmed the presence of remaining Cu (I) iodide on the surface despite being washed several times. The traces of copper were removed by immersion of the substrates in a 0.05% EDTA aqueous solution⁵⁷ and checked by XPS. Chemical compositions on the surfaces of the modified silicon surfaces are reported in Tables 2.11-2.13 and the area of Pt 4d and Si 2s XPS signals in Table 2.14.

Table 2.11. Chemical composition on the Si-Pt substrate immersed in 0.1 mM solution.

Name	Peak BE	FWHM eV	Area (P) CPS.eV	Atomic %
Si 2p	99.94	2.42	703678.23	45.83
C 1s	285.25	2.93	441497.70	28.92
O 1s	532.26	2.81	749101.50	20.30
Cu 2p _{3/2}	933.91	3.44	353099.27	2.27
N1s	400.29	3.55	40682.22	1.72
F 1s	688.77	2.79	31004.77	0.67
Pt 4f	76.82	4.92	38345.11	0.30

Table 2.12. Chemical composition on the Si-Pt substrate immersed in 1 mM solution.

Name	Peak BE	FWHM eV	Area (P) CPS.eV	Atomic %
Si 2p	99.91	2.44	598477.76	38.15
C 1s	285.37	3.09	501162.35	32.13
O 1s	532.21	2.89	712790.64	18.90
N 1s	400.27	2.98	100939.45	4.17
F 1s	688.37	2.84	150664.28	3.20
Cu 2p _{3/2}	934.18	4.00	445254.23	2.80
Pt 4f	74.51	2.36	106019.95	0.64

Table 2.13. Chemical composition on the Si-Pt substrate immersed in 10 mM solution.

Name	Peak BE	FWHM eV	Area (P) CPS.eV	Atomic %
C 1s	286.07	3.47	669173.33	39.68
Si 2p	99.93	2.44	396665.15	23.37
O 1s	532.38	2.91	509858.94	12.50
N 1s	400.37	2.94	312285.67	11.93
F 1s	688.40	2.82	519190.76	10.18
Cu 2p _{3/2}	934.10	3.80	235868.82	1.37
Pt 4f	74.35	2.79	310239.41	0.97

Table 2.14. Area ratios of the Pt 4d and Si 2s XPS signals in the survey spectra.

	Si 2s	Pt 4d _{5/2}	Pt 4d _{3/2}	Pt 4d _{5/2} / Si 2s	Pt 4d _{3/2} / Si 2s
0.1 M	770793	7638	5519	0.010	0.007
1.0 M	692701	36975	24951	0.053	0.036
10 mM	421920	163102	110049	0.39	0.261

The atomic percentage of the platinum element is increased when the concentration of **complex 7** in solution, is increased from 1×10^{-5} M to 1×10^{-3} M. However, the platinum element only represented around 1% of the overall chemical composition. The (Si 2s/ Pt 4d_{5/2}) and (Si 2s/ Pt 4d_{3/2}) ratio is increased from 0.007 to 0.261, which is very weak compared to previous study⁴⁶. A possible explanation for this is that the platinum (II) complex **6** was sufficiently large enough to induce some steric hindrances on the surface and limit the grafting on the substrate.

In conclusion, platinum (II) complexes were attached to silicon (100) substrate by stepwise and pre-synthesised methods. XPS analysis provided valuable information on the follow-up of the different surface modifications and surface coverages. Although the platinum (II) complex was successfully attached to the surface; only a little amount of the complex was actually covalently bond to the substrate. The low coverage did not allow further analysis of the substrates. The different strategies used in this chapter will need to undergo further optimisation in order to increase the surface coverage of the platinum (II) complex.

2.2.4. Functionalisation of gold substrates

Three platinum (II) complexes of varying chain lengths were prepared and are depicted in Figure 2.9.

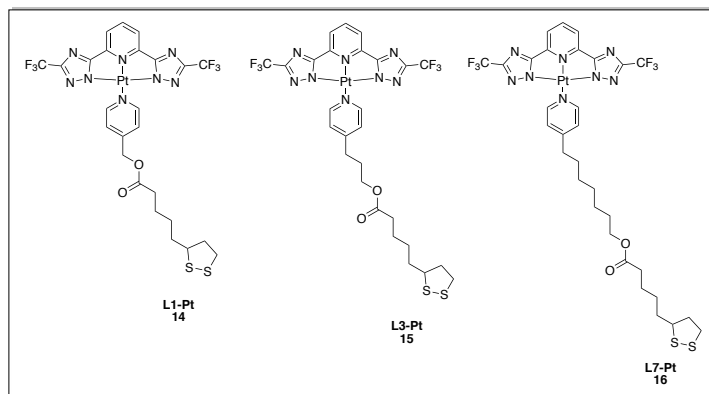


Figure 2.9. Chemical structures of the platinum (II) complexes used for the functionalisation of gold substrates. The numbers (L1, L3 and L7) represents the number of methyl groups between the pyridine and the ester functional group of the ancillary ligand.

2.2.4.1. Photophysical properties

Platinum (II) complexes L1-Pt, L3-Pt and L7-Pt were not soluble in most of the common nonpolar and polar protic organic solvents. Polar aprotic solvents such as THF or DMF dissolved these complexes more efficiently. The emission and excitation spectra of L1-Pt, L3-Pt and L7-Pt are displayed in Figure 2.10. Excited state lifetimes and photoluminescent quantum yields are reported in Table 2.15.

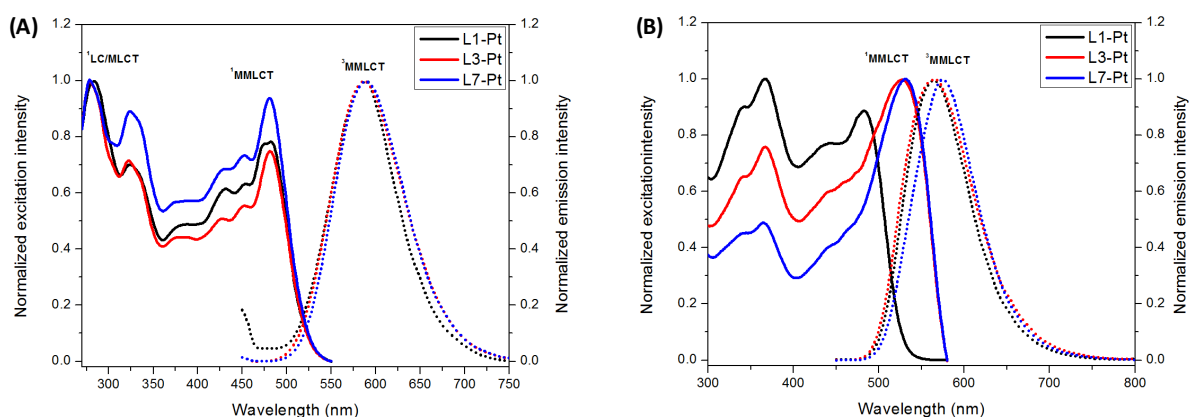


Figure 2.10. Normalised emission and excitation spectra of L1-Pt, L3-Pt and L7-Pt in DMF at a concentration of 5.0×10^{-5} M (A) and in solid state (B). $\lambda_{exc} = 400$ nm, $\lambda_{em} = 570$ or 590 nm.

Table 2.15. Photophysical properties of the three platinum(II) complexes

Sample	Medium	$\lambda_{\text{max,em}}$ (nm)	PLQY	τ (ns)
L1-Pt	DMF	587	< 0.01	7 (55%), 95(15%), 400 (31%)
	Solid	567	0.22	70 (49%), 260 (50%), 975 (1%)
L3-Pt	DMF	587	0.02	130 (21%) 395 (79%)
	solid	565	0.21	135 (76%), 310 (24%)
L7-Pt	DMF	591	0.03	130 (9%), 420 (91%)
	solid	576	0.30	35 (49%), 265 (9%), 120 (42%)

Although the platinum (II) complexes were partially dissolved in DMF, the emission spectra displayed a broad band centered at approximately 590 nm, which was attributed to the ³MMLCT. This indicates the presence of platinum aggregates in solution, confirmed by the presence ¹MMLCT bands between 400 nm and 500 nm in the excitation spectra.

2.2.4.2. Functionalisation of the gold substrates

The gold substrates were cleaned by UVO cleaning for 30 minutes and immersed in a 1.0×10^{-3} M DMF solution of platinum (II) complex for 6 days. The substrates were then thoroughly rinsed with DMF and ethanol and dried under a nitrogen flow. The substrates were stored under vacuum prior to analysis. The nature of the disulfide-gold bond and more broadly, the gold-sulfur bond remains unanswered⁶⁵. Whether it is a covalent bond or ionic bond, it is a very strong bond but it will not be discussed in this thesis.

2.2.4.3. X-ray photoelectron spectroscopy (XPS)

The high resolution XPS spectra were calibrated on the C-C component of the C 1s peak at 284.8 eV. The XPS survey scan and high resolution XPS spectra of C 1s, N 1s, O 1s, S 2p and Pt 4f signals for the three platinum (II) complexes L1-Pt, L3-Pt and L7-Pt are displayed in Figures 2.11, 2.12 and 2.13 respectively. The survey scans of the three complexes on gold indicated the presence of F 1s, O 1s, N 1s, C 1s, S 2p and Pt 4f, corresponding to all of the elements of the platinum (II) complexes (Figures 2.11-2.13, a). The chemical compositions on the surfaces of the functionalised gold substrates are reported in Tables 2.16-2.18. The atomic percentage of the platinum was approximately 1% for the three platinum (II) complexes on gold. The density of the platinum (II) complexes on the gold substrate was estimated by comparing the Au 4d and Pt 4f peaks intensities as reported in Table 2.19. The $(\text{Pt } 4f_{7/2} / \text{Au}$

$4d_{5/2}$) and (Pt $4f_{5/2}$ /Au $4d_{3/2}$) were calculated to be around 0.01 confirming the low density of the platinum (II) complexes on the substrate. The high resolution spectra of the Pt $4f$ signal was similar for the three complexes with two peaks at 72.6 eV and 77 eV, attributed to the spin orbit splitting into Pt $4f_{7/2}$ and Pt $4f_{5/2}$, respectively. The peak of the Pt $4f$ signal was close to the intense peak of the Au $4f$ signal. Consequently, the signal of the Pt $4f$ was not flat and was difficult to deconvolute (Figures 11-13, f).

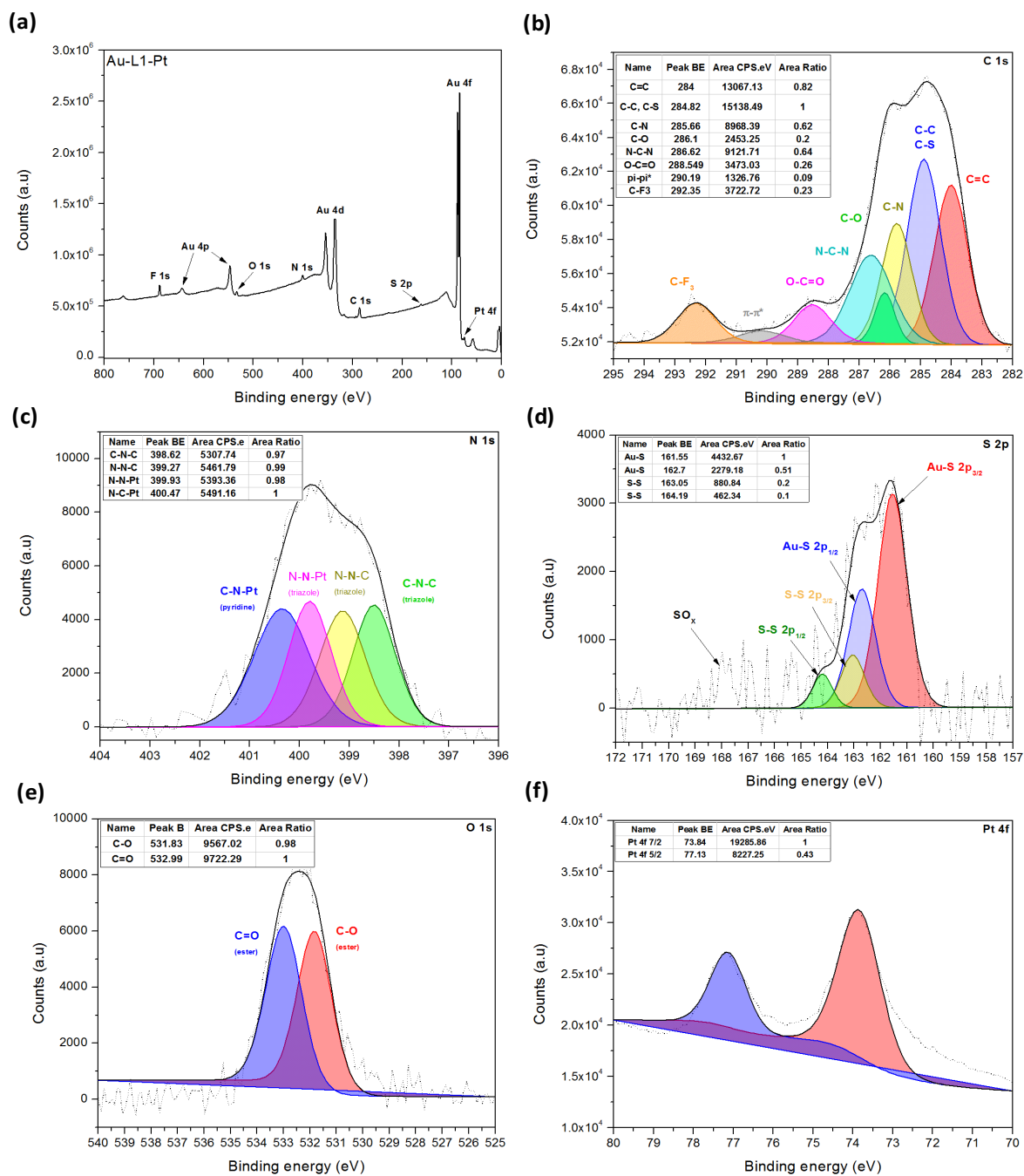


Figure 2.11. XPS survey scan (a) and high resolution XPS spectra of C 1s (b), N 1s (b), S 2p (d), O 1s (e), Pt 4f (f) of L1-Pt platinum(II) complexes on gold.

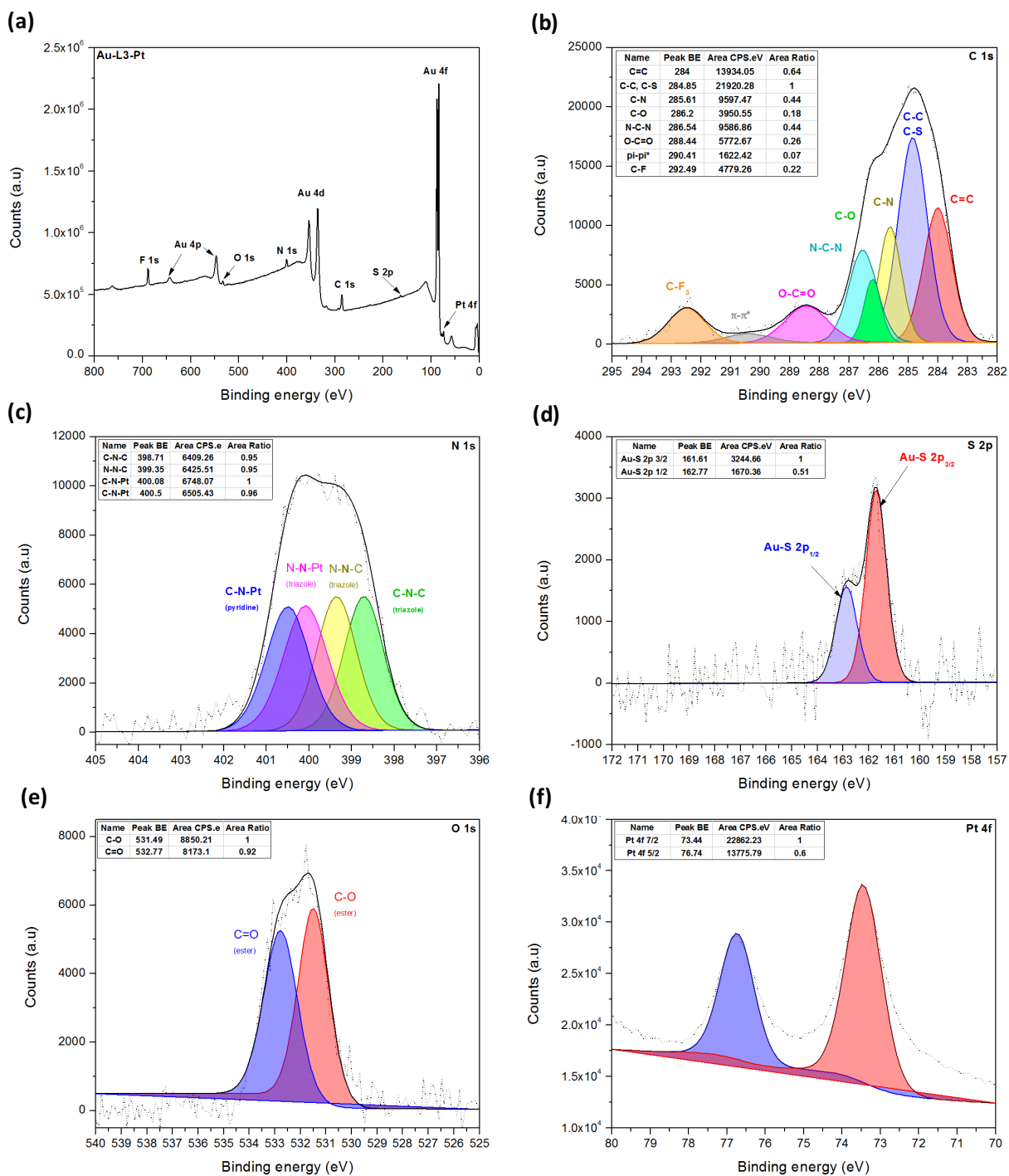


Figure 2.12. XPS survey scan (a) and high resolution XPS spectra of C 1s (b), N 1s (c), S 2p (d), O 1s (e), Pt 4f (f) of L3-Pt platinum(II) complexes on gold.

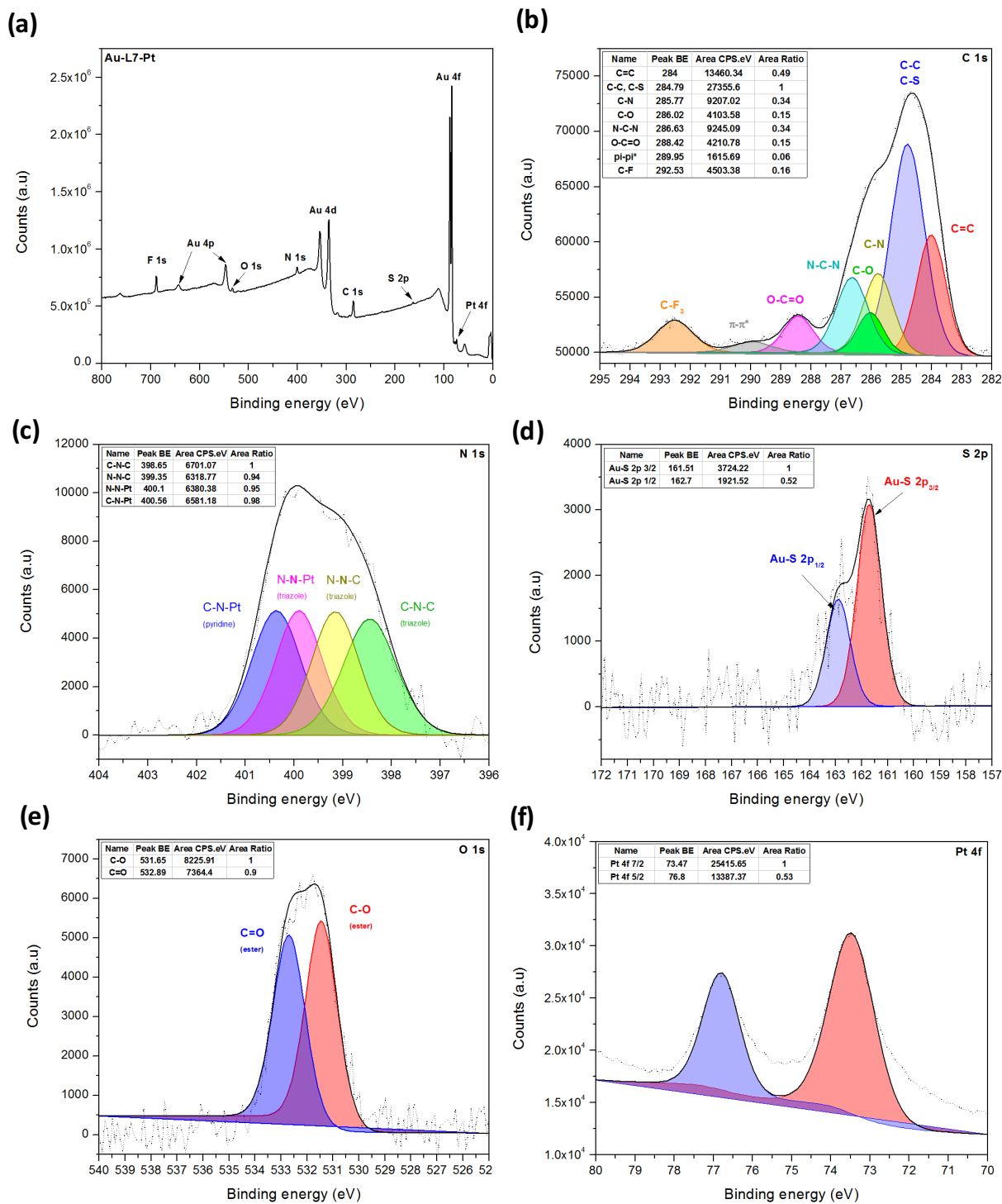


Figure 2.13. XPS survey scan (a) and high resolution XPS spectra of C 1s (b), N 1s (c), S 2p (d), O 1s (e), Pt 4f (f) of L7-Pt platinum(II) complexes on gold.

Table 2.16. Chemical composition of L1-Pt on gold substrate

Name	Peak BE	FWHM eV	Area (P) CPS.eV	Atomic %
Au 4f	84.33	2.57	10142388.86	34.76
C 1s	286.09	3.49	431673.97	34.60
N 1s	400.44	3.60	218868.91	11.30
F 1s	688.76	2.88	398149.51	10.55
O 1s	532.95	3.03	134923.71	4.47
S 2p	162.71	3.28	88031.88	3.48
Pt 4f	73.88	2.94	197712.26	0.84

Table 2.17. Chemical composition of L3-Pt on gold substrate

Name	Peak BE	FWHM eV	Area (P) CPS.eV	Atomic %
C 1s	286.06	3.29	522905.75	40.76
Au 4f	84.35	1.65	8731455.93	29.11
F 1s	688.82	2.81	477262.66	12.31
N 1s	400.71	1.93	220386.08	11.07
O 1s	533.05	3.05	96091.63	3.10
S 2p	163.02	2.91	69228.20	2.66
Pt 4f	73.95	2.93	241491.06	1.00

Table 2.18. Chemical composition of L7-Pt on gold substrate

Name	Peak BE	FWHM eV	Area (P) CPS.eV	Atomic %
C 1s	285.95	3.41	617386.95	42.97
Au 4f	84.27	2.56	9047251.72	26.93
F 1s	688.82	2.88	515891.49	11.88
N 1s	400.74	3.21	260273.83	11.67
S 2p	162.89	2.96	83638.50	2.87
O 1s	532.91	2.87	96346.59	2.77
Pt 4f	73.93	2.90	246507.61	0.91

Table 2.19. Area ratios of the Pt 4f and Au 4d XPS signals in the survey spectra.

	Au 4d _{5/2}	Au 4d _{3/2}	Pt 4f _{7/2}	Pt 4f _{5/2}	Pt 4f _{7/2} / Au 4d _{5/2}	Pt 4f _{5/2} / Au 4d _{3/2}
Au-L1-Pt	4619235	2880023	37117	26746	0,008	0,009
Au-L3-Pt	3787537	2460811	39192	27443	0,010	0,011
Au-L7-Pt	3716238	2500196	44701	29629	0,012	0,012

The high-resolution spectra of the O 1s signal was deconvoluted into two peaks with similar areas under the curve, both from the ester functional group of the complexes and the adventitious oxygen (Figures 2.11-2.13, e). The high-resolution XPS spectra of the N 1s signal were also similar for the three platinum (II) complexes. Indeed, the nitrogen atoms are located on the triazole and pyridine moieties of the CF₃ triazole ligands of the complex. The broad band of the N 1s signal was deconvoluted into 4 smaller peaks of equal area under the curves (Figures 2.11-2.13, c). The signal corresponding to the nitrogen of the pyridine (C-N-Pt) was at a higher binding energy (\approx 400.5 eV) due to the electropositive environment and the lack of a non-covalent bond. For a similar reason, the signal corresponding to the nitrogen of the triazole linked to the platinum atom (N-N-Pt) was also at a higher binding energy (400 eV). However, it was lower than the signal of the nitrogen from the pyridine due to the octet rule. The signal corresponding to the nitrogen of the triazole moiety surrounded by one atom of nitrogen and one atom of carbon (N-N-C) eventuated around 399.35 eV. Finally, the signal of the nitrogen of the triazole ligand surrounded by two atoms of carbon (C-N-C) was at the lower binding energy (388.65 eV) due to the electron withdrawing character of the nitrogen towards the carbon, which resulted in an increased electronegative environment. The high resolution spectra of the C 1s signal was also deconvoluted into numerous peaks (Figures 2.11-2.13, b). The carbon atoms surrounded by the most electron withdrawing groups have the highest binding energy. In decreasing order, CF₃ (295.5 eV), O-C=O (ester, 288.5 eV), N-C-N (pyridine, triazole, 286.6 eV), C-O (ester, adventitious, 286 eV), C-C-N (pyridine, triazole, 285.8 eV), C-C (284.8 eV) and C=C (pyridine, 284 eV) were the signals resulting in the broad band of the C 1s signal. Increasing the length of the ancillary ligand resulted in the increase of the number of CH₃ groups. Consequently, the contribution of the C-C peak (284.8 eV) in the C 1s signal increased from L1-Pt to L7-Pt. The high resolution spectra of the S 2p signal was very significant because of the binding through the Au-S bond. The S 2p region of the spectrum reveals the S 2p_{3/2} and S 2p_{1/2} at 161.7 eV and 162.9 respectively (Figures 2.11-2.13, d). Those two peaks were attributed to the binding of thiolate to gold⁵⁸. The disulfide functional groups of the platinum (II) complexes were bound to the gold substrate. A comparison of the high resolution XPS spectra of the S 2p signal of the disulfide from the complex powder and the thiolate from the platinum (II) complex attached to the gold is depicted in Figure 2.14. The spin-orbit components S 2p_{3/2} and S 2p_{1/2} display a 1.16 eV spacing and the ratio between their areas was 2:1. Disulfide bonds S 2p signal show two peaks at 163.2 eV and 164.2 eV.

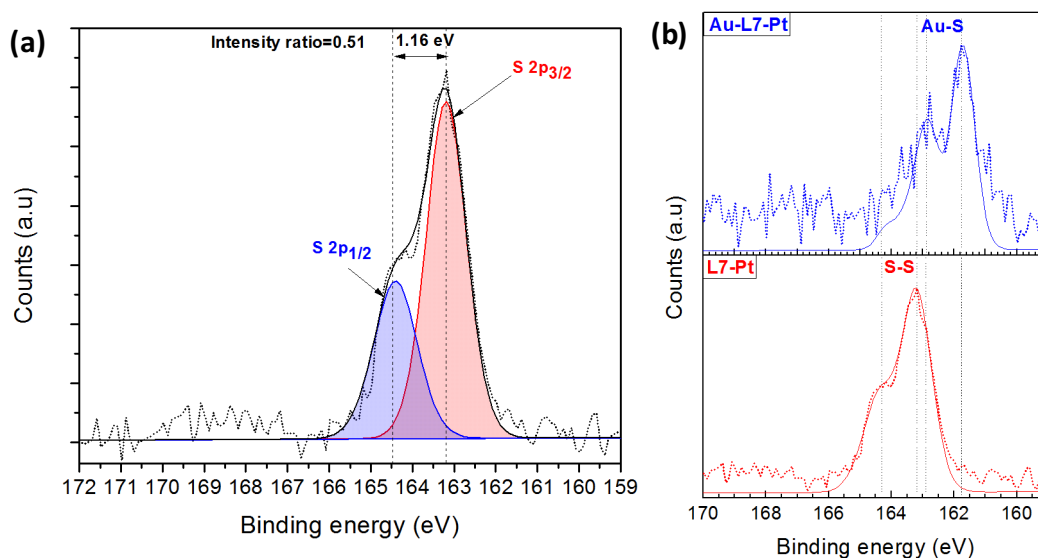


Figure 2.14. High resolution XPS spectra of the S 2p region of the disulfide bond of L1-Pt powder (a) and comparison of the S 2p signal from the disulfide and the thiolate-gold bond.

When the disulfide bond was broken and replaced by a sulfur-gold bond, the environment of the sulfur atom became more electronegative and the S 2p peaks were shifted to lower binding energies at 161.5 eV and 162.7 eV. It was then evident that the platinum (II) complexes were bound to the gold substrate. The presence of physisorbed platinum (II) complexes on the gold was also detected, along with the presence of the weak peaks at 163 eV and 164.2 eV from the unreacted disulfide bonds (Figure 2.11, d). The formation of the oxidized sulfur species was indicated by the presence of a low-lying band at 168 eV⁵⁸.

2.2.4.4. Water contact angle

Water contact angle measurements of the functionalised gold substrates are reported in Table 2.20. The water contact angle of the gold substrate after ozonolysis is around 52° which results in a slightly hydrophobic substrate. Upon functionalisation of the gold substrates with the three platinum (II) complexes, the water contact angle increased to approximately 62°. The values are similar for the three modified substrates. That was attributed to the presence of the same CF₃-triazole ligand on top of the substrates. Moreover, the XPS analysis indicated that the platinum coverage was limited and explained why the water contact angle did not vary before and after functionalisation of the gold substrates.

Table 2.20. Water contact angle of the modified gold substrates.

Au	Au-L1-Pt	Au-L3-Pt	Au-L7-Pt
$52 \pm 1^\circ$	$62 \pm 2^\circ$	$62 \pm 2^\circ$	$62 \pm 2^\circ$

2.2.4.5. Scanning electron microscopy (SEM)

SEM images of the three platinum (II) complexes drop-casted on a glass slide from a DMF solution (samples L_n-Pt) and the functionalised gold substrates (Au-L_n-Pt) are displayed in Figure 2.15.

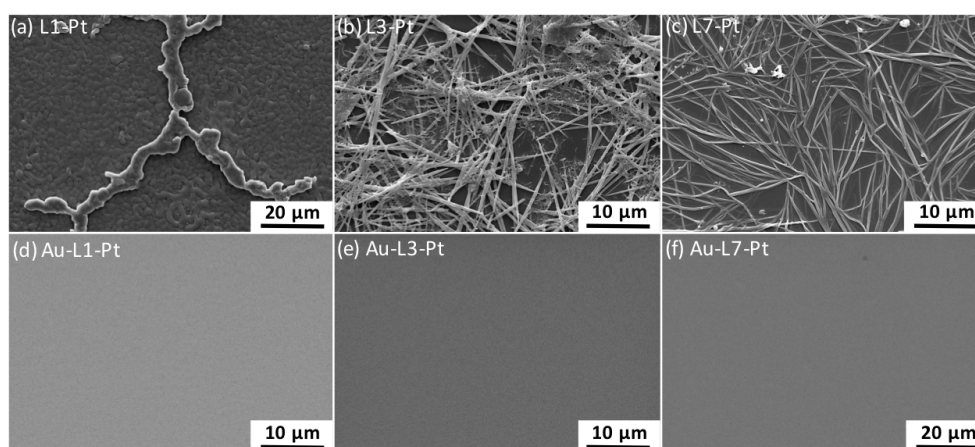


Figure 2.15. SEM images the drop casted platinum (II) complexes/DMF solution of a glass slide (a, b, c) and the functionalised gold substrates (d, e, f). The glass slides were recovered with a 40 nm layer of silver whereas the gold substrates were already conductive.

L1-Pt self-assembled into amorphous aggregates when drop-casted into a glass slide. L3-Pt self-assembled into a mixture of amorphous aggregates and fibers. L7-Pt self-assembled into interconnected fibers. As a general note, the longer the spacer of the platinum (II) complexes are, the more ordered the aggregates are. The SEM images of the functionalised gold substrates did not show any kind of aggregates or traces of platinum (II) complexes on the surface. It has been proven by XPS analysis that the platinum (II) complexes were covalently bound to the surface by gold-sulfur bond. However, the absence of platinum aggregates on the gold substrates implied the the platinum signal on the XPS spectra were most likely coming from platinum (II) complexes monomers attached to the surface or small aggregates undetected by SEM. It was envisaged that the platinum (II) complexes aggregated in DMF would be grafted to the gold surface. One possibility to explain the absence of platinum

aggregates on the gold substrates was the size of the structures. The successive washing of the gold substrates removed the aggregates which were not strongly attached to the substrate by gold-sulfur bond. Another explanation was that the disulfide groups of the platinum (II) complexes were not available in the structure to be linked to the gold substrate. For instance, the disulfide groups might be located in the interior of the fibers and thus not react with gold.

2.2.4.6. Confocal fluorescence microscope

Confocal fluorescence microscope images of the three platinum (II) complexes drop-casted on a glass slide from a DMF solution (samples Ln-Pt) and the functionalised gold substrates (Au-Ln-Pt) are displayed in Figure 2.16.

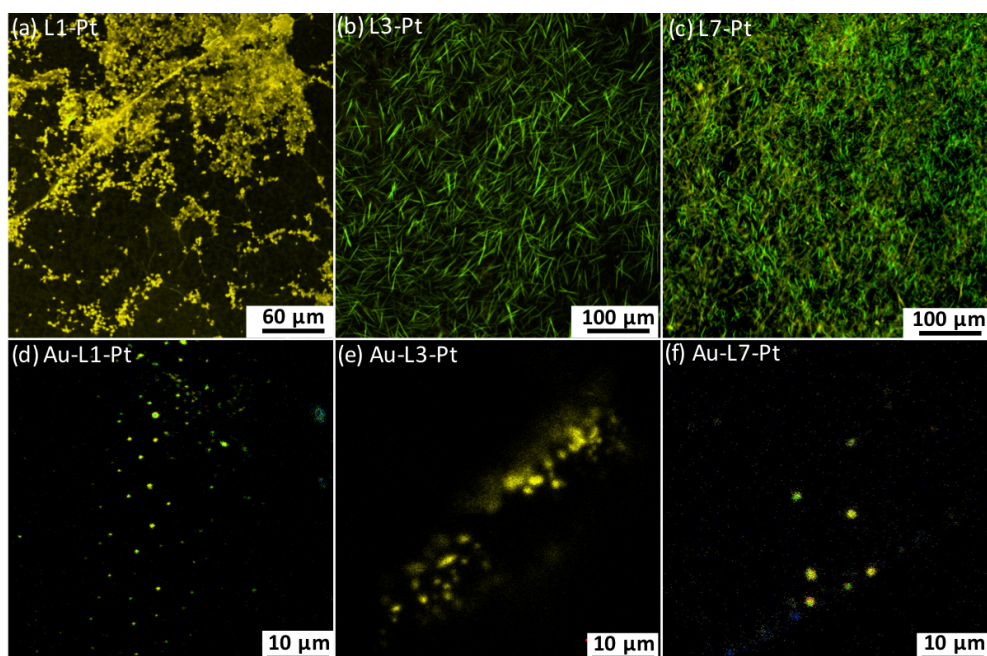


Figure 2.16. Confocal images of the functionalised gold substrates (a, b, c) and the drop casted platinum(II) complexes/DMF solution of a glass slide). $\lambda_{exc} = 405 \text{ nm}$ in lambda mode (real colors).

The same types aggregates observed on the SEM images (Figure 2.15) were observed on confocal images; yellow emissive amorphous aggregates for L1-Pt, green emissive fibers for L3-Pt and green-yellow interconnected fibers for L7-Pt. However, none of these particular aggregates were observed on the functionalised gold substrates. Islands of luminescent aggregates were observed on each of the gold substrates. The emission spectrum measured by the confocal microscopy displayed a broad band centered at approximately 570 nm, which could be attributed to $^3\text{MMLCT}$ band of the platinum (II) complexes. One possibility was that

the luminescence detected from the islands on the gold substrates was originating from the amorphous physisorbed platinum (II) complexes aggregates. The absence of fibers on the surface could be explained by the fact that they were not bound to the surface via the sulfur-gold bond and washed away when the substrates were rinsed.

2.2.4.7. Stability of the functionalised gold substrates.

In order to assess the stability of the modified surfaces, the functionalised gold substrates were stored at room temperature for 2 months. The high-resolution XPS spectra of the S 2p signal of the freshly prepared and 2 months old functionalised gold substrate are displayed in Figure 2.17.

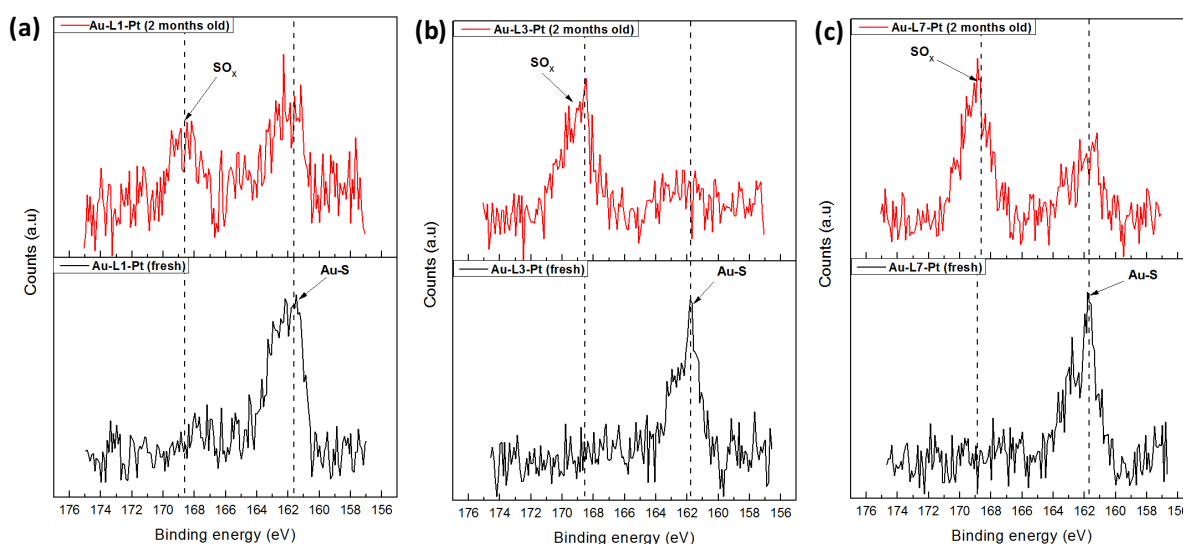


Figure 2.17. High resolution XPS spectra of the S 2p signal of Au-L1-Pt (a), Au-L3-Pt (b) and Au-L7-Pt (c) functionalised gold substrates freshly prepared (black lines, bottom) and after 2 months under standard atmosphere (red line, top).

The presence of a new peak around 168.5 eV suggested the formation of sulfur oxide species on the surface. The peak around 162.8 eV (previously attributed to the thiolate-gold (Au-S)) decreased in intensity, indicating the cleavage of the bonds^{58, 59}. The platinum (II) complexes were not bonded to the gold substrate but mainly physisorbed. It appears that the functionalised gold substrates have a limited stability upon exposure to standard conditions.

2.2.4.8. Removal of the platinum (II) complexes by hydrolysis of the ester functional group of the anchoring ligand⁵²

The three platinum (II) complexes previously used are bonded to the gold by a sulfur-gold bond. The anchoring ligand is linked to the platinum center by an ester functional group, which can be cleaved under the right conditions. As a result, the anchoring ligand remains on the surface, while the platinum center is removed. In order to demonstrate the cleavage of the ester bond and the selective recognition of the esterase agent toward this specific bond, a platinum (II) complex in which the ester bond was replaced by an amide bond was prepared (L0-amide-Pt). The chemical structure of the four platinum (II) complexes used for this test is depicted in Figure 2.18.

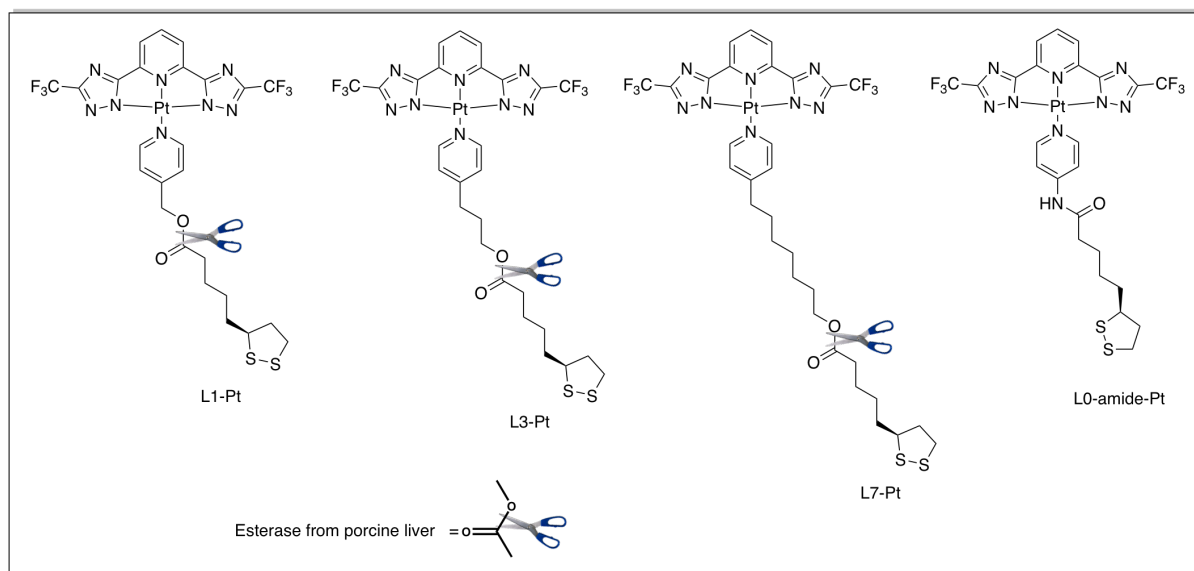


Figure 2.18. Chemical structures of the platinum(II) complexes used for the functionalisation of gold substrates and cleavage of the ester bond.

The four platinum (II) complexes were partially dissolved in DMF ($c = 1.0 \times 10^{-3}$ M) and freshly cleaned gold substrates were immersed in the solutions for 6 days. The modified substrates were then immersed in aqueous solutions containing the esterase agent for 1 day. The substrates survey scans and high-resolution XPS spectra of the Pt 4f signal are displayed in Figure 2.19. The survey scans showed the presence of small F 1s, N 1s and Pt 4f peaks only for the substrate functionalised with the platinum (II) complex containing the amide bond (Au-L0-Pt). The high resolution XPS spectra of the Pt 4f signal for all platinum (II) complexes prior to the cleavage of the ester bond show two peaks at 72.7 eV and 76 eV, attributed to the Pt 4f_{7/2} and Pt 4f_{5/2} respectively (Figure 2.19b). After incubation in an aqueous solution of the

esterase, only the gold substrate functionalised with L0-amide-Pt complex displayed clear Pt4f signals (Figure 2.19c).

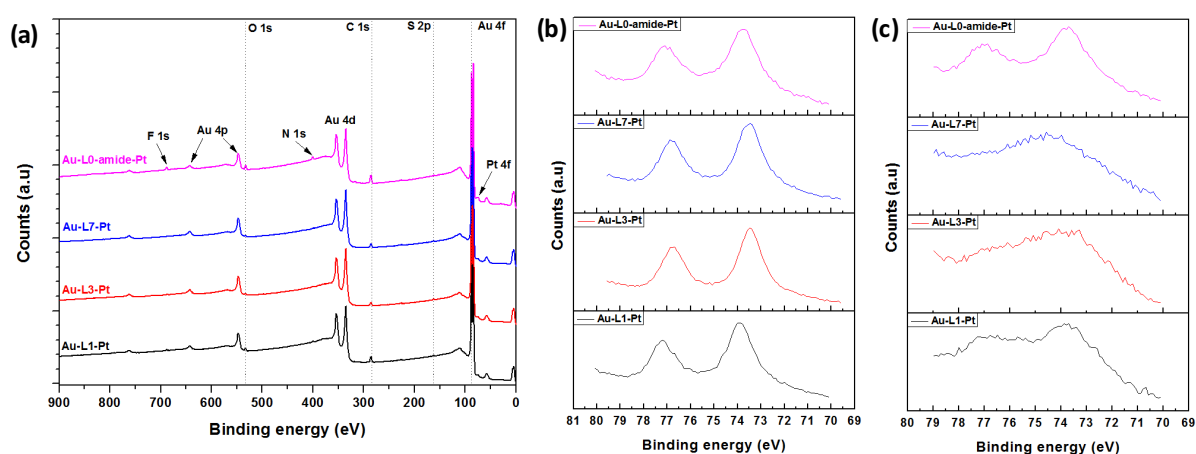
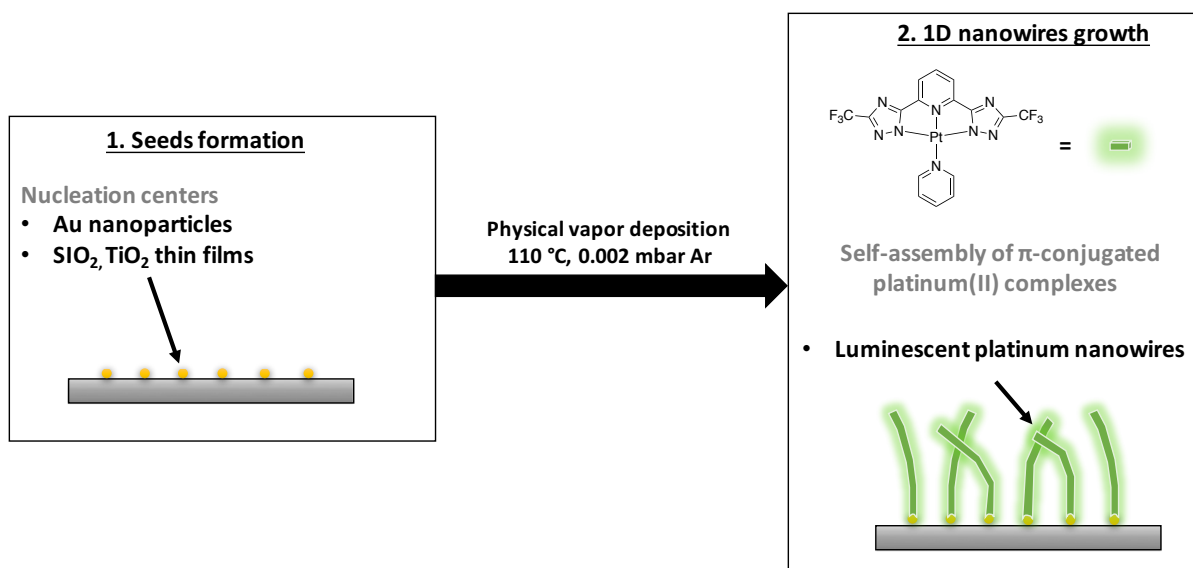


Figure 2.19. XPS survey scans of the functionalised gold substrates after cleavage of the ester bond (a) and high resolution XPS spectra of the Pt 4f signal before (b) and after (c) cleavage of the ester group.

It is worth noting that weak, unresolved Pt 4f peaks were also observed for the platinum (II) complex with the shorter spacer Au-L1-Pt. Upon increasing the length of the spacer from Au-L3-Pt to Au-L7-Pt, the Pt 4f peaks was gradually decreased. It can be concluded that the longer the platinum (II) complex is, the easier it is to cleave the ester bond. The modified gold substrates were highly sensitive toward esterase agents and could be used as sensing surfaces.

2.2.5. Growth of platinum (II) complexes nanowires by physical vapor deposition

The formation of single crystal organic nanowires strongly depends on the morphology and roughness of the substrate instead of its chemical composition. The formation of perylene and phthalocyanine nanowires on a wide variety of substrates have been previously reported⁶⁰⁻⁶¹. The formation of platinum (II) complex nanowires were achieved on three different substrates: mesoporous SiO₂ thin films, mesoporous TiO₂ thin films and gold nanoparticles deposited on silicon (100) and fused silica. The procedure is described in Scheme 2.11. The growth of supported platinum (II) complexes nanowires started with the formation of nucleation centers, *e.g* gold nanoparticles or mesoporous oxide substrates such as SiO₂ or TiO₂. The nanowires were obtained by controlling the temperature of the substrate between 90°C and 140°C (optimum value at 110°C) and sublimation of the complex. The nanowires prepared from this method were randomly distributed and bent⁴⁷.



Scheme 2.11. Illustration describing the PVD method used to grow nanowires of platinum (II) complex. 1) Nucleation centers were created on different substrates 2) Self-assembly of π -conjugated platinum (II) complexes at 110°C.

Formation of platinum nanowires on SiO₂ thin films⁶²

Thin, mesoporous SiO₂ films were deposited by Glancing Angle Deposition (GLAD). Stoichiometric SiO₂ thin films with a tilted columnar nanostructure and ~350 nm thickness were grown by glancing angle PVD from SiO₂ pellets at O₂ atmosphere pressure below 10⁻⁴ mbar. The substrates were placed at a glancing angle of 70° with respect to the evaporator source. SEM images of the SiO₂ mesoporous films and of the platinum nanowires formed on this substrate are depicted in Figure 2.20. On the thin, mesoporous SiO₂ films, the formation of platinum nanowires was not homogeneous. Most of the features that were formed on the surface of the films presented irregular shapes comparable to a polycrystalline formation. The density of the nanowires on SiO₂ was relatively low and can be explained by a predominant diffusion of the Pt-complex molecules through the open porosity of the SiO₂ layer.

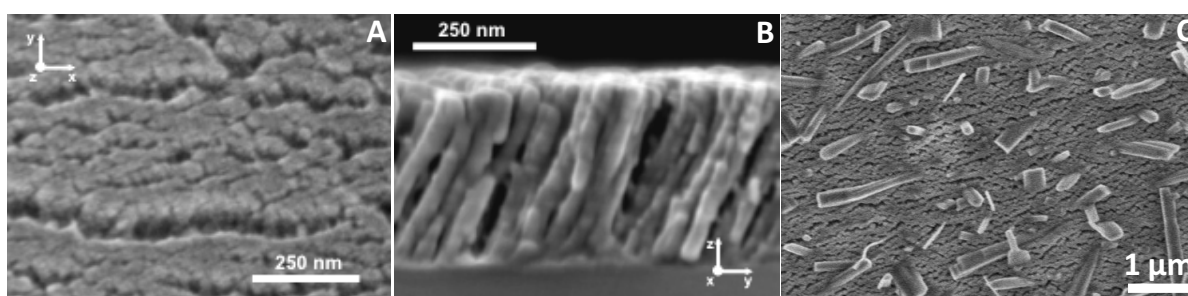


Figure 2.20. Normal view (A) and cross section (B) SEM images of the SiO₂ GLAD thin films. SEM images of the platinum (II) complex deposited on mesoporous SiO₂ thin film.

Formation of platinum nanowires on thin TiO₂ films

Thin TiO₂ films were fabricated in a microwave (2.45 GHz) ECR reactor with a down-stream configuration using titanium tetraisopropoxide (TTIP) as precursor. Total pressure in the chamber was settled at 1.5×10^{-2} mbar and plasma power at 400 W to maintain the substrates at room temperature during the fabrication process. SEM images of the TiO₂ mesoporous films and the platinum nanowires formed on this substrate are depicted in Figure 2.21.

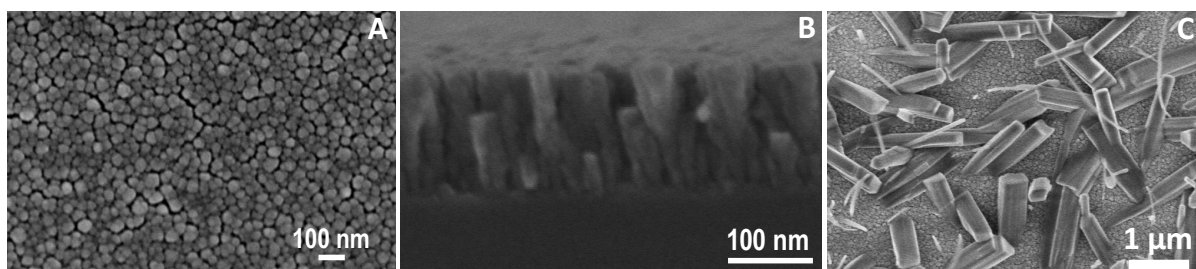


Figure 2.21. Normal view (A) and cross section (B) SEM images of the TiO₂ GLAD thin films. SEM images of the platinum(II) complex deposited on mesoporous TiO₂ thin film.

On the mesoporous TiO₂ thin films, the formation of platinum nanowires was similar to those on the SiO₂ films. However, the density of the platinum nanowires was higher on the TiO₂ films compared to the SiO₂ films.

Formation of platinum nanowires on gold nanoparticles deposited on silicon (100) and fused silica

Gold nanoparticles were deposited by high vacuum thermal evaporation of gold pellets onto silicon (100) wafers and fused silica slides. Three different substrates were prepared with varying thicknesses of the gold layer: Au1, Au2 and Au5 corresponding to 1 nm, 2 nm and 5 nm of equivalent thickness. Since it is very difficult to measure the exact amount of gold on the substrates, the concept of equivalent thickness is used in this case. The equivalent thickness represents the thickness of a homogenous gold layer covering the entire substrate. Deposition rate was settled at 5 nm/hour in the three cases. The substrate and evaporation cell were cooled at 23°C to avoid undesired heating. The base pressure was 3×10^{-6} mbar and $7-8 \times 10^{-6}$ mbar during deposition. SEM images of the gold nanoparticles deposited on silicon (100) and the platinum nanowires grown on Au1, Au2 and Au5 substrates are displayed in Figure 2.22.

Optimal results regarding the formation of Pt-complex NWs in high density were obtained for the Au nanoparticles. The total amount of gold (equivalent thickness) that controls the distribution of nanoparticles (density and size) plays a critical role in the formation of platinum nanowires in a homogeneous and high-density distribution. With an equivalent thickness of 1 nm (Au1-Pt), the density of platinum nanowires was relatively low. Upon increasing the equivalent thickness to 2 nm (Au2-Pt), the density of nanowires was increased. Finally, when the equivalent thickness of gold nanoparticles was increased to 5 nm, the density of nanowires was extremely high, resulting in a disorganized distribution of the nanowires.

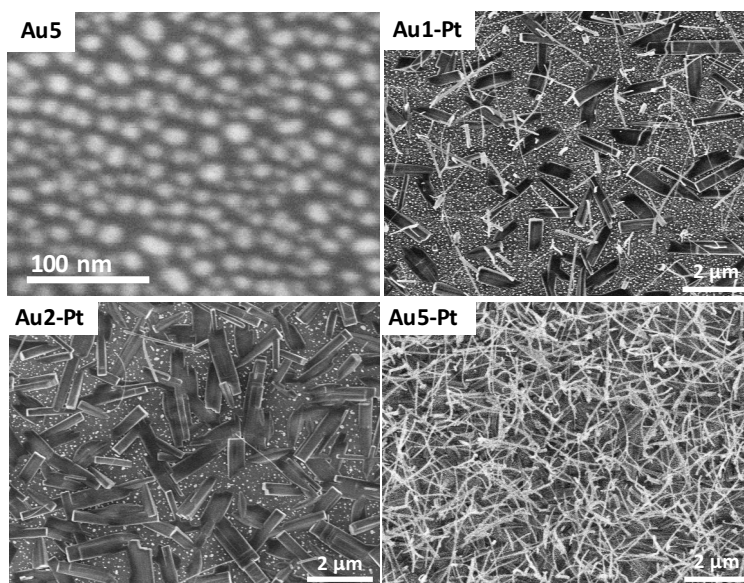


Figure 2.22. SEM images of gold nanoparticles on silicon (100) substrate with an equivalent thickness of 5 nm (Au5). Nanowires formed from platinum (II) complex (19) deposited on different gold nanoparticles of equivalent film thickness of 1 nm (Au1-Pt), 2 nm (Au2-Pt) and 5 nm (Au5-Pt).

Mechanochromic properties of the platinum (II) complex

The platinum (II) complex (19) displays mechanochromism upon grinding of the powder with a luminescence change from green to yellow visible under UV lamp, displayed in Figure 2.23.

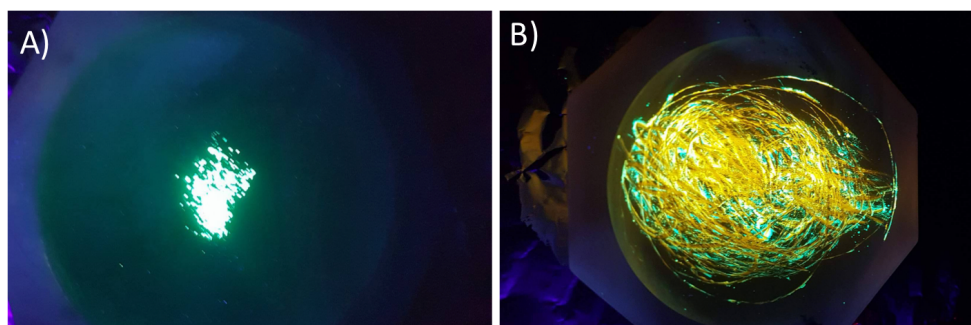


Figure 2.23. Photographs of the platinum (II) complex (**19**) under UV lamp (365 nm) before (A) and after grinding (B).

The mechanochromism properties have been demonstrated on the bulk material of complex **19** and have been previously reported⁶³. Similar behavior was also observed for the platinum nanowires grown from the gold nanoparticles on silicon (100) substrate. The mechanical stress was applied by a gentle pressing of a PDMS foil on the platinum nanowires of Au1-Pt substrate. The fluorescence microscope images of the Au1-Pt nanowires before and after application of a pressure are displayed in Figure 2.24.

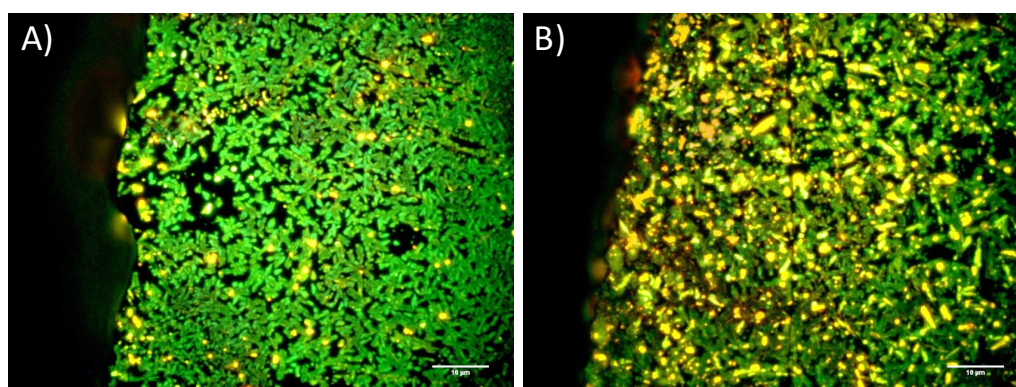


Figure 2.24. Fluorescence microscopy images of the platinum nanowires on Au (1nm) before (A) and after (B) mechanical activation of the nanowires by gently pressing it through a PDMS foil.

The platinum nanowires were mainly green emissive with some yellow emissive fibers prior to the application of mechanical stress. After application of the manual pressure, more yellow emissive nanowires were observed on the same area. The mechanical stress induced a decrease of the platinum-platinum distance resulting in more intense platinum-platinum interactions. As a consequence of the shorter distance between two platinum complexes, the emission was shifted to higher wavelengths from green to yellow. However, the pressure was

applied with a relatively large PDMS foils on nanowires of different lengths. As a consequence, the pressure force was mainly applied on the longest nanowires which underwent the red-shift in emission. The nanowires, which had no or little pressure applied maintained their green emission. The mechanochromism effect is observed on the platinum (II) complex powder and nanowires. The next proposed step would be to apply a controlled force via an AFM tip on a single fiber and observe its mechanochromic properties.

2.3. Conclusion

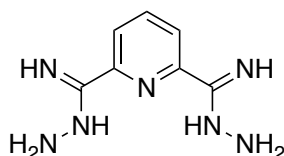
Silicon wafers were modified by wet chemical routes, which led to the covalent attachment of platinum (II) complexes. The XPS spectra demonstrate the expected surface modification. However, when the platinum (II) complexes were covalently bond to the surface the coverage was relatively low, hindering further photophysical characterisation. The functionalisation of gold substrates was achieved by using platinum (II) complexes bearing disulfide moieties on ancillary ligands. Most of the complexes were attached to the surface, although a small amount of physisorbed complexes could be detected by XPS. A few luminescent islands of platinum (II) complexes aggregates were observed by confocal fluorescence microscopy. The density of complexes on the surface was also relatively low. Addition of *tris*-(2-carboxyethyl) phosphine hydrochloride ($\text{TCEPH}^+\text{Cl}^-$) as a reducing agent for the disulfide bond or longer immersion time of the gold substrates did not improve the density of platinum (II) complexes on the surface. A different method based on sublimation of the platinum (II) complexes by PVD led to the formation of nanowires grown epitaxially to the surface. The density of platinum (II) complexes nanowires was relatively high when grown from gold nanoparticles on a silicon (100) substrate. Moreover, platinum nanowires showed a bright luminescence with an emission wavelength that could be tuned by application of a force. In order to further characterize the mechanochromism properties from the bulk (powder) to the nanoscale (fibers), further detailed AFM-fluorescence microscopy coupled studies are needed.

2.4. Experimental Part

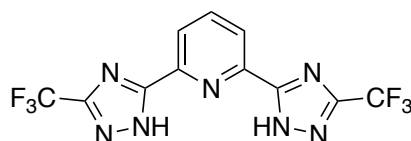
2.4.1. General information

All reactions were carried out under nitrogen atmosphere. All solvents and reagents were received from Aldrich, Fluka or TCI and were used without further modifications. K_2PtCl_4 was purchased from Precious Metal Online (PMO). $PtCl_2(DMSO)_2$ was prepared by previously-reported synthetic procedures¹. Column chromatography was performed on silica gel 60 (particle size 63-200 μm , 70-230 mesh ASTM, Merck). NMR spectra were recorded on a Bruker Avance 400 spectrometer. ^1H NMR, ^{13}C NMR and ^{19}F NMR chemical shifts (δ) of the signals are given in parts per million and referenced to residual protons in the deuterated solvents. The signal splitting are abbreviated as follows: s, singlet; d, doublet; t, triplet; q, quadruplet; m, multiplet. Coupling constants (J) are given in Hertz. Electrospray ionization mass spectrometry (ESI-MS) was carried out on a MicroTOF (Bruker) mass spectrometer equipped with an electrospray source by the mass spectrometry service of the University of Strasbourg. Elemental analysis was performed by the analytical service of physical measurements and optical spectroscopy by the University of Strasbourg.

2.4.2. Synthesis

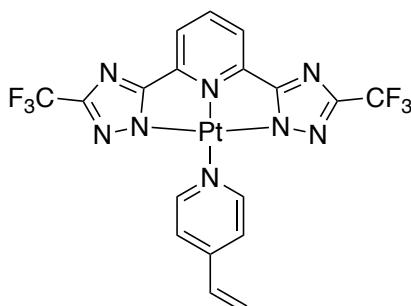


Pyridine-2,6-bis(carbohydrazonamide) (**1**). In a 500 mL round bottom flask, 2,6-pyridinecarbonitrile (5 g, 38.7 mmol, 1 eq) was dissolved in 100 mL of ethanol, then 40 mL of hydrazine monohydrate (40 mL, 825 mmol, 21.3 eq) was added and the flask closed with a rubber septum. The resulting solution was stirred at room temperature for 3 days. A thick white precipitate rapidly formed. After 3 days, a white precipitate was obtained. The suspension was filtered and the precipitate was then rinsed with ethanol several times. A white powder was obtained (m = 6.915 g, 35.8 mmol, yield 92.5%).



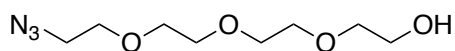
2,6-bis(3-(trifluoromethyl)-1H-1,2,4-triazol-5-yl) pyridine (**2**). In a 250 mL round bottom flask, 2,6-carboximidehydrazide (**1**) (2.28g, 11.8 mmol, 1 eq) was suspended in 25 ml of diethylene

glycol dimethylether and sonicated until a fine white suspension was formed. Trifluoroacetic acetate (3.6 mL, 25.3 mmol, 2.14 eq) was added slowly at room temperature. The suspension dissolved during this addition and was slowly heated up to 162 °C for 2 hours. The suspension rapidly transformed into an orange-brown clear solution and then into a turbid brown mixture when cooled down at room temperature. 70 mL of distilled water and 2 mL of HCl 37% was then added to the reactional mixture. The brown mixture solidified onto the walls of the flask. The solution was heated up at 90 °C overnight. A clear yellow solution with a brown solid on the walls was obtained. The solution was cooled down and stirred at room temperature for another 4 hours. The yellow/white/brown precipitate was filtered off and rinsed thoroughly with water and petroleum ether. It was dried overnight in an oven at 70 °C. A tan coloured powder was obtained (m = 3.561 g, 10.2 mmol, yield 86.4 %). ¹H NMR (acetone-*d*₆, 400 MHz, ppm) δ: 8.33–8.40 (m); ¹⁹F NMR (acetone-*d*₆, 376 MHz, ppm) δ: -65.80 (s, CF₃); ¹³C NMR (acetone-*d*₆, 100 MHz, ppm) δ: 156.42 (s), 156.04–154.88 (q, *J* = 39 Hz), 146.05 (s), 141.36 (s), 124.55–116.53 (q, *J* = 268 Hz), 123.82 (s). HR-ESI-MS (*m/z*): C₁₁H₅F₆N₇Na [M+Na]⁺, calcd. 372.040, found 372.035.

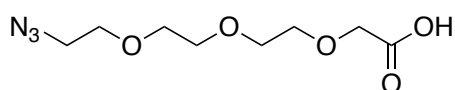


Complex 3. In a 50 mL two-neck round-bottom flask, compound **7** (86 mg, 0.248 mmol, 1.05 eq) and PtCl₂(DMSO)₂ (100 mg, 0.236 mmol, 1.0 eq) were suspended in 15 mL of acetonitrile. N,N-diisopropylethylamine (82 μL, 0.472 mmol, 2.0 eq) was added to the suspension followed by 4-vinylpyridine (26 μL, 0.236 mmol, 1.0 eq) and then the mixture was heated at 80 °C overnight under N₂ atmosphere. An orange precipitate formed when the mixture was cooled. The crude was purified by column chromatography using ethylacetate and cyclohexane 1:1 as the mobile phase. The final product was rinsed with a minimal amount of methanol and filtered. The orange solid was dried under vacuum for two days (m = 70 mg, 0.108 mmol, yield 46%). ¹H NMR (CDCl₃, 400 MHz, ppm) δ: 9.59 (d, *J* = 6.1 Hz, 2H), 8.04 (t, *J* = 7.9 Hz, 1H), 7.84 (d, *J* = 7.9 Hz, 2H), 7.58 (d, *J* = 6.1 Hz, 2H), 6.78 (dd, *J* = 17.5, 10.8 Hz, 1H), 6.23 (d, *J* = 17.5 Hz,

1H), 5.80 (d, $J = 10.9$ Hz, 1H); ^{19}F NMR (CDCl_3 , 376 MHz, ppm) δ : -64.26 (s, 6H); HR-MS (ESI) m/z : $\text{C}_{18}\text{H}_{11}\text{F}_6\text{N}_8\text{Pt} [\text{M}+\text{H}]^+$, calcd. 648.065, found 648.062.

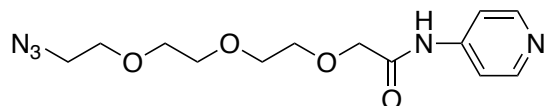


*2-(2-(2-(2-azidoethoxy)ethoxy)ethoxy)ethan-1-ol (4)*⁴². A 250-mL round bottom flask equipped with an oval-shaped magnetic stir bar was charged with tetraethylene glycol (50.9 g, 262 mmol, 10 eq) in tetrahydrofuran (10 mL). An aqueous solution (10 mL) containing sodium hydroxide (1.68 g, 42 mmol, 1.6 eq) was added to the flask, and *p*-toluenesulfonyl chloride (5 g, 26.2 mmol) dissolved in tetrahydrofuran (30 mL), was added dropwise to the mixture at 0 °C and stirred while maintaining this temperature for 3 hr. The reaction was diluted with ice-cold water (150 mL) and extracted into dichloromethane (3 x 100 mL). The combined organic layers were rinsed with water (2 x 300 mL), dried over MgSO_4 , filtered, and concentrated to yield a clear oil product (6.9 g, 19.7 mmol, 75%). Sodium azide (4.3 g, 65.5 mmol, 2.5 eq) was added to the tosylate intermediate, and the mixture was dissolved in absolute ethanol (200 mL). The reaction was stirred under reflux overnight, cooled to room temperature, and then diluted with water (150 mL). The mixture was concentrated by rotary evaporation to approximately 150 mL, and the product was extracted into ethyl acetate (3 x 150 mL), dried with MgSO_4 , filtered, and concentrated to yield a pale yellow liquid (3.822 g, 17.4 mmol, 66% yield over two steps). ^1H NMR (400 MHz, CDCl_3 , ppm) δ : 3.70 (m, 2H), 3.65 (m, 10H), 3.62 (m, 2H), 3.40 (t, $J = 5.0$ Hz, 2H); ^{13}C NMR (100 MHz, CDCl_3 , ppm) δ : 72.61, 70.88, 70.85, 70.78, 70.55, 70.22, 61.95, 50.84; HR-MS (ESI): calculated for $\text{C}_8\text{H}_{17}\text{N}_3\text{NaO}_4$, 242.1111; found 242.1115.

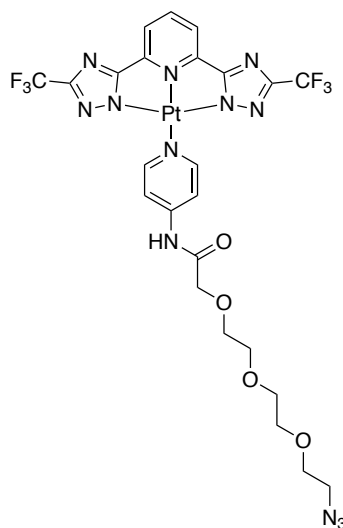


2-(2-(2-(2-azidoethoxy)ethoxy)ethoxy)acetic acid (5). A solution of azido alcohol **1** (3.822 g, 17.4 mmol) in acetone (100 mL) was cooled to 0°C. Freshly prepared Jones reagent (44 mL) was then added. The reaction mixture was then left to warm to room temperature and stirred vigorously overnight. Propan-2-ol was added dropwise to the orange suspension until a green colour was observed, and then the reaction mixture was filtered over Celite to remove chromium (IV) oxide. The mixture was then concentrated in vacuum to obtain the crude product. The oil residue was purified by flash column chromatography, and eluted with

dichloromethane/methanol (9:1) to give an oil weighing 1.8 g (75% yield). ^1H NMR (400 MHz, CDCl_3 , ppm) δ : 4.17 (s, 2H), 3.77 (m, 2H), 3.72 - 3.68 (m, 8H), 3.40 (m, $J = 5.0$ Hz, 2H); ^{13}C NMR (100 MHz, CDCl_3 , ppm) δ : 172.07, 71.78, 70.91, 70.61, 70.33, 70.26, 69.03, 50.83 HR-MS (ESI): calculated for $\text{C}_8\text{H}_{15}\text{N}_3\text{NaO}_5$, calc. 256.0904; found 256.0885.

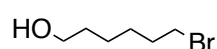


2-(2-(2-(2-azidoethoxy) ethoxy) ethoxy)-N-(pyridin-4-yl) acetamide (6). In a 250 mL round bottom flask, azido acid **2** (950 mg, 3.74 mmol, 1 eq), 4-aminopyridine (382 mg, 4.11 mmol, 1.1 eq) and DCC (847 mg, 4.11 mmol, 1.1 eq) were dissolved in THF (40 mL) and stirred at room temperature overnight. A white precipitate was formed during the course of the reaction. The solution was then filtered off and concentrated under vacuum. The crude was purified by column chromatography using ethylacetate as an eluent. ^1H NMR (400 MHz, CDCl_3 , ppm) δ : 8.95 (s, 1H), 8.51 (d, $J = 6.2$ Hz, 2H), 7.58 (d, $J = 6.5$ Hz, 2H), 4.13 (s, 2H), 3.76 (m, 6H), 3.71 (m, 2H), 3.66 (m, 2H), 3.35 (m, $J = 5.0$ Hz, 2H); ^{13}C NMR (100 MHz, CDCl_3 , ppm) δ : 169.38, 150.89, 144.51, 113.95, 71.48, 70.86, 70.72, 70.58, 70.36, 70.23, 50.80 HR-MS (ESI): calculated for $\text{C}_{13}\text{H}_{20}\text{N}_5\text{O}_4$, calcd. 310.1510; found 310.1504.

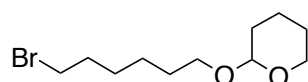


Complex 7. In a 50 mL two-neck round-bottom flask, compound **3** (350 mg, 1.0 mmol, 1.05 eq) and $\text{PtCl}_2(\text{DMSO})_2$ (422 mg, 1.0 mmol, 1.0 eq) was suspended in 25 mL of acetonitrile. After the addition of *N,N*-diisopropylethylamine (348 μL , 2.0 mmol, 2 eq), the reaction mixture turned to a clear yellow solution. Ligand **3** (310 mg, 1.0 mmol, 1.0 eq) was added and the mixture heated at 75°C overnight under N_2 atmosphere. The crude was purified by column

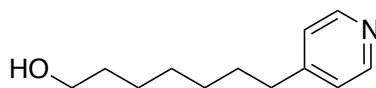
chromatography using ethylacetate as a mobile phase. The final product was then rinsed with a minimum amount of methanol and filtered. An orange solid was collected and dried under vacuum for two days (351 mg, 0.412 mmol, yield 41%). ^1H NMR (CDCl_3 , 400 MHz, ppm) δ : 9.53 (d, $J = 6.2$ Hz, 2H), 9.13 (s, 1H), 8.02 (t, $J = 8.0$ Hz, 1H), 7.93 (d, $J = 8.0$ Hz, 2H), 7.82 (m, 2H), 4.20 (m, 2H), 3.79 (m, 2H), 3.42 (m, 4H); ^{19}F NMR (CDCl_3 , 376 MHz, ppm); -64.23 (s, CF_3); ^{13}C (CDCl_3 , 100 MHz, ppm) δ : 178.16, 170.26, 155.63, 154.15, 149.09, 147.41, 143.00, 118.34, 115.75, 71.57, 71.06, 70.44, 70.23, 50.80, 29.86, 14.24; HR-MS (ESI) m/z : $\text{C}_{24}\text{H}_{23}\text{F}_6\text{N}_{12}\text{O}_4\text{Pt}$ $[\text{M}+\text{H}]^+$, calcd. 852.1513, found 852.1501. Elemental analysis: calcd. C 33.85%, N 19.74%, H 2.60%, found C 33.74%, N 19.60%, H 2.63%



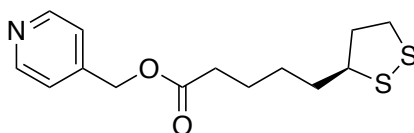
6-bromohexan-1-ol (**8**). 1,6-hexane-diol (12 g, 101.5 mmol, 1.0 eq) was dissolved in anhydrous toluene (100 mL) and the solution was heated at 120 °C before the dropwise addition of 48% hydrobromic acid (15 mL, 132.5 mmol, 1.3 eq). After the addition was completed, the reaction mixture was stirred under reflux for 96 hrs. The solvent was removed under reduced pressure, and then the residue was purified by silica gel column chromatography (EtAc/petroleum ether, 1:4). The final product was obtained as a yellow oil (14.988 g, 82.8 mmol, yield 81.5%). ^1H NMR (CDCl_3 , 400 MHz, ppm): δ 4.05 (t, $J = 6.9$, 1H), 3.64 (t, $J = 6.9$ Hz, 2H), 3.41 (t, $J = 6.9$ Hz, 2H), 1.87(m, 2H), 1.58 (m, 2H), 1.47 (m, 2H), 1.39 (m, 2H); HR-MS (ESI) m/z : $\text{C}_6\text{H}_{13}\text{BrO}$ $[\text{M}+\text{H}]^+$, calcd. 181.07, found 182.9.



2-((6-bromohexyl) oxy) tetrahydro-2H-pyran (**9**). 6-bromo-1-hexanol (14 g, 77.3 mmol, 1 eq), pyridinium para-toluenesulfonate (PPTs) (1.94 g, 7.73, 0.1 eq) and 3,4-dihydro-2H-pyran (10.6 mL, 115.9 mmol, 1.5 eq) were dissolved in dichloromethane (100 mL). The reactional mixture was stirred at room temperature for 4 hours, and then concentrated in vacuum. The obtained residue was purified by silica gel column chromatography using a mixture ethyl acetate / petroleum ether (1:100) as an eluent. A clear oil was obtained as the final product. (14.641 g, 55.2 mmol, 71.4%). ^1H NMR (CDCl_3 , 400 MHz, ppm): δ 4.56 (d, $J=4.1$ Hz, 1H), 3.85 (t, $J = 9.4$ Hz, 1H), 3.72 (dd, $J = 9.4$ Hz, 6.8 Hz, 1H), 3.49 (m, 1H), 3.38 (m, 3H), 1.87 (m, 3H), 1.70 (t, $J=10.6$ Hz, 1H), 1.58 (m, 2H), 1.47 (m, 4H), 1.40 (m, 4H); HR-MS (ESI) m/z : $\text{C}_{11}\text{H}_{21}\text{BrO}_2$ $[\text{M}+\text{Na}]^+$, calcd. 287.06, found 287.06.

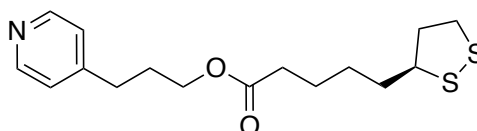


7-(pyridin-4-yl)heptan-1-ol (10). In a 100 mL Schlenk flask, diisopropylamine (5.6 mL, 39.6 mmol, 1.5 eq) was added to dry THF (30 mL) under argon atmosphere. The solution was cooled to $-70\text{ }^{\circ}\text{C}$ and *n*-butyllithium 1.6 M in hexane (20 mL, 31.68 mmol, 1.2 eq) was added dropwise to the solution. The resulting solution was stirred at this temperature for one hour. The solution was then left to warm to room temperature. In a 250 mL round bottom flask, 4-picoline (3.1 mL, 31.68 mmol, 1.2 eq) was solubilized in dry THF (100 mL) and cooled to $-70\text{ }^{\circ}\text{C}$. Then, the aforementioned prepared solution of LDA was added dropwise after which the solution was stirred for another 45 min. The resulting solution was left to warm to room temperature. In a 500 mL round bottom flask, the above-prepared 4-picoline solution was added to a cooled solution ($-70\text{ }^{\circ}\text{C}$) of 2-(6-bromohexyloxy) tetrahydro-2H-pyran (**9**) (7 g, 26.4 mmol, 1 eq) in dry THF (50 mL). The resulting solution was stirred for one hour and left to warm to room temperature. Finally, the solution was stirred at room temperature overnight. The reaction mixture was poured into water and the THF and cyclohexane was removed under reduced pressure. The crude product was acidified with 10 mL HCl (37%), stirred for 2 hours, rinsed with diethyl ether (3x50 mL), basified with K_2CO_3 , extracted with dichloromethane (2x50 mL) and dried with sodium sulfate anhydrous. The desired product was isolated from the resulting residue using silica gel column chromatography with ethyl acetate / cyclohexane (7:3) as an eluent. Pale, yellow oil was obtained as the final product. (1.203 g, 6.22 mmol, yield 23.6%). ^1H NMR (CD_2Cl_2 , 400 MHz, ppm) δ : 8.46 (d, $J = 6.0$ Hz, 2H), 7.12 (d, $J = 6.0$ Hz, 2H), 4.07 (t, $J = 6.4$ Hz, 2H), 3.57 (m, 1H), 3.16 (m, 1H), 3.12 (m, 1H), 2.69 (t, $J = 7.3$ Hz, 2H), 2.46 (m, 1H), 2.30 (t, $J = 7.4$ Hz, 2H), 1.98 (m, 1H), 1.68 (m, 4H), 1.45 (m, 2H) $\text{C}_{12}\text{H}_{19}\text{NO}$ $[\text{M}+\text{H}]^+$, calcd. 194.15, found 194.16.

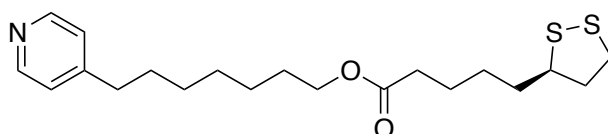


Pyridin-4-ylmethyl 5-(1,2-dithiolan-3-yl)pentanoate (11). 4-pyridine carbinol (570 mg, 5.22 mmol, 1.9 eq) and EDC.HCl (615 mg, 3.2 mmol, 1.16 eq) were dissolved in 100 mL of dried CH_2Cl_2 then TEA (445 μL , 3.2 mmol, 1.16 eq) was added under a nitrogen atmosphere. After the mixture was stirred for 10 minutes, α -lipoic acid (570 mg, 2.75 mmol, 1 eq) and DMAP (130 mg, 1.06 mmol, 0.4 eq) were added and the reactional mixture was stirred at room

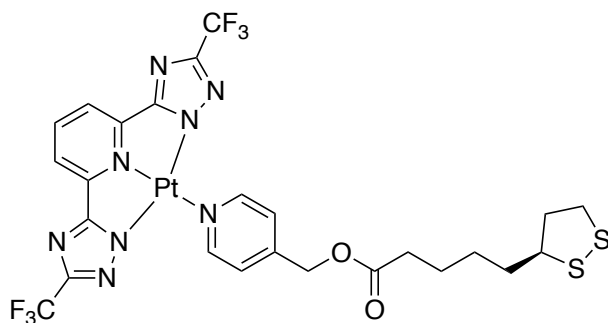
temperature overnight. A white solid instantaneously formed and dissolved after stirring. The solution turned orange due to the atmosphere. The organic phase was rinsed with 8% NaHCO₃ solution (8 mg in 100 mL water) (3 x 100 mL) and water (2 x 50 mL). Then the CH₂Cl₂ fraction was dried with Na₂SO₄, filtered off and evaporated until dry. The residue was purified by column chromatography with silica gel using a mixture of Ethyl acetate/ cyclohexane (2:1) as an eluent to obtain a viscous yellow oil product (536 mg, 1.8 mmol, yield 65.5%). ¹H NMR (CD₂Cl₂, 400 MHz, ppm) δ: 8.46 (d, J = 6.0 Hz, 2H), 7.12 (d, J = 6.0 Hz, 2H), 5.52 (s, 2H), 3.62 (m, 1H), 3.17 (m, 1H), 3.13 (m, 1H), 2.60 (t, J = 7.5 Hz, 2H), 2.49 (m, 1H), 1.92 (m, 1H), 1.77 (m, 4H), 1.52 (m, 2H); C₁₄H₁₉NO₂S₂ [M+H]⁺, calcd. 298.0930, found 298.0953; Elemental analysis: calcd. C 56.54%, N 4.71%, H 6.44%, found C 56.34%, N 4.74%, H 6.55%.



3-(pyridin-4-yl)propyl 5-(1,2-dithiolan-3-yl) pentanoate (12). A-lipoic acid (1.14 g, 5.5 mmol, 1 eq) and EDC.HCl (1.23 g, 6.4 mmol, 1.16 eq) were dissolved in 100 mL of dried CH₂Cl₂ then TEA (890 μL, 6.4 mmol, 1.16 eq) was added under nitrogen atmosphere. After the mixture was stirred for 10 minutes, 4-pyridine propanol (1.43 g, 10.44 mmol, 1.9 eq) and DMAP (260 mg, 2.12 mmol, 0.4 eq) were added and the reactional mixture was stirred at room temperature overnight. The organic phase was rinsed with 8% NaHCO₃ solution (8 mg in 100 mL water, 3 x 100 mL) and water (2 x 50 mL). Then the CH₂Cl₂ fraction was dried with Na₂SO₄, filtered and evaporated until dry. The residue was purified by column chromatography with silica gel using a mixture of Ethyl acetate/ acetone (2:1) as an eluent to obtain a viscous yellow oil product. (680 mg, 2.09 mmol, 38%). ¹H NMR (CD₂Cl₂, 400 MHz, ppm) δ : 8.46 (d, J = 6.0 Hz, 2H), 7.12 (d, J = 6.0 Hz, 2H), 4.07 (t, J = 6.4 Hz, 2H), 3.57 (m, 1H), 3.16 (m, 1H), 3.12 (m, 1H), 2.69 (t, J = 7.3 Hz, 2H), 2.46 (m, 1H), 2.30 (t, J = 7.4 Hz, 2H), 1.98 (m, 1H), 1.68 (m, 4H), 1.45 (m, 2H); ¹³C (CD₂Cl₂, 100 MHz, ppm) δ: 173.88, 152.16, 150.19, 124.40, 64.82, 57.03, 40.82, 39.10, 35.68, 35.18, 29.20, 26.40, 25.32; C₁₆H₂₃NO₂S₂ [M+Na]⁺, calcd. 348.1062, found 348.1068. Elemental analysis: calcd. C 59.04%, N 4.30%, H 7.12%, found C 59.15%, N 4.30%, H 7.16%.

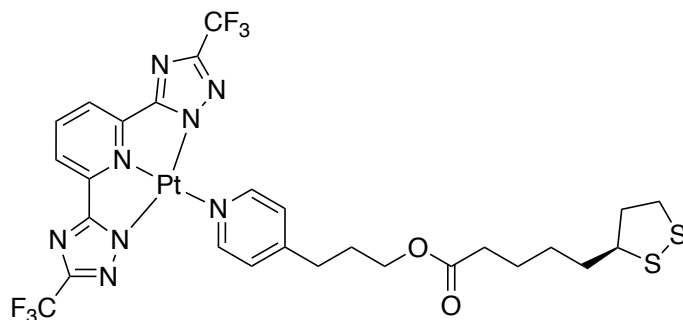


7-(pyridin-4-yl)heptyl 5-(1,2-dithiolan-3-yl) pentanoate (**13**). A-lipoic acid (0.825g, 4.0 mmol, 1 eq) and EDC.HCl (0.9 g, 4.68 mmol, 1.16 eq) were dissolved in 100 mL of dried CH₂Cl₂ then TEA (637 μL, 4.68 mmol, 1.16 eq) was added under a nitrogen atmosphere. After the mixture was stirred for 10 minutes, 7-(pyridin-4-yl) heptan-1-ol (**10**) (1.17 g, 6.05 mmol, 1.5 eq) and DMAP (196 mg, 1.61 mmol, 0.4 eq) were added and the reaction mixture was stirred at room temperature for 2 days. The organic phase was rinsed with 8% NaHCO₃ solution (8 mg in 100 mL water) (3 x 100 mL) and water (2 x 50 mL). Then the CH₂Cl₂ fractions were dried with Na₂SO₄, filtered off and evaporated until dry. Column chromatography was performed on the residue with silica gel using a mixture of Ethyl acetate/ acetone (2:1) as an eluent to yield a viscous yellow oil product. (537 mg, 1.41 mmol, 35.2%). ¹H NMR (CD₂Cl₂, 400 MHz, ppm) δ : 8.43 (d, J = 6.0 Hz, 2H), 7.11 (d, J = 6.0 Hz, 2H), 4.03 (t, J = 6.7 Hz, 2H), 3.57 (m, 1H), 3.17 (m, 1H), 3.12 (m, 1H), 2.60 (t, J = 7.3 Hz, 2H), 2.45 (m, 1H), 2.29 (t, J = 7.3 Hz, 2H), 1.90 (m, 1H), 1.68 (m, 10H), 1.45 (m, 2H); ¹³C (CD₂Cl₂, 100 MHz, ppm) δ: 173.88, 152.16, 150.19, 124.40, 64.82, 57.03, 40.82, 39.10, 35.68, 35.18, 34.61, 30.82, 29.60, 29.20, 26.40, 25.32; C₂₀H₃₁NO₂S₂ [M+H]⁺, calcd. 382.19, found 382.18. Elemental analysis: calcd. C 62.95%, N 3.67%, H 8.19%, found C 62.57%, N 3.77%, H 8.11%.



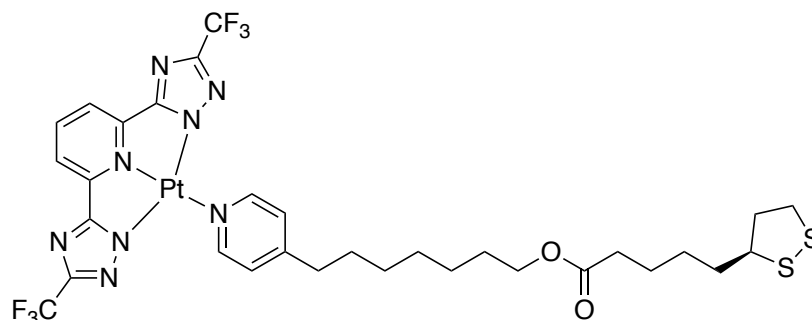
Complex 14. In a 50 mL two-neck round-bottom flask, the tridentate ligand CF₃-trz-py (**2**) (349 mg, 1.0 mmol, 1.05 eq), and PtCl₂(DMSO)₂ (400 mg, 0.95 mmol, 1.0 eq) were suspended in 150 mL of methanol. After addition of triethylamine (265 μL, 1.9 mmol, 2.0 eq) to the suspension, a solution of pyridin-4-ylmethyl 5-(1,2-dithiolan-3-yl) pentanoate (**11**) (134 mM in methanol) (7.1 mL, 0.95 mmol, 1.0 eq) was added and the mixture heated at 65°C under N₂ atmosphere overnight. A turbid yellow-orange solution rapidly formed. After the solution cooled to room temperature, the reaction mixture was evaporated under vacuum. The crude product was then dissolved in ethylacetate/cyclohexane (1:1) and absorbed onto silica (0.063 – 0.200 mm), which was loaded onto a column packed with silica gel. The compound was separated by column chromatography using ethyl acetate/cyclohexane (1:1) as the eluent

mixture. The first fraction was the product, which was collected and dried under vacuum. The crude product was then washed with a minimum amount of methanol and filtered. The yellow powder was dried under vacuum for two days. (295 mg, 0.351 mmol, yield 37%). ^1H NMR (acetone d^6 , 400 MHz, ppm) δ : 9.22 (d, J = 6.5 Hz, 2H), 8.14 (t, J = 7.9 Hz, 1H), 7.57 (d, J = 7.9 Hz, 2H), 7.48 (d, J = 6.6 Hz, 2H), 5.53 (s, 2H), 3.64 (m, 1H), 3.19 (m, 1H), 3.13 (m, 1H), 2.60 (t, J = 7.5 Hz, 2H), 2.50 (m, 1H), 1.94 (m, 1H), 1.76 (m, 4H), 1.56 (m, 2H); ^{19}F NMR (CDCl_3 , 376 MHz, ppm) δ : -64.71; $\text{C}_{25}\text{H}_{23}\text{F}_6\text{N}_8\text{O}_2\text{PtS}_2$ $[\text{M}+\text{H}]^+$, calcd. 840.0933, found 840.0890. Elemental analysis: calcd. C 35.76%, N 13.34%, H 2.64%, found C 35.61%, N 13.17%, H 2.69%.

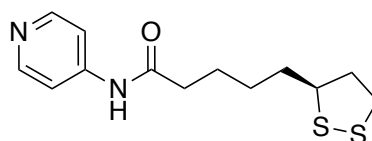


Complex 15. In a 50 mL two-neck round-bottom flask, the tridentate ligand CF_3 -trz-py (**2**) (346.4 mg, 0.992 mmol, 1.05 eq), and $\text{PtCl}_2(\text{DMSO})_2$ (400 mg, 0.947 mmol, 1.0 eq) were suspended in 150 mL of methanol. After the addition of triethylamine (265 μL , 1.894 mmol, 2.0 eq) to the suspension, 3-(pyridin-4-yl) propyl 5-(1,2-dithiolan-3-yl) pentanoate (**12**) (solution of 120 mM in methanol) (7.85 mg, 0.947 mmol, 1.0 eq) was added and the mixture heated at 80°C under N_2 atmosphere overnight. A turbid yellow-orange solution quickly formed. The solution was cooled to room temperature, and the reaction mixture was evaporated under vacuum. The crude product was then dissolved in ethylacetate/cyclohexane (1:1) and absorbed onto silica (0.063 – 0.200 mm), which was loaded onto a column packed with silica gel. The compound was separated by column chromatography using ethyl acetate/cyclohexane (1:1) as the eluent mixture then a 2:1 mixture. The first fraction was the product, which was collected and dried under vacuum. The crude product was then rinsed with a minimum amount of methanol and filtered. The yellow–orange solid was dried under vacuum for two days. (331 mg, 0.381 mmol, 40%). ^1H NMR (acetone d^6 , 400 MHz, ppm) δ : 9.33 (d, J = 6.5 Hz, 2H), 8.24 (t, J = 7.9 Hz, 1H), 7.72 (d, J = 7.9 Hz, 2H), 7.53 (d, J = 6.6 Hz, 2H), 4.18 (t, J = 6.2 Hz, 2H), 3.56 (m, 1H), 3.14 (m, 1H), 3.06 (m, 1H), 2.95 (t, J = 7.9 Hz, 2H), 2.44 (m, 1H), 2.30 (t, J = 7.3 Hz, 2H), 2.15 (m, 2H), 1.87 (m, 1H), 1.69 (m, 4H), 1.61 (m, 2H); ^{19}F NMR

(CDCl₃, 376 MHz, ppm) δ : -64.69; C₂₇H₂₇F₆N₈O₂PtS₂ [M+H]⁺, calcd. 868.1246, found 868.124. Elemental analysis: calcd. C 37.37%, N 12.91%, H 3.02%, found C 36.67%, N 12.56%, H 3.11%.

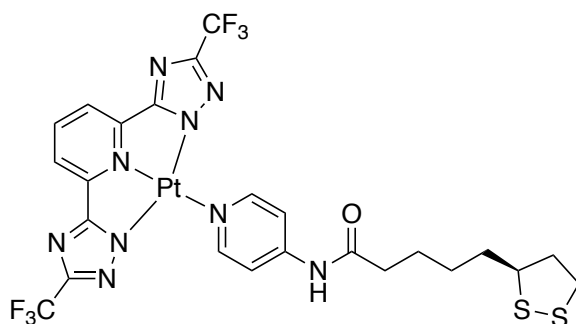


Complex 16. In a 50 mL two-neck round-bottom flask, the tridentate ligand CF₃-trz-py (**2**) (349 mg, 1.0 mmol, 1.05 eq), and PtCl₂(DMSO)₂ (400 mg, 0.95 mmol, 1.0 eq) were suspended in 25 mL of methanol. Triethylamine (265 μ L, 1.9 mmol, 2.0 eq) was then added to the suspension. A solution of 7-(pyridin-4-yl) heptyl 5-(1,2-dithiolan-3-yl) pentanoate (**13**) (65.5 mmol.L⁻¹ in methanol) (14.5 mL, 0.95 mmol, 1.0 eq) was also added and the mixture heated at 65°C under N₂ atmosphere overnight. A turbid yellow-orange solution rapidly formed. The solution solidified to the walls of the round bottom flask. The solution was left to cool to room temperature, and the reaction mixture was evaporated under vacuum. The crude product was then dissolved in ethylacetate/cyclohexane (1:1) and absorbed onto silica (0.063 – 0.200 mm), which was loaded onto a column packed with silica gel. The compound was separated by column chromatography using ethyl acetate/cyclohexane (1:1) as the eluent mixture. The first fraction was the product, which was collected and dried under vacuum. The crude product was then rinsed with a minimal amount of methanol and filtered. The orange powder was dried under vacuum for two days. (293 mg, 0.317 mmol, 33%). ¹H NMR (CD₂Cl₂, 400 MHz, ppm) δ : 9.31 (d, J = 6.5 Hz, 2H), 7.95 (t, J = 7.62 Hz, 1H), 7.62 (d, J = 7.9 Hz, 2H), 7.31 (d, J = 6.6 Hz, 2H), 4.06 (t, J = 6.7 Hz, 2H), 3.56 (m, 1H), 3.15 (m, 1H), 3.11 (m, 1H), 2.76 (t, J = 7.3 Hz, 2H), 2.45 (m, 1H), 2.30 (t, J = 7.3 Hz, 2H), 1.89 (m, 1H), 1.63 (m, 10H), 1.46 (m, 2H); ¹⁹F NMR (CDCl₃, 376 MHz, ppm) δ : -64.55; [M+H]⁺, calcd. 924.1873, found 924.1879. Elemental analysis: calcd. C 40.30%, N 12.13%, H 3.71%, found C 40.19%, N 11.97%, H 3.69%.

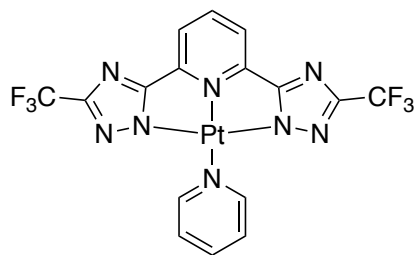


5-(1,2-dithiolan-3-yl)-N-(pyridin-4-yl)pentanamide (17). A solution of α -lipoic acid (200mg, 0.965 mmol, 1 eq) and HOBu.xH₂O (153 mg, 1.17 mmol, 1.17 eq) in dry DMF (5 mL) was cooled

to 0°C upon which EDC.HCl (209 mg, 1.09 mmol, 1.13 eq) was added and stirred, maintaining the temperature until the EDC.HCl had completely dissolved. The solution was left to warm to room temperature and stirred for another hour. A solution of N-ethylmorpholyne (116 mg, 1.007 mmol, 1.04 eq) and 4-aminopyridine (182 mg, 1.93 mmol, 2 eq) in dry DMF (7 mL) was added to the reactional mixture and stirred overnight. A yellow clear solution was obtained. The solution was dried and purified with a chromatography column using dichloromethane/acetone (1:1) as an eluent. The desired product, a pale yellow oil, was obtained. (142 mg, 0.50 mmol, 52%). ¹H NMR (CDCl₃, 400 MHz, ppm) δ : 8.47 (d, J = 5.3 Hz, 2H), 7.5 (d, J = 6.3 Hz, 2H), 3.57 (m, 1H), 3.18 (m, 2H), 3.12 (m, 1H), 2.46 (m, 1H), 2.40 (m, 2H), 1.91 (m, 1H), 1.71 (m, 4H), 1.51 (m, 2H) ; ¹³C NMR (CDCl₃, 100 MHz, ppm) δ: 172.09, 150.21, 145.72, 113.78, 56.48, 40.39, 38.63, 37.54, 34.72, 28.91, 25.03 ; HR-ESI-MS (m/z) : C₁₃H₁₉N₂O₂ [M+H]⁺, calcd. 283.0933, found 283.0946.

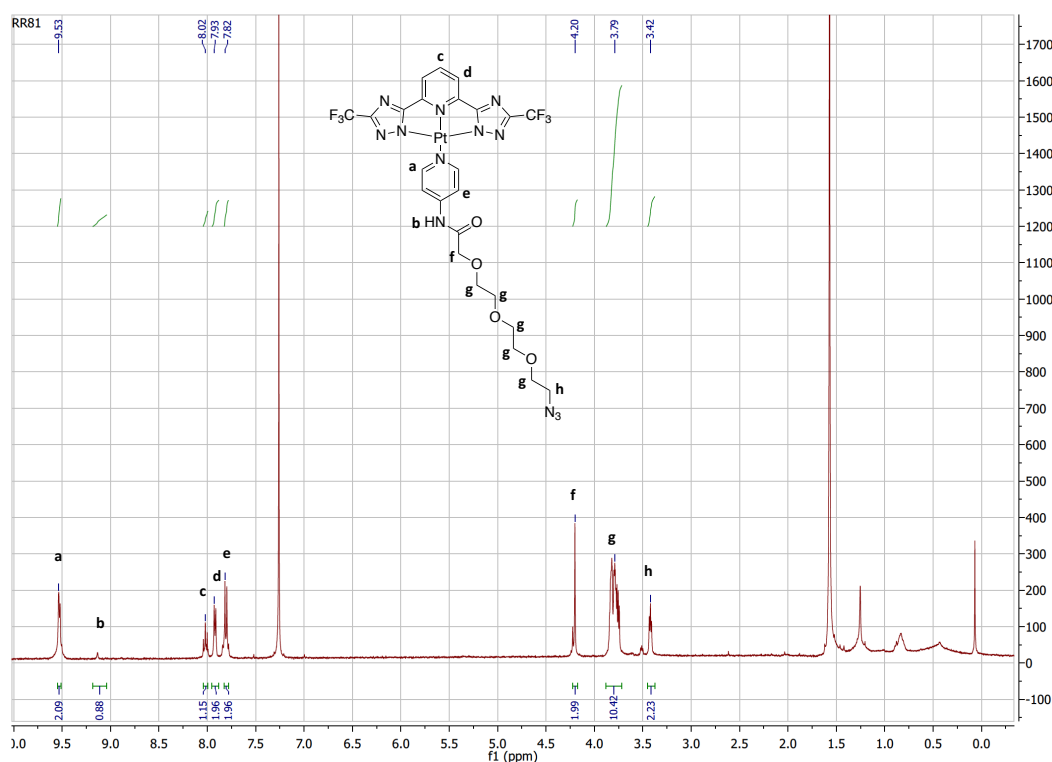


Complex 18. In a 50 mL two-neck round-bottom flask, the tridentate ligand CF₃-trz-py (**2**) (86 mg, 0.248 mmol, 1.05 eq) and PtCl₂(DMSO)₂ (100 mg, 0.236 mmol, 1.0 eq) were suspended in 15 mL of ethanol. After the addition of triethylamine (66 μL, 0.472 mmol, 2.0 eq) to the suspension, 5-(1,2-dithiolan-3-yl)-N-(pyridin-4-yl) pentanamide (**17**) (47.8 mg, 0.236 mmol, 1.0 eq) was then added and the mixture heated at 65°C overnight under N₂ atmosphere. An orange precipitate rapidly formed. The crude was purified by column chromatography using ethylacetate / cyclohexane 1: 1 as the mobile phase. The final product was rinsed with a minimal amount of methanol and filtered. The orange solid was dried under vacuum for two days. (m= 80mg, 0.097 mmol, yield 41%). ¹H NMR (CDCl₃, 400 MHz, ppm) δ : 9.41 (d, J = 6.5 Hz, 2H), 7.98 (t, J = 7.9 Hz, 1H), 7.73 (d, J = 7.9 Hz, 2H), 7.66 (d, J = 6.6 Hz, 2H), 3.63 (m, 1H), 3.17 (m, 2H), 3.12 (m, 1H), 2.50 (m, 3H), 1.98 (m, 1H), 1.81 (m, 4H), 1.53 (m, 2H); ¹⁹F NMR (CDCl₃, 376 MHz, ppm) δ: -64.23; HR-MS (ESI) m/z: C₂₄H₂₂F₆N₉O₁S₂Pt [M+H]⁺, calcd. 825.094, found 825.082; Elemental analysis: calcd. C 34.95%, N 15.29%, H 2.57%, found C 34.95%, N 14.50%, H 2.84%.



Complex 19. In a 50 mL two-neck round-bottom flask, the tridentate ligand CF₃-trz-py (**2**) (200 mg, 0.573 mmol, 1.05 eq) and PtCl₂(DMSO)₂ (230 mg, 0.46 mmol, 1.0 eq) were suspended in 25 mL of acetonitrile. N,N-diisopropylethylamine (100 μL, 0.576 mmol, 1eq) was added and the reaction mixture turned to a clear yellow solution. Pyridine (50 μL, 0.621 mmol, 1.2 eq) was then added and the mixture heated at 83°C overnight under N₂ atmosphere. The crude was purified by column chromatography using ethyl acetate and cyclohexane 3: 2 as the eluent mixture. The final product was then rinsed with a minimum amount of methanol and filtered. A yellow solid was collected and dried under vacuum for two days. (244 mg, 394 μmol, yield 72.1%). ¹H NMR (THF-d₈, 400 MHz, ppm) δ: 9.71 (d, J = 6.2 Hz, 2H), 8.24 (t, J = 8.0 Hz, 1H), 8.22 (t, J = 8.0 Hz, 1H), 7.89 (d, J = 6.5 Hz, 2H), 7.76 (t, J = 8.0 Hz, 2H); ¹⁹F NMR (THF-d₈, 376 MHz, ppm) δ: -64.79 (s, 6H); HR-MS (ESI) m/z: C₁₆H₈F₆N₈Pt [M+H]⁺, calcd. 622.0497, found 622.0487; Elemental analysis: calcd. C 30.93%, N 18.03%, H 1.30%. C 30.85%, N 17.88%, H 1.53%.

Detailed ¹H NMR spectra of platinum(II) complex **7**.



2.4.3. Surface preparation

Cleaning and etching of the substrates

Prior to use, the silicon wafers (p-type, <100>, 2 cm²) were cleaned by successive sonications in acetone, methanol, and 2-propanol. Substrates were then rinsed with distilled water and then placed into piranha solution (H₂SO₄: H₂O₂ (3:1), *warning: caustic!*) at 100°C for 1 hr. The samples were then removed from the acidic solution, rinsed with copious amounts of water and dried under streaming nitrogen. The silicon substrates were etched in the 5% HF(aq) solution for 5 min. During the etching process, the wafers were occasionally agitated to remove bubbles that formed on the surface. The samples were removed from the HF solution, rinsed thoroughly with water, and dried under a nitrogen flow.

UV-induced coupling of 4-vinylpyridine

The hydrogen-terminated silicon substrates were immersed in a 10 mL of 20 vol % ethanol solution of 4-vinylpyridine. The solution was purged with argon for 5 min and subjected to UV irradiation (1000 W) for 30 min. The substrates were removed from the 4-vinylpyridine ethanol solution, rinsed thoroughly with ethanol and dried under a nitrogen flow. Pyridine-terminated substrates (Si-4VP) were then placed into a methanol solution containing the tridentate CF₃ ligand (1.0 mmol, 3.66 mg), PtCl₂(DMSO)₂ (1.05 mmol, 4.22 mg) and TEA (1.05 mmol, 2.8 μL) and heated at 65°C under nitrogen overnight. The samples were then rinsed with ethanol, sonicated for 1 min in ethanol, rinsed with ethanol and dried under nitrogen.

Acetylenation of the substrates

The etched substrates (Si-H) were loaded into the glovebox for further modifications. A saturated solution of PCl₅ in chlorobenzene (0.6-0.7 M) was prepared and heated at 60°C for 1 h prior to use to ensure complete dissolution of the PCl₅. The silicon substrates were added with a few grains of benzoyl peroxyde (3-4 mg/mL of chlorobenzene) and heated to 90°C for 50 min. Subsequently, the samples were rinsed with anhydrous THF several times and immediately used for the acetylenylation step. The chlorinated wafers (Si-Cl) were immersed in a sodium acetylide (18% in xylenes/ light mineral oil) suspension and heated to 130°C for 5 h. At the end of the reaction, the substrates were removed from the solution, rinsed thoroughly with anhydrous THF, and then rinsed with anhydrous methanol. The samples were

then immersed into a fresh solution of anhydrous methanol, taken out of the glovebox, sonicated for 10 min, and then dried under a nitrogen flow.

CuAAC click-chemistry of ligand 6 and platinum (II) complex 7 on acetylenated substrates

The acetylenated substrates (Si-III) were immersed in an anhydrous dichloromethane or methanol solution containing the azide terminated ligand **6** (10^{-3} M) and copper iodide (10 mol %) for 4 days. The substrates were then rinsed with methanol, sonicated in methanol for 5 min and rinsed again with methanol. The functionalised substrates (Si-L) were then placed into a methanol solution containing the tridentate CF_3 ligand (1.0 mmol, 3.66 mg), $\text{PtCl}_2(\text{DMSO})_2$ (1.05 mmol, 4.22 mg) and TEA (1.05 mmol, 2.8 μL) and heated at 65°C under nitrogen overnight. The samples were then rinsed with ethanol, sonicated for 1 min in ethanol, rinsed with ethanol and dried under nitrogen. The direct coordination of complex **7** on the acetylenated substrated was carried out in a dichloromethane solution containing the complex **7** (10^{-3} M) and copper iodide (10 mol%) for 4 days under a gentle agitation with an orbital shaker. The substrates were rinsed with dichloromethane, sonicated in dichloromethane for 5 min, rinsed with dichloromethane and methanol and dried with streaming nitrogen. The substrates were stored under vacuum prior to analysis.

Functionalisation of gold substrates

The gold substrates (30 nm layer on silicon with 5 nm Ti priming layer) were cleaned using a UVO cleaner for 1 hr. The gold surfaces were immersed in a 1 mM solution of complex **14-16**, **18** in DMF for 6 days. The solutions were gently agitated with an orbital shaker to avoid precipitation of the platinum (II) complexes. The samples were rinsed with DMF, ethanol, sonicated 5 min in ethanol, rinsed with ethanol and dried under a nitrogen blow. The samples were stored under vacuum until analysis.

2.4.4. Photophysics

All of the absorption measurements in this report were recorded on a UV-3600 Shimadzu UV-Vis-NIR spectrophotometer, baseline and solvent corrected with UV Probe software. Quartz cuvettes were used for this purpose. Steady-state measurements were recorded on a HORIBA Jobin-Yvon IBH FL-332 Fluorolog 3 spectrometer equipped with a 450 W Xenon arc lamp, double grating excitation and emission monochromators.

2.4.5. Water contact angle

Water contact angles were determined on a Krüss DSA 100 goniometer. The measurement started 30 seconds after deposition of a 10 μ L water droplet on the substrate. The average value of 30 measurements was taken. The water contact angle was all measured with 3 separate spots for each substrate

2.4.6. X-ray photoelectron spectroscopy (XPS) measurements

The XPS measurements were all carried out by a Thermo Scientific K-Alpha X-ray Photoelectron Spectrometer using a monochromatic AlK α radiation ($h\nu = 1486.6$ eV). Survey spectra were obtained after 25 scans and the measurements were performed with a 200 eV analyzer pass energy and a 1 eV energy step size to calculate the atomic percentages. High resolution XPS spectra of the different elements were obtained after 10 scans with a 50 eV analyzer pass energy and a 0.1 eV energy step size to obtain the chemical state information. The binding energies of each element were all referenced to carbon C 1s peak at 284.8 eV.

2.4.7. Scanning electron microscopy (SEM)

SEM characterization was performed employing a FEI scanning electron microscope Quanta FEG 250, at an acceleration voltage of 10 KV. Samples were prepared by drop-casting a solution of platinum (II) complex onto a glass slide, and then a plasma-induced deposition of a 40 nm thick layer of silver was added.

2.4.8. Confocal fluorescence microscopy

All of the fluorescence images were taken by using Zeiss LSM 710 confocal microscope system with 63 \times magnification, numerical aperture, and a 1.3 of Zeiss LCI Plan-NEOFLUAR water immersion objective lens (Zeiss GmbH). The samples were excited by continuous wave (cw) laser at 405 nm. The emissions of the complexes were collected in the range from 400 to 750 nm. In addition, the lambda-mode acquisition technique was performed to observe the emission spectra of the two complexes after cell internalization. The raw data was processed in lambda-mode by using linear un-mixing tool available in the ZEN 2011 software package (Zeiss GmbH). All images were captured by using the same software.

2.4.9. Physical vapor deposition (PVD)

Conditions for the formation of the NWs were selected after conducting different experiments adjusting the temperature and type of substrate. Sublimation of the Pt-complex was carried out in a commercial available OLED thermal source (Lesker) at 0.002 mbar of Argon, with the distance between the evaporation cell and sample holder fixed at 8 cm. Substrate temperature was varied between 90 to 140 °C, optimal results were obtained at 110 °C. Growth rates were monitored by a Quartz Crystal Microbalance (QCM) located at the same distance from the evaporation cell as the sample at a fixed (nominal value) 0.4 Å/s (density 0.5). In a standard experiment, a nominal thickness of 1000 Å was deposited on the substrate.

2.6. References

1. Abraham Ulman, *Chem. Rev.*, **1996**, *96*, 1533-1554.
2. J. Christopher Love, Lara A. Estroff, Jennah K. Kriebel, Ralph G. Nuzzo, George M. Whitesides, *Chem. Rev.*, **2005**, *105*, 1103-1169.
3. Steffen Onclin, Bart Jan Ravoo, and David N. Reinhoudt, *Angew. Chem. Int. Ed.*, **2005**, *44*, 6282 – 6304.
4. J. Justin Gooding, Simone Ciampi, *Chem. Soc. Rev.*, **2011**, *40*, 2704–2718.
5. Sagiv, *J. Am. Chem. Soc.*, **1980**, *102*, 92–98.
6. R. G. Nuzzo, D. L. Allara, *J. Am. Chem. Soc.*, **1983**, *105*, 4481–4483.
7. Yaw S. Obeng and Allen J. Bard, *Langmuir*, **1991**, *7*, 195-201.
8. Juan Madoz, Boris A. Kuznetzov, Francisco J. Medrano, Jose L. Garcia, Victor M. Fernandez, *J. Am. Chem. Soc.*, **1997**, *119*, 1043-1051.
9. Marinella Govoni, Remko A. Bakker, Ineke van de Wetering, Martine J. Smit, Wiro M. B. P. Menge, Henk Timmerman, Sigurd Elz, Walter Schunack, Rob Leurs, *J. Med. Chem.*, **2003**, *46*, 5812-5824.
10. Paula M Mendes, *Chem. Soc. Rev.*, **2008**, *37*, 2512–2529.

11. Samuel J. Adams, David J. Lewis, Jon A. Preece, Zoe Pikramenou, *ACS Appl. Mater. Interfaces*, **2014**, *6*, 11598–11608.
12. S. Kobayashi, T. Nishikawa, T. Takenobu, S. Mori, T. Shimoda, T. Mitani, H. Shimotani, N. Yoshimoto, S. Ogawa, Y. Iwasa, *Nature materials*, **2004**, *3*, 317-322.
13. Rajaa Farran, Damien Jouvenot, Frédérique Loiseau, Jérôme Chauvin, Alain Deronzier, *Dalton Trans.*, **2014**, *43*, 12156-12159.
14. Sidharam P. Pujari, Luc Scheres, Antonius T. M. Marcelis, Han Zuilhof, *Angew. Chem. Int. Ed.*, **2014**, *53*, 6322 – 6356.
15. M. Grandbois, M. Beyer, M. Rief, H. Clausen-Schaumann, H. E. Gaub, *Science*, **1999**, *283*, 1727 – 1730.
16. N. Herzer, S. Hoepfener, U. S. Schubert, *Chem. Commun.*, **2010**, *46*, 5634 – 5652.
17. H. E. Ries, Jr., H. D. Cook, *J. Colloid Sci.*, **1954**, *9*, 535 – 546.
18. P. Thissen, M. Valtiner, G. Grundmeier, *Langmuir*, **2010**, *26*, 156 – 164.
19. D. L. Allara, R. G. Nuzzo, *Langmuir*, **1985**, *1*, 45 – 52.
20. A. Raman, R. Quiçones, L. Barriger, R. Eastman, A. Parsi, E. S. Gawalt, *Langmuir*, **2010**, *26*, 1747-1754.
21. Q. Ye, F. Zhou, W. Liu, *Chem. Soc. Rev.*, **2011**, *40*, 4244 – 4258.
22. M. Rosso, M. Giesbers, A. Arafat, K. Schron, H. Zuilhof, *Langmuir*, **2009**, *25*, 2172 – 2180.
23. T. K. Mischki, R. L. Donkers, B. J. Eves, G. P. Lopinski, D. D. M. Wayner, *Langmuir*, **2006**, *22*, 8359 – 8365.
24. Qin, G.; Zhang, R.; Makarenko, B.; Kumar, A.; Rabalais, W.; Romero, J. M. L.; Rico, R.; Cai, C. Highly Stable, *Chem. Commun.*, **2010**, *46*, 3289–3291.
25. D. Xu, E. T. Kang, K. G. Neoh, Yan Zhang, A. A. O. Tay, S. S. Ang, M. C. Y. Lo and K. Vaidyanathan, *J. Phys. Chem. B*, **2002**, *106*, 12508-12516.
26. Rosso, M., Arafat, A., Schroën, K.; Giesbers, M.; Roper, C. S., Maboudian, R.; Zuilhof, H., *Langmuir*, **2008**, *24*, 4007–4012.

27. Simone Ciampi, Till Böcking, Kristopher A. Kilian, Michael James, Jason B. Harper, J. Justin Gooding, *Langmuir*, **2007**, *23*, 9320-9329.
28. Matthew R. Linford, Christopher E. D. Chidsey, *J. Am. Chem. Soc.*, **1993**, *115*, 12631–12632.
29. M. R. Linford, P. Fenter, P. M. Eisenberger and C. E. D. Chidsey, *J. Am. Chem. Soc.*, **1995**, *117*, 3145–3155.
30. Simone Ciampi, Jason B. Harper and J. Justin Gooding, *Chem. Soc. Rev.*, **2010**, *39*, 2158–2183.
31. J. Christopher Love, Lara A. Estroff, Jennah K. Kriebel, Ralph G. Nuzzo, George M. Whitesides, *Chem. Rev.*, **2005**, *105*, 1103-1169.
32. Richter, S.; Poppenberg, J.; Traulsen, C. H.-H.; Darlatt, E.; Sokolowski, A.; Sattler, D.; Unger, W. E.; Schalley, C. A., *J. Am. Chem. Soc.*, **2012**, *134*, 16289–16297.
33. Fioravanti, G.; Haraszkiwicz, N.; Kay, E. R.; Mendoza, S. M.; Bruno, C.; Marcaccio, M.; Wiering, P. G.; Paolucci, F.; Rudolf, P.; Brouwer, A. M., *J. Am. Chem. Soc.*, **2008**, *130*, 2593–2601.
34. Seitz, O.; Dai, M.; Aguirre-Tostado, F.; Wallace, R. M.; Chabal, Y. J., *J. Am. Chem. Soc.*, **2009**, *131*, 18159–18167.
35. N. Tuccitto, I. Delfanti, V. Torrisi, F. Scandola, C. Chiorboli, V. Stepanenko, F. Würthner, A. Licciardello, *Phys. Chem. Chem. Phys.*, **2009**, *11*, 4033–4038.
36. Douglas G. Brown, Phil A. Schauer, Javier Borau-Garcia, Brandon R. Fancy, and Curtis P. Berlinguette, *J. Am. Chem. Soc.*, **2013**, *135*, 1692–1695.
37. Hiroaki Maeda, Ryota Sakamoto, Yoshihiko Nishimori, Junya Sendo, Fumiyuki Toshimitsu, Yoshinori Yamanoi, Hiroshi Nishihara, *Chem. Comm.* **2011**, *47*, 8644-8646.
38. Hatzor, A.; Moav, T.; Cohen, H.; Matlis, S.; Libman, J.; Vaskevich, A.; Shanzer, A.; Rubinstein, I., *J. Am. Chem. Soc.*, **1998**, *120*, 13469–13477.
39. V. H. Houlding; V. M. Miskowski, *Coord. Chem. Rev.*, **1991**, *111*, 145-152.
40. V. M. Miskowski; V. H. Houlding, *Inorg. Chem.*, **1991**, *30*, 4446-4452.
41. Strassert, Cristian A., Chen-Han Chien, Maria D. Galvez Lopez, Dimitrios Kourkoulos, Dirk Hertel, Klaus Meerholz, and Luisa De Cola, *Angew. Chem., Int. Ed.* **2011**, *50*, 946-950.
42. Po, Charlotte, Anthony Yiu-Yan Tam, Keith Man-Chung Wong, and Vivian Wing-Wah Yam, *J. Am. Chem. Soc.*, **2011**, *133*, 12136-12143.

- 43 Mauro, Matteo, Alessandro Aliprandi, Cristina Cebrián, Di Wang, Christian Kübel, and Luisa De Cola. *Chem. Commun.*, **2014**, *50*, 7269-7272.
44. Lu, Wei, Yong Chen, V. A. L. Roy, Stephen Sin-Yin Chui, and Chi-Ming Che. *Angew. Chem. Int. Ed.*, **2009**, *48*, 7621–7625.
23. 45. Alessandro Aliprandi, Matteo Mauro, Luisa De Cola, *Nature Chem.* **2016**, *8*, 10–15.
46. Deb Kumar Bhowmick, Linda Stegemann, Manfred Bartsch, Naveen Kumar Allampally, Cristian A. Strassert, Helmut Zacharias, *J. Phys. Chem. C*, **2015**, *119*, 5551–5561.
47. Manuel Macias-Montero, A. Nicolas Filippin, Zineb Saghi, Francisco J. Aparicio, Angel Barranco, Juan P. Espinos, Fabian Frutos, Agustin R. Gonzalez-Elipe, Ana Borrás, *Adv. Funct. Mater.*, **2013**, *23*, 5981–5989.
48. Q. Liao, H. Fu, J. Yao, *Adv. Mater.*, **2009**, *21*, 1.
49. Ana Borrás, Myriam Aguirre, Oliver Groening, Carlos Lopez-Cartes, Pierangelo Groening, *Chem. Mater.*, **2008**, *20*, 7371–7373.
50. Sang Won Jeong, David F. O'Brien, *J. Org. Chem.*, **2001**, *66*, 4799-4802.
51. Benoît Frisch, Christophe Boeckler, Francis Schuber, *Bioconjugate Chem.*, **1996**, *7*, 180-186.
52. Mei-Jin Li, Xing Liu, Mei-Juan Nie, Zhao-Zhen Wu, Chang-Qing Yi, Guo-Nan Chen, Vivian Wing-Wah Yam, *Organometallics*, **2012**, *31*, 4459–4466.
53. Cicero, R. L.; Linford, M. R.; Chidsey, C. E. D., *Langmuir*, **2000**, *16*, 5688.
54. Rosemary D. Rohde, Heather D. Agnew, Woon-Seok Yeo, Ryan C. Bailey, and James R. Heath, *J. Am. Chem. Soc.*, **2006**, *128*, 9518-9525.
55. E. Joseph Nemanick, Patrick T. Hurley, Bruce S. Brunshwig, Nathan S. Lewis, *J. Phys. Chem. B*, **2006**, *110*, 14800-14808.
56. Kolb, H. C.; Finn, M. G., Sharpless, K. B., *Angew. Chem. Int. Ed.*, **2001**, *40*, 2004-2021.
57. Simone Ciampi, Till Böcking, Kristopher A. Kilian, Michael James, Jason B. Harper, J. Justin Gooding, *Langmuir*, **2007**, *23*, 9320-9329.
58. Willey, T. M.; Vance, A. L.; Bostedt, C.; van Buuren, T.; Meulenburg, R. W.; Terminello, L. J.; Fadley, C. S., *Langmuir*, **2004**, *20*, 4939–4944.

59. Dong, Y.; Abaci, S.; Shannon, C.; Bozack, M. J., *Langmuir*, **2003**, *19*, 8922–8926.
60. A. Borrás, M. Aguirre, C. Lopez-Cartes, O. Groening, and P. Groening, *Chemistry of Materials*, **2008**, *20*, 7371-7273.
61. A. Borrás, O. Groening, M. Aguirre, F. Gramm, P. Groening, *Langmuir*, **2010**, *26*, 5763-5771.
62. Oulad-Zian, Y., Sanchez-Valencia, J.R., Oliva, M., Parra-Barranco, J., Icaire, M., Aparicio, F.J., Mora-Boza, A., Espinos, J.P., Yubero, F., Gonzalez-Elipe, A.R., Barranco, A., Borrás, A., *Adv. Opt. Mater.*, **2016**, *7*, 1124-1131.
63. Damiano Genovese, Alessandro Aliprandi, Eko A. Prasetyanto, Matteo Mauro, Michael Hirtz, Harald Fuchs, Yasuhiko Fujita, Hiroshi Uji-I, Sergei Lebedkin, Manfred Kappes, Luisa De Cola, *Adv. Funct. Mater.*, **2016**, *26*, 5271–5278.
64. Peigen Cao, Ke Xu, James R. Heath, *J. Am. Chem. Soc.*, **2008**, *130*, 14910–14911.
65. Hannu Häkkinen, *Nature Chem.*, **2012**, *4*, 443-455.

Chapter 3

Encapsulation of platinum(II) complexes by PMMA-PMAA diblock copolymer

Abstract: This chapter describes a method developed for the entrapment of platinum(II) complex in water. It was not only demonstrated that the platinum(II) complex was encapsulated inside the PMMA-PMAA particles, but also that the photoluminescence properties of the platinum-loaded particles were tunable by adjusting different parameters. Optimisation of the method in order to obtain monodisperse particles suitable for further applications was also discussed.

3.1. Introduction

Supramolecular chemistry represents a very important area in a number of research fields, such as chemistry, biology, and material science, mainly owing to its relevance to assembly of randomly oriented molecules to highly ordered supramolecular structures through a delicate balance of non-covalent interactions¹. Supramolecular organometallic nanostructures have attracted a great deal of attention in the last few years because of the possibility to fabricate functional materials with superior properties compared to the bulk. In particular, square-planar Pt(II) complexes with filled d_z^2 orbitals have been known to show a high tendency towards stacking through weak non-covalent metal...metal and/or π - π ligand-ligand interactions. The self-organization of luminescent platinum(II) complexes has been used in the last decade as an efficient bottom-up approach towards preparation and development of new molecular structures from the nanometer up to micrometer scale²⁻⁶. Phosphorescent platinum(II) complexes are also known for their high photoluminescence quantum yield, long excited state lifetimes (compared to organic fluorescent labels), tunable emission and significant Stokes shift^{7,8}. Studies on platinum(II) system showing drastic color changes in solution upon a change in the composition of the solvents due to metal-metal and π - π interactions associated with aggregate formation were reported⁹⁻¹¹.

Metallo-supramolecular block copolymer self-assemblies have attracted a lot of attention for an alternative strategy of the encapsulation of platinum(II) complexes. A metal-ligand complex is used as a supramolecular linker between the hydrophilic and hydrophobic blocks and the amphiphilic block copolymer. Several studies report the synthesis of block copolymer containing transition metal complexes units and their self-assembled properties. Sleiman et al. reported the first detailed study on the self-assembly of diblock copolymers containing the luminescent metal complex $\text{Ru}(\text{bpy})_3^{2+}$. They evidenced the reproducible formation of numerous morphologies in solution including vesicles, micelles or tubules which all contain $\text{Ru}(\text{bpy})_3^{2+}$ within the micellar core/ vesicle wall¹². Yam et al. have reported an amphiphilic platinum (II)-containing diblock copolymer¹⁸. They have demonstrated the micellisation properties of such molecules and the remarkable photophysical changes upon pH and solvent variations that could induce drastic UV-vis and emission spectral changes via modulation of Pt...Pt and π - π stacking interactions both in aqueous and organic media.

A more versatile approach is the encapsulation of platinum(II) complexes in soft structures, such as micelles or vesicles. A few reports were found on the incorporation of cationic platinum(II) complexes into an anionic sodium dodecyl sulfate (SDS) surfactant in aqueous solution¹⁴⁻¹⁶. An enhancement of the photophysical properties was always observed with an increase of the emission intensity of several orders of magnitude. Rod- and sheet-like aggregates with remarkable photophysical properties in water were also observed¹⁷. De Cola et al. recently reported a highly reactive platinum precursor that enables the facile labelling of aza-heterocyclic compounds in aqueous media through the formation of highly emissive platinum(II) complex aggregates inside Pluronic P123 micelles¹⁸. A luminescent assay for the in situ labelling, detection and differentiation of pyridines, imidazoles, and related species in aqueous solution and biological environment was developed and based on the remarkable spectroscopic properties of Pt(II) aggregates.

Another approach based on the electrostatic interaction between the positively charged platinum(II) complex ions and negatively charged polymer chains were reported by Yam and coworkers¹⁹. Upon deprotonation of poly (acrylic acid), the platinum(II) complexes were able to self-assemble onto the polyelectrolyte chain inducing remarkable photophysical changes. Bu et al. reported the preparation of luminescent polymeric hybrids formed by platinum(II) complexes and block copolymers. The incorporation of cationic platinum(II) complexes into anionic block copolymers led to the formation of luminescent architectures from spherical or rod-like micelles to vesicles^{20,21}. In both cases, the platinum(II) cations were brought into close proximity with each other leading to Pt...Pt and π - π stacking interactions.

While previous reports favour a bottom-up approach, e.g. encapsulation of single platinum complexes into different carriers, a top-down strategy involving the encapsulation of formed self-assembled structures has not been demonstrated.

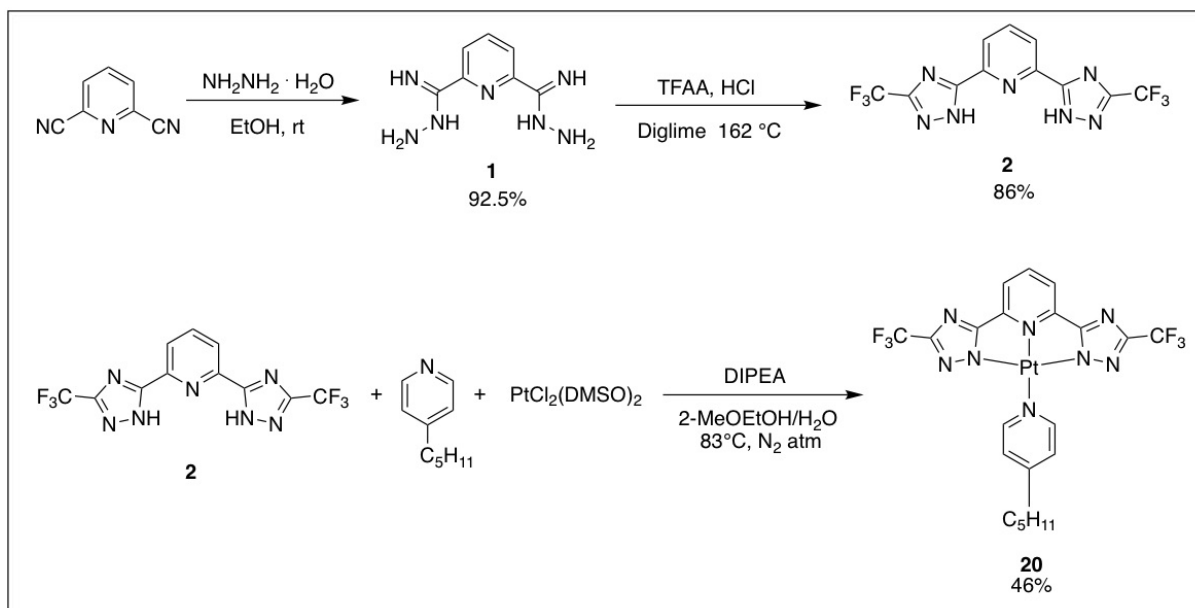
Block copolymers such as polystyrene-*b*-poly(acrylic acid) or polystyrene-*block*-poly(ethylene oxide) and their self-assembled architectures have played a key role in the development of carriers and undergo self-assembly into various nanosized morphologies as a result of the energetic repulsion effect between blocks in selective solvents²²⁻²⁴. While the self-assembly of block copolymers has been extensively investigated, there is no report on the formation of particles formed from diblock copolymers containing luminescent platinum(II) complexes.

To facilitate the encapsulation of neutral hydrophobic complexes, poly (methyl methacrylate-*co*-methacrylic acid) (PMMA-PMAA) diblock copolymer were chosen. It consisted of a long

hydrophobic PMMA block and a short hydrophilic PMAA chain and tended to self-organize in water into spherical micelles²⁵. Moreover, the hydrophobic core of the spherical particles might be a suitable environment for the neutral platinum(II) complexes. In order to study the role of the platinum(II) complexes during the encapsulation by PMMA-PMAA, one hydrophobic and one amphiphilic platinum(II) complex were prepared. Interestingly, both complexes self-assembled in water to form highly luminescent supramolecular structures. Herein, we report a general method for preparing a pure, surfactant-free, stable, aqueous suspension of platinum (II)-loaded PMMA-PMAA particles. The encapsulation is based on the flash injection of a solution containing the platinum(II) complex and poly (methyl methacrylate-co-methacrylic acid) (PMMA-PMAA) into water, followed by removal of the organic solvent²⁶. This is in contrast to previous examples of the metallosupramolecular polymer, in which the metal is covalently bonded to the polymer moiety; here the amphiphilic BCP and the platinum(II) complex are two distinct molecules which interact with each other when they are injected into water. The presence of the polymeric shell allows the control of the morphology of the aggregates and the emission color tuning from green to blue with enhanced excited state lifetimes and photoluminescence quantum yields. Assemblies of platinum(II) complexes within a polymer matrix, spatially confined to spherical geometry at the nanometer to micrometer scale and stable for months at a time may be appealing for biological, or sensing applications. To our knowledge, this represents the first example of self-assembled neutral platinum(II) complexes into polymer particles.

3.2. Results and discussions

3.2.1. Synthesis of the platinum(II) complex



Scheme 3.1. Chemical structures of the platinum(II) complex **20**.

The platinum(II) complexes were all prepared accordingly to a methodology described in previous chapters as depicted in Scheme 3.1⁴. The tridentate ligand **2**, was coordinated to the platinum ion by deprotonation of the two triazole moieties with $\text{PtCl}_2(\text{DMSO})_2$ as a precursor, and heated in the presence of a base under nitrogen atmosphere. The coordination sphere was completed by the addition of the corresponding ancillary ligand. The platinum(II) complexes were obtained after column chromatography purification as a yellow powder. The complexes were further characterized by ^1H NMR, ^{19}F NMR, ^{13}C NMR, elemental analysis and mass spectrometry.

3.2.2. Preparation of polymer particles

Generally, for block copolymers consisting of glassy hydrophobic blocks at room temperature such as PMMA-PMAA ($T_{g,\text{PMMA}} = 105^\circ\text{C}$), a co-solvent method is frequently used²⁷. The amphiphilic diblock copolymers were dissolved in a common solvent such as DMF, dioxane, or THF, which are suitable solvents for both blocks. Then a selective solvent, for example, water (which is a non-solvent for the hydrophobic chain), is slowly added to the solution. The

aggregates were quenched in an excess of water to freeze the kinetics process and morphologies. Finally, the common solvent was removed by dialysis of the resulting solution against water. Next, a basic method for the preparation of aqueous dispersion of polymeric particles was used. A solution of PMMA-PMAA (PMAA : 1.6 mol %) in THF was stirred overnight and then a 2 mL solution with a selected concentration was flash injected in 8 mL of distilled water while sonicating. The organic solvent was rapidly removed under vacuum and the solutions were allowed to stand at room temperature for two days. The size and morphology of the formed particles was confirmed by electron microscopy. The SEM images in Figure 3.1 display the dried PMMA-PMAA particles on a glass slide and the recovered gold.

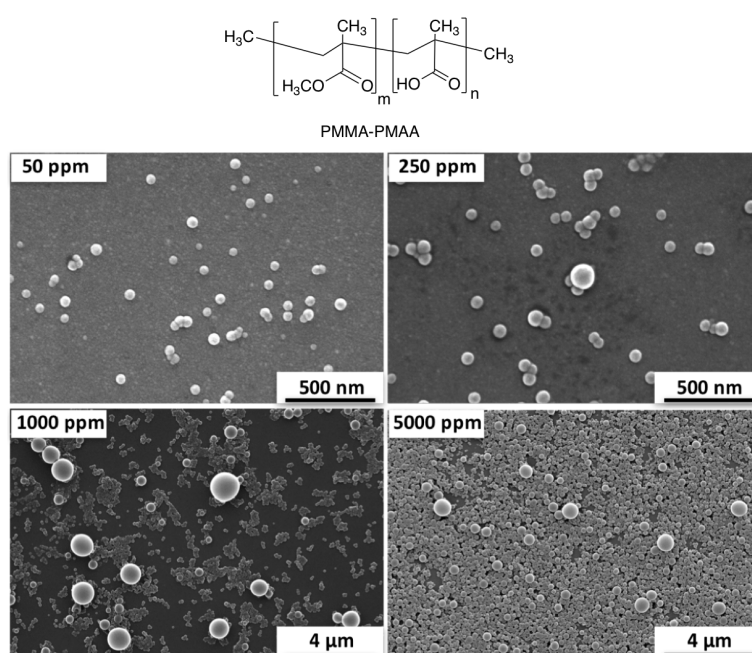


Figure 3.1. SEM images of the PMMA-PMAA particles formed from a THF/polymer solution flash-injected in water at selected concentrations and schematic representation of the polymer aggregates.

At a lower concentration, small particles were observed and the number and size of the particles increased. At 1000 ppm (ppm unit represents mg.L^{-1}) concentration, for a PMMA-PMAA diblock copolymer with a relatively long hydrophobic PMMA block, a mixture of spherical micelles and larger particles was observed. Such morphologies were already reported in a previous work of Eisenberg and coworkers and have been defined as large compound micelles (LCMs)²². LCMs consist of an aggregation of inverse micelles, where the outer surface is stabilized in solution by a thin layer of hydrophilic chains. These micelles are

spherical, solid, highly dispersive and contain some very large specimens. The effect of PMMA-PMAA concentration on the morphology of the aggregates can be interpreted by the fact that the aggregation number (N_{agg} , the average number of polymer chain in an aggregate) is a function of polymer concentration. An increase in the aggregation number yields larger core dimensions. This process is energetically favourable because the larger core sizes result in a smaller number of aggregates, and therefore a smaller total interfacial area and a lower total interfacial energy between the core and the non solvent²⁸.

Dynamic light scattering (DLS) in Figure 3.2, a) displays the intensity percentage of the particles in solution. Three peaks were observed: the first peak around 100 nm corresponding to the smaller particles, and the second peak around 320 nm, which are considered to be the particles of medium diameter or aggregates of smaller particles. A less intense peak above 1000 nm were also observed, which were attributed to either the larger particles of aggregates or smaller particles. It is also worth mentioning that the particles solution was not filtered before analysis, therefore it is possible that dust or contaminants may have resulted in the presence of a half peak above 5000 nm in some samples. The number percentages displayed in Figure 3.2, b) shows a single peak at 100 nm corresponding to the average diameter of the majority of the polymer particles.

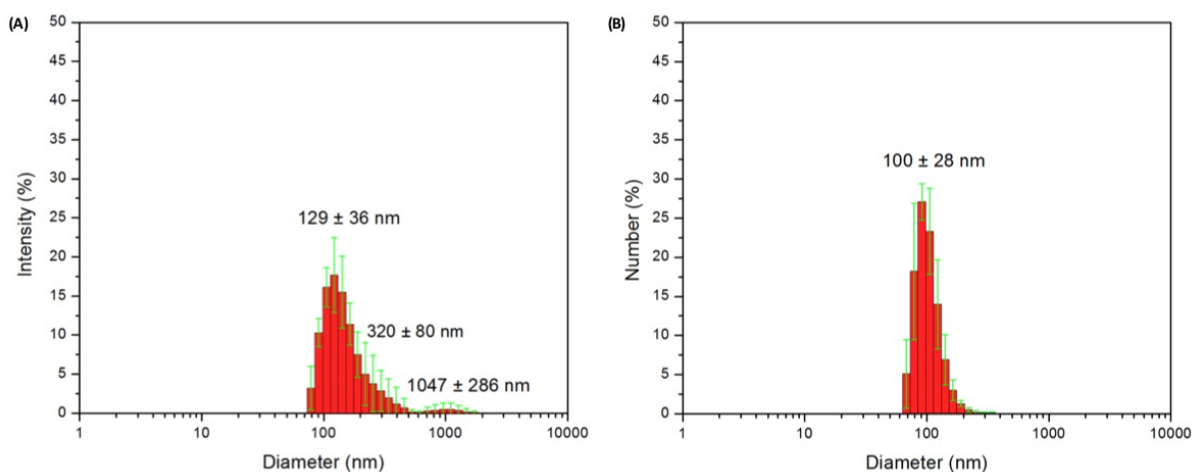


Figure 3.2. DLS measurement of the PMMA-PMAA particles formed from flash-injection of a 5000 ppm PMMA-PMAA/THF solution in water.

The nature of a suitable solvent can play an important role in the formation of various aggregates, since the organic solvent directly affects the dimensions of both hydrophobic domains and hydrophilic coronas of the aggregates²⁹. Dissolution of the polymer is optimal

when the values of the solubility parameters (δ) for the polymer and the solvent are similar. If these values diverge, the polymer chain dimensions decrease. The solubility parameter value δ of PMMA ($\delta = 18.0$) is closer to that of THF ($\delta = 18.5$) compared to acetone (19.7). As a consequence, the degree of mobility and swelling of the PMMA cores of the micelles are higher in THF than in acetone, which facilitates the micelles growth. As a result, the particles formed by flash-injection in water from a polymer/acetone solution were extremely small in size and hence difficult to observe by SEM (Figure 3.3). When THF was used instead of acetone, larger particles were observed for the same concentration.

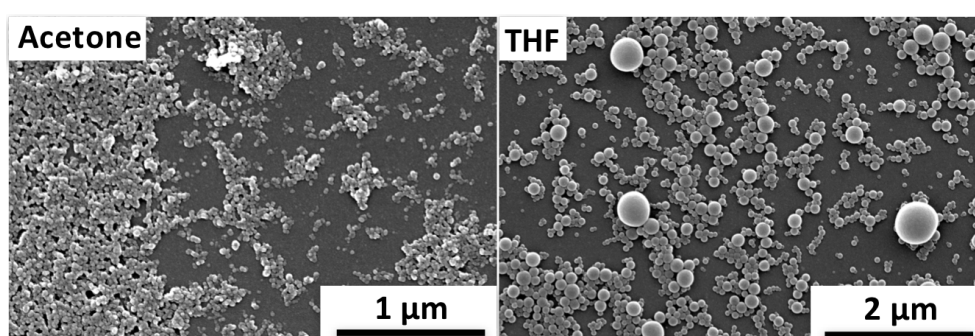


Figure 3.3. SEM images of PMMA-PMAA particles formed from flash-injection of a 5000 ppm polymer/acetone (left) or polymer/THF (right) solution in water.

The choice of the solvent for PMMA-PMAA is crucial regarding the size and morphology of the particles. Generally, the closer the solubility parameters of the polymer and the solvent are, the more swollen the particles will be. The most common solvents used in literature were THF, dioxane and DMF. The solvents' effect on the morphologies of the polymer aggregates has previously been studied²⁹. A selected list of solvents with their solubility parameters and dielectric constants was reported in Table 3.1³⁰. PMMA-PMAA was used with a platinum(II) complex, which is an emissive compound, and hence it was necessary to verify that the polymer was not emissive. Emission spectra of the PMMA-PMAA particles in water are displayed in Figure 3.4.

Table 3.1. Solubility parameters and dielectric constants of some common solvents.

Solvents	Solubility parameter (δ)	Dielectric constant
Cyclohexane	16.8	2.02
Ethyl acetate	18.2	6.02
THF	18.5	7.5
Acetone	19.7	20.7
Dichloromethane	20.2	8.93
Dioxane	20.5	2.2
DMF	24.7	36.7
Methanol	29.7	32.7
Water	48.0	80.1
PMMA	18.0	

When excited at 400 nm, the Raman peak of the water was detected at 460 nm for all the solutions. This Raman peak was the result of inelastic scattering of the incoming light from the solvent. Raman scattering occurs from all solvents and the shift between the excitation wavelength and the Raman peak is always constant in energy. Raman scattering is located in the same emission region as the platinum(II) complex but has a rather low yield and thus will not interfere with its emission. One way to shift this Raman band was to excite the solution at a lower excitation wavelength. For example, when the solution was excited at 350 nm, the Raman peak was located around 400 nm.

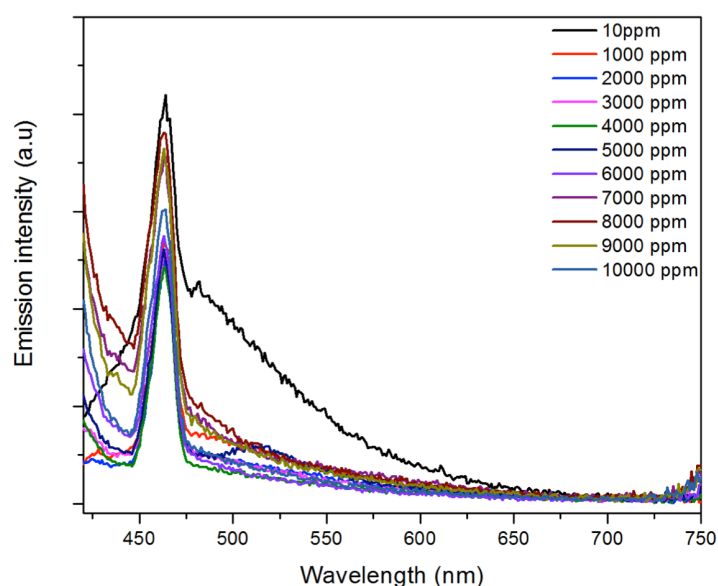


Figure 3.4. Emission spectra of the PMMA-PMMA particles in water at different concentrations. $\lambda_{exc} = 400$ nm. The peak observed at 460 nm was the Raman peaks.

3.2.3. Encapsulation of platinum(II) complexes in PMMA-PMAA particles

The encapsulation of platinum(II) complexes into PMMA-PMAA diblock copolymers in aqueous solutions was performed according to previous literature reports with some modifications³¹. First of all, PMMA-PMAA and the desired platinum(II) complex were dissolved separately in THF. Then 2 mL THF solutions containing both the platinum(II) complex and PMMA-PMAA were prepared. The concentration of the platinum(II) complex was maintained consistently at 5 ppm and the concentration of PMMA-PMAA was gradually increased in each solution. 2 mL THF solution with different PMAA-PMAA/platinum(II) complex ratios were obtained. The ratio between the PMMA-PMAA diblock copolymer and the platinum (II) complex will be from herein referred to as **R** as displayed in Table 3.2.

concentration Pt(II) complex [ppm]	5	5	5	5	5	5	5	5	5	5	5	5	5	5	5	5	5	5
concentration PMMA-PMAA [ppm]	0	5	25	50	100	250	500	750	1000	1250	1500	2000	2500	3000	3500	4000	4500	5000
PMMA-PMAA/ Pt(II) complex (R)	0	1	5	10	20	50	100	150	200	250	300	400	500	600	700	800	900	1000

Table 3.2. Concentrations of platinum(II) complex **20** and PMMA-PMAA diblock copolymers in each solution and the corresponding ratio **R**.

An amount of 2 mL of the freshly prepared mixture was rapidly flash-injected into 8 mL of distilled water while the mixture was sonicated. The organic solvent was then removed by evaporation under reduced pressure and the solutions were left to stand for two days in ambient conditions before analysis. The method of flash-injecting the PMMA-PMAA/platinum(II) complex solution into an aqueous solution resulted in an instantaneous high water content, which allowed the system to be kinetically frozen. Henceforth, the system maintains its morphological and photophysical properties in solution for a considerable amount of time after the removal of the organic solvent. Photography of the solutions under normal light and UV lamp (365 nm) was undertaken and are displayed in Figure 3.5. At the lowest **Rs**, the solutions were transparent and clear. Upon increasing the concentration of the PMMA-PMAA, the solutions became more turbid due to the formation of larger particles and aggregates. Under UV lamp, the solutions have a yellow-orange emission which was

originating from the platinum(II) complex aggregates formed in water. At higher **Rs**, the luminescence from the solution was blue-shifted upon increasing the ratio.

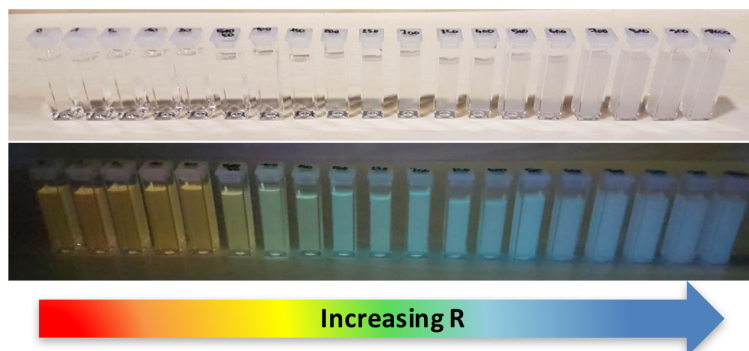


Figure 3.5. Photography of the PMMA-PMAA/platinum(II) complex **20** solutions in water under normal light (top) and UV lamp (bottom) upon increasing **R** from left to right.

3.2.3.1. Photophysical properties

Platinum(II) complex

As reported for similar platinum(II) complexes^{4,6}, those luminescent compounds have a high tendency to aggregate due to platinum-platinum interactions stabilized by π - π stacking. When the distance between the metal complexes is shorter than 3.5 Å, a new molecular orbital is formed which leads to metal to metal ligand charge transfer (MMLCT) states. The absorption and emission spectra of the complex in THF is displayed in Figure 3.6. The spectra was dominated by intense π - π^* transition between 250 nm and 320 nm, which was attributed to the tridentate ligand and to the substituted pyridine. A less intense broad band centered at approximately 400 nm was associated with the metal to ligand charge transfer ¹MLCT, band involving the d_{z^2} orbital of the platinum and the π^* orbital of the pyridine. Emission spectra of the complex displayed weak structured blue emission bands with maximas at 460 nm, 490 nm and two shoulders at 520 nm and 560 nm. The photoluminescent quantum yield (PLQY) of the complex was measured below 1% by the integrating sphere coupled with a short excited state lifetime of 10 ns. All the photophysical properties of the complex are reported in Figure 3.6 and Table 3.3.

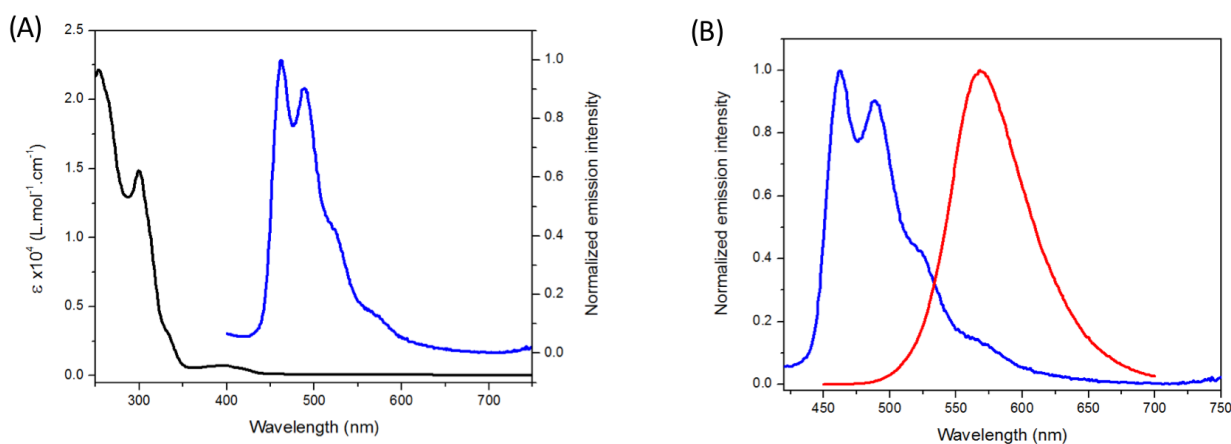


Figure 3.6. a) Absorption (black) and normalized emission (blue) spectra of the platinum(II) complex **20** in THF. b) Normalized emission spectra of the platinum complex in THF (blue) and water (red) showing the emission of the platinum(II) monomer (blue) and aggregates (red). $\lambda_{exc} = 300$ nm.

Table 3.3. Photophysical properties of the platinum(II) complex **20** in different mediums.

Medium	Conditions (T) [K]	air equilibrated			
		λ_{max} [nm]	$\lambda_{max,em}^{a),b)}$ [nm]	PLQY	$\langle \tau_{obs} \rangle$ [ns]
THF	298	300, 330, 400	462, 492, 520 (sh)	< 0.01	10
2-MeTHF	298	300, 340, 400	463, 493, 520 (sh)	< 0.01	5
2-MeTHF	77		451, 481, 514, 550		7420
solid	298		569	0,7	450

PMMA-PMAA/platinum(II) complex system

The emission and excitation spectra of the PMMA-PMAA/ platinum(II) complex mixture in water are displayed in Figure 3.7. The absorption spectra of those solutions were not considered to be applicable because of the scattering due to the turbidity of the solution. The spectras were all measured under the same conditions (excitation and emission wavelength and slit's width), for the comparison of the intensites of the signals. The excitation spectra were measured at an emission wavelength of 570 nm in order to monitor the presence of

platinum-platinum interaction through the $^1\text{MMLCT}$ bands between 400 and 500 nm. The complex **20** alone in water ($R=0$) showed a broad band centered at 572 nm attributed to $^3\text{MMLCT}$ transition which was a strong indication of the presence of platinum-platinum interaction through self-assembly in a bad solvent for the platinum(II) complex. The strong platinum-platinum interactions may also be observed in the excitation spectra by the presence of intense $^1\text{MMLCT}$ structured bands between 400 and 500 nm (see Figure 3.7, b). Surprisingly for $R=1$, a hypsochromic shift from 572 nm to 585 nm was observed. For $R=5$, $R=10$ and $R=20$; the $^3\text{MMLCT}$ bands were still observed in emission and excitation. For $R=50$, a decrease in intensity of $^3\text{MMLCT}$ bands coupled with an increase in intensity of $^3\text{LC/MLCT}$ was the result of the interaction between the platinum(II) complex and PMMA-PMAA diblock copolymer.

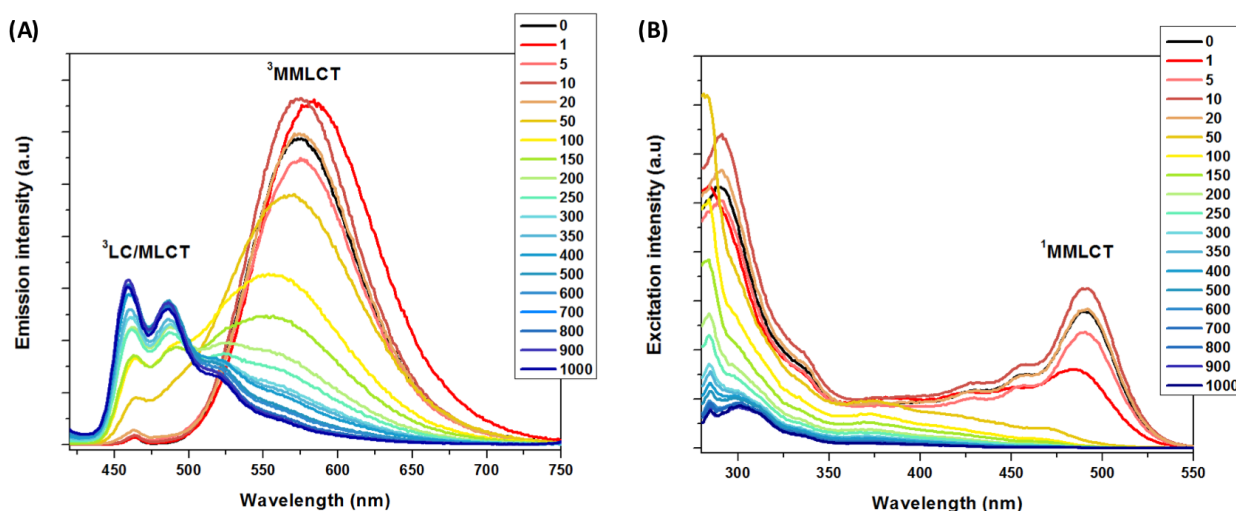


Figure 3.7. (a) Emission and (b) excitation spectra of PMMA-PMAA-Platinum(II) complex **20** system in water. The values on the right of the spectra referring to the PMMA-PMAA/platinum(II) complex ratio R . $\lambda_{exc} = 400 \text{ nm}$, $\lambda_{em} = 570 \text{ nm}$.

Interestingly, even though the emission still showed a broad band centered at approximately 570 nm, the excitation spectra did not show any intense $^1\text{MMLCT}$ bands between 400 nm and 500 nm anymore. As a preliminary conclusion, the addition of a sufficient amount of PMMA-PMAA to the platinum(II) complex in water resulted in a change of the nature of the platinum-platinum interaction. Such a behaviour was also observed when the ratio R was increased. For $50 < R < 300$ an hypsochromic effect was observed from 570 nm to 550 nm coupled with an increase in intensity from the peaks at 460 nm, 490 nm and 520 nm in the emission spectra.

The decrease of the $^1\text{MMLCT}$ bands in the excitation spectra also suggested a decrease of platinum-platinum interactions. Finally, at a higher ratio ($R > 300$), a slight increase in the intensity of the $^3\text{LC/MLCT}$ bands at 460 nm, 490 nm and 520 nm were observed while the broad band at 550 nm decreased in intensity. The emission spectra for $R = 1000$ was very similar to the emission of the platinum(II) complex monomer in THF where no platinum-platinum interactions were observed. The excitation spectra did not display any signals due to the weak intensity of the emission spectra at 570 nm. It may be concluded that a sufficient amount of PMMA-PMAA prevents any platinum-platinum interactions in aqueous solution. One hypothesis was that the platinum(II) complex was “diluted and embedded” into the PMMA-PMAA matrix of the particles. Excited state lifetimes of each solution were also measured and reported in Table 3.4. In order to measure the lifetimes from both $^3\text{LC/MLCT}$ and $^3\text{MMLCT}$ bands, the detection wavelength was set at 515 nm at the isobestic wavelength. The PMMA-PMAA/platinum(II) complex system in water has a multi-exponential decay because of the presence of various types of complex’s aggregates. The complex 20 in water alone ($R = 0$) has an average excited state lifetime of 410 ns and may be deconvoluted into three exponential decays. Surprisingly, for $R = 1$ and 5 when the emission was slightly red-shifted, the average lifetime of the system was decreased from 400 ns to 300 ns and maintained a tri-exponential decay. For $R = 10$ and 20, the average lifetime was 400 ns, similar to the platinum(II) complex aggregates in water. Interestingly, the excited state lifetime of the system for $R = 50$ was significantly increased to 1150 ns with the appearance of a long excited state lifetime of 6650 ns as part of the deconvoluted signal. Such an increase of the lifetime was correlated with the rise of the $^3\text{LC/}^3\text{MLCT}$ in emission. Upon increasing R from 50 to 500, the excited state lifetime was gradually increased from 1150 ns to 2550 ns. The system showed a tri-exponential decay which can be decomposed into three decays; one “short” lifetime around 450 ns, an “intermediate” lifetime around 1750 ns, and a “long” lifetime around 8500 ns. Those three signals could be observed in every lifetime measurement and the percentage of the longer lifetimes was gradually increased upon increasing R . Conversely, the percentages of the “short” and “intermediate” decay in the average lifetime was decreasing proportionally to the increase of the “long” lifetime upon increasing R .

Table 3.4. Photophysical properties of the PMMA-PMAA/platinum(II) **20** system in water. a) $\lambda_{exc} = 400$ nm, b) $\lambda_{exc} = 405$ nm, $\lambda_{em} = 515$ nm.

R	Solvent	Emission max ^{a)}	Lifetime ^{b)} (ns)	Average lifetime (ns)
0	Water	572	75 (12%), 310 (42%), 600 (46%)	410
1	Water	584	40 (17%), 250 (64%), 680 (18%)	300
5	Water	575	40 (17%), 240 (68%), 670 (14%)	280
10	Water	575	60 (15%), 290 (69%), 1030 (15%)	390
20	Water	463, 574	60 (19%), 300 (70%) 1290 (11%)	400
50	Water	463, 571	480 (37%), 1380 (61%), 6650 (2%)	1150
100	Water	463, 492, 554	450 (40%), 1460 (56%), 7730 (3%)	1260
150	Water	463, 492, 552	470 (41%), 1610 (55%), 8520 (4%)	1420
200	Water	462, 488, 524, 553(sh)	400 (42%), 1600 (52%), 8520 (7%)	1550
250	Water	461, 491, 524, 555 (sh)	460 (44%), 1720 (49%), 8840 (8%)	1720
300	Water	460, 490, 520 (sh)	350 (37%), 1580 (52%), 8300 (11%)	1900
350	Water	460, 490, 520 (sh)	460 (44%), 1870 (45%) 9150 (11%)	2065
400	Water	460, 490, 520 (sh)	400 (42%), 1820 (46%) 9020 (13%)	2150
500	Water	460, 490, 520 (sh)	405 (40%), 1940 (43%) 9160 (17%)	2550
600	Water	460, 490, 520 (sh)	1150 (74%), 7940 (26%)	2920
700	Water	460, 490, 520 (sh)	1180 (71%), 8200 (29%)	3250
800	Water	460, 490, 520 (sh)	1180 (70%), 8300 (30%)	3300
900	Water	460, 490, 520 (sh)	1110 (66%), 8150 (34%)	3520
1000	Water	460, 490, 520 (sh)	1100 (66%), 8070 (34%)	3500

For $R > 500$, the excited state lifetime was characterized by a relatively long bi-exponential decay with a lifetime range of 2550 ns to 3500 ns upon increasing R . Interestingly, the lifetime may be deconvoluted into a bi-exponential decay with two components being approximately $\tau_1 = 1150$ ns and $\tau_2 = 8150$ ns. Upon increasing R , the percentage of τ_2 in the excited state lifetime was increased while the percentage of τ_1 was decreased proportionally resulting in longer lifetime of the system. Those lifetime values are similar to the excited state lifetime of the platinum(II) complex in 2-MeTHF at 77K ($\tau = 7420$ ns, table 3.3). The excited state lifetime of complex **20** interacting with PMMA-PMAA in water may be compared to the excited state lifetime of the platinum(II) complex at 77K where most of the non-radiative relaxations are prevented by the rigidochromism effect. The emission and excitation spectra as well as the excited state lifetime and the photoluminescent quantum yield are strongly dependent on the environmental rigidity³². One hypothesis was that the platinum(II) complex was indeed encapsulated into the PMMA-PMAA particles, thus resulting in longer lifetimes and a blue-shifted emission. To comprehend the platinum(II) complex interactions with PMMA-PMAA in water for $R = 200$, the excited state lifetimes were measured at 4 different detection wavelengths as displayed in Figure 3.8.

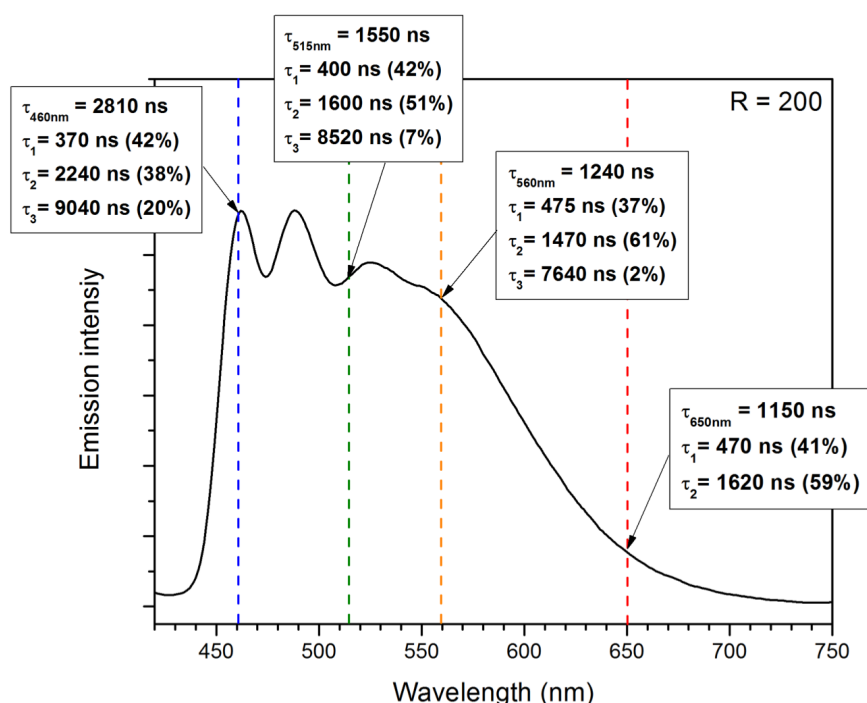


Figure 3.8. Emission spectra of the PMMA-PMAA/platinum(II) complex **20** system in water for $R = 200$ and excited state lifetimes measured at 460 nm, 515 nm, 560 nm and 650 nm. $\lambda_{exc} = 400$ nm (emission), $\lambda_{exc} = 405$ nm (lifetime).

The emission measured from the PMMA-PMAA/platinum(II) complex system in water for $R=200$ was interpreted as the combination of two signals; structured bands at 460 nm, 490 nm and 520 nm from the $^3LC/MLCT$ transition of blue emissive platinum(II) complex and a broad band centered at approximately 570 nm from the 3MMLCT of the green-yellow emissive platinum(II) complex aggregates. At 650 nm, only the yellow-orange emissive complex was emitting, the excited state lifetime had a bi-exponential decay $\tau_1 = 470$ ns (41%) and $\tau_2 = 1620$ ns (59%) with an average lifetime of 1150 ns. At 460nm, only the blue-emissive platinum(II) complex was emitting, the excited state lifetime had a tri-exponential decay; $\tau_1 = 370$ ns (42%), $\tau_2 = 2240$ ns (38%) and $\tau_3 = 9040$ ns (20%) with an average lifetime of 2810 ns. Two platinum(II) complex species were clearly identified by the excited state lifetime measurements. If the lifetime was measured at a wavelength when both species were emitting, e.g at 515 nm or 560 nm, it would appear to be the combination of the lifetime of the two platinum(II) species. The excited state lifetime at 515 nm was a tri-exponential decay; $\tau_1 = 370$ ns (42%), $\tau_2 = 1600$ ns (51%) and $\tau_3 = 8520$ ns (7%) with an average lifetime of 1550 ns. The excited state lifetime at 560 nm was also a tri-exponential decay; $\tau_1 = 475$ ns (42%), $\tau_2 = 1470$ ns (51%) and $\tau_3 = 7640$ ns (2%) with an average lifetime of 1240 ns. At 515 nm, the lifetime was longer than the lifetime measured at 560 nm and the percentage of the longer decay around 8000 ns was higher at 515 nm (7%) than at 560 nm (2%). It is also worth mentioning that the excited state measurement showed a very rapid decay at the beginning of the measurement between 0 and 200 ns as displayed in Figure 3.9. This was observed for all the measurements and was attributed to either the laser source or the presence of a species with a very short lifetime. The first hypothesis was chosen and the excited state lifetime decays were fitted without accounting for the rapid decay at the beginning. The excited state lifetimes reported in Table 4 were measured at 515 nm at the isobestic wavelength of the two species, in order to measure the excited state lifetimes of the two platinum(II) complex species simultaneously. This distribution may be controlled by the ratio R between the PMMA-PMAA and the platinum(II) complex. At a low R , the platinum(II) complex was mainly present as green emissive species but upon increasing the R , the green emissive species gradually turned into a blue emissive species. Between $R = 50$ and $R=500$, the two species were emitting in solution and their distribution could be tuned by varying R . For $R >500$, the platinum(II) complex was mainly emitting a blue colour.

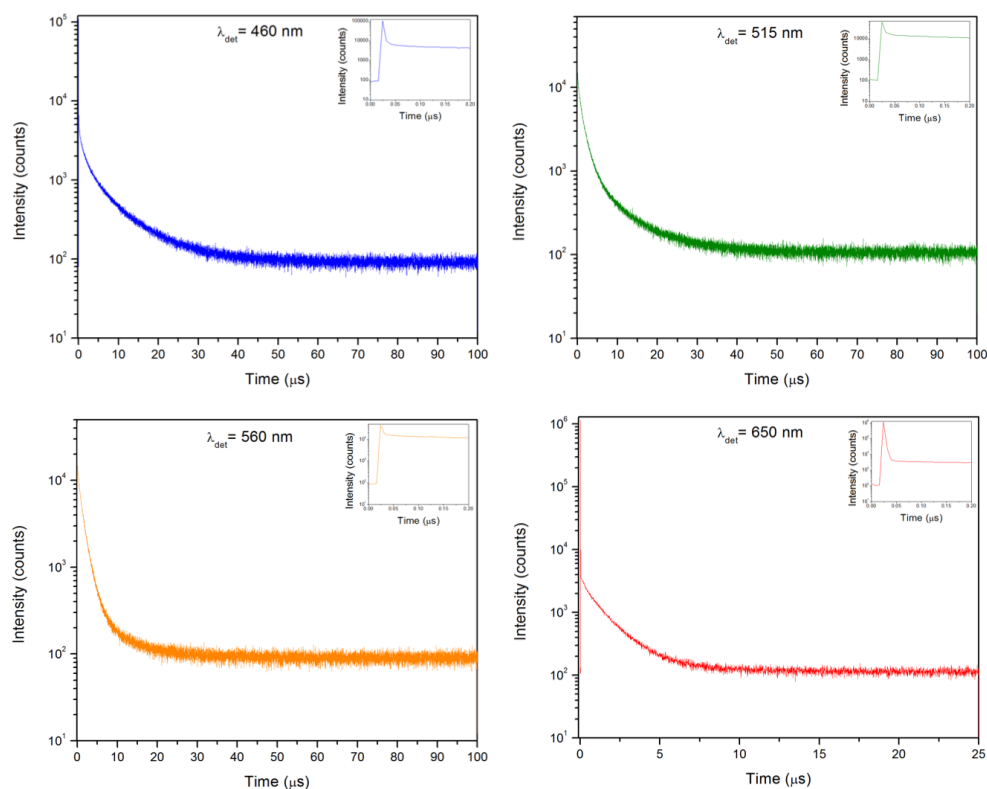


Figure 3.9. Excited state lifetime decay of the PMMA-PMAA/platinum(II) complex **20** system in water for $R = 200$ at 460 nm, 515 nm, 560 nm and 650 nm. $\lambda_{exc} = 405$ nm. Inset showed the decay between 0 and 200 ns.

3.2.3.2. Scanning electron microscopy (SEM)

SEM of the PMMA-PMMA/platinum(II) complex system in water was performed to observe the different steps of the encapsulation of the self-assembled complex. Selected SEM images of the system are displayed in Figure 3.10. At $R = 0$, few platinum fibers were observed alongside amorphous material. The concentration of the platinum(II) complex in each solution was relatively low ($5 \text{ ppm} = 7.3 \times 10^{-6} \text{ M}$) which explained the small amount of fibers observed. When PMMA-PMAA was added to the platinum(II) complex, a mixture of fibers and particles was observed for $R = 1, 5, 10, 20$. At $R = 50$, polydisperse PMMA-PMAA particles were observed however the platinum(II) fibers were not observed. Upon increasing R , the number and the size of the PMMA-PMMA particles theoretically increased. The formation of the PMMA-PMAA particles associated with the disappearance of the fibers suggests the encapsulation of the platinum(II) complex. In order to correlate the photophysical properties

of the system in solution to the morphology of the particles, the next step involved performing confocal imaging of the dried solution.

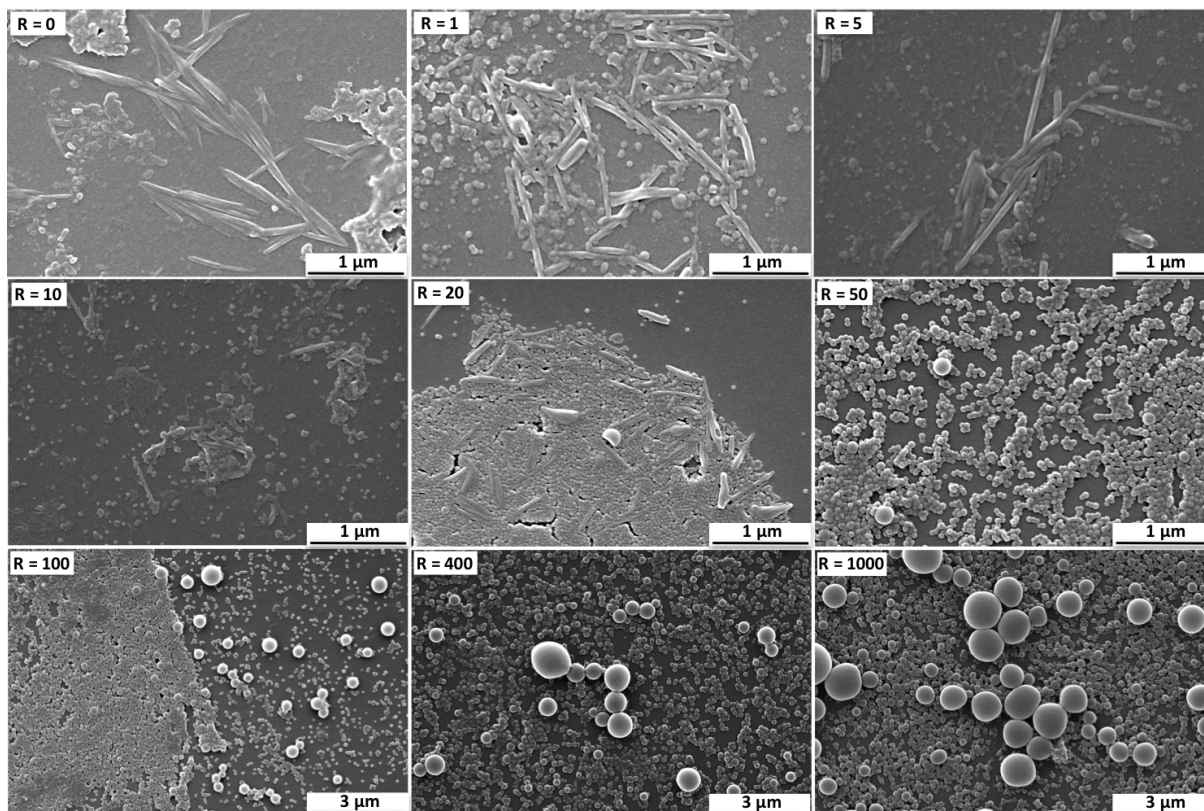
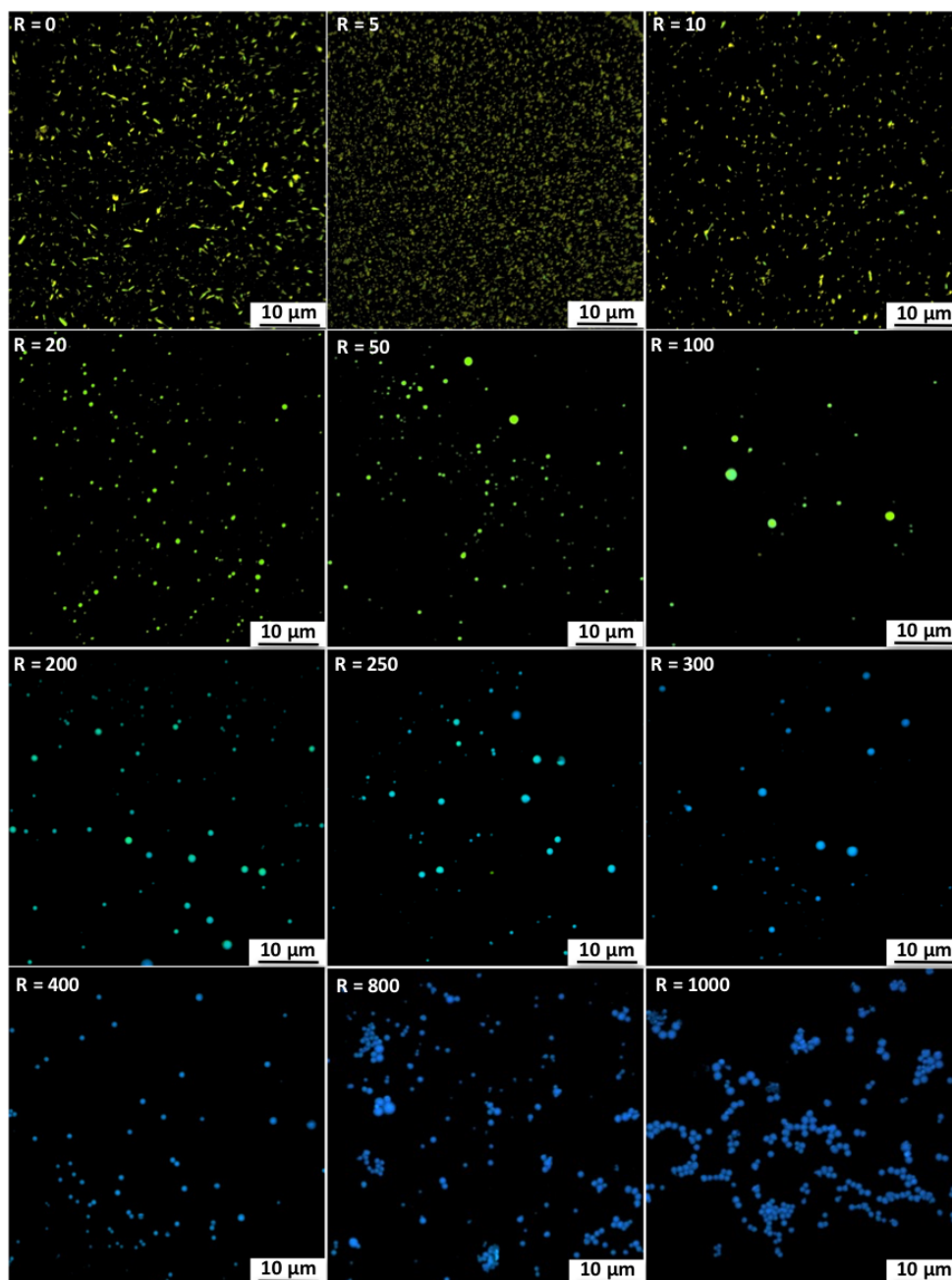


Figure 3.10. SEM images of the PMMA-PMAA/platinum(II) complex 20 system. The solutions were drop-casted on a glass slide and dried under standard conditions. The substrate was then sputtered with gold.

3.2.3.3. Confocal fluorescence microscopy

The resulting confocal fluorescence microscopy images displayed in Figure 3.11 provided an insight on the photophysical properties of the PMMA-PMAA/platinum(II) complex system. As mentioned previously, the low concentration of the platinum(II) complex in solution limited the number of larger platinum(II) fibers formed. Nevertheless, for $R = 0$, small yellow-green emissive fibers were observed. For $R = 5$ and 10, yellow emissive aggregates were observed; however, the specific morphology of the aggregates were unable to be confirmed. This also confirmed the small bathochromic effect for low ratios ($R < 10$), which resulted in a red shift which was observed in the emission spectra. At $R = 20$, green emissive particles were observed



*Figure 3.11. Confocal images of PMMA-PMAA/platinum(II) complex **20** system. The solutions were drop-casted onto a glass slide and dried under standard conditions before imaging. The real emission colors were obtained by using lambda-mode acquisition ($\lambda_{exc} = 405 \text{ nm}$).*

and small emissive aggregates were no longer detected. As a preliminary conclusion, when the PMMA-PMAA/ complex **20** ratio reaches a certain value, i.e $R = 20$ in this case, the platinum(II) complex encapsulates into the polymer particles. For $R = 50$ and 100 , green emissive particles were also observed in accordance with the emission measured in solution. Interestingly, from $R = 100$ to $R = 300$, the emission from the particles were gradually blue-

shifted from green emissive particles ($R = 100$) to blue emissive particles ($R = 300$). Remarkably, the luminescence observed from a single particle was a result of a mixture of green and blue emissive platinum(II) complex. The contribution of the green emissive species was decreasing whilst the contribution of the blue emissive species was increasing upon increasing R . Consequently, the confocal images showed particles emitting various shades between green and blue, e.g turquoise, cyan, azure, etc. For $R > 300$, the blue emissive species was dominant in the particles and resulted in a blue emission. It is also worth mentioning that the emission originating from a single particle was homogeneously distributed over the polymer particle and was not specifically located in the outer shell of the particles. Confocal images of PMMA-PMAA/ platinum (II) complex particles at $R = 50, 200$ and 1000 with their corresponding emission spectra recorded by the microscope are displayed in Figure 3.12.

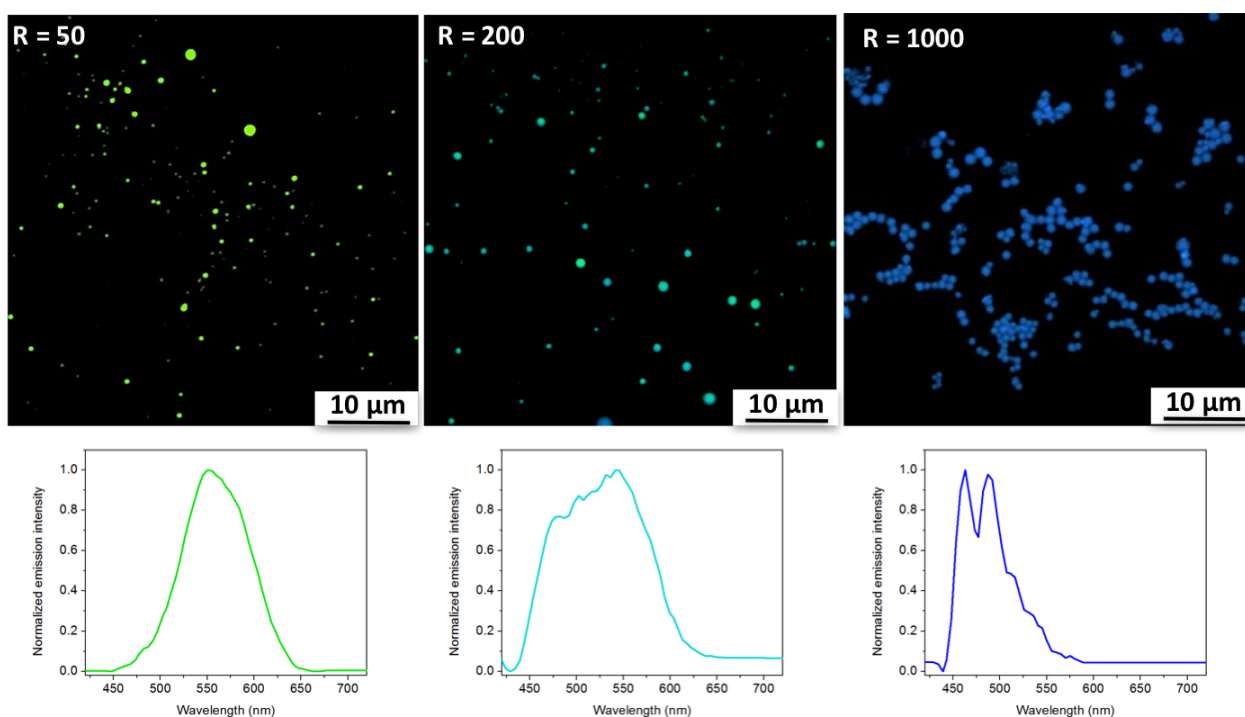


Figure 3.12. Confocal images of the PMMA-PMAA/platinum(II) complex **20** for $R = 50, 200$ and 1000 at their corresponding emission spectra. The real emission colors were obtained by using lambda-mode acquisition. ($\lambda_{exc} = 405 \text{ nm}$)

The encapsulation of complex **20** into the PMMA-PMAA particles was successful and displayed intriguing photophysical properties. The platinum fibers originally formed in the aqueous media was replaced by platinum(II)-loaded particles with tunable photophysical properties,

influenced by the PMMA-PMAA/ complex **20** ratio **R**. The platinum-loaded particles had a green coloured emission at the beginning of the encapsulation at a low **R** (**R** = 50) and blue emission at higher ratio (**R** > 300). Between those two values, the emission emanating from the particles was a mixture between the green and blue emissive coloured particles. It was concluded that the encapsulation of the platinum(II) complex by PMMA-PMAA resulted in the formation of two luminescent platinum(II) complex species; a blue emissive species with a long excited state lifetime (2810 ns) and a green emissive species with a shorter excited state lifetime (1150 ns). Those lifetime values are higher than the usual lifetimes observed for platinum(II) complex aggregates in solution (400 ns) which was believed to be caused by the rigidochromic effect inside the PMMA-PMAA particles. Remarkably, those two species co-existed inside a single particle with an emission influenced by the amount present of each species. However, the mechanism of encapsulation is not understood yet and would require the study of higher concentrations of platinum(II) complex in solution to observe the fate of the fibers in presence of PMMA-PMAA.

3.2.4. Influence of the concentration of platinum(II) complex

PMMA-PMAA and the desired platinum(II) complex were dissolved separately in THF. Then 2 mL THF solutions containing both the platinum(II) complex and PMMA-PMAA were prepared. The concentration of the platinum(II) complex was kept constant at 100 ppm and the concentration of PMMA-PMAA was gradually increased in each solution (refer to Table 3.5).

concentration Pt(II) complex [ppm]	100	100	100	100	100	100	100	100	100	100	100	100	100	100	100	100	100	100
concentration PMMA-PMAA [ppm]	0	100	500	1000	2000	5000	10000	15000	20000	25000	30000	40000	50000	60000	70000	80000	90000	100000
PMMA-PMAA/ Pt(II) complex (R)	0	1	5	10	20	50	100	150	200	250	300	400	500	600	700	800	900	1000

*Table 3.5. Concentration of platinum(II) complex **20** and PMMA-PMAA diblock copolymer in each solution and corresponding ratio **R**.*

Photographs of the solutions under normal light and UV lamp (365 nm) are displayed in Figure 3.13. At the lowest **R**, the solution was transparent and clear. Upon increasing the concentration of the PMMA-PMAA, the solutions became more turbid due to the formation

of larger particles and aggregates. At $R > 400$, the concentration in PMMA-PMAA was too high and caused the formation of large solid chunks of polymer in solution. Those chunks were luminescent and were removed from the solutions. Under the UV lamp, the solution at the lowest R had a bright yellow-orange emission which was emanating from the platinum(II) complex aggregates formed in water. At a higher R , the emission coming from the solution was blue-shifted upon increasing the ratio.

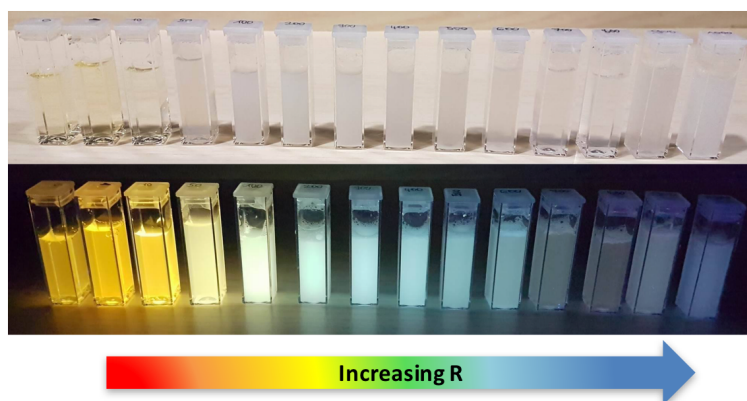


Figure 3.13. Photographs of the PMMA-PMAA/platinum(II) complex **20** solutions in water under normal light (top) and UV lamp (bottom) upon increasing R from left to right.

3.2.4.1. Photophysical properties

The solution of the removed PMMA-PMAA aggregates was not as emissive as the other solutions due to the loss of the platinum(II) complexes entrapped inside the solid particles. The emission and excitation spectra of the PMMA-PMAA/ platinum(II) complex mixture in water is displayed in Figure 3.14. The absorption spectra of those solutions were not significant because of the scattering due to the turbidity of the solutions. All the spectra were measured under the same conditions (excitation wavelength, emission wavelength and slit's width) in order for the intensity of each spectrum to be compared. The excitation spectra were measured at an emission wavelength of 570 nm in order to monitor the presence of the platinum-platinum interactions through $^1\text{MMLCT}$ bands between 400 and 500 nm. The platinum(II) complex alone in water ($R=0$) showed a broad band centered at 570 nm attributed to $^3\text{MMLCT}$ transition which was a strong indication of the presence of platinum-platinum interaction through self-assembly in an unsuitable solvent. The strong platinum-platinum interactions may also be observed in the excitation spectra by the presence of intense

$^1\text{MMLCT}$ structured bands between 400 and 500 nm. For $R=1$, a small hypsochromic shift from 570 nm to 575 nm was observed. For $R=5$ and $R=10$, the $^3\text{MMLCT}$ bands were still observed in emission and excitation. For $R=20$ and 50, a decrease in the intensity of $^3\text{MMLCT}$ band coupled with an increase of intensity of $^3\text{LC/MLCT}$ was the result of the interaction between the platinum(II) complex and PMMA-PMMA diblock copolymer.

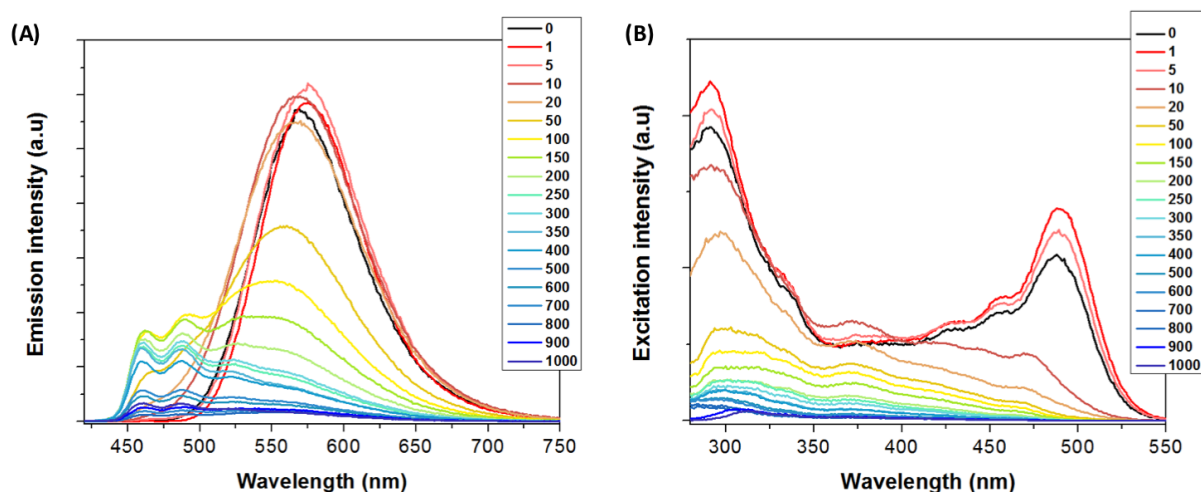


Figure 3.14. (A) Emission and (B) excitation spectra of PMMA-PMMA-Platinum(II) complex **20** system in water. The values on the right of the spectra were referring to the PMMA-PMAA/platinum(II) complex ratio R . $\lambda_{exc} = 400 \text{ nm}$, $\lambda_{em} = 570 \text{ nm}$.

Interestingly, even though the emission still showed a broad band centered at approximately 570 nm, the excitation spectra did not display any intense $^1\text{MMLCT}$ bands between 400 nm and 500 nm. The emission of the PMMA-PMAA/platinum(II) complex remained similar in value at 100 ppm or 5 ppm. For $50 < R < 300$, a hypsochromic effect was observed from 570 nm to 550 nm, coupled with an increase in intensity from the peaks at 460 nm, 490 nm and 520 nm in the emission spectra. The decrease of the $^1\text{MMLCT}$ bands in the excitation spectra also suggested the decrease of the platinum-platinum interactions. Finally, at a higher ratio ($R > 300$), the solution started to be saturated in PMMA-PMAA. As a result, if the emission of the solution were blue-shifted towards the $^3\text{LC/MLCT}$ bands, a decrease in emission would be observed due to the loss of material. The excited state lifetimes of each solution were also measured and reported in Table 3.6. In order to measure the lifetimes from both the $^3\text{LC/MLCT}$ and $^3\text{MMLCT}$ bands, the detection wavelength was set at 515 nm at the isobestic wavelength.

Table 3.6. Photophysical properties of the PMMA-PMAA/platinum(II) complex **20** system in water. a) $\lambda_{exc} = 400$ nm, b) $\lambda_{exc} = 405$ nm, $\lambda_{em} = 515$ nm.

R	PLQY	Emission max ^{a)}	Lifetime ^{b)} (ns)	Average lifetime (ns)
0	0.45	569	90 (29%), 260 (52%), 550 (19%)	270
1	0.46	575	160 (31%), 340 (68%), 1310 (1%)	290
5	0.50	575	95 (15%), 280 (68%), 910 (15%), 2000 (2%)	375
10	0.49	570	160 (15%), 570 (54%), 1180 (31%), 3770 (1%)	710
20	0.43	570	120 (15%), 650 (40%), 1180 (44%), 5150 (1%)	880
50	0.41	561	460 (39%), 1360 (59%), 6630 (2%)	1100
100	0.36	460, 490, 550	540 (45%), 1550 (51%), 8040 (3%)	1320
150	0.33	530	720 (55%), 1850 (40%), 8620 (5%)	1570
200	0.27	460, 490, 520, 553(sh)	600 (47%), 1810 (46%), 8830 (7%)	1700
300	0.26	460, 490, 520, 560 (sh)	200 (16%), 1020 (54%), 2760 (16%), 9270 (6%)	1550
350	0.23	460, 490, 520, 560 (sh)	140 (20%), 760 (44%), 2040 (28%), 8500 (8%)	1600
400	0.22	460, 490, 520, 560 (sh)	460 (45%), 1690 (46%), 8430 (8%)	1700
500	0.25	460, 490, 520, 560 (sh)	410 (43%), 1570 (49%), 8150 (18%)	1590
600	-	460, 490, 520, 560 (sh)	440 (42%), 1620 (50%), 8340 (8%)	1640
700	-	460, 490, 520 (sh), 548	400 (40%), 1420 (55%), 7750 (5%)	1340
800	-	460, 490, 520, 560 (sh)	430 (40%), 1370 (56%), 7460 (4%)	1220
900	-	460, 490, 520, 560 (sh)	480 (37%), 1470 (61%), 7660 (2%)	1240

The platinum(II) complex in water alone ($R=0$) had an average excited state lifetime of 270 ns and could be deconvoluted into three exponential decays. Immediately after the PMMA-PMAA was added to the platinum(II) complex ($R > 1$), a longer exponential component was observed which was attributed earlier to the signal from the encapsulated platinum(II) complexes. The average lifetime of the signal was longer upon increasing R . When the solution was saturated in polymer and the big aggregates were removed from the solution, the lifetime stabilized between 1200 ns and 1700 ns. The limit of encapsulation of platinum(II) complex was reached when the concentration of PMMA-PMAA was too high. Nevertheless, a benefit of using a higher concentration of the platinum(II) complex was the possibility to measure the photoluminescent quantum yield with the integrating sphere. The PLQY of the platinum(II) aggregates formed at $R = 0$ in water was 45%. This value was slightly increased from 45% to 50% at $R = 10$. Once the platinum(II) complex started to be encapsulated, a decrease in the PLQY was observed from 50% ($R = 10$) to 20-25% ($R = 500$). Beyond a ratio of 500, a significant amount of aggregates were lost during the removal of the large PMMA-PMAA aggregates and the intensity of the emission of the solution was no longer high enough to be measured. The PLQY of the blue emissive particles was measured between 20% and 25%. The emission of the platinum(II) complex monomer in THF and the encapsulated platinum(II) complex were quite similar, however the PLQY was significantly higher once the platinum(II) complex was encapsulated. One reason for this result, as mentioned previously, was that the rigid environment of the polymer core prevented most of the non radiative decay, significantly increasing the excited state lifetime and PLQY. The photoluminescent quantum yield of the green emissive particles was measured to be around 40%. Particles with the emission emanating from a mixture of both species ($20 < R < 300$) had a PLQY measurement between 20% and 40%.

In order to investigate the encapsulation of the platinum(II) complex into PMMA-PMAA particles, a more detailed study was carried out where R was between 0 and 175. The emission spectra of the study is displayed in Figure 3.15. Beginning with a pure $^3\text{MMLCT}$ transition band centered around 570 nm for $R < 10$, the rise of the $^3\text{LC/MLCT}$ was gradually observed upon increasing R from 10 to 150. The study also showed that the intensity of the $^3\text{LC/MLCT}$ emanating from the blue emissive platinum(II) complex could be tuned precisely by selecting the appropriate ratio between PMMA-PMAA and the platinum(II) complex. The small bathochromic effect from 570 nm to 550 nm was carefully studied and it was concluded that

the effect reflected the transition from the platinum(II) complex aggregates to the the green emissive platinum-loaded particles. At $R = 175$, the intensity of the $^3\text{LC/MLCT}$ bands was, for the first time, higher than the intensity of the $^3\text{MMLCT}$ bands.

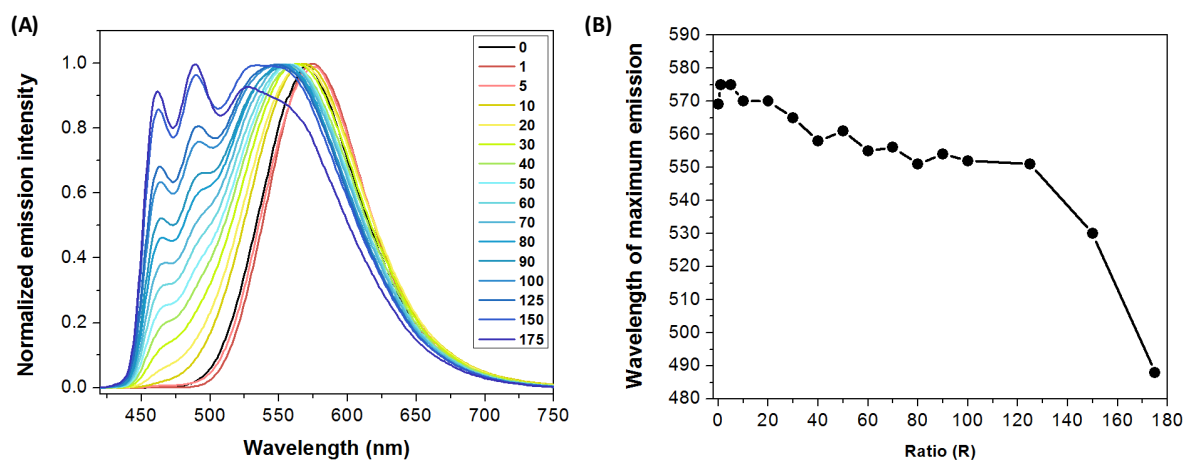


Figure 3.15. a) Normalized emission spectra of the PMMA-PMAA/platinum(II) complex 20 system in aqueous solution. b) plot of the values of the wavelength of maximum intensity versus R .

3.2.4.2. Electron microscopy (SEM AND STEM)

SEM imaging of the PMMA-PMAA/platinum(II) complexes in water was performed to visualize the interaction between the two compounds (see Figure 3.16). For $R = 0$, the platinum(II) complex was self-assembling into rigid fibers upon flash-injection in water. Similar morphology was already observed for the same platinum(II) complex in dichloromethane⁴. For $R = 2$, the rigid fibers were replaced by long and flexible fibers. Moreover, PMMA-PMAA particles were also observed alongside the fibers. The polymer had a significant effect on the morphology of the platinum(II) fibers which could justify the small photophysical changes observed prior to effective encapsulation. For $R = 5$ and $R = 10$, well-defined polymer particles and long, flexible platinum fibers were observed. Sometimes aggregation of PMMA-PMAA was observed around some platinum (II) fibers forming a bead-on-string morphology. They were distinguishable with a protruding PMMA-PMAA central part and thin ending platinum(II) fibers on each side. A SEM image of the bead-on-string morphology with the EDX spectra measurements at three areas of the aggregate is displayed in Figure 3.17. When the electron beam was focused on the core of the structure,

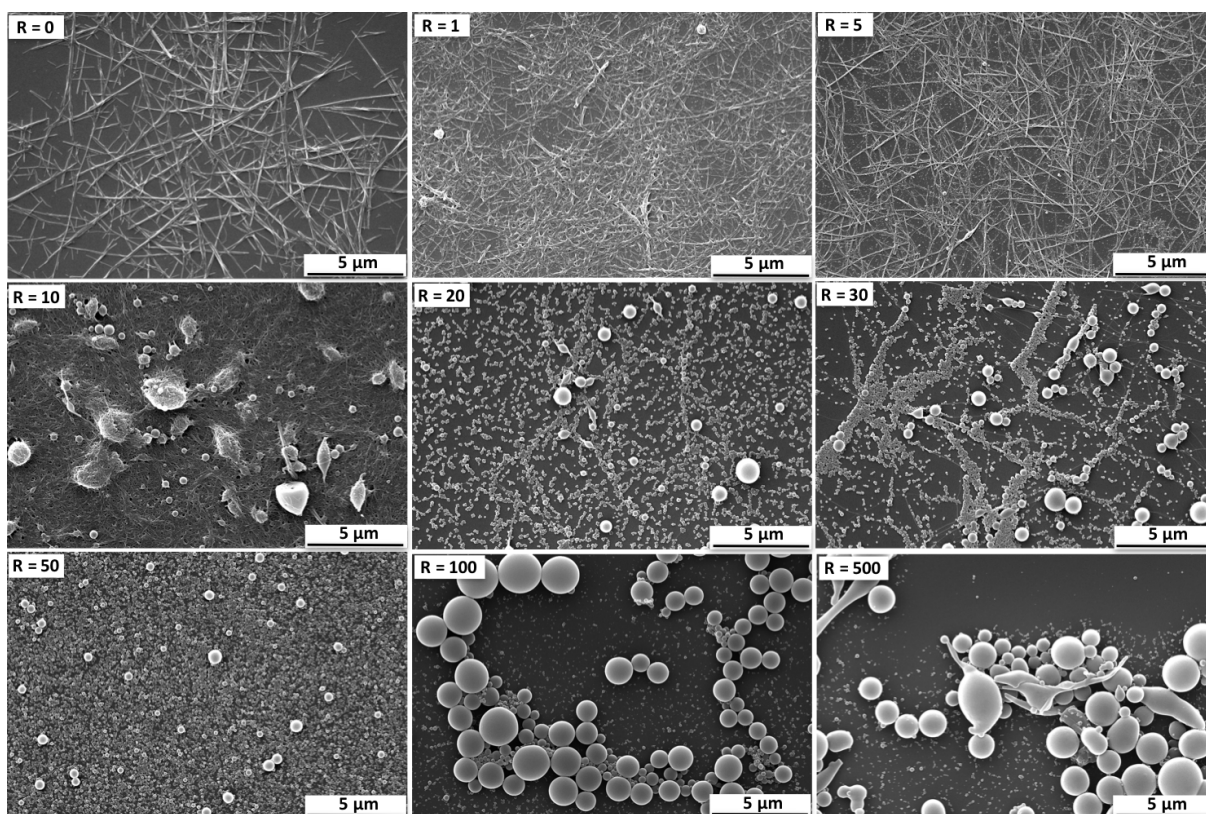


Figure 3.16. SEM images of the PMMA-PMAA/platinum(II) complex **20** system. The solutions were drop-casted on a glass slide and dried under standard conditions. The substrate was then sputtered with gold.

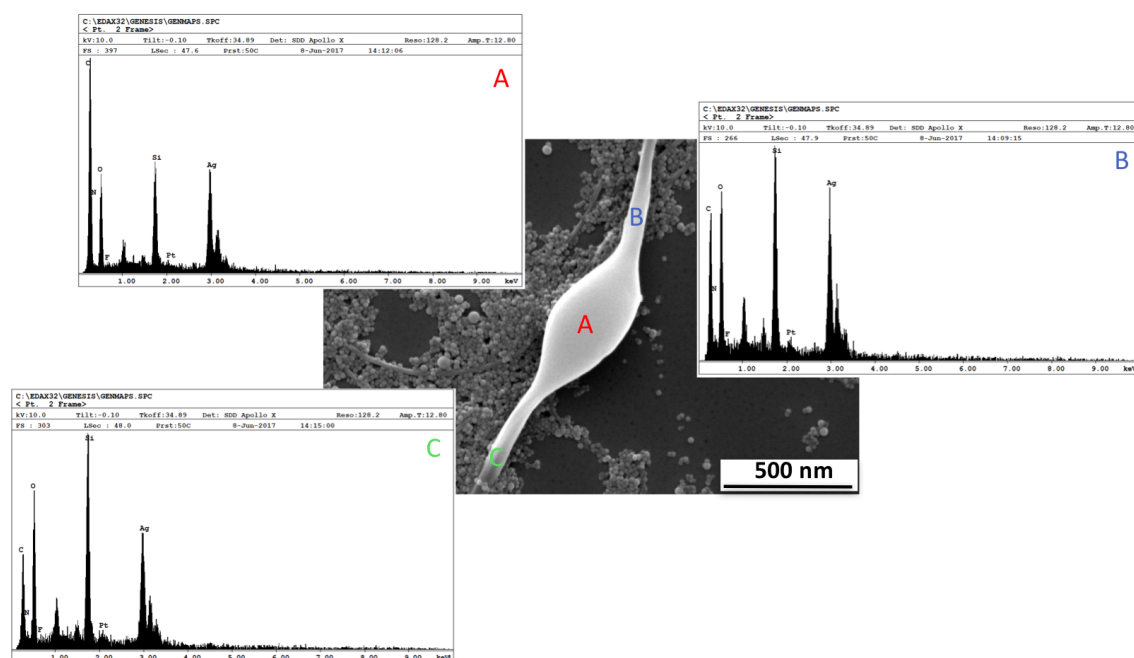


Figure 3.17. SEM image of a bead-on-string morphology of PMMA-PMAA/platinum(II) complex **20** aggregates for $R = 15$. EDX spectra at three areas of the morphology: the core (A), the narrowing (B) and the end (C).

the platinum signal (2.10 eV) was barely detected (A). The PMMA-PMAA particle was too thick for the platinum inside to be detected. At the limit between the core and the extremities (B), the fiber was recovered by a thin layer of PMMA-PMAA, evidenced by the platinum peak detected on the EDX spectra. Finally, when the electron beam was focused at the ending of the fibers' structure (C), the platinum peak was clearly present around 2.10 eV.

The bead-on string morphology was observed at $R = 20$, despite the number of fibers decreasing. Long platinum fibers surrounded by PMMA-PMAA particles of various diameters were also observed. At $R = 50$, only polydisperse PMMA-PMAA particles were observed meaning that most of the platinum(II) complex was encapsulated into the polymer particles. At $R = 100$, highly polydisperse polymer particles were observed. At a higher ratio, e.g $R = 500$, after removal of the large aggregates from the solution, were polydisperse particles of various shapes and sizes. When the solution was saturated in PMMA-PMMA, the control of the size and shape of the particles was not possible. In order to observe the PMMA-PMAA/platinum(II) system, scanning transmission electron microscopy (STEM) was also performed. The STEM images of each solution are displayed Figure 3.18.

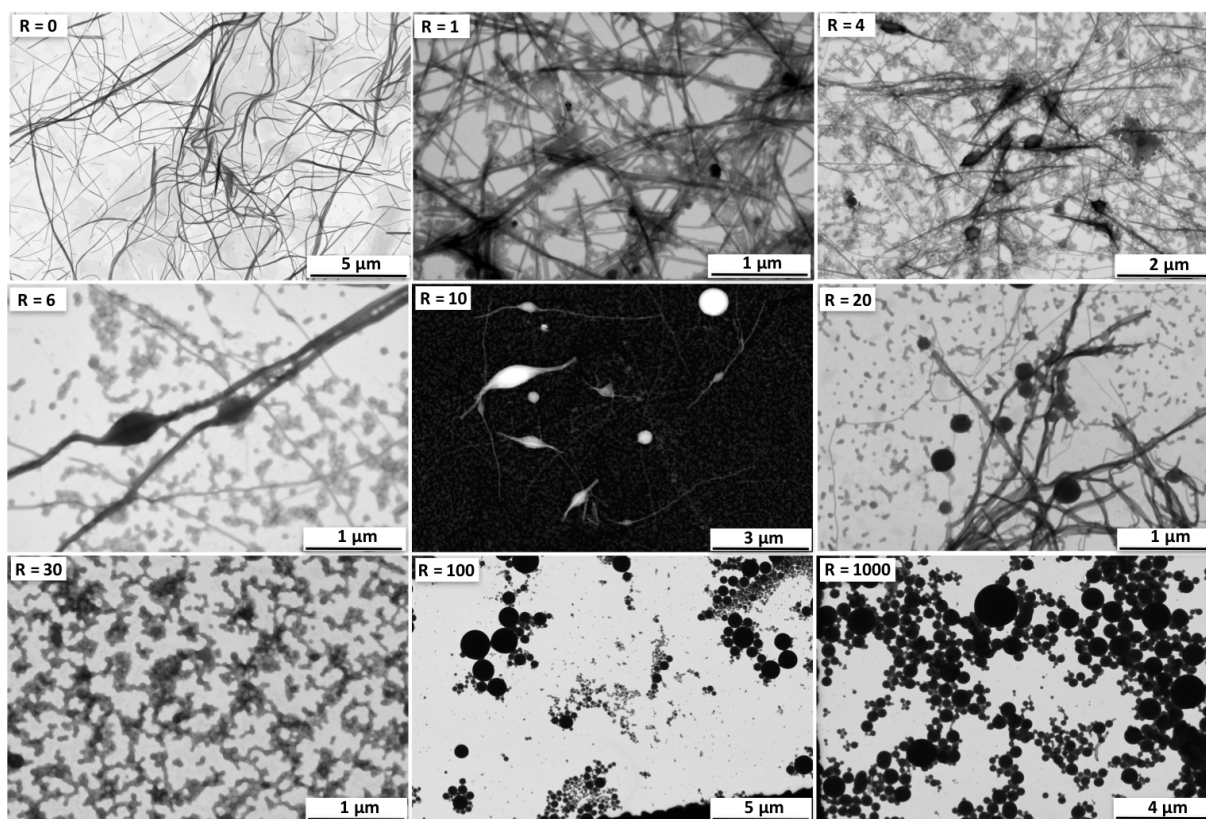


Figure 3.18. STEM images of the PMMA-PMAA/platinum(II) complex 20 system. The solutions were drop-casted on a copper grid and dried at normal condition.

The platinum fibers were easily distinguishable by STEM in bright field at $R = 0$. When PMMA-PMMA was mixed with the platinum(II) complex, fibers surrounded by polymer particles were observed. The bead-on-string morphology viewed by SEM was also observed by STEM. Due to the difference in electron density between PMMA-PMMA and the platinum, a difference in contrast was distinguished between the polymer core and the fibers ($R = 6$). Switching to a High-Angle Annular Dark-Field (HAADF) detector may increase the contrast between PMMA-PMMA and platinum. In a HAADF-STEM image, components with heavy elements for example, platinum, appear to be brighter compared to the dark carbon matrix background. At $R = 10$, the platinum fibers appeared brighter than the polymer particle and the internal structure of the bead-on string morphology was observed. It can be concluded that the fibers were passing through the particles while retaining its' morphological integrity. Finally, at a higher ratio R , platinum-loaded particles were mainly observed. It was worth noting that once the platinum(II) complex was encapsulated into the polymer particles, there was no signal on the EDS spectra or contrast in the STEM image that could confirm the presence of the platinum(II) complexes inside the particles. Nevertheless, the confocal images displayed previously showed that the luminescence of the solution was emanating from either the platinum(II) fibers or the platinum(II)-loaded particles with tunable emission. Different methods were then explored to verify the presence of the platinum inside the PMMA-PMMA particles.

3.2.4.3. Transmission electron microscopy (TEM)

TEM images of the PMMA-PMMA/platinum(II) complex system for $R = 40$ are displayed in Figure 3.19. Although the electron beam of the TEM is known to be considerably stronger than that of the STEM, no contrast could be observed inside the particles. One reason for this may be that the thickness of the inner part of the particle was too wide to view any contrast inside. Another reason may be that the size of the platinum(II) complex once encapsulated was too small to be detectable.

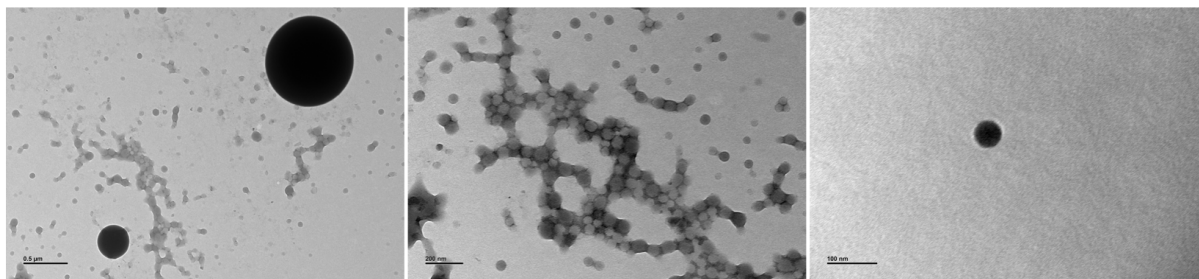


Figure 3.19. TEM images of the PMMA-PMAA/platinum(II) complex **20** for $R = 40$. The solution was drop-casted onto a copper grid and dried in the over for 30 min.

3.2.4.4. Focused-Ion Beam (FIB)

The difference between the FIB and the SEM is that the former utilises an ion beam while the latter utilises an electron beam. The use of an ion beam provides images of a higher quality due to the faster acceleration of the ions and allows etching on the surface or on nanostructures when the energy of the ions source is high enough. Some of the PMMA-PMMA particles were sufficiently large and thus the ion beam could only etch half of the structures. FIB images of the PMMA-PMMA/platinum(II) complex before and after etching are displayed in Figure 3.20. The solution was drop-casted on a glass slide and dried under standard conditions. The substrate was then sputtered with gold. Large particles were located for $R = 100$ on the surface of the substrate (top). The wrinkles observed on the surface of the particles were due to the gold sputtered on the surface. After the etching of half of the particles by the ion beam, the inside of the particles could be observed. The particles were not hollow and were filled with an amorphous material. Any specific features were observed inside the particles and any traces of platinum(II) complex was also observed. To determine the presence of the platinum(II) fibers in the polymer particles, a bead-on-string aggregates was etched to study the middle section inside the particle. However, no specific features were observed inside the particle. It was concluded that the ion beam was too powerful and melted the particle. The images at the bottom of Figure 3.20 display PMMA-PMMA aggregates wrapped within long and flexible platinum fibers. After the ion beam etching, neither the interior morphology of the particle nor the platinum fibers could be observed. The ion beam was too powerful to maintain the morphology of structures. It is also worth noting that not only the particles and fibers were destroyed but also the

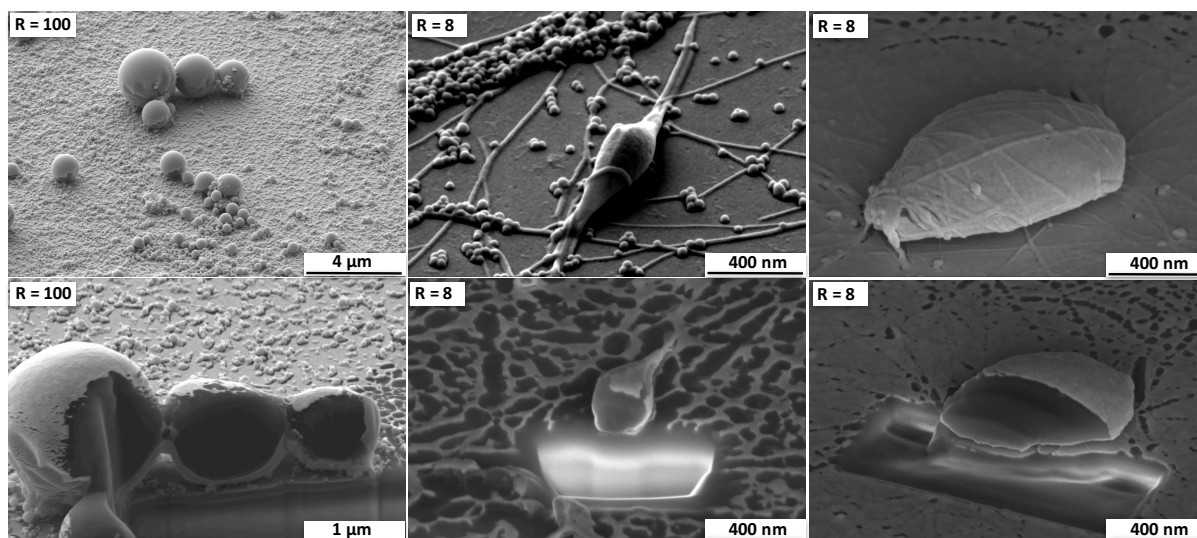


Figure 3.20. FIB images of the PMMA-PMAA/platinum(II) complex **20** system before (right) and after (left) etching by the ion beam.

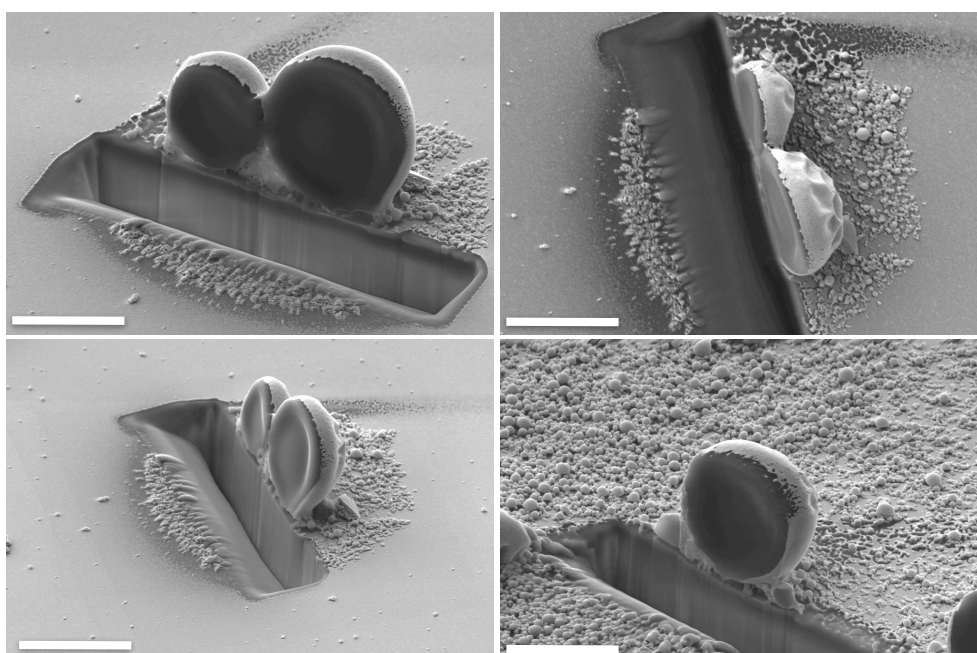


Figure 3.21. FIB images PMMA-PMAA/platinum(II) complex **20** system ($R = 50$) after etching by the ion beam. Scale bar: $3 \mu\text{m}$.

gold sputtered on the surface of the substrate. Decreasing the power of the ion beam would prevent the etching of the particles. FIB images of PMMA-PMAA particles etched by the ion beam are displayed in Figure 3.21. The different image perspectives show that the particles maintained their morphology even though they were exposed to a powerful beam. Moreover, the inside of the particles were confirmed amorphous and the core was curved, suggesting

there was leakage after exposure to the ion beam. FIB provided more resolved images of the PMMA-PMMA/platinum(II) complex system at a different ratio **R** but the main objective was not obtained: the detection of the platinum(II) complex inside the particles.

3.2.4.5. High resolution HAADF-STEM

To locate and highlight the presence of the platinum(II) complex inside the PMMA-PMAA particles, high-angle annular dark-field scanning transmission electron microscopy (HAADF-STEM) was performed (refer to Figure 3.22). In a HAADF-STEM image, components with heavy elements appear bright against the dark carbon matrix background. The images show single and dual particles with diameters between 50 nm and 100 nm. Larger particles were not observed, as the solution was drop-casted on the grid for 5 min before being blown away with a nitrogen flow and absorbed on a tissue. This method limited the presence of impurities on the sample but also removed the larger particles, which did not stick to the surface. Strong evidence of the presence of platinum inside the particles was shown in the EDX spectra. When the measurement was performed on an empty spot of the grid, no platinum signal was observed whereas when the measurement was performed on the particle containing white dots, a relatively low but significant platinum peak was detected. The signal could not have been increased because a longer exposure to the electron beam would affect the morphology of particles and destroy them. For **R** = 30, the emission spectra mainly displayed a broad band centered at approximately 560 nm which was attributed to ³MMCLT transition due to platinum-platinum interactions. Such interactions were observed in platinum(II) complex fibers of micrometer size. It was interesting to observe that the emission was emanating from small dots inside the PMMA-PMAA particles and not from larger aggregates. Furthermore, this raises the question of how many platinum(II) complexes were required to obtain the emission emanating from platinum-platinum interaction. Although the amount of PMMA-PMMA and platinum(II) complex in the solution was known, it was impossible to determine the concentration of platinum(II) complex per particles. Nevertheless, the detection of the platinum peak in the polymer particles confirmed that the emission was emanating from the platinum(II) complex.

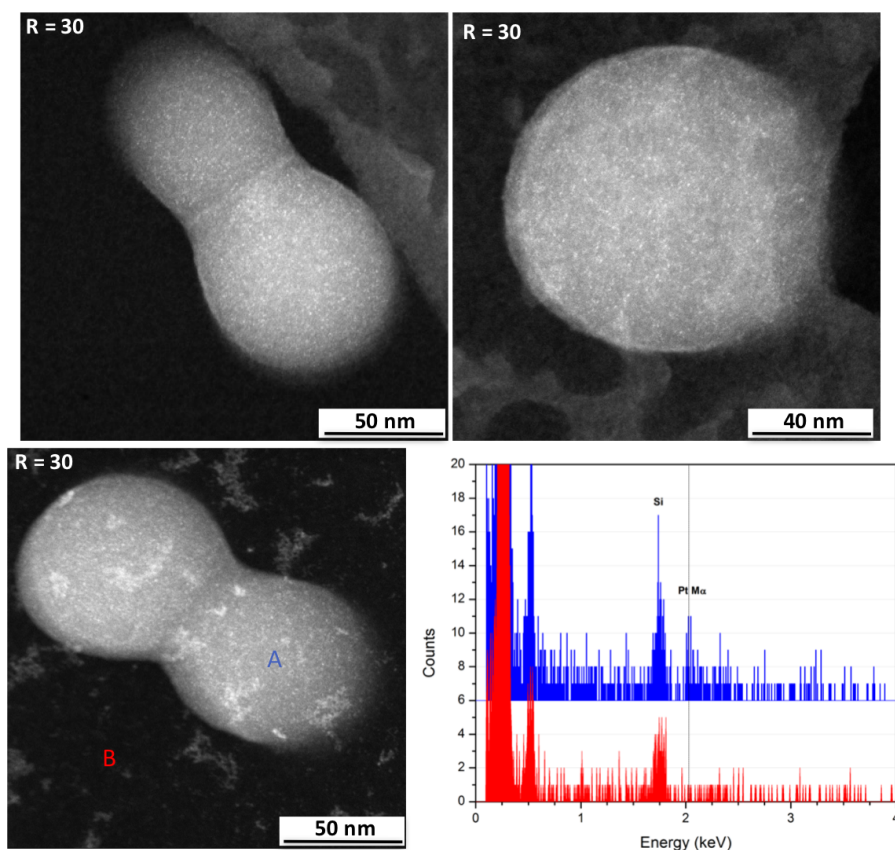
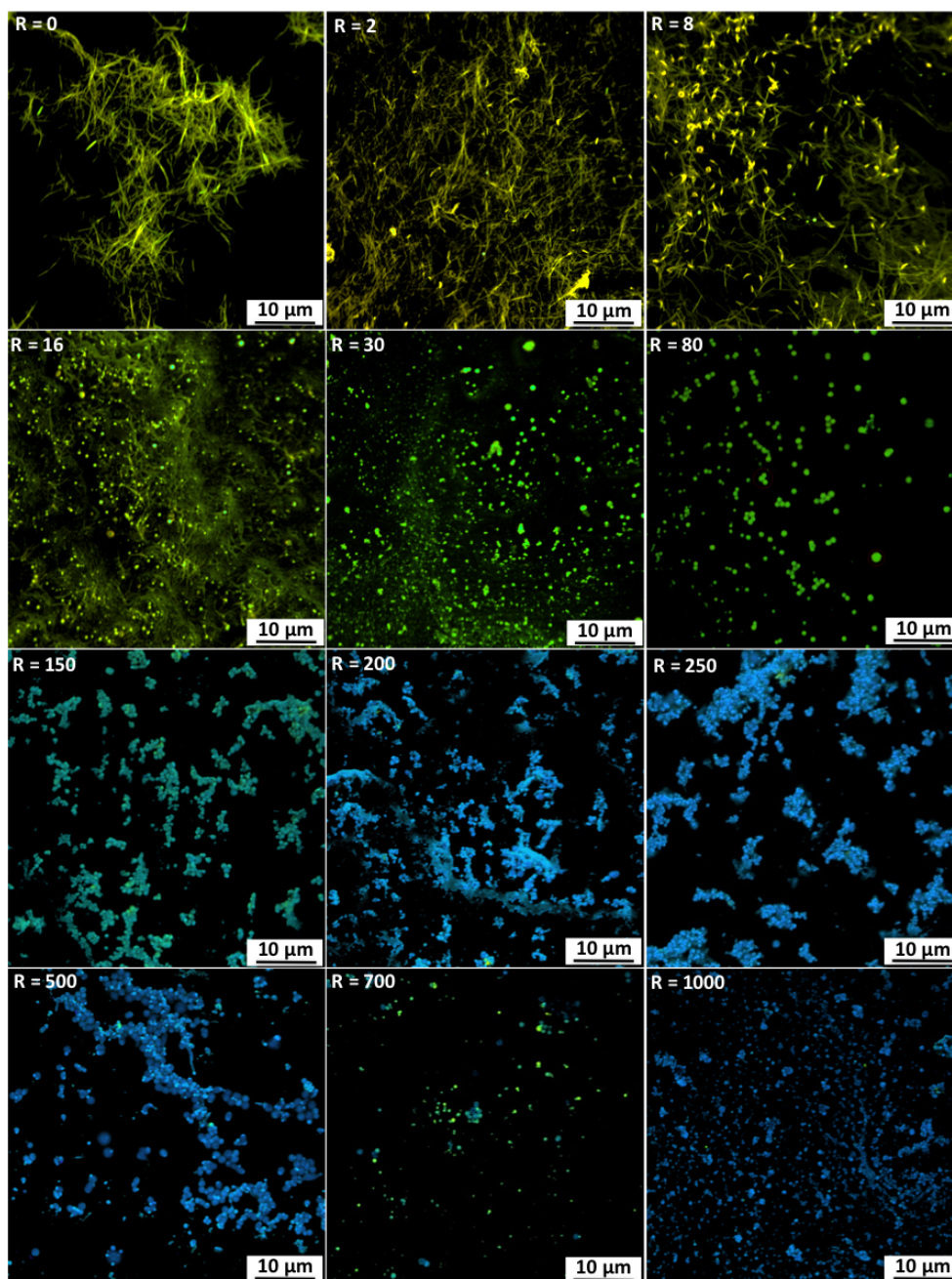


Figure 3.22. HAADF-STEM images of platinum(II) complex **20**-loaded PMMA-PMAA particles for $R = 30$, and energy dispersive X-ray spectra of one of the aggregates containing the white dots (A) and an empty spot (B). The signal of the platinum was highlighted around 2.0 keV.

3.2.4.6. Fluorescence confocal microscopy

The fluorescence confocal images of PMMA-PMAA/platinum(II) complex system are displayed in Figure 3.23. The platinum(II) complex alone ($R = 0$) self-assembled into green-yellow emissive fibers. When R was low, e.g. $R = 2$, long and flexible yellow emissive fibers were observed in accordance with the emission measured in solution. For $R = 8$, the bead-on-string morphology was observed with a bright yellow emissive center part and less emissive yellow-green fibers at the extremities. For $R = 16$, yellow-green emissive platinum-loaded particles and fibers were observed. For $R = 30$, the encapsulation was almost complete and green emissive particles were mainly observed with some green emissive fibers. For $R = 80$, well-defined green emissive particles were observed.



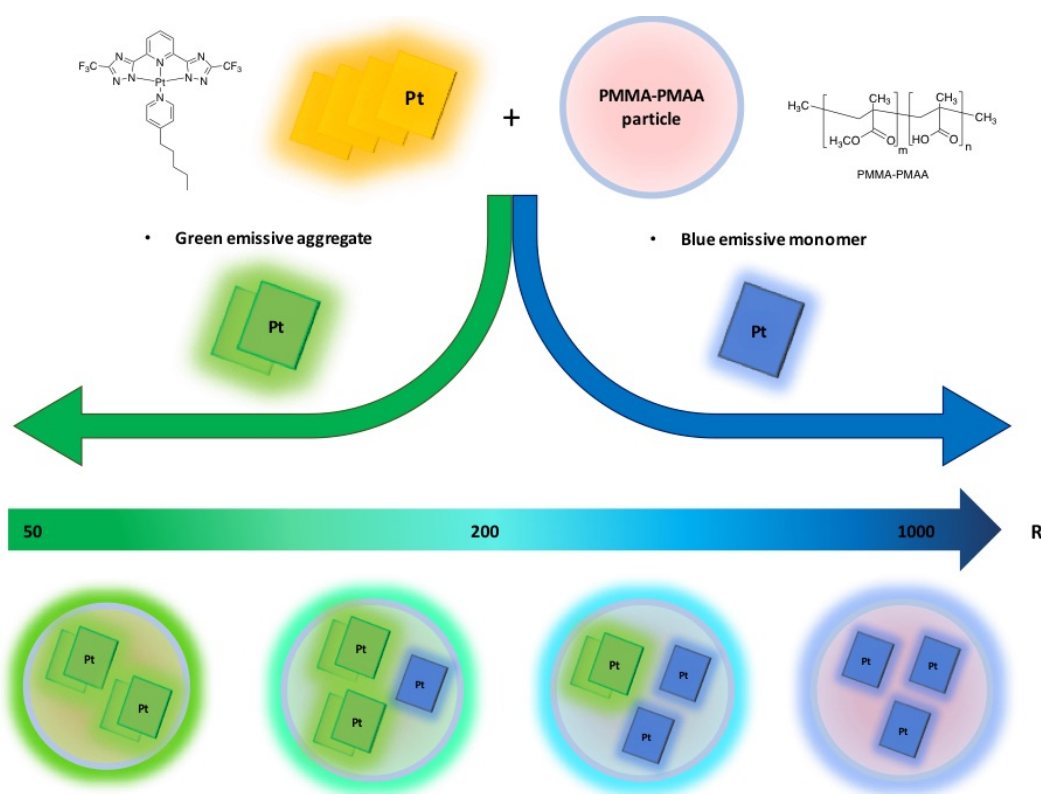
*Figure 3.23. Confocal images PMMA-PMAA/platinum(II) complex **20** system. The solutions were drop-casted on a glass slide and dried under standard conditions before imaging. The real emission color was obtained by using lambda-mode option ($\lambda_{exc} = 405\text{nm}$).*

The blue-shift measured in emission was also from the particles. From $R = 80$ to 250, the particles were gradually emitting from green to blue. However, the concentration of PMMA-PMAA in solution was very close to the saturation point and thus well-defined particles were no longer observed. The loss of control on the morphology of the particles was coupled with the loss of control of the photophysical properties. For $R = 700$, the platinum-loaded particles

was expected to have a blue emission. Instead, each particle was emitting different colors with a color range between green and blue. The confocal fluorescence images showed the different steps of the encapsulation of the platinum(II) complex from the yellow-green emissive fibers, passing through the yellow emissive bead-on-string aggregates, the green emissive particles and then the blue-emissive particles.

3.2.4.7. Intermediate conclusion

The encapsulation of a platinum(II) complex by PMMA-PMAA particles was successfully achieved by mixing the two compounds in an organic solvent prior to flash-injection to water. The platinum(II)-loaded particles showed emission ranging from green to blue with relatively long lifetimes and a high quantum yield. The photophysical properties of the hybrid particles were easily tuned by changing the PMMA-PMAA/platinum(II) ratio (**R**). The encapsulation mechanism was summed up in scheme 3.2.



*Scheme 3.2. Schematic representation of the encapsulation of platinum(II) complex into PMMA-PMAA particles and resulting photophysical properties depending on the PMMA-PMAA/platinum(II) complex **20** system ratio (**R**). The red area of the PMMA-PMAA particle represents the hydrophobic core and the blue area the hydrophilic shell.*

To date, this is the first known report on the encapsulation of platinum(II) complex with tunable photophysical properties. In order to study the versatility of the method, modifications of some parameters were required. In the following sections; solvents, order of PMMA-PMAA/platinum(II) complex mixing, speed of THF/water mixing, and the method of the removal of the organic solvent will be studied.

3.2.5. Effect of the organic solvent: acetone vs THF

The platinum(II) complex and PMMA-PMAA diblock were soluble in THF (which is soluble in water). When the water content was adjusted to 80% in a THF/water mixture, the platinum(II) complex self-assembled into fibers while PMMA-PMMA was forming particles. One advantage of using THF was that the swollen particles were formed in aqueous media and thus were easily observed under the confocal microscope. One disadvantage of using large particles was that they could not be used for in vitro study, where monodisperse and smaller particles are preferably used. The choice of solvent was crucial to determine the size of the particles. As mentioned previously, the closer the solubility parameters of the polymer and the solvent are, the larger the particles will be. One strategy to decrease the size of the particles was to replace THF with acetone. The images of the particles are displayed in Figure 3.3. The size of the particles was successfully reduced. For this reason, the same procedure above was employed except the THF was replaced with the acetone. Platinum(II) complex and PMMA-PMAA diblock copolymer were both soluble in acetone which was miscible with water. Photographs of the solutions under normal light and UV lamp are displayed in Figure 3.24. The same trend was observed whether acetone or THF was used. For the low **R**s, yellow-orange emissive solutions were observed and the luminescence was gradually blue-shifted upon increasing **R**. The main difference between the two studies was that the solutions were less turbid when the concentration in PMMA-PMMA was increasing in acetone. One reason for this may be that the size of the particles was smaller and fewer aggregates were formed. The luminescent properties of the solution were confirmed by the emission and excitation spectra displayed in Figure 3.25. For **R** = 0, a broad band centered at approximately 570 nm was characteristic of platinum-platinum interactions observed in emission. Upon increasing the **R**, a small red-shift

in emission was observed until $R = 10$. The blue-shift and decrease in the intensity of the broad band of the $^3\text{MMLCT}$ coupled with an increase of the $^3\text{LC/MLCT}$ bands were observed, which marked the beginning of the encapsulation of the platinum(II) complex. The emission spectra were stabilized for $R > 500$ meaning that most of the platinum(II) complex was encapsulated and emitted blue inside the PMMA-PMAA particles. The excitation spectra showed structured bands between 400 and 500 nm, attributed to $^1\text{MMLCT}$ transition. These bands were decreasing in intensity upon increasing R .

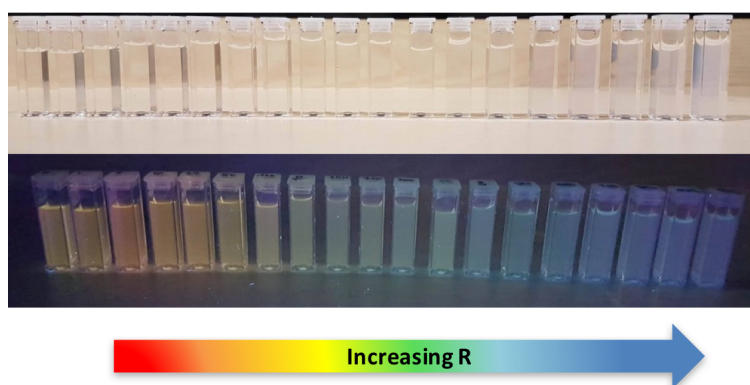


Figure 3.24. Photographs of the PMMA-PMAA/platinum(II) complex **20** solutions in water under normal light (top) and UV lamp (bottom) upon increasing R from left to right.

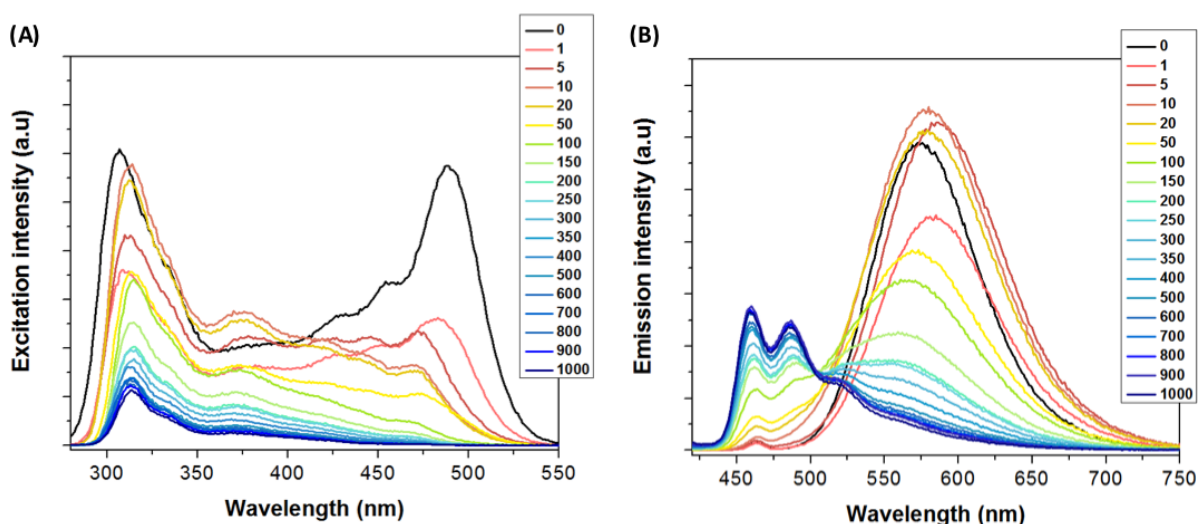


Figure 3.25. (A) Emission and (B) excitation spectra of PMMA-PMMA/platinum(II) complex **20** system in water. The values on the right of the spectra refer to the PMMA-PMAA/platinum(II) complex ratio R . $\lambda_{exc} = 400 \text{ nm}$, $\lambda_{em} = 570 \text{ nm}$.

Table 3.7. Photophysical properties of the PMMA-PMAA/platinum(II) complex **20** system in water. a) $\lambda_{exc} = 400$ nm, b) $\lambda_{exc} = 405$ nm, $\lambda_{em} = 515$ nm.

R	Solvent	Emission max^{a)}	Lifetime^{b)} (ns)	Average lifetime (ns)
0	Water	573	275 (27%), 580 (73%)	500
1	Water	585	190 (22%), 500 (78%), 1730 (0.5%)	440
5	Water	585	150 (29%), 480 (70%), 2390 (1%)	400
10	Water	580	115 (26%), 455 (64%), 1180 (10%), 6110 (0.3%)	450
20	Water	579	280 (54%), 1080 (37%) 5430 (9%)	670
50	Water	460, 573	420 (75%), 1250 (23%), 7630 (1%)	670
100	Water	460, 490, 561	470 (43%), 1450 (54%), 8670 (3%)	1210
150	Water	460, 490, 559	460 (42%), 1540 (54%), 9200 (4%)	1415
200	Water	460, 490, 520, 557	470 (43%), 1650 (51%), 9690 (6%)	1600
250	Water	460, 490, 520, 553	460 (43%), 1690 (52%), 9750 (6%)	1650
300	Water	460, 490, 520 (sh)	440 (43%), 1730 (49%), 9830 (8%)	1800
350	Water	460, 490, 520 (sh)	500 (42%), 1800 (51%) 9920 (7%)	1840
400	Water	460, 490, 520 (sh)	460 (43%), 1890 (47%) 10100 (11%)	2150
500	Water	460, 490, 520 (sh)	450 (42%), 1990 (45%) 10330 (13%)	2410
600	Water	460, 490, 520 (sh)	470 (44%), 2150 (42%), 10500 (14%)	2590
700	Water	460, 490, 520 (sh)	410 (40%), 2030 (43%), 10220 (17%)	2740
800	Water	460, 490, 520 (sh)	390 (40%), 2070 (42%), 10230 (17%)	2820
900	Water	460, 490, 520 (sh)	390 (40%), 2090 (42%), 10240 (18%)	2870

1000 Water 460, 490, 520 (sh) 1240 (71%), 8890 (29%) 3480

The emission and excitation spectra of PMMA-PMAA/platinum(II) complex in acetone were similar to those in THF. The solvent appeared to have no effect on the encapsulation of the platinum(II) complex. In addition, the excited state lifetimes of the solutions were also reported in Table 3.7. Similar measurements were observed in THF, with slightly shorter lifetimes when the emission was red-shift for $R < 10$ and gradual increase for $10 < R < 1000$. The excited state lifetime showed a multi-exponential decay when more than one platinum species (platinum aggregates or encapsulated platinum(II) complex) was present in solution and a bi-exponential decay when the blue emissive platinum(II) complex inside the particles was dominant for $R = 1000$.

SEM images of the solutions drop-casted on a glass substrate are displayed in Figure 3.26.

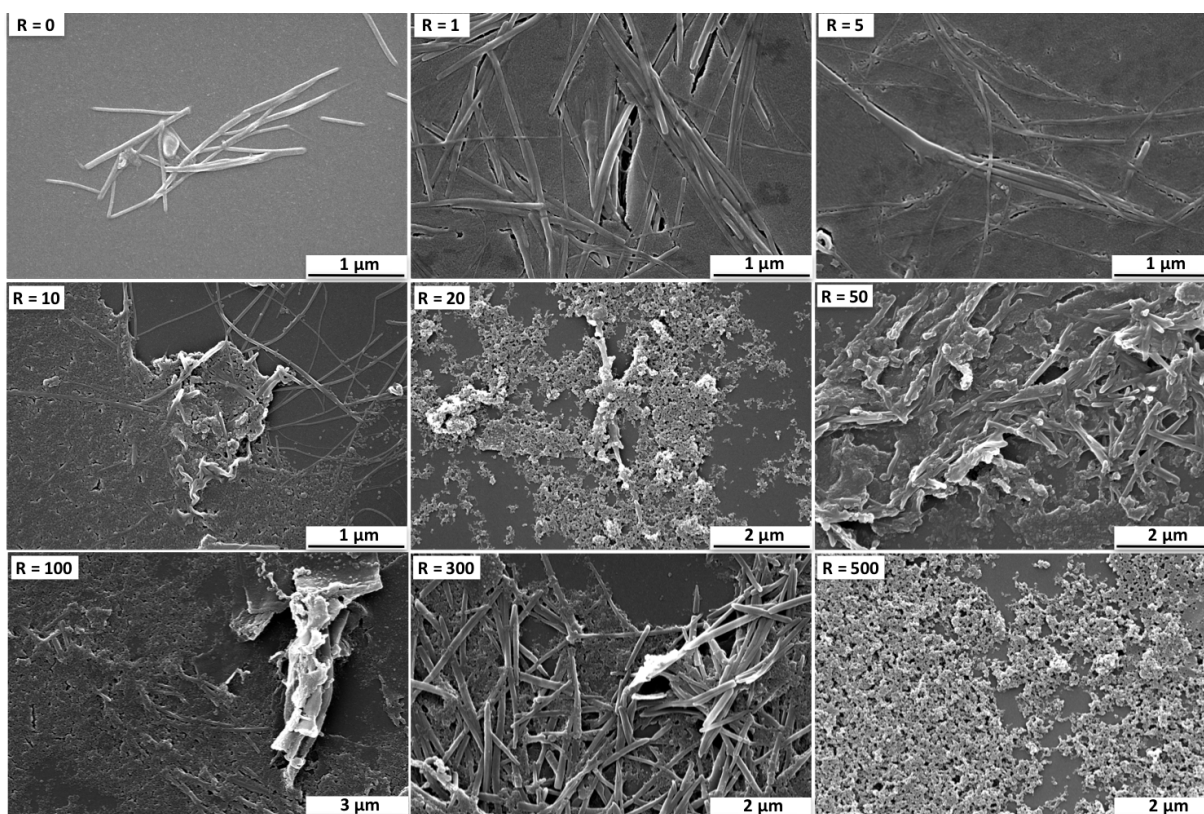


Figure 3.26. SEM images of the PMMA-PMAA/platinum(II) complex 20 system. The solutions were drop-casted on a glass slide and dried under standard conditions. The substrate was then sputtered with gold.

The platinum(II) complex self-assembled into small rods. When PMMA-PMAA was added, the rods were more elongated and flexible. Upon increasing R to a higher ratio the number of

fibers was decreasing while the number of small PMMA-PMAA particles was increasing. At $R = 300$, platinum rods were still observed on the SEM images meaning that the encapsulation the platinum(II) complex in acetone was not as efficient as in THF. Finally for $R = 500$, only aggregates of small sized particles were observed. Confocal fluorescence microscope images of the solution are displayed in Figure 3.27.

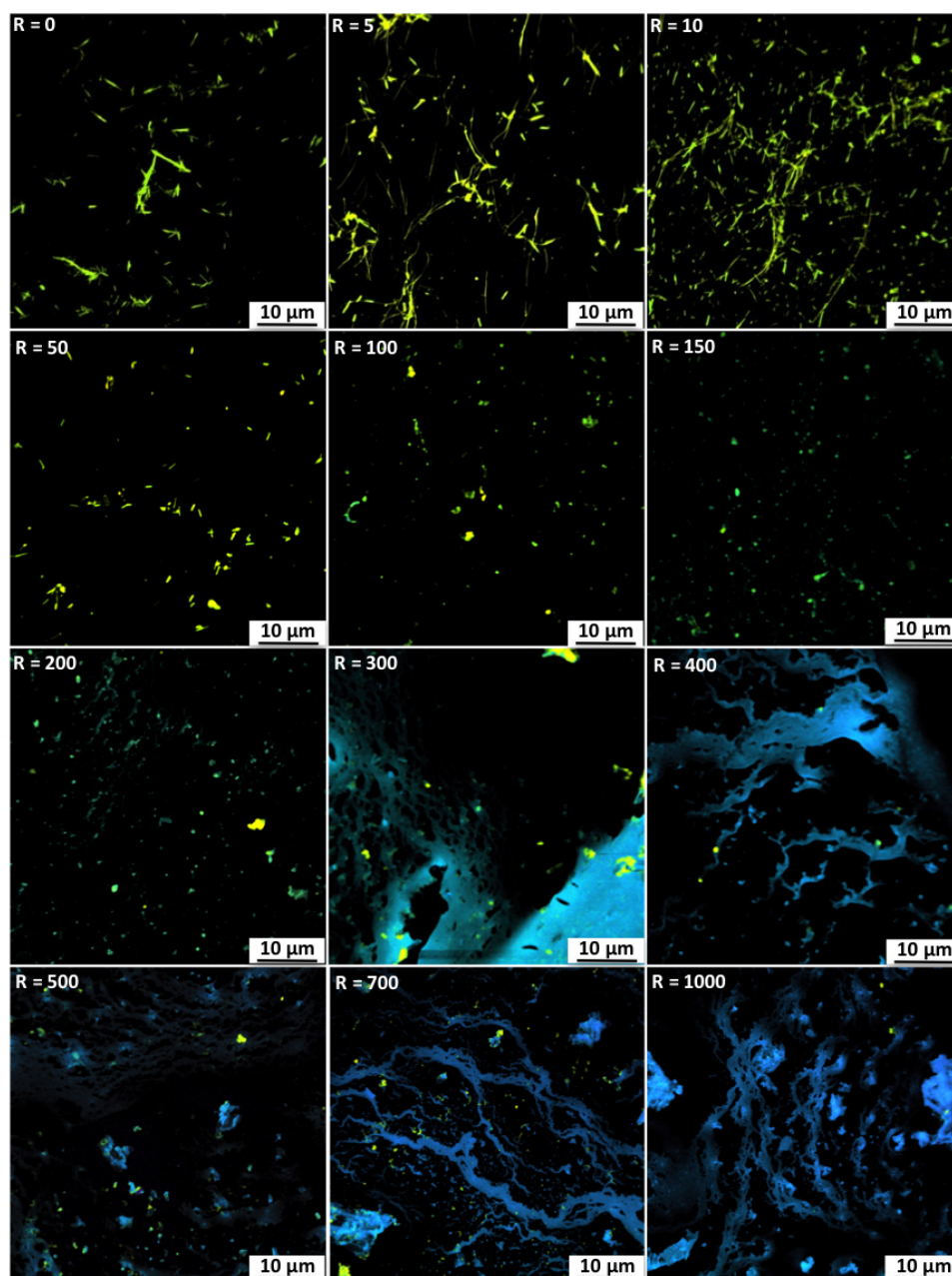


Figure 3.27. Confocal images of PMMA-PMAA/platinum(II) complex **20** system. The solutions were drop-casted on a glass slide and dried under standard conditions before imaging. The real emission color was obtained by using lambda-mode option ($\lambda_{exc} = 405\text{nm}$).

The yellow-green emissive rods were observed for $R = 0$ and were slightly red-shifted. When $50 < R < 150$, small yellow rods with green emissive particle aggregates were observed. As expected, the particles were barely visible because of their small size and only aggregation of particles were detected. Upon increasing R , the luminescence of the polymer aggregates changed from green to blue emissive particles. Yellow emissive aggregates were also observed, which originated from the remaining platinum rods as observed in the SEM images in Figure 3.26. This confirmed that most of the platinum(II) complex was encapsulated regardless of the size of the PMMA-PMAA particles. However, the encapsulation was not complete as platinum fibers were still observed even at high ratios.

The selection of the solvent played an important role on the morphology of the PMMA-PMAA particles. The use of acetone instead of THF significantly decreased the size of the particles. However, the encapsulation of the platinum(II) complex was successful even though it was not complete. Platinum(II)-loaded particles with tunable photophysical properties were obtained depending on the PMMA-PMAA/platinum(II) complex ratio R . Due to the small size of the particles and their tendency to aggregate, visualisation of the transformation of the platinum(II) complexes from fibers to particles was not clearly observed. This study also revealed that the size of the particles did not affect the encapsulation of the platinum(II) complex, meaning that the platinum(II) aggregates or monomer species were responsible for the green or blue emissions, were small and could fit inside small particles. The preparation of smaller platinum(II)-loaded particles may be of interest in bio-imaging or bio-applications.

3.2.6. Order of PMMA-PMAA and platinum(II) mixing

In the aforementioned experiments, the PMMA-PMAA and the platinum(II) complex were consistently combined in the organic solvent before being flash-injected in water. In this section, the order of the addition into water will be studied.

Firstly, the platinum(II) complex was formed in water according to the method described previously. The platinum(II) complex was dissolved in THF and 2 mL solutions with identical concentrations in platinum ($c = 5$ ppm) were prepared. Each THF/platinum(II) complex was flash-injected in 8 mL of distilled water while sonicating for 5 minutes. The organic solvent was then removed by evaporation under reduced pressure and the solutions were left to

stand for two days under ambient conditions before further analysis. Photographs of the solutions of platinum fibers are displayed in Figure 3.28. The solutions were all crystal clear and had a yellow luminescence. Secondly, the PMMA-PMAA solutions were prepared according to the method previously. PMMA-PMAA was dissolved in THF and 2 mL solution with different concentrations was prepared. The concentration of each solution is reported in Table 3.2. Each THF/PMMA-PMAA solution was flash-injected in 8 mL of the aqueous solution containing the platinum fibers while sonicating for 5 minutes. THF was then removed by evaporation under reduced pressure and the solutions were left to stand under ambient conditions for two days before analysis. Photographs of the final solutions are displayed in Figure 3.29. The solutions were more turbid and the luminescence of the solutions was shifted from yellow to blue upon increasing **R**. The encapsulation of the platinum fibers appeared to be effective when PMMA-PMAA was added after the platinum(II) complex.

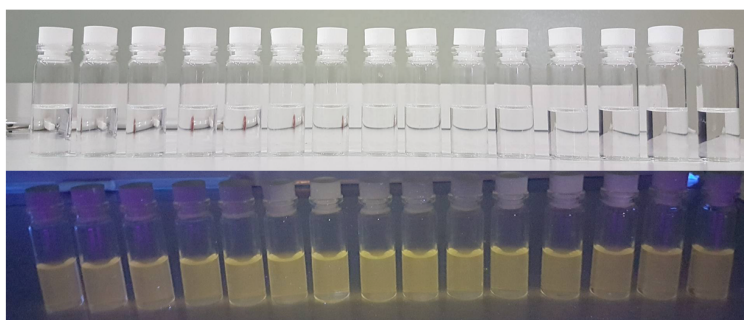


Figure 3.28. Photography of the platinum fibers in water under normal light (top) and UV irradiation (bottom).

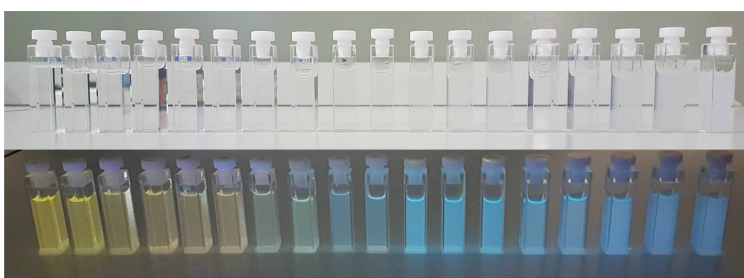


Figure 3.29. Photographs of the PMMA-PMAA/platinum(II) complex **20** solution in water. The PMMA-PMAA solution was added to an aqueous solution containing the platinum fibers.

Normalized emission and excitation spectra are displayed in Figure 3.30 and the corresponding excited state lifetimes in Table 3.9. As expected, a decrease in the intensity of the $^3\text{MMLCT}$ bands around 570 nm coupled with an increase of the $^3\text{LC/MLCT}$ bands between 450 and 550 nm was observed upon increasing **R**. The excited state lifetimes of the PMMA-

PMAA/platinum(II) complex solutions are reported in Table 3.9. As expected, the average lifetime was stagnated at low R and increasing for $R > 50$. It is worth noting that the lifetime was a bi-exponential decay starting at $R = 300$ and above. This signified that the entire the platinum(II) complex was encapsulated into the the polymer particles and that the blue emissive platinum(II) species was dominant in the particles. This was confirmed by the emission spectra as all the spectra were similar for $R > 300$. When the platinum(II) complex and PMMA-PMAA was added simultaneously, a ratio of 600 was necessary to obtain a bi-exponential decay and a pure blue emission. The encapsulation was more effective than when the PMMA-PMMA was added to the aqueous platinum fibers solution.

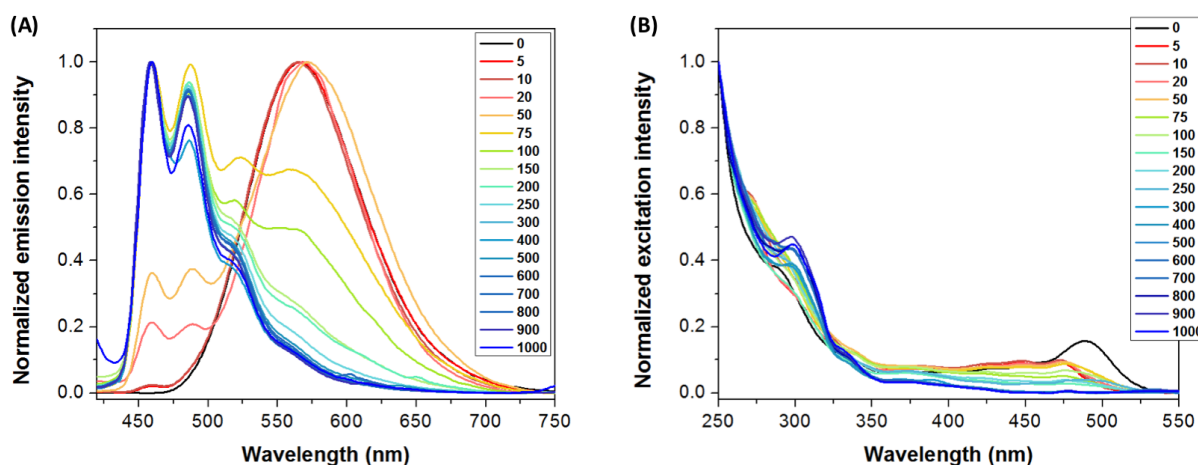


Figure 3.30. Normalized (A) Emission and (B) excitation spectra of PMMA-PMMA-Platinum(II) complex **20** system in water. The values on the right of the spectra refer to the PMMA-PMAA/platinum(II) complex ratio R . $\lambda_{exc} = 300$ nm, $\lambda_{em} = 570$ nm.

Table 3.9. Photophysical properties of the PMMA-PMAA/platinum(II) complex **20** system in water. a) $\lambda_{exc} = 400$ nm, b) $\lambda_{exc} = 405$ nm, $\lambda_{em} = 515$ nm.

R	Solvent	Emission max ^{a)}	Lifetime ^{b)} (ns)	Average lifetime (ns)
0	Water	566	325 (47%), 580 (53%)	460
5	Water	568	115 (17%), 420 (78%), 850 (5%)	390
10	Water	565	160 (15%), 500 (83%), 1450 (1%)	460
20	Water	571	320 (73%), 730 (26%), 5440 (1%)	470
50	Water	460, 572	320 (74%), 780 (25%), 4920 (1%)	490
100	Water	460, 490, 555	310 (72%), 1170 (25%), 6830 (3%)	720
150	Water	463, 490, 554	260 (52%), 1350 (39%), 7175 (8%)	1250
200	Water	460, 490, 520 (sh)	260 (49%), 1600 (41%), 8560 (10%)	1650
250	Water	460, 490, 520 (sh)	290 (47%), 1720 (40%), 8740 (13%)	2000
300	Water	460, 490, 520 (sh)	980 (73%), 7410 (27%),	2740
400	Water	460, 490, 520 (sh)	950 (70%), 7410 (30%)	2880
500	Water	460, 490, 520 (sh)	930 (69%), 7420 (31%)	2960
600	Water	460, 490, 520 (sh)	1030 (69%), 7900 (31%)	3170
700	Water	460, 490, 520 (sh)	1080 (65%), 8150 (35%)	3580
800	Water	460, 490, 520 (sh)	860 (65%), 7710 (35%)	3250
900	Water	460, 490, 520 (sh)	830 (61%), 7450 (39%)	3400
1000	Water	460, 490, 520 (sh)	820 (63%), 7600 (37%)	3340

3.2.7. Effect of the method of removal of the organic solvent

When a THF or acetone solution containing PMMA-PMAA/platinum(II) complex was added to distilled water, the subsequent removal of the organic solvent from the mixture could play an important role on the final photophysical and morphological properties of the system. Water can form azeotrope with other organic solvents, and the removal of the organic solvent by distillation or under pressure might be challenging³³. Moreover, after leaving the solution to stand for 2 days, traces of THF or acetone could still be detected. Although it did not affect the photophysical properties of the encapsulated platinum(II) complex, the presence of a small amount of organic solvent could be prejudicial for bio-application. One method consistently reported in literature is to dialyse the mixture against water^{45'-48'}. The THF was replaced by distilled water while the bulk of the PMMA-PMAA/platinum(II) aggregates would remain in the dialysis bag. To study the effect of the method of removal of the organic solvent, three THF solutions containing the same concentration in platinum(II) complex ($c = 100 \text{ ppm}$) and PMMA-PMAA ($c = 5000 \text{ ppm}$) for a ratio $R = 50$ were prepared. Each solution was flash-injected in 8 mL of distilled water while sonicating for 5 min. The first solution was then sealed and left at 80% water content, while the second solution was evaporated under pressure and left to stand under ambient conditions (as previously reported). The third solution was dialysed against water for 2 days. Photographs of the three solutions are displayed in Figure 3.31.

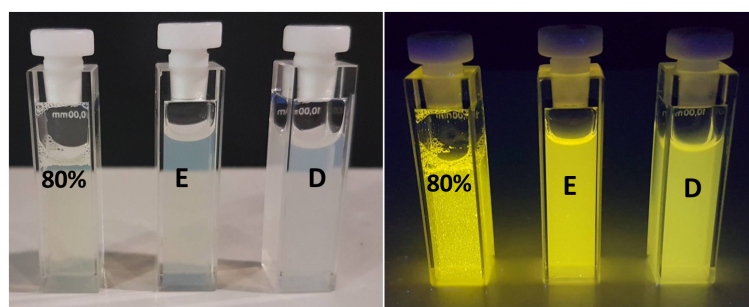


Figure 3.31. Photographs of the PMMA-PMAA/platinum(II) complex **20** system in 80% water content in THF/water mixture (80%, right cuvette), evaporated under reduced pressure (middle cuvette, E) and dialysed against water (D, left cuvette) under normal light (right) and UV lamp (left).

The three solutions were turbid due to the high concentration of PMMA-PMAA. Under the UV lamp ($\lambda_{\text{exc}} = 365 \text{ nm}$), the solution at 80% water content was viewed to be yellow emissive and

aggregates were observed. The solution that was evaporated was also yellow emissive but no aggregation was observed. The solution which was dialysed did not show any aggregates and was green-yellow emissive. Normalized emission and excitation spectra of the solutions are displayed in Figure 3.32.

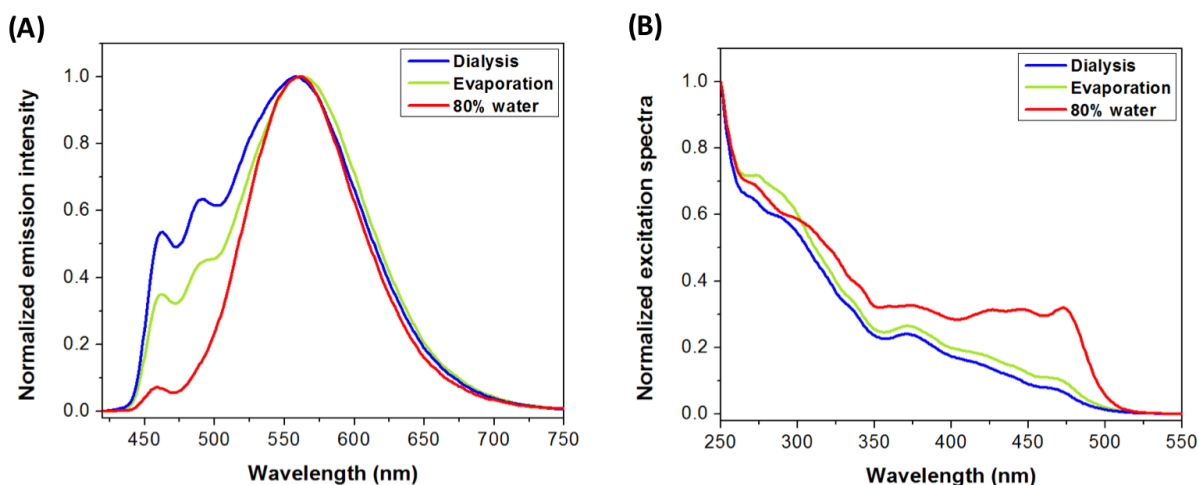


Figure 3.32. Normalized (A) Emission and (B) excitation spectra of PMMA-PMMA-platinum(II) complex **20** system in 80% water (red curves), evaporated (green curve) and dialysed (blue curve). $\lambda_{exc} = 300 \text{ nm}$, $\lambda_{em} = 560 \text{ nm}$.

The normalized emission spectra revealed the presence of the $^3\text{MMLCT}$ bands for the three solutions. More importantly, the spectra showed $^3\text{LC/MLCT}$ bands at 460 nm and 490 nm which could be used as reference of the encapsulation of the platinum(II) complex. The more intense the bands were, the more platinum(II) complex was encapsulated. When the PMMA-PMAA/platinum(II) complex was left at 80% water content, the contribution of the $^3\text{LC/MLCT}$ was very low compared to the $^3\text{MMLCT}$. When the solution was evaporated the contribution of the $^3\text{LC/MLCT}$ bands was increased. Finally, when the solution was dialysed, the contribution of the $^3\text{LC/MLCT}$ bands was the most significant aspect. Normalized excitation spectra showed $^1\text{MMLCT}$ bands between 400 nm and 500 nm when the water content of the solution was 80%, suggesting the presence of platinum fibers in solution. When the solutions were evaporated or dialysed, those bands decreased in intensity, which indicated the encapsulation of the platinum(II) complexes. PLQY and excited state lifetime of the three solutions are reported in Table 3.11.

Table 3.11. Photophysical properties of the PMMA-PMAA/platinum(II) complex **20** system in water. a) $\lambda_{exc} = 400$ nm, b) $\lambda_{exc} = 405$ nm, $\lambda_{em} = 515$ nm.

R	Solvent	Emission max ^{a)}	Lifetime ^{b)} (ns)	Average lifetime (ns)	PLQY
50	80% Water	460, 560	275 (40%), 510 (60%), 2950 (0.5%)	420	0.52
50	Water (evaporation)	460, 490, 561	260(38%), 1020 (59%), 3370 3%	800	0.37
50	Water (Dialysis)	460, 490, 558	380 (32%), 1180 (65%), 4970 (2%)	1000	0.43

In accordance with the emission and excitation spectra, the solution at 80% water content had an average lifetime of 420 ns and a PLQY of 52%, typical values from platinum fibers. When the solution was evaporated, an average lifetime of 800 ns and a PLQY of 37% was obtained. Those values are similar to the values reported previously. Finally, when the solution was dialysed against water, a longer average lifetime of 1000 ns and a higher PLQY of 43% were measured, better values than those observed when the solution was evaporated. Those results confirmed that the encapsulation of the platinum(II) complex was the most efficient when the solution was dialysed. SEM images of the three solutions are displayed in Figure 3.33. When the solution was evaporated, relatively small PMMA-PMAA particles and a few long platinum fibers were observed. When the solution was dialysed, only polymer particles were observed. Finally, when the solution was kept at 80% water content, haystacks of long and flexible platinum fibers were observed. Polymer particles and amorphous materials surrounded those fibers. If the PMMA-PMAA/platinum(II) complex ratio was the same for each solution, the final result was still dependent on the amount of THF present in solution. When no THF was present in solution, as in the case of dialysis, only platinum-loaded particles were observed. Conversely, when the water content was left at 80%, long and flexible fibers along with some polymer particles were observed. In this case, the aggregation process was directed by the platinum(II) complex. Finally, when the solution was evaporated with traces of THF was still present in solution, a mixture of platinum-loaded particles and a few platinum fibers were observed. This trend was confirmed by the confocal fluorescence images shown in Figure 3.34. Bright green emissive fibers were observed at 80% water content while only

yellow-green emissive particles were observed when the solution was dialysed. When the solution was evaporated, a mixture of yellow-green emissive particles and fibers was observed.

In conclusion, complete removal of the organic solvent by dialysis enhanced the encapsulation of the platinum(II) complex by PMMA-PMAA particle.

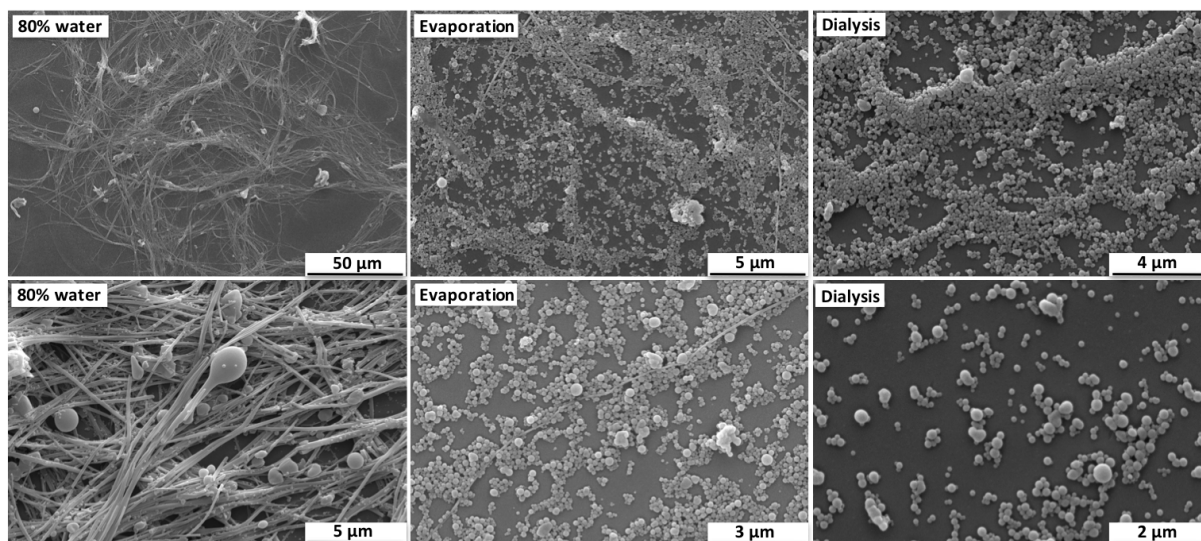


Figure 3.33. SEM images of the PMMA-PMAA/platinum(II) complex **20** solution when the solution was evaporated (top), dialysed (middle), and left at 80% water content (bottom).

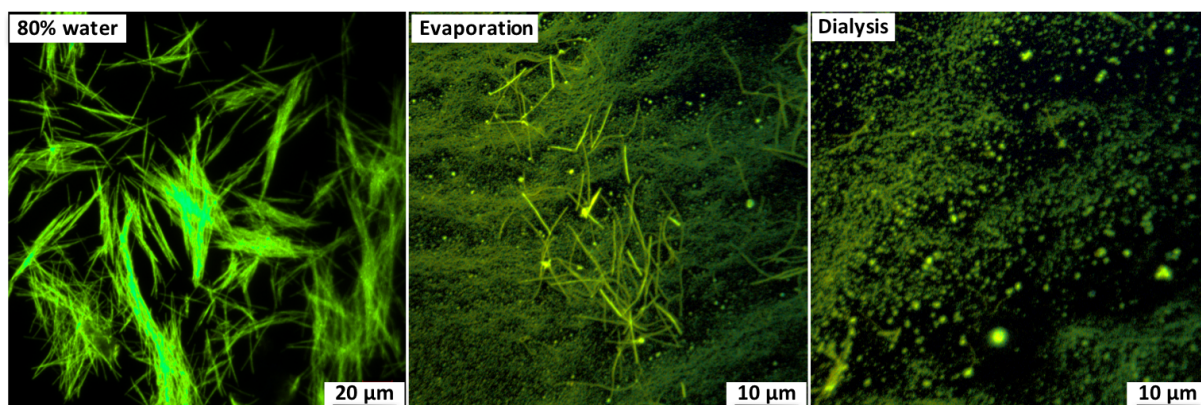


Figure 3.34. Fluorescence confocal microscope images the PMMA-PMAA/platinum(II) complex **20** solution when the solution was evaporated, dialysed and left at 80% water content. The real emission color was obtained by using lambda-mode option ($\lambda_{\text{exc}} = 405\text{nm}$).

3.2.8. Effect of the method of addition of water on the encapsulation of the platinum(II) complex

To improve the monodispersity of the particles and the encapsulation efficiency of the polymer particles, the method of addition of the PMMA-PMAA/platinum(II) complex/THF solution to the water was modified and the removal of the organic solvent was conducted by dialysis. Monodispersed platinum-loaded particles were obtained by gradual addition of water to the PMMA-PMAA/platinum(II) complex/ THF mixture at a rate of 1 drop/10 seconds while stirring. Then the THF/water mixture was immediately dialysed against water for 2 days. Photographs of the dialysed solutions are displayed in Figure 3.35.

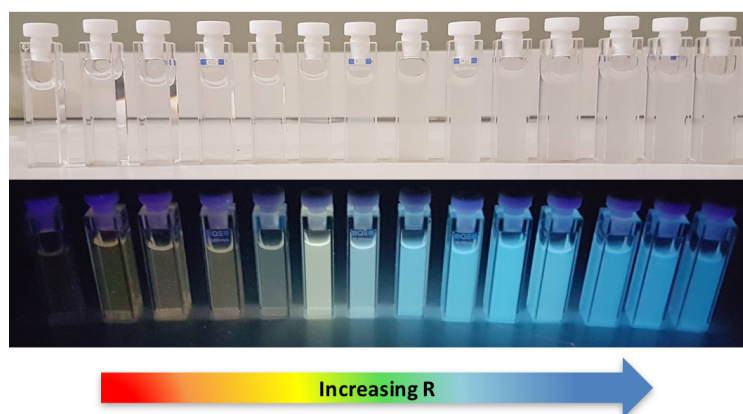


Figure 3.35. Photographs of the PMMA-PMAA/platinum(II) complex **20** solutions in water under normal light (top) and UV lamp (bottom) upon increasing R from left to right.

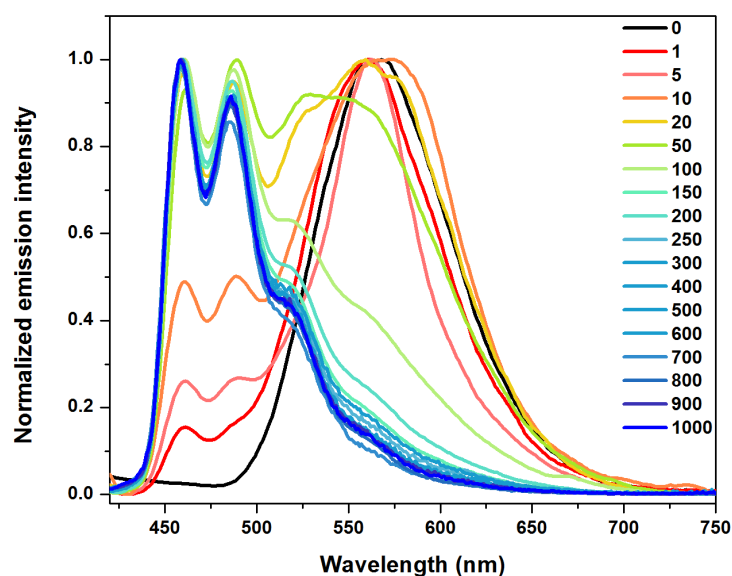


Figure 3.36. Normalized emission spectra of the dialysed emission spectra. The values on the right of the spectra refer to the PMMA-PMAA/platinum(II) complex **20** ratio R . $\lambda_{exc} = 300$ nm.

The luminescence originating from the solution at the left of the photo ($R = 0$) was very weak compared to the other solutions. The platinum fibers were very emissive and such a low intensity meant that the amount of platinum(II) complex in solution was very low. It was concluded that the fibers diffused with the THF outside of the membrane pores during the dialysis (regenerated cellulose, 1000 Da). Upon addition of PMMA-PMAA to all of the solutions ($R > 1$), the luminescence was brighter, translating to a higher concentration of platinum(II) complex in the solutions. PMMA-PMAA prevented the diffusion of the platinum(II) complex out of the dialysis bag by either encapsulating it or aggregating around the platinum fibers, resulting in a larger and heavier aggregation that enabled it to pass through the membrane's pores. Normalized emission intensity of the dialysed solutions are displayed in Figure 3.36 and the excited state lifetimes are reported in Table 3.13. There was a small amount of platinum fibers in solution when $R = 0$, which was confirmed by the fact that the emission spectra started relatively high at 420 nm. Upon increasing R , the intensity of the $^3\text{LC/MLCT}$ bands at 460 nm, 490 nm and 520 nm was quickly increasing while the $^3\text{MMLCT}$ band around 570 nm was initially blue-shifted to 560 nm and then decreased in intensity. It is worth noting that the rise of the $^3\text{LC/MLCT}$ bands were observed from $R = 1$ and above. The dialysis removed most of the platinum fibers and the intensity of the $^3\text{MMLCT}$ band was decreased compared to $^3\text{LC/MLCT}$ bands. The excited state lifetimes were also longer upon increasing R . A bi-exponential decay occurred when $R = 200$, indicating that all of the platinum(II) complex was encapsulated and were blue emissive inside the PMMA-PMAA particles. After the PMMA-PMAA/platinum(II) complex / THF was flash-injected in water and the organic solvent removed by evaporation, a bi-exponential decay was obtained for $R = 600$ (refer to Table 3.4). The encapsulation of the platinum(II) complex was more efficient when the water was added gradually to the PMMA-PMAA/platinum(II) complex / THF mixture and dialysed against water.

Table 3.13. Photophysical properties of the PMMA-PMAA/platinum(II) complex **20** system in water. a) $\lambda_{exc} = 400$ nm, b) $\lambda_{exc} = 405$ nm, $\lambda_{em} = 515$ nm.

R	Solvent	Emission max^{a)}	Lifetime^{b)} (ns)	Average lifetime (ns)
0	Water	569	195 (51%), 440 (49%),	310
1	Water	460, 490, 559	200 (41%), 410 (58%), 2260 (1%)	340
5	Water	460, 490, 560	300 (84%), 700 (15%), 4900 (1%)	385
10	Water	460, 490, 557	280 (66%), 620 (33%), 5020 (1%)	420
20	Water	460, 490, 520, 554	320 (64%), 820 (34%), 6430 (1%)	570
50	Water	460, 490, 520, 555	360 (33%), 1250 (33%), 6430 (3%)	1100
100	Water	463, 490, 520	370 (38%), 1400 (56%), 7460 (6%)	1350
150	Water	460, 490, 520 (sh)	860 (89%), 4940 (11%)	1315
150	Water	460, 490, 520 (sh)	350 (39%), 1590 (49%), 8200 (13%)	1950
200	Water	460, 490, 520 (sh)	350 (37%), 1470 (54%), 7890 (10%)	1690
250	Water	460, 490, 520 (sh)	1050 (77%), 7130 (23%)	2460
300	Water	460, 490, 520 (sh)	1070 (79%), 7200 (21%)	2330
400	Water	460, 490, 520 (sh)	950 (69%), 7120 (31%)	2840
500	Water	460, 490, 520 (sh)	1120(71%), 7750 (29%)	3070
600	Water	460, 490, 520 (sh)	1080 (72%), 7610 (28%)	2930
700	Water	460, 490, 520 (sh)	980 (64%), 7520 (36%)	3320
800	Water	460, 490, 520 (sh)	940 (66%), 7500 (34%)	3200
900	Water	460, 490, 520 (sh)	1040 (69%), 7500 (31%)	3050
1000	Water	460, 490, 520 (sh)	910 (63%), 7300 (37%)	3310

SEM images of the PMMA-PMAA/platinum(II) complex system dialysed against water are shown in Figure 3.37.

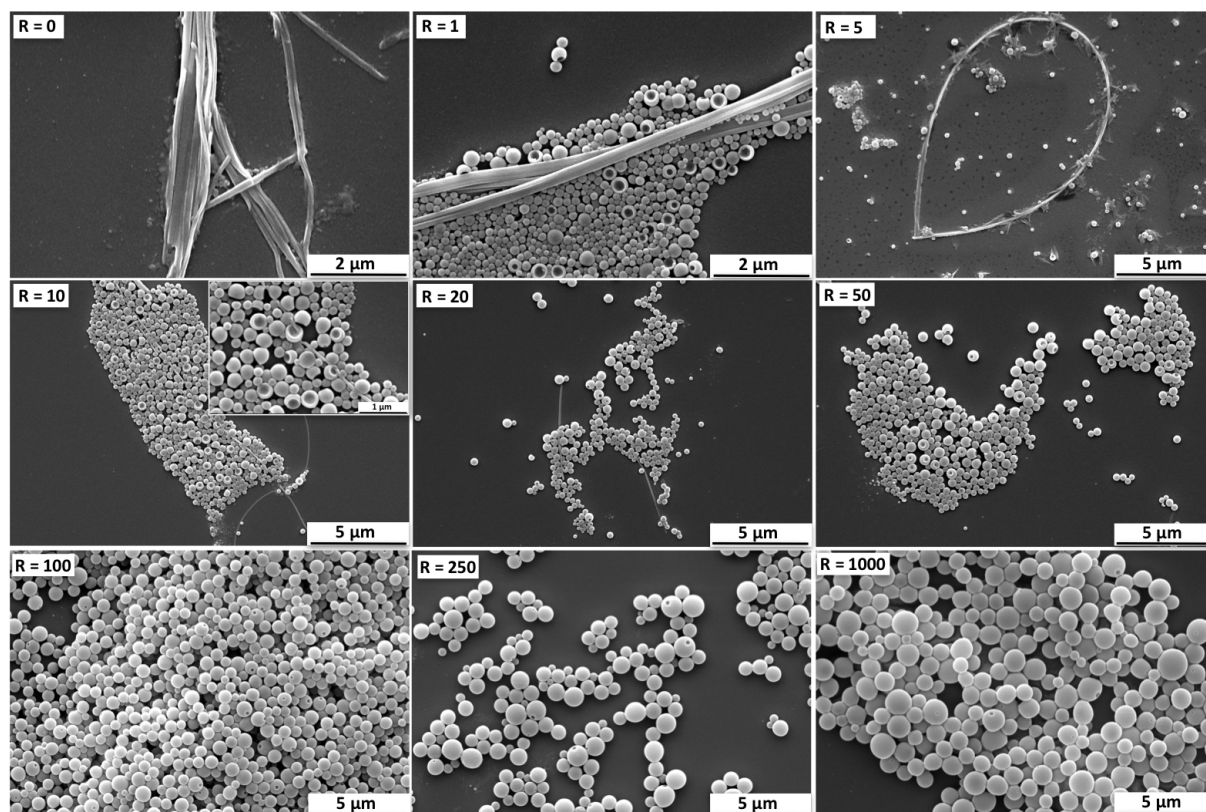


Figure 3.37. SEM images of the PMMA-PMAA/platinum(II) complex **20** system. The solutions were drop-casted on a glass slide and dried under standard conditions.

For $R = 0$, platinum fibers were observed by SEM. When PMMA-PMAA was added to the solution, a mixture of platinum fibers and bowl-shaped particles and particles with indentations were observed during the dialysis. Polymer hollow particles have previously been reported in literature³⁴⁻³⁶. The deformation on the surface was caused by pressure difference between the interior and the exterior of the particles during mixing of the two solvents. When the water content was increased in solution, the difference in water concentration between the interior and exterior of the particles drove the diffusion of the organic solvent to the exterior and diffusion of the water to the interior. The rate of diffusion of the organic solvent out of the hydrophobic core was faster than the diffusion of the water in, resulting in the generation of negative pressure inside the particles, which led to the formation of indentation or collapse of the particles. When the pressure was equalized between the interior and the exterior of the particles, the shape of the particles had frozen due to the large excess of water in the solvent mixture. Bundles of platinum fibers forming

large rings were also observed ($R = 5$). The number of platinum fibers was decreasing and the PMMA-PMAA particles were constricting upon increasing R . For the highest ratio, only monodisperse platinum-loaded particles with small indentations on the surface were observed. Confocal fluorescence microscope images of the PMMA-PMAA system in water are displayed in Figure 3.38.

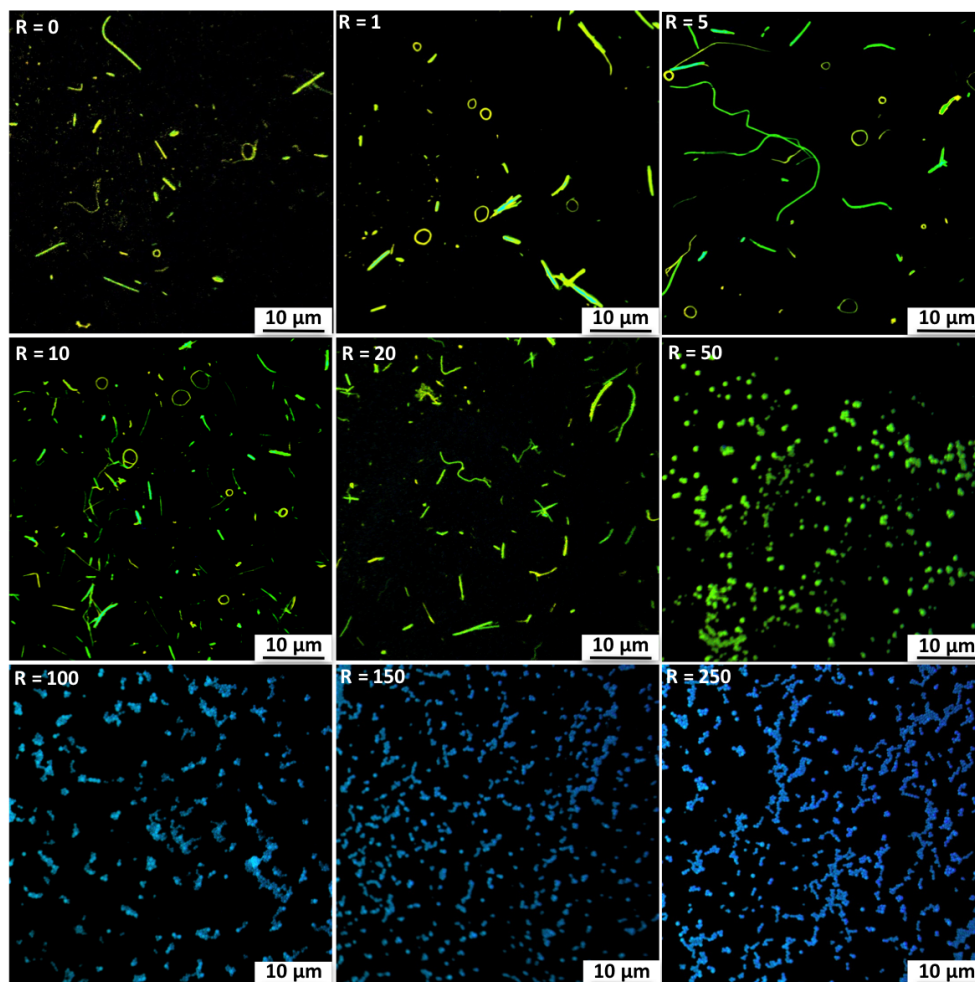


Figure 3.38. Confocal images of PMMA-PMAA/platinum(II) complex **20** system. The solutions were drop-casted on a glass slide and dried under standard conditions before imaging. The real emission color was obtained by using lambda-mode option ($\lambda_{exc} = 405nm$).

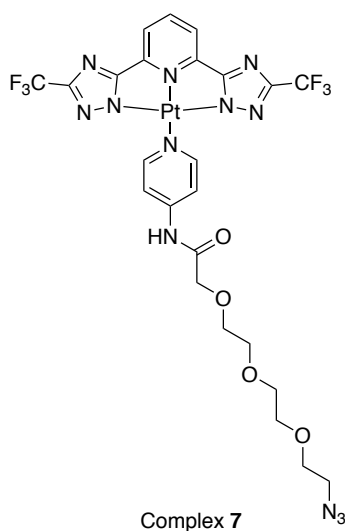
Green emissive fibers with yellow emissive rings were observed at low ratios ($R < 20$). The yellow emissive rings were the ring-forming platinum fibers bundle observed by SEM. For $R = 50$, green emissive particles were observed and upon increasing R , the green particles were replaced by blue emissive particles.

In conclusion, gradual addition of water to the PMMA-PMAA/platinum(II) complex / THF mixture followed by dialysis against water to remove the organic solvent, provides well-

defined monodisperse platinum-loaded particles with tunable emission from green to blue. Small defects on the surfaces of the particles were observed but did not affect the encapsulation properties of PMMA-PMAA diblock copolymer.

3.2.9. Influence of the platinum(II) complex on the encapsulation

Thus far, only one platinum(II) complex was attempted for the encapsulation by PMMA-PMAA diblock copolymer. In order to prove the versatility of the method, platinum(II) complexes with different photophysical and morphological properties were encapsulated by PMMA-PMAA. All the platinum-loaded particles were prepared using the same methods as previously. An amphiphilic neutral platinum(II) complex was chosen for these experiments (Scheme 3.3).



Scheme 3.3. Chemical formula of the amphiphilic neutral platinum(II) complex 7.

Photographs of the PMMA-PMAA/platinum(II) complex ($c = 5$ ppm) solutions in water are displayed in Figure 3.39. Emission and excitation spectra of the solution are shown in Figure 3.40 and the excited state lifetimes are reported in Table 3.14.

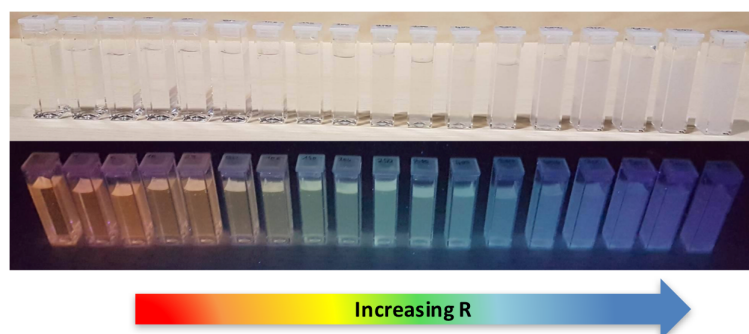


Figure 3.39. Photographs of the PMMA-PMAA/platinum(II) complex **7** solutions in water under normal light (top) and UV lamp (bottom) upon increasing R from left to right.

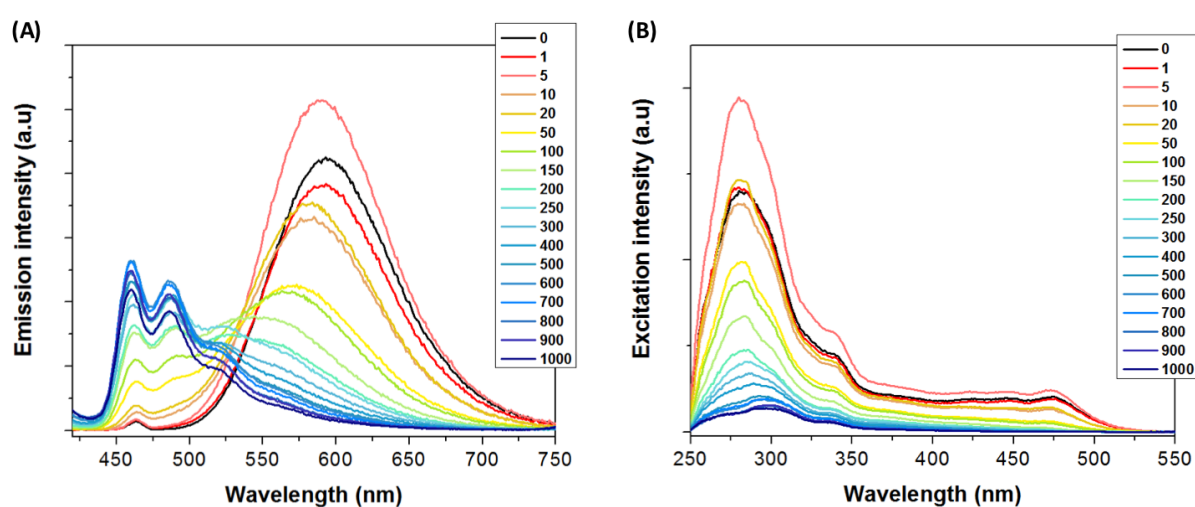


Figure 3.40. (A) Emission and (B) excitation spectra of PMMA-PMMA/ complex **7** system in water. The values on the right of the spectra refer to the PMMA-PMAA/platinum(II) complex ratio R . $\lambda_{exc} = 400 \text{ nm}$, $\lambda_{em} = 590 \text{ nm}$.

Replacing the hydrophobic platinum(II) complex (known to be more stable in the hydrophobic core of the PMMA-PMAA particles) with an amphiphilic molecule did not affect the encapsulation properties of the diblock copolymer. The same encapsulation behavior was observed for the amphiphilic platinum(II) complex; green emissive particles were obtained when the ratio R was around 50. Upon increasing R , the concentration in platinum(II) complex per particles was decreasing, inducing a blue-shift in the emission of the particles. The PMMA-PMAA diblock copolymer disassembled the aggregates and encapsulated them into its particles core regardless of whether the platinum(II) complex self-assembled into fibers or into torroidal particles in water.

Table 3.14. Photophysical properties of the PMMA-PMAA/platinum(II) complex **7** system in water. a) $\lambda_{exc} = 400$ nm, b) $\lambda_{exc} = 405$ nm, $\lambda_{em} = 525$ nm.

R	Solvent	Emission max ^{a)}	Lifetime ^{b)} (ns)	Average lifetime (ns)
0	Water	593	230 (46%), 530 (54%)	390
1	Water	593	250 (34%), 810 (66%)	620
5	Water	591	150 (17%), 740 (75%), 1520 (8%)	700
10	Water	460, 585	210 (25%), 910 (71%), 2750 (4%)	800
20	Water	460, 584	320 (33%), 1025 (65%) 2290 (2%)	870
50	Water	460, 573	360 (38%), 1190 (59%), 6320 (3%)	1000
100	Water	460, 490, 570	380 (40%), 1280 (57%), 7115 (3%)	1110
150	Water	460, 490, 544	360 (39%), 1320 (57%), 7120 (4%)	1180
200	Water	460, 490, 520, 560(sh)	380 (40%), 1380 (40%), 7450 (5%)	1300
250	Water	460, 490, 520 (sh)	390 (41%), 1440 (52%), 7630 (6%)	1390
300	Water	460, 490, 520 (sh)	1010 (87%), 6300 (13%)	1680
400	Water	460, 490, 520 (sh)	400 (40%), 1650 (49%) 8240 (11%)	1850
500	Water	460, 490, 520 (sh)	320 (37%), 1520 (50%) 7830 (13%)	1900
600	Water	460, 490, 520 (sh)	1070 (78%), 7160 (22%)	2400
700	Water	460, 490, 520 (sh)	1000 (76%), 6890 (24%)	2440
800	Water	460, 490, 520 (sh)	990 (73%), 6970 (27%)	2590
900	Water	460, 490, 520 (sh)	930 (71%), 6830 (29%)	2610
1000	Water	460, 490, 520 (sh)	1100 (66%), 8070 (34%)	2630

3.3. Conclusion

Encapsulation of a hydrophobic platinum(II) complex was successfully achieved by using PMMA-PMAA diblock copolymers in water. Platinum fibers initially formed in water were encapsulated by the polymer particles until the PMMA-PMAA/platinum(II) complex ratio was high enough to encapsulate most of the platinum(II) complex. The photophysical properties of the platinum-loaded particles were easily tunable by varying the ratio **R**. Green emissive particles with enhanced PLQY were obtained when the **R** was relatively low. Upon increasing the PMMA-PMAA/platinum(II) complex ratio, the luminescence of the particles was gradually shifted from green to blue with longer lifetimes, due to the rigidochromism effect within the polymer particles. Parameters such as solvents composition, order of addition into water and the concentration in platinum(II) complex, had a small influence on the morphology or the photophysical properties of the platinum-loaded particles. The various methods used to improve the homogeneity of the particles and the encapsulation efficiency could be applied to most of the platinum(II) complexes and could be extended to different molecules with interesting properties. Such particles with enhanced and tunable photoluminescent properties could be used for bio-imaging applications and further functionalisation of the outer shell of the particles could render them suitable for bio-imaging.

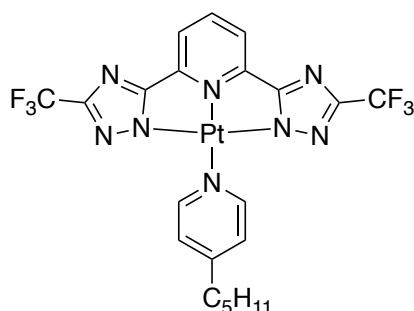
3.4. Experimental Section

3.4.1. General information

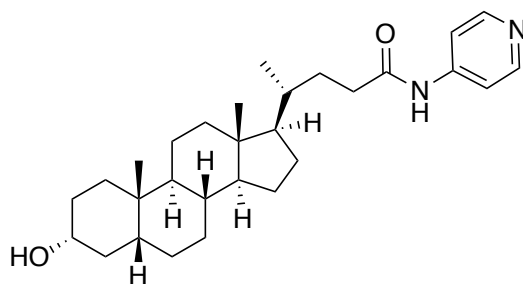
All the solvents and chemicals were used as received from Sigma-Aldrich or Fluka without any further purification. The synthesis of complexes **3**, **7**, **18**, **19** was previously reported in chapter **2**. Complex **20** was synthesized exactly as reported in the literature⁴. K_2PtCl_4 was purchased from Precious Metal Online (PMO). $PtCl_2(DMSO)_2$ was prepared from previously reported synthetic procedures¹. Column chromatography was performed on silica gel 60 (particle size 63-200 μm , 70-230 mesh ASTM, Merck). NMR spectra were recorded on a Bruker Avance 400 spectrometer. ¹H NMR, ¹³C NMR and ¹⁹F NMR chemical shifts (δ) of the signals are given in parts per million and referenced to residual protons in the deuterated solvents. The signal splitting are abbreviated as follows: s, singlet; d, doublet; t, triplet; q, quadruplet; m,

multiplet. Coupling constants (J) are given in Hertz. Electrospray ionization mass spectrometry (ESI-MS) was carried out on a MicroTOF (Bruker) mass spectrometer equipped with an electrospray source by the mass spectrometry service of the University of Strasbourg. Elemental analysis was performed by the analytical service of physical measurements and optical spectroscopy by the University of Strasbourg.

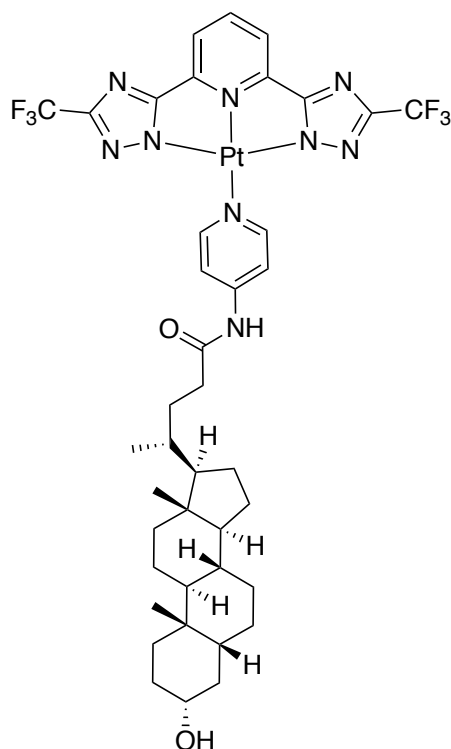
3.4.2. Synthesis



Complex 20⁴. In a 50 mL two-neck round-bottom flask, tridentate ligand **2** (200 mg, 0.573 mmol, 1.05 eq) and PtCl₂(DMSO)₂ (230 mg, 0.46 mmol, 1.0 eq) were suspended in 15 mL of 2-MeOEtOH and 5 mL of H₂O 3 :1. Upon addition of N,N-diisopropylethylamine (100 μL, 0.576 mmol, 1eq), the reaction mixture turned to a clear yellow solution. 4-undecylpyridine (90.5 μL, 0.546 mmol, 1.2 eq) was added and the mixture heated at 83°C overnight under N₂ atmosphere. A yellow precipitate was quickly formed. The crude was purified by column chromatography using ethyl acetate and cyclohexane 1: 1 as mobile phase. The final product was then washed with a minimal amount of methanol and filtered. A yellow solid was collected and dried under vacuum for two days (167 mg, 0.255 mmol, yield 46.6%). ¹H NMR (acetone-d₆, 400 MHz, ppm) δ: 9.23 (d, J = 6.2 Hz, 2H), 8.20 (t, J = 8.0 Hz, 1H), 7.64 (d, J = 8.0 Hz, 2H), 7.43 (d, J = 6.5 Hz, 2H), 2.81 (m, 2H), 1.79 (m, 2H), 1.43 (m, 4H), 0.96 (t, J=6.9, 3H); ¹⁹F NMR (acetone-d₆, 376 MHz, ppm) δ: -64.78 (s, 6H); HR-MS (ESI) m/z: C₁₈H₂₀F₆N₇O₂Pt [M+HCOOH]⁺, calcd. 692.13, found 692.13; Elemental analysis: calcd. C 36.48%, N 16.20%, H 2.62%, found C 36.26%, N 15.89%, H 2.72%.



(*R*)-4-((3*R*, 5*R*, 8*R*, 9*S*, 10*S*, 13*R*, 14*S*, 17*R*)-3-hydroxy-10,13-dimethylhexadecahydro-1*H*-cyclopenta[*a*]phenanthren-17-yl)-*N*-(pyridin-4-yl) pentanamide³⁷ (**21**). A solution of lithocholic acid (1.0 g, 2.66 mmol, 1 eq) and triethylamine (410 μ L, 3.0 mmol, 1.1 eq) in dry THF (100 mL) was stirred at room temperature. Ethyl chloroformate (290 μ L, 3.0 mmol, 1.1 eq) was added and the resulting turbid white solution was stirred for 45 min. 4-aminopyridine (310 mg, 3.0 mmol, 1.1 eq) was introduced to the flask and the reaction mixture stirred for 24 h. At the end of the reaction the triethylamine salt was filtered off and the solvent evaporated under reduced pressure. The unreacted 4-aminopyridine and lithocholic acid were removed by aqueous bicarbonate solution followed by refluxing in acetonitrile. The resulting white powder was filtered and dried under vacuum (400 mg, 0.88, yield 33%). ¹H NMR (CD₂Cl₂, 400 MHz, ppm) δ : 8.44 (d, *J* = 6.4 Hz, 2H), 7.46 (d, *J* = 6.3 Hz, 2H), 7.34 (s, 1H), 3.57(m, 1H), 2.34 (dddd, *J* = 66.5, 15.3, 10.0, 5.5 Hz, 2H), 2.00-1.00 (m, 11-CH₂), 1.54 (s, 3H), 1.26 (s, 2H), 0.96 (d, *J*= 6.3 Hz, 3H), 0.92 (s, 3H), 0.66 (s, 3H); ¹³C NMR (CD₂Cl₂, 100 MHz, ppm) δ : 172.88, 151.25, 113.76, 72.28, 57.10, 56.61, 43.34-21.41, 18.80, 12.38; HR-ESI-MS (*m/z*) : C₂₉H₄₄N₂O₂ [M+H]⁺, calcd. 453.3476, found 453.3439.



Complex 22. In a 50 mL two-neck round-bottom flask, tridentate ligand **2** (347 mg, 0.994 mmol, 1.05 eq) and $\text{PtCl}_2(\text{DMSO})_2$ (400 mg, 0.947 mmol, 1.0 eq) were suspended in 20 mL of acetonitrile. Upon addition of *N,N*-diisopropylethylamine (330 μL , 0.1894 mmol, 2.0 eq) to the suspension, compound **21** (429 mg, 0.994 mmol, 1.0 eq) was added and the mixture heated at 80°C under N_2 atmosphere overnight. A yellow precipitate rapidly formed. The crude was purified by column chromatography using ethylacetate/methanol 95: 5 as the mobile phase. The orange solid was dried under vacuum for two days ($m = 137$ mg, 0.138 mmol, yield 15%). ^1H NMR (THF- d_8 , 400 MHz, ppm) δ : 9.95 (s, 1H), 9.49 (d, $J = 6.6$ Hz, 2H), 8.23 (t, $J = 7.9$ Hz, 1H), 7.91 (d, $J = 8$ Hz, 2H), 7.87 (d, $J = 6.9$ Hz, 2H), 3.45 (m, 1H), 2.47 (m, 2H), 2.00-1.00 (m, 11- CH_2), 1.29 (s, 2H), 1.00 (d, $J = 6.4$ Hz, 3H), 0.94 (s, 3H), 0.71 (s, 3H); ^{19}F NMR (CDCl_3 , 376 MHz, ppm) δ : -65.10; (HR-MS (ESI) m/z : $\text{C}_{40}\text{H}_{48}\text{F}_6\text{N}_9\text{O}_2\text{Pt}$ [$\text{M}+\text{H}$] $^+$, calcd. 995.348, found 995.354).

3.2.1. Preparation of the PMMA-PMAA diblock copolymer nanoparticles.

PMMA-PMAA particles were prepared by “flash-injection” technique²⁶. The block copolymer was dissolved by stirring in acetone or THF overnight. Then solutions at varying concentrations were prepared. A 2 mL of the freshly-prepared PMMA-PMAA/acetone or THF solution was rapidly added to 8 mL of distilled water while the mixture was sonicated. The organic solvent was removed by evaporation under reduced pressure and the solutions were left to stand for

two days at ambient condition before analysis. The resulting aqueous suspensions were clear for low concentrations of PMMA-PMMA and more turbid for higher concentrations of the polymer.

3.2.2. Encapsulation of platinum(II) complexes into PMMA-PMAA diblock copolymer nanoparticles

Platinum(II)-loaded polymer particles were prepared in a similar manner as described above. PMMA-PMMA and complex **20** were distinctively dissolved in acetone or THF. Solutions at different concentrations of PMMA-PMAA but with a constant concentration of complex **20** (5 or 100 ppm) were prepared. 2 mL of the freshly-prepared mixture was rapidly flash-injected into 8 mL of distilled water while the mixture was sonicated. The organic solvent was removed by evaporation under reduced pressure and the solutions were left to stand for two days at ambient condition before analysis. The same method was employed for all the platinum(II) complexes tested in this chapter. Another alternative for the preparation of platinum-loaded particles has also been described. The distilled water was gradually added to the complex **20**/PMMA-PMAA/THF mixture at a rate of 1 drop/10 sec while stirring. The resulting mixture was then dialysed against water for 2 days.

3.4.3. Photophysics

All the absorption measurements in this report were recorded on a UV-3600 Shimadzu UV-Vis-NIR spectrophotometer, and were baseline and solvent corrected with UV Probe software. Quartz cuvettes were used for this purpose. Steady-state measurements were recorded on a HORIBA Jobin-Yvon IBH FL-332 Fluorolog 3 spectrometer equipped with a 450 W Xenon arc lamp, double grating excitation and emission monochromators.

Time-resolved measurements up to 5 μ s were performed using the TCSPC option on a FluoTime 300 (PicoQuant). The excitation source was mounted directly on the sample chamber at 90° to a double grating emission monochromator and collected by a PicoHarp 300 (PicoQuant) single-photon-counting detection module. Signals were collected using the software FluroFit, PicoQuant For excited state lifetimes > 10 μ s, a different experimental setup was utilised, by equipping the FluoTime 300 with a FL-1040 phosphorescence module

including a 70-W xenon flash tube. The signal was recorded on the PDL 820 single-photon-counting detector and collected with multichannel scalling (MCS).

Absolute quantum yield measurements were performed using a Hamamatsu Photonics absolute PL quantum yield measurement system. This setup is equipped with a L0799-001 CW Xenon light source (150 W), a monochromator, a C7473 photonic multi-channel analyzer and an integrating sphere.

3.4.4. Scanning electron microscopy (SEM) Scanning Transmission electron microscopy (STEM)

SEM characterization was performed employing a FEI scanning electron microscope Quanta FEG 250, at an acceleration voltage of 10 KV. Samples were prepared by drop-casting a solution of platinum(II) complex onto a glass slide, and subsequent plasma-induced deposition of a 40 nm thick layer of silver.

STEM characterization was performed employing a FEI scanning electron microscope Quanta FEG 250, at an acceleration voltage of 20 kV. Samples were prepared by drop-casting a solution of platinum(II) complex onto a copper grid (400 mesh, Agar Scientific) coated with Formvar/carbon film.

3.4.5. Fluorescence confocal microscopy

All of the fluorescence images were taken by using Zeiss LSM 710 confocal microscope system with 63 × magnification, numerical aperture, NA, 1.3 of Zeiss LCI Plan-NEOFLUAR water immersion objective lens (Zeiss GmbH). The samples were excited by continuous wave (cw) laser at 405 nm. The emission of the complexes was collected in the range from 400 to 750 nm. In addition, the lambda-mode acquisition technique was performed to observe the emission spectra of the two complexes after cell internalization. The raw data, collected in lambda-mode, was processed using linear un-mixing tool available in ZEN 2011 software package (Zeiss GmbH). All images were performed using the same software.

3.5. References

1. Lehn, J. M. *Science* **2002**, *295*, 2400–2403; Elemans, J. A. A. W., van Hameren, R., Nolte, R. J. M., Rowan, A. E. *Adv. Mater.* **2006**, *18*, 1251–1266.
2. Strassert, Cristian A., Chen-Han Chien, Maria D. Galvez Lopez, Dimitrios Kourkoulos, Dirk Hertel, Klaus Meerholz, and Luisa De Cola, *Angew. Chem., Int. Ed.* **2011**, *50*, 946-950.
3. Po, Charlotte, Anthony Yiu-Yan Tam, Keith Man-Chung Wong, and Vivian Wing-Wah Yam, *J. Am. Chem. Soc.*, **2011**, *133*, 12136-12143.
4. Mauro, Matteo, Alessandro Aliprandi, Cristina Cebrián, Di Wang, Christian Kübel, and Luisa De Cola. *Chem. Commun.*, **2014**, *50*, 7269-7272.
5. Lu, Wei, Yong Chen, V. A. L. Roy, Stephen Sin-Yin Chui, and Chi-Ming Che. *Angew. Chem. Int. Ed.*, **2009**, *48*, 7621 –7625.
6. Alessandro Aliprandi, Matteo Mauro, Luisa De Cola, *Nature Chem.* **2016**, *8*, 10–15.
7. V. H. Houlding; V. M. Miskowski, *Coord. Chem. Rev.*, **1991**, *111*, 145-152.
8. V. M. Miskowski; V. H. Houlding, *Inorg. Chem.*, **1991**, *30*, 4446-4452.
9. Yam, V. W. W., Wong, K. M. C., Zhu, N. Y. *J. Am. Chem. Soc.* **2002**, *124*, 6506–6507.
10. Yam, V. W. W., Chan, K. H. Y., Wong, K. M. C., Zhu, N. *Chem. Eur. J.* **2005**, *11*, 4535–4543.
11. Aliprandi, A., Genovese, D., Mauro, M., De Cola, L. *Chem. Lett.* **2015**, *44*, 1152–1169.
12. Kimberly L. Metera and Hanadi Sleiman, *Macromolecules*, **2007**, *40*, 3733-3738.
13. Vivian Wing-Wah Yam, Yongchen Hu, Kenneth Hoi-Yiu Chan and Clive Yik-Sham Chung. *Chem. Commun.*, **2009**, *41*, 6216–6218.
14. Li-Zhu Wu, Tsz-Chun Cheung, Chi-Ming Che, Kung-Kai Cheung, Michael H. W. Lamb, *Chem. Commun.*, **1998**, *10*, 1127-1128.
15. N. A. Larew, A. R. V. Wassen, K.E. Wetzels, M. M. Machala and S. D. Cummings, *Inorg. Chim. Acta*, **2010**, *263*, 57-62.
16. K.Y Wong, W.W.S. Lee, *J. Photochem. Photobiol. A Chem.*, **1997**, *102*, 231-235.
17. N. Liu, B. Wang, W. Liu, W. Bu, *J. Mater. Chem. C*, **2013**, *1*, 1130-1136.
18. Stephan Sinn, Frank Biedermann and Luisa De Cola, *Chem. Eur. J.* **2017**, *23*, 1 – 8.

19. C. Yu, K. M. C. Wong, K. H. Y. Chan, V. W. W. Yam, *Angew. Chem Int. Ed*, **2005**, *44*, 791-794.
20. Nijuan Liu, Baoyan Wang, Weisheng Liu and Weifeng Bu, *Chem. Commun.*, **2011**, *47*, 9336–9338.
21. N. Liu, Q. He, W. Bu, *Langmuir*, **2015**, *31*, 2262–2268.
22. Zhang, L., Eisenberg, A., *Science* **1995**, *268*, 1728-1731.
23. Cui, H., Chen, Z., Zhong, S., Wooley, K.L., Pochan, D.J., *Science* **2007**, *317*, 647-650.
24. Discher, D. E., Eisenberg, A., *Science*, **2002**, *297*, 967-973.
25. Feng Li, Mike Schellekens, Jens de Bont, Ron Peters, Ad Overbeek, Frans A. M. Leermakers, Remco Tuinier, *Macromolecules*, **2015**, *48*, 1194–1203.
26. Szymanski, C., Wu, C., Hooper, J., Salazar, M.A., Perdomo, A., Dukes, A., McNeill, J.D. *J. Phys. Chem. B*, **2005**, *109*, 8543-8546.
27. L. Zhang and A. Eisenberg, *J. Am. Chem. Soc.*, **1996**, *118*, 3168–3181.
28. Yiong Mai and Adi Eisenberg, *Chem. Soc. Rev.*, **2012**, *41*, 5969-5985
29. Y. Yu, L. Zhang and A. Eisenberg, *Macromolecules*, **1998**, *31*, 1144–1154.
30. Values selected from Hansen's 1971 parameters listed in Handbook of Solubility Parameters, Allan F. M. Barton. Ph.D., *CRC Press*, **1983**, 153-157.
31. Pösel, E., Schmidtke, C., Fischer, S., Peldschus, K., Salamon, J., Kloust, H., Tran, H. *ACS Nano*, **2012**, *4*, 3346–55.
32. Mark Wrighton, David L. Morse, Wrighton, M.; Morse, D. L., *J. Am. Chem. Soc.*, **1974**, *96*, 998– 1003.
33. Moore, Walter J., *Physical Chemistry*, 3rd Prentice-Hall, 1962, 140–142.
34. T. Azzam and A. Eisenberg, *Langmuir*, **2010**, *26*, 10513–10523.
35. K. T. Kim, J. Zhu, S. A. Meeuwissen, J. J. L. M. Cornelissen, D. J. Pochan, R. J. M. Nolte and J. C.M. van Hest, *J. Am. Chem.Soc.*, **2010**, *132*, 12522–12524.
36. Sang Hyuk IM, Unyong Jeong and Younan Xia, *Nature materials*, **2005**, *5*,671-675.
37. Ahonen, Kari V., Manu K. Lahtinen, Miika S. Löfman, Anniina M. Kiesilä, Arto M. Valkonen, Elina I. Sievänen, Nonappa, and Erkki T. Kolehmainen, *Steroids*, **2012**, *77*, 1141–1151

Chapter 4

Morphogenic effect of solvent mixture on aggregates of an amphiphilic platinum(II) complex

Abstract: This chapter describes the different morphologies of a platinum(II) complex in different solvent mixture. Relationship between the nature of the solvent mixture and the morphology of the aggregates was studied in detail. The photophysical properties of each of the platinum aggregates was explored and rationalised.

4.1. Introduction

Supramolecular chemistry represents a very important area in numerous research fields, including chemistry, biology, and materials science. One of the aims is the assembly from randomly oriented molecules to highly ordered supramolecular structures through covalent and non-covalent interactions¹. In particular, assemblies of amphiphilic molecules have attracted widespread attention due to their ability to form highly ordered aggregates with interesting morphologies in solution such as micelles, vesicles, and fibers via differential interactions of the hydrophilic and hydrophobic moieties with the solvent²⁻⁴. Amphiphilic vesicle forming polymers have been examined for their potential applications in drug delivery and as model systems of biomembranes⁵, while amphiphiles bearing organic chromophoric dyes have been investigated with the aim to construct highly ordered nanostructures for optoelectronic applications⁶. Most of the studies have been focused on the investigation of amphiphilic polymers and amphiphiles bearing organic chromophoric dyes, whereas amphiphilic transition metal complexes have been less explored⁷⁻¹¹. Numerous reports have explored the structure-property relationships influencing luminescent properties of square-planar Pt(II) complexes^{12,13}. These fundamental works have offered an understanding on how the luminescence of these systems can be tuned and used in a large variety of applications, including electroluminescent materials such as organic light emitting diodes (OLEDs)¹⁴, sensitizers for photovoltaic materials¹⁵ and biomolecule applications¹⁶. Factors that play a large role in influencing the luminescent properties of platinum (II) complexes include the platinum-platinum interactions, π - π stacking, and other intermolecular interactions that can lead to aggregation. Metal-metal interaction between platinum(II) complexes can be monitored and tuned by varying parameters such as temperature¹⁷, solvent¹⁸, mechanical forces¹⁹, or the presence of different counterions. These interactions are weak under standard conditions and sensitive to the surrounding environment. The formation of functional architectures, such as luminescent self-assembled 1D fibers and 2D structures with defined distances between metal centers of adjacent platinum (II) complexes, have been exploited to create electronic devices such as field effect transistors (FET) and semi conductors²⁰. Amphiphilic sulfonate-pendant platinum(II) complexes with different lengths of alkyl chains have been developed and studied for their luminescent properties²¹. The spectroscopic properties are found to be associated with the formation of self-assembled nanostructures. It

has been discovered that the introduction of an alkyl chain can have a drastic effect on controlling the molecular packing, resulting in sheet-like structures for short alkyl chains, and cylindrical micelles for long alkyl chains. The change in morphology can be rationalised by the different hydrophilic and hydrophobic interactions occurring between the amphiphilic molecule, the solvents and the interactions between two platinum (II) complexes. Amphiphilic anionic platinum(II) complexes have been investigated to show aggregation in water through platinum-platinum interaction and π - π stacking²². An interesting partial deaggregation-aggregation process and a morphological transformation from vesicles to fibers has been demonstrated upon variation of the solvent composition. Well-defined platinum (II) complex structures such as nanowires²⁰, tubes²¹, rod-like aggregates²³, sheet-like aggregates²¹, vesicles²² or rings²⁴ are commonly reported in the literature. Due to the rich spectroscopic and luminescence properties of square-planar d^8 platinum (II) complexes, it was envisaged that neutral amphiphilic platinum (II) complexes could be used to probe the formation of supramolecular assemblies and to also study the correlation between the morphological transformation and spectroscopic changes. In the previous chapter, a platinum(II) complex self-assembling into toroidal particles was observed in a THF/water mixture. The discovery of such an uncommon morphology for a platinum (II) complex motivated the work accomplished in this chapter. Indeed, although numerous morphologies have been reported previously, only two or three different aggregates were observed per platinum (II) complex¹²⁻²⁴. Herein, we report the preparation of several aggregates of a single amphiphilic platinum (II) complex and the changes upon variation of the solvent composition, mixture, method of mixing and concentration. The amphiphilic character of the complex allows the modification of the hydrophilic/hydrophobic interactions depending on the solvent conditions and is stabilized by platinum-platinum interactions and π - π stackings. The morphological changes are systemically controlled by electron microscopy and luminescence techniques. A comprehensive mechanism for the formation of the different aggregates of platinum(II) complexes is also proposed.

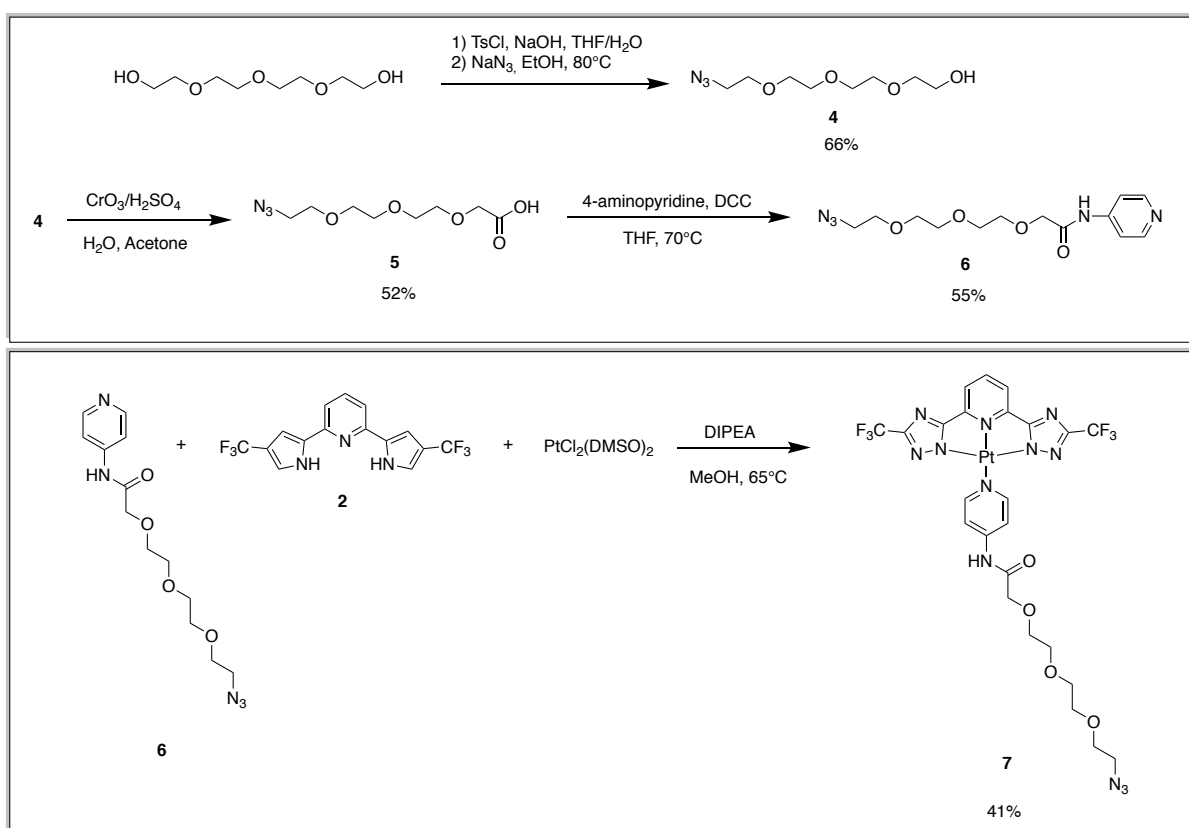
4.2. Results and discussion

The results and discussion section was divided in three parts. First, investigation of the self-assembly of the platinum(II) complex in THF/H₂O mixture at two different concentrations was carried out. Secondly, the rate and the order of addition of the two solvents were examined.

Finally, the relationship between the nature of the organic solvent and the aggregate morphology of the platinum (II) complex was also studied.

4.2.1. Synthesis of the complex

The synthetic route for the preparation of the platinum (II) complex was displayed in Scheme 4.1 and was previously discussed in Chapter 2.



Scheme 4.1. Synthetic route of ancillary ligand **6** and platinum (II) complex **7**.

4.2.2. Preparation of the platinum aggregates in THF/water mixture

The platinum (II) complex was dissolved in THF (concentration $\approx 1 \times 10^{-3} \text{ mol} \cdot \text{L}^{-1}$) and diluted to reach a final concentration of $5 \times 10^{-5} \text{ mol} \cdot \text{L}^{-1}$ in 10 mL of THF/H₂O mixture. The appropriate amount of THF was added and then distilled water was added dropwise (1 drop/10 s) while stirring until the final volume of the THF/ water solution was 10 mL as reported in Table 4.1. The solutions were stirred for 48 hours to prevent the appearance of transient morphologies and to negate the effect of the rate of stirring. To prepare aggregates, the complex was first dissolved in a common solvent (*e.g.* THF or DMF) and then a non-solvent (H₂O), for the platinum (II) complex, water, was added. As water was gradually added, the ability of the

organic solvent to solubilise the platinum(II) complex decreased. The aggregation began when the critical water content (CWC) was reached. The CWC is usually defined as the water content at which micellization starts for a polymer²⁵. The same principle can be applied for the amphiphilic platinum(II) complex as its self-assembly will start at a specific water content for any organic solvent/ water mixture. Since water is a good solvent only for the polyethyleneglycol chain, addition of water to the organic solvent forces the system to reorganize to avoid interactions between the platinum moiety of the complex and the H₂O molecules. At a certain point after the addition of water, the platinum (II) complex starts to aggregate and precipitation can occur as well as a change in color. In the early stages of aggregation, a thermodynamic equilibrium was operative between the monomers and the aggregates. As more water was added and the solvent progressively diffused out from the aggregate cores, the structure of the aggregates became kinetically frozen and do not change anymore²⁶. The self-assembly of platinum (II) complex in solution was observed by photophysical analysis in conjunction with electron microscopy. As a result of these experiments, parameters such as the rate, order of addition of the water to the complex/ THF solution and the concentration in platinum (II) complex were then investigated.

Solution	1	2	3	4	5	6	7	8	9	10	11
Volume of platinum(II) complex 7/THF solution	0.3	0.3	0.3	0.3	0.3	0.3	0.3	0.3	0.3	0.3	0.3
Added volume of THF	9.7	8.7	7.7	6.7	5.7	4.7	3.7	2.7	1.7	0.7	0
Added volume of H₂O	0	1	2	3	4	5	6	7	8	9	9.7
H₂O content (%)	0	10	20	30	40	50	60	70	80	90	97

Table 4.1. Volume of platinum(II) complex 7 solution, THF and water added to each solution in mL.

4.2.2.1. Photophysical characterisation

The CWC at which the platinum (II) complex started to aggregate was determined by photophysical analysis. Normalized emission and excitation spectra of the platinum (II) complex 7 in THF/ water solutions were displayed in Figure 4.1. From 0 to 65% water content,

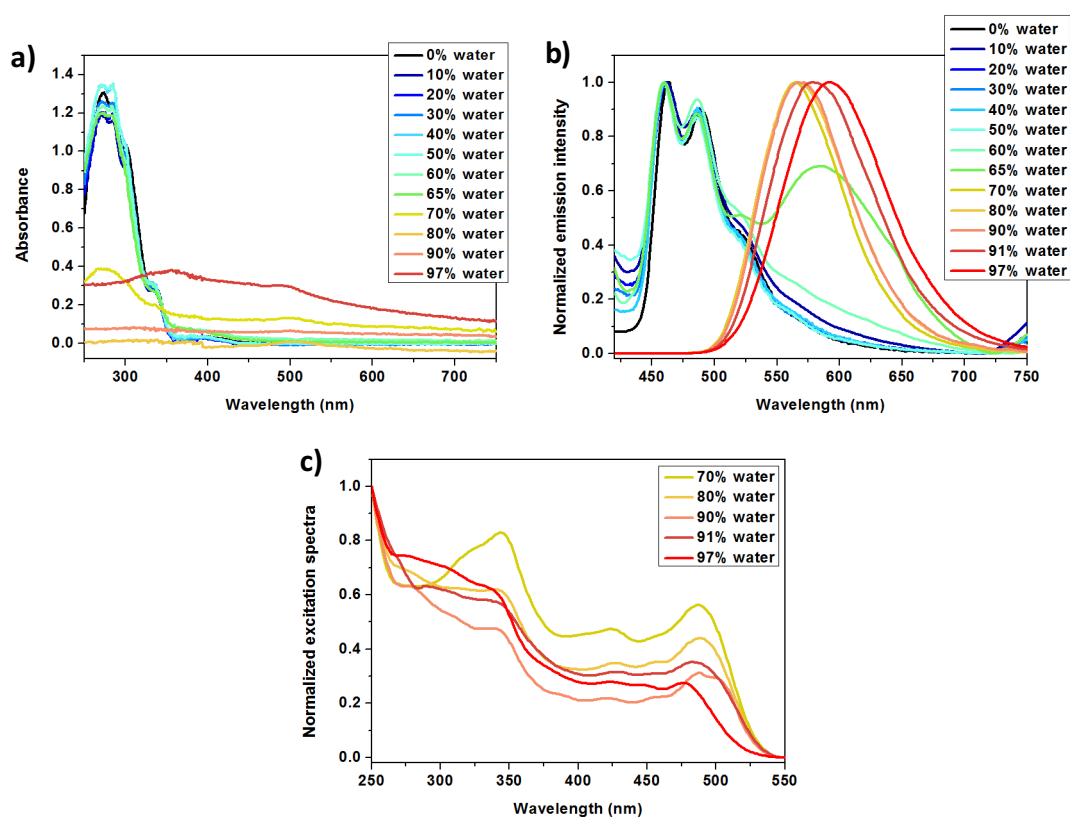


Figure 4.1. Absorption (a) and emission (b) and excitation (c) spectra of complex 7 in different THF/water mixture. $\lambda_{exc} = 300 \text{ nm}$, $\lambda_{em} = 570 \text{ or } 590 \text{ nm}$.

the absorption spectra clearly show intense bands between 270 and 320 nm, which can be attributed to a spin-allowed singlet ligand-centered (1LC) transition, involving mainly the $\pi-\pi^*$ transitions of the pyridine and the tridentate ligand of the complex. The broad weak band centered at 400 nm can be attributed to the energetically lowest-lying singlet metal-to-ligand charge transfer transition (1MLCT) involving the d orbitals of the platinum(II) and the π^* orbital of the ligand. The band at 340 nm can be attributed to a mixture of MLCT and LC transition. Above 65% water content, those bands disappear and only unstructured spectra were observed. This change in absorption was the result of the the aggregation of the platinum(II) complex in solution. From 0 to 60%, the emission spectra had identical profiles with structured bands at 460, 490 and 520 nm. The related transitions were mainly due to the contribution of the vibrational progression of a triplet ligand centered transition (3LC) and a weak triplet metal-to-ligand charge transfer transition (3MLCT). At 65% water content, a ground-state aggregation was present and evidenced by the broad Metal-Metal-to-Ligand Charge Transfer (3MMLCT) band between 550 and 600 nm, and the structured bands at 460, 490 and 520 nm.

Table 4.2. Photophysical properties of platinum (II) complex **7** in different THF/water mixture and morphology of aggregates observed by SEM. $\lambda_{em} = 300$ nm. Excited state lifetime values were measured at the maximum of emission in each solution.

Solvent mixture	Morphology	$\lambda_{em,max}$ (nm)	τ (ns)	PLQY
THF	amorphous	462, 490, 520 (sh)	3	< 0.01
10% water	amorphous	462, 490, 520 (sh)	3	< 0.01
20% water	amorphous	460, 490, 520 (sh)	3	< 0.01
30% water	amorphous	461, 490, 520 (sh)	3	< 0.01
40% water	amorphous	460, 490, 520 (sh)	3	< 0.01
50% water	amorphous	459, 490, 520 (sh)	3	< 0.01
60% water	amorphous	460, 490, 520 (sh), 560 (sh)	3	< 0.01
65% water	amorphous rods	460,490, 520, 584	5 (56%), 19 (39%), 53 (5%)	< 0.01
70% water	amorphous rigid fibers	565	410	0.60
80% water	rigid fibers	567	380 (96%), 840 (4%)	0.68
90% water	rigid fibers toroidal	572	380	0.61
91% water	small fibers toroidal	579	370 (19%), 555 (81%)	0.63
97% water	toroidal	592	530	0.67

At 70% and above water content, only the 3 MMLCT band was observed in the emission profiles, which was proof of the presence of the platinum (II) complex aggregates. It is also worth noting that this 3 MMLCT band is red-shifted upon increasing the water content from 70% to 97% meaning possible change in the aggregation state of the platinum(II) complex. In order to complete the photophysical study, and to overcome the difficulty of obtaining information from the absorption spectra of the aggregates, excitation spectra of the different

solutions were performed (refer to Figure 4.1c). The spectra show the presence of broad bands between 400 and 550 nm, attributed to the ¹MMLCT due to the aggregation of the platinum (II) complex. The red-shift observed in emission when the water content is above 70% can be correlated to a decrease in intensity of the ¹MMLCT bands in excitation and a possible change in conformation upon increasing the water content. Finally, excited state lifetimes and photoluminescent quantum yields (PLQY) were also measured and reported in Table 4.2. Below 70% water content, the excited state lifetimes and photoluminescent quantum yields are similar to those observed in pure THF when the platinum (II) complex molecularly dissolved in solution. Above 70% water content, long excited lifetimes were measured between 380 ns and 550 ns due to the aggregated state of the platinum(II) complex in solution. An increase of those lifetimes was also observed upon increasing the water content, which is in correlation with the red-shift observed in emission. Some of those lifetimes, especially those at 91% water content (a combination of the lifetimes from 80% and 97% water content), have a bi-exponential decay. This may be another indication of the presence of at least two different types of aggregates of the platinum (II) complex. The photoluminescence quantum yield of the molecularly dissolved platinum (II) complex is below 1% at the integrating sphere, while those of the aggregates are between 60% and 70%. Such an increase of the overall photophysical properties of the platinum (II) complex is the result of the platinum-platinum interactions leading to MMLCT transition with longer lifetimes and higher quantum yields.

4.2.2.2. Study of the morphology of the platinum (II) complex aggregates

Direct observations of the morphologies were made by scanning electron microscopy (SEM) and scanning transmission electron microscopy (STEM). For samples with water contents below 60%, the morphologies observed by SEM are the results of solvent evaporation off the SEM glass coverslip and do not represent the morphologies in solution (Figure 4.2). The photophysical properties have previously demonstrated that the platinum (II) complex is molecularly dissolved below 65% water content. The complex organizes itself into amorphous aggregates between 10% to 50% water content. It is worth observing that close to the CWC (60% water content), a honeycomb pattern was observed on the SEM glass coverslip. At 65% water content where the first ³MMLCT band was observed in emission, rod-like aggregates and some amorphous materials were observed on SEM. A further increase of H₂O (to 70%

water content) led to the formation of long and rigid fibers surrounded by the remaining amorphous material.

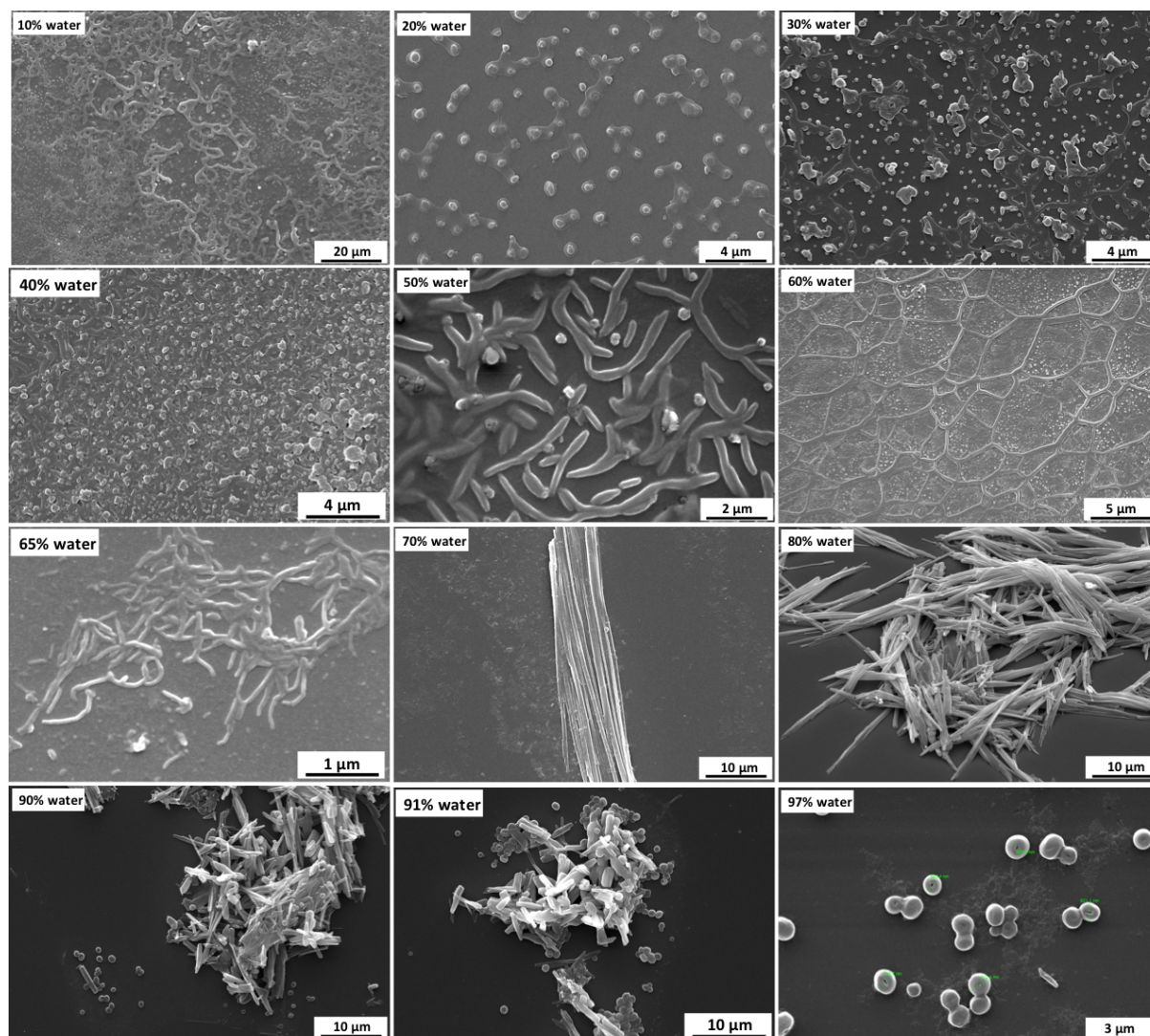


Figure 4.2. SEM images of the platinum(II) complex in THF/ water mixture after drop casting on glass slide and evaporation of the solvents for water content below 60%.

As more water was added, only rigid fibers were observed (80% water content), whereas at 90% water content the formation of toroidal aggregates was characterized by an average size of 729 ± 91 nm. The number and size of fibers decreased while the number of toroidal particles increased until a full population of tores was observed (at 97% water content).

Table 4.2 summarises the morphologies and the photophysical properties of the platinum (II) complex aggregates formed in solutions in different H₂O contents.

Finally, the correlation between the photophysical properties and SEM imaging was confirmed by fluorescence confocal microscopy. The solution was excited with a 405 nm laser (refer to

Figure 4.3). For clarity, the amorphous materials were colored in green, the fibers in yellow and the toroids in orange. The honeycomb pattern was observed at 60% water content and the formation of the fibers at 70% water content. The morphological changes of the fibers from 80 to 90% was observed under confocal microscopy. At 97% water content, the toroidal particles were observed throughout all the samples.

While the formation of fibers from platinum(II) complexes have previously been described in the literature^{27,28}, large toroidal aggregates with enhanced photophysical properties are yet to be reported. Figure 4.4 summarizes the different aggregates of complex 7 observed at different water content. Upon increasing the water content to above 90%, there was configuration of toroidal particles and the formation of the platinum-platinum and π - π stacking interactions, indicated by the presence of ³MMLCT emission and excitation bands. Moreover, the presence of hydrophobic-hydrophobic interactions in highly polar solvent mixture would stabilize the toroidal aggregates²⁴. A slight decrease of the water content to 80% resulted in the formation of fibers with the alignment of platinum(II) complexes resulting in metallophilic interactions. It is also believed that decreasing the polarity of the mixture (decreasing the water content) would gradually transform the toroidal particles to fibers. This theory was supported by the presence of a mixture of toroidal particles and fibers at 90% and 91% water content in the SEM images of Figure 4.2.

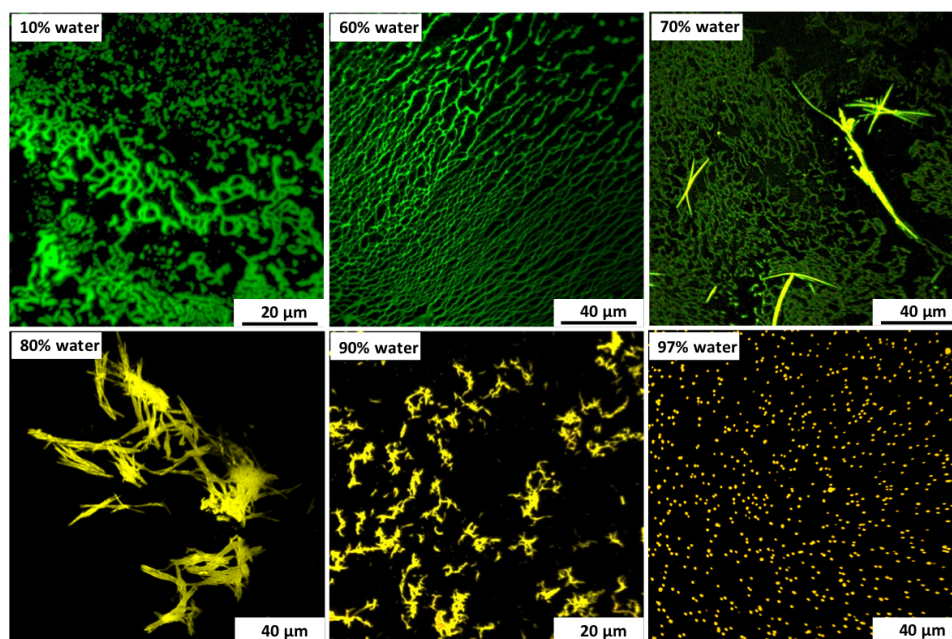


Figure 4.3. Confocal fluorescence images of platinum (II) complex aggregates in different THF/water mixtures with a platinum (II) complex concentration of $5 \times 10^{-5} M$. $\lambda_{exc} = 405 \text{ nm}$. False colours.

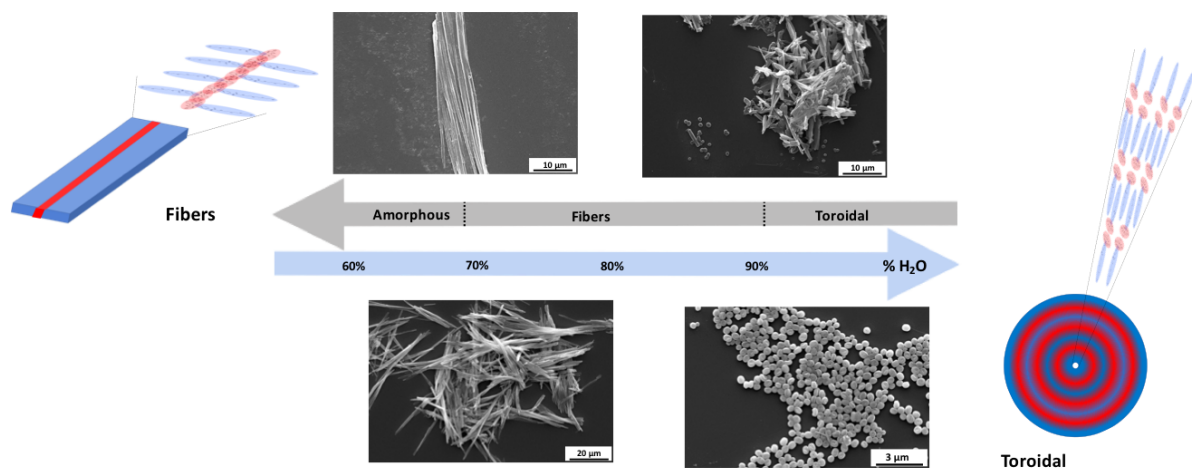


Figure 4.4. Schematic representation of the self-assembly of platinum (II) complex in THF/water mixtures and observed morphologies. The red area indicates the platinum-platinum interactions and the blue area indicates the polyethylene glycol ancillary ligand interacting via hydrogen bonding.

4.2.2.3. Stability upon dilution in water

In order to study the stability of the platinum (II) complex aggregates and observe the thermodynamically stable aggregates, the previously prepared solutions were diluted in water. 100 μL of each solution was diluted by adding 900 μL of water. As a result, the water content was increased from 10% to 91%, 20% to 92%, etc. It is expected that the previously formed fibers and toroidal particles will maintain their morphological integrity upon dilution. However, when complex **7** was molecularly dissolved in the THF/water mixture (below 70% water content), new types of aggregates were formed as a result of the the dilution in water which increased the overall water content of the mixture.

Photophysical properties

The normalized emission and excitation spectra for each solution were measured and are displayed in Figure 4.5.

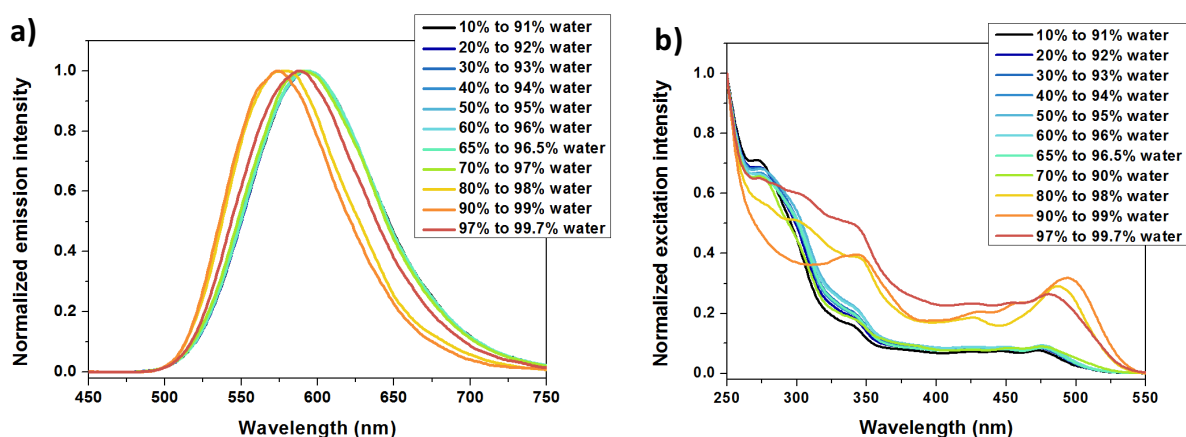


Figure 4.5. a) Emission and b) excitation spectra of the platinum (II) complex diluted 10 times in water. $\lambda_{exc} = 300$ nm, $\lambda_{exc} = 570$ or 590 nm, depending on the sample.

The emission of all diluted solutions are dominated by the $^3\text{MMLCT}$ band due to the platinum-platinum interaction. The dilution of solutions consisting of a water content below 70% triggered the self-assembly of the platinum (II) complex. The dilution of the solutions above 70% water content did not appear to affect the emission properties, which suggested that the aggregates formed prior to dilution maintained their morphologies in solution. The excitation spectra of the aggregates revealed significant data. Although the emission spectra show the $^3\text{MMLCT}$ band centered around 570 or 590 nm, the excitation spectra were quite different. It has been previously reported that at 80% water content, the platinum (II) complex tends to form rigid fibers, showing an emission at 565 nm and excitation bands between 400 and 550 nm, attributed to $^1\text{MMLCT}$. At 97% water content, platinum (II) complex tends to self-assemble into toroidal aggregates with an emission centered at 590 nm and less intense excitation bands compared to the platinum (II) complex fibers. Finally, the emission band was centered at approximately 590 nm for the newly formed aggregates in diluted solutions with initial water contents below 70%. However, the excitation bands between 400 and 550 nm were very weak compared to those from the fiber or the toroidal morphologies. All of the photophysical properties of the diluted solutions are reported in Table 4.3.

Table 4.3. Photophysical properties of platinum (II) complex in diluted THF/water mixtures and the morphologies of the aggregates observed by SEM. $\lambda_{em} = 300$ nm. Excited state lifetimes were measured at the maximum of emission of each solution.

Solvent mixture	Morphology	$\lambda_{em,max}$ (nm)	τ (ns)
10% → 91% water	small tores	593	680
20% → 92% water	small tores	592	630
30% → 93% water	small tores	592	620
40% → 94% water	small tores	593	480 (25%), 660 (75%)
50% → 95% water	small tores small fibers	593	330 (11%), 615 (89%)
60% → 96% water	small tores cylinders rods	593	280 (12%), 600 (88%)
70% → 97% water	small tores fibers	590	330 (48%), 630 (52%)
80% → 98% water	fibers	580	330 (83%), 540 (17%)
90% → 99% water	fibers toroids	574	345 (92%), 650 (8%)
97% → 99.7% water	toroidal	589	350 (56%), 560 (44%)

Study of the morphology of the platinum (II) aggregates

To assess the morphology of the aggregates, aliquots of the diluted solutions were drop-casted onto glass slides for SEM, then onto a copper grid for STEM, and left to dry. The different morphologies observed are shown in Figure 4.6. Dilution of the initial 10% to 50% water content solution in water resulted in a drastic increase of the water content (from 10% to 91%, 50% to 95% water content) and the formation of small toroidal aggregates, uniform in size and appearance. The outside diameters of the aggregates were measured to be 225 ± 27 nm and 233 ± 17 nm via SEM and STEM, respectively, while the cross-section diameters were measured to be 94 ± 14 nm (by SEM) and 92 ± 11 nm (by STEM). Dilution of the 50%

water solution in water led to the formation of a mixture of small toroidal aggregates and small rigid fibers. Interestingly, the dilution of 60% water led to the formation of a mixture toroidal aggregates, rods and, more surprisingly, cylinders and fan-shaped aggregates. Those morphologies were observed by SEM and more precisely by STEM in Figure 4.7. The rods observed by SEM and STEM had uniform diameters but various lengths. The diameter was measured to be 71 ± 7 nm on the SEM images and 51 ± 7 nm on the STEM images. These differences can be accounted for by the layer of silver sputtered on the sample for the SEM imaging. Furthermore, the diameter of the rods was almost two times smaller than the diameter of the small toroidal aggregates. This may suggest that the formation of those rods is due to the elongation and stretching of the toroidal aggregates. On the SEM (top left) and STEM (top right) picture in Figure 4.7 (top-left), rod-like aggregates connected to its ends (to form a loop-like shape) can be observed. As mentioned above, spherical cylinders and fan-shaped cylinders can be observed with an average length of 485 ± 68 nm and width of 300 ± 50 nm. Some organized patterns can be observed within the different cylinders, although further work is needed to clarify their nature. The various morphologies and dimensions were reported in Table 4.4. The size of the aggregates was measured on the SEM and STEM images and the average value of 30 aggregates was calculated. It is worth noting that the outside diameter of the larger toroidal aggregates is approximately three times higher than the outside diameter of the smaller toroidal aggregates. Upon dilution, the concentration of complex 7 is divided by 10. As a consequence, the outside diameters and the number of toroidal aggregate layers decreases with the concentration.

Dilution of THF/H₂O mixtures containing fibres and toroidal aggregates (*e.g* 70% H₂O content and above) did not affect the morphology of the aggregates. The presence of small toroidal aggregates along with rigid fibers verify the fact that the fibers retain their morphology while the amorphous aggregates self-assembled into smaller aggregates. The dilution of the platinum (II) complex in THF/water mixture enabled the formation of new morphologies with enhanced photophysical properties, and the testing of the stability of the pre-formed aggregations before dilution.

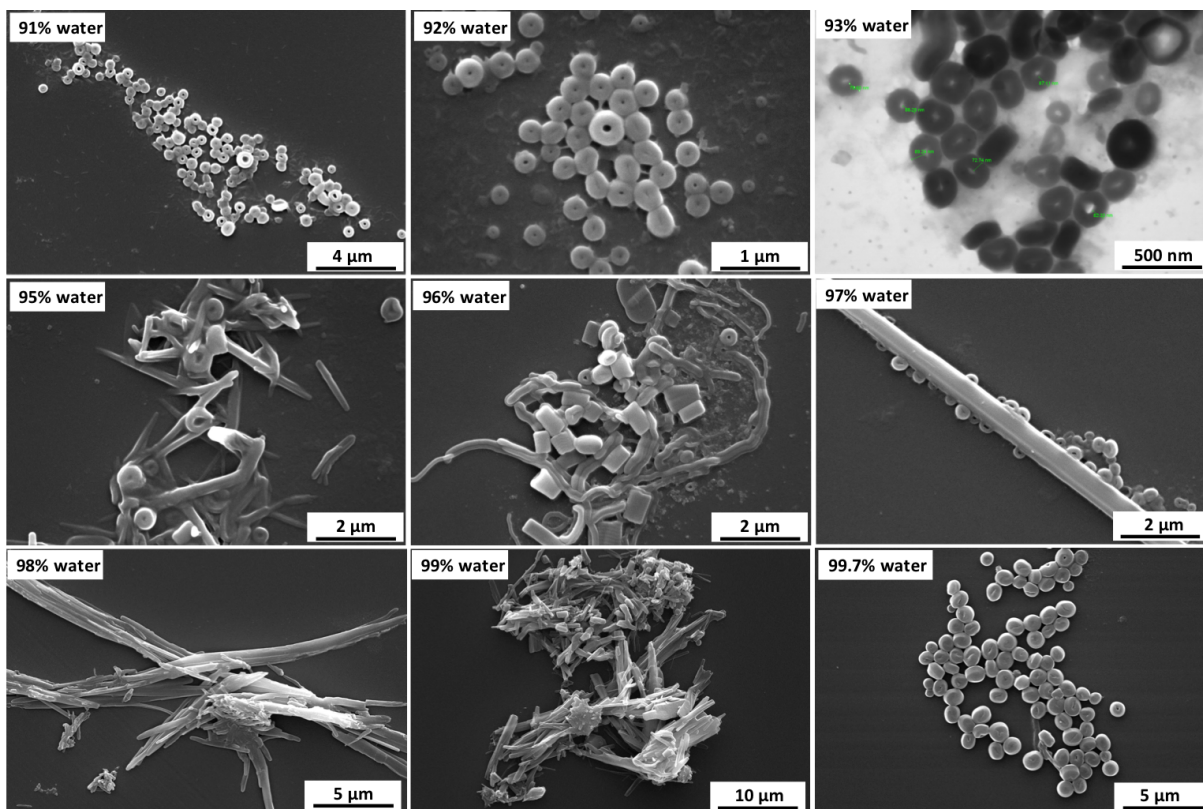


Figure 4.6. SEM and STEM images of the platinum(II) complex aggregates after dilution in water.

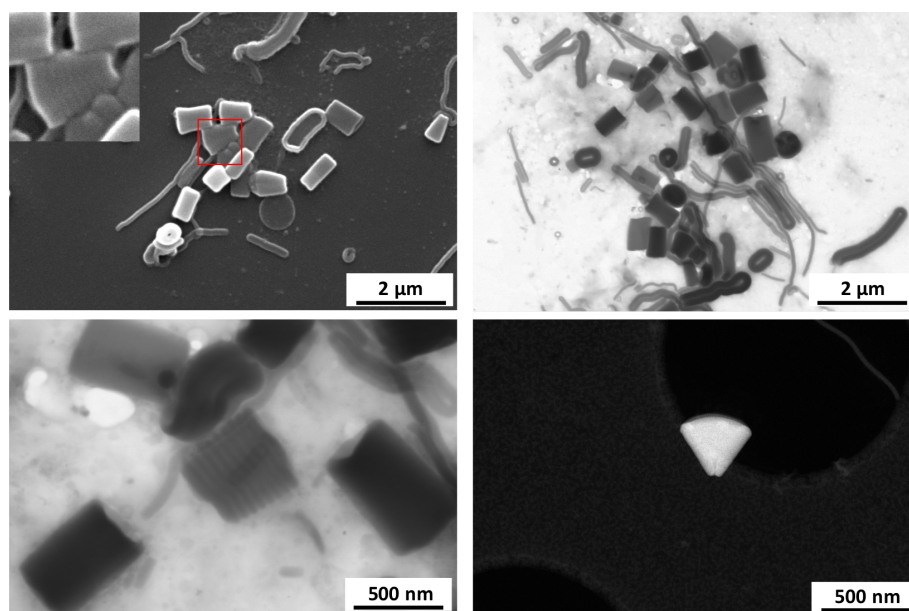


Figure 4.7. SEM and STEM images of the platinum (II) complex cylinders, rods and fan-shaped morphologies observed in diluted 60% water content solution.

Morphology	Method	Outside diameter (nm)	Cross section diameter (nm)
Large tores	SEM	729 ± 91	-
Small tores	SEM	225 ± 27	94 ± 14
	STEM	233 ± 17	92 ± 11
rods	SEM	71 ± 7	-
	STEM	51 ± 7	-
cylinders	STEM	485 ± 68 (length)	
		300 ± 50 (width)	

Table 4.4. Various platinum (II) complex aggregates observed upon dilution in water and their average dimensions.

4.2.3. Effect of the concentration on the self-assembly properties of the platinum (II) complex

The initial concentration of complex **7** in THF can play an important role in the self-assembly of the platinum (II) complexes in THF/water mixtures²⁹. The complex was dissolved in THF ($\approx 1 \times 10^{-3} \text{ mol.l}^{-1}$) and then poured into different vials in order to obtain a predetermined final concentration of $5 \times 10^{-6} \text{ mol.l}^{-1}$ in 10 mL of THF/water mixture. The solutions were stirred for 48 hours to prevent the appearance of transient morphologies and to negate the effect of the rate of stirring. The photophysical properties are shown in Figure **4.8** and Table **4.5**. The CWC was not influenced by the change of the platinum (II) complex concentration. The self-assembly was triggered between 60% and 70% water content solutions and correlated with the shifting of the emission bands from ³LC/MLCT (below 70%) to ³MMLCT (above 70%) in the emission spectra. A red-shift was also observed upon increasing the water content to 97%. These results are consistent to those reported previously and suggest that the aggregates have transformed morphologically. There was a significant increase of the excited state lifetimes, from 3 ns to 380 ns, which suggested the formation of aggregates between 60% and

70% water content. The morphological transformation from fibers to toroidal particles at above 90% water content resulted in an increase of the excited state lifetime from 380 to 560 ns.

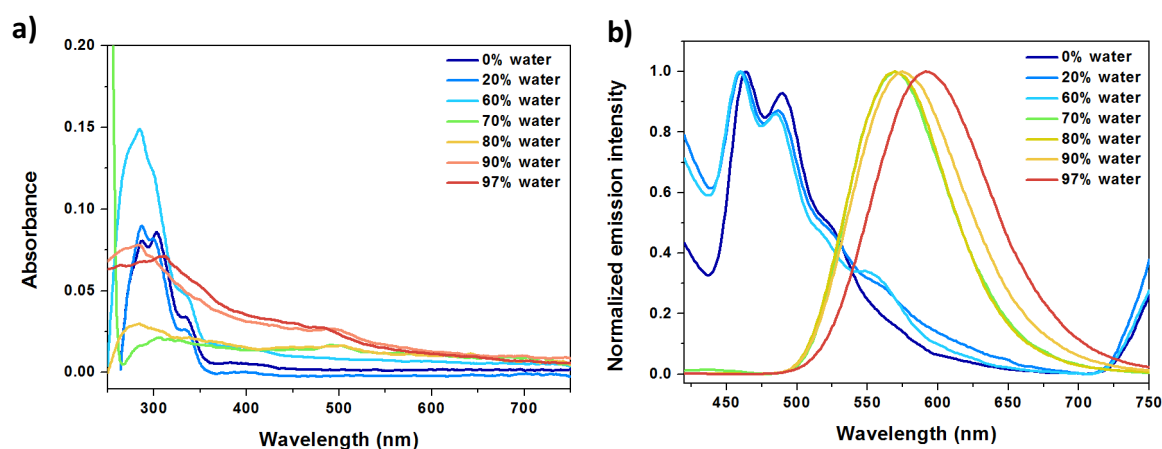


Figure 4.8. a) Emission and b) excitation spectra of the platinum(II) complex in THF/water mixture. $\lambda_{exc} = 300$ nm, $\lambda_{exc} = 570$ or 590 nm.

Table 4.5. Photophysical properties of platinum (II) complex in different THF/water mixtures and morphologies of the aggregates observed by SEM. $\lambda_{em} = 300$ nm. Excited state lifetimes were measured at the maximum of emission of each solution.

Solvent mixture	Morphology	$\lambda_{em,max}$ (nm)	τ (ns)
THF	amorphous	464, 490, 520 (sh)	3
10% water	amorphous	460, 489, 520 (sh)	3
20% water	amorphous	459, 490, 520 (sh)	3
30% water	amorphous	461, 489, 520 (sh)	3
40% water	amorphous	461, 490, 520 (sh)	3
50% water	amorphous	460, 491, 520 (sh)	3
60% water	amorphous	460, 490, 520 (sh)	3
70% water	rigid fibers	570	380 (97%), 910 (3%)

80% water	rigid fibers	570	365 (97%), 860 (3%)
90% water	toroidal particles	575	350 (80%), 585 (20%)
	rigid fibers		
97% water	toroidal particles	591	315 (10%), 560 (90%)

SEM images of the dropcasted solution are displayed in Figure 4.9. At 70% water content, platinum(II) complex self-assembled into fibers with a small amount of amorphous material. At 80% water content, rigid fibers were formed. At 90% water content, a mixture of fibers and small toroidal aggregates were formed. Finally, at 97% water content, mainly small toroidal particles were formed. Decreasing the concentration in platinum(II) complex in the final THF/water mixture did not affect the nature of the aggregates (fibers or toroidal aggregates). The only noticeable difference was a significant decrease of the size of the toroidal particles from ca. 730 nm ($c = 5 \times 10^{-5}$ M) to 230 nm ($c = 5 \times 10^{-6}$ M).

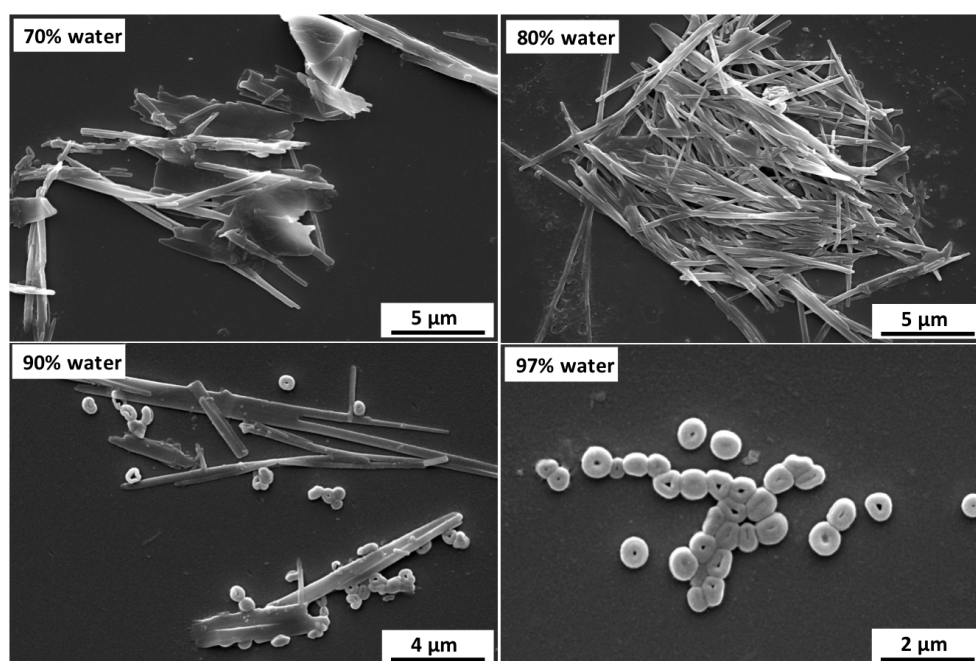


Figure 4.9. SEM images of the platinum(II) complex in THF/ water mixture after drop casting on glass slide and evaporation of the solvents.

4.2.4. Effect of the rate of addition

The effect of the rate of addition of water to the solution of platinum(II) complex in THF was examined in this section. Instead of gradually adding the water, e.g 1 drop/10 s, the water was flash-injected via a syringe into the platinum (II) complex/THF solution while stirring. The

different solutions were stirred for 48 hrs prior to the photophysical study, SEM, STEM and confocal imaging. The photophysical properties of each solution were reported in Figure 4.10 and Table 4.6. The CWC, at which the platinum (II) complex starts to self-assemble, was determined by UV-vis and emission spectroscopy. As previously reported, the aggregation can be followed by the change in emission from $^3\text{LC/MLCT}$ to $^3\text{MMLCT}$. This transition occurred between 60% and 70% water content. Flash-injecting water instead gradual addition to the THF solution does not affect the CWC. The emission spectra did not vary considerably from gradual addition to flash-injection. The only observable change was a higher photoluminescent quantum yield at 97% water content upon flash-injection (77%) compared to gradual addition (67%).

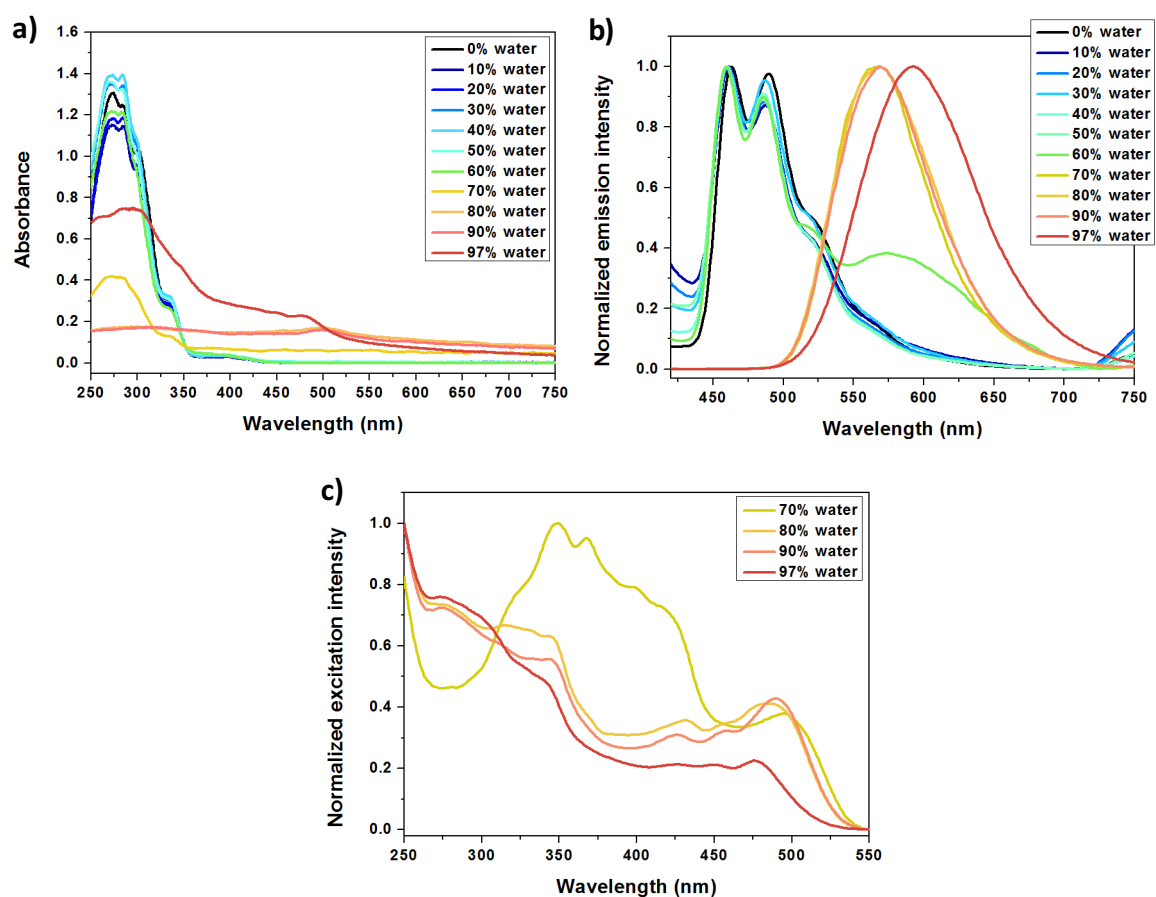


Figure 4.10. Absorption (a) and emission (b) and excitation (c) spectra of the platinum(II) complex in different THF/water mixture. $\lambda_{em} = 300 \text{ nm}$, $\lambda_{exc} = 570\text{-}590 \text{ nm}$.

Electron and confocal microscopy enabled the study of different types of platinum (II) complex aggregates formed at various THF/water mixtures. As previously reported, the CWC was reached between 60% and 70% water content. Prior to that, mainly amorphous morphologies

were observed after the evaporation of the solvents on the SEM glass coverslips (refer to Figure 4.11). The honeycomb pattern was also observed at 60% water content, when the water was added gradually or flash-injected in THF. At 70% water, long rigid fibers were observed surrounded by amorphous materials. At 80% water content, fibers were mainly observed. It was observed that some of the fibers formed by flash-injection were wider (up to 5 μm) and thinner, and almost transparent. At 90% water content, long and rigid fibers were replaced by a mixture of smaller, less flexible fibers and rods. Finally, at 97% water content, mainly small, entangled rod-like aggregates were observed on the SEM. The effect of the rate of addition of water on the platinum (II) was not negligible as it enabled the formation of fibers of various morphological properties.

Table 4.6. Photophysical properties of platinum (II) complex in different THF/water mixtures and the morphologies of the aggregates observed by SEM. $\lambda_{em} = 300 \text{ nm}$. Excited state lifetime were measurements at the maximum of emission of each solution.

Solvent mixture	Morphology	$\lambda_{em,max}$ (nm)	τ (ns)	PLQY
THF	amorphous	462, 490, 520 (sh)	3	< 0.01
10% water	amorphous	462, 490, 520 (sh)	3	< 0.01
20% water	amorphous	460, 490, 520 (sh)	3	< 0.01
30% water	amorphous	461, 490, 520 (sh)	3	< 0.01
40% water	amorphous	460, 490, 520 (sh)	3	< 0.01
50% water	amorphous	459, 490, 520 (sh)	3	< 0.01
60% water	amorphous	460, 490, 520 (sh), 574	3	< 0.01
70% water	amorphous fibers	567	410	< 0.01
80% water	fibers	568	380 (96%), 840 (4%)	0.68
90% water	fibers rods	569	380	0.64
97% water	small rods	592	530	0.77

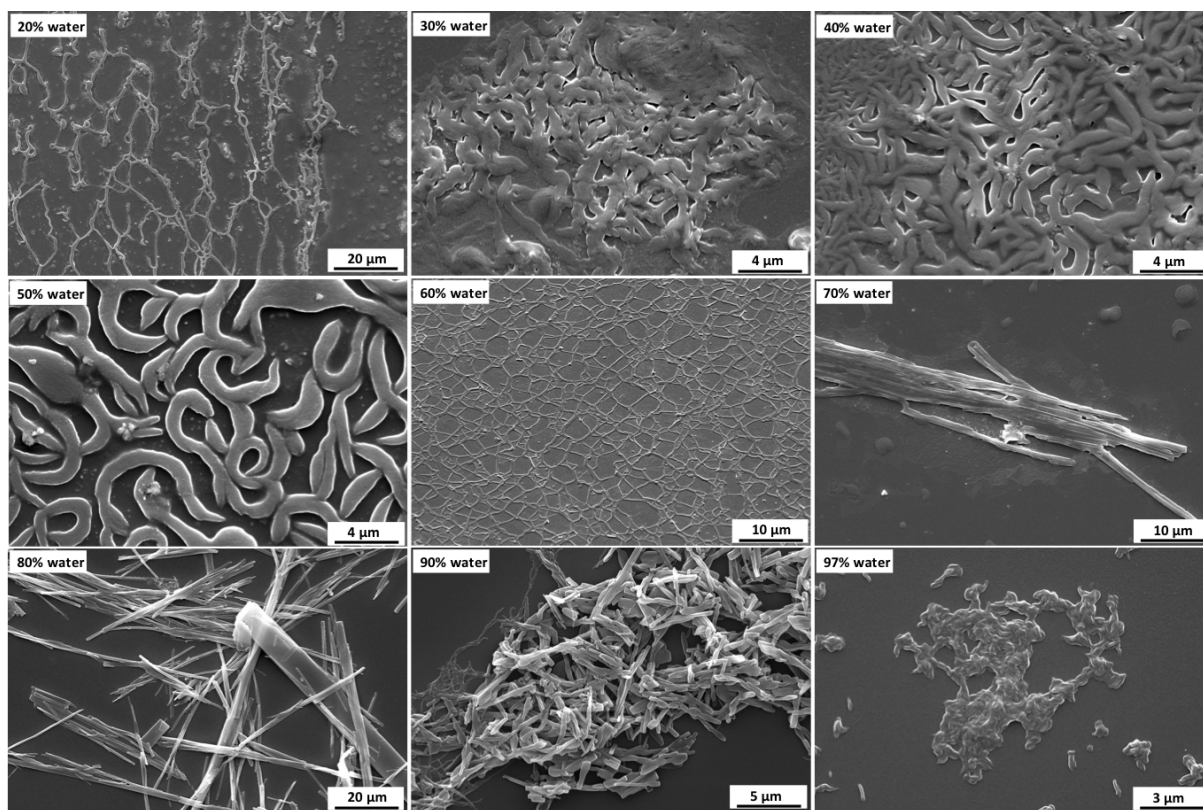


Figure 4.11. SEM images of the platinum (II) complex in THF/water mixtures after drop casting onto glass slides and the evaporation of the solvents

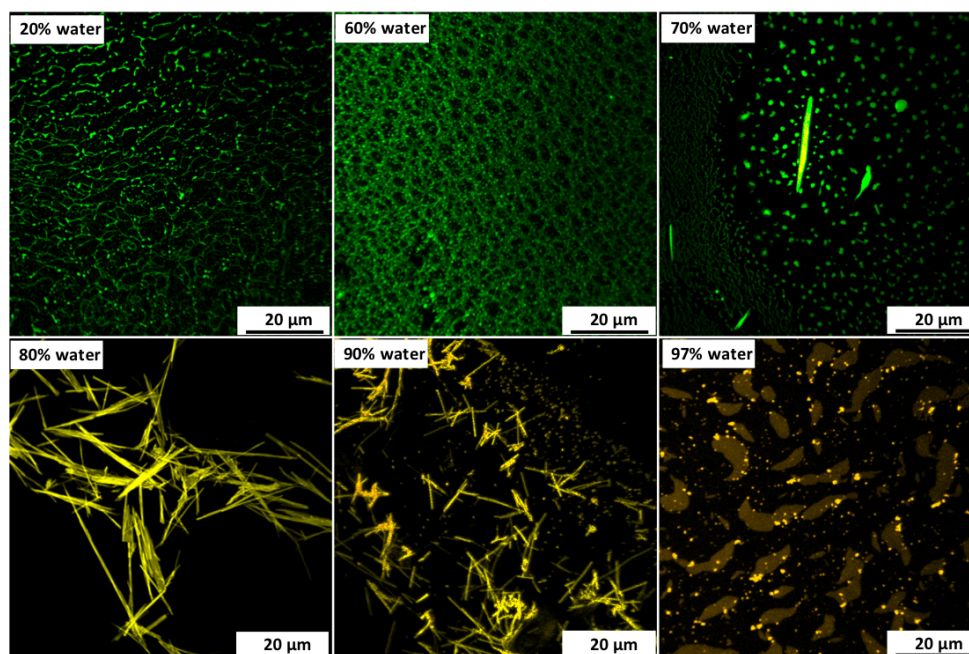


Figure 4.12. Confocal images of the platinum (II) complex aggregates in THF/water mixtures. $\lambda_{exc} = 405 \text{ nm}$. False colors.

Moreover, rod-like aggregates were formed instead of toroidal particles at 97% water content. The morphologies of the aggregates observed by SEM and their photophysical properties were reported in Table 4.6. Confocal fluorescence microscopy was also performed in order to correlate the photophysical properties and the morphologies. For optimal clarity, the amorphous materials were colored in green, the fibers in yellow and the toroidal-aggregates in orange, as shown in Figure 4.12

As expected, the fibers were observed at 70% water content, surrounded by amorphous aggregates. At 80% water content, only long fibers were observed whereas shorter fibers and rod-like aggregates were observed at 90% water content. Finally, at 97% water content, bundles of entangled rods are mainly observed. The morphology of the platinum (II) complex and the conditions required to obtain them were summarised in Figure 4.13. Platinum fibers were formed, when the water was either flash-injected or gradually added to the THF/complex 7 mixture, between 60% and 80% water content. However, rod-like aggregates were formed instead of the toroidal particles in above 90% water content solutions. In such conditions, the platinum (II) complex self-assemble into aggregates and do not evolve. The rods can be considered as kinetically trapped aggregates at high water contents. When the polarity of the solvent is slightly decreased, the rods are no longer frozen in solution and can reorganize into a more favourable morphology. This accounts for the presence of a mixture of rods and fibers at 90% water content and the complete transformation from rods to fibers at 80% water content.

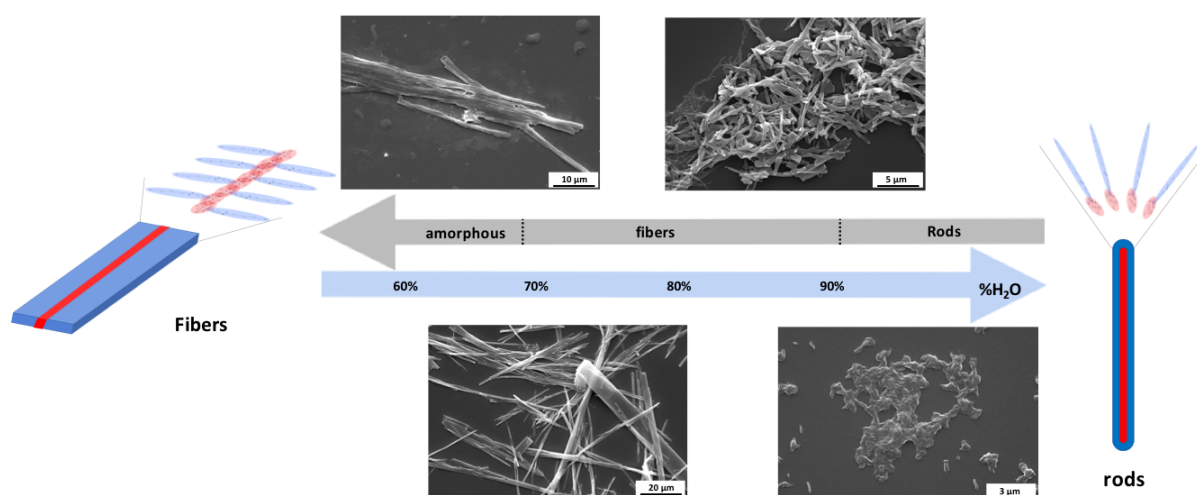


Figure 4.13. Schematic representation of the self-assembly of platinum (II) complex in THF/water mixture and the observed morphologies of the aggregates.

Stability upon dilution in water

In order to study the stability of the previously reported morphologies, 100 μL of each solution was diluted in 900 μL of water. The emission and excitation spectra of the diluted solutions are displayed in Figure 4.14 and the excited state lifetimes reported in Table 4.7. The SEM images are depicted in Figure 4.15.

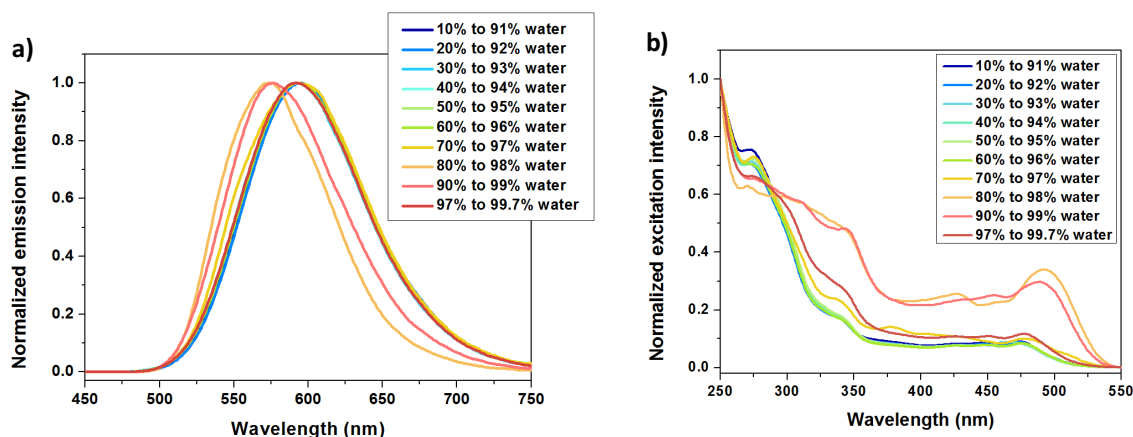


Figure 4.14. a) Emission and b) excitation spectra of the platinum(II) complex diluted 10 times in water. $\lambda_{exc} = 300 \text{ nm}$, $\lambda_{exc} = 570 \text{ or } 590 \text{ nm}$.

Table 4.7. Photophysical properties of platinum(II) complex in different THF/water. $\lambda_{em} = 300 \text{ nm}$. Excited state lifetimes were measured at the maximum of emission of each solution.

Solvent mixture	Morphology	λ_{max} (nm)	average lifetime
10% \rightarrow 91% water	rods small tores	594	655
20% \rightarrow 92% water	small tores	595	630
30% \rightarrow 93% water	small tores	593	310 (9%), 640 (91%)
40% \rightarrow 94% water	small tores cylinders rods	592	450 (13%), 660 (87%)
50% \rightarrow 95% water	small tores cylinders rods	593	305 (11%), 610 (89%)
60% \rightarrow 96% water	small tores cylinders rods	594	290 (8%), 640 (92%)

70% → 97% water	rods small toroidal aggregates	595	330 (33%), 630 (67%)
80% → 98% water	fibers	574	360 (96%), 800 (4%)
90% → 99% water	rods	576	320 (56%), 530 (44%)
97% → 99.7% water	small rods	592	130 (12%), 580 (12%)

As expected, the morphologies and photophysical properties of the previously formed aggregates were retained upon dilution (initial water content above 70%). The dilution enabled the superior visualisation of the brittle and semi-transparent fibers at 98% water content. Rod-like aggregates of the same diameter but various lengths were observed at 99% water content. Below 70% water content, small toroidal particles, rod-like aggregates, and spherical cylinders were observable by SEM.

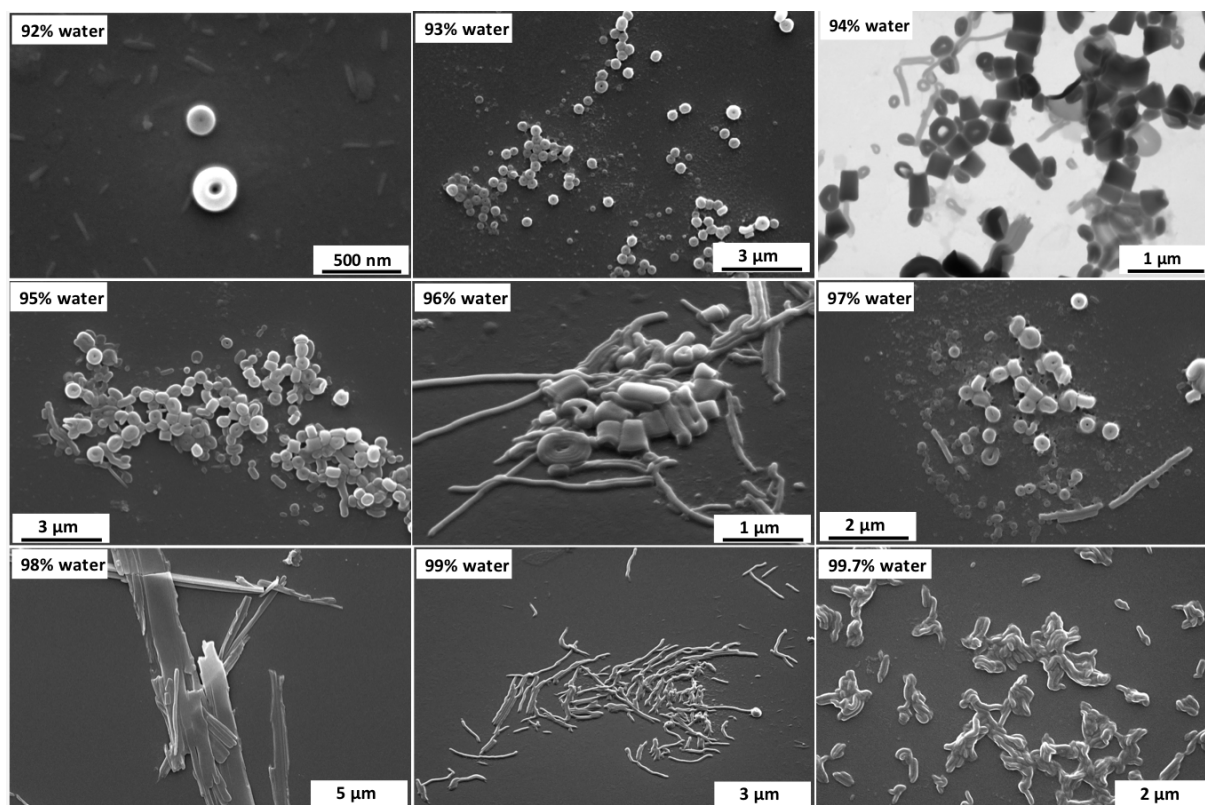


Figure 4.15. SEM and STEM images of the platinum (II) complex aggregates after dilution in water.

4.2.5. Study of the morphology of the fibers at 80% water content via gradual-addition and flash-injection methods.

As previously mentioned, the morphology of the platinum (II) complex fibers formed from flash-injection or gradual addition of water at 80% water content were a little dissimilar despite the fact that their photophysical properties were identical, as shown in Figure 4.16. When the water was gradually added to THF while stirring, long, sharp and rigid fibers were principally formed. However when flash-injection was conducted, a mixture of long, sharp fibers and wider, semi-transparent fibers were formed.

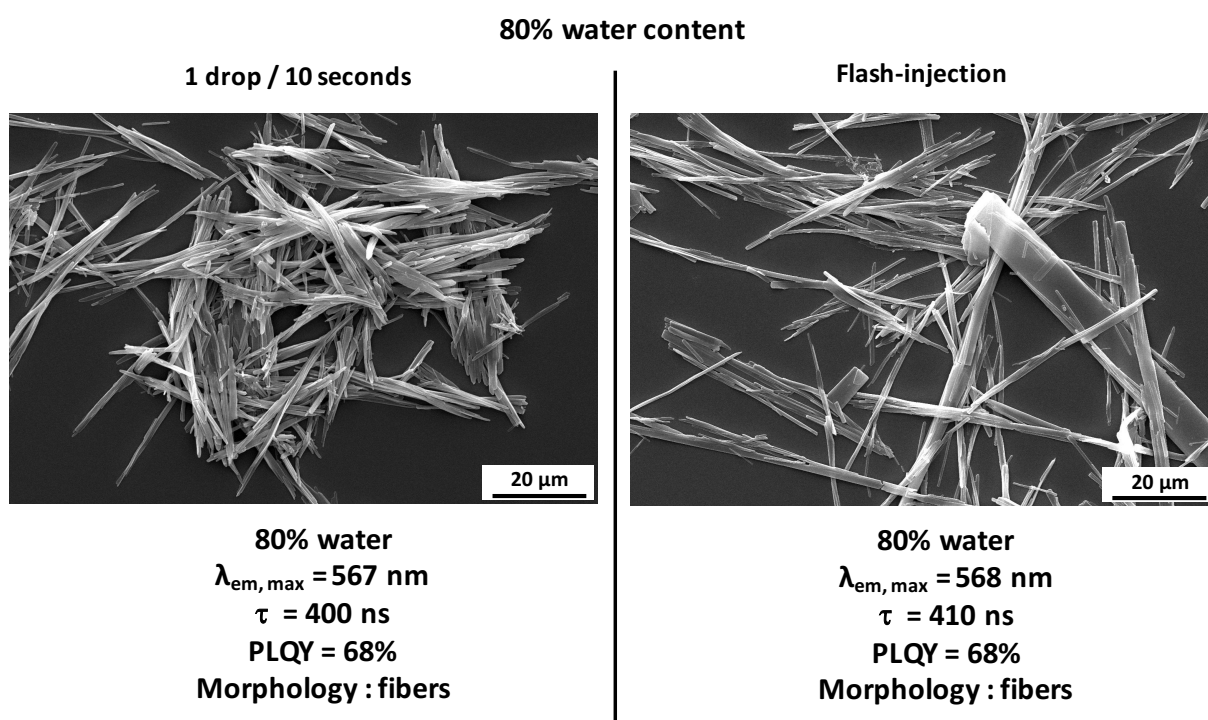


Figure 4.16. Morphology and photophysical properties of the two kind of platinum(II) fibers formed at 80% water content in THF/ water mixture.

To further study those fibers, the two solutions were left at ambient temperature while stirring to specifically remove the THF by evaporation for 48 hrs. The removal of the organic solvent enabled the growth of the fibers. The SEM images of the two types of fibers are displayed in Figures 4.17 to 4.18. In the first case, with the gradual addition of water; long, robust and thick fibers were obtained . In the second case, when the water was flash-injected ; thin, long and almost transparent ribbons were primarily observed along with robust fibers. It is worth noting that those fibers were very brittle when they did not lay flat on the substrate.

In Figure 4.18, breaking points could be observed any point in time when those fibers were in contact with the robust fibers. It was then possible to manipulate not only the photophysical properties of the platinum (II) complex aggregates but also the mechanical properties of the fibers formed at 80% water content.

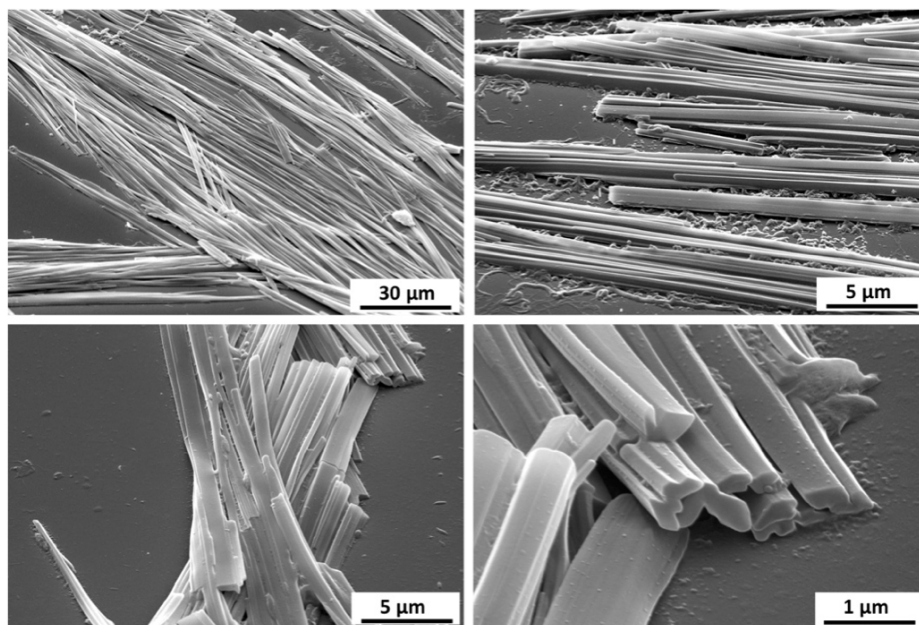


Figure 4.17. SEM images from the fibers obtained by gradual addition after evaporation of the organic solvent

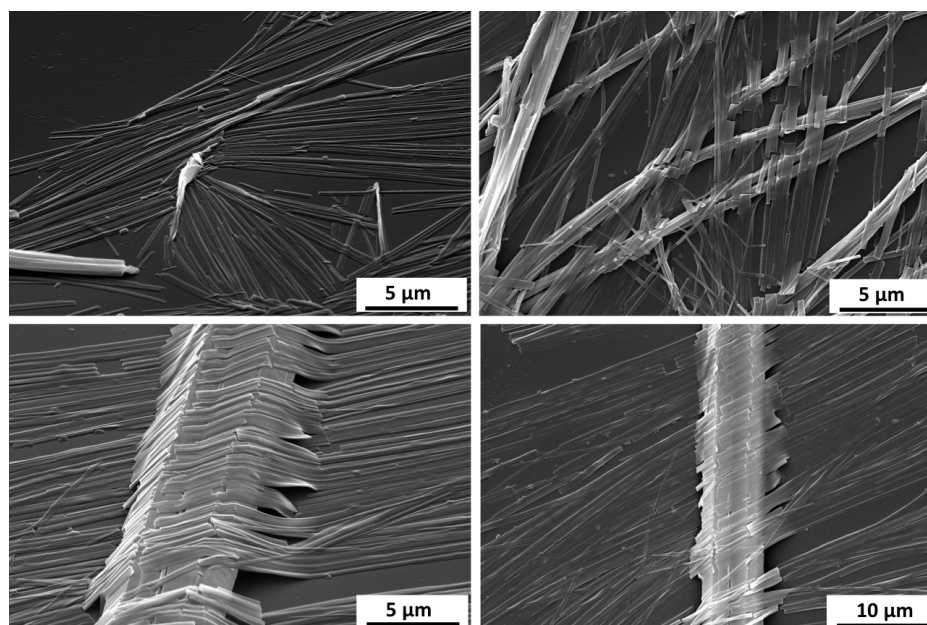


Figure 4.18. SEM images from the fibers obtained by flash-injection after evaporation of the organic solvent.

4.2.6. Effect on the addition order of THF and water

Previously, the platinum (II) complex was firstly dissolved in THF, and then water was gradually added while stirring. The addition of water to the THF enabled the platinum (II) complex to organize itself to form the most thermodynamically stable morphology for any THF/ water mixture. If the platinum (II) complex in THF was added to water, it would result in a non-favourable condition for crystal growth and it would adopt the most kinetically stable morphology. To verify this, two different experiments were conducted. In the first experiment, 9.5 mL of water was gradually added to a 0.5 mL of platinum (II) complex solution. In the second experiment, 0.5 mL of the platinum (II) complex solution in THF was gradually added to 9.5 mL of water. The rate of addition for both methods was set at $500 \mu\text{L}\cdot\text{h}^{-1}$. The two solutions had the same final concentration of platinum (II) complex, $c = 5 \times 10^{-5} \text{ M}$ in 10 mL of THF/water (5:95) solution. The photophysical and morphological properties of both solutions were then studied. The two solutions appeared to be different under standard light and UV lamp, as displayed in Figure 4.19. When the water was gradually added to the platinum (II) complex THF solution, a yellow precipitate was formed at the bottom of the cuvette (right cuvette) and emitted yellow under UV lamp. When the platinum (II) THF solution was added to the water, an orange suspension was formed (left cuvette) and displayed a bright orange emission under UV lamp.

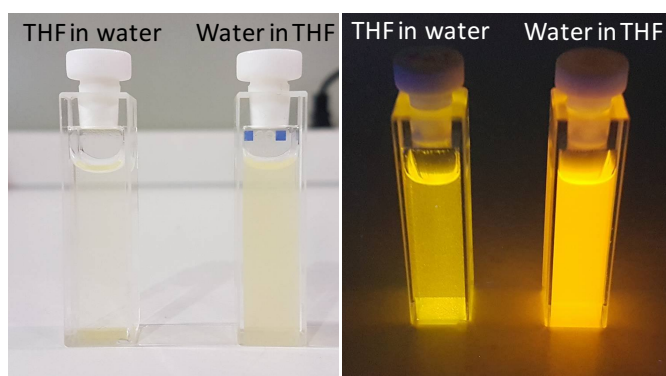


Figure 4.19. Photography of the two solutions prepared from addition of water to the platinum (II) complex THF solution (left cuvette) and the opposite (right cuvette) under standard light (right photo) and UV lamp (left photo).

The emission and excitation spectra of those two solutions were recorded and displayed in Figure 4.20. The excitation spectra of the two solutions show the $^1\text{MMLCT}$ bands between 400 nm and 550 nm, due to the platinum-platinum interaction. As previously mentioned, the

presence of intense $^1\text{MMLCT}$ bands can be interpreted as the formation of fiber aggregates. However, when the platinum (II) complex THF solution was added to the water, a small hypsochromic effect was observed in emission from 575 nm to 593 nm. When water was added to THF, the band was centered at approximately 575 nm, which is typical for platinum (II) complex fibers. When the THF was added to the water, the $^3\text{MMLCT}$ band was centered at approximately 590 nm, which was previously attributed to the presence of rods and toroidal particles. The lifetimes and PLQY in Table 4.8 also confirmed the photophysical properties of both morphologies.

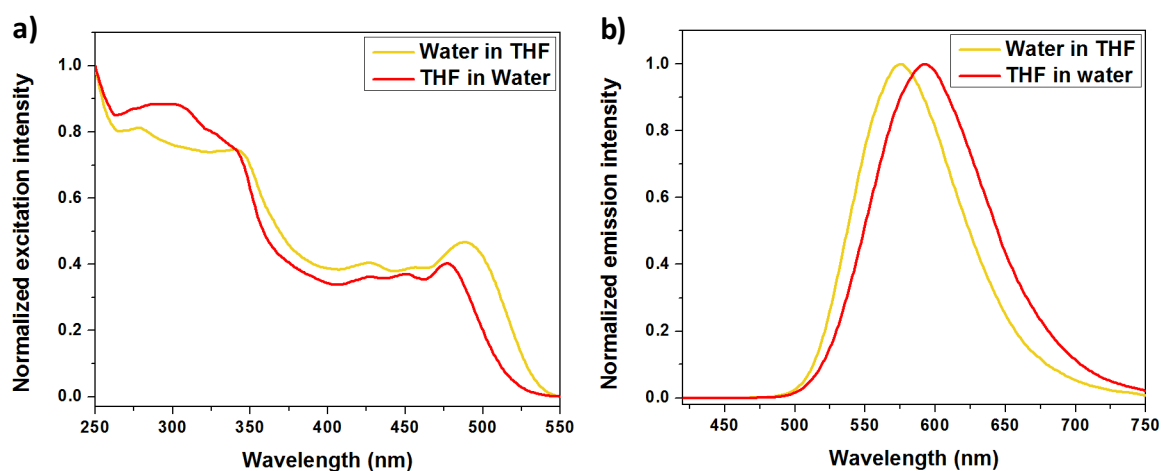


Figure 4.20. a) Excitation and b) emission spectra of the two solutions prepared from addition of water in the platinum(II) complex THF solution (yellow curves) and the opposite (red curves). $\lambda_{exc} = 300 \text{ nm}$, $\lambda_{exc} = 570 \text{ or } 590 \text{ nm}$.

Table 4.8. Photophysical properties of the two solutions prepared from addition of water in the platinum(II) complex THF solution (top line) and the reversal (bottom line).

Solvent mixture	Morphology	$\lambda_{em,max}$ (nm)	τ (ns)	PLQY
95% water (Water in THF)	Fibers	575	345 (88%), 630 (12%)	0.63
95% water (THF in water)	Rings, sheets	593	385 (15%), 615 (85%)	0.81

To confirm all the hypotheses deduced from the study of the photophysical properties; SEM, STEM and confocal microscopy were performed. As deduced, when the water was added to

THF, platinum fibers were formed (see Figure 4.21). It can be argued that at 95% water content the platinum (II) complex will form toroidal particles.

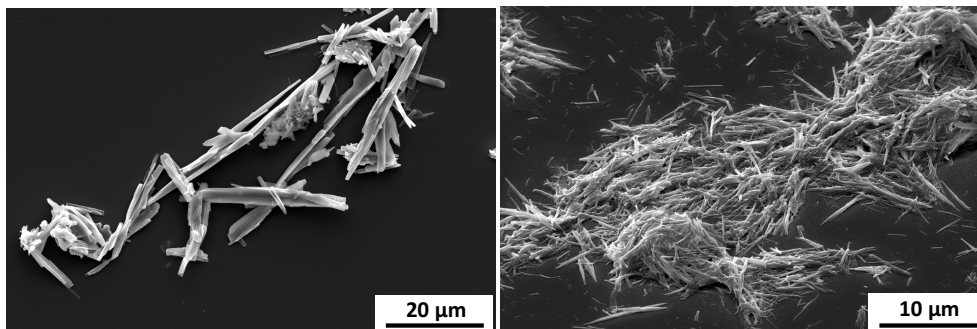


Figure 21. SEM images of the fibers prepared by addition of water to the platinum (II) complex THF solution.

In this experiment, the water was added very gradually ($500 \mu\text{L}\cdot\text{h}^{-1}$) compared to previously ($3 \text{ mL}\cdot\text{h}^{-1}$), to allow the fibers more time to grow and to ensure no resulting change in morphology once they are formed. This was also confirmed by the fact that the fibers retained their morphology when diluted in water, as shown previously. When the platinum (II) complex THF solution was added to water, very different morphologies were observed by SEM, as shown in Figures 4.22 and 4.23. One type of aggregates consisted of sheet-like structures, which were thin and transparent (Figure 4.22). The intersection of two sheets appeared to give rise « plateaux », which were observable by SEM and STEM. This behaviour can be compared to tectonic plates, where the intersection line between two plates gives rise to mountains. The platinum (II) complex sheets were observed by confocal fluorescence microscopy. The sheets-like aggregates were very thin and thus difficult to observe by microscopy. The emission was yellow and originating from islands within the sheet-like aggregates.

The second morphology observed for this solution was platinum « rings » of different sizes and shapes (Figure 4.23). These were different from the toroidal particles, which were very homogeneous in size, shape and a smaller inner diameter²⁴. The platinum rings observed in Figure 4.23 were not homogeneous in size. The STEM images also showed that those types of aggregates were quite flexible as several folded rings could be observed along with varying shaped rings. The diameter of the cross-section ($59 \pm 15 \text{ nm}$) was also comparable to one type of the rod-like aggregates and the photophysical properties were similar. It can be hypothesized that those platinum rings were a particular organization of closed rod-like

aggregates. The platinum (II) rings were also observed by confocal microscopy, however the resolution was quite low due to the small diameter of the rings. Nevertheless, the rings

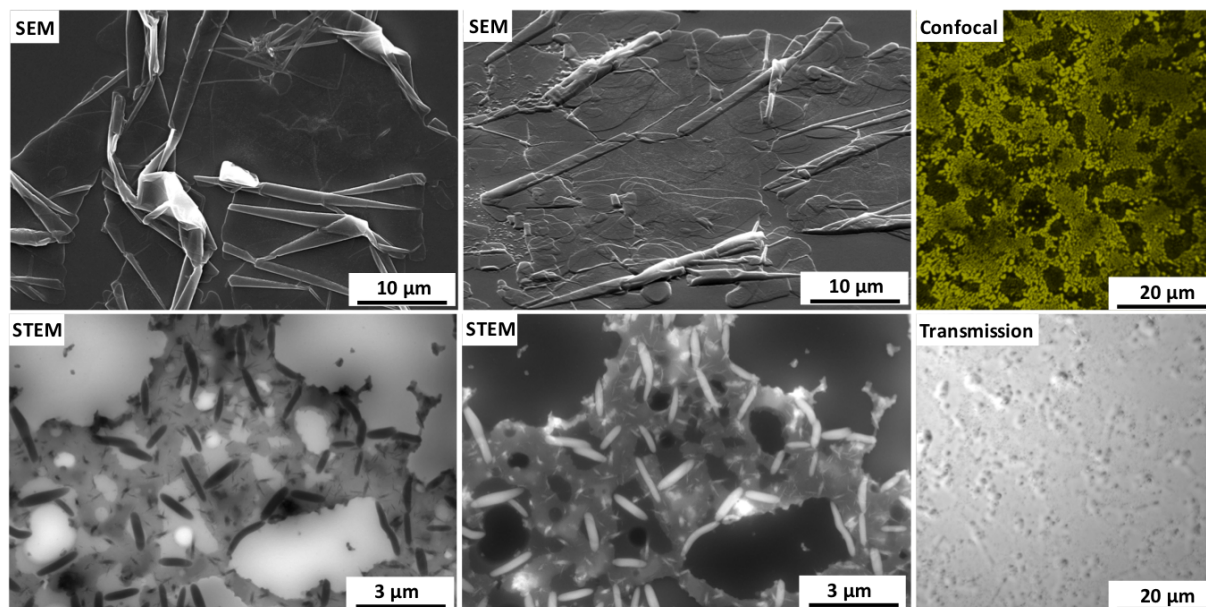


Figure 4.22. SEM and STEM (BF and HAADF mode) images of the platinum (II) complex sheets observed when the platinum (II) complex THF was added to the water. Transmission and confocal fluorescence images of platinum (II) complex sheets. The emission are false colors. $\lambda_{exc} = 405 \text{ nm}$.

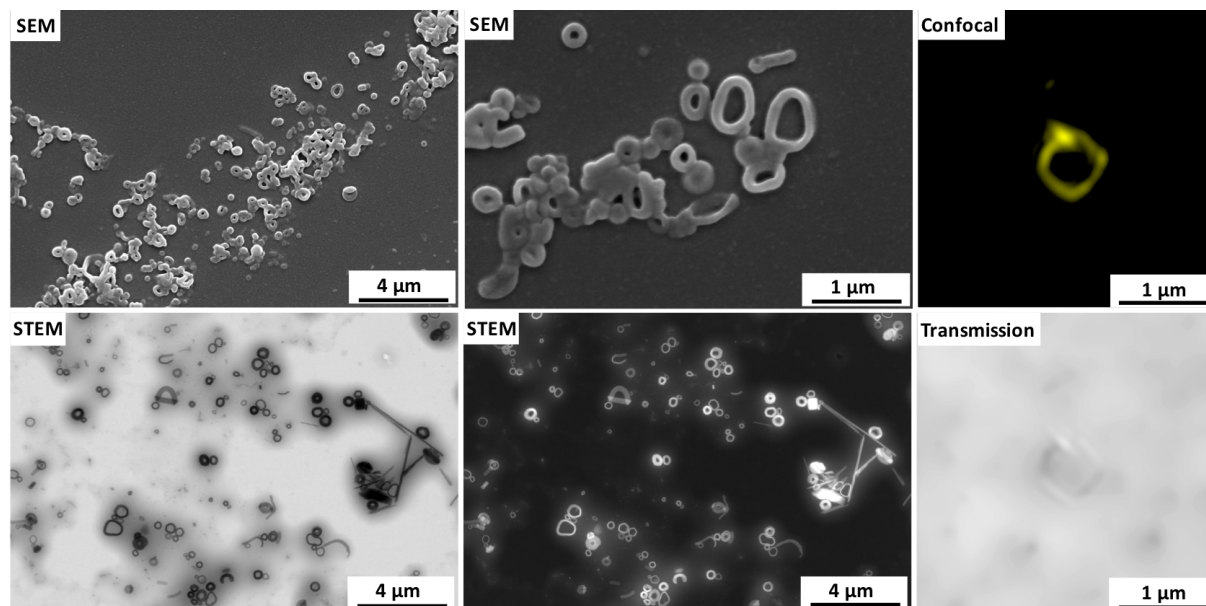


Figure 4.23. SEM and STEM (BF and HAADF mode) images of the platinum (II) complex rings observed when the platinum (II) complex THF was added to the water. Transmission and confocal fluorescence images of platinum (II) complex sheets. The emission are false colors. $\lambda_{exc} = 405 \text{ nm}$

could be distinctively observed by microscopy and the emission pattern matched the shape of the rings. The presence of these two new morphologies highlighted the crucial role played by the addition of water to the THF/complex **7** mixture during the early stages of the formation of platinum aggregates. In addition to the cylinders, rods and fan-shaped structures were observed at high water content. Rings and sheet-like aggregates are two structures that can also be obtained through varying the method of addition. The platinum (II) complex was manipulated to adapt the most stable morphology in order to minimize the interaction between the hydrophobic part, *e.g.* triazole-platinum moiety, with water. The reorganization of the rod-like aggregates into rings showed that the two ends of a rod could connect to form new rings with the same cross section diameter.

4.2.7. Role of the solvent on the aggregation of the platinum (II) complex.

The THF/water mixture was used to form different types of platinum aggregates. THF is a good solvent due to the fact that the platinum(II) complex was soluble, and that it was miscible with water. Solvents can be roughly classified into two categories: polar and nonpolar. The dielectric constant of the solvent provides an approximative measurement of the solvent's polarity. Generally, the dielectric constant of a solvent is an acceptable predictor of the solvent's ability to dissolve common ionic compounds, such as salts. The strong polarity of water is indicated by a high dielectric constant ϵ of 88. Solvents with a dielectric constant of less than 15 are generally considered to be nonpolar. The polarity, dipole moment, polarizability and hydrogen bonding of a solvent determines what type of compounds can be dissolved and with what other solvents it is miscible with. Generally, polar solvents dissolve polar compounds and non-polar solvents dissolve non-polar compounds. The Hansen solubility parameters contain information about the inter-molecular interactions with other solvents and also with polymers, pigments, and nanoparticles etc. The solubility parameters δ and dielectric constants ϵ for some common solvents were reported in Table **4.9**. To study the effect of the solvent on the self-assembly of the platinum (II) complex, dioxane and DMF was used to compare with THF. Dioxane is a nonpolar solvent while DMF is a polar aprotic solvent. The platinum (II) complex was soluble in both solvents and became miscible when the water was added. The same method was utilised to trigger the aggregation. Platinum (II) complex was dissolved in dioxane and DMF and the water was added to solution with different THF or

DMF/ water ratios but with the same predetermined final concentration ($c = 5 \cdot 10^{-5}$ M). The solution was stirred for 2 days prior to the photophysical and morphological studies.

Table 4.9. Solubility and polarity properties of some common solvents.

Solvents	Solubility parameter (δ)	Dielectric constant ϵ
Cyclohexane	16.8	2.02
Ethyl acetate	18.2	6.02
THF	18.5	7.5
Acetone	19.7	20.7
Dichloromethane	20.2	8.93
Dioxane	20.5	2.2
DMF	24.7	36.7
Methanol	29.7	32.7
Water	48.0	80.1

4.2.7.1. Self-assembly of platinum(II) complex in dioxane/water mixture

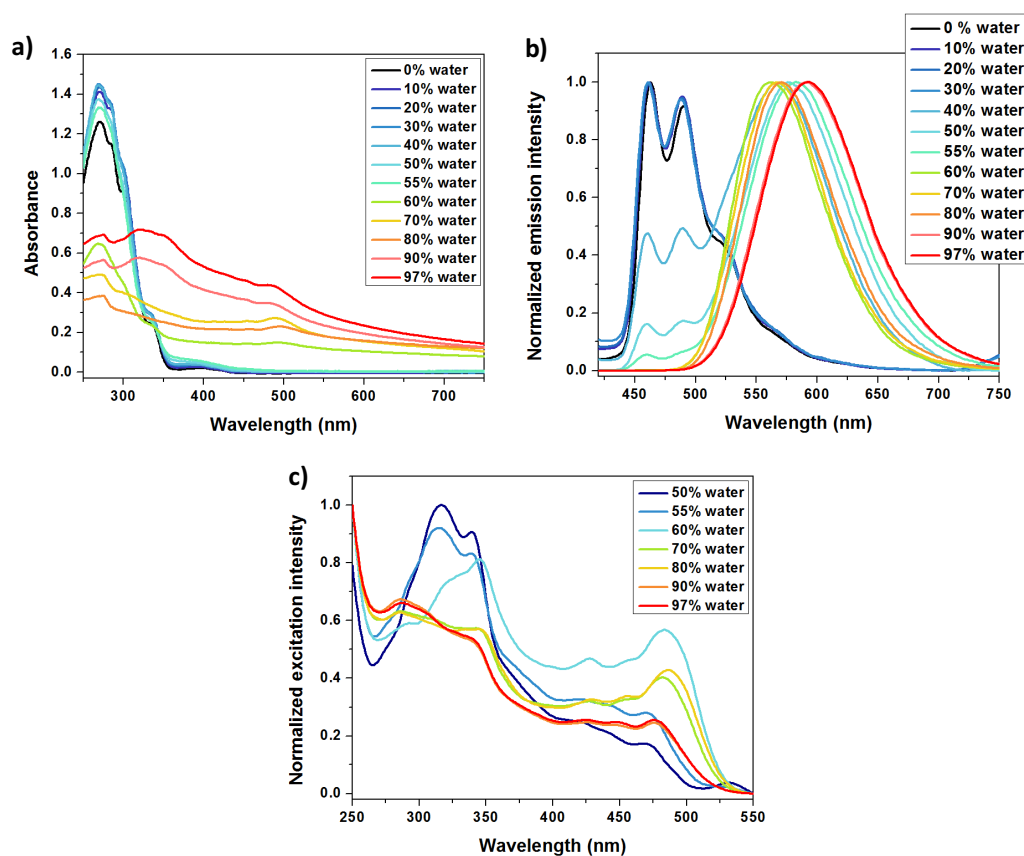


Figure 4.24. a) absorption b) emission and c) excitation spectra of the platinum(II) complex in different dioxane/water mixture. $\lambda_{exc} = 300$ nm, $\lambda_{exc} = 570$ or 590 nm.

The absorption, emission and excitation spectra of the dioxane/water platinum (II) complex solutions were displayed in Figure 4.24. The CWC at which the aggregation began was determined at 40% water content when the ³MMCLT band appeared in emission, even though ³LC/MLCT bands at 460 and 490 nm were still present. Nevertheless, the absorption and excitation spectra did not show any signs of platinum-platinum interactions. The decrease of the ¹LC band around 300 nm in absorption was observed at 60% water content. The intensity of the ¹MMLCT bands was between 400 and 550 nm in excitation and was the highest at 60% water content. A gradual red-shift in emission was observed when the water content was increased. The excited state lifetimes and photoluminescent quantum yields were reported in Table 4.10. When the platinum (II) complex was dissolved in dioxane/water mixture at water content below 40%, the average lifetime was measured at 5 ns and the PLQY below 1%. When the aggregation began at 40% water content, a bi-exponential decay was observed with a very short lifetime of around 3 ns and a longer lifetime measurement around 430 ns. This component was characteristic of platinum-platinum interactions and aggregation of platinum (II) complexes. The short lifetime component meant that the aggregation was not complete.

Table 4.10. Photophysical properties of the platinum (II) complex in dioxane/water mixture

Solvent mixture	Morphology	$\lambda_{em,max}$ (nm)	τ (ns)	PLQY
Dioxane	amorphous	463, 490, 520 (sh)	5	< 0.01
10% water	amorphous	462, 490, 520 (sh)	5	< 0.01
20% water	amorphous	461, 490, 520 (sh)	5	< 0.01
30% water	amorphous	461, 490, 520 (sh)	5	< 0.01
40% water	amorphous rods	461, 490, 567	3 (57%), 430 (43%)	< 0.01
50% water	amorphous rods toroidal	461, 490, 576	3 (51%), 15 (28%), 210 (6%), 510 (15%)	< 0.01

55% water	amorphous	460, 490, 582	8 (45%), 28 (31%),	0.015
	toroidal		260 (8%), 510 (16%)	
	toroidal			
60% water	rigid fibers	562	400 (99%), 1000 (1%)	0.42
70% water	semi-rigid fibers	567	425 (99%), 1000 (1%)	0.60
80% water	flexible fibers	571	410 (98%), 840 (2%)	0.60
90% water	flexible fibers	591	370 (19%), 555 (81%)	0.75
	toroidal			
97% water	toroidal	593	475 (51%), 580 (49%)	0.56

At 60% water content, a long excited state lifetime was measured in conjunction with a high photoluminescent quantum yield. At 90% water content, a longer lifetime around 530 ns was measured, signifying a change in morphology of the platinum (II) complex. The morphology of the aggregates was then studied by electron microscopy and the images are displayed in Figure 4.25. Below 40% water content, the SEM images only show the amorphous platinum (II) complex, as predicted, considering the photophysical properties. Between 40% and 60% water content, amorphous material was observed along with rod-like aggregates, and large, spherical aggregates. At 60% water content, long and sharp needles were observed. From 70% to 80% water content, the quality of the fibers degraded as they were more flexible and less rigid. At 90% water content, a mixture of flexible fibers and toroidal particles was observed. Finally, at 97% water content, mainly toroidal aggregates and undefined structures were observed by SEM. The CWC for dioxane was determined around the 50% water content solution, despite the presence of the ³MMLCT band at 40% water content solution. Dioxane enabled the formation of sharp needled and fibers of various shapes.

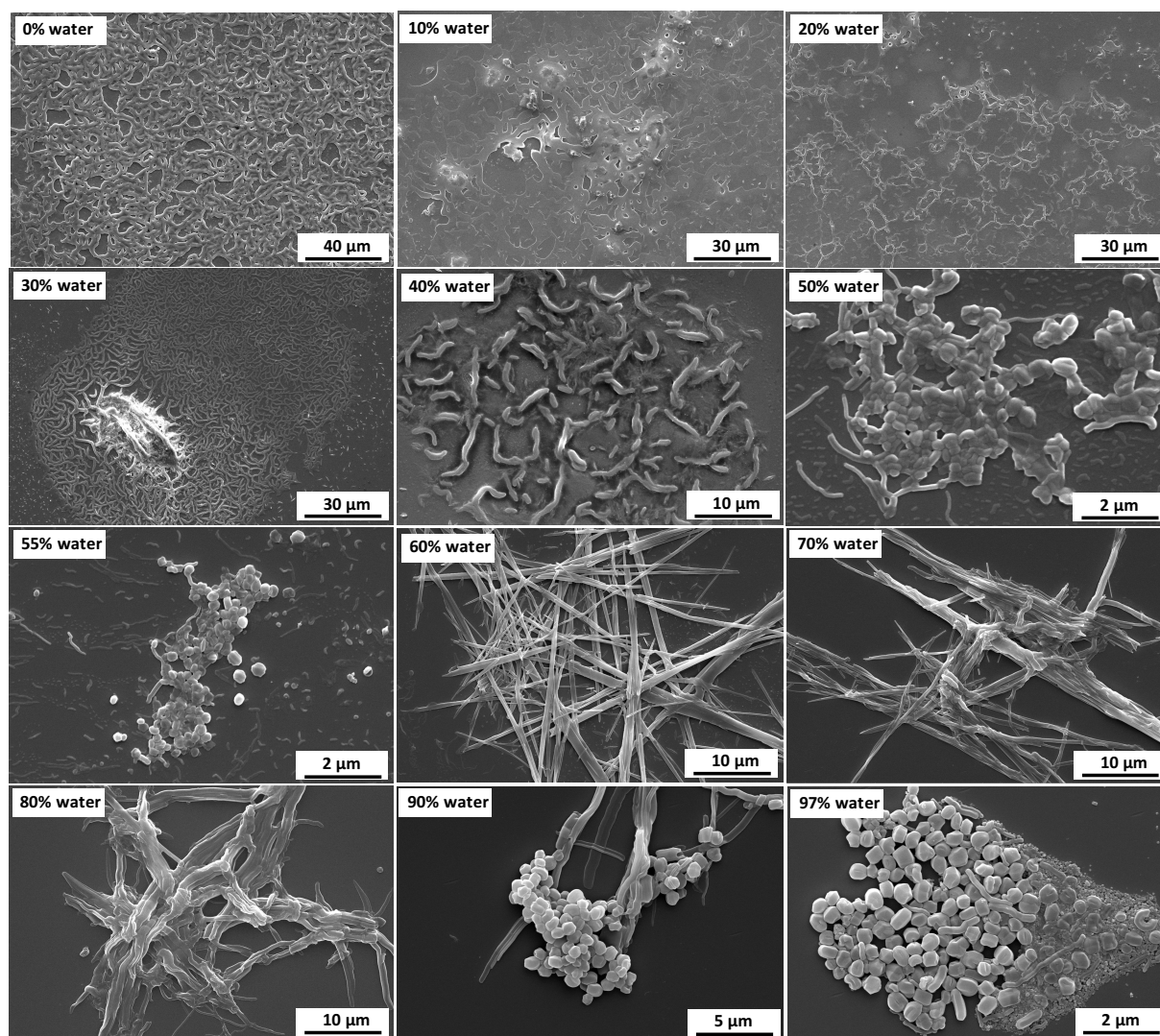


Figure 4.25. SEM images of the platinum (II) aggregates formed after evaporation of drop-casted solution at different dioxane/water ratios.

4.2.7.2. Self-assembly of platinum (II) complex in DMF/water mixtures

Platinum (II) complex was dissolved in DMF and the water was added to the solution with different DMF/ water ratios but with the same predetermined final concentrations ($c = 5.10^{-5}$ M). The solutions were stirred for 2 days prior to the photophysical and morphological study. The absorption, emission and excitation spectra of the dioxane/water platinum (II) complex solutions are displayed in Figure 4.26. The excited state lifetimes and photoluminescent quantum yields are reported in Table 4.11.

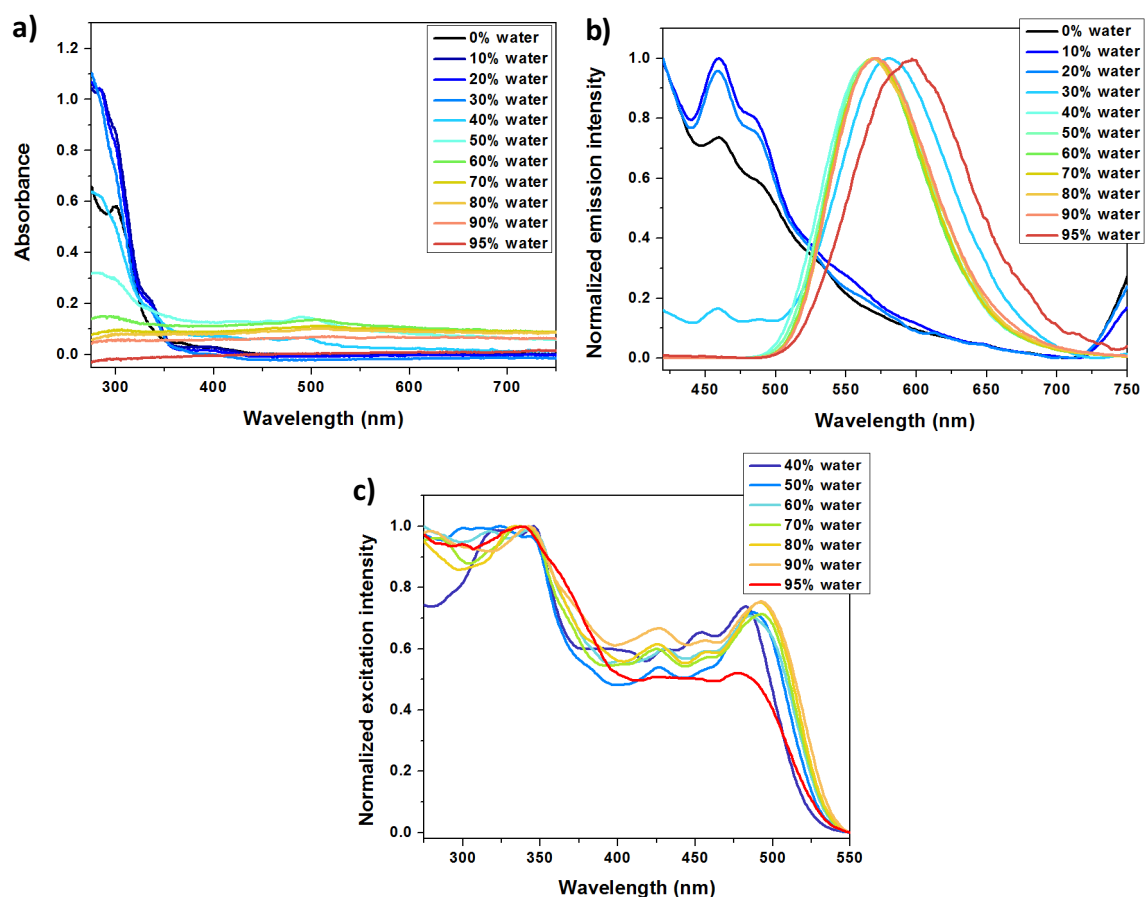


Figure 4.26. a) Absorption b) emission and c) excitation spectra of the platinum (II) complex in different dioxane/water mixtures. $\lambda_{exc} = 300$ nm, $\lambda_{em} = 570$ or 590 nm.

Table 4.11. Photophysical properties of the platinum (II) complex in DMF/water mixtures

Solvent mixture	Morphology	$\lambda_{em,max}$ (nm)	τ (ns)	PLQY
DMF	amorphous	460, 490(sh)	7	< 0.01
10% water	amorphous	460, 490 (sh)	7	< 0.01
20% water	amorphous	459, 490 (sh)	7	< 0.01
30% water	amorphous	459, 580	7	< 0.01
40% water	amorphous fibers	569	440	0.40
50% water	amorphous fibers	569	405	0.58

60% water	amorphous fibers	570	385	0.61
70% water	amorphous fibers	571	380	0.62
80% water	toroidal fibers rods	570	372 (99%), 1060 (1%)	0.62
90% water	toroidal fibers rods	571	380	0.62
95% water	toroidal rods	597	120 (14%), 505 (86%)	0.52

The CWC was determined by the presence of ³MMLCT broad band around 570 nm in emission and the decrease of the ¹LC band at 300 nm in absorption. It was estimated to be at 30% water content, which is the lowest among the three solvents tested. Although the platinum (II) complex was soluble in DMF, it is still considered a bad solvent for the complex due to the fact that the self-assembly occurred at a low water content. Between 40% and 90% water content, the ³MMLCT band was centered at approximately 570 nm. In addition, intense ¹MMLCT bands were observed between 400 nm and 550 nm. Those bands were characteristic of the formation of fibers. At 95% water content, the ³MMLCT band was red-shifted and the ¹MMLCT bands decreased in intensity which signified a change in morphology. The excited state lifetime and photoluminescent quantum yield of each solution was reported in Table 4.11. At below 40% water content, the lifetime was 7 ns and the PLQY below 1%, similar to the values obtained when the platinum (II) complex was dissolved in DMF. From 40% to 90 % water content, the excited lifetime was measured around 400 ns and PLQY around 60%, which were constant and in accordance with the formation of fibers. At 97% water content the excited state lifetime was increased around 500 ns and the PLQY slightly decreased around 52%, due to the change in morphology. The morphology of the aggregates was studied by SEM and displayed in Figure 4.27.

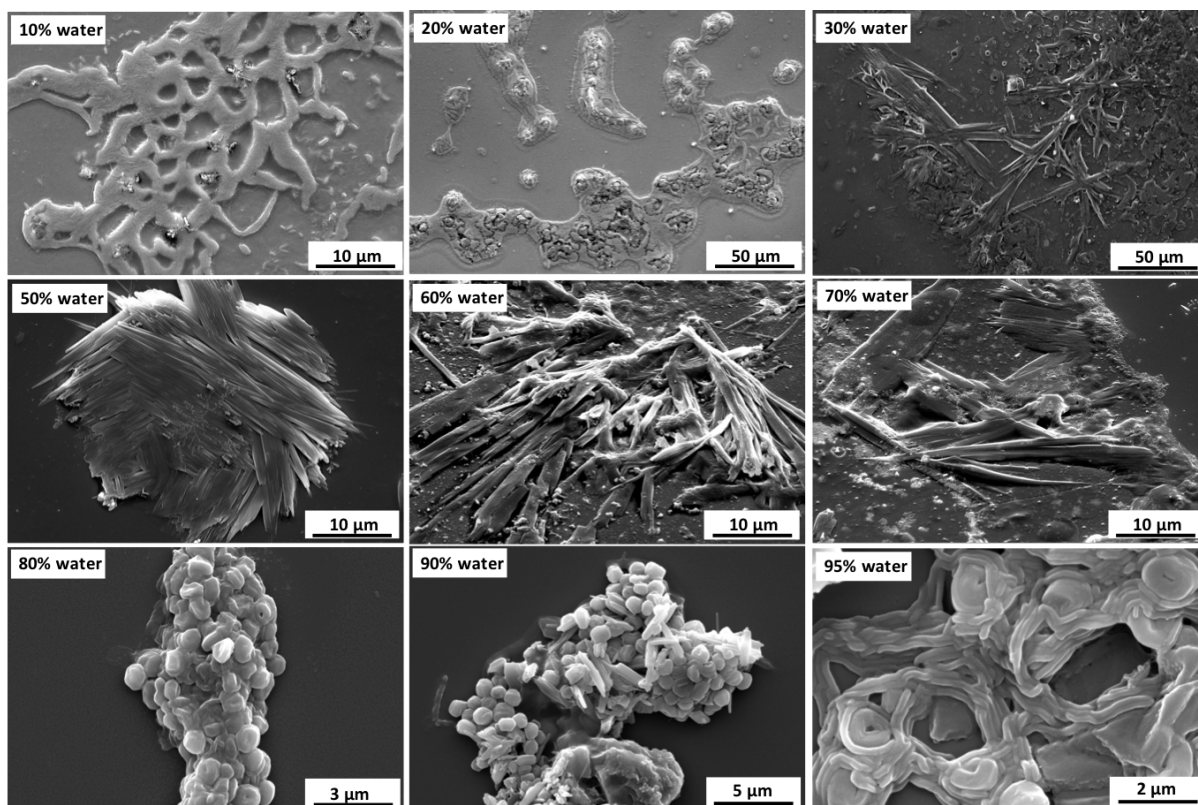


Figure 4.27. SEM images of the platinum (II) aggregates formed after evaporation of drop-casted solution at different dioxane/water ratio.

The imaging of the platinum aggregates was more complex than for the THF/ water or dioxane/water mixtures. Between 0% and 30% water content, amorphous material was observed. Between 40% and 70% water content, fiber-like aggregates were observed. Nevertheless, those fibers were different to those observed for the THF or dioxane water mixtures. They were not as well defined and were generally surrounded by amorphous material, even though they shared the same photophysical properties. At 80% and 90% water content, a mixture of toroidal particles, rods and fibers were observed. Finally, at 95% water content, entangled toroidal particles and rods could be observed. As a general conclusion, DMF may be a suitable solvent to dissolve insoluble platinum (II) complexes, however, electron microscopy showed a mixture of undefined aggregates. The wavelength of maximum emission intensity as a function of the water content in various solvents for THF, dioxane and DMF are displayed in Figure 4.28. The increase of the wavelength of maximum emission intensity from 460 nm to around 570 nm defined the CWC for each solvents mixture. The lower the CWC, the worst the solvent is for the platinum (II) complex. Regarding this, the best solvent is THF out of the three solvents, followed by dioxane and then DMF.

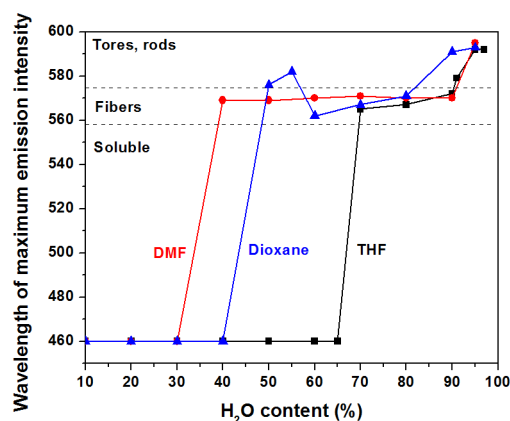


Figure 4.28. Wavelength of maximum emission intensity as a function of the water content in various solvents. The morphologies observed at different emission wavelengths are also reported.

4.2.8. Energy dispersive spectra (EDS) of platinum (II) complex aggregates

Electron microscopy can reveal a lot of information of about the morphology of the platinum (II) complex and coupled with energy dispersive spectroscopy can prove that the morphology observed was the platinum (II) complex.

Fibers

Platinum fibers were the simplest morphological structures to characterize by EDS due to their size and the density. Carbon (0.277 keV), nitrogen (0.392 keV), oxygen (0.525 keV), fluorine (0.677) and platinum (2.048 keV) peaks were observed on the EDS. Also, sodium (1.041 keV), aluminum (1.486 keV), silicon (1.739 keV), and potassium (3.312 keV) were consistently present. The substrates were sputtered with silver (2.984 keV) instead of gold (2.12 keV) to prevent the overlapping between the platinum and gold signals.

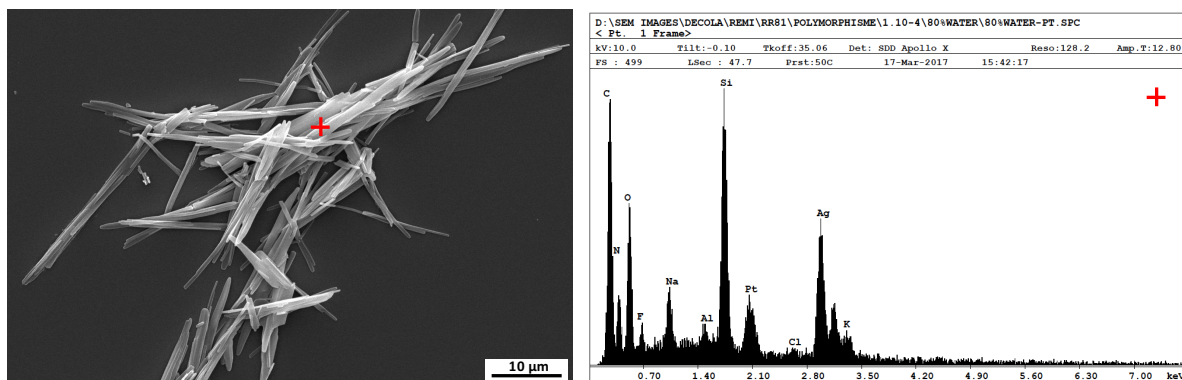


Figure 4.29. SEM and corresponding EDS spectra of the aggregates. The red cross marks the point where the EDS measurement was performed.

Large toroidal particles

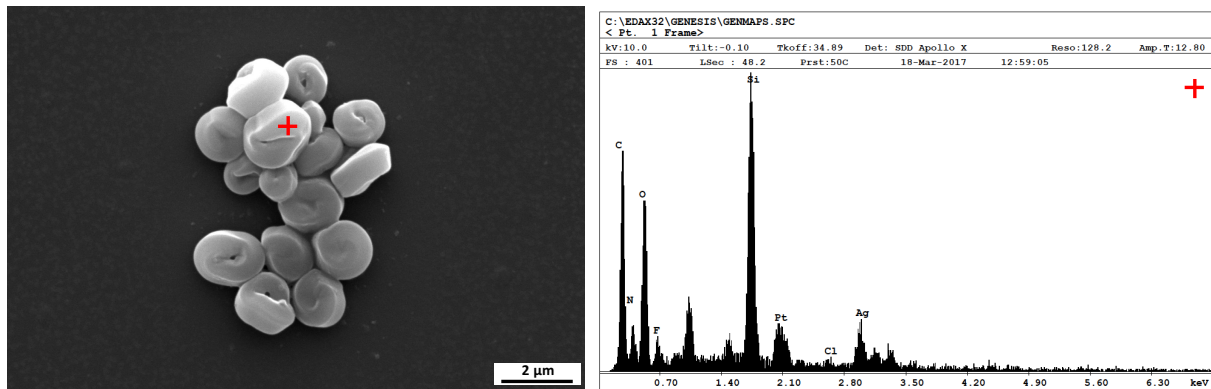


Figure 4.30. SEM and corresponding EDS spectra of the aggregates. The red cross marks the point where the EDS measurement was performed.

Platinum toroidal particles were also relatively easy to characterize by EDS due to their size and the density of the platinum. Carbon (0.277 keV), nitrogen (0.392 keV), oxygen (0.525 keV), fluorine (0.677) and platinum (2.048 keV) peaks were observed on the EDS.

Small toroidal particles

Small platinum toroidal particles were more challenging to characterize by EDS but a clear signal could be observed. Carbon (0.277 keV), nitrogen (0.392 keV), oxygen (0.525 keV), fluorine (0.677) and platinum (2.048 keV) peaks were observed on the EDS.

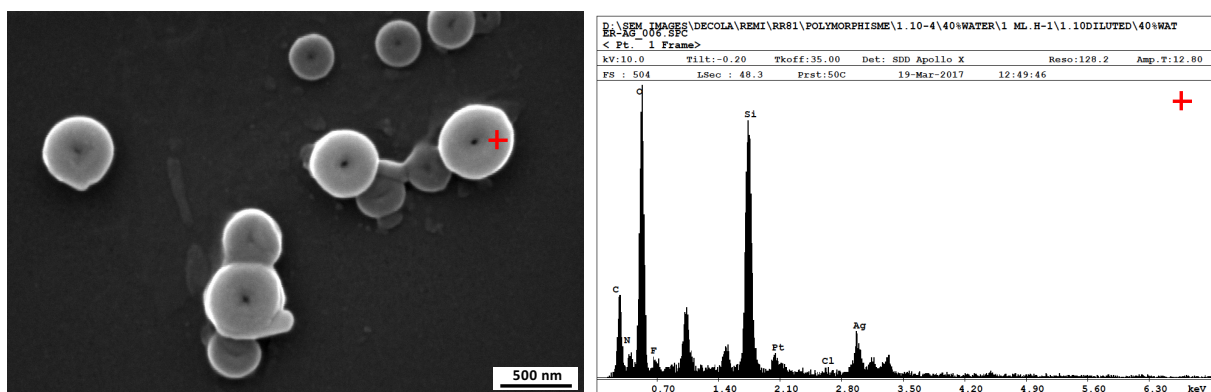


Figure 4.31. SEM and corresponding EDS spectra of the aggregates. The red cross marks the point where the EDS measurement was performed.

Spherical cylinder

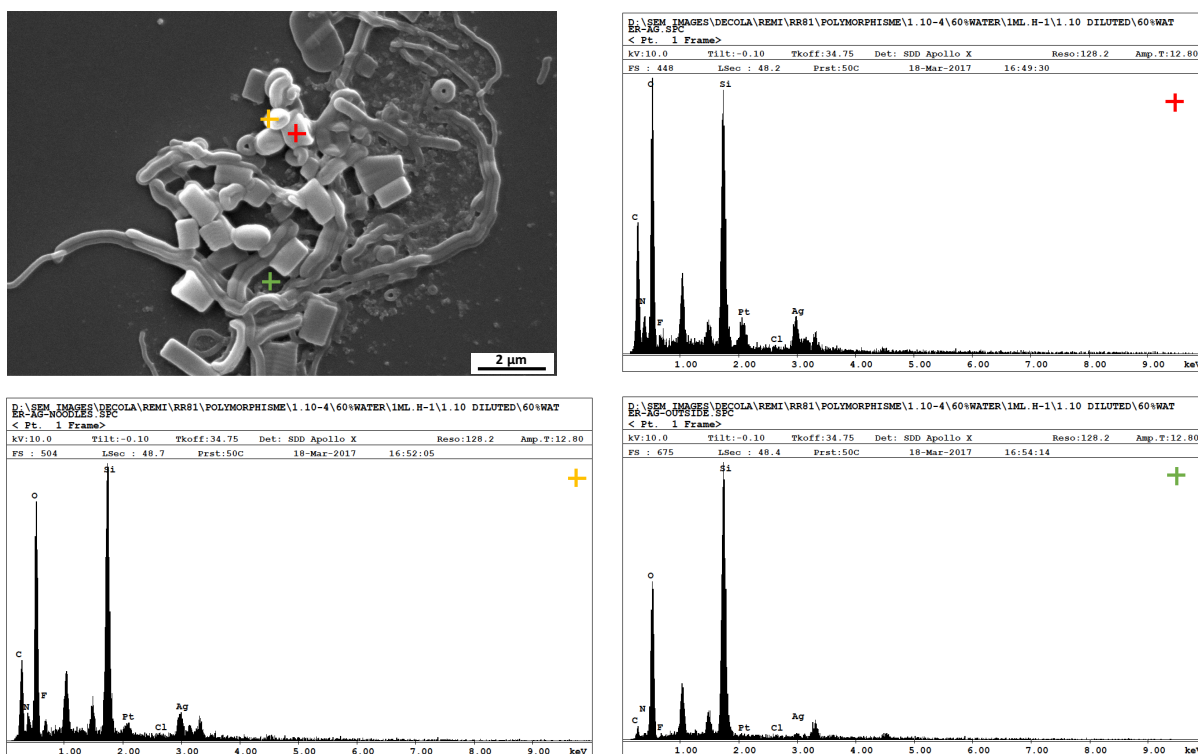


Figure 4.32. SEM and corresponding EDS spectra of the aggregates. The red, orange and green crosses mark the points where the EDS measurement was performed.

Platinum spherical cylinders were also difficult to characterize by EDS but a clear signal could be observed. The orange and red crosses mark two different cylinders while the green cross marks an empty spot. Carbon (0.277 keV), nitrogen (0.392 keV), oxygen (0.525 keV), fluorine (0.677) and platinum (2.048 keV) peaks were observed on the EDS for the cylinders while sodium (1.041 keV), aluminum (1.486 keV), silicon (1.739 keV), potassium (3.312 keV) and silver (2.984 keV) were observed on the empty spot.

Rods

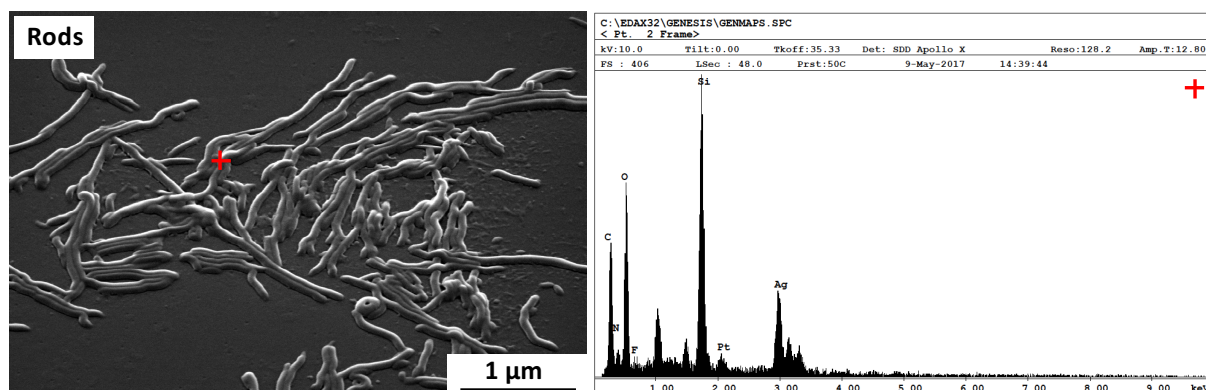


Figure 4.33. SEM and corresponding EDS spectra of the aggregates. The red, orange and green crosses mark the points where the EDS measurement was performed.

Platinum rods were also difficult to characterize by EDS because of their smaller sizes and diameters. A weak but clear signal could be observed. Carbon (0.277 keV), nitrogen (0.392 keV), oxygen (0.525 keV), fluorine (0.677) and platinum (2.048 keV) peaks were observed on the EDS. The fluorine peak was barely detected.

Sheets

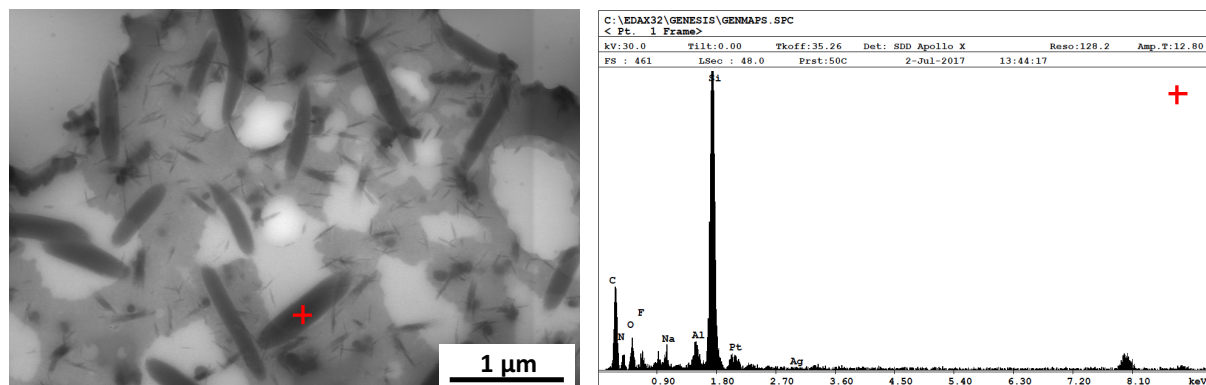


Figure 4.34. STEM (BF) and corresponding EDS spectra of the aggregates. The red, orange and green crosses mark the points where the EDS measurement was performed.

Platinum sheets were the most difficult aggregate to characterize due to the fact that they were very thin compared to the other morphologies. The issue was solved by using a copper grid and and STEM mode. Once the morphology was located, EDS was possible. Carbon (0.277 keV), nitrogen (0.392 keV), oxygen (0.525 keV), fluorine (0.677) and platinum (2.048 keV) peaks were observed on the EDS. An additional peak at 8.04 keV was detected and was originating from the copper from the grid.

Rings

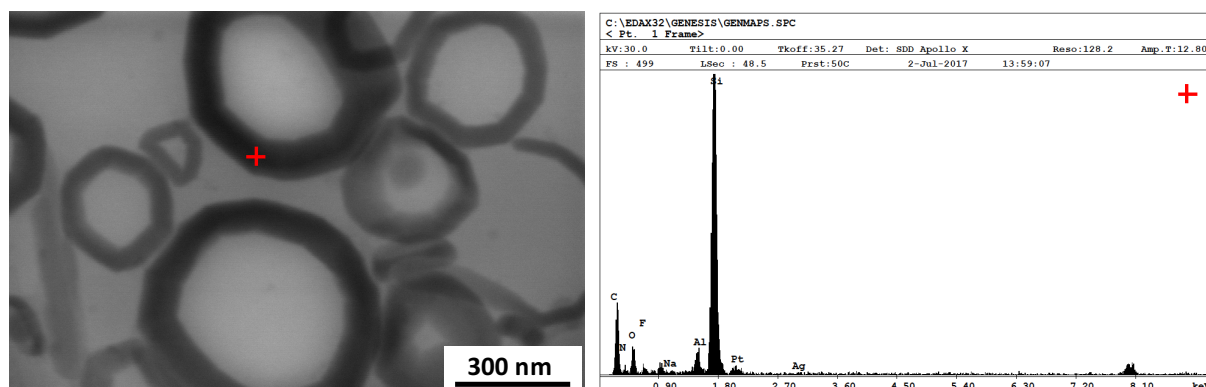
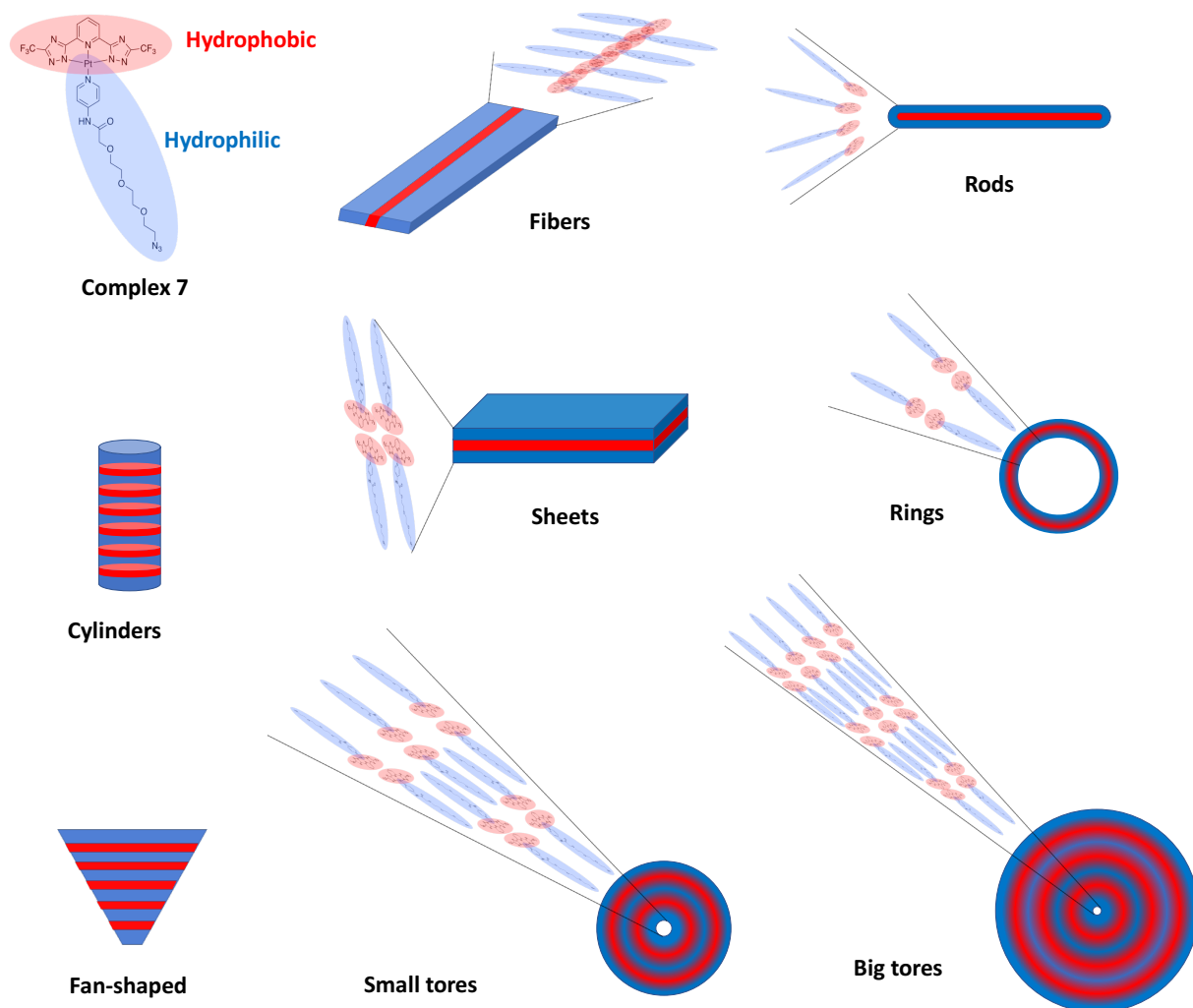


Figure 4.35. STEM (BF) and corresponding EDS spectra of the aggregates. The red, orange and green crosses mark the points where the EDS measurement was performed.

Platinum rings were also difficult to characterize and the same method as for the sheets was used. Carbon (0.277 keV), nitrogen (0.392 keV), oxygen (0.525 keV), fluorine (0.677) and platinum (2.048 keV) peaks were observed on the EDS. Those peaks were weaker compared to the other morphologies due to the the small size of the particles.

4.3. Conclusion

The results show that it is possible to control the self-assembly of the platinum (II) complex depending on the concentration, the organic solvent, and the rate and order of addition of the water. The platinum (II) complex was able to adopt multiple morphologies in different conditions. These morphologies included fibers, rods, cylinders, fan-shaped aggregates, small and large toroidal particles, sheet-like aggregates and rings (Scheme 2). The formation of eight different types of aggregates is unprecedented for a single platinum (II) complex and reveals the variety of morphologies that can be adopted depending on the different parameters used. Interestingly, it was observed that each morphology has its own photophysical properties which render them unique. Some aggregates such as fibers or toroidal particles were easy to obtain individually in solution while other morphologies, for example, rod-like aggregates, sheet-like aggregates or cylinders coexisted in solution. One challenge would be to separate those coexisting morphologies in order to study them individually. Those findings will likely contribute to the use of platinum (II) self-assembled aggregates of different shapes and properties for applications in material science. It would be also greatly beneficial if the morphology of those aggregates could change upon specific stimuli to prepare responsive materials with different properties.



Scheme 4.2. Simplified representation of the aggregates of platinum (II) complex 7 observed in THF/ water mixture. The red area represents the hydrophobic core and the blue area represents the hydrophilic tail of complex 7.

4.4. Experimental Section

4.4.1. Preparation of the platinum aggregates

To prepare the platinum aggregates, deionized water (as a precipitant), was added at a rate of 1 drop/10 s or flash-injected with vigorous stirring into the into the organic solvent containing the platinum (II) complex 7 in the common solvent (THF, dioxane, or DMF). The final volume of the mixture of solvents was consistently 10 mL and the final concentration in complex 7 was 5×10^{-5} or 5×10^{-6} M for the diluted solutions. The solution was sealed to avoid the evaporation of solvents and stirred for 48 hours before analysis.

4.4.2. Photophysics

All the absorption measurements in this report were recorded on a UV-3600 Shimadzu UV-Vis-NIR spectrophotometer, and were baseline and solvent corrected with UV Probe software. Quartz cuvettes of path length xxx mm were used for this purpose. Steady-state measurements were recorded on a HORIBA Jobin-Yvon IBH FL-332 Fluorolog 3 spectrometer equipped with a 450 W Xenon arc lamp, double grating excitation and emission monochromators.

Time-resolved measurements up to 5 μ s were performed using the TCSPC option on a FluoTime 300 (PicoQuant). The excitation source was mounted directly on the sample chamber at 90° to a double grating emission monochromator and collected by a PicoHarp 300 (PicoQuant) single-photon-counting detection module. Signals were collected using the software FluroFit, PicoQuant for excited state lifetimes > 10 μ s, a different experimental setup was utilised, by equipping the FluoTime 300 with a FL-1040 phosphorescence module including a 70-W xenon flash tube. The signal was recorded on the PDL 820 single-photon-counting detector and collected with multichannel scalling (MCS).

Absolute quantum yield measurements were performed using a Hamamatsu Photonics absolute PL quantum yield measurement system. This setup is equipped with a L0799-001 CW Xenon light source (150 W), a monochromator, a C7473 photonic multi-channel analyzer and an integrating sphere.

4.4.3. Scanning electron microscopy (SEM) and scanning transmission electron microscopy (STEM)

SEM characterization was performed employing a FEI scanning electron microscope Quanta FEG 250, at an acceleration voltage of 10 KV. Samples were prepared by drop-casting a solution of platinum (II) complex onto a glass slide, followed by plasma-induced deposition of a 40 nm thick layer of silver.

STEM characterization was performed employing a FEI scanning electron microscope Quanta FEG 250, at an acceleration voltage of 20 kV. Samples were prepared by drop-casting a solution of platinum (II) complex onto a copper grid (400 mesh, Agar Scientific) coated with Formvar/carbon film.

4.4.4. Confocal fluorescence microscopy

All of the fluorescence images were taken by using the Zeiss LSM 710 confocal microscope system with 63 X magnification, numerical aperture, NA, 1.3 of Zeiss LCI Plan-NEOFLUAR water immersion objective lens (Zeiss GmbH). The samples were excited by continuous wave (cw) laser at 405 nm. The emission of the complexes was collected in the range from 400 to 750 nm. In addition, the lambda-mode acquisition technique was performed to observe the emission spectra of the two complexes after cell internalization. The raw data was processed by using a linear un-mixing tool available in the ZEN 2011 software package (Zeiss GmbH) and collected in lambda-mode. All images were performed by using the same software.

4.5. References

1. Lehn, J. M, *Science*, **2002**, *295*, 2400–2403; Hoeben, F. J. M.; Jonkheijm, P.; Meijer, E. W.; Schenning, A. P. H., *J. Chem. Rev.*, **2005**, *105*, 1491–1546
2. Zhang, L. F.; Eisenberg, A., *Science*, **1995**, *268*, 1728–1731.
3. Zhang, L. F.; Yu, K.; Eisenberg, A., *Science*, **1996**, *272*, 1777–1779.
4. Meijer, E. W., *Science*, **1995**, *268*, 1592–1595
5. Yan, X.; He, Q.; Wang, K.; Duan, L.; Cui, Y.; Li, J., *Angew. Chem., Int. Ed.*, **2007**, *46*, 2431–2434.
6. Rao, K. V.; George, S., *J. Org. Lett.*, **2010**, *12*, 2656–2659; Jiang, B. P.; Guo, D. S.; Liu, Y., *J. Org. Chem.*, **2010**, *75*, 7258–7264.
7. Chung, C. Y. S.; Chan, K. H. Y.; Yam, V. W. W., *Chem. Commun.*, **2011**, *47*, 2000–2002
8. Golubkov, G.; Weissman, H.; Shirman, E.; Wolf, S. G.; Pinkas, I.; Rybtchinski, B., *Angew. Chem., Int. Ed.*, **2009**, *48*, 926–930
9. Chen, Y.; Li, K.; Lloyd, H. O.; Lu, W.; Chui, S. S. Y.; Che, C. M., *Angew. Chem. Int. Ed.*, **2010**, *49*, 9968–9971
10. Kishimura, A.; Yamashita, T.; Aida, T., *J. Am. Chem. Soc.* **2005**, *127*, 179–183
11. J. F. Gohy, B. G. G. Lohmeijer, S. K. Varshney, B. Decamps, E. Leroy, S. Boileau, U. S. Schubert, *Macromolecules*, **2002**, *35*, 9748–9755.
12. K.M.C. Wong, V.W.W. Yam, *Coord. Chem. Rev.*, **2007**, *251*, 2477–2488.
13. F.N. Castellano, I.E. Pomestchenko, E. Shikhova, F. Hua, M.L. Muro, N. Rajapakse, *Coord. Chem. Rev.*, **2006**, *250*, 1819–1828.

14. D'Andrade, B. W.; Brooks, J.; Adamovich, V.; Thompson, M. E.; Forrest, S. R. *Adv. Mater.* **2002**, *14*, 1032-1036; Brooks, J.; Babayan, Y.; Lamansky, S.; Djurovich, P. I.; Tsyba, I.; Bau, R.; Thompson, M. E. *Inorg. Chem.* **2002**, *41*, 3055-3066. Adamovich, V.; Brooks, J.; Tamayo, A.; Alexander, A. M.; Djurovich, P. I.; D'Andrade, B. W.; Adachi, C.; Forrest, S. R.; Thompson, M. E. *New, J. Chem.* **2002**, *26*, 1171-1178; S. C. F. Kui, I.H.T. Sham, C.C.C. Cheung, C.W. Ma, B.P. Yan, N.Y. Zhu, C.M. Che, W.F. Fu, *Chem. Eur. J.*, **2007**, *13*, 417-435.
15. E.A.M. Geary, L.J. Yellowlees, L.A. Jack, I.D.H. Oswald, S. Parsons, N. Hirata, J.R. Durrant, N. Robertson, *Inorg. Chem.*, **2005**, *44*, 242-250.
16. K.M.C. Wong, W.S. Tang, B.W.K. Chu, N.Y. Zhu, V.W.W. Yam, *Organometallics*, **2004**, *23*, 3459.
17. V. W. Yam, K. H. Chan, K. M. Wong and B. W. Chu, *Angew. Chem. Int. Ed.*, **2006**, *45*, 6169-6173.
18. J. R. Kumpfer, S. D. Taylor, W. B. Connick and S. J. Rowan, *J Mater Chem*, **2012**, *22*, 14196-14204.
19. K. M. Wong and V. W. Yam, *Acc. Chem. Res.*, **2011**, *44*, 424-434.
20. M. Y. Yuen, V. A. Roy, W. Lu, S. C. Kui, G. S. Tong, M. H. So, S. S. Chui, M. Muccini, J. Q. Ning, S. J. Xu and C. M. Che, *Angew. Chem. Int. Ed.*, **2008**, *47*, 9895-9899; Chi-Ming Che, Hai-Feng Xiang, Stephen Sin-Yin Chui, Zong-Xiang Xu, V. A. L. Roy, Jessie Jing Yan, Wen-Fu Fu, P. T. Lai, Ian D. Williams, *Chem. Asian J.*, **2008**, *3*, 1092-1103; ong-Young Noh, Jang-Joo Kim, Yuji Yoshida, Kiyoshi Yase, *Adv. Mater.* **2003**, *15*, 699-702; Nam Seob Baek, Steven K. Hau, Hin-Lap Yip, Orb Acton, Kung-Shih Chen, and Alex K.-Y. Jen, *Chem. Mater.* **2008**, *20*, 5734-5736.
21. Charlotte Po, Anthony Yiu-Yan Tam and Vivian Wing-Wah Yam, *Chem. Sci.*, **2014**, *5*, 2688.
22. C. Po; A. Y. Tam; K. M. Wong; V. W. Yam, *J. Am. Chem. Soc.*, **2011**, *133*, 12136-12143
23. S. Y. L. Leunga, K. M. Ch. Wonga, V. W. W. Yam, *PNAS*, **2016**, *113*, 2845-2850.
24. H. L. A. Yeung, S. Y. L. Leung, A. Y. Y. Tam, V. W. W. Yam, *J. Am. Chem. Soc.*, **2014**, *136*, 17910-17913.
25. Lifeng Zhang, Adi Eisenberg, *J. Am. Chem. Soc.*, **1996**, *118*, 3168-3181.
26. Zhang, L; Eisenberg, A., *Macromol. Symp.*, **1997**, *113*, 221.
27. M. Mauro, A. Aliprandi, C. Cebrian, D. Wang, C.Kübel, L. De Cola, *Chem. Commun.*, **2014**, *50*, 7269-7272.
28. A. Aliprandi, M. Mauro, L. De Cola,, *Nature Chem.*, **2016**, *8*, 10-15.
29. D. E. Discher and A. Eisenberg, *Science*, **2002**, *297*, 967-973.

Chapter 5

Supramolecular co-assembly of two luminescent platinum (II) complexes

Abstract: This chapter describes the co-assembly of two luminescent platinum (II) complexes. The two platinum (II) complexes were chosen due to their tendency to form fiber-like aggregates when placed individually in dioxane/water mixtures. The objective was to study the photophysical and morphological properties of the new aggregates from two different platinum (II) complexes added simultaneously to dioxane/water mixtures.

5.1. Introduction

Supramolecular fibers are one dimensional (1D) aggregates, in which units are connected through noncovalent interactions. These aggregates play an integral role in material chemistry, medicine and molecular electronics¹. The vested interest to study one dimensional materials is due to their unusual properties compared to the bulk material in the field of electrical conductivity², low-dimensional magnetism³ and non linear optics⁴. 1D aggregates of square-planar platinum (II) complexes showed intriguing spectroscopic and luminescence properties.

For several years, numerous reports were published on the synthesis and properties of materials composed of interacting metal ions along the backbone of a chain⁵. One of the oldest one-dimensional structures based on platinum which was correctly synthesized and analysed almost 200 years ago, was the Magnus' green salt $[\text{Pt}(\text{NH}_3)_4][\text{PtCl}_4]$ ⁶. It was discovered that the structure of of the Magnus's green salt involved a backbone of linearly arranged platinum atoms separated by 3.23-3.25 Å⁷. The relatively short Pt-Pt distances are the origin of the semiconducting properties of the Magnus' green salt⁸. The main disadvantage of such structures was their insolubility in water or common organic solvents which was restrictive for further applications⁹. In order to increase the solubility of these salts, $[\text{Pt}(\text{NH}_2\text{R})_4][\text{PtCl}_4]$ complexes (R is long alkyl chain) were prepared. These complexes were pink due to the increase of the Pt-Pt spacing and generally resulted in a loss of conductivity of the wire¹⁰, with a few exceptions¹¹.

One of the most studied classes of materials is the family of partially oxidized tetracyanoplatinate salts, commonly referred to as Krogmann salts¹². The square-planar $[\text{Pt}(\text{CN})_4]^{n-}$ anions in these materials form infinite stacks in the solid state based on the overlap of the d_z^2 orbitals normal to the plane of the molecule. These materials represent the first synthetically designed « wires » based on inorganic and were extensively studied for their conductivity properties. A new class of platinum chains based on alternating cations and anions of the types $[\text{Pt}(\text{CNR})_4]^{2+}$ (R = *i*Pr, *c*-C₁₂H₂₃, *p*-(C₂H₅)C₆H₄) and $[\text{Pt}(\text{CN})_4]^{2-}$ has been reported¹³. Some of these materials show pronounced and reversible color changes upon exposure to volatile organic compounds or solvent molecules from the gas phase¹⁴. This phenomenon is known as vapochromism¹⁵ and has been studied extensively. Vapochromism in crystalline $(\text{Pt}(\text{CNR})_4)[\text{Pt}(\text{CN})_4]$ salts arises from highly anisotropic packing forces that enable

solvent vapors to reversibly penetrate the interior of the material to form a new crystalline structures with precisely determined solvent chromophore interactions¹⁶. The colors exhibited for those platinum (II) complexes in the solid-state were dependent on the extent of the metal-metal interaction and π - π stacking of the polypyridyl ligands. The first example of a platinum (II) complex showing a pronounced color change upon varying the composition of the solvent mixture was reported by Yam and coworkers¹⁷. The luminescent platinum (II) diynyl complexes with a terpyridyl chelating ligand were molecularly dissolved in acetonitrile, and the addition of diethyl ether in solution resulted in changes of colors of the solution, from yellow to green to blue. The color changes were attributed to the formation of soluble platinum aggregates in solution. Since the complex was insoluble in diethyl ether, the molecule would tend to aggregate in an acetonitrile/diethyl ether mixture as a result of the reduced solvation. Such remarkable photophysical changes in the solvent composition were a milestone in the solvent-induced aggregation of platinum (II) complex referred to as solvatochromism. Numerous works on the formation of platinum aggregates such as nanosheets¹⁸, liquid crystals¹⁹ gels²⁰, fibers^{21,22} or wire^{23,24} with interesting luminescent, semiconducting, or gelating properties were reported. The correlation between the morphological changes and photophysical properties of an amphiphilic anionic platinum (II) complex was also studied by Yam and coworkers²⁵. Depending on the composition of an acetone/water mixture, the platinum (II) complex aggregated into fibers or vesicles and the morphological transformations were investigated via spectroscopy.

Several studies to further understand the mechanism of fiber assembly and dynamics have been carried out^{26,27} due to the importance of 1D self-assembled fibers in the aforementioned fields. *De Cola* and coworkers showed that platinum fibers were the result of a slow nucleation step followed by a fast elongation process²⁸. The control of the length of the 1D platinum fibers was also achieved by seeded growth polymerization²⁹ and was an important feature of further applications. These fibers also displayed mechanochromism upon pressure application delivered through atomic force microscopy (AFM)³⁰. The majority of the platinum aggregates reported to date undergo single-component self-assembly with the platinum (II) complex serving as the only monomeric species¹⁷⁻³⁰. In the last few months, the first supramolecular co-assembly between a platinum (II) complex and poly(ethylene glycol)-*b*-poly(acrylic acid) (PEG-*b*-PAA) diblock copolymer in aqueous solution was reported³¹. The resulting co-assembly

Both platinum (II) complexes had similar photophysical properties when dissolved in dioxane: a short excited state lifetime around 3 ns and a low PLQY below 1%. The emission spectra were both similar and showed structured bands at 460, 490 and 520 nm originating from the $^3\text{LC}/\text{MLCT}$ nature of the transition. When complex 25/dioxane solution was flash-injected into distilled water, blue-emissive fibers were formed as shown in Figure 5.1. When complex 7/dioxane solution was flash-injected in water, green-yellow emissive fibers were formed as shown in Figure 5.2.

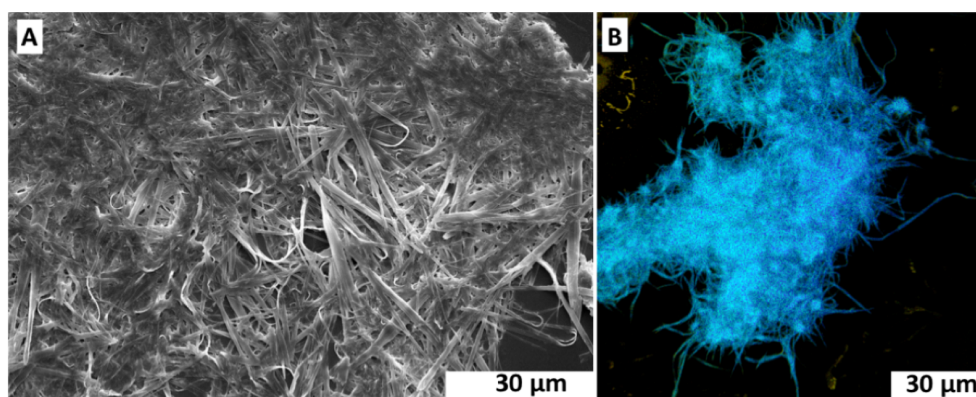


Figure 5.1. a) SEM and b) fluorescence confocal images of the fibers formed from complex 25 in water. The solution was drop-casted on a glass slide and dried under standard conditions. $\lambda_{\text{exc}} = 405 \text{ nm}$ in lambda mode.

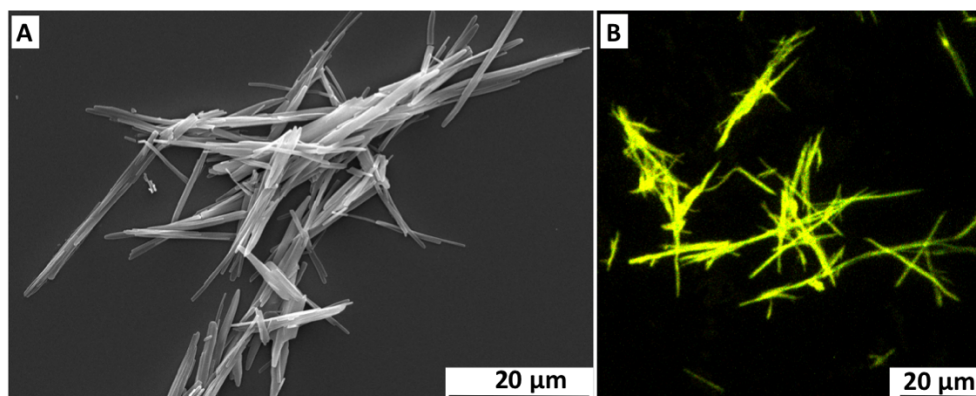


Figure 5.2. a) SEM and b) fluorescence confocal images of the fibers formed from complex 7 in water. The solution was drop-casted on a glass slide and dried under standard conditions. $\lambda_{\text{exc}} = 405 \text{ nm}$ in lambda mode.

There were two reasons that these particular platinum (II) complexes were chosen for the co-assembly. Firstly, they both formed fiber-like aggregates between 60% to 80% water content

in a water/dioxane mixture. The self-assembly of the two platinum (II) complexes could be triggered at the same time under the same conditions. Secondly, the photophysical properties of the two fibers were quite different and could be used as references during the co-assembly of the two platinum (II) complexes.

5.2.2. Co-assembly at 70% water content in dioxane/water mixture.

Complex 25 and complex 7 were separately dissolved in 1,4 dioxane ($c \approx 1.0$ mM solution). A 3 mL dioxane solution containing the two platinum (II) complexes at different concentrations were prepared and 7 mL of distilled water was added drop-wise (1 drop/ 10 seconds) to the dioxane/platinum (II) complexes while stirring. The final concentrations of the two platinum (II) complexes in the 10 mL dioxane/water mixture are reported in Table 5.1 along with the corresponding complex 25: complex 7 feed ratios. The solutions were then sealed to prevent any evaporation of the solvents and left to stand for 4 days prior to analysis.

complex 25 (mol.l ⁻¹)	5x10 ⁻⁵	5x10 ⁻⁵	5x10 ⁻⁵	5x10 ⁻⁵	5x10 ⁻⁵	5x10 ⁻⁵	5x10 ⁻⁵	5x10 ⁻⁵	3.75x10 ⁻⁵	2.5x10 ⁻⁵	2x10 ⁻⁵	1.5x10 ⁻⁵	1x10 ⁻⁵	5x10 ⁻⁶	0
complex 7 (mol.l ⁻¹)	0	5x10 ⁻⁶	1x10 ⁻⁵	1.5x10 ⁻⁵	2x10 ⁻⁵	2.5x10 ⁻⁵	3.75x10 ⁻⁵	5x10 ⁻⁵	5x10 ⁻⁵	5x10 ⁻⁵	5x10 ⁻⁵	5x10 ⁻⁵	5x10 ⁻⁵	5x10 ⁻⁵	5x10 ⁻⁵
Complex 25 : complex 7	1 : 0	1 : 0.1	1 : 0.2	1 : 0.3	1 : 0.4	1 : 0.5	1 : 0.75	1 : 1	0.75 : 1	1 : 0.5	1 : 0.4	1 : 0.3	1 : 0.2	1 : 0.1	0 : 1

Table 5.1. Concentration of the two platinum (II) complexes in 10 mL dioxane/water mixture solutions and ratio between the two complexes.

Photographs of the solutions containing the two platinum (II) complexes are displayed in Figure 5.2. The four solutions on the right of the photograph mainly contain complex 7 with ratios from 0:1 to 0:3 and these solutions displayed similar yellow luminescence. Upon increasing the concentration in complex 25 from 0.4:1 to 0.75:1 feed ratios, the solutions were orange emissive. At an equimolar 1:1 feed ratio, the solution remained orange emissive, however a precipitate was observed. At a 1: 0.75 molar ratio, a bright whitish emission was observed. From 1: 0.5 to 0.2 feed ratios, the solutions were emitting from white to blue. The solution at 1: 0.1 was slightly blue-green emissive. Finally, the solution containing only complex 25 was green emissive. Any clear trends were observed in the photographs.

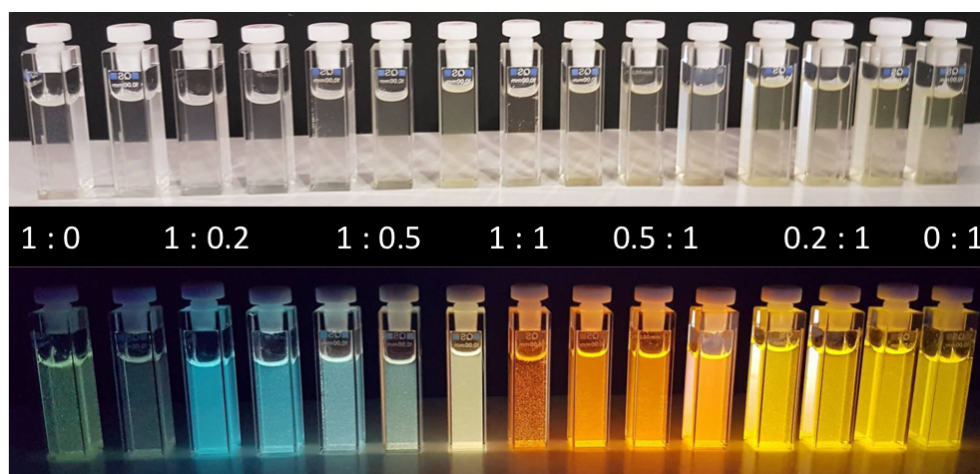


Figure 5.2. Photographs of the complex **25**/complex **7** dioxane/water solutions at 70% water content under standard light (to) and UV lamp (top, 365 nm). The values represent the complex **25**: complex **7** feed ratio for each solution.

Photophysical characterisation

Normalized emission and excitation spectra are displayed in Figures 5.3 and 5.4. The excited state lifetimes and photoluminescent quantum yields (PLQY) measured from the solutions are reported in Table 5.2. The emission spectra for 1 :0 in Figure 5.3 (black curve) showed three emission peaks at 465 nm, 495 nm and 530 nm and a shoulder at 570 nm. According to previous literature^{28',31}, these peaks were originating from the ³LC/MLCT transition from the blue emissive fibers. It appeared that two aggregates were present in solution due to the unusually high intensity of the peaks at 530 nm and the shoulder peak at 570 nm. The excited state was measured at 460 nm with an average lifetime at 450 ns while the excited state lifetime measured at 570 nm was around 2350 ns. It was reported that complex **25** self-assembled into blue-emissive fibers, green emissive fibers and yellow-orange emissive micelles^{28'}. A mixture of at least two of those aggregates was present in solution. Upon slightly increasing the concentration of complex **7**, the peaks at 530 nm and 570 nm was decreasing and a pure ³LC/MLCT emission profile was observed (Figure 5.3, A, blue curve). As the concentration of complex **7** in solution was increased, the ³LC/MLCT bands at 465 and 495 nm decreased in intensity while the peak at 570 nm increased in intensity (Figure 5.3, B) When complex **25** and **7** were equimolarly present in dioxane/water mixture, a broad single band centered at approximately 595 nm was observed (Figure 5.3, B, red curve).

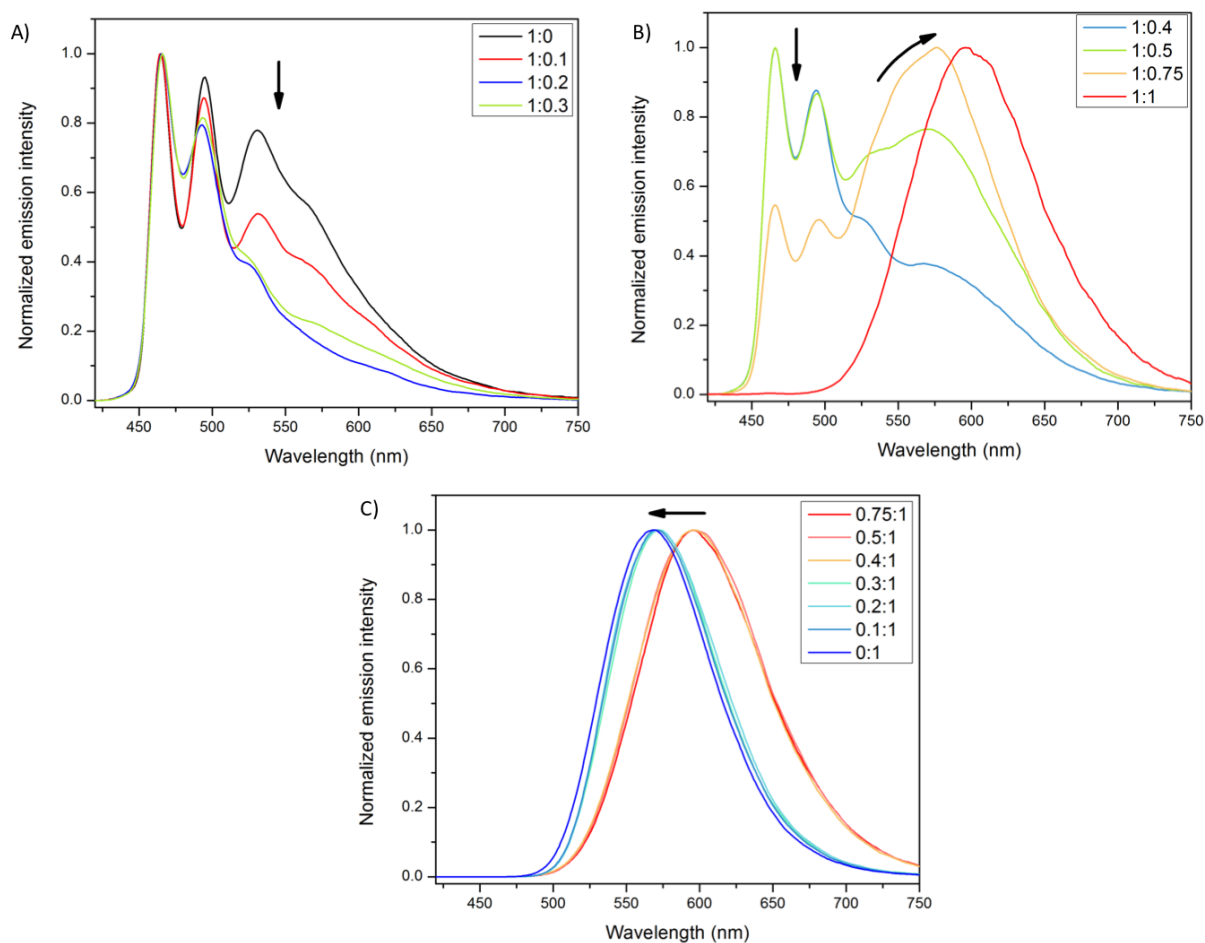


Figure 5.3. Normalized emission spectra of the complex **25**/complex **7** mixture in a 70% water content dioxane/water mixture. The arrows represent the trends of the emission spectra upon variation of the ratio between the two platinum (II) complexes. $\lambda_{exc} = 300$ nm.

The absence of bands at 465 nm and 495 nm indicated the disappearance of the blue emissive fibers in solution and the red shift indicated the formation of different types of platinum-platinum interactions. When the complex **25**: complex **7** ratio was in between 1:1 and 0.4:1, the emission bands were centered at approximately 595 nm. When the ratio was in between 0.3: 1 and 0: 1, the emission band was centered at approximately 570 nm (Figure 5.3, C). This confirmed the presence of two types of platinum aggregates. The signal at 570 nm originated from the platinum fibers formed from complex **7**. This was evidenced by the structured 1 MMLCT bands in the excitation spectra in Figure 5.4, D. The broad band centered at approximately 590 nm in emission was not yet attributed. The excitation spectra did not provide any other useful data

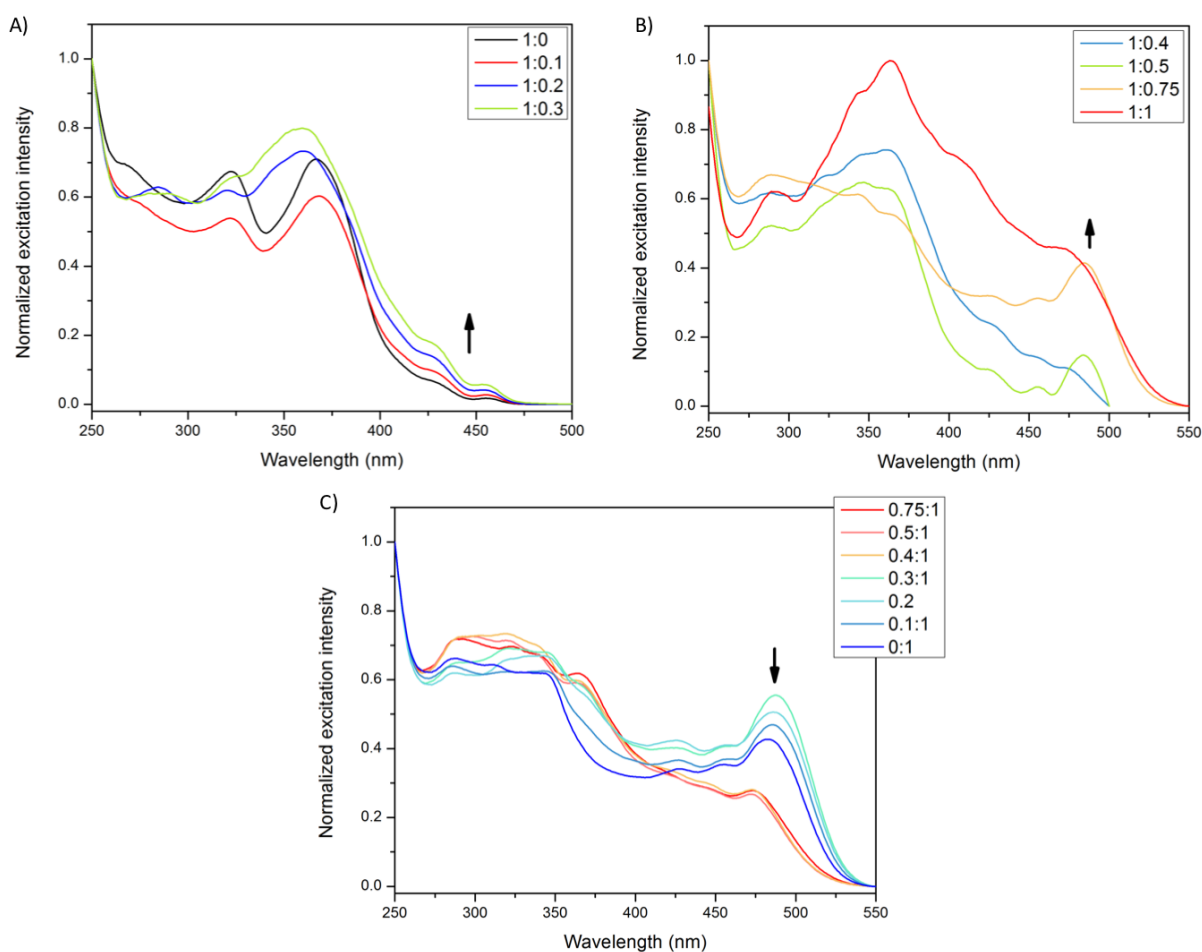


Figure 5.4. Normalized excitation spectra of the complex 25/complex 7 mixture in a 70% water content dioxane/water mixture. The arrows represent the trend of the emission spectra upon variation of the ratio between the two platinum (II) complexes. $\lambda_{em} = 520, 570$ or 590 nm (maximum of intensity of the corresponding emission spectra).

relating to the morphology of the platinum aggregates (Figure 5.4). The PLQY of the solutions are reported in Table 5.2. When complex 25 was dominant in solution, the PLQY was measured to be approximately 10%. Upon increasing the concentration of complex 7 in solution, the PLQY was gradually increasing until obtaining an average value of 60%. This value was similar for the aggregate emitting at 570 nm and 595 nm. The fibers emitting at 570 nm had an average lifetime of 420 ns and the aggregate emitting at 595 nm had an average lifetime of 570 ns. As mentioned previously, when a mixture of two emission profiles were observed, the excited lifetimes were measured at both wavelengths (Table 5.2). Complex 25 had a « short » excited state lifetime of 450 ns at 465 nm and a « long » lifetime of 2350 ns at

570 nm. When a small amount of complex **7** was added in solution (1 :0. 1), the lifetime at 570 ns was decreased from 2350 ns to 1240 ns.

*Table 5.2. Photophysical properties of the complex **25**: complex **7** dioxane/water solution (70% water content). $\lambda_{exc} = 405$ nm, λ_{em} was the wavelength of maximum intensity. When more than two peaks were present in the emission spectra, the detection wavelength for the excited state lifetime measurements was typed in bold in the emission max column.*

Complex 25 : complex 7	PLQY	Emission max	Lifetime (ns)	Average lifetime (ns)
1:0	0.12	465, 495, 530, 570 (sh)	100 (24%), 370 (52%), 850 (22%), 3310 (1%)	450
1:0	0.12	465, 495, 530, 570 (sh)	790 (65%), 3350 (20%), 8000 (15%)	2350
1:0.1	0.10	465, 495, 530, 570 (sh)	130 (27%), 500 (65%), 1360 (8%)	470
1:0.1	0.10	465, 495, 530, 570 (sh)	740 (86%), 2760 (10%) 8210 (4%)	1240
1:0.2	0.23	465, 495, 525 (sh)	180 (13%), 690 (55%) 1160 (33%)	780
1:0.3	0.28	465, 495, 525 (sh), 570 (sh)	500 (31%), 1200 (69%)	980
1:0.4	0.29	465, 495, 525 (sh), 570	470 (32%), 1200 (68%)	970
1:0.4	0.29	465, 495, 525, 570 (sh)	720 (80%), 1470 (20%)	870
1:0.5	0.35	465, 495, 525, 570	420 (32%), 1160 (68%)	920
1:0.5	0.35	465, 495, 525, 570	500 (74%), 1180 (26%)	675
1:0.75	0.47	465, 495, 575	450 (36%), 1250 (64%)	970
1:0.75	0.47	465, 495, 575	450 (89%), 1210 (11%)	540

1 :1	0.62	595	50 (8%), 570 (92%)	530
0.75:1	0.60	595	330 (5%), 580 (95%)	570
0.5 :1	0.50	597	580	580
0.4 :1	0.60	597	575	575
0.3 :1	0.59	570	420 (96%), 660 (4%)	430
0.2 :1	0.57	570	410 (97%), 670 (3%)	420
0.1 :1	0.65	570	410 (98%), 740 (2%)	420
0 :1	0.60	570	400 (98%), 790 (2%)	405

From 1 :0.2 to 1 :0.75 feed ratios, the excited state lifetime measured at 465 nm was approximately 950 ns, similar to the value previously reported in literature²⁹. The values measured at 570 nm decreased from 1240 ns to 540 ns. This change was attributed to the formation of new platinum-platinum aggregates that were emitting at 595 ns. Those photophysical measurements were quite interesting and were evidence of some type of interaction between the two platinum (II) complexes in a dioxane/water mixture. A superimposition of the emission profile in the emission and excitation spectra with peak intensities dependant on the concentration of the platinum (II) complex should have been observed. Conversely, a red-shift was observed in emission when the complex **25**: complex **7** ratio was between 1:1 and 0.4 :1. Surprisingly, there was a catalytic effect of complex **7** on the formation of blue-emissive fibers of complex **25**. It was observed that a mixture of blue emissive fibers and yellow-orange emissive fibers were present when complex **25** was dissolved alone the dioxane/water mixture. Upon addition of a small amount of complex **7** (1 :0.1 and 1 :0.2 ratio), the emission peaks at 535 nm and 570 nm decreased and a pure ³LC/MLCT signal originating from the blue-emissive fibers was observed. An increase of the peak at 570 nm was expected as the result of the formation of agggregates of complex **7**.

Electron microscopy

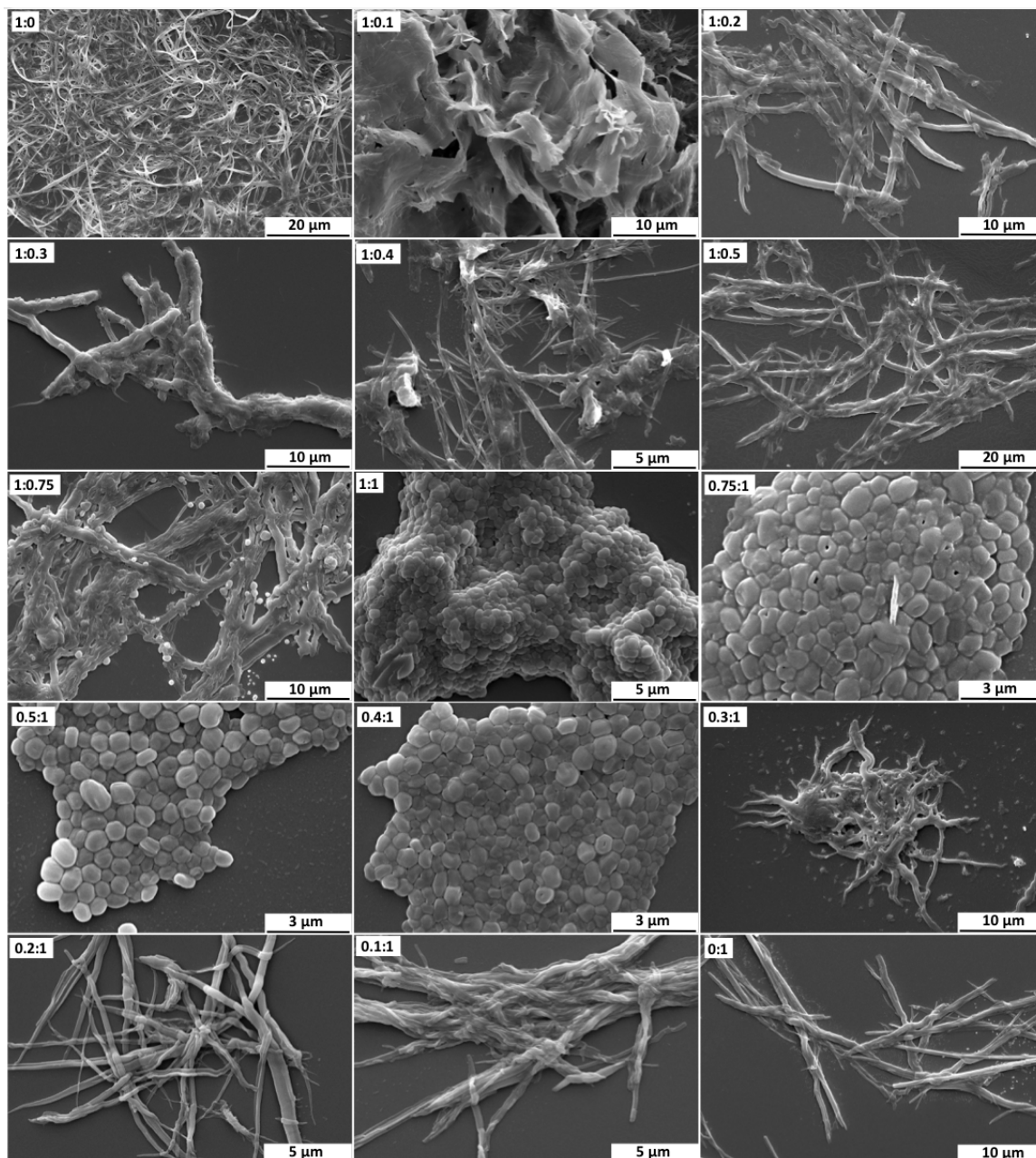


Figure 5.5. SEM images of complex 25: complex 7 dioxane/water mixture. The solutions were drop-casted on a glass slide and evaporated under standard conditions.

In order to study the morphology of the complex 25/complex 7 aggregates, SEM images of the drop-casted solution on a glass slide are displayed in Figure 5.5. Complex 25 alone (1:0) formed a haystack of flexible and thin ribbon-like aggregates upon addition in water. When a small amount of complex 7 was added (1 :0.1), a mixture of sheet-like and fiber-like aggregates were observed. When the concentration in complex 7 was increased (1 :0.2 to 1 :0.5), thick

platinum fibers were observed on the SEM images. At a 1 :0.75 ratio, a mixture of thick fibers and hexagonal particles were observed. When the concentration in complex **7** was equal to or higher than the concentration of complex **25** in solution (1:1 to 0.4:1), only hexagonal shaped particles were observed. Finally, when the concentration of complex **7** was dominant (0.3:1 to 0 :1), an entanglement of thick and flexible fibers were observed.

Confocal fluorescence microscopy

Confocal fluorescence imaging of the complex **25**: complex **7** solutions drop-casted on a glass slide and dried under standard conditions are displayed in Figure **5.6**. Haystacks of blue emissive fibers were observed when complex **25** was alone in solution. Yellow-orange emissive amorphous material was also present along with the fibers. This confirmed the fact that the self-aggregation of complex **25** into fibers was not complete and that kinetically trapped platinum vesicles were still present in solution²⁹. When the concentration in complex **7** was slightly increased (1 :0.1), the blue emissive sheet-like aggregates were observed with yellow-orange emissive vesicles. The thick fibers observed when the concentration in complex **7** was increased (1 :0.2 to 1 :0.75) were orange emissive. The hexagonal-shaped aggregated in solution when the concentration in complex **7** was higher than the concentration in complex **25** (1:1 to 0.4:1), and were also yellow-orange emissive. Finally, when complex **7** was dominant (0.3:1 to 0:1), yellow-green emissive fibers were observed by fluorescence microscopy. The shapes of the aggregates observed under the microscope was consistent with the shapes observed by SEM. However, there were significant differences observed between the photophysical properties measured in solution and the emission profile observed by fluorescence microscopy. For example, for the complex **25**: complex **7** with a feed ratio of 1 :0.2, the solution was blue-emissive and the emission spectra showed structured ³LC/MLCT bands at 465, 495 and 520 nm. Conversely, the fibers observed by confocal imaging were orange emissive and the emission spectra showed a broad band centered at approximately 585 nm, attributed to ³MMLCT due to the new platinum-platinum interactions as displayed in Figure **5.7**. The evaporation of the solvent mixture during the drying of the drop-casted solution on the glass slide is suspected to have caused the formation of a new type of aggregates.

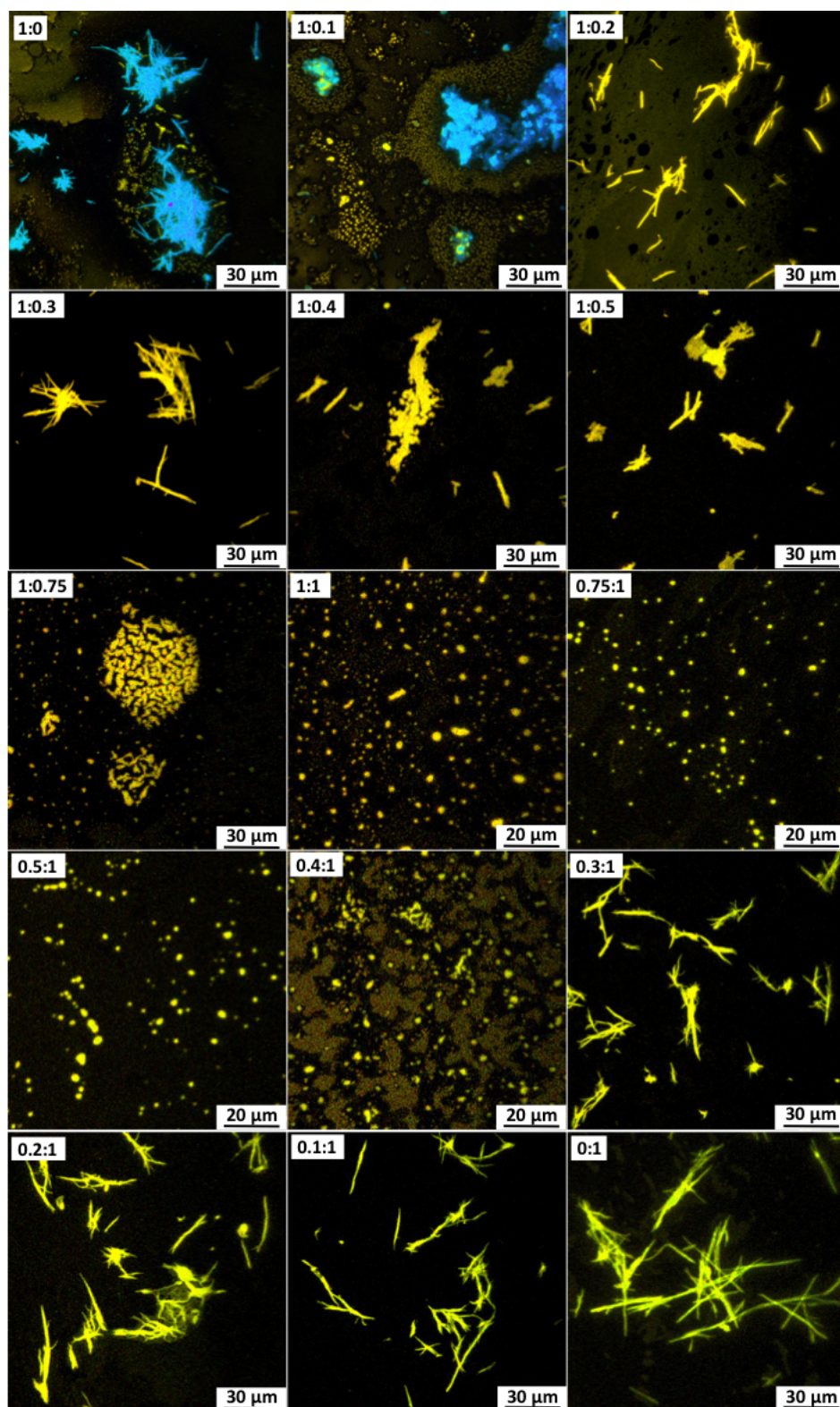


Figure 5.6. Confocal imaging of the complex 25: complex 7 dioxane/water solution (70% water content) dried on a glass slide. $\lambda_{exc} = 405 \text{ nm}$ in lambda mode (real emission).

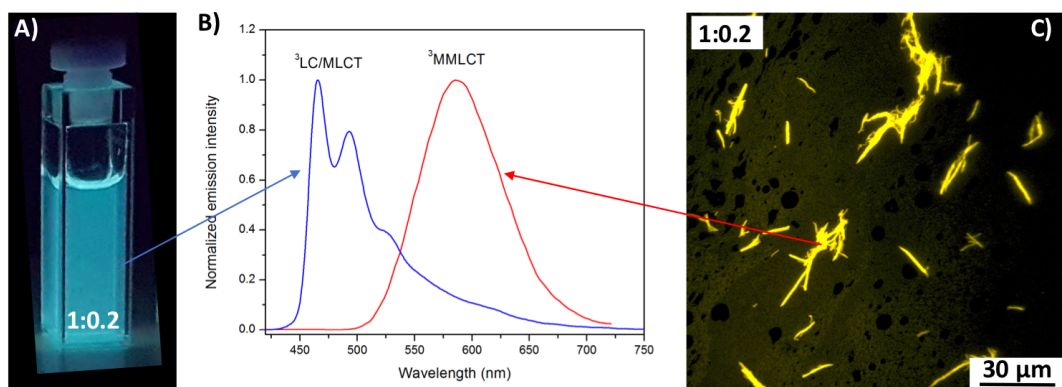


Figure 5.7. a) Photograph of the complex **25**: complex **7** (1:0.2) dioxane/water solution and c) confocal imaging on the solution dried on a glass slide and b) their corresponding normalized emission intensity. $\lambda_{exc} = 300 \text{ nm}$ for the solution and $\lambda_{exc} = 405 \text{ nm}$ for the confocal imaging (real color).

The aggregates inducing the blue-emission were not observed either by SEM or confocal as the sample was already dried. For this reason, real time imaging by confocal microscopy was considered necessary. One drop of the solution was drop-casted on a glass slide and fluorescence images were recorded every 20 seconds for 36 minutes. Selected images are displayed in Figure 5.8.

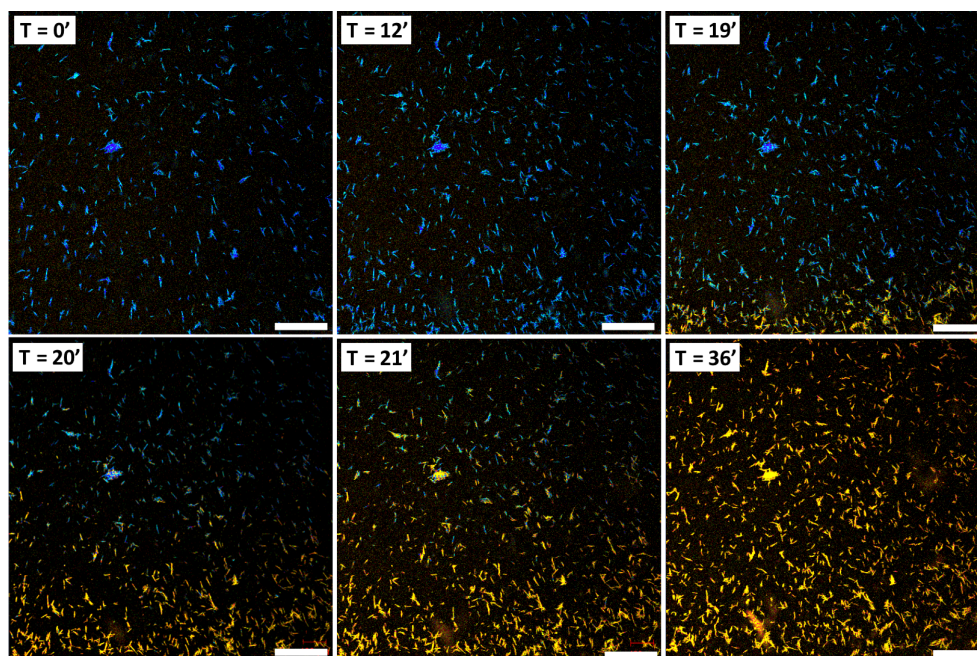


Figure 5.8. Real-time confocal imaging of the drop-casted solution of complex **25**: complex **7** (1 :0.2) dioxane/water mixture (70% water content). $\lambda_{exc} = 405 \text{ nm}$ (real colors). Scale bar: 200 μm . The values indicate the number of minutes from the beginning of the recording.

At the beginning of the imaging ($t=0'$), numerous blue emissive fibers were observed in solution. These fibers were migrating to the edge of the droplet as observed at $t=12'$. Surprisingly, the luminescence of the fibers rapidly changed from blue to orange ($t=19'$ to $t=21'$). At the end of the experiment, all the platinum fibers were orange emissive even if they were still in solution. When all of the solvents had evaporated, orange emissive fibers were observed, as displayed in Figure 5.7. To investigate the red-shifted emission of the fibers upon evaporation of the solvent mixture, dioxane and water were compared. Both solvents have very similar boiling point (100°C against 101°C for dioxane at ambient temperature) and density ($1.0\text{ g}\cdot\text{ml}^{-1}$ against $1.033\text{ g}\cdot\text{ml}^{-1}$), which made them ideal candidates for the solvent mixture. However, the vapor pressure of the dioxane was 38 mbar at 20°C whereas the vapor pressure of water was 23.4 mbar at 20°C . In standard conditions where the atmospheric pressure was close to 1000 mbar, the solvent with the higher vapor pressure will generally evaporate first. In a dioxane/water mixture, it is suspected that the dioxane will evaporate before the water and modify the mixture composition in the droplet. It is of particular interest that the luminescence shift of the fibers from blue to orange was propagating from the exterior to the interior of the droplet. The droplet was evaporating from the exterior to the interior. As a result, the solvent mixture composition was firstly modified at the exterior of the droplet due to the evaporation of the dioxane and was then propagating to the interior. As a conclusion, the luminescence shift of the fibers was induced by an increase of the water content in the solvent mixture. In order to demonstrate this theory, the dioxane/water mixture containing complex **25** and complex **7** (1 :0.2) was dialysed against water. In this example, the platinum fibers remained in solution and only the solvent composition was changed. Photophysical and morphological characterisation of the dialysed solution is displayed in Figure 5.9. As expected, the luminescence of the solution was shifted from blue to orange. The normalized emission spectra displayed a distinct difference between the structured $^3\text{LC}/\text{MLCT}$ bands at 465, 495 and 525 nm and the broad band centered at approximately 610 nm. The emission was significantly red-shifted compared to the 585 nm measured by confocal microscopy on the dried sample (Figure 5.7). The SEM and confocal images confirmed that the emission was originating from thick entangled fibers. Such extreme changes in the photophysical properties was due to the increase of the water content resulting in an increase the polarity of the solvent mixture. The ability of a chemical substance to change color due to a change in solvent polarity is referred to as solvatochromism and has previously

been reported for platinum (II) complexes^{20,28}. However, in those articles, the color change was attributed to a morphological transformation. In this case, the shape of the platinum fibers remained consistent upon increasing the solvent polarity. Moreover, the positive solvatochromism was only observed when complex **25** and **7** were mixed together and formed “hybrid” and stimuli-responsive aggregates in a dioxane/water mixture. Indeed, blue-emissive fibers formed from complex **25** or yellow-green emissive fibers formed from complex **7** did not show any solvatochromic effect. It is worth noting that depending on the feed ratios between the two complexes in solution, either fibers or hexagonal particles were formed, while the two platinum (II) complexes alone formed fibers.

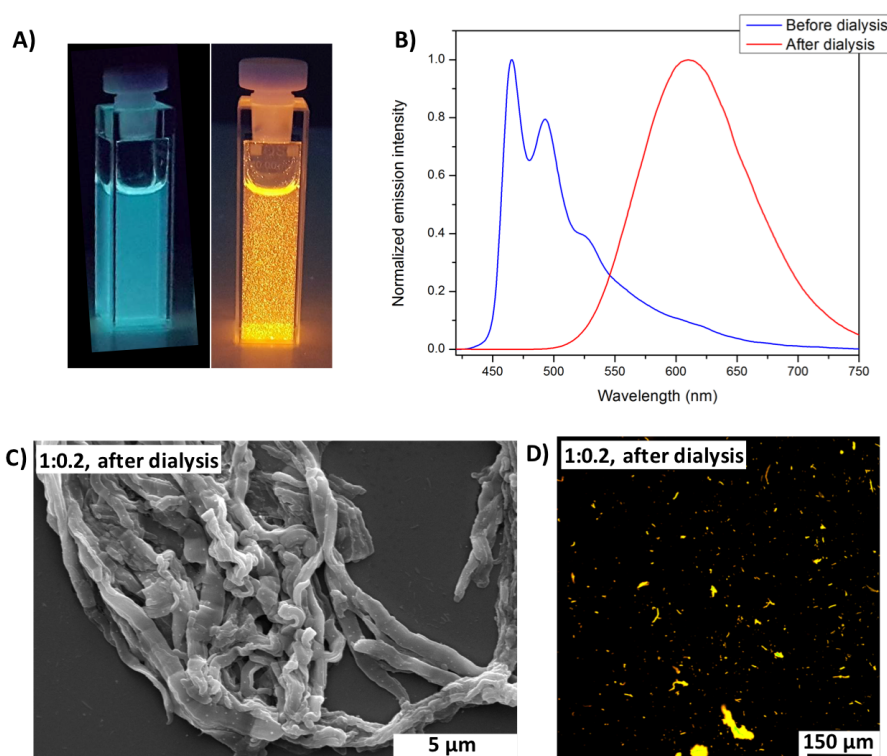


Figure 5.9. A) Photograph of the solution containing complex **25** and complex **7** (1 :0.2 feed ratio) before and after dialysis against water and b) corresponding normalized emission spectra. $\lambda_{exc} = 300 \text{ nm}$. C) SEM and d) confocal images of the platinum aggregates after dialysis. $\lambda_{exc} = 405 \text{ nm}$ in lambda mode (real colors).

In order to conduct a detailed study of the solvatochromism of those “hybrid” fibers, the solvent composition was modified and the complex **25**: complex **7** feed ratios were narrowed down between 1:0 and 1:1.

5.2.3. Co-assembly at 80% water content in dioxane/water mixture.

Solutions containing complex **25** and **7** in a dioxane/water solution at 80% water content were prepared via the same method described previously. Complex **25** and complex **7** were separately dissolved in 1,4 dioxane ($c \approx 1.0$ mM solution). A 2 mL dioxane solution containing the two platinum (II) complexes at different concentrations were prepared and 8 mL of distilled water was added drop-wise (1 drop/ 10 seconds) to the dioxane/platinum (II) complexes while stirring. The final concentrations of the two platinum (II) complexes in the 10 mL dioxane/water mixture are reported in Table 5.3 along with the corresponding complex **25**: complex **7** feed ratios. The solutions were sealed to prevent any evaporation of the solvents and left to stand for 4 days prior analysis.

Table 5.3. Concentrations of the two platinum (II) complexes in 10 mL dioxane/water mixture solutions and ratio between the two complexes.

complex 25 (mol.l ⁻¹)	5×10^{-5}	5×10^{-5}	5×10^{-5}	5×10^{-5}	5×10^{-5}	5×10^{-5}	5×10^{-5}	5×10^{-5}	5×10^{-5}	0
complex 7 (mol.l ⁻¹)	2.5×10^{-6}	5×10^{-6}	7.5×10^{-6}	1.0×10^{-5}	1.25×10^{-5}	1.5×10^{-5}	2.0×10^{-5}	2.5×10^{-5}	5×10^{-5}	5×10^{-5}
Complex 25 : complex 7	1 : 0.05	1 : 0.1	1 : 0.15	1:0.2	1 : 0.25	1 : 0.3	1 : 0.4	1 : 0.5	1 : 1	0 : 1

Photographs of the solutions containing the two platinum (II) complexes are displayed in Figure 5.10. The four solutions on the left on the picture containing mainly complex **25** had a blueish luminescence. Upon increasing the concentration of complex **7**, the luminescence of the solutions was red-shifted until a bright yellow-orange emission was obtained at a 1:1 ratio. Complex **7** alone in solution had a yellow-green emission (cuvette on the right of the photograph).

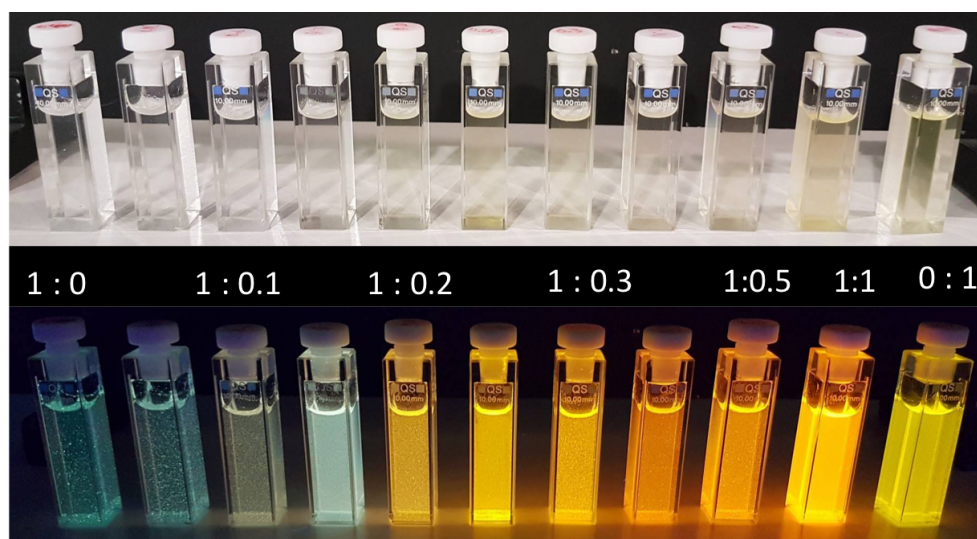


Figure 5.10. Photographs of the complex 25/complex 7 dioxane/water solutions at 80% water content under normal light (to) and UV lamp (top, 365 nm). The values represent the complex 25: complex 7 molar feed ratios for each solution.

Photophysical characterisation

Normalized emission and excitation spectra of the different solutions are shown in Figure 5.11. Complex 25 displayed the usual ³LC/MLCT structured bands at 465, 495 and 530 nm in emission. Upon increasing the concentration of complex 7, these bands decreased in intensity while a broad band centered at approximately 585 nm emerged (1 :0.05 to 1 :0.2). This broad band was attributed to ³MMLCT transition due to platinum-platinum interactions. A red shift of the broad band from 585 nm to 605 nm was observed and attributed to the formation of a new type of platinum aggregates. As reported previously, the emission of complex 7 in the dioxane/water mixture was centered at approximately 570 nm. The normalized excitation spectra did not show any ¹MMLCT bands between 400 and 500 nm for complex 25 in solution. However, the increase of the complex 25: complex 7 feed ratio led to the emergence of those bands as a result of platinum-platinum interactions. Excited state lifetime and PLQY of the solutions are reported in Table 5.4. Those values are similar to the values at 70% water content. The blue emissive fibers had a lifetime of around 450 ns. Upon increasing the concentration in complex 7, new aggregates formed with an average lifetime of 560 ns. An increase of the PLQY was also observed from around 8% for the blue emissive fibers to a maximum of 78% for the hexagonal aggregates formed at a 1 1 ratio.

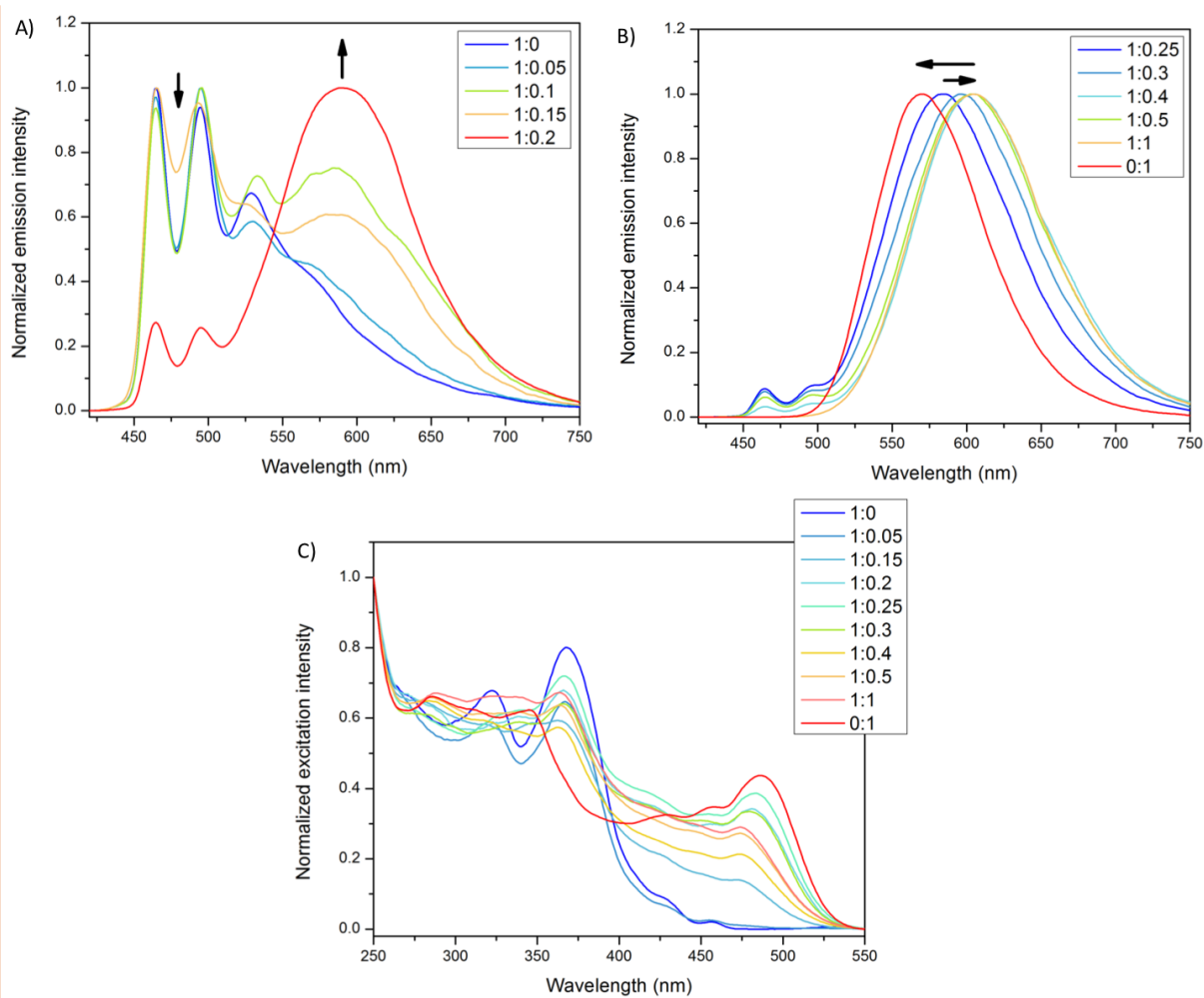


Figure 5.11. a), b) Normalized emission spectra and c) excitation spectra of the complex **25**/complex **7** mixture in a 80% water content dioxane/water mixture. The arrows represent the trend of the emission spectra upon variation of the ratio between the two platinum (II) complexes. $\lambda_{exc} = 300$, $\lambda_{em} = 570-600$ nm (maximum of intensity of the corresponding emission spectra).

Table 5.4. Photophysical properties of the complex 25: complex 7 dioxane/water solutions (80% water content). $\lambda_{exc} = 405$ nm, λ_{em} was the wavelength of maximum intensity. The detection wavelength was typed in bold in the emission max column when more than two peaks were present in the emission spectra.

Complex 25 : complex 7	PLQY	Emission max	Lifetime (ns)	Average lifetime (ns)
1 :0	0.08	465 , 495, 530, 570 (sh)	190 (50%), 630 (47%), 2450 (3%)	460
1 :0.05	0.08	465 , 495, 530, 570 (sh)	200 (49%), 610 (49%), 2330 (2%)	450
1 :0.1	0.12	465 , 495, 530, 570, 585	180 (48%), 550 (50%) 2170 (2%)	410
1 :0.1	0.12	465, 495, 525, 585	660 (95%), 3130 (4%) 9840 (1%)	840
1 :0.15	0.31	465 , 495, 525(sh), 570 (sh)	330 (25%), 880 (73%), 2600 (1%)	760
1 :0.15	0.31	465, 495, 525 (sh), 585	660 (96%), 1500 (4%)	700
1 :0.2	0.30	465 , 495, 590	120 (36%), 475 (59%), 1440 (5%)	400
1 :0.2	0.30	465, 495, 590	560 (100%)	560
1 :0.25	0.43	585	540 (100%)	540
1 :0.3	0.45	597	550 (100%)	550
1 :0.4	0.40	605	570 (100%)	570
1 :0.5	0.45	605	570 (100%)	570
1:1	0.78	605	565 (100%)	565
0 :1	0.64	570	400 (99%), 990 (1%)	405

Electron microscopy

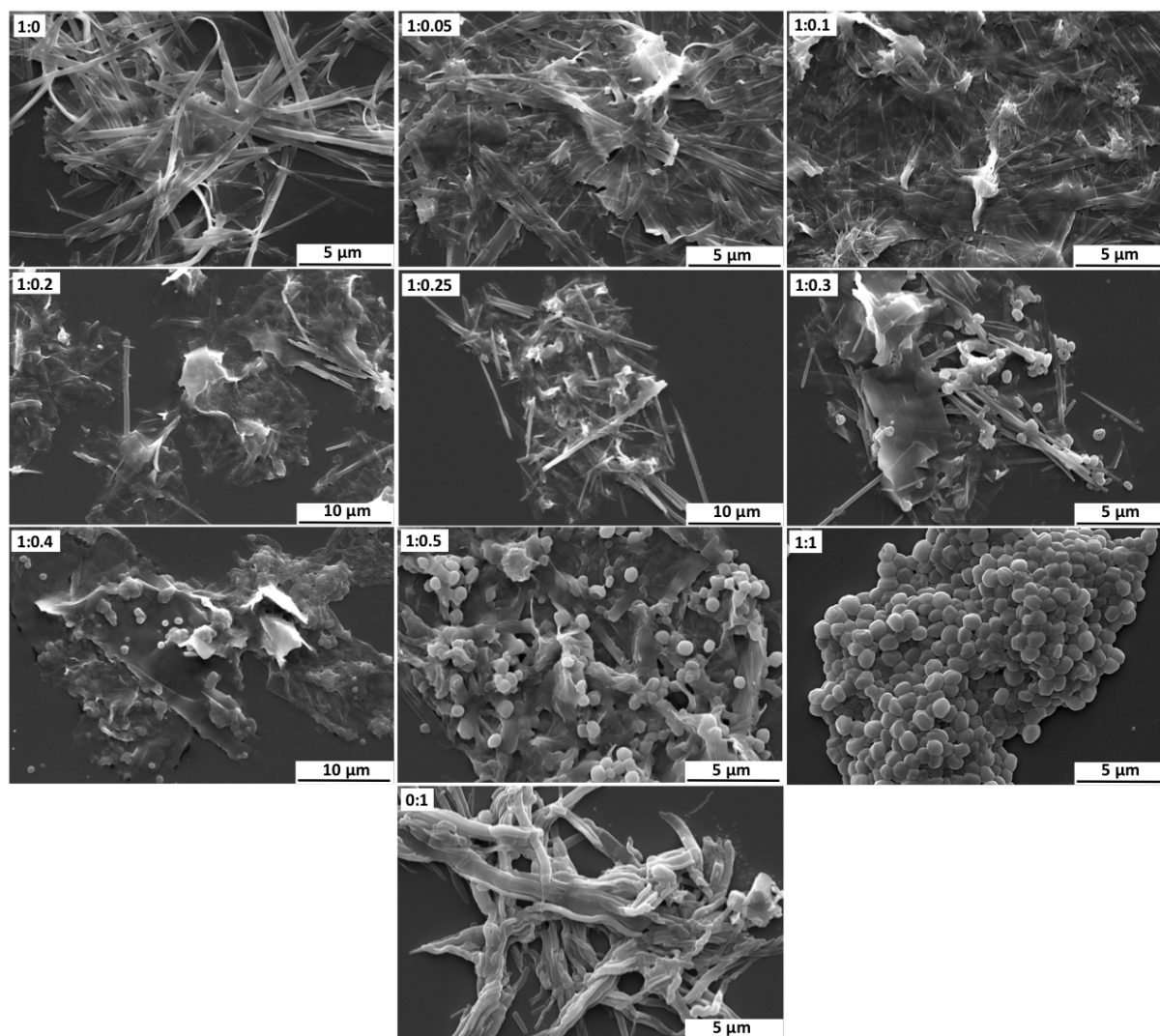


Figure 5.12. SEM images of complex 25 : complex 7 dioxane/water mixture. The solutions were drop-casted on a glass slide and evaporated under standard conditions.

In order to investigate the morphology of the platinum aggregates, SEM images of different solutions dried on a glass slide were conducted and are displayed in Figure 5.12.

Complex 25 in a dioxane/water mixture at 80% water content also formed flexible ribbons. Upon increasing the concentration in complex 7, the ribbons became almost transparent, sheet-like aggregates. Moreover, the presence of needle-like aggregates was also observed at 1 :0.2 and 1 :0.25 ratio. Further increase of the complex 25: complex 7 feed ratio led to the formation of the hexagonal particles along with needle and transparent ribbon-like aggregates (1 :0.3 to 1 :0.5). At an equimolar 1 :1 ratio, only hexagonal particles were observed. When complex 7 was isolated in a dioxane/water mixture, fibers of different shapes and sizes were

observed. Finally, in order to correlate the photophysical properties with the morphology of the aggregates, confocal images were compared.

Confocal fluorescence microscopy

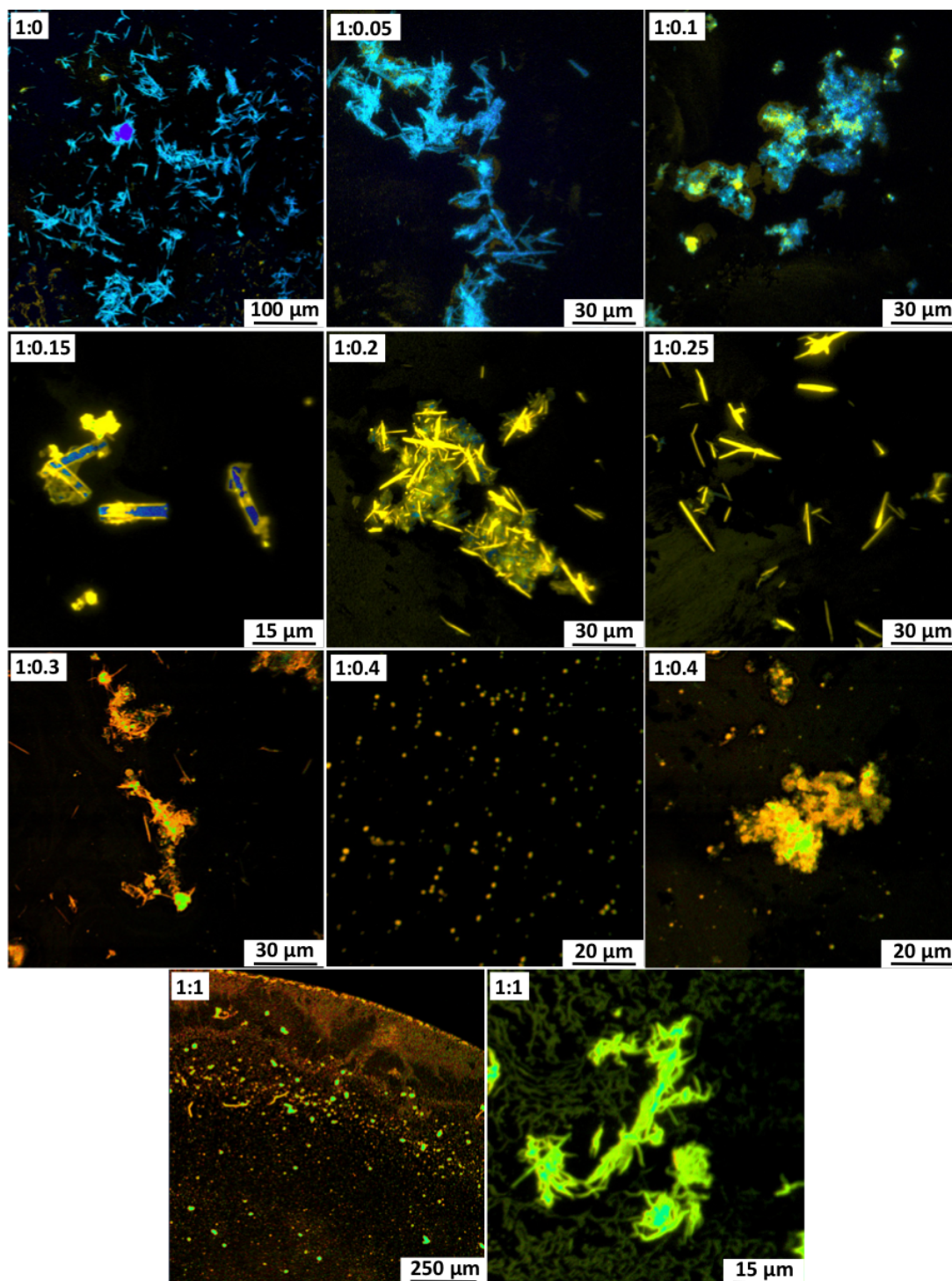


Figure 5.13. Confocal imaging of the complex 25: complex 7 dioxane/water solution (80% water content) dried on a glass slide. $\lambda_{exc} = 405 \text{ nm}$ in lambda mode (real emission).

These images are displayed in Figure 5.13. Complex **25** self-assembled into blue-emissive ribbons in the dioxane/water mixture. Upon slightly increasing the concentration in complex **7**, the blue emissive ribbons remained with some yellow green patches (1 :0.05 and 1 :0.1). Interestingly, at a 1 :0.15 ratio, blue emissive ribbons coated with a yellow layer were observed. At this point, the two platinum (II) complex did not co-assemble together but separately. At 1 :0.2 and 1.0.25, yellow emissive needles were observed on the confocal images. Neither complex **25** or complex **7** self-assembled into this particular type of aggregates and the yellow emissive fibers were the result of the co-assembly between the two platinum (II) complexes. Further increase of the concentration of complex **7** led to the formation of orange emissive hexagonal particles (1 :0.3 to 1 :1). Eventually, complex **7** formed yellow-green emissive fiber-like aggregates.

Contrary to the solutions at 70% water content, any significant differences between the luminescence of the solutions and aggregates observed by confocal were measured for solutions at 80% water content. To ensure the absence of solvatochromism, real time confocal imaging of a droplet of the 80% water content solution at a ratio of 1 :0.2 was performed and is shown in Figure 5.14.

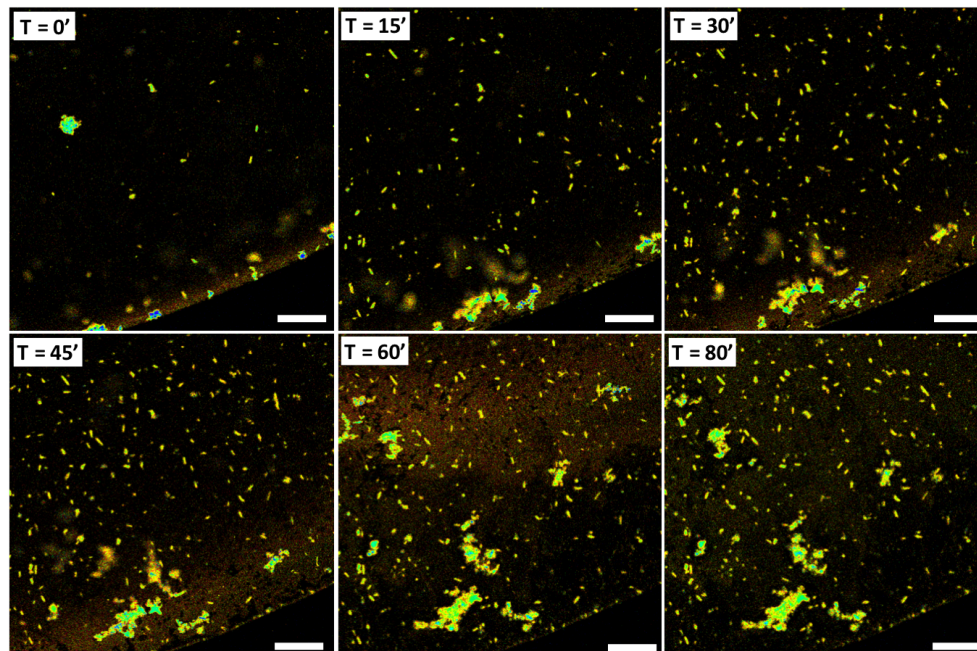


Figure 5.14. Real-time confocal imaging of the drop-casted solution of complex **25**: complex **7** (1 :0.2) dioxane/water mixture (70% water content). $\lambda_{exc} = 405 \text{ nm}$ (real colors). Scale bar: 100 μm .

The migration of the platinum aggregates to the outskirts of the droplet was observed for the first 45 minutes followed by the complete evaporation of the droplet at $t = 80$ min. Between the start and the completion of the experiment no emission shifts were observed on the platinum (II) aggregates. A mixture of yellow needles and blue emissive patches was observed at the start and at the end. Although the co-assembly of the two platinum (II) complexes resulted in the formation of new yellow-emissive fibers, any solvatochromic effect upon evaporation of the droplet was still also observed. At 80% water content in a dioxane/water mixture, the water content was too high to observe the solvatochromic effect.

5.2.4. Co-assembly at 60% water content in dioxane/water mixture.

Solutions containing complex **25** and **7** in a dioxane/water solution at 60% water content were prepared via the same method described previously. Complex **25** and complex **7** were separately dissolved in 1,4 dioxane ($c \approx 1.0$ mM solution). A 4 mL dioxane solution containing the two platinum (II) complexes at different concentrations were prepared and 6 mL of distilled water was added drop-wise (1 drop/ 10 seconds) to the dioxane/platinum(II) complexes while stirring. The final concentration of the two platinum (II) complexes in the 10 mL dioxane/water mixture are reported in Table 5.5 with the corresponding complex **25**: complex **7** feed ratios. The solutions were sealed to prevent any evaporation of the solvents and left to stand for 4 days prior analysis.

complex 25 (mol.l ⁻¹)	5×10^{-5}	5×10^{-5}	5×10^{-5}	5×10^{-5}	5×10^{-5}	5×10^{-5}	5×10^{-5}	5×10^{-5}	0
complex 7 (mol.l ⁻¹)	2.5×10^{-6}	5×10^{-6}	7.5×10^{-6}	1.0×10^{-5}	1.5×10^{-5}	2.0×10^{-5}	2.5×10^{-5}	5×10^{-5}	5×10^{-5}
Complex 25 : complex 7	1 : 0.05	1 : 0.1	1 : 0.15	1:0.2	1 : 0.3	1 : 0.4	1 : 0.5	1 : 1	0 : 1

Table 5.5. Concentrations of the two platinum (II) complexes in 10 mL dioxane/water mixture solutions and ratios between the two complexes.

Photographs of the solutions containing the two platinum (II) complexes are shown in Figure 5.15. The three solutions on the left on the picture mainly consisted of complex **25** and had a bluish luminescence. Upon increasing the concentration of complex **7**, the luminescence of the solutions was red-shifted until a yellow-orange emission was obtained at a 1:1 ratio.

Complex **7** alone had a bright yellow emission. In the previous chapter, it was determined that the self-assembly of complex **25** initiated at a water content of 55% in a dioxane/water mixture. As a result, only a small amount of fibers at 60% water content was expected and the luminescence of the solutions under UV light was less intense at 60% water content compared to the 70% or 80% water content solutions.

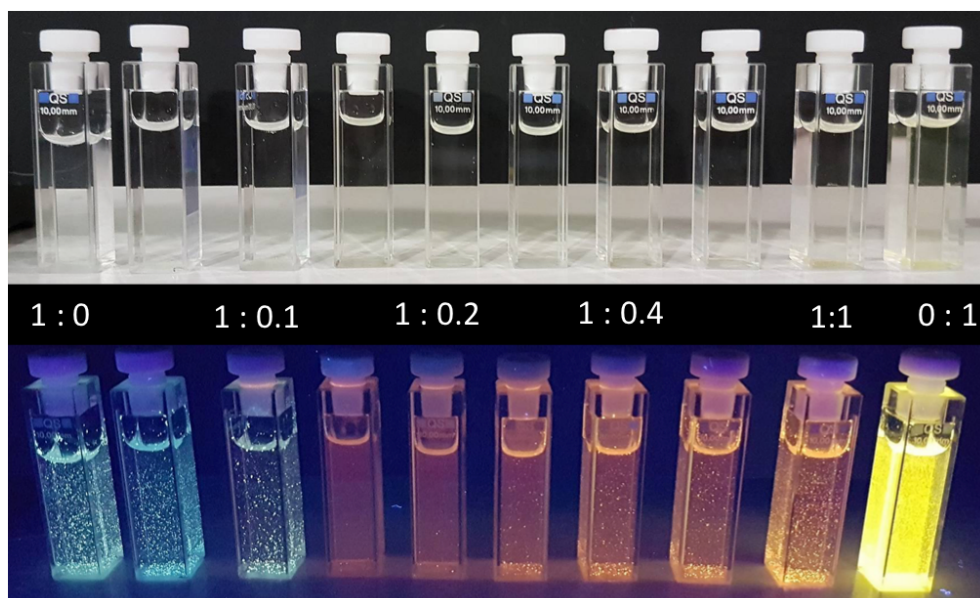


*Figure 5.15. Photographs of the complex **25**/complex **7** dioxane/water solutions at 60% water content under normal light (bottom) and UV lamp (top, 365 nm). The values represent the complex **25**: complex **7** feed ratios for each solution.*

Photophysical characterisation

Normalized emission and excitation spectra of the solutions are displayed in Figure 5.16. The emission spectra appeared to contain similar trends to those observed at the 70% and 80% water content mixtures. Upon increasing the complex **25**: complex **7** feed ratio, the structured $^3\text{LC/MLCT}$ bands at 465, 495 and 530 nm were decreasing in intensity while a broad $^3\text{MMLCT}$ band centered at approximately 605 nm was rapidly emerging. Complex **7** alone displayed the usual broad band centered at 565 nm attributed to the platinum-platinum interaction in the platinum fibers. The normalized excitation spectra did not show any $^1\text{MMLCT}$ bands between 400 and 500 nm except for the complex **7** alone, indicating the absence or the limited amount of platinum fibers in solution. PLQY and excited state lifetimes of the solutions are reported

in Table 5.6. Two significant differences were observed compared to the photophysical properties at 70% and 80% water content solutions.

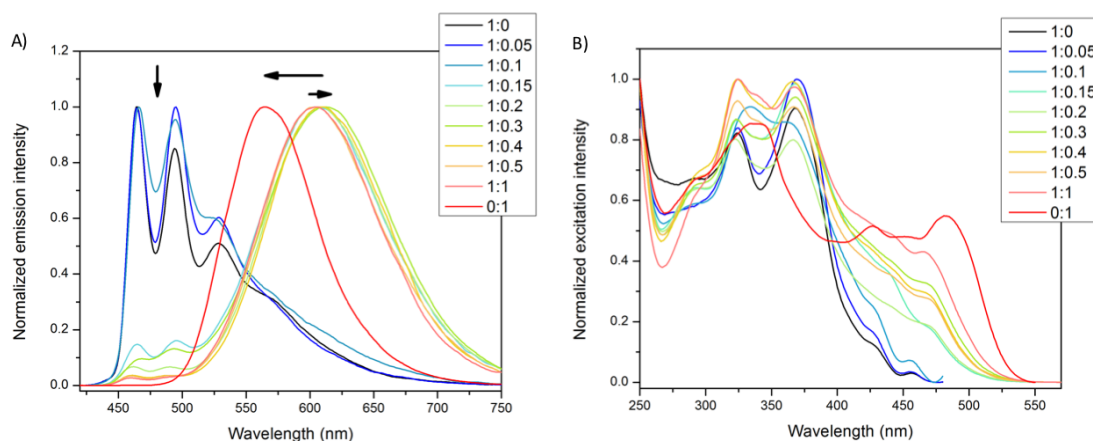


Figure 5.16. a), b) Normalized emission and c) excitation spectra of the complex **25/complex 7** mixture in a 60% water content dioxane/water mixture. The arrows represent the trend of the emission spectra upon variation of the ratio between the two platinum (II) complexes. $\lambda_{exc} = 300$, $\lambda_{em} = 490, 570$ or 600 nm (maximum of intensity of the corresponding emission spectra).

Firstly, the PLQY of the solutions were very low when the two platinum (II) complexes were mixed together in solution. This was also observed for complex **7** alone, which showed a PLQY of 45% at 60% water content instead of a PLQY of 60%, which was previously measured. The excited state lifetimes of the solutions were also relatively short when measured at 600 nm for ratios between 1 :0.15 and 1 :1. Indeed, the signal was deconvoluted into 4 signals: 2 very short decays of 10 ns and 45 ns corresponding approximately at 85% of the overall decay, and two longer decays of 130 ns and 575 ns. The excited state lifetime of 575 ns was previously attributed at the mixed platinum aggregates. However, at 60% it was only representing 5% of the overall excited state lifetime. The shorter decays were attributed to the platinum (II) complexes monomers in solution. One reason attributed to the fact that the emission profile mainly consisted of a broad band around 600 ns rather than the structured bands at 465, 495 and 539 nm was that the PLQY of the aggregates was significantly higher than the PLQY of the monomers (40% against 1%). Consequently, the intensity of the $^3\text{MMLCT}$ band was significantly higher than the intensity of the $^3\text{LC/MLCT}$ bands. Also, the concentration of platinum monomers was significantly higher than the concentration of platinum aggregates.

Table 5.6. Photophysical properties of the complex 25: complex 7 dioxane/water solutions (60% water content). $\lambda_{exc} = 405$ nm, λ_{em} was the wavelength of maximum intensity. The detection wavelength was typed in bold in the emission max column when more than two peaks were present in the emission spectra.

Complex 25 : complex 7	PLQY	Emission max	Lifetime (ns)	Average lifetime (ns)
1 :0	0.07	465 , 495, 530, 570 (sh)	120 (39%), 490 (56%), 1660 (5%)	405
1 :0.05	0.02	465 , 495, 530	190 (37%), 550 (60%), 1910 (3%)	450
1 :0.1	0.02	465 , 495, 530	180 (23%), 660 (73%) 1450 (4%)	580
1 :0.15	0.01	465, 495, 604	25 (53%), 85 (41%), 540 (5%), 1440 (10%)	85
1 :0.2	0.01	465, 495, 609	20 (39%), 65 (49%), 200 (10%), 580 (2%)	75
1 :0.3	0.01	465, 495, 610	10 (36%), 45 (47%), 140 (12%), 590 (4%)	65
1 :0.4	0.015	608	10 (39%), 45 (46%), 140 (12%), 560 (3%)	60
1 :0.5	0.02	605	10 (35%), 45 (47%), 135 (13%), 570 (5%)	70
1:1	0.02	605	10 (36%), 40 (47%), 130 (11%), 575 (7%)	75
0 :1	0.45	565	380 (97%), 680 (3%)	390

Electron microscopy

SEM images of the dried solutions are displayed in Figure 5.17. The images showed well-defined platinum ribbons for the complex 25 alone. A small addition of complex 7 caused the slight narrowing of the width of the ribbons (1 :0.05). When the concentration of complex 7

was further increased (1 :0.1 to 1 :1), only a limited amount of platinum fibers was observed along with amorphous platinum aggregates. These entangled amorphous aggregates were previously reported in chapter 4 and observed upon evaporation of solvent mixture containing platinum monomers. SEM image of complex 7 alone (0:1) displayed a mixture of platinum fibers and amorphous material. The SEM images confirmed a small degree of aggregation of the platinum (II) complexes mixture at 60% water content. Although the two platinum (II) complexes formed fibers separately at 60% water content, they rarely formed any type of aggregates when mixed together.

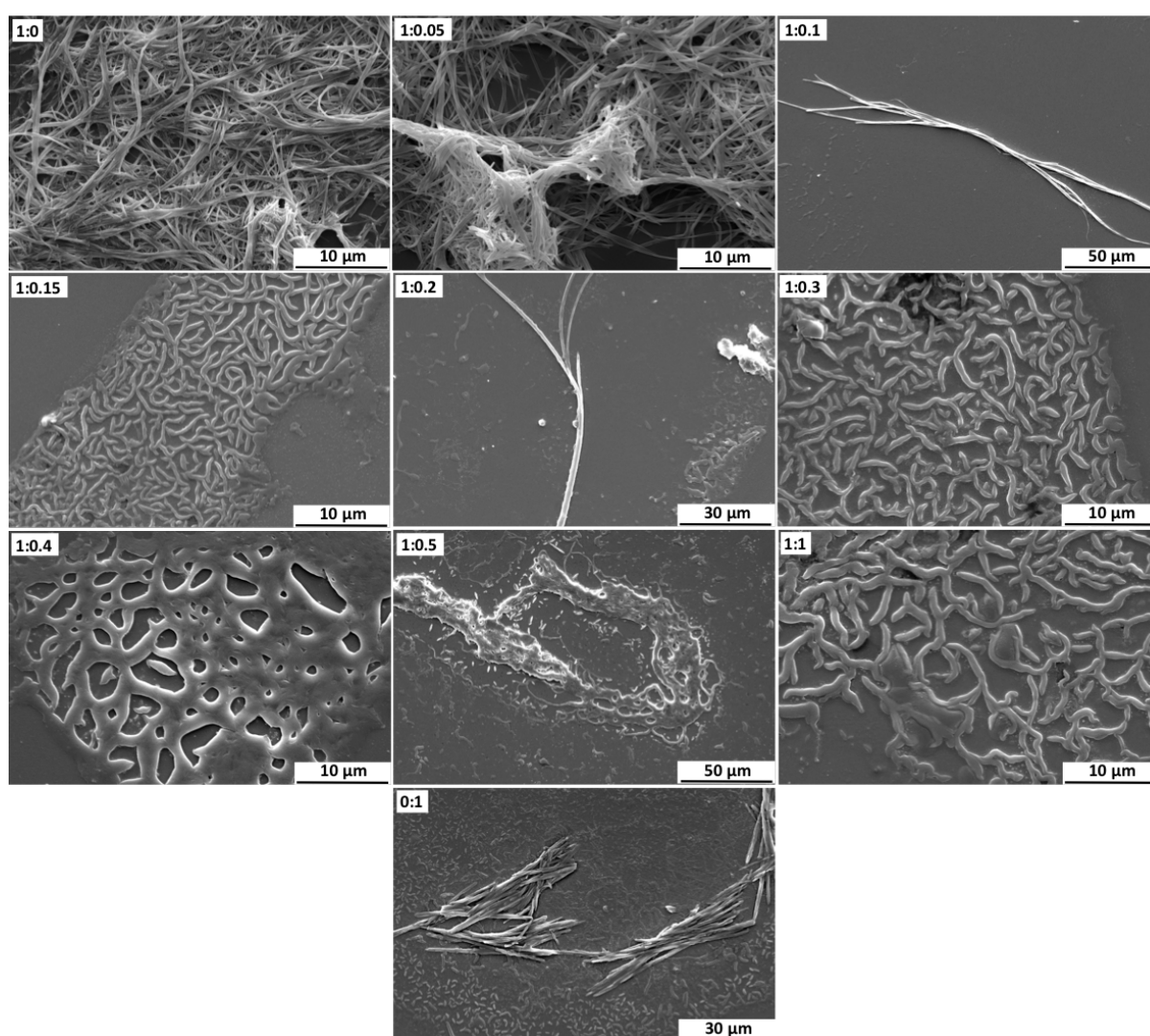


Figure 5.17. SEM images of complex 25: complex 7 dioxane/water mixture. The solutions were drop-casted on a glass slide and evaporated under standard conditions.

Fluorescence confocal microscopy

Finally, the confocal imaging of the dried solutions is displayed in Figure 5.18. Complex **25** self-assembled into entangled blue emissive ribbons surrounded by amorphous orange-emissive material. Upon increasing the concentration in complex **7** (1 :0.05), a mixture of yellow and blue emissive fibers was observed.

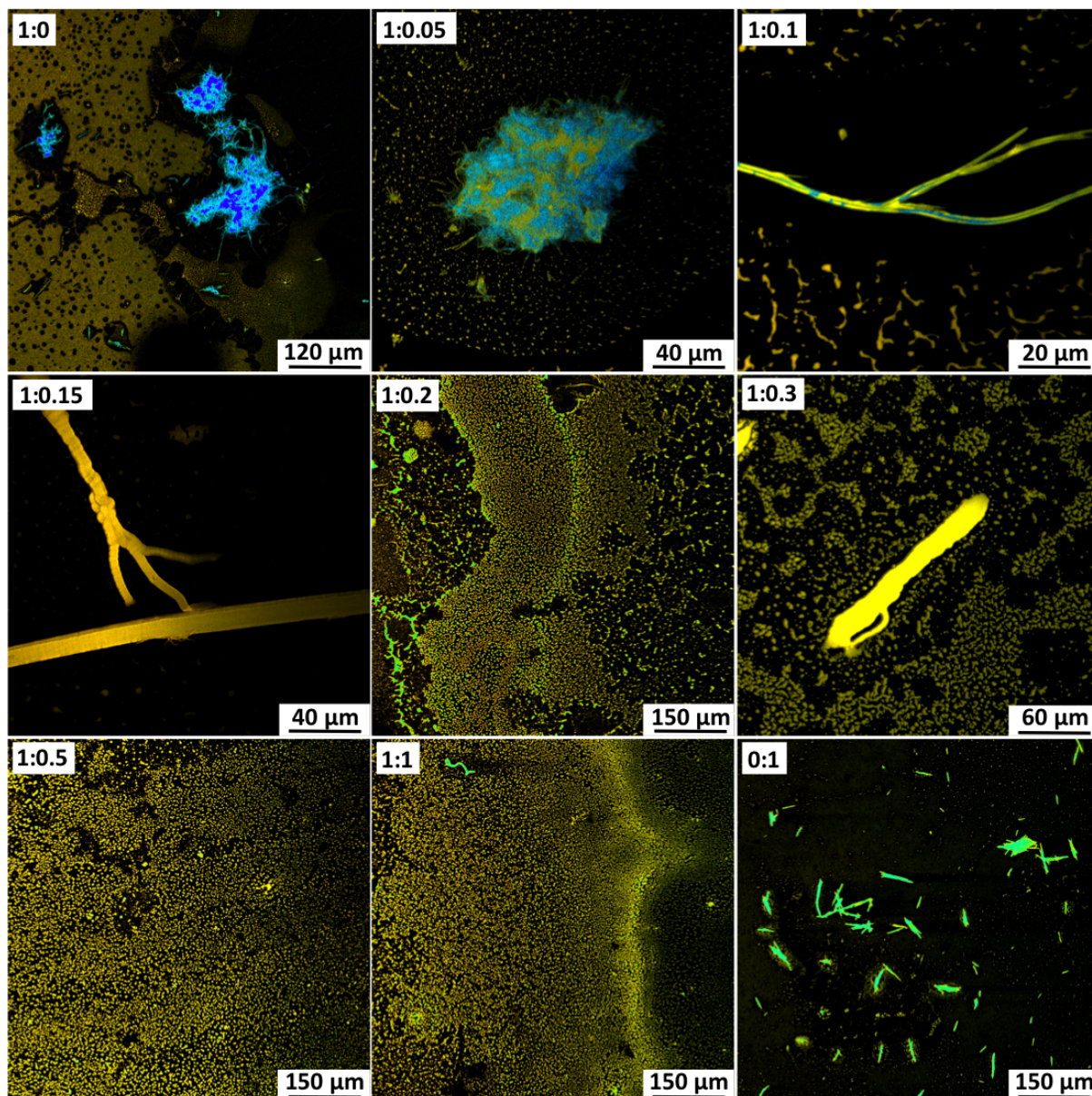


Figure 5.18. Confocal imaging of the complex **25** : complex **7** dioxane/water solution (60% water content) dried on a glass slide. $\lambda_{exc} = 405 \text{ nm}$ in lambda mode (real emission).

At 1 :0.1 feed ratio, only a few long blue emissive fibers coated with a yellow-emissive layer were observed. For complex **25**: complex **7** ratios between 1.0.1 and 1:1, yellow-green emissive amorphous aggregates were mainly observed. Some sparse, yellow-orange large fibers were also observed. Complex **7** alone formed green emissive fibers. Real time confocal imaging of the droplet of the 60% water content solution and feed ratios of 1 :0.15 and 1 :0.2 were performed and are displayed in Figures **5.19** and **5.20** respectively. A few long blue emissive fibers were observed at $t = 0$ min. Upon evaporation of the droplet and modification of the water content, the luminescence of the fibers was shifted from blue to orange within 5 minutes. The confocal images at 39 min displayed rigid orange emissive fibers and the same fibers at 50 min and 64 min were still orange emissive but were bent shaped. Interestingly, when the luminescent transition was complete, the fibers rigidity was broken. It is noteworthy that at $t = 64$ min the droplet was almost evaporated resulting in a high concentration of amorphous visible on the background. At $t = 70$ min, the droplet was dried and the same yellow-green emissive fibers surrounded by orange emissive amorphous material was observed. The difference in emission was explained by the difference of the surrounding environment (solution vs solid). The orange emission of the fibers is deduced to be due to the orange emission of the amorphous material in the background. Another possible explanation is that the emission observed under the confocal microscope was affected by the microscope settings. The droplet is spherical and it was almost impossible to maintain the fibers in the same focal plane during the course of the recording. In order to follow the propagation of the luminescence switch in the fibers, detailed real time imaging was displayed in Figure **5.20**. At $t = 0$ min, three rigid blue emissive fibers were present. At $t = 30$ min, the beginning of the luminescence change was observed at the extremities of the fibers. The switch was complete within 5 minutes from the extremities to the center of the fibers. A small curvature at the tip of the fibers were observed just before the complete evaporation of the fibers at $t = 67$ minutes. At 60% water content, a positive solvatochromism from blue to yellow green emissive fibers was observed upon evaporation of the dioxane/water droplet. Remarkably, this solvatochromism triggered a change in the morphology of the fibers. After the luminescence transition was complete, the fibers became more flexible. To further understand the change in rigidity, X-ray diffraction measurements were performed on the fibers formed from the two platinum (II) complexes separately and from the co-assembled fibers.

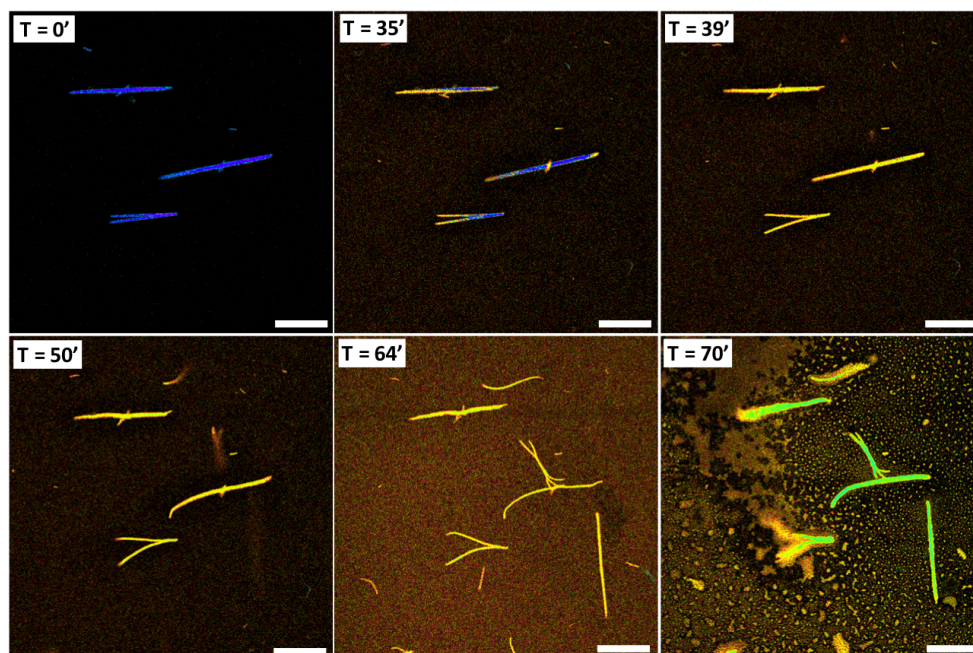


Figure 5.19. Real-time confocal imaging of the drop-casted solution of complex 25: complex 7 (1 :0.15 feed ratio) dioxane/water mixture (60% water content). $\lambda_{exc} = 405 \text{ nm}$ (real colors). Scale bar: 200 μm .

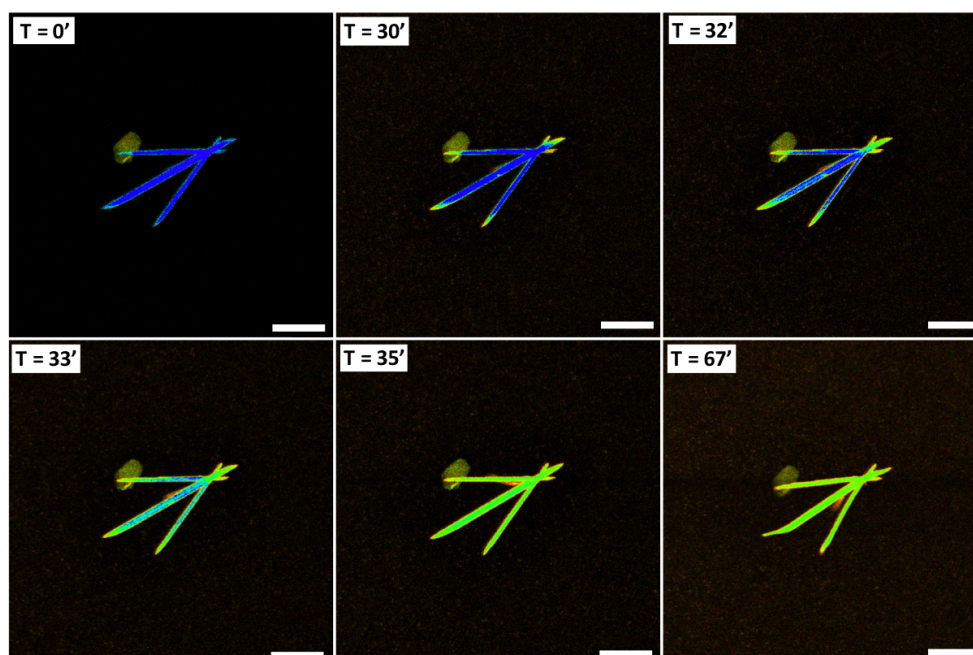


Figure 5.20. Real-time confocal imaging of the drop-casted solution of complex 25: complex 7 (1 :0.2 feed ratio) dioxane/water mixture (60% water content). $\lambda_{exc} = 405 \text{ nm}$ (real colors). Scale bar: 50 μm .

5.2.5. X-ray diffraction pattern

Unit cell and lattice parameters of the aforementioned platinum aggregates are summarised in Table 5.7. Blue-emissive ribbons formed from complex **25** at 60%, 70%, 80% (Figure 5.21) water content were highly microcrystalline with an XRD pattern defined as monoclinic (P2) with $a=22.95 \text{ \AA}$, $b=2.50 \text{ \AA}$, $c=12.99 \text{ \AA}$ and $\beta=87.91^\circ$, similar to values previously reported in literature³⁰. The zoom on the distances (Figure 5.21, insets) did not show any peak between 3 and 3.5 \AA due to the absence of platinum-platinum interactions. The XRD patterns for complex **7** at 60%, 70% and 80% water content were comparably dissimilar (Figure 5.22). That was explained by the changing morphology of complex **7** upon variation of the water content. Small peaks at 3.47 \AA and 3.5 \AA were detected in the zoom on the distances. These peaks were attributed to platinum-platinum interactions and π - π stacking between adjacent complex **7** molecules. Finally, XRD measurements on the co-assembled aggregates were also performed. As previously demonstrated, the emission and morphology of the fibers changed upon evaporation of the solvent. For this reason, the XRD patterns displayed in Figure 5.23 were those from the final orange emissive fibers. The initial blue, rigid fibers were unable to be measured, as they were only stable in a dioxane/water mixture. The co-assembled aggregates at 60% water content displayed a crystalline pattern defined as orthorhombic (C222) unit cell. The co-assembled aggregates at 70% water also displayed an orthorhombic (pna21) unit cell. Interestingly, a peak at 3.41 \AA , which was typical for metallophilic interactions, was only detected at 70% water content. The co-assembled aggregates at 80% water content had an XRD pattern defined as monoclinic (P2) unit cell with lattice parameters $a = 23.09 \text{ \AA}$, $b = 2.55 \text{ \AA}$, $c = 12.81 \text{ \AA}$, $\beta=88.55^\circ$. Those values were similar to the ones observed for the blue emissive ribbons formed by complex **25**. The confocal image (Figure 5.13) shows blue emissive ribbons coated with an orange emissive layer and accounts for the similar XRD pattern for complex **25** and 1 :0.2 feed ratio aggregates at 80% water. The XRD pattern confirmed the formation of new platinum-platinum interactions for the fibers formed from the co-assembly of the two complexes when dried and orange emissive. The XRD patterns of the initial blue emissive fibers were not measurable because they were only present in solution.

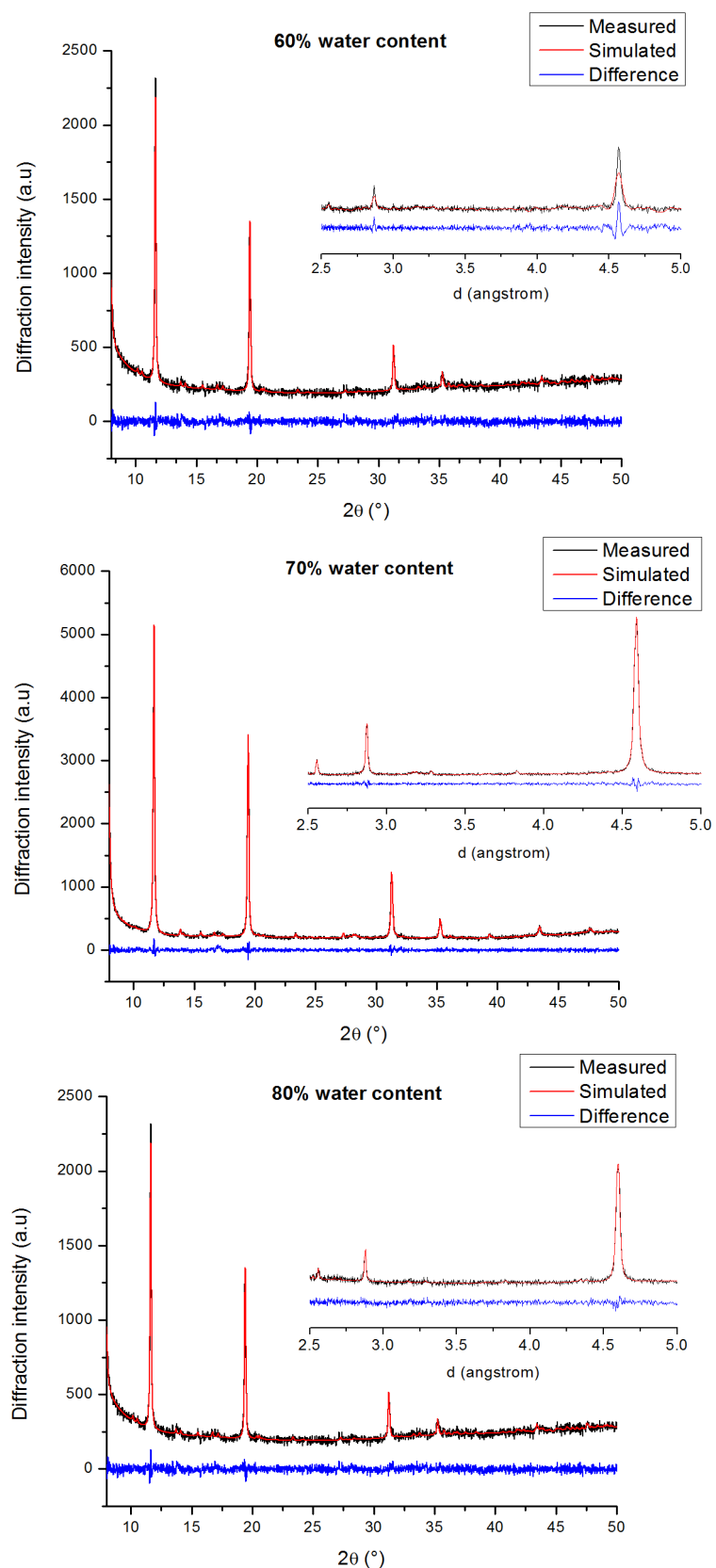


Figure 5.21. Measured XRD graphs of complex **25** aggregates formed from a 60%, 70% and 80% water content dioxane/water mixture and corresponding zoom on the 2.5-5.0 Å region of the XRD patterns where typical platinum-platinum distances are expected.

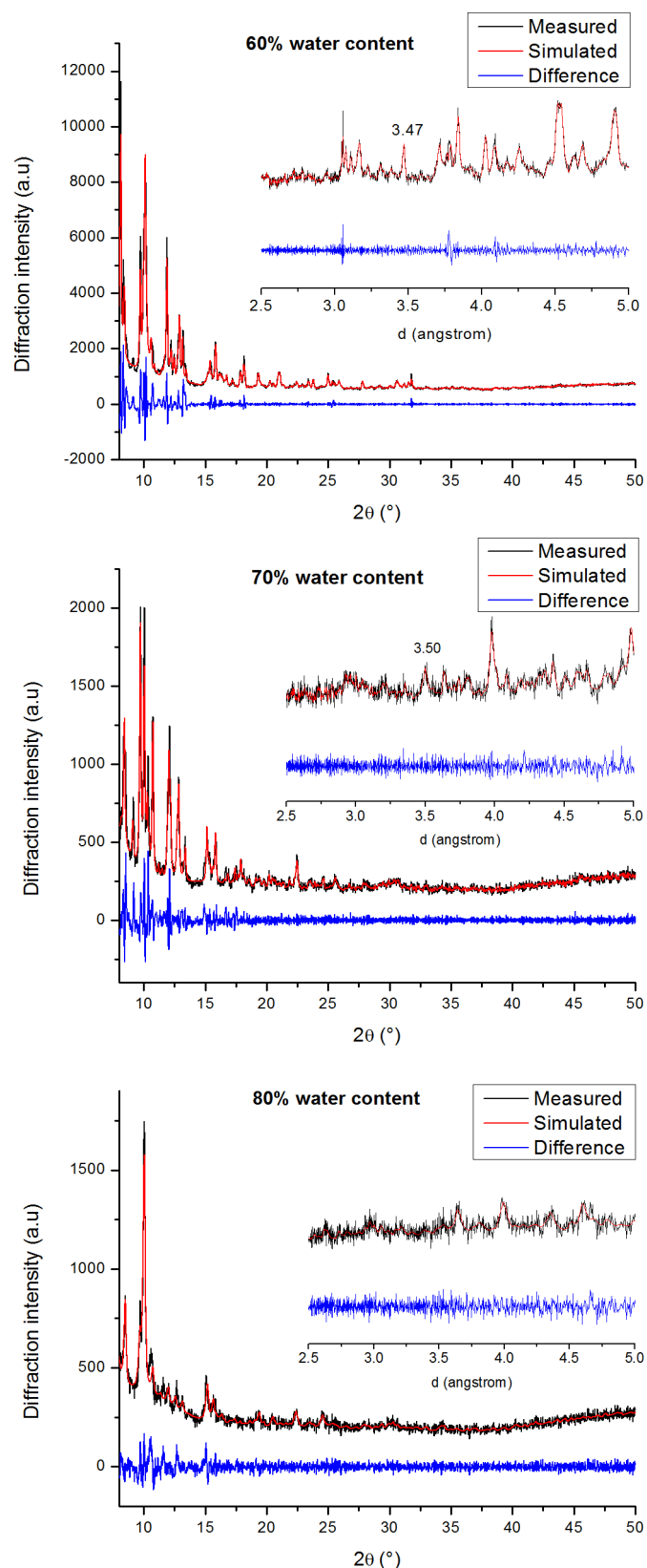


Figure 5.22. Measured XRD graphs of complex **7** fibers formed from a 60%, 70% and 80% water content dioxane/water mixture and corresponding zoom on the 2.5-5.0 Å region of the XRD patterns where typical platinum-platinum distances are expected.

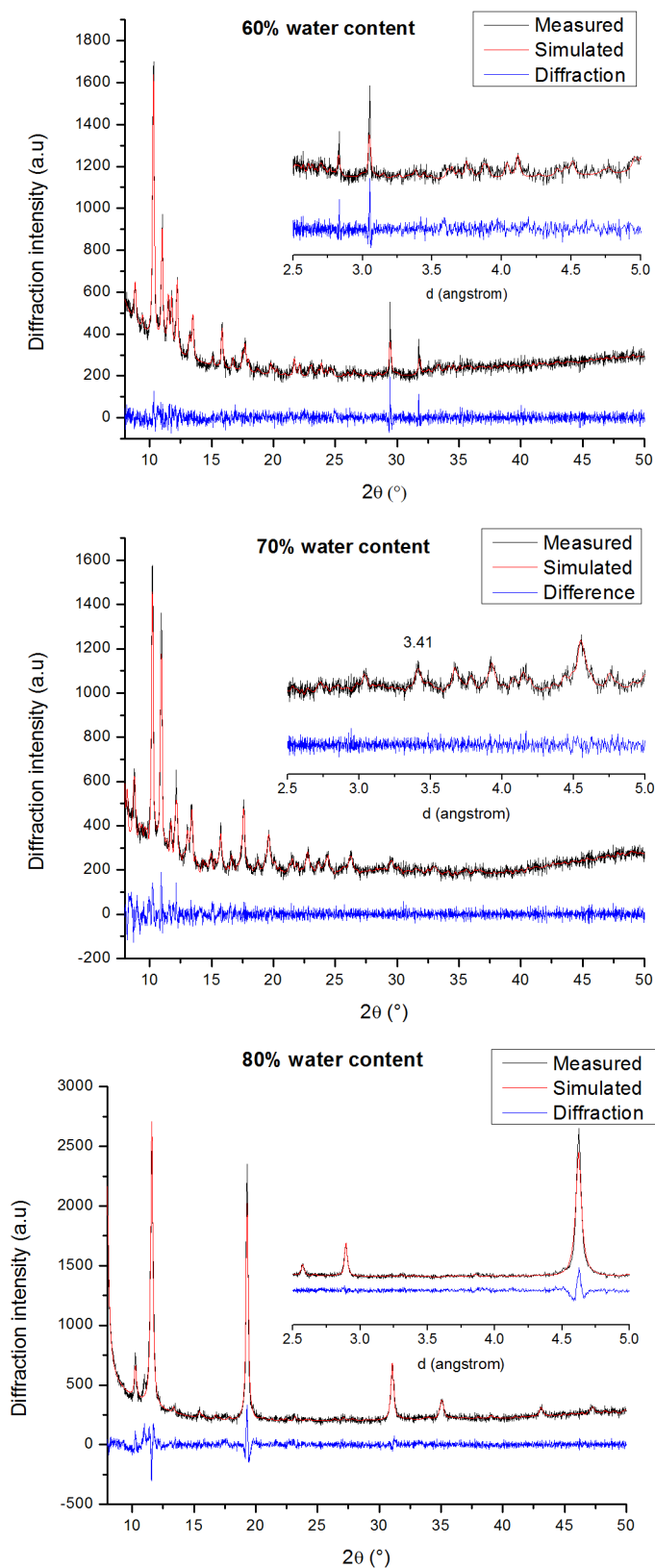


Figure 5.23. Measured XRD graphs of complex **25**: complex **7** (1:0.2 feed ratio) aggregates formed from a 60%, 70% and 80% water content dioxane/water mixture and corresponding zoom on the 2.5-5.0 Å region of the XRD.

Table 5.7. Unit cell and lattice parameters of the platinum aggregates determined by XRD.

	Water content	Crystal class	Space group	a(Å)	bÅ)	c(Å)	$\alpha(^{\circ})$	$\beta(^{\circ})$	$\gamma(^{\circ})$	Rwp
Complex 7	60%	Orthorombic	P212121	69.77	25.17	8.95				9.2
	70%	Monoclinic	P2	44.38	21.80	9.52		93.94		9.1
	80%	Cubic	P-43n	32.95						7.2
Complex 25	60%	Monoclinic	P2	22.95	2.50	12.99				8.2
	70%	Monoclinic	P2	22.95	2.50	12.99		87.91		8.9
	80%	Monoclinic	P2	22.95	2.50	12.99		87.91		6.4
(1 :0.2) mixture	60%	Orthorombic	C222	60.19	3.34	26.90				6.4
	70%	Orthorombic	Pna21	30.30	27.13	30.82				7.5
	80%	Monoclinic	P2	23.09	2.55	12.81		88.55		7.3

Furthermore, the interpretation of the XRD patterns is not sufficient enough to conclude the presence of platinum-platinum interactions. The density of fibers on the surface is too low to ascertain that the X-ray beam hit the aggregates. Thus, more sophisticated and precise measurements are needed.

5.2.6. Selected Area Electron Diffraction (SAED)

SAED measurements of the fibers formed from complex **25**, complex **7** and the 1:0.2 feed ratio mixtures at 70% water content are displayed in Figure **5.24**. The morphology and the orientation of the different fibers were obtained by viewing the shadow image in the central disk of a strongly defocused diffraction pattern. The blue emissive fibers formed by complex **25** showed a complicated SAED pattern with several diffraction points. The XRD pattern previously indicated the absence of platinum-platinum interactions. However, for complex **7** and the 1:0.2 feed ratio mixture, strongly streaked diffraction spots corresponding to a lattice period of 3.36 Å along the fiber's axis which confirmed the presence of metal-metal interactions and π - π stacking between platinum (II) complexes molecules. Interestingly, the lattice period is identical for both complex **7** and the mixture, suggesting that similar organisation occurred in the two types of fibers. It is worth noting that the SAED pattern acquisitions were performed with an electron beam at a very low dose to prevent damage of the crystal structures. The pattern observed from the fibers formed by complex **7** is similar but less intense than that of the fibers from the 1:0.2 mixture in similar experimental conditions. The lower resistance of the fibers to the electron beam accounted for this difference in pattern. The difference of lattice parameters measured from XRD and SAED can

be accounted for by the different sample preparation conditions and the low accuracy of the XRD beam.

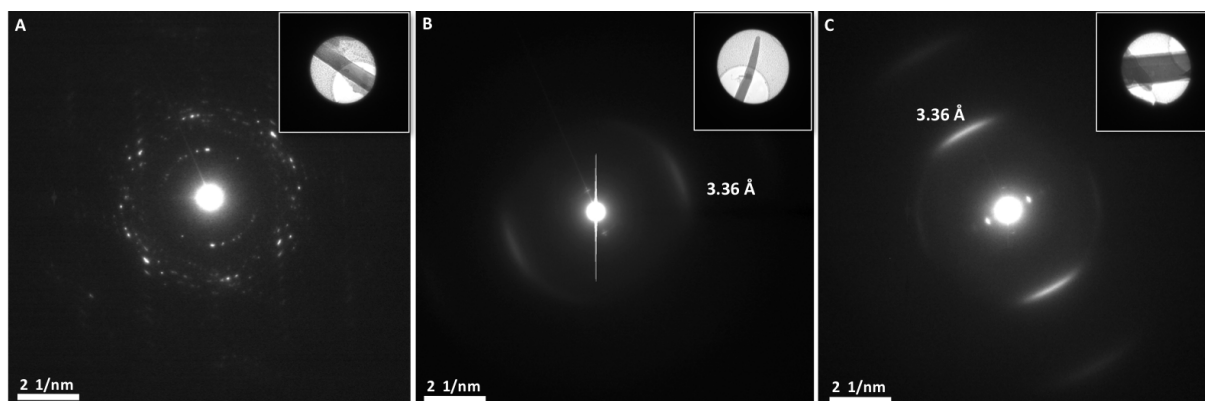


*Figure 5.24. SAED patterns and corresponding shadow images of the fibers formed by complex **25** (A), complex **7** (B) and the platinum (II) complexes mixture (1:0.2 feed ratio) (C) in a dioxane/water (70% water content). The numerical values in (B) and (C) indicates the *d* spacing.*

5.2.7. Reversibility

A change in the emission of the co-assembled fibers was observed under the confocal microscope for water content below 80%. It was demonstrated that the emission of the fibers was sensitive to the surrounding environment. In 70% water content dioxane/ water mixture, the aggregates formed from the mixture of complex **25** and **7** (feed ratio 1:0.2) were blue emissive. Upon dialysis against water, the emission of the fibers were red-shifted from 460-490 nm to 610 nm (Figure 5.9). In order to study the reversibility of the luminescence transition, the water content solution containing the orange emissive aggregates was re-adjusted to 70% water content in a dioxane/water mixture by addition of dioxane in the dialysed solution. Normalized emission and photographs of the solution under UV lamp over time are displayed in Figure 5.25. It was noted that 24 hrs after the addition of dioxane, ¹LC/MLCT bands at 465 and 495 nm were increasing in intensity while the broad band was slightly blue-shifted from 610 nm to 603 nm. After 48 hrs, the structured bands between 460 and 490 nm were dominant and a broad peak at 570 nm remained. After two more days, the intensity of the broad band was slightly decreasing in intensity but did not completely disappear. It appeared that the system did not return to its original state. The broad band or shoulder around 570 nm indicated the presence of some yellow emissive aggregates. The

photographs of the solution at different water contents also showed the blue emission of the platinum aggregates before dialysis (left cuvette), followed by a red shift after dialysis (middle cuvette) and a mixture of whitish aggregates and orange luminescence on the walls of the cuvettes.

The excited state lifetimes and PLQY of the complex **25**: complex **7** solution upon variation of the water content is reported in Table 5.8.

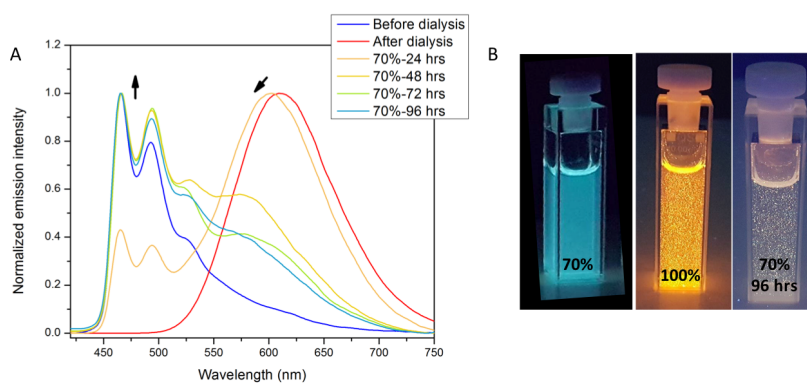


Figure 5.25. a) Normalized emission spectra and photograph of the solution under UV lamp. $\lambda_{exc} = 300 \text{ nm}$.

It was observed that 24 hrs after the addition of dioxane to obtain a 70% water content, the PLQY of the solution had decreased to 1%. After 48 hrs, the PLQY was slightly increased to 4% and did not evolve after time. This value was significantly less than the 12% PLQY observed originally. Moreover, the excited state lifetime of the solution after 24 hrs at 70% water content was relatively short. When the lifetime was measured at 465 nm, a multi-exponential decay resulting in an average lifetime of 65 ns was measured. Such a short lifetime with the presence of extremely short lifetime decays of 1 and 45 ns suggested the presence of molecularly dissolved platinum (II) complexes. That hypothesis was in accordance with the low PLQY. After 48 hours, the excited state lifetime measured at 465 nm and 570 nm was stabilised around 420 ns and 840 ns, respectively. An excited state of 420 ns was attributed to the presence of blue emissive fibers in solution similar to those measured before dialysis against water. The signal at 570 nm was attributed to another type of aggregate. The photophysical measurements showed that the luminescent switch from orange to blue emissive fibers was not completely reversible and not as rapid as the blue to orange transition. SEM images of the platinum fibers at each step are displayed in Figure 5.26. After dialysis against water, the fibers were thicker than at 70% water. When the water content of the

solution mixture was re-adjusted to 70%, only a few large platinum aggregates were observed. Finally, real time confocal imaging of the fibers obtained after 4 days at 70% water content are shown in Figure 5.27.

Table 5.8. Photophysical properties of the complex 25: complex 7 dioxane/water solution. λ_{exc} = 405 nm, λ_{em} was the wavelength of maximum intensity. The detection wavelength for the excited state lifetimes measurements was highlighted in bold in the emission max column

Conditions	PLQY	Emission max	Lifetime (ns)	Average lifetime (ns)
70% water	0.12	465 , 495, 525	100 (24%), 370 (52%), 850 (22%), 3310 (1%)	450
100% water	0.55	610	345 (13%), 575 (87%)	550
70% water-24 hrs	0.01	465 , 495, 603	1 (83%), 45 (5%), 370 (8%), 880 (4%)	65
70% water-24 hrs	0.01	465, 495, 603	40 (41%), 520 (51%), 1030 (8%)	360
70% water-48 hrs	0.04	465 , 495, 525, 570	400 (61%), 790 (39%)	570
70% water-48 hrs	0.04	465, 495, 525, 570	785 (98%), 3310 (2%)	840
70% water-72 hrs	0.04	465 , 495, 525, 570	8 (22%), 140 (14%), 540 (52%), 970 (12%)	410
70% water-72 hrs	0.04	465, 495, 525, 570	720 (80%), 1470 (20%)	870
70% water-96 hrs	0.04	465 , 495, 525, 570(sh)	42 (14%), 330 (38%), 640 (47%), 1860 (1%)	440
70% water-96 hrs	0.04	465, 495, 525, 570(sh)	770 (98%), 3230 (2%)	820

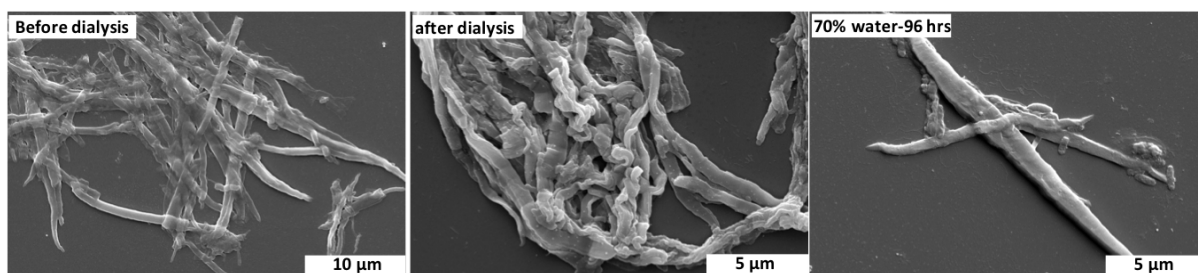


Figure 5.26. SEM images of the complex **25**: complex **7** (1 :0.2 feed ratio) aggregates at 70% (before dialysis), 100% (after dialysis), and back at 70% water content after 4 days.

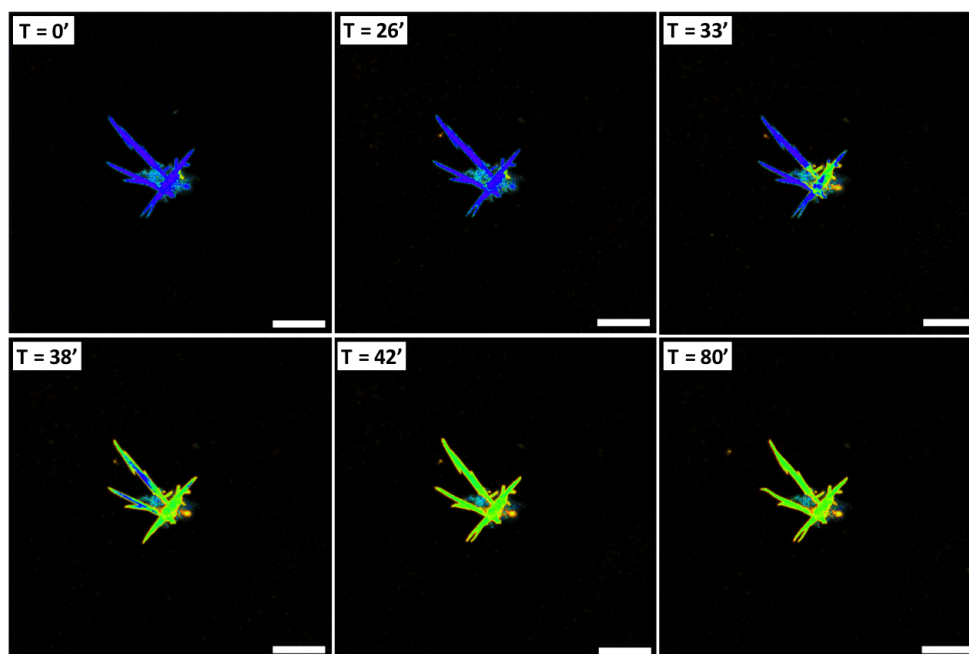


Figure 5.27. Real-time confocal imaging of the drop-casted solution of complex **25**: complex **7** (1 :0.2) dioxane/water mixture (70% water content-for 4 days). $\lambda_{exc} = 405 \text{ nm}$ (real colors). Scale bar: 50 μm .

The real time confocal imaging showed the luminescence transition from blue to yellow green fibers, obtained after 4 days at 70% water content. This confirmed the reversibility of the hybrid fibers formed from two different platinum (II) complexes. However, the number of aggregates was decreasing compared to what was previously observed (refer to Figures 5.6 and 5.8). Another experiment was conducted to confirm the reversibility of the luminescence switch. A droplet from a 60% water content solution containing complex **25**: complex **7** aggregates at a feed ratio of 1 :0.2, was drop-casted onto a glass slide and real time confocal imaging was performed (Figure 5.28). From $t = 0 \text{ min}$ to $t = 44 \text{ min}$, the evaporation and the modification of the solvent mixture triggered the luminescent transition. Once the fibers were

yellow-green emissive, a drop of a dioxane/water solution at 60% water content (without platinum (II) complexes) was added to the evaporating droplet. This resulted in a mixture composition of around 70% water content. At t=48 minutes, the fibers returned to their original blue emission with the exception of their tips. Upon evaporation of the droplet, a second luminescent transition from blue to yellow-green was observed.

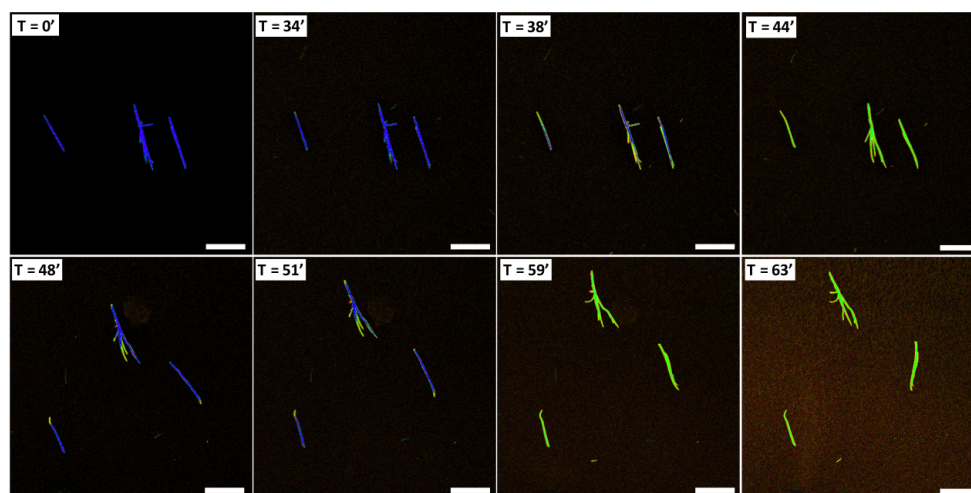


Figure 5.28. Real-time confocal imaging of the drop-casted solution of complex **25**: complex **7** (1 :0.2 feed ratio) dioxane/water mixture (70% water content-for 4 days). $\lambda_{exc} = 405 \text{ nm}$ (real colors). Scale bar: 100 μm .

However, the composition of the solvent in the droplet was not precisely known, for example, at t =44 minutes. A 60% water content droplet instead of 70% water content droplet was added after 45 minutes to ensure that the the water content was low enough to trigger the luminescent transition. It is worth noting that the partial luminescence change from yellow-green to blue was instanteneous after the addition of the droplet at 44 minutes.

5.2.8. Aging

In order to obtain larger platinum fibers, a proposed method was to seal a 60% water content dioxane/water solution containing the two platinum (II) complexes (1 :0.15 feed ratio) for a month. The SEM images in Figure 5.17 show that after 4 days, a few fibers were observed. At 60% water content, the rate of the self-assembly process was reduced by the solvation of the platinum (II) complexes by dioxane. As a result, fewer and longer fibers will be obtained at 60% after a month, for example. Real time confocal imaging of the longer fibers is displayed

in Figure 5.29. Micrometer sized fibers were observed under the microscope and displayed a luminescence transition upon evaporation of the droplet.

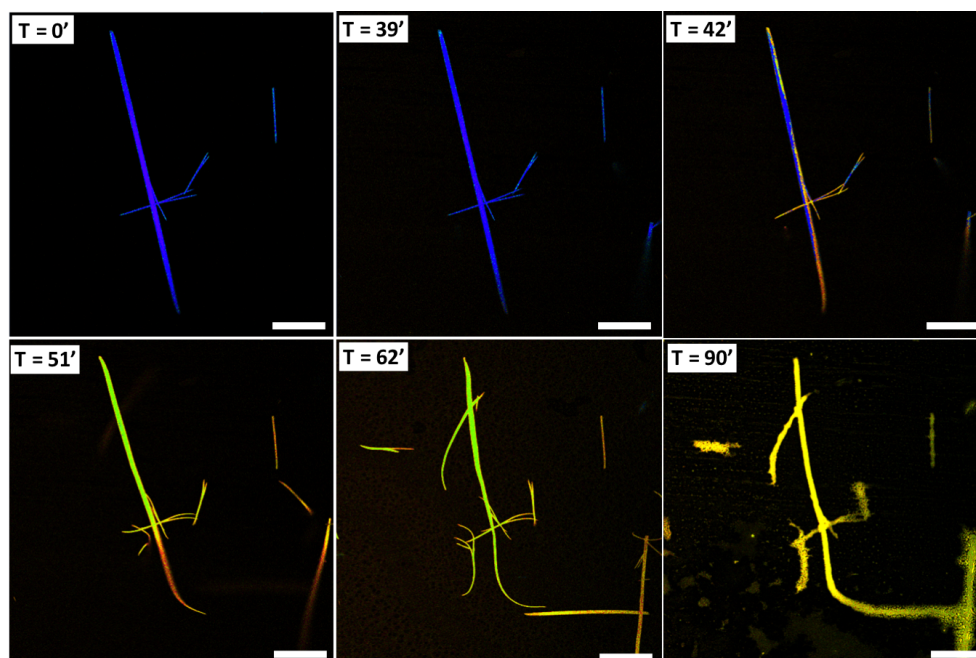


Figure 5.29. Real-time confocal imaging of the drop-casted solution of complex 25: complex 7 (1 :0.15 feed ratio) dioxane/water mixture (60% water content) after a month. $\lambda_{exc} = 405 \text{ nm}$ (real colors). Scale bar: 100 μm .

The change in emission was accompanied by the deformation of the fiber, attributed to the change in crystallinity. The last image at $t = 90 \text{ min}$ shows the real emission of the fibers after refocusing when the droplet was mainly evaporated.

5.3. Conclusion

1D crystalline structures were formed by the supramolecular co-assembly of two platinum (II) complexes. It was demonstrated that the crystalline structures were defined by the water content in a dioxane/water mixture and the feed ratio between the two platinum (II) complexes. Moreover, the fibers formed from the mixture of the two complexes at specific ratios and at water contents between 60% and 70% showed an intriguing luminescent transition from blue to yellow in the visible region. Such a change in the photophysical properties of the fibers was triggered by an increase of the water content in solution or upon evaporation of the solvent. This positive solvatochromism was induced by the change of the

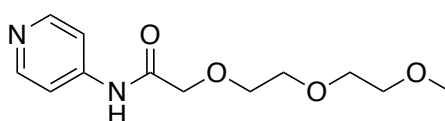
crystallinity of the fibers, resulting in the formation of platinum-platinum interactions within the aggregates and rise of MMLCT transition. The luminescent switch can be controlled by the water content in solution and is a reversible process. Moreover, microsized fibers could be obtained upon slow crystallization. Further investigation of the co-assembly of platinum (II) complexes could initiate a pathway to new structures with spectacular photophysical and stimuli-responsive properties. Another exciting challenge would be to co-assemble more than two different platinum (II) complexes in solution which could lead to even more intriguing photophysical and morphological properties.

5.4. Experimental part

5.4.1. General information

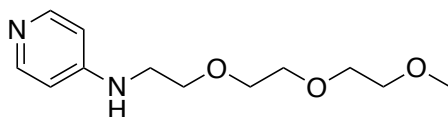
All the solvents and chemicals were used as received from Sigma-Aldrich or Fluka without any further purification. The synthesis of complex **7** was previously reported in chapter 2. Complex **25** was synthesized exactly as reported in the literature^{28'}. K_2PtCl_4 was purchased from Precious Metal Online (PMO). $PtCl_2(DMSO)_2$ was prepared from previously reported synthetic procedures¹. Column chromatography was performed on silica gel 60 (particle size 63-200 μm , 70-230 mesh ASTM, Merck). NMR spectra were recorded on a Bruker Avance 400 spectrometer. 1H NMR, ^{13}C NMR and ^{19}F NMR chemical shifts (δ) of the signals are given in parts per million and referenced to residual protons in the deuterated solvents. The signal splitting are abbreviated as follows: s, singlet; d, doublet; t, triplet; q, quadruplet; m, multiplet. Coupling constants (J) are given in Hertz. Electrospray ionization mass spectrometry (ESI-MS) was carried out on a MicroTOF (Bruker) mass spectrometer equipped with an electrospray source by the mass spectrometry service of the University of Strasbourg. Elemental analysis was performed by the analytical service of physical measurements and optical spectroscopy by the University of Strasbourg.

5.4.1.1. Synthesis

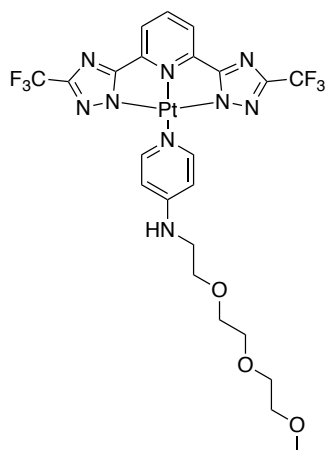


2-(2-(2-methoxyethoxy)ethoxy)-N-(pyridin-4-yl)acetamide (**23**). The starting triethylene glycol chain 2-[2-(2-methoxyethoxy)ethoxy]acetic acid (10 g, 55.13 mmol) and 4-aminopyridine (3.5

g, 37.17 mmol) were dissolved in 50 mL of chloroform. *N,N'*-dicyclohexylcarbodiimide (DCC) (11.5 g, 55.13 mmol) was gradually added to the mixture and a white precipitate was formed. The reactional mixture was stirred at room temperature for one hour and refluxed for 4 hours. The solution was filtered off and concentrated under vacuum. The crude product was purified by column chromatography using ethylacetate/methanol 9:1 mixture as an eluent. The pure compound was obtained as a pale yellow oil product. (m = 5.8 g, Yield 61%). ^1H NMR δ (CD_2Cl_2 , 400 MHz, ppm) 9.03 (s, 1H), 8.50 (d, $J = 8.0$ Hz, 2H), 7.60 (d, $J = 8$ Hz, 2H), 4.13 (s, 2H), 3.72-3.80 (m, 6H), 3.60-3.62 (m, 2H), 3.37 (s 3H), ^{13}C NMR (CD_2Cl_2 , 100 ppm) δ 169.90, 151.17, 145.08, 114.28, 72.27, 72.01, 71.23, 70.94, 70.50, 59.16. HR-ESI-MS (m/z): $\text{C}_{12}\text{H}_{18}\text{N}_2\text{O}_4$ $[\text{M}+\text{Na}]^+$, calc 277.115, found 277.115.



N-(2-(2-(2-methoxyethoxy)ethoxy)ethyl)pyridin-4-amine (**24**). Compound **23** (5.5 g, 21.62 mmol) was dissolved in anhydrous THF (5mL) and added dropwise to a 30 mL suspension of LiAlH_4 in THF 1 M at 0°C under a nitrogen atmosphere. The mixture was then stirred at room temperature overnight. 30 mL of methanol was gradually added to the reactional mixture at 0° under nitrogen. The resulting mixture was filtered with neutral alumina and the filtrate evaporated under vacuum. The crude product was purified by column chromatography on neutral alumina using acetone/MeOH (10:1) as eluent. The pure compound was obtained as a yellow oil product. (m = 2.5 g, yield 48%). ^1H NMR δ (CD_2Cl_2 , 400 MHz, ppm) 8.13 (d, $J = 8.0$ Hz, 2H), 6.44 (d, $J = 8$ Hz, 2H), 4.74 (s, 1H), 3.64-3.69 (m, 6H), 3.58-3.63 (m, 6H), 3.50-3.52 (m, 2H), 3.28-3.34 (m, 5H), ^{13}C NMR (CD_2Cl_2 , 100 ppm) δ 154.02, 150.50, 108.18, 72.51, 71.01, 70.94, 69.61, 59.16, 42.86. HR-ESI-MS (m/z): $\text{C}_{12}\text{H}_{20}\text{N}_2\text{O}_3$ $[\text{M}+\text{H}]^+$, calc 241.154, found 241.155.



Complex 25. Triazole ligand **2** (200 mg, 0.573 mmol, 1 eq) and platinum precursor $\text{PtCl}_2(\text{DMSO})_2$ (242 mg, 0.573 mmol, 1 eq) were dissolved in 20 mL of acetonitrile. *N,N*-diisopropylethylamine (DIPEA) (100 μL , 1.145 mmol, 2 eq) was added and the clear yellow solution stirred for 10 minutes. Ancillary ligand **24** (179 mg, 0.745 mmol) dissolved in 5 mL of acetonitrile was added to the solution and the reactional mixture was stirred at 60 °C under nitrogen overnight. The yellow crude product was purified by column chromatography using cyclohexane/ethylacetate (1:4) and then ethylacetate/acetone (4:1) as mobile phase. The pure product was obtained after recrystallization in acetonitrile as a yellow solid. Yield 130 mg, 36%. ^1H NMR (CD_2Cl_2 , 400 MHz) δ : 9.01 (d, $J = 8$ Hz, 2H), 8.04 (t, $J = 8$ Hz, 1H), 7.78 (d, $J = 8$ Hz, 2H), 5.87 (m, 1H), 3.78–3.76 (m, 2H), 3.70–3.61 (m, 6H), 3.57–3.54 (m, 2H), 3.47–3.43 (m, 2H), 3.37 (s, 3H); ^{19}F NMR (CD_2Cl_2 , 376 MHz, ppm) δ : 64.54 (s). HR-ESI-MS (m/z): $\text{C}_{23}\text{H}_{23}\text{F}_6\text{N}_9\text{NaO}_3\text{Pt} [\text{M}+\text{Na}]^+$, calcd. 805.137, found: 805.136. Elemental analysis: calcd. C 35.30%; H 2.96%; N 16.11%; found C 35.12%; H 3.05%; N 15.79%.

5.4.2. Photophysics

All the absorption measurements in this report were recorded on a UV-3600 Shimadzu UV-Vis-NIR spectrophotometer, and were baseline and solvent corrected with UV Probe software. Quartz cuvettes were used for this purpose. Steady-state measurements were recorded on a HORIBA Jobin-Yvon IBH FL-332 Fluorolog 3 spectrometer equipped with a 450 W Xenon arc lamp, double grating excitation and emission monochromators.

Time-resolved measurements up to 5 μs were performed using the TCSPC option on a FluoTime 300 (PicoQuant). The excitation source was mounted directly on the sample

chamber at 90° to a double grating emission monochromator and collected by a PicoHarp 300 (PicoQuant) single-photon-counting detection module. Signals were collected using the software FluroFit, PicoQuant For excited state lifetimes > 10 μ s, a different experimental setup was utilised, by equipping the FluoTime 300 with a FL-1040 phosphorescence module including a 70-W xenon flash tube. The signal was recorded on the PDL 820 single-photon-counting detector and collected with multichannel scalling (MCS).

Absolute quantum yield measurements were performed using a Hamamatsu Photonics absolute PL quantum yield measurement system. This setup is equipped with L0799-001 CW Xenon light source (150 W), a monochromator, a C7473 photonic multi-channel analyzer and an integrating sphere.

5.4.3. Scanning electron microscopy (SEM) and Scanning transmission electron microscopy (STEM)

SEM characterization was performed employing a FEI scanning electron microscope Quanta FEG 250, at an acceleration voltage of 10 KV. Samples were prepared by drop-casting a solution of platinum (II) complex onto a glass slide, and the subsequent plasma-induced deposition of a 40 nm thick layer of silver.

STEM characterization was performed employing a FEI scanning electron microscope Quanta FEG 250, at an acceleration voltage of 20 kV. Samples were prepared by drop-casting a solution of platinum (II) complex onto a copper grid (400 mesh, Agar Scientific) coated with a Formvar/carbon film.

5.4.4. Fluorescence confocal microscopy

All of the fluorescence images were taken by using Zeiss LSM 710 confocal microscope system with 63 \times magnification, numerical aperture, NA, 1.3 of Zeiss LCI Plan-NEOFLUAR water immersion objective lens (Zeiss GmbH). The samples were excited by continuous wave (cw) laser at 405 nm. The emission of the complexes was collected in the range from 400 to 750 nm. In addition, the lambda-mode acquisition technique was performed to observe the emission spectra of the two complexes after cell internalization. All images were performed by using the same software.

5.4.5. X-ray diffraction (XRD) measurement

The XRD patterns of all the samples were obtained by Bruker AXS D2 Phaser (LYNXEYE detector) using Ni-filtrated Cu-K α radiation ($\lambda = 1.5406 \text{ \AA}$) with 1 mm of air-scattering slit and 0.1 mm of equatorial slit. Solutions were drop-casted on the surface of single crystal Si wafer (cut of (911)) and dried at room temperature. XRD patterns were collected with degree step of 0.016° and time step increments of 20 sec/step from 8 to 60° . The peak fitting was done using Bruker DIFFRACplus TOPAS (TOtal Pattern Analysis Solutions).

5.5. References

1. T. Aida, E. W. Meijer, S. I. Stupp, *Science*, **2012**, *335*, 813–817.
2. Kagoshima, S.; Nagasawa, H.; Sambongi, T. *One-Dimensional Conductors*; Springer: Heidelberg, Germany, **1988**.
3. Steiner, M.; Villian, J.; Windsor, C. G., *Adv. Phys.*, **1976**, *25*, 87.
4. Yamamoto, K.; Kamata T.; Yoshida, Y.; Yase, K.; Mizukami, F.; Ohta, T., *Adv. Mater.* **1998**, *10*, 13.
5. *Extended Linear Chain Compounds*, Vo I. 1 \pm 3 (Ed.: J. S. Miller), Plenum, New York, **1982**.
6. Magnus, G. *Pogg. Ann.*, **1828**, *14*, 239; Magnus, G. *Ann. Chim. Phys. Se´r. 2*, **1829**, *40*, 110.
7. Rodgers, M. L. ; Martin, D. S. *Polyhedron* **1987**, *6*, 225 ; Atoji, M. ; Richardson, J. W.; Rundle, R. E., *J. Am. Chem. Soc.*, **1957**, *79*, 3017 ; Miller, J. R, *J. Chem. Soc.*, **1965**, 713.
8. Gomm, P. S. ; Thomas, T. W.; Underhill, A. E., *J. Chem. Soc. A*, **1971**, 2154.
9. Miller, J. R., *Proc. Chem. Soc.*, **1960**, 318; Cradwick, M. E. ; Hall, D.; Phillips, R. K., *Acta Crystallogr. B*, **1971**, *27*, 480.
10. Breimi, J.; Brovelli, D.; Caseri, W.; Hähner, G.; Smith, P.;Tervoort, T., *Chem. Mater.*, **1999**, *11*, 977.
11. Margherita Fontana, Henry Chanzy, Walter R. Caseri, and Paul Smith Albertus P. H. J. Schenning and E. W. Meijer, *Chem. Mater.*, **2002**, *14*, 1730-1735.
12. K. Krogmann, *Angew. Chem.*, **1969**, *81*, 10-17; *Angew. Chem. Int. Ed. Engl.*, **1969**, *8*, 35.
13. C. E. Buss, C. E. Anderson, M. K. Pomije, C. M. Lutz, D. Britton, K. R. Mann, *J. Am. Chem. Soc.*, **1998**, *120*, 7783 ; C. E. Buss, K. R. Mann, *J. Am. Chem. Soc.*, **2002**, *124*, 1031.

14. Buss, C. E.; Anderson, C. E.; Pomije, M. K.; Lutz, C. M.; Britton, D.; Mann, K. R. *J. Am. Chem. Soc.*, **1998**, *120*, 7783-77901; Exstrom, C. L.; Sowa, J. R., Jr.; Daws, C. A.; Janzen, D.; Mann, K. R.; Moore, G. A.; Stewart, F. F., *Chem. Mater.*, **1995**, *7*, 15-17.
15. Nagel, C. C. U.S. Patent 4,834,909, **1989**.
16. Exstrom, C. L.; Pomije, M. K.; Mann, K. R., *Chem. Mater.*, **1998**, *10*, 942; Miller, J. R., *J. Chem. Soc.*, **1965**, 713.
17. Vivian Wing-Wah Yam, Keith Man-Chung Wong, and Nianyong Zhu, *J. Am. Chem. Soc.*, **2002**, *124*, 6506-6507.
18. Yong Chen, Kai Li, Wei Lu, Stephen Sin-Yin Chui, Chun-Wah Ma, and Chi-Ming Che, *Angew. Chem. Int. Ed.*, **2009**, *48*, 9909–9913.
19. Wei Lu, Yong Chen, V. A. L. Roy, Stephen Sin-Yin Chui, and Chi-Ming Che, *Angew. Chem. Int. Ed.*, **2009**, *48*, 7621–7625.
20. Anthony Yiu-Yan Tam, Keith Man-Chung Wong, Guoxin Wang and Vivian Wing-Wah Yam, *Chem. Commun.*, **2007**, 2028–2030; Cristian A. Strassert, Chen-Han Chien, Maria D. Galvez Lopez, Dimitrios Kourkoulos, Dirk Hertel, Klaus Meerholz, and Luisa De Cola *Angew. Chem. Int. Ed.* **2011**, *50*, 946–950.
21. Wei Lu, V. A. L. Roy and Chi-Ming Che, *Chem. Commun.*, **2006**, 3972–3974.
22. Yinghui Sun, Kaiqi Ye, Hongyu Zhang, Junhu Zhang, Lan Zhao, Bao Li, Guangdi Yang, Bai Yang, Yue Wang, Siu-Wai Lai, and Chi-Ming Che, *Angew. Chem.*, **2006**, *118*, 5738–5741.
23. Wei Lu, Stephen Sin-Yin Chui, Kwan-Ming Ng, and Chi-Ming Che, *Angew. Chem. Int. Ed.* **2008**, *47*, 4568–4572
24. Mai-Yan Yuen, V. A. L. Roy, Wei Lu, Steven C. F. Kui, Glenna So Ming Tong, Man-Ho So, Stephen Sin-Yin Chui, Michele Muccini, J. Q. Ning, S. J. Xu, and Chi-Ming Che, *Angew. Chem. Int. Ed.* **2008**, *47*, 9895–9899
25. Charlotte Po, Anthony Yiu-Yan Tam, Keith Man-Chung Wong, and Vivian Wing-Wah Yam, *J. Am. Chem. Soc.* **2011**, *133*, 12136–12143.
26. Tuomas P. J. Knowles; Christopher A. Waudby; Glyn L. Devlin, Samuel I. A. Cohen; Adriano Aguzzi; Michele Vendruscolo; Eugene M. Terentjev, Mark E. Welland, Christopher M. Dobson, *Science*, **2009**, *326*, 1533–1537.
27. F. Würthner, T. E. Kaiser, C. R. Saha-Möllner, *Angew. Chem. Int. Ed.*, **2011**, *50*, 3376–3410.
28. Aliprandi, A., Mauro, M., and De Cola, L., *Nat. Chem.*, **2016**, *8*, 10–15.

29. Robinson, M.E., Lunn, D.J., Nazemi, A., Whittell, G.R., De Cola, L., and Manners, I., *Chem. Commun.*, **2015**, *51*, 15921–15924.
30. Damiano Genovese, Alessandro Aliprandi, Eko A. Prasetyanto, Matteo Mauro, Michael Hirtz, Harald Fuchs, Yasuhiko Fujita, Hiroshi Uji-I, Sergei Lebedkin, Manfred Kappes, and Luisa De Cola, *Adv. Funct. Mater.*, **2016**, *26*, 5271–5278.
31. Kaka Zhang,¹ Margaret Ching-Lam Yeung, Sammual Yu-Lut Leung, Vivian Wing-Wah Yam, *Chem 2*, **2017**, 825–839.

Chapter 6

Instrumental techniques

Abstract: This chapter briefly describes all the instruments and experimental techniques used for this thesis. These techniques include UV-Vis absorption, emission and excitation spectroscopy techniques. The methods of obtaining the excited state lifetimes and photoluminescence quantum yield measurements are also described. Electron microscopy and spectroscopy techniques including X-ray photoelectron spectroscopy (XPS), scanning electron microscopy (SEM), scanning transmission electron microscopy (STEM) and transmission are also described. Additional instruments used such as confocal fluorescence microscopy or X-ray diffraction techniques were also described.

6.1. Absorption spectroscopy^{1,2}

UV-Vis spectrometry is the quantitative measurement of the reflection and the transmission properties of a molecule in solution as a function of the wavelength. The transmittance (T) is the ratio between the intensity of the light passing through the sample (transmitted light, I) and the intensity of the incident light (I_0), defined as:

$$T = \frac{I}{I_0} \quad (\text{eq. 6.1})$$

The absorbance is defined as either the negative logarithm of the transmittance or the logarithm of the ratio between the intensity of the incident light (I_0) and the intensity of the transmitted light (I).

$$A = -\log T = -\log \frac{I}{I_0} = \log \frac{I_0}{I} \quad (\text{eq. 6.2})$$

Beer Lambert's law also defines absorbance, which is generally stated as:

$$A = \varepsilon \cdot l \cdot c \quad (\text{eq. 6.3})$$

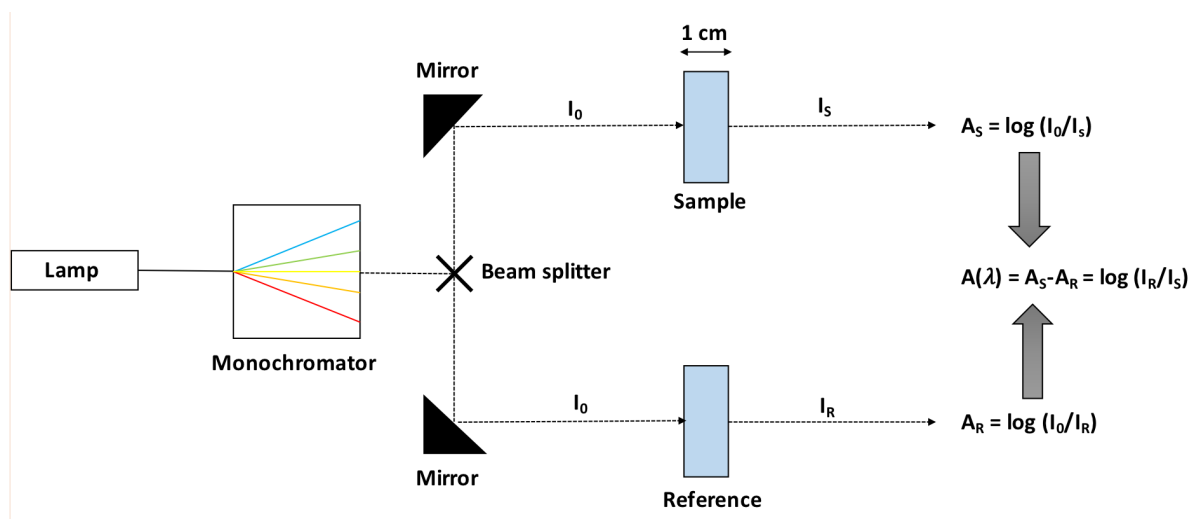
where A is the absorbance or optical density (no unit)

ε is the molar extinction coefficient ($\text{L} \cdot \text{mol}^{-1} \cdot \text{cm}^{-1}$),

l is the optical path or the width of the cuvette (cm)

c is the concentration of the molecule in solution ($\text{mol} \cdot \text{L}^{-1}$)

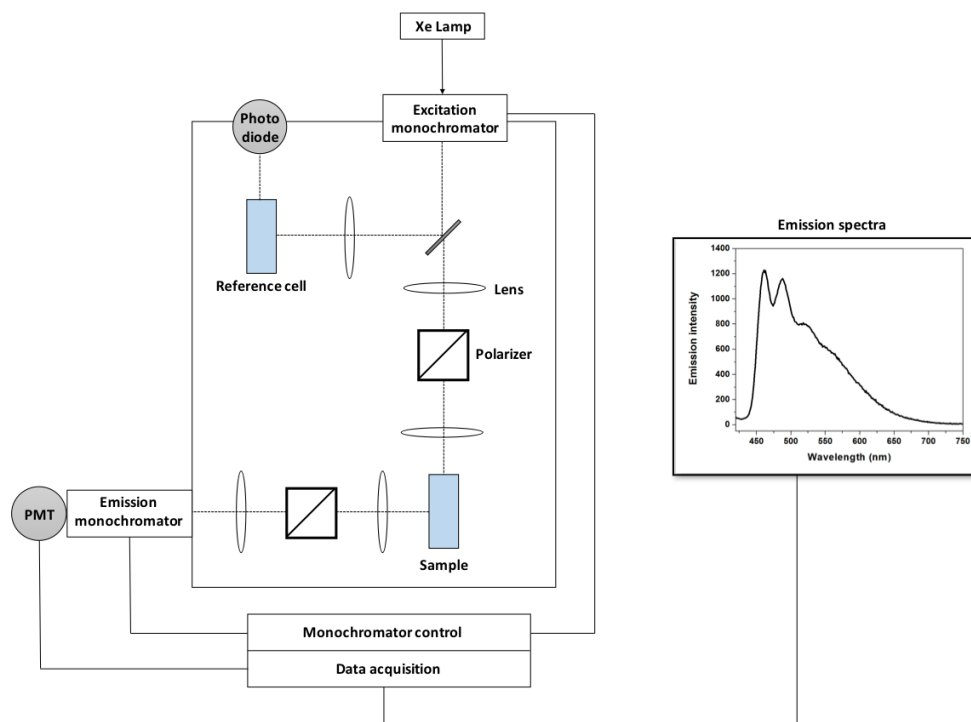
The schematic representation of the double-beam UV-Vis spectrophotometer is displayed in Scheme 6.1. The lamp emits radiation of all wavelengths within the spectral region. The radiation from the lamp is passed through a monochromator, which selects a specific wavelength and splits the light beam into two light beams. One light beam passes through the reference sample containing the pure solvent and the other light beam passes through the solution containing the absorbing species. The intensities of the two light beams were converted into absorbance. The absolute absorbance of the sample was calculated by subtracting the absorbance of the sample from the absorbance of the reference. The measurements were performed on a Shimadzu UV-3600 double-beam UV-VIS-NIR spectrophotometer. The polystyrene and quartz cuvettes had an optical path of 1 cm.



Scheme 6.1. Schematic representation of the double-beam UV-VIS spectrophotometer. The radiation from the lamp passes through a monochromator, which selects a specific wavelength. The monochromatic light is split by a beam splitter into two light beams, which passes through the sample and reference solutions.

6.2. Emission and excitation spectroscopy²

An emission spectrum displays the intensity of the emitted light of the sample versus the emission wavelength at a constant excitation wavelength. The excitation spectrum displays the intensity of the excited light versus the scanned excitation wavelength at a selected emission wavelength. The emission and excitation spectra are not absolute measurements and depend on the instruments used and the selected experimental parameters. In this thesis, all the emission and excitation spectra were recorded on a HORIBA Jobin-Yvon IBH FL-322 Fluorolog 3 spectrofluorometer, illustrated in Scheme 6.2. A 450 W xenon arc lamp was mounted on the fluorolog and was the source of the exciting light. The radiation beam passed through a monochromator, which selected a specific excitation wavelength and then directed it to a reference detector and to the sample. The emission of the luminescent sample solution was collected at a 90° angle compared to the incident light, and then passed through another monochromator (2.1 nm/mm dispersion; 1200 grooves/mm) before reaching the detector. Two different detectors were available for use in the laboratory, a TBX-04 single photon-counting detector, which was used in the UV-VIS region, and a Hamamatsu R2658P photomultiplier, which was used in the NIR (Near Infrared) region. 375 nm long pass optical filters were regularly utilised to decrease the intensity of undesired wavelengths in the excitation beam.



Scheme 6.2. Schematic representation of the fluorescence spectrophotometer.

6.3. Photoluminescence quantum yield measurement³

The photoluminescence quantum yield can be measured by using the integrating sphere instrument, which provides an absolute measurement or by using relative actinometry with a fluorescent reference.

6.3.1. Relative actinometry measurement

$\text{Ru}(\text{bpy})_3\text{Cl}_2 \cdot x\text{H}_2\text{O}$ (tris(bipyridine) ruthenium(II) chloride hydrate) was used as a reference due to the fact that it has similar photophysical properties to those of platinum(II) complexes. The photoluminescence quantum yields were calculated using the following equation:

$$\Phi_S = \Phi_R \left[\frac{A_R(\lambda_R)}{A_S(\lambda_S)} \right] \left[\frac{I_R(\lambda_R)}{I_S(\lambda_S)} \right] \left[\frac{D_S}{D_R} \right] \left[\frac{n_S^2}{n_R^2} \right] \quad (\text{eq 6.4})$$

Φ is the luminescence quantum yield

A is the absorbance at the excitation wavelength (λ)

I is the intensity of the excitation light at the excitation wavelength (λ)

D is the integrated intensity of the luminescence

n is the refractive index of the solvent

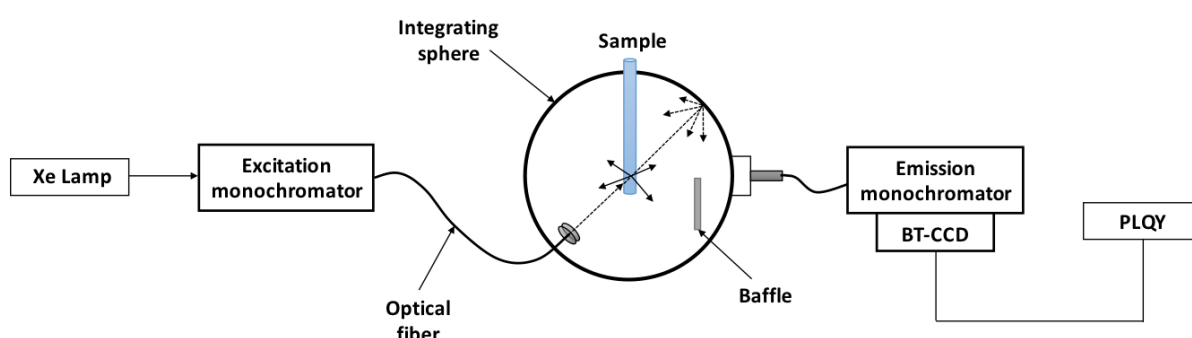
The subscripts R and S refer to the reference and sample, respectively.

The photoluminescence quantum yield measurements were carried out at identical excitation wavelengths for both the sample and the reference. As a result, $\frac{I_R(\lambda_R)}{I_S(\lambda_S)}$ is equal to 1 and equation 4 was simplified to:

$$\Phi_S = \Phi_R \left[\frac{A_R(\lambda_R)}{A_S(\lambda_S)} \right] \left[\frac{D_S}{D_R} \right] \left[\frac{n_S^2}{n_R^2} \right] \quad (\text{eq. 6.5})$$

6.3.2. Integrating sphere

Absolute luminescence quantum yields were measured using an integrating sphere illustrated in Scheme 6.3.



Scheme 6.3. Schematic representation of the integrating sphere. BT-CDD refers to the Back Thinned-Charge Coupled Device.

The light source used was a Xenon lamp and the incident beam passed through a monochromator, which selected the appropriate wavelength. The monochromatic beam then entered the integrating sphere via an optical fiber. The radiations emitted by the sample then entered a second monochromator via another optical fiber and then to the detector. In order to compare the intensity of the emitted light, a reference (quartz tube containing the pure solvent) was measured prior to the sample measurement. The software corrected the quantum yield of the sample with the quantum yield of the reference to generate the absolute photoluminescence quantum yield according to equation 6.6:

$$\Phi = \frac{N_{emission}}{N_{absorption}} = \frac{\int_{\lambda}^{\lambda} \{I_{em}^S(\lambda) - I_{em}^R(\lambda)\} d\lambda}{\int_{\lambda}^{\lambda} \{I_{ex}^R(\lambda) - I_{ex}^S(\lambda)\} d\lambda} \quad (\text{eq. 6.6})$$

$N_{absorption}$ is the number of photons absorbed by the sample

$N_{emission}$ is the number of photons emitted by the sample

I_{em} is the intensity of the emission and I_{ex} is the intensity of the excitation light

h is the Planck's constant and c is the velocity of the light

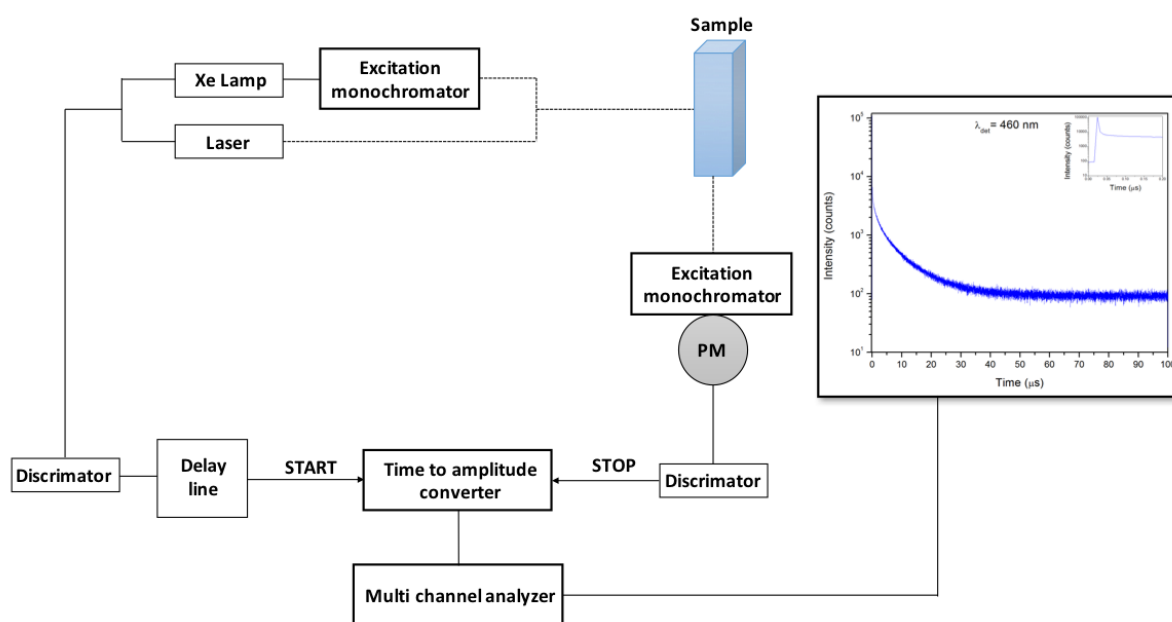
R and S superscripts refer to the sample and reference, respectively.

All the measurements were performed on a Hamamatsu Photonics absolute PL quantum yield measurement system (C9920-02) equipped with a L9799-01 CW Xenon light source (150 W), a monochromator, a C7473 photonic multichannel analyzer, and an integrating sphere. The data was analysed with U6039-05 PLQY software (Hamamatsu Photonics, Ltd., Shizuoka, Japan).

6.4. Excited state lifetime measurements

Time-resolved experiments were conducted using the principle of Time-Correlated Single Photon Counting (TCSPC). The schematic diagram of the experiment setup is shown Scheme 6.4. The pulsed light source used was a flash lamp or a laser. Each pulse generates an electrical signal to the START input of the Time-to-Amplitude Converter (TAC). Next, the detector generates an electrical response after the photon is emitted from the excitation pulse, which is then directed as a STOP signal to the TAC. The START pulse initiates the charging of the capacitor, while the STOP pulse terminates it. Therefore, the final voltage is proportional to the time between the START and the STOP pulses and this data is stored in a histogram. The x -axis in this histogram represents the time difference between the START and STOP signal and the y -axis represents the number of photons detected for this time difference. The numerous repetitive measurements collected provided an optimal statistical fit for the time distribution of the emitted photons. Time-resolved measurements up to the value of $10\mu\text{s}$ were performed using the TCS C option on a Fluorolog 3 spectrometer (Horiba-Jobin-Yvon Inc.). Two NanoLEDs (402 nm; FWHM < 750ps and 431 nm; FWHM < 200 ps) with repetition rates between 10 kHz and 1 MHz were used to excite the samples. The excitation source was directed to the sample chamber at a 90° angle to a double grating emission monochromator (2.1 nm/mm dispersion; 1200 grooves/mm) and collected by a TBX-4-X single-photon-counting detector. Signals were collected using an IBH DataStation Hub photon counting module and data analysis was performed using the DAS6 software (HORIBA Jobin Yvon IBH). For excited state lifetime measurements of $>10\mu\text{s}$, a Fluorolog 3 spectrometer equipped with a FL-1040 phosphorescence module and a 70-W xenon flash tube (full-width at half maximum, FWHM = 3 μs) with a variable flash rate (0.05–25 Hz) was used. The signals were then recorded

on the TBX-4-X single photon counting detector and collected with a multichannel scaling (MCS) card in the IBH DataStation Hub photon-counting module. The data analysis was then performed using the aforementioned method. The multichannel analyzer consisted of a multichannel card. The peak amplitude is stored if the input pulse amplitude falls within the threshold of the lower level and upper level discriminators, which enables the control and logic circuits. The signal intensities were collected in different channels for the duration of a predetermined time. After this predetermined time, an intensity counter moves to the next channel. The acquisition time is then reached, and the collected total light intensities in all the channels are counted and correlated to the time frames of each channel. At the end of the measurements an intensity-time profile was constructed. The profile was then deconvoluted with one or several exponential decays and the optimal fit was selected by minimizing the reduced chi squared function (χ^2) and visual inspection of the weighted residuals.



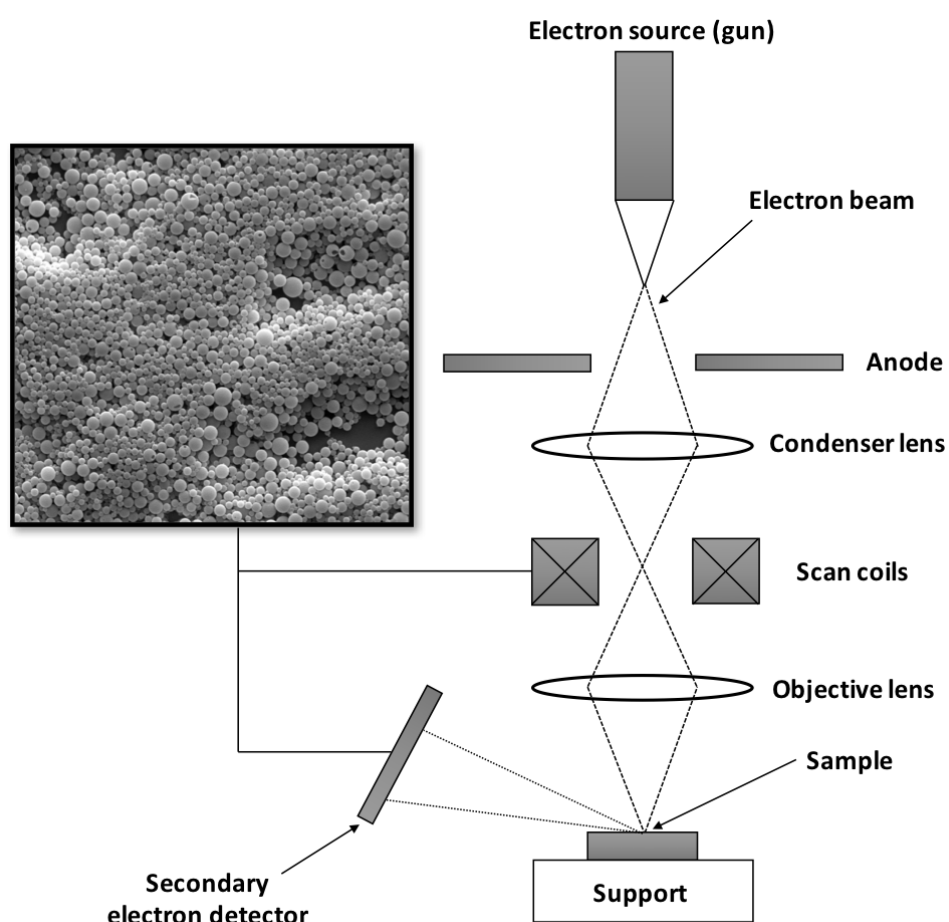
Scheme 6.4: Schematic representation of a single photon counting setup.

6.5. Scanning electron microscopy

The schematic diagram of a simplified SEM setup is shown in Scheme 6.5. The electron source (gun) emits electrons, which then passes through a condenser lens to emit a thin electron beam. The magnetic field is produced by the scan coils, and deflects the electron beam back and forward. The electron beam is focused by the objective lens to a spot of 1 nm to 5 nm in

size and then the beam scans the sample surface in a raster pattern. Primary electrons from the electron beam interact with the atoms of the sample surface, which results in the emission of the secondary electrons. The secondary electron detector detects these secondary electrons and an image of the sample is produced. The backscattered electrons of the electron beam can also be used to create contrasting images of specific regions in the sample.

The samples used in the SEM in this thesis were covered by a 40 nm thick silver or gold layer, and then investigated using a FEI Quanta FEG 250 instrument.

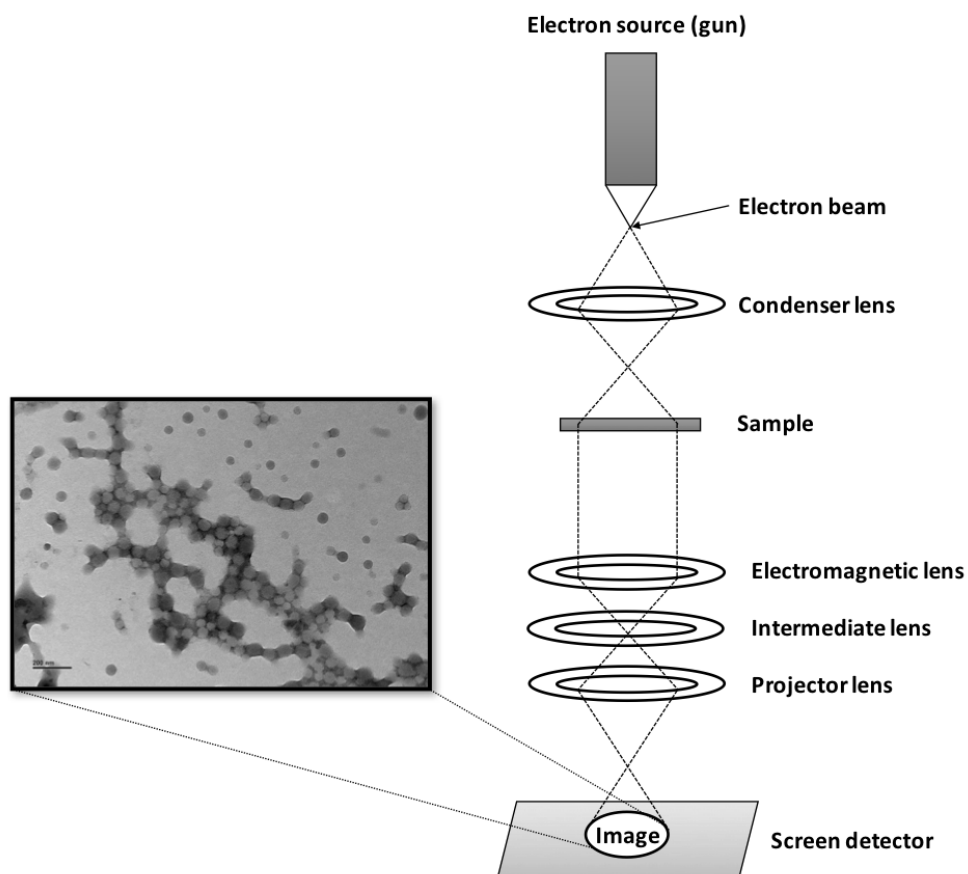


Scheme 6.5. Schematic representation of the SEM setup.

6.6. Transmission electron microscopy

The schematic representation of the TEM setup is shown in Scheme 6.6. The electron gun emits electrons that travel through the vacuum column of the microscope. The electron beam is first condensed into a thinner beam by passing through electromagnetic lens, and then it reaches the sample. Depending on the density of the material present in the sample, some of the electrons are scattered and the remaining unscattered electrons pass through the sample.

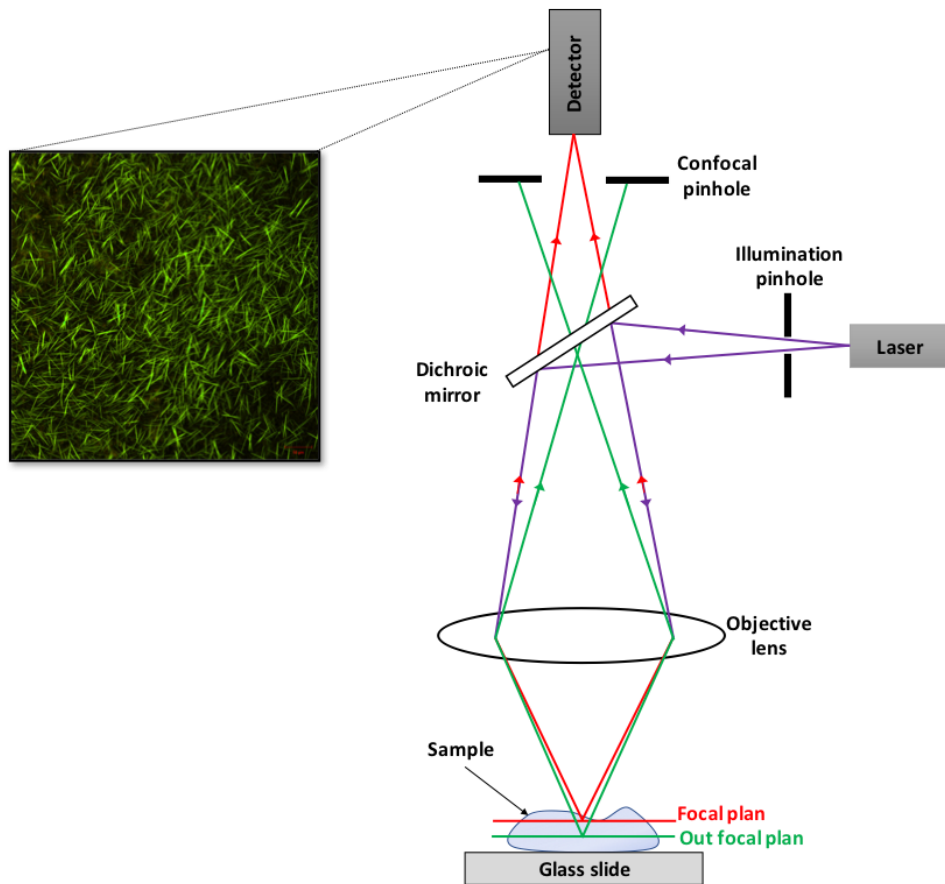
These electrons are then focused by the electromagnetic lens and directed to the fluorescent screen at the bottom of the microscope. A shadow image of the sample with its different components is displayed in varying darkness depending on the density or thickness of the material.



Scheme 6.6. Schematic representation of the TEM setup

Transmission electron microscopy (TEM) characterization was performed using an image corrected FEI Titan 80-300 electron microscope. The microscope was operated at 300 kV in scanning TEM mode (STEM) with a selected spot size of 0.2 nm using a high-angle annular dark field (HAADF) detector. Energy dispersive X-ray (EDX) spectroscopy was performed with a nominal beam diameter of 0.3 nm using an EDAX s-UTW EDX detector. The sample was prepared by drop-casting from aqueous suspension onto carbon coated tungsten grids (Quantifoil).

6.7. Confocal fluorescence microscopy



Scheme 6.7. Schematic representation of a fluorescence confocal microscope

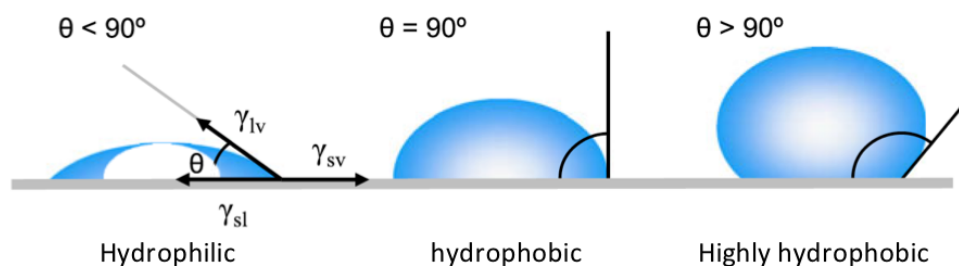
Simplified representation of a fluorescence confocal microscope is displayed in Scheme 6.7. Laser scanning fluorescence confocal microscopy offers several advantages over conventional mainstream fluorescence microscopes. Two major advantages include the ability to control the depth of field and eliminate out-of-focus luminescence. The latter is known as spatial filtering, which eliminates out-of-focus light or flare in specimens that are thicker than the plane of focus by illuminating the objective through a pinhole. The specimen is focused and the light then passes through the pinhole and reaches a detector (usually a PMT). A disadvantage of this technique is that the total signal level is lower, despite increasing the specific signal-to-noise ratio for the features of interest. Magnification can be electronically adjusted by altering the scanning laser-sampling period without increasing the objective (zoom factor). Increasing the zoom factor reduces the specimen area scanned and

simultaneously reduces the scanning rate. However, a high zoom factor may lead to the increase of photobleaching.

Confocal fluorescence microscopy was performed with a Zeiss LSM 710 confocal microscope system with a 10 to 63x magnification objective.

6.8. Water contact angle

A droplet of water was carefully deposited onto the different substrates and the angle between the substrate and the curvature of the droplet was measured, as demonstrated in Scheme 6.8. On a hydrophilic surface, the water droplet tends to spread across the surface and the contact angle is relatively small. On a hydrophobic surface, the water droplet adopts a dome shape and the water contact angle is between approximately 30° to 90°. When the surface is highly hydrophobic, the water angle is above 90° and the water droplet tends to retract itself.



Scheme 6.8. Schematic illustration of the water contact angle measurements.

6.9. X-ray photoelectron spectroscopy

Scheme 6.9 shows the function of an XPS instrument. An incident X-ray (200~2000eV) is first applied under vacuum, and a 1s electron is ejected from the atom. The photoelectron is then collected by the electron multiplier detector and analysed by the electron spectrometer to acquire the kinetic energy (E_{kin}). The binding energy of the electron (EB) identifies the electron both from its parent element and the atomic energy level. It can be described as below:

$$E_b = h\nu - E_{kin} - W_f \quad (\text{eq. 6.7})$$

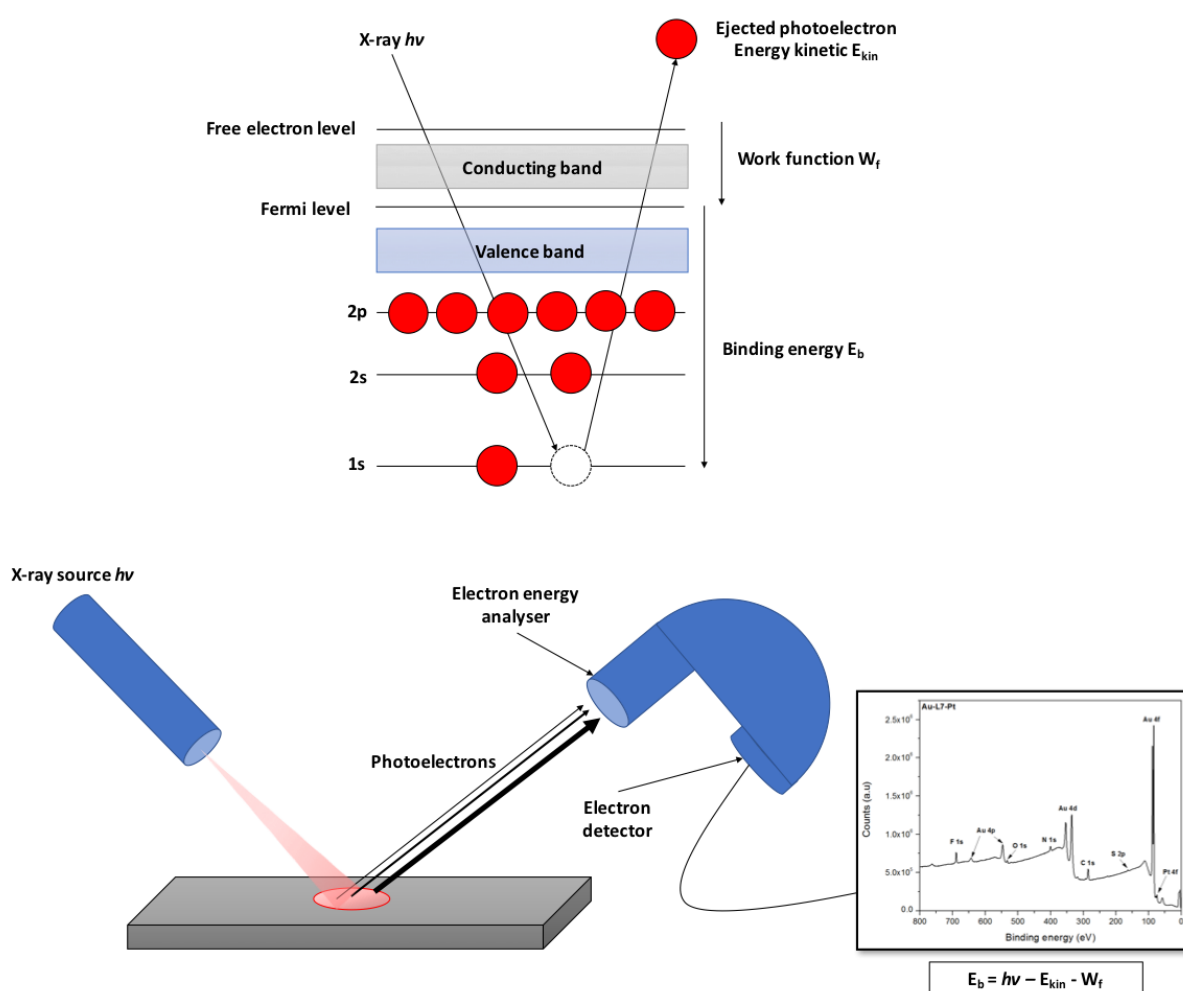
$h\nu$ is the X-ray energy

E_{kin} is the kinetic energy of the photoelectron

W_f the spectrometer work function.

The binding energy can therefore be determined from those three parameters, which are either known as constants, or are measurable.

In this thesis, the XPS measurements were performed using a Thermo Scientific K-Alpha X-ray Photoelectron Spectrometer with a monochromatic AlK α radiation ($h\nu = 1486.6$ eV; $\lambda = 8.340113\text{\AA}$). Survey measurements were performed with a 200 eV analyzer pass energy and a 1 eV energy step size to calculate the atomic concentrations. Element scans were performed with 50 eV analyzer pass energy and a 0.1 eV energy step size to obtain the chemical state information. All the obtained binding energies were referenced from the carbon 1s peak, originating from the residual CO₂, at 284.80 eV.



Scheme 6.9. Schematic representation of the X-ray photoelectron spectroscopy (XPS).

6.10. X-ray diffraction

A monochromatic X-ray is directed to the sample with a glancing angle θ (Scheme 6.10). Each crystalline plane of the sample reflects a small fraction of the incident beam. The radiation is scattered in a specular fashion by the atoms of the crystalline system and undergoes constructive interference. For a crystalline solid, the incident waves from adjacent planes are separated by an interplanar distance d . The difference of the optical path is equal to $2d \sin\theta$ and related to the incident wavelength λ by the Bragg equation:

$$2d \sin\theta = n\lambda \quad (\text{eq. 6.8})$$

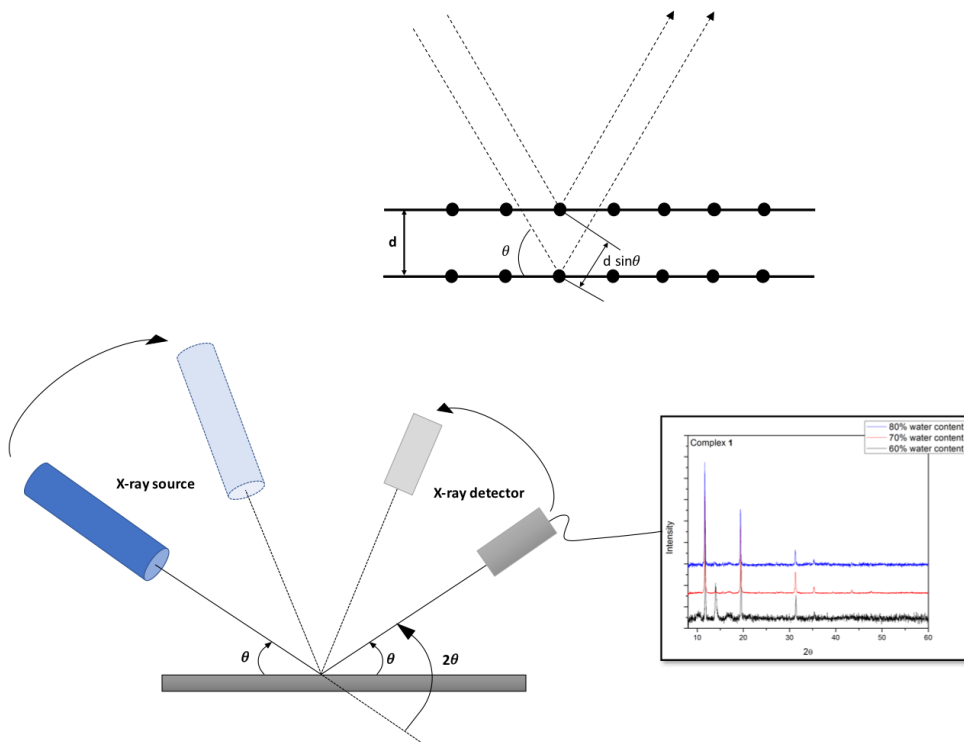
n is the positive integer

λ is the wavelength of the incident X-ray beam (nm)

d is the distance between adjacent planes of atoms, d-spacing (nm)

θ glancing angle ($^{\circ}$ C)

A diffraction pattern is obtained by measuring the intensity of the scattered waves as the function on the scattering angle. Very strong intensities known as Bragg peaks are obtained in the diffraction pattern at the points where the scattering angles satisfy Bragg condition.



Scheme 6.10. Schematic representation of the X-ray diffraction setup.

6.11. References

1. B. Valeur, *Molecular fluorescence: principles and applications*, 2001
2. N. J. Turro, V. Ramamurthy and J. C. Scaiano, *Principles of molecular photochemistry: an introduction*, 2009.
3. H. Ishida, S. Tobita, Y. Hasegawa, R. Kato and K. Nozaki, *Coord. Chem. Rev.*, **2010**, *254*, 2449-2458.

Acknowledgements

My PhD journey was not easy, however I was fortunate enough to be surrounded by amazing people who supported me professionally and personally throughout this journey.

Firstly, I would like to express my sincere gratitude to Prof. Luisa De Cola, my teacher and supervisor. You gave me the desire to do a PhD. I remember attending the first course you taught on hybrids materials and photophysics. After that, you welcomed me into your group for my master's internship and then for my PhD. At times it was tough, however I understand that you were hard on me to help me become a better scientist. I would like to thank you for that.

I would like to thank the University of Strasbourg for the great quality of education provided during my studies and for financing my PhD.

I would also like to thank Dr. Matteo Mauro and Dr. Alessandro Aliprandi, who taught me everything I know on photophysics and platinum (II) complexes. I wish we had had more time together to explore more aspects of the chemistry.

I would like to thank Dr. Brian DiMarco, Dr. Charles Lochenie, Dr. Leana Travaglini and Dr. Simone Silvestrini for correcting my thesis. Also, a special thank you to Simone and his wife Federica, who also welcomed me in your house when I needed a place to stay.

The French system is known for its excessive red tape and paperwork. I would not have completed the required paperwork without the assistance of Claire Menouna Ekani. Thank you for your loyalty and for your friendship.

I would like to extend my gratitude to Ines Below-Lutz for ensuring that I had the required equipment in the lab at all times. Thank you for also being a good confidante.

Throughout the last few years, I have had the chance to work with amazing people who have not only helped me with my work but who are also my friends.

I would like to start with you, John Ddungu. We spent a lot of time together, whether it was in my car, in our office in KIT or on the couch of my flat as you were often considered as a member of our flat. I wish you the very best in the completion of your thesis.

Next, I would like to thank Dr. Youssef Atoini for all the late night sessions we had in the lab, and the XRD measurements you completed for me. I also enjoyed hanging out with you and

playing cards. I am going miss our Champions' League game nights and you bagging out Paris Saint Germain and me with FC Barcelona.

For similar reasons, I would like to thank Dr. Riccardo Totovao. I will not forget our crazy night sessions, not only in the lab but also on the dance-floor. Thank you for your support.

The next person I am grateful for is Luca Capaldo. When I started my PhD three years ago you were a Masters student. We were working together on the same project and you were my fume-hood partner. It was a pleasure to work with you and have fun with you in the lab.

I would like to especially thank Dr. Ingrid Cabrera Puiz, my best friend in the lab. It was always a pleasure to talk to you and spend time together outside of the lab.

Dr. Christof Stähler, thank you for cleaning the fume-hood that you never used. Thank you for sharing your love of hiking and for your good spirit.

I would like to thank my tall Dutch friend Annet for our intense card games and the talks we had.

We always have a crazy Italian person in every group and in mine was Dr. Serena Carrara. I would like to thank you for your kindness, our visit together in Dublin and for your moral support.

Another crazy Italian coworker I would like to mention now is Dr. Elena Longhi. You were my partner in the lab for many years and kept the place tidy and clean.

The Italian community in the lab consisted of many people. I had the chance to meet these many colourful and lively people that I would like to mention now: Nadia, Federica, Laura, Martina, Alessandro, Matteo, Agostino, Camilla, Beatrice, Guisepe, Giacomo, Marco, Maurizio, Valentina, Vitali, Etienne. Yes, indeed that's a lot of Italians. A special thought to Matteo Bessi, I wish I had had more time to get to know you better.

The Spanish speaking community was also well represented in the lab. I would like to thank Amparo, Leticia, Cristina, Mariel and Alberto for their extreme kindness and for always being uplifting, you girls are the best.

I would like to thank my American colleague Rebecca for her bubbly nature and for all the good moments we had.

I would also like to thank the French people of the lab Mike, Etienne and Loic for their friendship and support.

We also had a strong Asian community in the lab. I will start with the Indonesians, Dedy and Eko. Thank you both for your assistance with the confocal microscope and XPS. You guys know

your stuff. Then there was also Pengkun, (Chinese) and Chien-Wei (Taiwanese). You guys are so cool and funny.

I would like to also thank the German community, Dr. Biedermann and Dr. Sinn (with his wife and kid) for assisting me scientifically but also when I spent some time in KIT.

We also had some visiting students with whom I created special bonds with in a short amount of time. In particular, my friends Mateusz and Natália.

Some of the results presented in this thesis have been done by Dr. Eloise Devaux (FIB) and Dr. Mohamed El Garah (AFM) and Dr. Di Wang and Dr. Christian Kübel (HAADF-TEM). Thank you for helping me with my research.

Lastly, thanks to anyone not mentioned above that also assisted me with my thesis, you know who you are. I would like to now make some more personal acknowledgements.

Firstly, I would like to thank the flatmates that I have lived with throughout my PhD: Nina, Thibault, Laura Germier, Camilla, Faustine, Laura Outan, Didem, Natalia, Chloé and of course, Anna and her dog Cali. Thank you all for your support and friendship.

I would like to thank my neighbor Karim “freebox” Thank you for helping us out at anytime I needed something and also for the TV show nights.

I would also really like to thank my closest friends who supported and encouraged me during my thesis. In particular, I would like to thank my best friend and best man, Bastien Heitz. Thank you for your friendship, your hospitality and being so supportive of me.

I would also like to thank Vincent and Céline, the funniest and sweetest couple I know. Thank you guys for your ongoing support,

I would also like to thank my friend Matsouf. Thank you for helping me to choose the most important ring that I have had to buy. You are the kindest man I know.

On a more personal note, I would like to thank my family for their unconditional support and encouragement. Thank you mum and dad, for making me who I am today. I would never have succeeded if you both hadn't taught me the value of hard work and perseverance.

I would also like to thank my brothers, Antoine and Jacky, and my sister Chloe, for their ongoing support.

I would like to thank my grandmother, Paulette, whom I am very close with, for all her support. I would like to thank all of the other members of my family for their support including Gratiene, Olivier, Ali, Camille, Léo, Thomas, Martin, Eden and Lou.

Finally, I could not conclude these acknowledgements without mentioning my perfect wife-to-be, Belinda Hughes. I met you before I started my PhD and you have been on my side ever since. You have always encouraged and supported me, despite being separated by two oceans, three continents, 24 hrs flight and 10 hours time difference. Thank you for everything and the best is yet to come for us.

Curriculum Vitae

ROUQUETTE REMI

Born: January, 4th 1989

Nationality: French

Age: 29

Email: remi.rouquette@hotmail.fr

Phone: 0403 807 709

Address :

4/15 Angelo Street

2134, Burwood, NSW

Australia

Education

2014-2017: PhD thesis in the group of Prof. Luisa De Cola, University of Strasbourg, FRANCE

2012 - 2014: Master of Physics and Chemistry in materials (honours), specialty "Physics and chemistry of materials", University of Strasbourg, FRANCE

2012: Bachelor of Physics and Chemistry, University of Strasbourg, FRANCE

2007: Scientific Bacalaureate in Chemistry and Physics (honours), Lycée Charles de Foucauld, Lyon, FRANCE

Research experience

October 2014-October 2017: PhD research: "*Spatially confined hybrid (photo-)active self-assembled materials with tunable properties*", University of Strasbourg, Institut des Sciences and d'Ingénierie Supramoléculaire (ISIS), FRANCE. Supervisor: Prof. Luisa De Cola. Financed by the university of Strasbourg.

February 2014 to June 2014: Final research project for the Master of Science graduation, University of Strasbourg, Institut des Sciences and d'Ingénierie Supramoléculaire (ISIS), FRANCE. Supervisor: Dr. Matteo Mauro. Director: Prof. Luisa De Cola. Financed by ciRFC. "*Hybrid organic-organometallic soft structures: preparation, properties and applications*" *Preparation, encapsulation and characterization of Platinum(II) complexes with amphiphilic diblock copolymers in aqueous media for cellular uptake.*

March 2014 to June 2013: Master I internship at ISIS, University of Strasbourg, FRANCE.

Supervisor: Dr. Matteo Mauro. Director: Prof. Luisa De Cola.

“Aggregation in neutral Pt(II) complexes bearing tridentate dianionic (N^{^-}N^{^-}N^{^-}) ligand”

Preparation of Pt complexes and study of the self-assembled properties by photophysical measurements.

Knowledge and Skills

Organic and organometallic synthesis: Preparation, purification and characterization of Platinum(II) complexes, synthesis of ligands, preparation of polymer particles.

Instrumental techniques : UV-visible absorption

Fluorescence emission and excitation

Photoluminescent absolute and relative quantum yield

Excited lifetime measurements

Dynamic light scattering (DLS)

Scanning Electron Microscopy (SEM)

Scanning Transmission Electron Microscopy (STEM)

¹H, ¹³C, ¹⁹F Nuclear magnetic resonance (NMR)

X-ray photoelectron spectroscopy (XPS)

Confocal fluorescence microscopy

X-ray diffraction (XRD)

Information Systems: Microsoft office, Chem Office, Topspin, NMR notebook, MestReNova LITE, Scifinder, Zotero, Avantage, Origin, Image J, Zen.

Languages: French (native tongue)

English (TOEIC: 895)

Personal skills

Able to work independently in a highly interdisciplinary and international environment, solve problems, present results and discuss them.

Interests

Sport: badminton, fitness and basketball

Travelling

Tutoring

Publications

1. "Encapsulation of platinum(II) complexes by PMMA-PMAA diblock copolymer" [Remi Rouquette](#), Di Wang, Christian Kübel, Luisa De Cola, (to be submitted)
2. "Supramolecular co-assembly of two luminescent platinum(II) complexes" [Remi Rouquette](#), Youssef Atoini, Di Wang, Christian Kübel, Luisa De Cola, (manuscript under preparation)

Scientific meetings

10th ISMSC **2015** (International Symposium on Macrocyclic and Supramolecular Chemistry) in Strasbourg, organizing team.

30th ECIS **2016** (European colloidal and interfaces Society) in Rome, *hybrid platinum-loaded polymer particles*, poster contribution.

21st ICP **2017** (International Conference on Photochemistry) in Strasbourg, *Luminescent platinum(II) complexes-polymer particles*, oral presentation.

References

Prof. Luisa De Cola
Institut de Science et d'Ingénierie Supramoléculaires
Laboratoire de Chimie et des Biomatériaux Supramoléculaires
Université de Strasbourg
8, allée Gaspard Monge
67083 Strasbourg France
Phone: +33 (0)3 68855220
Fax: +33 (0)3 68855242
Email: decola@unistra.fr

